INTERNATIONAL DOCTORAL
SCHOOL OF THE USC

Andrés Manuel
Álvarez Constantino

PhD Thesis

Catalytic methodologies for the valorization of C2 hydrocarbons and mechanistic studies

Santiago de Compostela, 2024

Doctoral Programme in Chemical Science and Technology

INTERNATIONAL DOCTORAL SCHOOL OF THE USC

DOCTORAL THESIS

CATALYTIC METHODOLOGIES FOR THE VALORIZATION OF C2 HYDROCARBONS AND MECHANISTIC STUDIES

Author

Andrés Manuel Álvarez Constantino

Supervisor/s: Martín Fañanás Mastral

Tutor: Martín Fañanás Mastral

DOCTORAL PROGRAMME IN CHEMICAL SCIENCE AND TECHNOLOGY

SANTIAGO DE COMPOSTELA

2024

The data organization in the corresponding sections of the present thesis dissertation was conducted in accordance with the DOG 167/2024, article 34.2, which states that *the doctoral thesis should include, as a minimum, an abstract, an introduction, the objectives and hypotheses, the general methodology, the analysis of the results and their discussion, the general conclusions and the bibliography. These parts should be clearly indicated in the thesis to facilitate its identification and reading.*

The format of the manuscript was adapted to the criteria *of homogeneity, typographic readability and functional ease* included in the recommended guidelines provided by the International PhD School of the University of Santiago de Compostela (EDIUS), as carried out by the Publications and Scientific Exchange Service.

ABBREVIATIONS

	4
4-CzlPN	1,2,3,5-Tetrakis(carbazol-9-yl)-4,6-dicyanobenzene
	A
ATR	Atenuated Total Reflectance
	B
$BARF_4$	Tetrakis[3,5-bis(trifluoromethyl)phenyl]borate
BET	Bromodomain and Extra-Terminal Motif
BINAP	2,2′-bis(diphenylphosphino)-1,1′-binaphthyl
BIPHEP	2,2'-Bis(diphenylphosphino)-1,1'-biphenyl
B_2pin_2	Bis(pincolato)diboron
	C
CAAC	Cyclic(alkyl)(amino)carbene
COD	Cyclooctadiene
CPCM	Conductor-like Polarizable Continuum Model
	D
dan	1,8-Diaminonaphthalene
dba	Dibenzylideneacetone
DCE	Dichloroethane
DCM	Dichloromethane
DFT	Density functional theory
DIAs	Distortion interaction analysis
DMA	*N*,*N*-dimethyl acetamide
DMAP	Dimethyl amino pyridine
DMF	Dimethyl formamide
DMSO	Dimethyl sulfoxide
dr (*or* d.r.)	Diastereomeric ratio
dtbbpy	4,4′-Di-*tert*-butyl-2,2′-dipyridyl
	E
EDCI	*N*-(3-dimethylaminopropyl)-*N'*-ethylcarbodiimide hydrochloride
EnT	Energy transfer
EPR	Electron Paramagnetic Resonance
er (*or* e.r.)	Enantiomeric ratio
EWG	Electron withdrawing group
	F
FMO	Frontier molecular orbitals
	G
GnRH	Gonadotropin-Releasing Hormone
	H
HAT	Hydrogen atom transfer
HOBT	1-Hydroxybenzotriazole hydrate
HPLC	High Performance Liquid Cromatography
	I
iefpcm	Integral equation formalism polarizable continuum model
IMes	1,3-Bis(2,4,6-trimethylphenyl)-2-imidazolidinylidene
IPr	1,3-Bis(2,6-diisopropylphenyl)-2-imidazolidinylidene

ISC	Inter System Crossing

L

LDA	Lithium diisopropylamide
LG	Leaving group

M

MOC	Methoxycarbonyl
MsCl	Mesityl chloride

N

NCI	Non-covalent interaction
NHC	*N*-heterocyclic carbene
NMM	*N*-methylmorpholine
NMR	Nuclear Magnetic Resonance

P

PCET	Proton-coupled electron transfer
Phen	Phenantroline
ppm	Parts per million
Ppy	Phenylpiridine

R

RE	Reductive elimination
rpm	Revolutions per minute

S

SCRF	Self-consistent reaction field
SET	Single electron transfer
SIMes	1,3-Bis(2,4,6-trimethylphenyl)imidazolinium chloride
SIPr	1,3-Bis(2,6-diisopropylphenyl)-4,5-dihydroimidazolium tetrafluoroborate
SMD	Solvent Model Density
STING	Stimulator of Interferon Genes

T

TBAF	Tetrabutyl ammonium fluoride
TFA	Trifuoroacetate
TFAA	Trifuoroacetic anhydride
TFAH	Trifuoroacetic acid
THF	Tetrahydrofuran
TRIP thiol	2,4,6-triisopropylbenzenethiol
TS	Transition state

U

uHPLC	ultra High Performance Liquid Cromatography

Z

ZPE	Zero point energy

ABSTRACT

This thesis dissertation presents a compilation of the principal results obtained in the investigation of the design, development and mechanistic analysis of Cu and Fe-catalyzed allylation reactions. The Cu-catalyzed transformations have been focused on multicomponent allylboration reactions, which involve a boron source, an unsaturated compound (alkynes, allenes and acetylene) and allylic substrates (allylic *gem*-dichlorides and phosphates). With regard to the Fe-catalyzed transformations, these involved the use of ethane and allylic chlorides.

The use of allylation reactions in literature is widespread, with the objective of installing a nucleophilic moiety in a double bond, which subsequently migrates while eliminating the leaving group. In this field, the generation of transient nucleophilic species has emerged as a powerful alternative to classical organometallic reagents, toward reach greener methodologies. Moreover, the utilization of alternative, underutilized carbon sources in fine chemistry – such as acetylene and ethane –is highly sought after in order to diversify the available chemical feedstocks and overcome the high oil-dependent tendency.

This thesis dissertation is structured in a manner in which the obtained insights and improved abilities from one project were transferred into the next project, enabling the effective pursuit of the identified objectives. Firstly, we have explored the diastereo- and enantioselectivity of Cu-catalyzed allylboration of alkynes and allenes with allylic *gem*-dichlorides using computational approaches. DFT calculations were conducted, complemented with distortion-interaction and non-covalent interactions analyses, which afforded a deep understanding of the behavior of underutilized allylic *gem*-dichlorides in allylboration reactions. Insights were gained regarding the supramolecular interactions established between the ligand and the leaving groups, *via* cation-bridge interaction, and were rationalized in accordance with cation size and outcome selectivity.

Then, the acquired mechanistic insights were transferred to the development of a multicomponent diastereo- and enantioselective Cu-catalyzed allylboration of acetylene, utilizing allylic phosphates and allylic *gem*-dichlorides. This process is catalyzed by a chiral NHC-sulfonate bearing copper catalyst, operates under ambient pressure, and provides chiral skipped dienes displaying a stereodefined and orthogonally functionalized olefins with excellent levels of chemo-, regio-, enantio- and diastereoselectivity. Computational studies of the reaction mechanism, based on DFT calculations and non-covalent interaction analysis, indicate the presence of a cation-bridge interaction which is responsible for the observed stereoselectivity. The combination of the stereochemical features and the orthogonal functionalization make the products privileged structural motifs, allowing access to the complete set of stereoisomers of the chiral skipped diene core through simple enantio- and diastereodivergent pathways. The synthetic utility of the method is demonstrated by the enantioselective synthesis of three bioactive natural skipped diene products, namely (+)-Nyasol, (+)-Hinokiresinol and (+)-Phorbasin C, and other related synthetically relevant chiral molecules.

Finally, the experience gained in working with gaseous reagents, was subsequently applied to the development of a direct $FeCl_3$ photoredox HAT catalyzed direct $Csp^3–Csp^3$ allylation of ethane. The process is catalyzed by inexpensive $FeCl_3·6H_2O$ in combination with collidine, which serves a double role as both ligand and a base. It occurs in commercially available glass

reactors and allows for the alkylation of a range of allylic chlorides, bearing several alkyl C−H bonds and functional groups. The synthetic utility of the catalysis was illustrated with the synthesis of 2-phenylpentanoic acid, a molecule with significant synthetic relevance. An extensive combination of experimental techniques was employed to gain insight into the reaction mechanism, including radical trapping, deuterium scrambling, MS spectroscopy, UV-Vis spectroscopy, EPR spectroscopy and X-ray diffraction analysis. These techniques support the role of the collidine as a ligand which accounts for the higher photocatalyst stability and the suppression of side C−H chlorination reactivity.

RESUMO

A presente tese doutoral compila os principais resultados obtidos no estudo referente ao deseño, desenvolvemento e análise mecanística de reaccións de alilación catalizadas mediante catalizadores de Cu e Fe. A catálise de Cu centrouse en reaccións multicompoñente de alilboración, nas que se involucraron unha fonte de boro, un composto insaturado (alquinos, alenos e acetileno) e compostos alílicos (dicloruros e fosfatos). No que respecta á catálise de Fe, esta implicou o uso de etano e cloruros alílicos.

Na primeira sección desta memoria, realizouse unha revisión bibliográfica dos traballos máis relevantes relativos á estrutura e reactividade da alilboración de alquinos e alenos. Ao longo deste texto, expúxose a relevancia da metodoloxía resaltando as súas principais vantaxes en comparación co uso de compostos organometálicos estequiométricos: a xeración catalítica das especies nucleófilas, maior tolerancia de grupos funcionais sensibles a condicións extremas e o uso de condicións de reacción máis suaves.

Durante a devandita sección, fíxose un percorrido bibliográfico analizando cada etapa elemental involucrada no ciclo catalítico das reaccións de alilboración catalizadas por Cu: (1) borocupración do composto insaturado, (2) adición oxidante ao composto alílico e (3) eliminación redutora. En primeiro lugar, presentouse a selectividade asociada ao paso número 1, profundando nos efectos estéricos e electrónicos que controlan a rexioselectividade durante a inserción do intermedio Cu^{I}-Bpin en alquinos e alenos. Para iso, utilizáronse reaccións de protoboración como exemplo, posto que permiten a análise directa (tras protonólise do enlace Cu^{I}-C) do complexo formado tras a borocupración. A continuación, examinouse en detalle a etapa da substitución alílica, que inclúe tanto a adición oxidante como a eliminación redutora. En canto á adición oxidante, esta transcorre de forma *anti* ao grupo saínte, o que facilita as interacción orbitais entre o HOMO do complexo de Cu^{I} e o LUMO do composto alílico. Tras a formación do Cu^{III}-π-alilo, o efecto dos ligandos sobre o catalizador regula a rexioselectividade da eliminación redutora. Se os ligandos inducen efecto *trans* sobre o Cu (un deles ten maior carácter σ-dador ca o outro), as interaccións orbitais favorecerán o ataque sobre a posición γ do alilo. Para finalizar a sección, estudáronse as reaccións enantioselectivas de alilboración de alquinos e alenos catalizadas por Cu, resaltando os principais factores, derivados de interaccións entre o ligando e substrato, que regulan a enantioselectividade nos sistemas mencionados.

Na segunda sección introduciuse o acetileno, produto de partida para a realización de parte desta tese. Tras unha breve introdución das súas propiedade químico-físicas, dos métodos de produción e dos usos a nivel industrial, o relato fixo fincapé nas súas aplicacións sintéticas no ámbito da química fina. Neste contexto, unha recente explosión de novas metodoloxías publicadas principalmente polo grupo do Prof. Zhu permitiu diversificar enormemente o potencial sintético do acetileno aplicando diferentes estratexias, englobando a fotocatálise de Ir ou organofotocatálise, e a catálise de Cu, Ni e Rh. De feito, cómpre resaltar que os autores levaron a cabo múltiples sínteses, totais e formais, de compostos con actividade biolóxica baseados nas metodoloxías desenvoltas. Porén, o uso de acetileno en reaccións enantioselectivas continuou limitado aos protocolos baseados na catálise de Rh desenvoltos polo Prof. Krische, nos anos 2006 e 2007, para realizar reaccións de acoplamento redutor con adehídos e iminas. Cómpre mencionar que recentemente o grupo do Prof. Echavarren publicou unha nova aplicación sintética en reacción de oxovinilación con catálise de Au, obtendo enantioselectividades moderadas.

Na terceira sección, de forma similar, introduciuse o etano, produto de partida para a realización de parte desta tese. Primeiramente fíxose unha breve mención ás súas propiedades, remarcando a dificultade que conleva a súa funcionalización dada a ausencia de electróns en nubes-π. A seguir presentáronse as metodoloxías catalíticas homoxéneas máis recentes que permiten a súa transformación de forma selectiva. Neste contexto sitúanse os traballos de Pérez (2011), Sanford (2016), Chang (2021) e Hartwig e Pérez (2021), para a formación de enlaces C-C, C-B, C-N e C-N, respectivamente. Porén, os métodos reportados continúan a ser específicos para un sistema catalítico e determinando. Recentemente, a activación de enlaces C-H non-activados por medio de metodoloxías fotocatalíticas de Transferencia de Átomos de Hidróxeno (HAT, polas siglas en inglés) situáronse como unha forma xeral con capacidade de activación de alcanos lixeiros e a súa transformación en diferentes produtos, mediante adicións radicalarias. Neste contexto, reportáronse diversas alternativas de sistemas catalícos basados en Fe, Ti, Ce, W e Acridinios. Porén, a maioría das reaccións quedaron limitadas a transformacións de adición radicalaria sobre aceptadores de Michael, limitando as posibilidades sintéticas dos alcanos lixeiros e abundantes.

Neste contexto no que se desenvolveu a presente tese doutoral, comprender os mecanismos de reacción para poder posteriormente extraer e aplicar as principais características chave, co fin de ampliar o alcance das metodoloxías catalíticas a compostos actualmente infravalorados, situouse como principal motivación do traballo, dividido en tres grandes seccións de resultados e discusión.

Na primeira sección (3.1) estudáronse os mecanismos de alilboración enantio- e diastereoselectiva de alquinos e alenos mediante catálise de Cu, usando dicloruros alílicos xeminais.

Como primeiro obxectivo desta tese doutoral, propúxose estudar as reaccións mencionadas mediante cálculos computacionais, co fin de lograr establecer os principais motivos tras o excelente control da enantio- e diastereoselectividade. Ambas metodoloxías involucran o uso de ligandos tipo NHC con un grupo sulfonato, que se coñece que establece interaccións supramoleculares co grupo saínte do alilo por medio de unha ponte catiónica.

En primeiro lugar considerouse o uso dos alquinos como pronucleófilos, cuxa reacción daba lugar á obtención do estereoisómero maioritario (*Z*,*R*). Neste caso, atopouse que baixo presencia de LiO^tBu, excelentes selectividades eran acadadas. Porén, o uso de NaO^tBu levou a unha drástica baixada nos niveis de estereoselectividade. Tras estudar o perfil de reacción mediante cálculos DFT considerando Li^+, observouse que a etapa elemental correspondente á adición oxidante determina tanto a velocidade de reacción como a estereoquímica, e atopáronse 4 posibles estados de transición que darían lugar aos catro posibles produtos derivados da catálise: (*Z*,*R*), (*Z*,*S*), (*E*,*R*), (*E*,*S*). Polo tanto, a adición oxidante transcorre de xeito estereoselectiva. Tras analizar as catro estruturas, púidose observar de forma certeira que o enantiómero minoritario (*S*) está desfavorecido por mor de repulsións estéricas entre o alilo e o Bpin, levándoo a requirir unha maior enerxía de activación que o (*R*), para ambas configuracións da olefina: $\Delta G(Z,R) < \Delta G(E,R) < \Delta G(Z,S) < \Delta G(E,S)$. A seguir, tras explorar o perfil de reacción considerando Na^+, en lugar de Li^+, observouse a mesma tendencia, mais a diferencia de enerxías entre (*Z*,*R*)-Na e (*E*,*R*)-Na veuse significativamente diminuída. Tras analizar as enerxías de interacción-distorsión (DIAs) e as interaccións non covalentes (NCI) das estruturas, púidose comprobar como o efecto do catión e a disposición do alilo xogan un

papel crucial para resultar no produto *Z* ou *E*, facendo que o maior radio catiónico do Na^+ sexa capaz de proporcionar unha extra estabilización ao isómero *E*.

En segundo lugar, considerouse o uso de alenos como pronucleófilos, cuxa reacción deu lugar á obtención do estereoisómero maioritario (*Z*,*S*). De xeito similar, os estudos de optimización da reacción atoparon unha importante dependencia entre o catión da base e a estereoselectividade obtida na reacción, sendo excelente con KO^{t}Bu mentres que LiO^{t}Bu levou a unha importante caída nos valores. Tras analizar o perfil de reacción considerando K^+, encontráronse dous complexos de Cu-σ-alilos en equilibrio, derivados da borocupración do aleno, exhibindo un comportamento como pro-*R* e pro-*S*. A ruta derivada do Cu-σ-alilo pro-*S* resultou ser máis favorable en enerxía, en consonancia cos resultados experimentais. De forma similar ao anterior caso, a adición oxidante volveu comportarse como a etapa determinante da velocidade de reacción, así como a determinante da estereoquímica. Tras analizas as interaccións non covalentes na adición oxidante, observouse de forma inequívoca que a coordinación do alilo ao pro-*R* ou pro-*S* determina a posibilidade de establecer unha ou dúas pontes catiónicas co ión K^+, respectivamente, favorecendo así a ruta cara o estereoisómero maioritario (*Z*,*S*). Con respecto á diastereoselectividade, esta ven determinada así mesmo pola coordinación do alilo ao complexo pro-*S*. Cando o alilo adopta a configuración necesaria para dar lugar á estereoquímica contraria, o ligando sufre unha reorganización espacial que implica á creación de repulsións estéricas que desfavorecen a formación do isómero (*E*,*S*). No referente ao efecto do catión na enantioselectividade, tras analizar o perfil de reacción considerando Li^+, púidose ver claramente como o menor radio catiónico deste impide que se estableza a segunda ponte catiónica, aproximando en enerxías ambas rutas.

Na segunda sección (3.2) estudouse a alilboración de acetileno enantio- e diastereoselectiva mediante catálise de Cu, usando fosfatos alílicos e dicloruros alílicos xeminais.

Como segundo obxectivo desta tese doutoral, propúxose desenvolver unha nova metodoloxía enantioselectiva usando acetileno como produto de partida para acceder 1,4-dienos quirais e multifuncionais, que posteriormente puidesen ser aplicadas na síntese de produtos de alto valor engadido, como estratexia de valorización deste hidrocarburo.

Dada a relevancia dos 1,4-dienos debido á súa presencia en múltiples produtos naturais e con actividade biolóxica (antibióticos, axentes antimicóticos ou citotóxicos) o seu acceso dende moléculas simples, baratas e abundantes é de especial interese para facilitar o acceso ás mesmas, ou derivados. Ademais, o uso de acetileno daría lugar a un patrón de substitución nas olefinas resultantes que non se pode acceder usando alquinos non gasosos. A metodoloxía descrita require o uso de B_2pin_2, acetileno e un substrato alílico, en presenza de un catalizador de Cu cun ligando quiral. O proceso dá lugar á xeración, de forma catalítica, de un complexo nucleofílico de alquenilboril-cobre(I), que posteriormente reacciona co composto alílico por medio de unha adición oxidante, dando lugar a un alquenilboril-Cu^{III}-π-alilo. Dende este intermedio transcorre a eliminación redutora levando á liberación do 1,4-dieno.

Tras avaliar os diferentes parámetros da reacción, apoiándonos en resultados previos do grupo de investigación, acadouse unha combinación óptima para a realización da transformación. A combinación de CuCl co uso de un ligando tipo NHC-sulfonato, contando con un grupo moi voluminoso, foi chave para acadar uns altos niveis de enantioselectividade (*R*); xunto co uso de NaO^{t}Bu, crucial para o control da diastereoselectividade no uso de

dicloruros alílicos xeminais; chegando ao isómero maioritario (*R*,*Z*). Ademais a reacción puido ser escalada 5 veces, mantendo os altos niveis de selectividade para ambos substratos alílicos.

O alcance da reacción catalizada por cobre permitiu explorar diferentes alilos aromáticos, heteroaromáticos e alifáticos. De forma satisfactoria, o uso de un fosfato alílico cun centro quiral preinstalado foi ben tolerado, así como o uso do grupo metilo, que acostuma ser máis problemático na hora de conservar a enantio- e diastereoselectividade debido a súa pequena estérica.

Para comprender de forma máis precisa o requirimento de un ligando máis voluminoso que no caso dos alquinos normais, realizáronse cálculos computacionais a nivel de DFT usando o dicloruro como substrato modelo xa que o seu estudo cubriría ambos aspectos: enantio- e diastereoselectividade. Debido ao menor tamaño do acetileno, atopáronse dous camiños de reacción − moi próximos en enerxía − para acadar os enantiómeros (*R*,*Z*) e (*S*,*Z*). Enerxeticamente falando, cada par de rutas diferéncianse en máximo 1.1 kcal·mol. No referente á estrutura, a orientación da unidade de β-Bpin-alquenilo varía a súa orientación no espazo a cal está permitida debido ao tamaño do acetileno. Porén, a ruta máis favorable é a que proporciona o stereoisómero maioritario (*R*,*Z*). Cando se compararon os perfís enerxéticos para acceder ao diastereoisómetro minoritario (*E*) dende ambas posicións do β-Bpin-alquenilo, obtivéronse camiños de maior enerxía. De forma similar aos anteriores sistemas, a etapa da adición oxidante presentouse como a determinante da velocidade de reacción e da estereoquímica final.

Para racionalizar os resultados obtidos, analizáronse as interacción non covalentes nos estados de transición das adicións oxidantes. Na comparación entre ambos enantiómeros (*R*,*Z*) e (*S*,*Z*), viuse que a pesar de o último (minoritario) dispoñer de dúas interaccións de ponte catiónica co ión Na^+, é maior en enerxía debido a que a disposición que debe adoptar conleva á agudización de interaccións repulsivas entre o C_α e o sulfonato, así como a aparición de novas repulsións estéricas entre o alilo e o Bpin. No que corresponde á diastereoselectividade, os análises NCI revelaron que principalmente son as interaccións repulsivas entre o Bpin e o novo grupo voluminoso instalado no ligando as que fan que a conformación (*E*) exhiba unha maior enerxía de activación.

Posteriormente, leváronse a cabo diversas reaccións de sobre o 1,4-dieno derivado dos dicloruros alílicos xeminais posto que ambas olefinas presentan funcionalidades ortogonais con unha estereoquímica ben definida (*Z*,*Z*). Primeiramente, explotouse esta oportunidade para realizar transformacións enantio- e diastereodiverxentes. Para levar a cabo estas transformacións, aplicáronse diferentes secuencias de reaccións deseñadas para acceder dende un único 1,4-dieno ambos enantiómeros (*R*,*Z*,*Z*) e (*S*,*Z*,*Z*), así como os correspondentes diastereoisómeros (*S*,*Z*,*Z*), (*S*,*E*,*Z*), (*S*,*Z*,*E*) e (*S*,*E*,*E*) de forma modular e selectiva.

Para reforzar a idea da versatilidade sintética, levouse a cabo a síntese de produtos naturais e intermedios avanzados. Mediante unha rigurosa análise, púidose acadar de xeito satisfactorio os produtos naturais estereoisoméricos (+)-Nyasol e (+)-Hinokiresinol dende un intermedio común facendo uso da desenvolta diastereodiverxencia. Ademais, púidose acceder a un intermedio avanzado da (+)-Phorbasin C e de un inhibidor da hormona liberadora da gonadotropina (GnRH, polas siglas en inglés). A maiores, púidose acceder ao alcohol quiral (*R*)-3-metilpent-4-en-1-ol, cuxa síntese enantioselectiva constitúe un reto a pesar da súa aparente simplicidade, relevante intermedio en numerosas sínteses de moléculas complexas.

Na terceira sección (3.3) estudouse a alilación de etano por medio de activación C-H mediante fotocatálise de Fe, usando cloruros alílicos.

Como terceiro obxectivo desta tese doutoral, propúxose desenvolver unha nova metodoloxía que permitise funcionalizar etano para a formación de enlaces C-C mediante activación C-H. Neste sentido, estudouse a reacción de alilación, que dá lugar a olefinas terminais que poden ser sometidas a posteriores modificacións sintéticas para acceder a produtos de interese comercial.

Dada a abundancia natural do etano, provinte do gas natural, a diversificación das súas funcionalizacións constitúe un campo de gran interese co fin de poder acceder a unha maior variedade de substancias de forma directa, evitando funcionalizacións previas. Posto que a química actual para o seu acoplamento directo recae principalmente en reaccións tipo Giese, desenvolver novas rutas catalíticas é crucial para pór en valor a súa versatilidade e aplicabilidade. A metodoloxía descrita nesta sección de tese require o uso de etano e un cloruro alílico, en presenza de un fotocatalizador capaz de promover procesos HAT. O proceso dá lugar a un radical etilo que tras reaccionar co substrato alílico xera unha nova olefina terminal xunto coa liberación de un radical cloruro. Este radical sería en tanto o encargado de promover a reoxidación do fotocatalizador, dando lugar a un novo ciclo catalítico.

Tras unha extensa optimización das condicións de reacción na cal se avaliaron fotocatalizadores, bases, lonxitudes de onda, presións, complexos, ligandos e dilucións, atopamos que o uso de $FeCl_3 \cdot 6H_2O$ en combinación con 2 equivalentes de colidina conduce aos mellores resultados, mentres que o uso de sistemas baseados en traballos previos para a realización de adicións Giese non mostraron reactividade ou conduciron a detectar cantidades de produto inferiores ao 10% de rendemento.

A metodoloxía para a alilación de etano catalizada por ferro foi aplicada a varios cloruros alílicos con grupos aromáticos e heteroaromáticos instalados. Ademais, cómpre destacar que o uso de alilos con diversos enlaces C-H (tipo aqluilo, α-osíxeno, α-osíxeno e benzílicos, e alílicos) foron ben tolerados e non se observaron produtos derivados da súa activación. A presencia de enlaces tipo amida non supuxeron un problema e mesmo o uso de dienos foron ben tolerados no transcurso da reacción. Para exemplificar a relevancia das alilacións a nivel sintético, levouse acabo a síntese do ácido 2-fenilpentanoico, un intermedio amplamente usado na preparación de diversos compostos con actividade biolóxica.

Para ampliar e profundar no coñecemento na reacción, leváronse a cabo diferentes estudos e probas mecanísticas que permitiron coñecer de forma detallada os aspectos chave que regulan esta transformación catalítica. En primeiro lugar, para confirmar a natureza radicalaria da transformación, realizouse a reacción en presenza de TEMPO, podendo detectar a formación do complexo TEMPO-Et ao tempo que a total supresión de formación do correspondente produto derivado da alilación. A seguir, estudouse o tipo de mecanismo mediante probas de marcaxe isotópica usando un cloruro alílico selectivamente deuterado. Tras sometelo ás condicións de reacción, obtívose unha maioría (94:6) de alilación tipo S_H2', mentres que o restante viría de unha isomerización paralela do substrato no medio de reacción. Evidencias adicionais deste tipo de reacción serían as obtidas con unha mestura de cloruros alílicos primario/secundario que tras sometela á reacción deu lugar a un único produto con total control da estereoquímica da olefina, suxerindo que ambos están en equilibrio e a olefina terminal é a que reacciona.

Durante os estudos de optimización e do alcance da transformación, púidose observar de forma sistemática que varias condicións ou substratos non acadaban unha conversión total. Dadas as evidencias bibliográficas, realizamos un estudio con ciclohexano e tras analizar a reacción por GCMS puidemos detectar a formación de clorociclohexano, que derivaría de unha reacción secundaria entre o radical ciclohexilo e cloros radicais, consumindo así estas especies e suprimindo tanto a alilación como o HAT ou a rexeneración do catalizador. Por medio de reaccións estequiométricas púidose confirmar o rol esencial da colidina que atenúa a cloración do alcano, mentres que a súa ausencia supón unha formación extremadamente rápida de clorociclohexano, ao tempo que o catalizador queda inactivo.

O rol da colidina no transcurso da reacción catalítica foi avaliado tamén por medio de estudios de absorción de UV-Vis. De feito, os espectros obtidos tras analizar a reacción con e sen colidina mostran como a colidina atenúa a absortividade molar do $FeCl_3$. As mostras foron irradiadas e púidose comprobar como a súa ausencia supuxo un rápido consumo da banda correspondente ao Fe(III), o que indica a formación de Fe(II) o cal non é activo. Tras a análise do datos, púidose comprobar que ambos procesos son orde 2 con respecto á concentración de Fe, e como a ausencia de colidina acelera a fotodegradación en un orde de magnitude. Para contrastar e reforzar esta hipótese da desactivación por formación de Fe(II), medíronse espectros de EPR e púidose ver o consumo de Fe(III) e a súa transformación en unha especie paramagnética, moi probablemente Fe(II).

A consolidación do rol da colidina logrouse tras a cristalización e obtención da estrutura de Raios X correspondente a o complexo formado entre o $FeCl_3$ e a colidina. O complexo illado púxose en condicións de reaccións e observouse a súa capacidade de catalizar a alilación de etano.

1 INTRODUCTION

Sustainability in chemical synthesis has always been a major must that every chemist has tried to implement in every transformation over the years, and it is not just a modern trend. In fact, by the middle of the 20th century, some of the long-term negative effects of pollution were recognized, and different actions, such as the creation of regulatory agencies and the organization of international symposia, began to change the concept of chemical processes and derivatives, calling for designing chemicals, chemical processes and commercial products in a manner as to avoid the generation of toxics and waste.

Within this context, in 1998, Paul Anastas and John Warner co-authored *Green Chemistry: Theory and Practice,* a book in which they listed the 12 Principles of Green Chemistry: (1) prevent waste generation, (2) maximize the atom economy, (3) design less hazardous chemical synthesis, (4) design safer chemicals, (5) use safer solvents and auxiliaries only where necessary, (6) design energy-efficient protocols prioritizing ambient temperature and pressure, (7) use of renewable feedstocks, (8) reduce unnecessary functionalization steps, (9) generate catalytic reagents, (10) design chemical products that degrade into harmless products, (11) analyze pollution in real time, and (12) select substances that would allow chemicals accidents to be minimized.[1-2]

Incorporating as many of the 12 Principles as possible into the design and development of novel synthetic methods to produce high-value compounds remains a major mission of synthetic chemistry. Within this concern, catalyzed reactions have been historically narrowly associated with green and sustainable chemistry.[3] Actually, any common catalyzed transformation would generally account for several of the mentioned points in the list: prevention of use of stoichiometric amounts of highly reactive reagents − with the associated manipulation risk and generation of stoichiometric amounts of waste − by *in situ* formation of the reactive species; atom and step economy is enhanced by enabling new reactivity routes, avoiding multiple prefunctionalization steps; reactivity is increased, allowing reaction performance at milder conditions and shorter times; and, as consequence, all of these aspects would derive in more energy-efficient protocols.[2-3]

Beyond improving well-established transformations, one of the most valuable catalyst features is their ability to enable new reaction pathways. This characteristic is crucial and makes it singular since a number of industrial reactions require a catalyst because there is no other direct alternative in literature, making them so special.

In the present oil-dependent era, one of the major opportunities lies in the development of innovative catalytic methodologies based on earth-abundant metals (e.g., Cu, Fe), to upcycle underutilized carbon sources – such as acetylene or ethane, which were traditionally used as fuels – and their transformation into complex new molecules. This research is primarily aligned with the objective of identifying alternative raw materials to replace oil as carbon source, given the increasing scarcity of this resource. Given the synthetic potential of these kind of methodologies, not only the design but understanding these new reactivity routes at the atomistic level is highly desired and required since it would enhance the general understanding of reaction mechanisms, and would constitute an important shortcut to design, rationalize, and improve present and future synthetic protocols.[4-6]

The mechanistic analysis of the catalytic reactions is a complex and constantly evolving research field, given the relevance of the findings to the wider synthetic community. A variety of techniques have been applied and refined to elucidate reaction mechanisms, including spectroscopic experiments, kinetic studies or computational approaches.[7] Spectroscopic

measurements permit the gathering of information concerning changes in composition, structure and concentration over time. When these analyses are performed quantitatively, the collected data can be used to develop kinetic studies, furnishing information regarding the transition state of the rate-determining step, including even the effects of isotope substitution.[6-7] On the other hand, computational methods have been widely used for structure predictions and the calculation of energies associated with catalytic intermediates and transition states. The data allows to propose plausible explanations regarding the outcome reactions and the selectivity of the process, establishing a direct relationship with the structure of the catalyst.[4, 7] Currently, there is a growing application of these methods to predict optimum ligand/catalyst combinations, as well as reaction conditions under which the best performance might be expected.[5, 8] In order to achieve that, large amounts of data containing a good set of experimental results and a good set of descriptors must be available.

Given the relevance of both reaction development and mechanistic studies in catalysis, the present thesis combines the two described aspects. Herein, we describe our findings on the development of new allylation methodologies based on Cu and Fe catalysts. The discussion of the results is divided into three main blocks. Firstly, we included the computational studies concerning Cu-catalyzed enantio-, regio-, chemo- and diastereoselective allylboration of alkynes and allenes using allylic *gem*-dichlorides. In the second place, based on the obtained insights, we report the successful development of Cu-catalyzed enantio-, regio-, chemo- and diastereoselective acetylene allylboration, and its further application in the syntheses of complex molecular structures. Finally, the gained experience in working with gaseous reagents was transferred to direct C−H activation of ethane and used in subsequent allylation reaction. Furthermore, the new reported methodologies were subjected to exhaustive mechanistic studies involving computational tools (DFT calculations, NCI and DIAs analyses) and experimental (gas chromatography, UV-Vis absorption experiments, X-ray diffraction, EPR spectroscopy).

To cover all the studied aspects, the introduction section will begin focusing on the allylboration mechanism by explaining the process step-by-step, covering the most relevant studies and findings which are essential to understand how transformation takes place and how selectivity is dictated. Then, acetylene and its chemistry would be reviewed in order to contextualize the current state-of-the-art regarding its application in fine chemistry. Finally, ethane and its homogeneous catalyzed C−H functionalization would be explored, to allow the reader to understand the main protocols reported in literature.

1.1 MECHANISTIC OVERVIEW FOR COPPER-CATALYZED ALLYLBORATION OF ALKYNES AND ALLENES

The use of simple and abundant unsaturated hydrocarbons as pro-nucleophiles through their catalytic transformation into a transient organocopper species by reaction with a hydrosilane (or dihydrogen),[9-11] a silylborane,[12-14] or a diboron compound[15-17] (Figure 1.1.1), constitutes an interesting methodology for reaching diverse molecules from ready available starting materials, by trapping of the corresponding organocopper intermediate with a suitable reagent, resulting in a reductive, silylative, or borylative coupling, respectively.

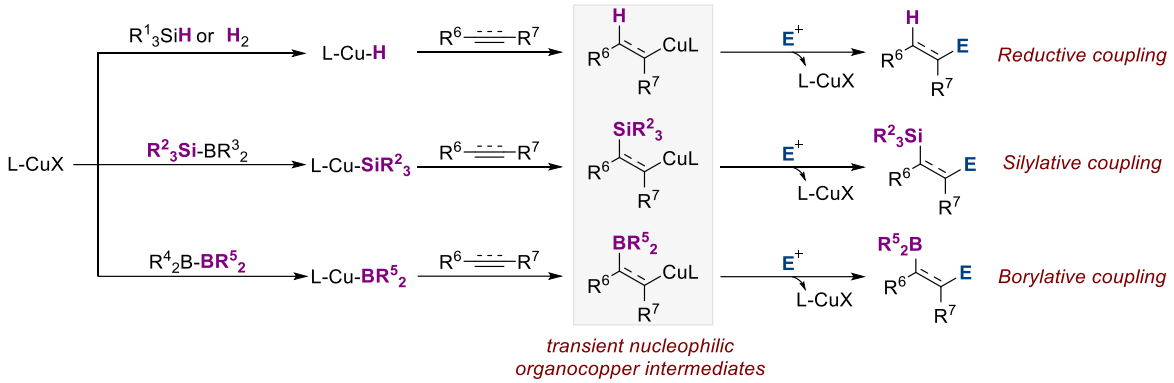

Figure 1.1.1. Main strategies to generate transient nucleophilic organocopper intermediates.

Copper-catalyzed allyboration of unsaturated hydrocarbons is a powerful strategy for accessing synthetically versatile densely functionalized molecules from simple starting materials. From a general vision, the reaction involves the catalytic formation of a borylated organocopper intermediate *via* borylcupration of the unsaturated hydrocarbon and subsequent allylic alkylation.[18-19]

In particular, alkyne allylboration reactions are three-component reactions where an alkyne, a diboron reagent and an allylic substrate react to yield a more complex structure with the formation of two new C−C and C−B bonds, leading to 1,4-diene structures. In this sense, it is noteworthy to mention that preliminary insights into the allylboration of alkynes were reported by Tortosa (2012)[20] and Yoshida (2013)[21] groups through single examples involving the copper-catalyzed coupling of diphenylacetylene and B_2pin_2 with allyl iodide and cinnamyl phosphate, respectively. The latter was shown to proceed with perfect γ-allylation selectivity under Cu/PCy_3 catalysis (Scheme 1.1.1). After these precedents, several methodologies were reported both in racemic and enantioselective fashion, together with the study of their corresponding mechanism.[18-19]

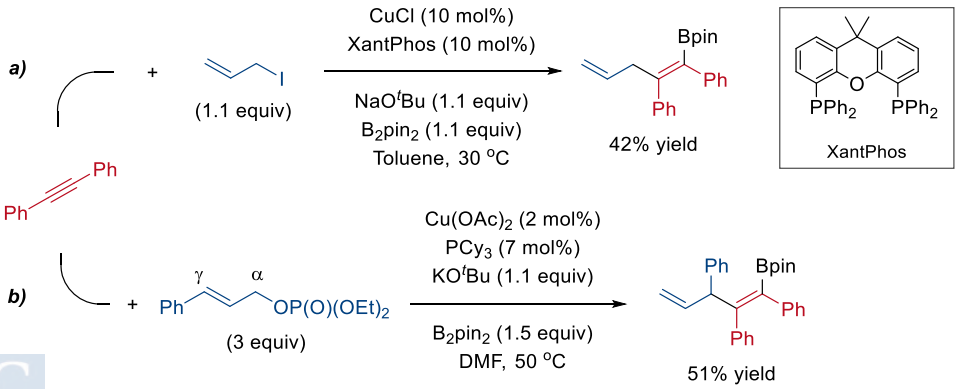

Scheme 1.1.1. First reported allylboration of alkynes by a) Tortosa and coworkers (2012) and b) by Yoshida and coworkers (2013).

The general catalytic cycle for this transformation is illustrated in Figure 1.1.2. The reaction starts with the reaction between LCu(I)−X (X=Cl or Br, generally) and a metal alkoxide which leads to a LCu(I)−OR complex. This species reacts with the diboron reagent through a σ-bond metathesis that results in the formation of a borylcopper complex. This intermediate must undergo a chemoselective insertion into the alkyne (rather than reacting with the allylic substrate) to yield the alkenylboryl copper complex **Int1**. Subsequent oxidative addition of the allylic substrate leads to the π-allylcopper(III) **Int2** which via a reductive elimination furnishes the desired borylated 1,4-diene.[18-19] This last step has to proceed faster than the competing isomerization to the thermodynamically more stable linear allylcopper complex **Int2'** which would lead to the linear (α) product after reductive elimination.

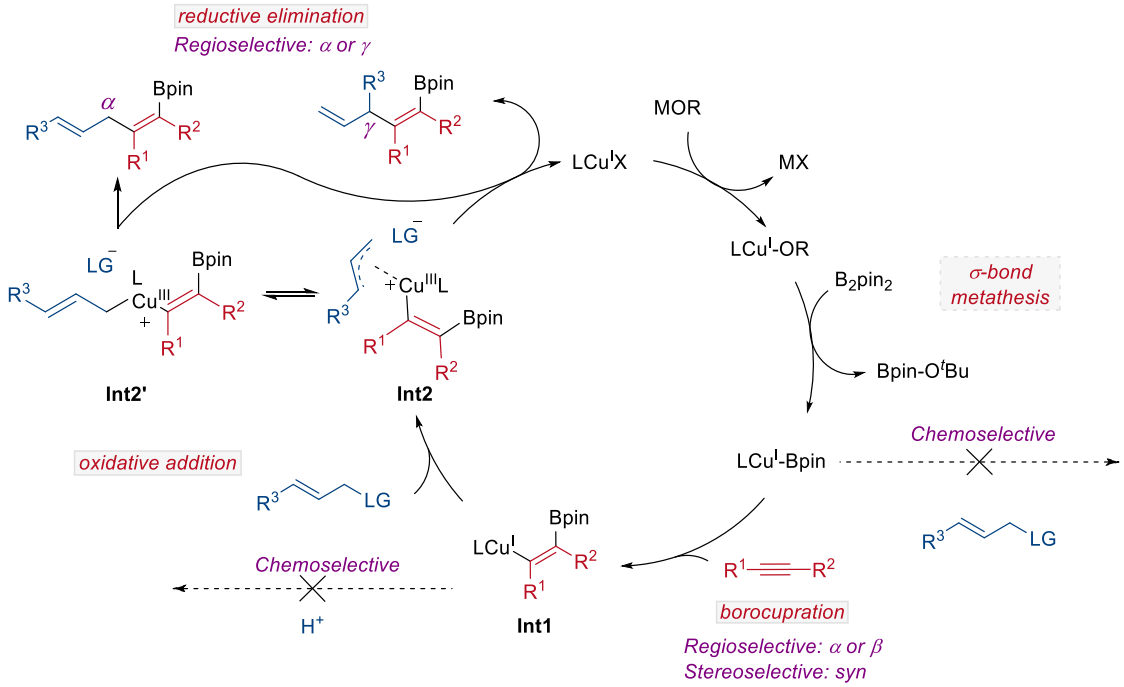

Figure 1.1.2. General catalytic cycle for Cu-catalyzed allylboration of alkynes.

If the reaction is run with an allene, instead of an alkyne, it is designated as an allene allylboration reaction which provides borylated 1,5-diene structures. Initial insights into this transformation were reported simultaneously by Tusji[22] and Hoveyda[23] in 2014, in a racemic and enantioselective fashion, respectively (Scheme 1.1.2). The general catalytic cycle for this transformation (Figure 1.1.3) resembles the one described above for the alkyne allylboration. However, it is important to highlight that an extra selectivity point is associated with this transformation since both double bonds of the allene can in principle undergo the borylcupration step, while the resulting allylcopper intermediate may undergo 1,3-metallotropic rearrangement thus leading to several possible reactive intermediates

As briefly discussed above, allyboration transformations are complex reaction networks of elemental steps that must occur with full control of selectivity. Therefore, in this first section of the introduction, the mechanistic intricacies will be explained in detail, analyzing every elemental step in order to understand, in an easy-to-follow way, every single selectivity point based on the electronic and structural properties of substrates and catalyst.

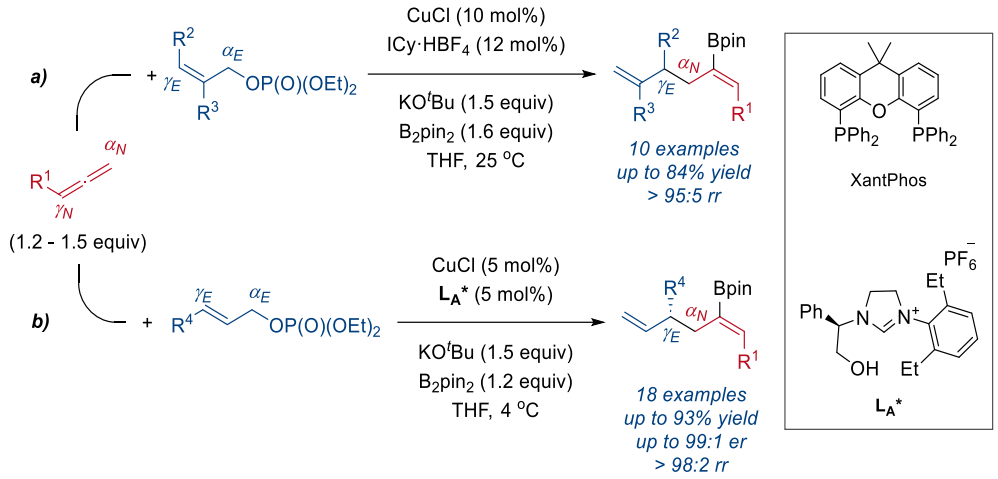

Scheme 1.1.2. First reported allylboration of allenes (2014) by a) Yoshida and coworkers (racemic) and b) by Hoveyda and coworkers (enantioselective).

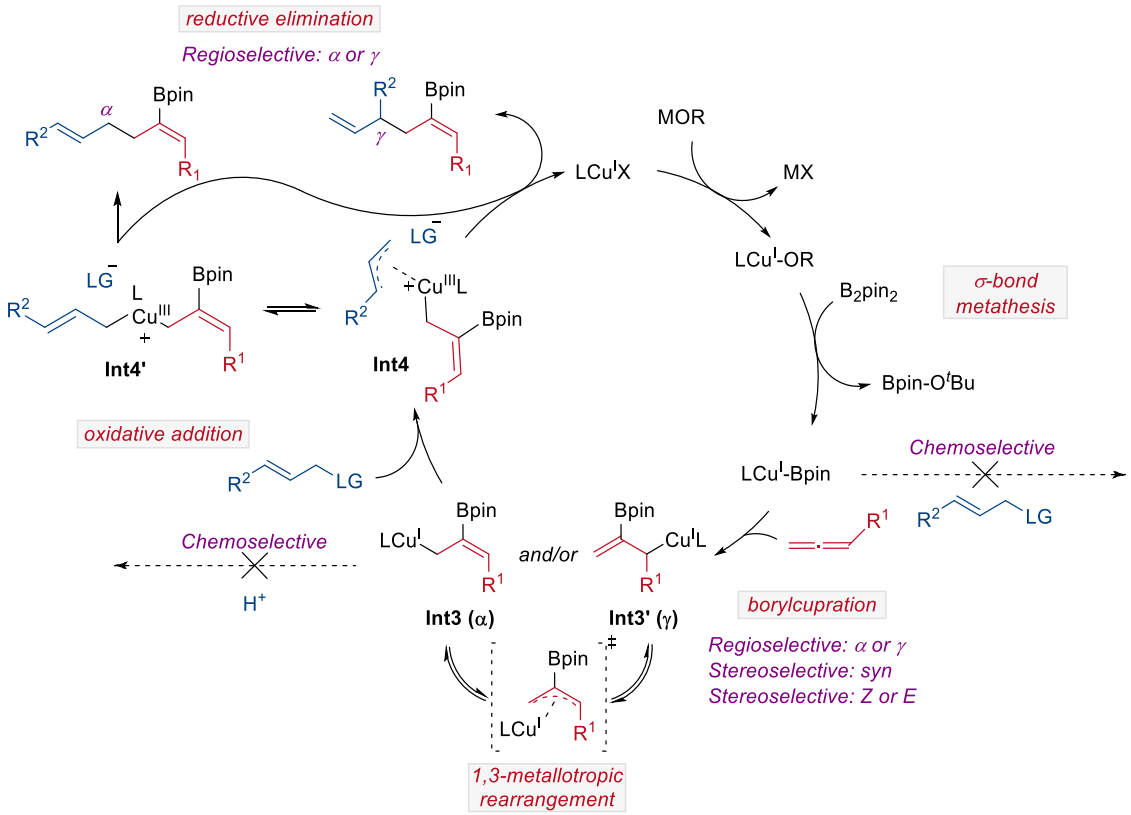

Figure 1.1.3. General catalytic cycle for Cu-catalyzed allylboration of allenes.

1.1.1 Borylcupration step

In order to study the borylcupration step, protoboration reactions are useful since the the product that results from the protonation of the C−Cu bond displays relevant information about the regio- and stereoselectivity of the formed borylcopper intermediate. Hence, along the present subsection, several alkyne and allene protoboration strategies will be discussed to depict a complete vision about the factors governing the different selectivity points.

1.1.1.1 Borylcupration of alkynes

In 2020, the group of Miyaura reported the first protoboration of terminal alkynes by using a stoichiometric combination of CuCl/KOAc/B_2pin_2 in DMF at room temperature.[24] After acidic work-up, the reaction gave rise to mixtures of terminal (β) and internal (α) borylation products. The regioisomeric ratios were observed to be influenced by the nature of the ligand and the alkyne substituent; however no general trends were found. ^{1}H NMR studies suggested that the active copper species was a CuCl-KOAc adduct, which in presence of B_2pin_2 led to the formation of a new signal at 1.19 ppm corresponding to, presumably, the Cu−Bpin complex (Scheme 1.1.3).

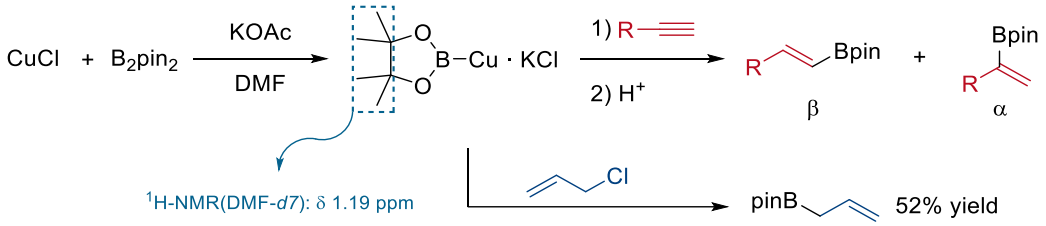

Scheme 1.1.3. Initial insights into Cu-Bpin formation and insertion in terminal alkynes.

Experimental evidence of the formation of the proposed boryl-copper complex was observed after adding allyl chloride to the preformed Cu-Bpin species, obtaining the corresponding allylboronate in 52% yield (Scheme 1.1.3). Some years later, different groups were able to isolate and characterize by X-ray diffraction analysis some boryl-copper complexes bearing *N*-heterocyclic carbenes (NHC) or phosphine ligands (Figure 1.1.4).

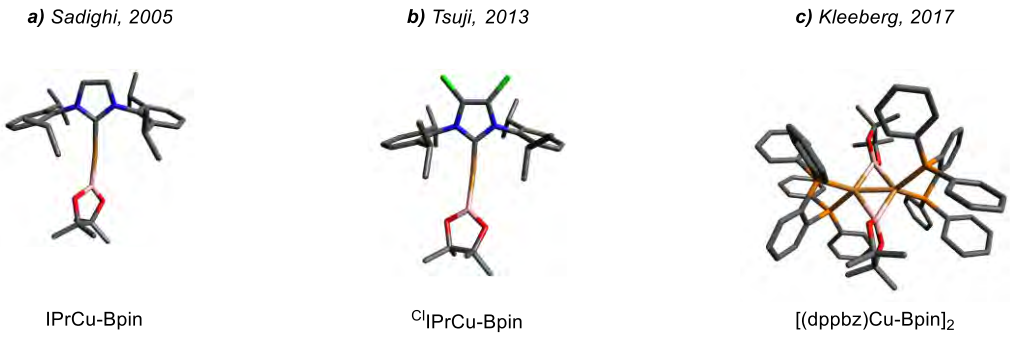

Figure 1.1.4. Examples of isolated LCu-Bpin complexes. Hydrogen atoms from X-ray structures were omitted for clarity. Crystallographic data obtained free of charge from The Cambridge Crystallographic Data Centre.

The pioneering work by Miyaura revealed the ability to generate nucleophilic alkenyl boryl copper complexes from alkynes and, therefore, set the basis for the development and understanding of catalytic methods based on the *in situ* generation of these nucleophilic species. Indeed, after the aforementioned work, several groups reported catalytic protocols where

regioselectivity was achieved, controlled, analyzed and explained. The most representative mechanistic studies, mainly focusing on the factors that govern the selectivity of the Cu-Bpin alkyne insertion step, are described below.

1.1.1.1.1 β-Carbon selectivity

Hoveyda and co-workers studied the regioselectivity in the copper-catalyzed protoboration of alkynes (Figure 1.1.4).[16] It was found that the use of a strong σ-donating and sterically hindered NHC ligand (*N*-adamantyl substituted NHC) was required for accessing the β-carbon selectivity insertion. Furthermore, reaction outcome was found to be β-selective independently from the alkyne nature (alky, aryl, propargylic ethers and propargylic amines were tested under reaction conditions) displaying β-selctivities higher than 73%. Main factors governing the selectivity are the higher electrophilicity and lower steric hindrance of the β-carbon atom (compared to the α-carbon) (Figure 1.1.4, a).[16, 25] This promotes the Bpin (nucleophilic and bulky) insertion into the β-position.

DFT calculations, performed by the groups of Hoveyda[16] and Liu[25], suggested that the regioselectivity determining step is the alkyne insertion stage. In fact, Frontier Molecular Orbital (FMO) analyses shown that strong σ-donating NHC ligands deforms the HOMO orbital from the Cu, injecting more electron density on the proximal orbital lobe to the NHC (*trans* effect). Consequently, the complex displays stronger interactions in the π-coordination complex due to the back-donation from the NHC-copper system to the alkyne (Figure 1.1.4, b). This effect induces a slightly bent structure and allows the alkyne to approach copper in an *anti*-trajectory. As π-backbonding makes the C_β LUMO even larger, the Cu-C_β distance would be small enough to favor β selectivity in B(pin) insertion (Figure 1.1.4, b: $\mathbf{TS_{inx1}}$). In contrast, when alkyne C_β π*-orbital (higher LUMO contribution position) overlaps with bigger Cu HOMO lobe – what would lead to more efficient orbital overlap – the bent structure is also adopted to promote C_α π*-orbital/HOMO interaction, leading to steric clashes between alkyne substituent and Bpin unit (Figure 1.1.4, b: $\mathbf{TS_{inx2}}$).

In the case of propargylic ethers and amines, electronics of the triple bond are modified due to the higher electronegativity of those functional groups (Figure 1.1.5, a). C_α π*-orbital becomes larger due to the heteroatom influence and, therefore, that position is turned more electrophilic than C_β. However, *trans* effect rules as well the selectivity outcome. When interaction between the bigger C_α π*-orbital and bigger Cu HOMO lobe is stablished, the orbital overlapping is highly efficient and steric clashes are minimum, leading to the β-borylated alkene (Figure 1.1.4, b: $\mathbf{TS_{inx3}}$). Conversely, when alkyne approaches with the contrary orientation, the *trans* effect leads to a poor orbital overlapping at the time steric clashes between the alkyne substituent and the Bpin moiety arises (Figure 1.1.4, b: $\mathbf{TS_{inx4}}$).

1.1.1.1.2 α-Carbon selectivity

The Hoveyda group developed a methodology based on SIMesCuCl catalysis, at -50 ºC or -15 ºC.[16] The protocol takes advantage of the lower σ-donating character of SIMes, compared to *N*-adamantyl substituted NHC from Figure 1.1.5) and the use of propargyl ethers and amines – due to the electronic modulation on the alkyne LUMO (Figure 1.1.6, a). The use of a less σ-donating ligand, result in a scenario where both back- and π-donation have similar contributions (Figure 1.1.5, b: $\mathbf{TS_{inx6}}$ and $\mathbf{TS_{inx6'}}$). In this situation, the alkyne approaches the

Cu complex in a planar fashion, and alkyne bent is negligible (Figure 1.1.5, b). By joining both effects, a symmetrical transition state is obtained where sterics between the NHC skeleton and alkyne substituent play the main role for the regioselectivity control (Figure 1.1.6, b: **TS_{inx5}**) promoting the formation of the α-vinylboronates.

Carretero laboratory published a methodology based on the use of P(^{t}Bu)$_3$CuCl as catalyst with alkynes bearing propargyl ethers, amines and sulfones.[26] During optimization studies, they found that less bulkier phosphines (e.g. PPh$_3$) were leading to β-borylated alkene

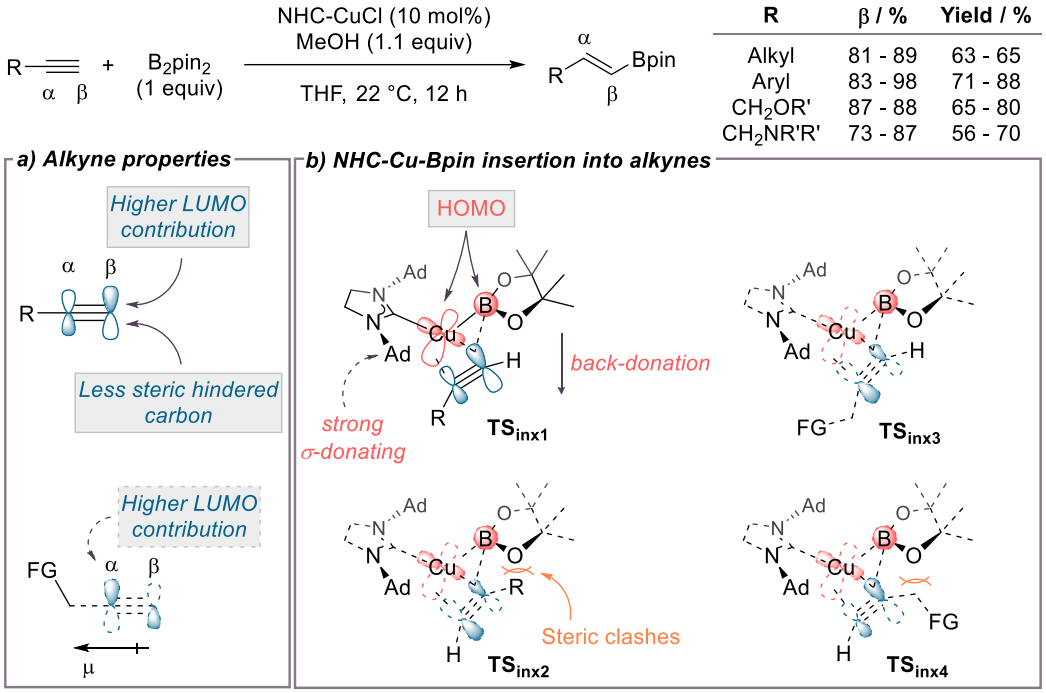

Figure 1.1.5. General reaction scheme and selectivity outcome related with electronic and structural properties governing ß-insertion. a) Electronic and structural properties of alkynes when R = Alkyl, Aryl and when FG = OR', NR'R'. b) Electronic and structural properties of transition states related with NHC-Cu-Bpin - alkyne insertion.

preferentially. However, the use of P(^{t}Bu)$_3$ (which displays a larger Tolman's cone angle than PPh$_3$, 145º vs 182º respectively) allowed them to selectively achieve the α-selective borylation. In the work, the authors claimed that selectivity was ruled by combining the presence of the propargyl directing group and the use of a bulky phosphine. This would lead to an orbital situation similar to the depicted in Figure 1.1.6, where steric clashes between phosphine and alkyne functionalized chain become main regulatory factor.

Recently, Engle and co-wokers reported the use of cyclic(alkyl)(amino)carbene (CAAC) ligands in a regioselective protoboration of alkynes (Figure 1.1.7).[27] Mechanistic analysis showed that α:β selectivity could be improved by increasing the σ-donor ability of the ligand (with comparable steric environment) or increasing the ligand bulkiness (with comparable electronic properties) (Figure 1.1.7). Compared with traditional NHC ligands, CAAC ligands exhibit a stronger σ-donor character combined with a bulky Dipp substituent. When using aryl or alkyl alkynes, higher LUMO lobe is located at the β-carbon. Therefore, α-selectivity will be achieved mainly because of the *trans*-effect that will favor the overlap between the proximal orbital lobe to the NHC and the β-position. On the other hand, when alkynes bearing propargylic heteroatoms are used, the most favored orbital interaction will be

the forged with the α-carbon of the alkyne instead. However, the presence of the sizable *N*-Dipp group engenders large steric repulsive interaction that will promote the borylation of the α-carbon. Moreover, recent ^{1}H-NMR and kinetic studies suggest that the borylcupration step is reversible and the nature of the electrophile would affect the regioselectivity outcome.[28]

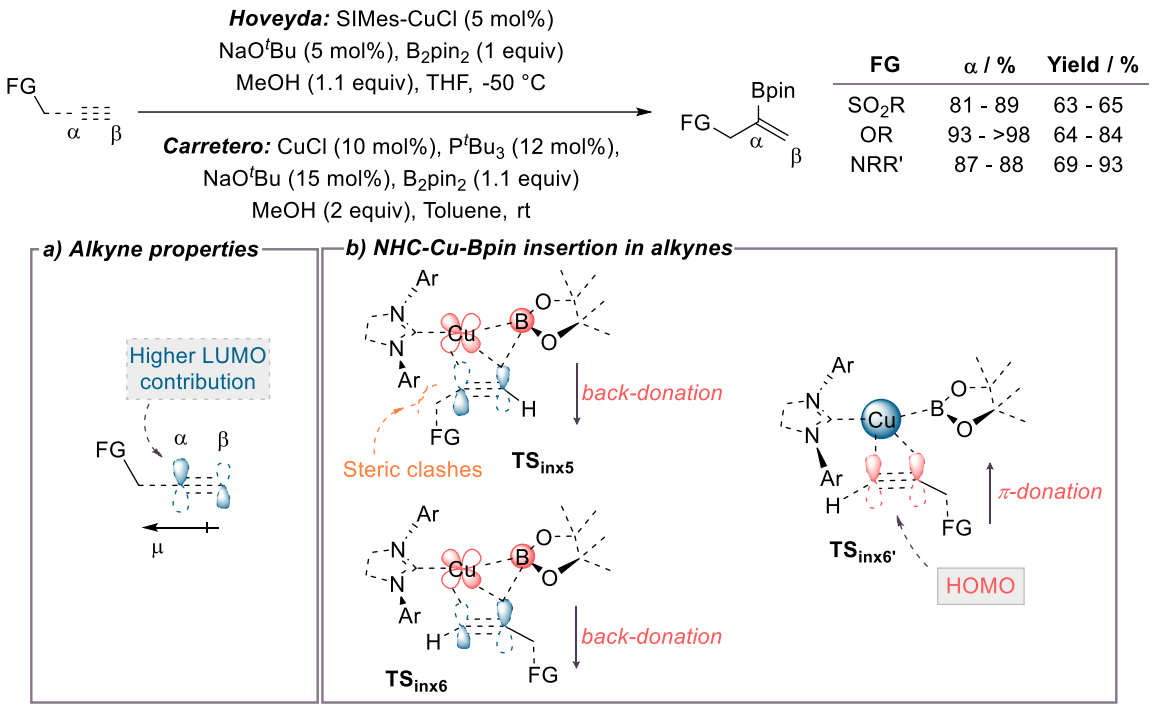

FG	α / %	Yield / %
SO_2R	81 - 89	63 - 65
OR	93 - >98	64 - 84
NRR'	87 - 88	69 - 93

Figure 1.1.6. General reaction scheme and selectivity outcome related with electronic and structural properties governing α-insertion for propargyl alkynes. a) Electronic properties of propargylic alkynes. b) Electronic and structural properties of transition states related with NHC-Cu-Bpin - alkyne insertion.

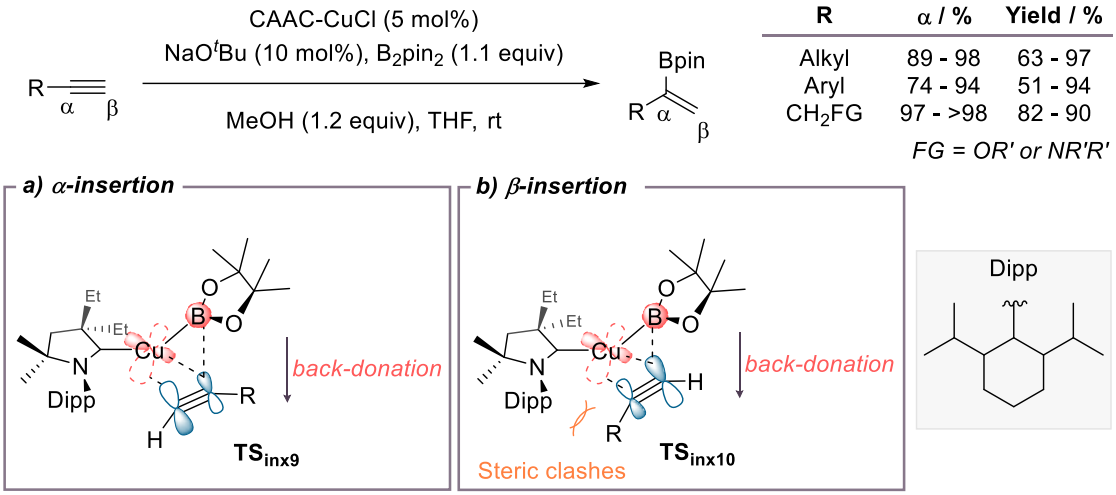

R	α / %	Yield / %
Alkyl	89 - 98	63 - 97
Aryl	74 - 94	51 - 94
CH_2FG	97 - >98	82 - 90

FG = OR' or NR'R'

Figure 1.1.7. General reaction scheme and regioselectivity outcome related with electronic and structural properties in Cu/CAAC-catalyzed alkyne protoboration.

Control over the regioselectivity can be also achieved by tuning the nature of the diboron compounds as reported by Yoshida and coworkers (Scheme 1.1.4).[29] In particular, when unsymmetrical diboron compounds such as pinB-Bdan are used, the less Lewis acidic boron atom is selectively transmetallated to copper during the σ-bond metathesis step. In this

case, SIPr-Cu-Bdan is formed and due to the lower Lewis acidity of the Bdan and the larger backbone from the NHC, steric hindrance between the alkyne and ligand becomes the main regulatory factor. Hence, α-insertion could be selectively achieved.

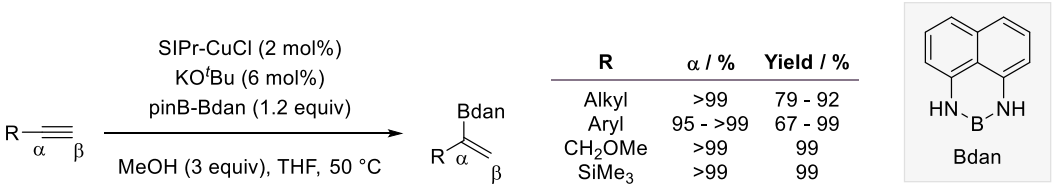

R	α / %	Yield / %
Alkyl	>99	79 - 92
Aryl	95 - >99	67 - 99
CH_2OMe	>99	99
$SiMe_3$	>99	99

Scheme 1.1.4. General reaction scheme and selectivity outcome for protoboration of alkynes with unsymmetrical diboron reagents.

The ability to enable the α-insertion was also reported by Fu[30] group through ligand control, without requiring the presence of an EWG on the alkyne. They reported the use of DMAP as ligand for the obtention of the Markonikov product with moderate selectivity in the alkylboration reaction of terminal alkynes with alkyl iodides and bromides, by using B_2pai_2 as boron source (Figure 1.1.8).[30] It is important to note, that the use of B_2pin_2 led also to α-insertion but in lower selectivities. FMO analysis allowed them to conclude that C_β contribution to LUMO is slightly larger than C_α (36.1% *vs* 32.2%) (Figure 1.1.8, a). In the case of the DMAP-Cu-Bpin complex, HOMO is mainly formed by Cu contribution (68.1% *vs* 20.2% of B atom) (Figure 1.1.8, b). Therefore, orbital overlap would be more efficient when Cu atom interacts with C_β as free energy profiles suggest, with a lower $\Delta G^{\ddagger}$ = 19.5 kcal·mol^{-1} for $\mathbf{TS_{inx7}}$ (*vs* 19.7 kcal·mol^{-1} for $\mathbf{TS_{inx8}}$).[25]

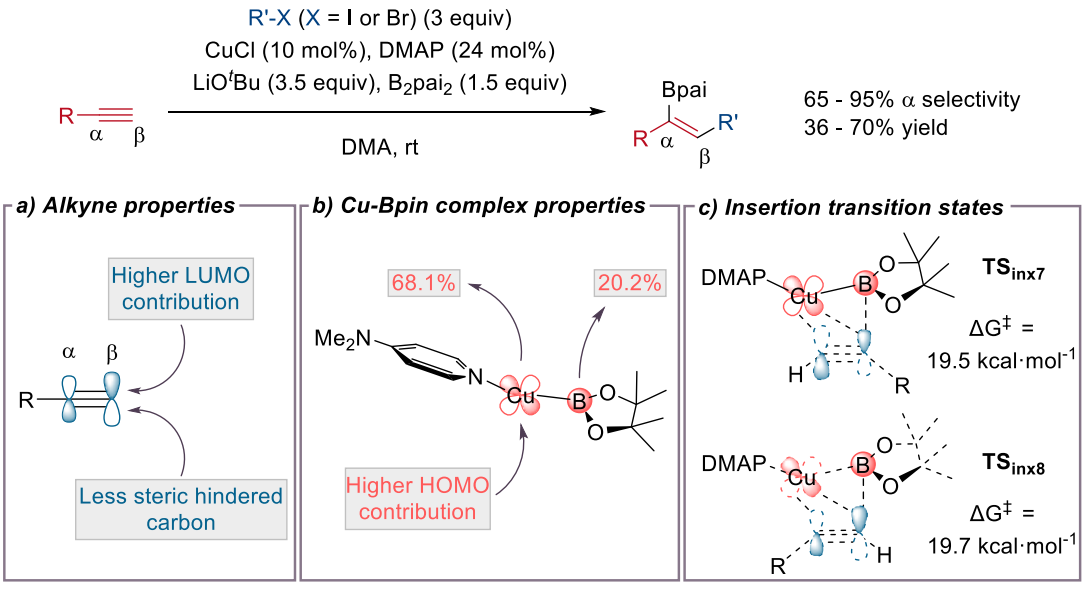

Figure 1.1.8. General reaction scheme, selectivity outcome and computed FMOs for electronic properties governing α-insertion with DMAP as ligand. a) Electronic and structural properties of propargylic alkynes. b) Electronic properties of DMAP-Cu-Bpin. c) Gibbs free energy for insertion transition states and FMO analysis. Computational details: B3LYP-D3/3-611++G(d,p)/SDD+*f* (Cu) (scrf=smd, DMA) // B3LYP-D3/6-31G(d)/LanL2DZ (I, Cu) (scrf=smd, DMA). DMA = dimethyl amide.

1.1.1.2 Borylcupration of allenes

Yuan and Ma developed a regiodivergent copper-catalyzed protoboration of allenes using B_2pin_2 and CuCl/Phosphine catalyst in ethereal solvents (Scheme 1.1.5).[31] The use of the

electron-rich monodentate P(*p*MeO-C_6H_4)$_3$, allowed to selectively obtain the (*Z*)-isomer **I.1** among the six possible regio- and stereoisomers. Further studies revealed that when using a bisphosphine like BIPHEP, the product ratio could be inverted towards **I.2**. The researchers conducted deuterium-labeling experiments and observed >90%-*d* incorporation at α and γ positions, for **(*Z*)-I.1** and **I.2** respectively. Accordingly, while for P(*p*-MeO-C_6H_4)$_3$ the reaction would proceed through the internal C=C bond (γ position), the bulkier BIPHEP would react with the terminal C=CH_2 (α position), and final Cu-C protonolysis would yield the products.

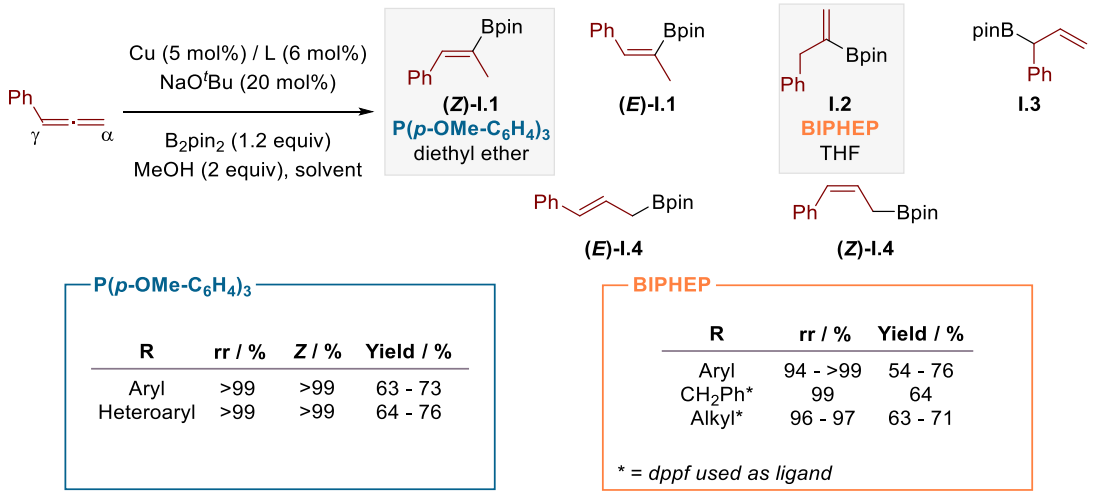

P(*p*-OMe-C_6H_4)$_3$

R	rr / %	*Z* / %	Yield / %
Aryl	>99	>99	63 - 73
Heteroaryl	>99	>99	64 - 76

BIPHEP

R	rr / %	Yield / %
Aryl	94 - >99	54 - 76
CH_2Ph*	99	64
Alkyl*	96 - 97	63 - 71

* = *dppf used as ligand*

Scheme 1.1.5. Representation of all 6 possible isomers from protoboration of allenes and optimized conditions for selective obtention of the indicated regioiromers.

More recently, in 2023, the Zhang group performed a deep DFT analysis of the reaction mechanism published by Yuan and Ma (Figure 1.1.9 and 1.1.10).[32] As previously stated by Yuan, borocupration step for P(*p*-MeO-C_6H_4)$_3$ was found to proceed more favorably on the more internal C=C bond, leading to the benzylic σ-allylboryl copper complex **Int2** ($\Delta G^{\ddagger}$ = 9.2 kcal·mol^{-1}) (Figure 1.1.8, right). Conversely, BIPHEP derived complex displays comparable energy barriers for both borocupration routes ($\Delta\Delta G^{\ddagger}$ = 0.1 kcal·mol^{-1}). Frontier Orbital analysis revealed that higher LUMO contribution on phenyl allene is located at the more internal C=C bond. Thus, orbital overlap with the Cu-complex HOMO would be more efficient at that position (**TS$_{1\text{-}2}$**) rather than the external one (**TS$_{1\text{-}3}$**). However, when BIPHEP is involved, the electronic effect competes with the steric clashes established between the phenyl allene and the ligand skeleton, destabilizing **TS$_{6\text{-}7}$**, thus making it similar in energy barrier than **TS$_{8\text{-}6}$**.

Upon analysis of the protoboration step, it was observed that the reaction with P(*p*-MeO-C_6H_4)$_3$ resulted in the selective generation of the benzylic σ-allylboryl copper complex intermediate **Int2**. However, this could easily isomerize to any of the others *via* 1,3-Cu shift (**TS$_{2\text{-}3}$**) or C−C bond rotation and subsequent 1,3-Cu shift (**TS$_{2'\text{-}3'}$**), displaying free energy barriers lower than 11.2 kcal·mol^{-1} (**TS$_{2\text{-}(Z)\text{-}I.1}$**) – referenced to the most stable primary (*E*)-σ-allyl copper complex **Int8** (Figure 1.1.10). Similarly, when the bulkier BIPHEP was used instead, isomerization steps (**TS$_{2\text{-}3}$** and **TS$_{2'\text{-}3'}$**) feature a lower free energy barrier than most favored protonolysis route (14.4 kcal·mol^{-1}, **TS$_{3\text{-}I.2}$**). It was therefore concluded that the final configuration in the product is established during the protonolysis step (**TS$_{2\text{-}(Z)\text{-}I.1}$** and **TS$_{3\text{-}I.2}$**) where sterics become the main regulatory factors.

One year later to Ma's work, Tsuji and coworkers reported an analogous procedure but using NHC ligands and toluene as the solvent (Scheme 1.1.6).[15] Similarly, they were able to selectively access both isomers **I.2** and **(*Z*)-I.1** when modifying catalyst from [(^{Me}IMes)CuCl] to [(^{Cl}IPr^{CPh_3})CuCl], respectively (Scheme 1.1.6). In order to elucidate how the mechanism works, the researchers performed stoichiometric experiments for each ligand and,

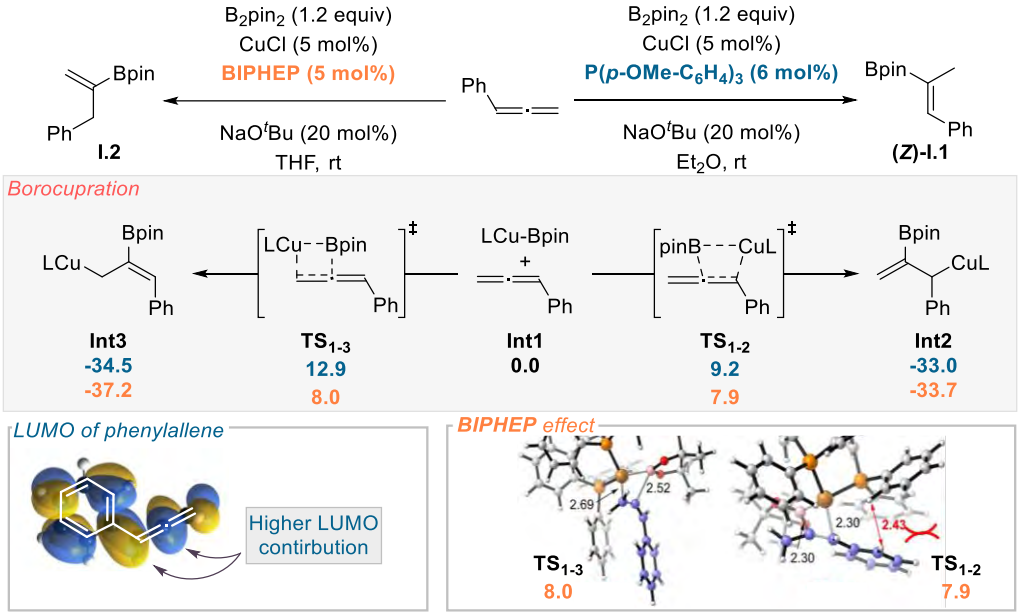

Figure 1.1.9. Electronic and structural properties governing selectivity in the Cu-catalyzed borylation of allenes using BIPHEP (orange) and P(C_6H_4OMe-*p*)$_3$ (blue) as ligand. The numbers are relative Gibbs energies in kcal·mol^{-1}. Computational details: MO6/6-311+G(d,p)/SDD (Cu) (scrf=iefpcm, *solvent*) // B3LYP-D3(BJ)/6-31G(d,p)/LanL2DZ (Cu). *solvent* = diethylether (P(C_6H_4OMe-*p*)$_3$) or tetrahydrofuran (BIPHEP). Images of phenylallene LUMO, **TS$_{1-3}$** and **TS$_{1-2}$** structures were extracted with permission from ref [32]. © 2023 Wiley-VCH GmbH.

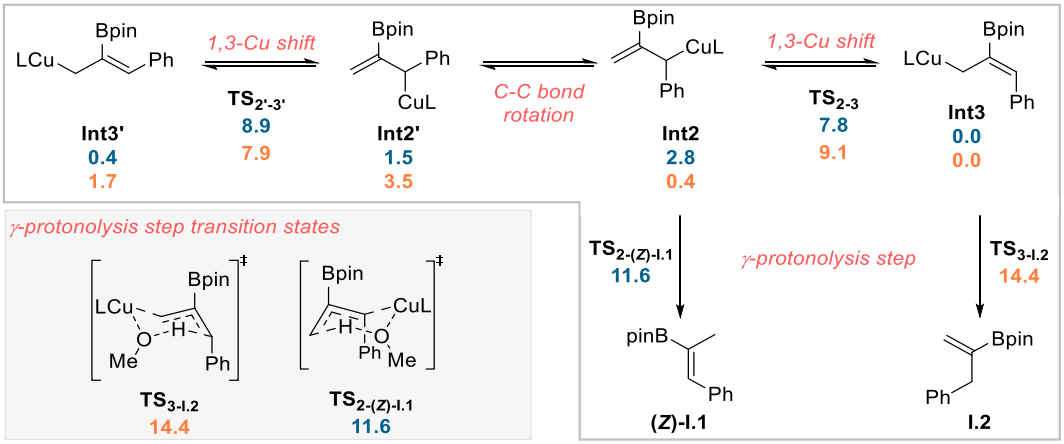

Figure 1.1.10. Structural properties governing protonolysis of allenes using BIPHEP (orange) and P(C_6H_4OMe-*p*)$_3$ (blue) as ligands. The numbers are relative Gibbs energies in kcal·mol^{-1}. Computational details: MO6/6-311+G(d,p)/SDD (Cu) (scrf=iefpcm, *solvent*) // B3LYP-D3(BJ)/6-31G(d,p)/LanL2DZ (Cu). *solvent* = diethylether (P(*p*-OMe-C_6H_4)$_3$) or tetrahydrofuran (BIPHEP).

utilizing ^{1}H-NMR and NOESY, they were able to identify the formation of the (*Z*)-σ-allyl copper species (**Int4** and **Int5**), and even isolate and characterize **Int4** by X-ray diffraction analysis (Scheme 1.1.6). When these isolated (*Z*)-σ-allyl intermediates were treated with MeOH, they provided similar results than observed in catalytic conditions, thus indicating that

while [(^{Me}IMes)CuCl] suffers a Cu-C bond protonolysis via an S_E2-like process, [(^{Cl}IPr)CuCl] would react in an S_E2' fashion.

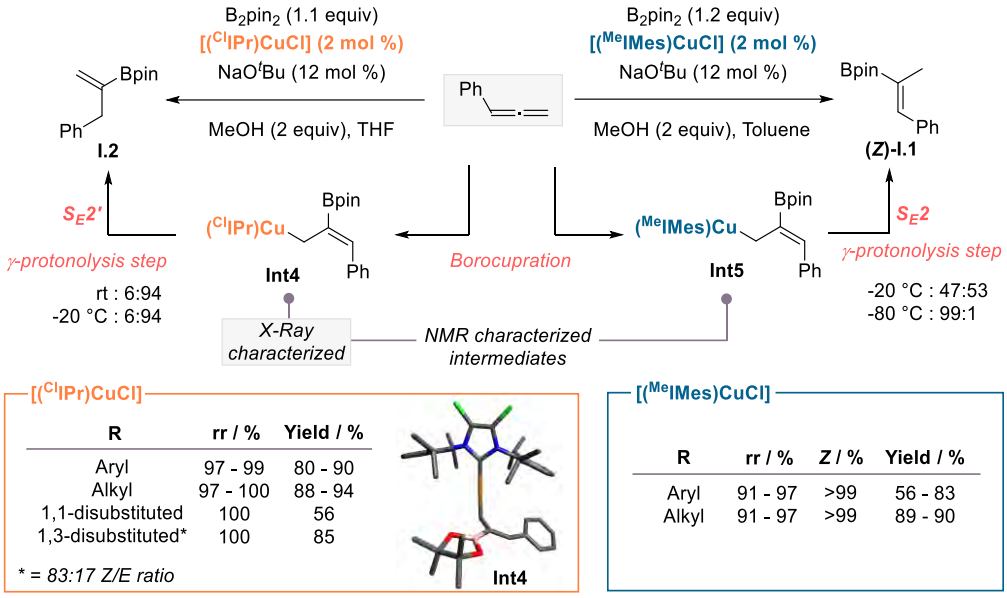

Scheme 1.1.6. Mechanistic analysis for NHC-Cu-catalyzed protoboration of allenes and main selectivity outcome. Ratios given in the γ-protonolysis step are referred to **(*Z*)-I.1**/**I.2** product ratio. Hydrogen atoms from X-ray structure of **Int4** were omitted for clarity. Crystallographic data obtained free of charge from The Cambridge Crystallographic Data Centre.

The group of Hoveyda also studied the protoboration of allenes under NHC-Cu catalysis.[33] It was found that **(*Z*)-I.1** could be selectively accessed when using IPr-CuCl as catalyst, while **I.2** was obtained with the less bulky *N*-methyl substituted NHC (IMe).

To disclose the mechanism ruling the observed selectivities, the researchers carried out DFT calculations using the small IMe-Cu-Bpin complex (Figure 1.1.11). According to their findings, borylcupration is more favored at the terminal C=CH_2 (α position) with a low energetic barrier of 7.2 kcal·mol^{-1} (3.7 kcal·mol^{-1} lower than borocupration at the γ position). Then, formed terminal (*Z*)-σ-allyl-Cu(I) complex **Int7** could easily isomerize through a 1,3-Cu shift (**TS$_{7\text{-}8}$**, $\Delta\Delta G^{\ddagger}$ = 12.5 kcal·mol^{-1}) to reach the internal σ-allyl-Cu(I) complex **Int8** (4.3 kcal·mol^{-1} higher in energy than **Int7**). Last protonolysis step from both routes was observed to display similar energies, but slightly lower for **Int8** ($\Delta\Delta G^{\ddagger}$ = -1.3 kcal·mol^{-1}, **TS$_{8\text{-}(Z)\text{-}I.6}$** vs **TS$_{7\text{-}I.5}$**).

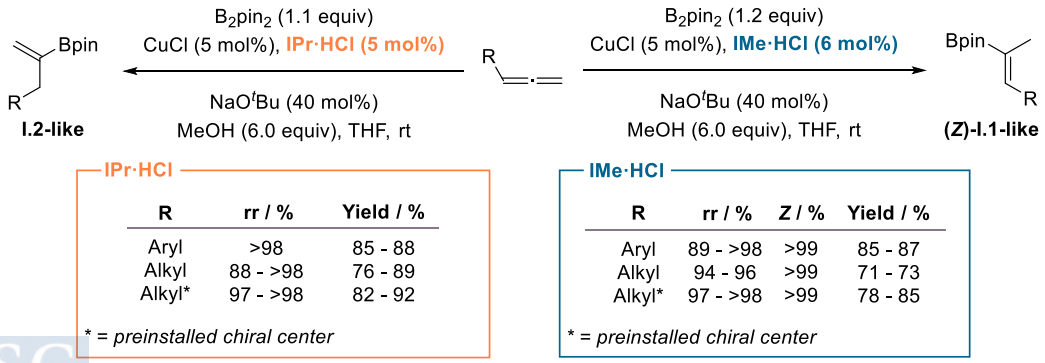

Scheme 1.1.7. General reaction scheme and selectivity outcome for Cu-catalyzed protoboration of allenes with IPr·HCl and IMe·HCl ligands.

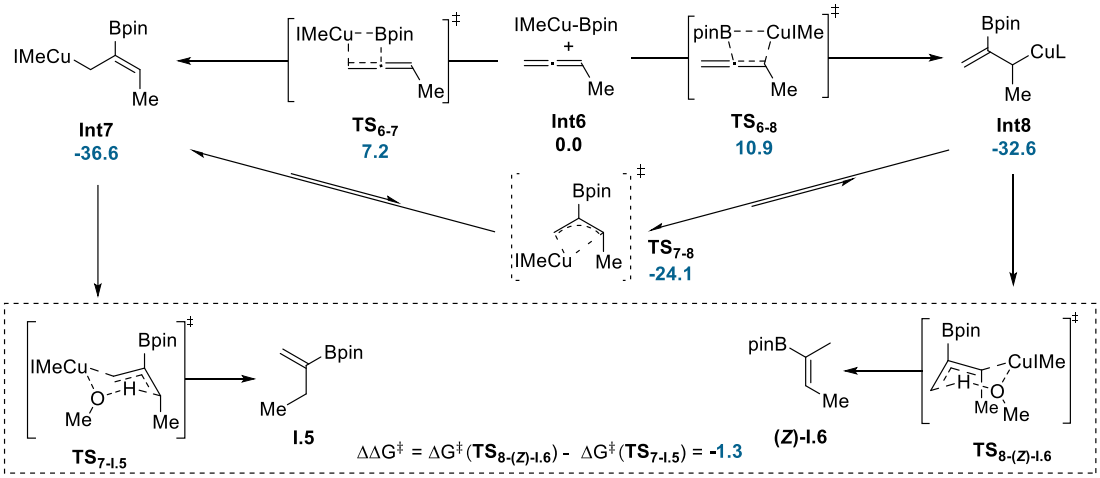

Figure 1.1.11. Mechanistic analysis for NHC-Cu-catalyzed protoboration of allenes. The numbers are relative Gibbs energies in kcal·mol^{-1}. Computational details: BP86/6-31G(d,p)/LanL2DZ (Cu) (scrf=pcm, THF).

Therefore, a Curtin-Hammett kinetic is established, where the less thermodynamically stable intermediate requires lower activation energy to reach product (Figure 1.1.11). In light of these findings, the authors proposed that in the case of using bulkier ligands, such as IPr·HCl, isomerization to the branched allylcopper intermediate **Int8** would be hampered by the steric hindrance of the NHC ligand would raise the isomerization energetic barrier, conducting the subsequent protonolysis step from **Int7** towards the **I.5**.

1.1.2 Copper-catalyzed allylic alkylation

Having discussed the main factors behind the regioselectivity of the borylcupration step, we may now proceed to disclose the subsequent step in the catalytic cycle of the allylboration reaction that is the allylic substitution. This process involves two elemental steps, i.e. the oxidative addition of the allylic substrate into the transient organocopper intermediate, and subsequent reductive elimination (Figure 1.1.2 and 1.1.3). In order to understand the reaction mechanism and the selectivities of the oxidative addition and reductive elimination steps, the mechanistic studies that have been conducted on the copper-catalyzed allylic alkylation with organometallic reagents will be discussed in the following paragraphs.

Over the last years many reports have been described for the copper-catalyzed coupling of organometallic reagents, such as organolithium,[34] Grignard reagents,[35-37] organotitanates,[38] organozincs[39-41] or alkylaluminium,[41] with different allylic substrates both in racemic and enantioselective fashion (Figure 1.1.12, a).[42-44] The mechanism of the transformation has attracted certain attention, mainly due to the effort to understand the factor that control the regio- (α versus γ alkylation) and stereoselectivity (*anti* or *syn* allylation) of the reaction (Figure 1.1.12, b).

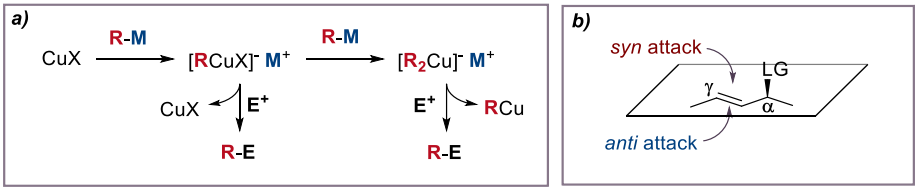

Figure 1.1.12. General mechanism of formation of organocopper(I) species and C-C bond formation. b) Schematic representation of multiple allylation pathways: α-carbon, γ-carbon, *syn*-face and *anti*-face fashions.

Goering and co-workers reported the first mechanistic proposal for this transformation.[45] Their proposal was based on an initial oxidative addition (OA) of the allylic substrate into the alkyl-Cu(I) that results in a σ- or π-allylcopper(III) intermediate which undergoes subsequent reductive elimination (RE) to furnish the final product (Figure 1.1.13). Despite the fact that this first proposal was published in 1981, no DFT studies on these intermediates were published until 2004 by the Nakamura group.[46]

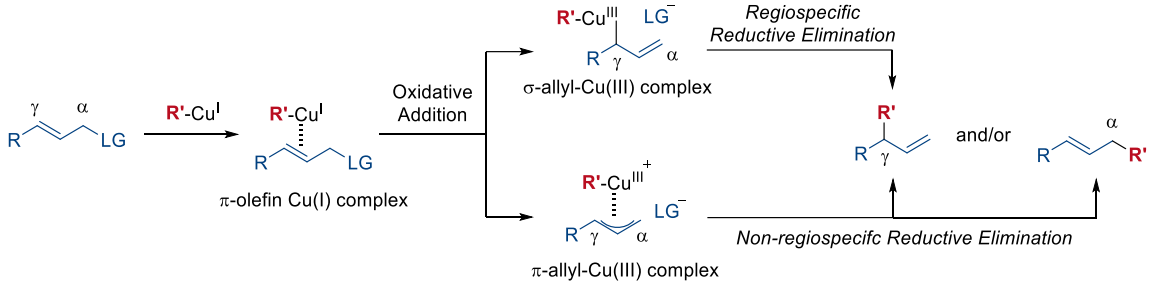

Figure 1.1.13. General mechanism of Cu-catalyzed allylic alkylation involving oxidative addition and reductive elimination steps proposed by Goering (1981).

Nakamura's DFT studies revealed that both the σ- and the π-allylcopper(III) intermediates exist as minima and undergo a rapid equilibration (**Int9-σ** and **Int9-π** respectively, $\Delta G^{\ddagger} = 9.8$ kcal·mol^{-1}), being the latter the more thermodynamically stable by 9.0 kcal·mol^{-1} (Figure 1.1.154 a). Reductive elimination was found to be much faster from the π-allylcopper(III) species than from the σ-complex ($\mathbf{TS^9_{\pi\text{–}RE}}$ *vs* $\mathbf{TS^9_{\sigma\text{-}RE}}$ respectively, $\Delta\Delta G^{\ddagger} = 4.5$ kcal·mol^{-1}), and its transition state structure resembles an enyl[σ+π] complex. Moreover, it was found that in a 1-substituted π-allylcopper(III) complexes, reductive elimination occurs at the more electrophilic position –in this case C_1 is bearing the less electrodonating substituent (Figure 1.1.14, b) – and the presence of a substituent with strong electrodonating character deforms the transition state geometry leading to an intermediate in which the Cu-Cα bond features a stronger σ-bond character (Figure 1.1.15, b). Additionally, it was established that the presence of a Lewis acid as a leaving group activator favors the formation of the *anti* and γ-selective product (Figure 1.1.14, c).[38, 47-48]

Orbital interactions involved in the reductive elimination step were deciphered by FMO analysis (Figure 1.1.15).[42] Considering the π-allylcopper(III) intermediate (**Int9-π**), interactions consist of allyl-to-copper donation (π-orbital to empty 4s orbital) and copper-to-allyl back-donation (3d orbital to non-bonding π*-orbital). As this intermediate evolves towards reductive elimination ($\mathbf{TS^9_{\pi\text{–}RE}}$), the complex adopts an enyl[σ+π] structure, where the Cu-C3 bond gets σ-bond character (back-donation) while the π-coordination to the double bond (donation) is still present. Finally, the Cu atom recovers its d-electrons while installing the Me ligand to the C3 position; and therefore Cu(III) is reduced to Cu(I).

1.1.2.1 γ-Carbon allylation

The γ-selective allylation, or S_N2'-type substitution reaction, has received major attention by synthetic chemists since it is a useful method for the generation of a new stereogenic center through the transformation of a trigonal carbon (Csp^2) to a tetrahedral (Csp^3). However, a general drawback of this methodology is the competing α-carbon allylation, or S_N2-type substitution reaction, that generally leads to a linear non-chiral compound. The works in which

the mechanistic intricacies that control chemoselectivity towards the S_N2' reaction pathway were studied and revealed are discussed below.

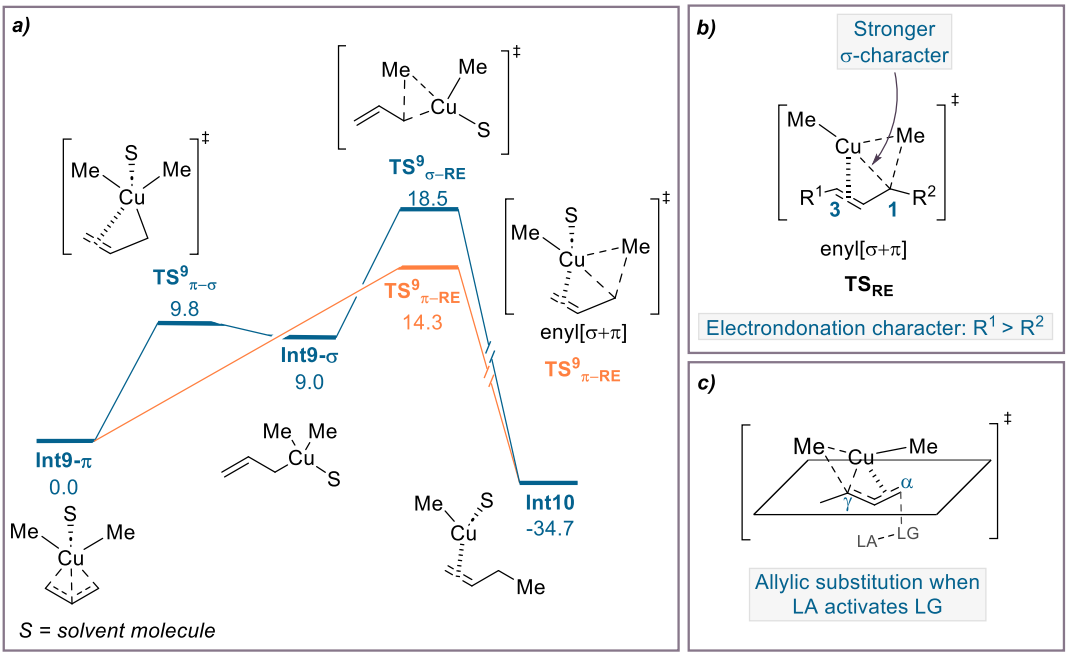

Figure 1.1.14. Computational mechanistic analysis of Cu-catalyzed allylic substitution. a) Gibbs free energy profiles (kcal·mol^{-1}) at 195.5 K for both feasible routes proposed routes based on RE from σ-allylcopper(III) (blue) and RE from π-allylcopper(III) (orange). b) Enyl-type reductive elimination transition state. c) Effect of Lewis acids on regio- and stereoselectivity. Computational details: B3LYP/6-31G(d)/SVP (Cu).

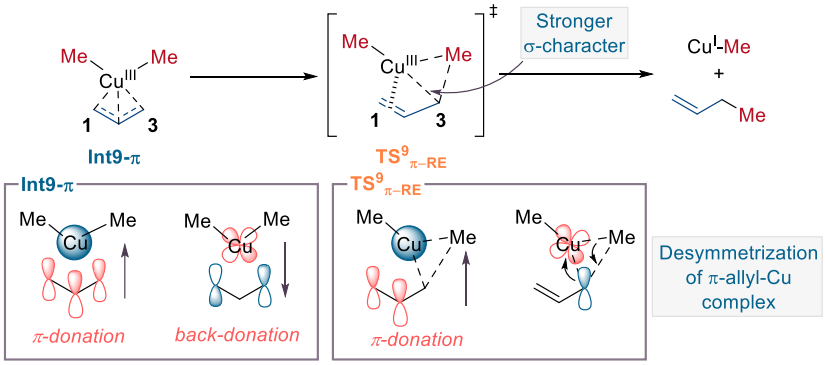

Figure 1.1.15. FMO analysis for reductive elimination step. Red orbitals represent HOMO and blue LUMO.

1.1.2.1.1 The Lewis acid effect

Initial insights into the regioselectivity of this transformation were reported in 1980 by Yamamoto and coworkers.[48] They reported that γ-selectivity is enhanced by the combination of Lewis acids with cuprates, when using allylic chlorides. The RCu·BF_3 combination was the most effective system in terms of both yield and regioselectivity, independently of the degree of substitution of the two ends of the allylic system (Scheme 1.1.8).[48] Later, in 1984, Corey and Boaz described the orbital interactions of organocuprates with allylic substrates.[49] According to them, the electron rich d orbital from copper would overlap the LUMO (π*) at the γ-carbon and, in a lesser extent, with the antibonding orbital (σ*) at α-position. This interaction would therefore favor the γ- and anti-selectivity.

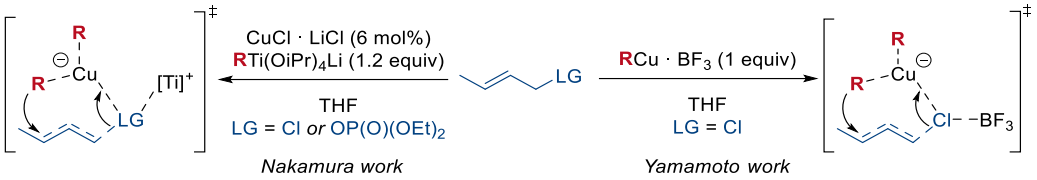

Scheme 1.1.8. Yamamoto and Nakamura works on copper-catalyzed γ-allylation using of Lewis acids.

In 1991, the Nakamura group studied the reaction of secondary allylic chlorides and phosphates in the presence of a Cu(I) catalyst and an organotitanium compound leading to diastereo- and regioselective allylation. (Scheme 1.1.8).[38] Despite the unclear nature of the reactive species, control experiments revealed that while organotitanium is inert to allyl chlorides, its absence in the reaction leads to a remarkable drop in selectivity . Therefore, Ti-to-Cu transmetallation would afford the in situ formed cuprate, and we may assume a Lewis acid role of the resulting titanium complex, enhancing the γ-selectivity either by weakening the C-LG bond, or by increasing sterics at the α-carbon through LG-[Ti] coordination, or by a combination of both, since it was reported that small Me group decreases regioselectivity.[48] It was also noted that reaction with allylic bromides showed moderate regioselectivity, exposing the relevance of the leaving group nature in the reaction outcome.

Subsequent studies regarding allylic alkylation reported the efficacy of incorporating a Lewis acid to modulate the reactivity towards the selective obtention of the γ-allylation product, and the activation of the leaving group.[50] For instance, Feringa and coworkers reported the use of the $BF_3{\cdot}OEt_2$/TMSOTf mixture – which in situ forms BF_2OTf (Scheme 1.1.9, a) – as a key factor to achieve high regio- and enantioselectivity when using allyl ethers as substrates.[51] Similarly, the research group of Alexakis demonstrated the important role of the Lewis acidity of the organoaluminun played in the activation of the leaving group in the desymmetrization of *meso*-hydrazines with trialkylaluminium reagents under copper catalysis (Scheme 1.1.9, b).[52] In this context, in 2009 the Nakamura group developed an enantioselective copper-catalyzed allylic substitution reaction with chiral aminohydroxyphosphine ligands by using diethylzinc reagent and allylic phosphates (Scheme 1.1.9, c).[53] This kind of bifunctional ligands were reported to coordinate the copper atom through the phosphine, while having the aminohydroxy part interacting with the zinc atom (**Int14**). The later would promote a non-covalent interaction with the phosphate group within the copper π-olefin complex. This situation fixes the structure acting as a template, promoting therefore excellent regio- (γ), stereo- (*anti*) and enantioselectivity.

1.1.2.1.2 The ligand effect

Further studies by Nakamura and coworkers helped to rationalize the stereo- and regioselectivity when cyclic allylic systems were used (Figure 1.1.16).[54] Experimental insights revealed that, when monoalkyl heterocuprate MeCu(CN)Li was used, the reaction displayed excellent *anti*-stereoselectivity and γ-regioselectivity (γ:α = 96:4). In sharp contrast, dialkyl cuprate Me_2CuLi performs also *anti*- yet entirely non-regioselective (γ:α = 50:50). A theoretical study for the Me_2CuLi system, showed that reaction proceeds through a square-planar olefin π-complex **Int15** from which the acetate is released in *anti*- fashion, yielding a symmetrical π-allylcopper(III) complex **Int9-π** (Figure 1.1.16, a). The *anti*- selectivity arises from the Cu $3d_{xz}$ HOMO and the C=C π*/C-O σ* LUMO interaction (Figure 1.1.16, c, d). From the π-allylcopper(III) species, reductive elimination proceeds, equally, at both α- and γ-positions.[54]

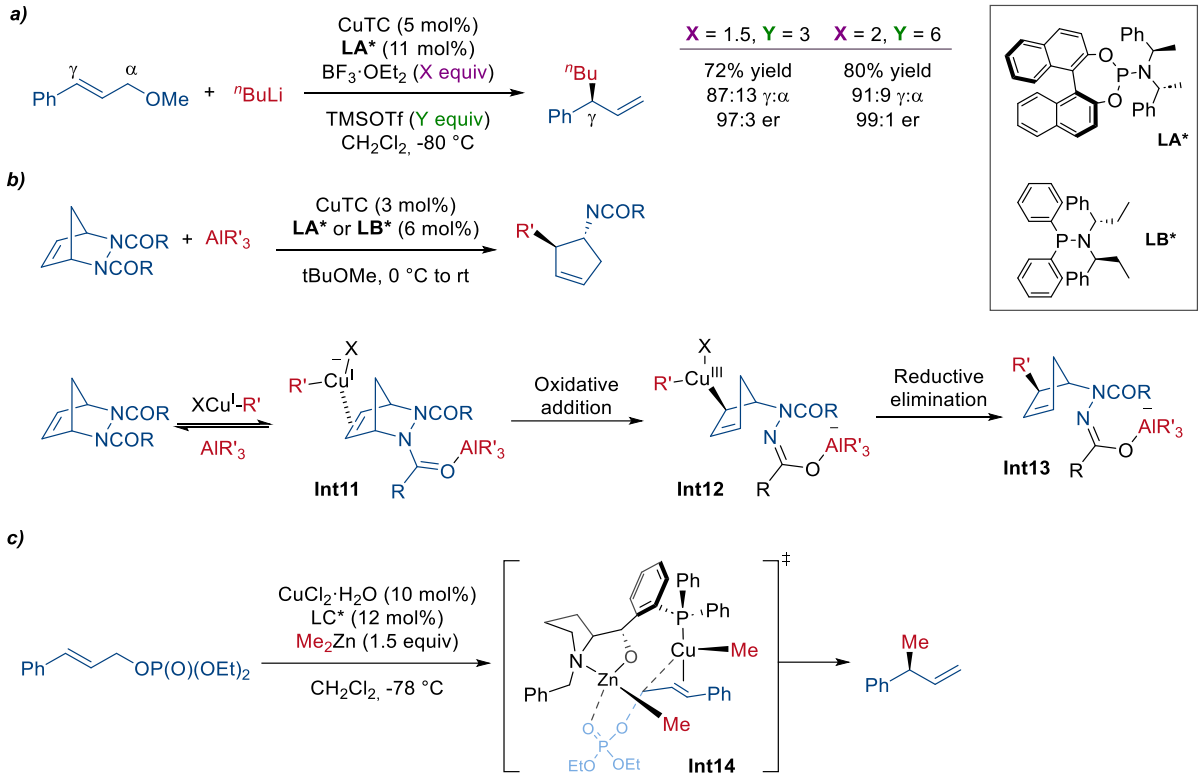

Scheme 1.1.9. Selected literature examples of leaving group activation using a Lewis acid.

Conversely, studies with heterocuprate MeCu(CN)Li revealed that the *trans* effect is the first regulatory factor for the γ-selectivity. It was found that oxidative addition transition state displaying the cyano ligand *syn* to the α-carbon is energetically lower than the one bearing the cyano in a *trans* position ($\Delta\Delta G^{\ddagger}$ = -3.2 kcal·mol^{-1}) (Figure 1.1.16, b). These transition states (**TS^{16}$_{OA}$** and **TS^{16}'$_{OA}$**) lead to enyl [σ+ π] copper(III) complexes (**Int17** and **Int17'**) that easily undergo reductive elimination. FMO analysis clarify the reason behind the selectivity. Cu $3d_{xz}$ HOMO is desymmetrized because of the different σ-donor abilities of the ligands (stronger for Me and weaker for CN). On other hand, C−OAc cleavage results in mixing C=C π*/C−O σ* orbitals and hence LUMO becomes larger on the γ-carbon (Figure 1.1.16, c). Therefore, better HOMO/LUMO overlap is stablished between the larger $3d_{xz}$ lobe with the larger LUMO lobe (Figure 1.1.16, d).[54] Very recently, Tambar and coworkers reported a similar study on the alkylation of allylic carbonates by using MeCu(CN)Li and Me_2CuLi that provided similar conclusions about the origin of the regioselectivity.[37]

1.1.3 Unsatutared hydrocarbons as pronucleophiles in enantioselective allylation reactions

Despite the exhibited efficiency of traditional protocols relying on the stiochiometic use of organometallic reagents, they present important drawbacks. They require prior preparation of the organometallic reagent, adding extra steps to the method. Moreover, in some cases, their relatively high reactivity and basicity can compromise the functional group tolerance of the reaction. Last, but not least the stoichiometric use of organometallic reagents inevitably generates stoichiometric amounts of inorganic waste. An advance in the Cu-catalyzed asymmetric allylic alkylation has been made by the employment of catalytically generated nucleophilic intermediates.

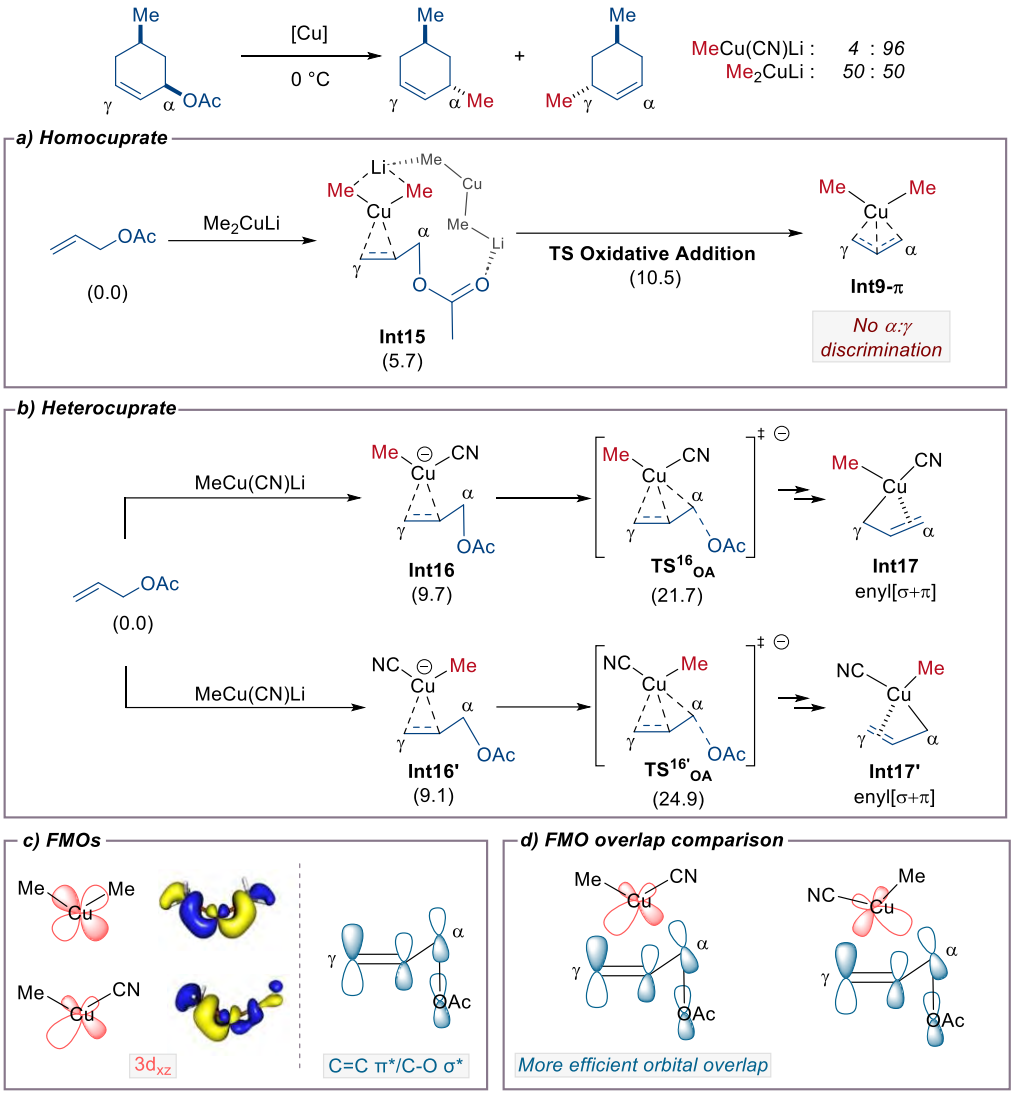

Figure 1.1.16. Computational mechanistic analysis regarding γ- and α-selectivity on copper-catalyzed alkylation of allylic acetates. a) Computed mechanism for homocuprate $[Me_2CuLi]_2$. b) Computed mechanism for heterocuprate MeCu(CN)Li. c) FMO representations for Cu HOMO ($3d_{xz}$) and allylic acetate LUMO (C=C π*/C-O σ*) orbitals. 3D orbital representation of $3d_{xz}$ was extracted with permission from ref. [37]. © 2023 The Authors. Angewandte Chemie International Edition published by Wiley-VCH GmbH. d) FMO overlap analysis. The numbers are relative ZPE corrected energies in kcal·mol^{-1}. Computational details: B3LYP/6-31+G(d)/SDD (Cu) (scrf=cpcm, THF).

1.1.3.1 Alkynes as pronucleophiles. Regio- and Enantioselective Allylboration of Alkynes

In our research group, we have long experience and deeply understand how this transformation takes place. [55] In fact, in 2019 we reported the first copper-catalyzed asymmetric allylboration of alkynes (Scheme 1.1.10).[56] The reaction – involving a terminal alkyne, an allylic bromide and B_2pin_2 – provides chiral-branched borylated 1,4-dienes with excellent levels of chemo-, stereo-, regio- and enantioselectivity. Ligand screening revealed that the use of a chiral Cu catalyst featuring a chiral sulfonate-bearing NHC ligand **Lc*** is key to achieve good efficiency and high levels of regio- and enantioselectivity (Scheme 1.1.10). The installation of the Bpin in the afforded products, well-known versatile functional group, allowed different transformations to afford complex and densely functionalized molecules.

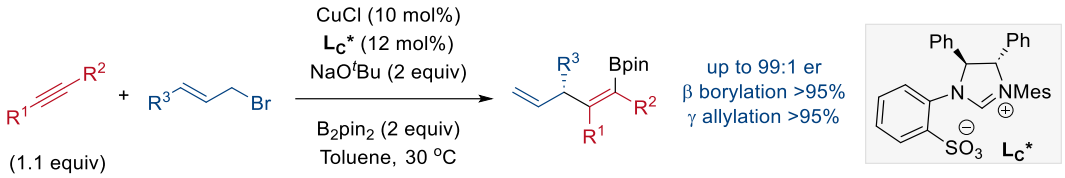

Scheme 1.1.10. General reaction conditions for Cu-catalyzed enantioselective allylboration of alkynes and allylic bromides using chiral sulfonate-bearing NHC ligands.

Factors that govern the regio- and enantioselectivity of the reaction were studied by DFT calculations. Regioselectivity in the borylcupration step was firstly addressed (Figure 1.1.17).[55] In order to discern how the process proceeds, three possible alkyne approaches to the NHC-Cu-Bpin complex **Int18** were considered: a) β-borylation from sulfonate face (**TS$_{Sulf-β}$**), b) α-borylation from sulfonate face (**TS$_{Sulf-α}$**) c) and β-borylation from mesityl face (**TS$_{Mes}$**). Optimized structure of **Int18** was found to proceed smoothly towards corresponding alkenyl boryl copper complex with an activation energy barrier of just 8.0 kcal·mol^{-1}. When alkyne orientation was switched to evaluate the α-borylation (**TS$_{Sulf-α}$**), a crowded geometry was observed mainly due to steric repulsions between the alkyne substituent, the Bpin and the mesityl groups. Alkyne approach from the mesityl face to give β-borylation (**TS$_{Mes}$**) also displayed higher energy than **TS$_{Sulf-β}$** as well.

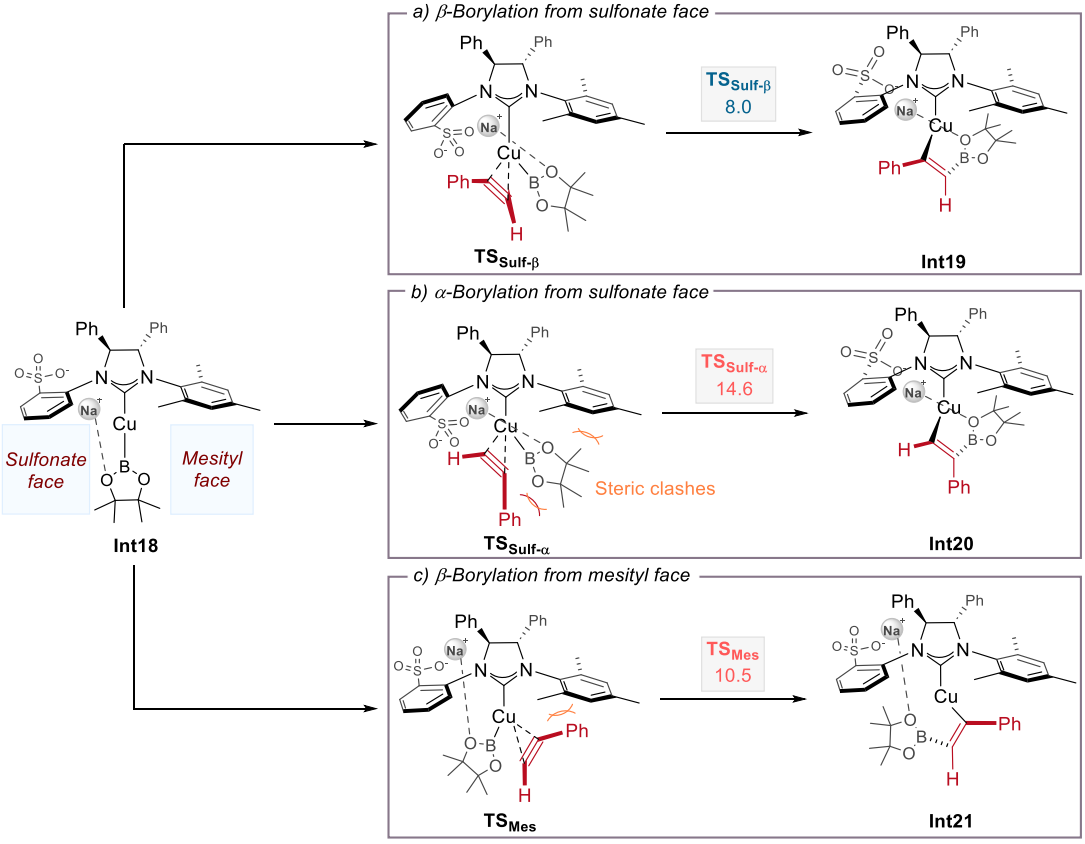

Figure 1.1.17. DFT evaluation of different alkyne-to-copper approachs towards borocupration step. The numbers are relative Gibbs energies in kcal·mol^{-1} and referred to the borocupration transition states. Computational details: ωB97XD/*def2*-TZVPP (srfc=smd, toluene) // ωB97XD/6-31G(d).

Among the different studied approaches for the allylation step, it was observed that the most favored one is the one in which the allyl bromide coordinates the alkenyl-Cu complex by the sulfonate face (**Int22** and **Int22'**). It was found that sulfonate-cation-leaving group

bridge is established,[57-59] and it helps to adopt the proper conformation – such a molecular template – in order to achieve the high levels of regio- and enantiodiscrimination (Figure 1.1.18). In this model, the adopted conformation would experience steric clashes for the minor enantiomer (**TS$_{OA}$-*R***) between the allyl moiety and the Bpin unit, favouring the **TS$_{OA}$-*S*** by 1.6 kcal·mol^{-1}.

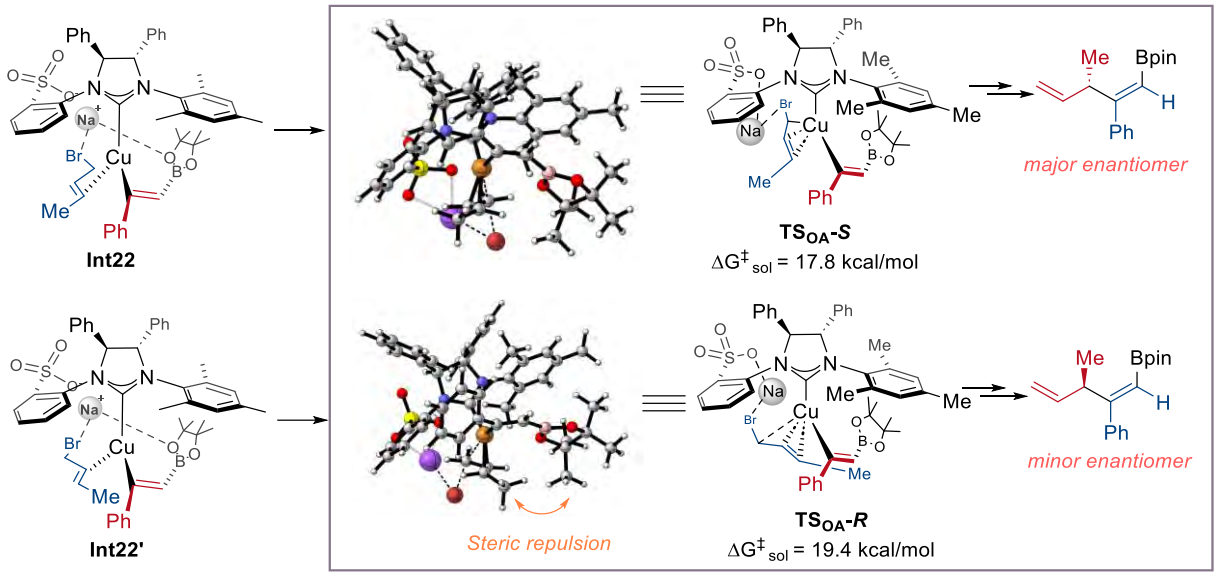

Figure 1.1.18. Cu-catalyzed enantioselective allylboration of alkynes and allylic bromides. DFT optimized geometries for oxidative addition transition state. Computational details: ωB97XD/*def2*-TZVPP (srfc=smd, toluene) // ωB97XD/6-31G(d).

1.1.3.2 Regio- and Enantioselective Allylboration of Allenes

The group of Hoveyda envisioned the use of those catalytic nucleophilic allyl copper intermediates in enantioselective allylic substitution reactions, i.e. an asymmetric allene allylboration (Figure 1.1.11).[23] Reaction was found to proceed with excellent levels of enantio- and regioselectivity, for both borocupration of allene and allylic substitution steps. In order to reach the excellent selectivity levels, a chiral heterocyclic ligand bearing a free alcohol **L$_D$***** (acting as chelating group) served as precursor to a bidentate catalyst. Ligand bulkiness was essential to reach high γ-selectivity in the allylation step, probably due to a fast reductive elimination to relieve steric repulsions in the formed complex,[42] meanwhile the large Bpin-substituted chiral chain was required to achieve the excellent enantioselectivity. Mechanistically, the authors proposed that the external C=C bond undergoes borylcupration. The resulting allyl-copper complex coordinates with the allylic phosphate leading to a tetrahedral Cu(I) intermediate and subsequent oxidative addition leads to a square planar Cu(III) complex, from where reductive elimination would occur. DFT modelling of the oxidative addition transition state revealed that enantioselectivity arises from steric repulsions established by (1) allylic substrate and Bpin unit installed on the ligand and (2) diethylphenyl ring from the ligand core and the Bpin unit installed on the allene moiety (Scheme 1.1.11).

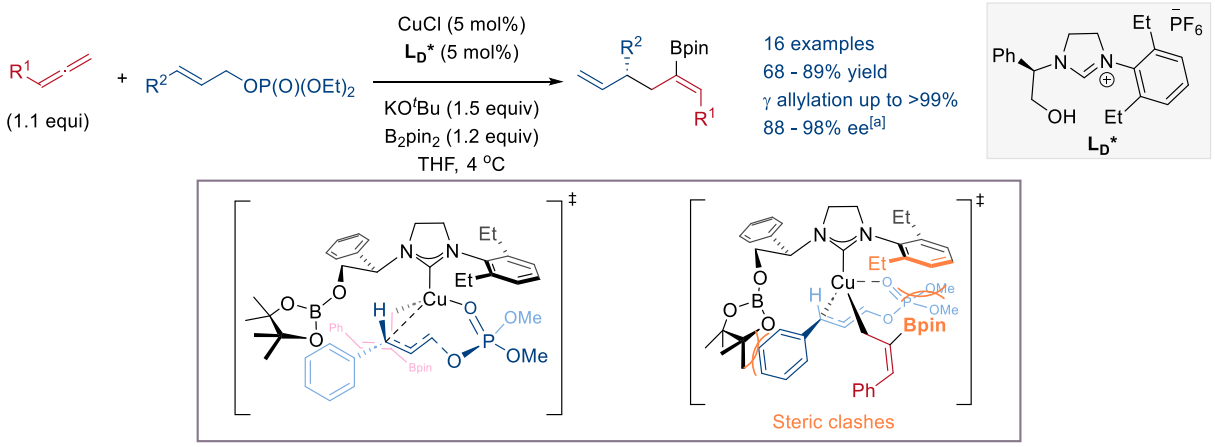

Scheme 1.1.11. Cu-catalyzed enantioselective allylboration of allenes and allylic phosphates. a) Reaction conditions. b) Schematic representation of oxidative addition transition states where key interactions govern enantioselectivity.

Very recently, our group reported an enantioselective transformation based on the allylation of allenes with allylic carbonates under dual Cu/Pd catalysis (Scheme 1.1.12). The reaction demonstrated to proceed with high levels of enantioselectivity, while providing borylated 1,5-dienes with contiguous chiral centers, in a diastereoselective manner.

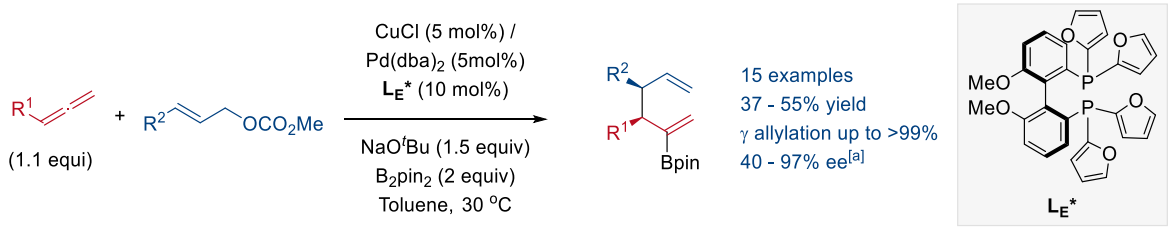

Scheme 1.1.12. Dual Cu/Pd catalyzed enantioselective allylboration of allenes with allylic carbonates. a) When R^2 = H enantiomeric excess drops drastically.

To provide a higher degree of detail on the reaction mechanism, an extensive study based on DFT calculations − using BIPHEP as ligand − in the context of the study of a enantioselective Cu/Pd-catalyzed allene allylboration reaction was performed.[60] As reported previously with BIPHEP (Figure 1.1.9 and 1.1.10),[31-32] borylcupration on the more internal C=C bond displayed lower energy than the external one, leading to **Int24** although both pathways have a similar energy span (Figure 1.1.19). Furthermore, the isomerization between all 6 possible σ-allyl copper species was evaluated and it was found that they can easily isomerize between each other towards the lower energy intermediate **Int25**. From this stage, transmetallation of the borylated allyl group, from Cu to Pd, would take place through a 6-membered transition state. Once the bis(allyl)Pd complex is formed, reaction undergoes reductive elimination to yield the final chiral diene.

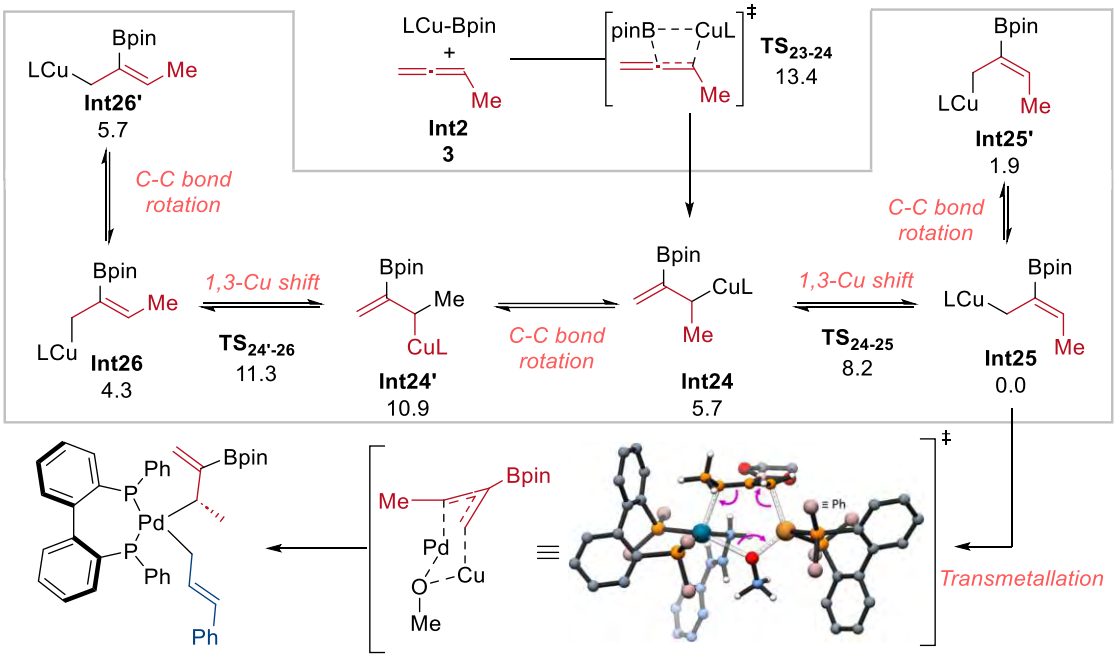

Figure 1.1.19. DFT computed isomerization of borylated σ-allyl-copper intermediates. The numbers are relative Gibbs energies in kcal·mol^{-1}. Computational details: B3LYP-D3/*def2*-TZVP/ *def2*-QZVP (Cu) (scrf=smd, toluene) // B3LYP-D3/6-31G(d,p)/SDD+*f* (Cu) (scrf=smd, toluene). L = BIPHEP. 3D molecular model extracted with permission from ref. [60]. Copyright © 2024 The Authors.

1.2 ACETYLENE. GENERAL ASPECTS AND STATE-OF-THE-ART OF CATALYTIC FUNCTIONALIZATION REACTIONS

Acetylene (C_2H_2) is the simplest hydrocarbon with a triple bond. From a physical point of view, acetylene is a colorless, nontoxic but narcotic gas, and is slightly lighter than air. Its C≡C triple bond and high positive energy of formation render acetylene into an unstable and highly reactive molecule (Table 1.2.1).

Table 1.2.1. Various physical properties of acetylene.

Various physical properties of acetylene	
Molecular mass	26.0379 g/mol.
Density (gaseous C_2H_2 at 1 bar)	1.095 kg/m^3 (288.15 K)
Enthalpy of formation	227.5 1.0 kJ/mol (298.15 K)
Gibbs free energy of formation	209.2 1.0 kJ/mol (298.15 K)
Entropy of formation	200.8 J mol^{-1} K^{-1} (298.15 K)
Vapor pressure	2.6633 MPa (273.15 K)

In terms of its chemical properties, due to its highly reactive character, it readily reacts with many elements and compounds and exhibits a large electrophilic character. The polarized C-H bond makes acetylene certainly acidic (pKa = 25), and consequently is very soluble in basic solvents due to the ability of forming hydrogen bonds with them (Table 1.2.2).

Table 1.2.2. Acetylene solubility coefficients in various solvents.

Acetylene solubility coefficients in various solvents (in mol kg^{-1} bar^{-1})			
Solvent	**C_2H_2 pressure / bar**	**− 20 °C**	**25 °C**
Methanol	0.98	1.979	0.569
1,2-Dichloroethane	0.4 – 1.05	0.569	0.218
n-Hexane	6.90	0.523	0.264
Toluene	0.98	0.619	0.214
Acetone	0.98	4.213	1.069
DMF	0.98	5.096	1.501
Ammonia	0.98	7.052	2.229

Regarding its electronic structure, according to molecular orbital theory, the C≡C bond in acetylene involves one σ-bond and two orthogonal π-bonds. The σ-bond is formed by two *sp*-hybrid orbitals from each carbon, and the two π-bonds are formed from the perpendicular *p*-orbitals. Alternatively, the so-called "bent" or "banana" bonds have been invoked to describe the multiple C–C bonds in acetylene (Figure 1.2.1).[61] Both models had been computationally evaluated and the superiority of one bond description over the other was observed to depend upon the studied system.[62] However, both display similar description level for acetylene.

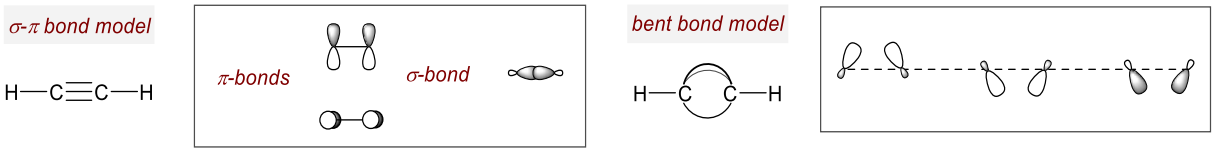

Figure 1.2.1. Electronic structure of acetylene according to both accepted models: σ-π bond model and bent bond model.

1.2.1 Industrial production and use of acetylene

Nowadays, due to the uncertain future about oil production, there is a general agreement that coal and natural gas, relevant raw materials for acetylene manufacture, will last longer.[63] In fact, current worldwide acetylene production is over five million tons per year.[64] Nowadays, four acetylene obtention routes remain remarkably active for the commercial production of acetylene: carbide route (Figure 1.1.2, a), partial combustion of natural gas or Sachsse process (Figure 1.1.2, b), the arc process or Hüls process ((Figure 1.1.2, c) and the hydrocarbon cracking (Figure 1.1.2, d). [65-66] All these are high-temperature processes, requiring a large amount of energy, being the main difference among them how the necessary energy is generated and transferred.

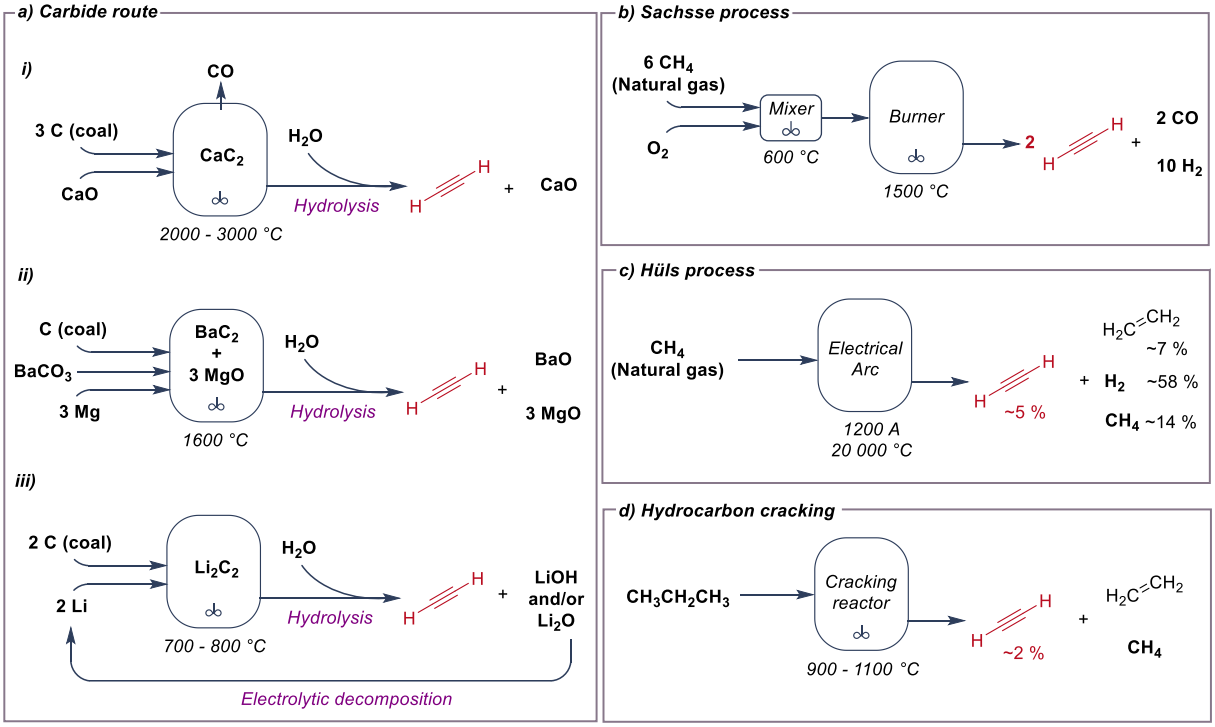

Figure 1.2.2. a) Formation of acetylene from diverse acetylenides by using (i) calcium carbide, (ii) barium carbide and (ii) lithium carbide. b) Partial combustion of natural gas to produce acetylene. c) Electrothermal process for acetylene production. d) Hydrocarbon cracking process.

1.2.1.1. Industrial applications

Acetylene displays a very rich chemistry, with a variety of applications in the chemical industry. These are based on vinylation or addition reactions with acids or protic sources, ethynylation of ketones to form alcohols (Favorskii reaction), carbonylation with CO_2 leading to acrylates, and dimerization, oligomerization or polymerization transformations (Figure 1.2.3).[63, 65] Nowadays, despite the absolute predominancy of petroleum as hydrocarbon source, the chemical industry still continued to use acetylene in the synthesis of vinyl chloride (for polyvinyl chloride synthesis, PVC), vinyl acetate, acrylic acid (for polyacrylic acid preparation, PAA) and acetylenic chemicals such as 1,4-butynediol. Regarding this last one, the acetylene route represents the predominant commercial production process currently available.[65-67]

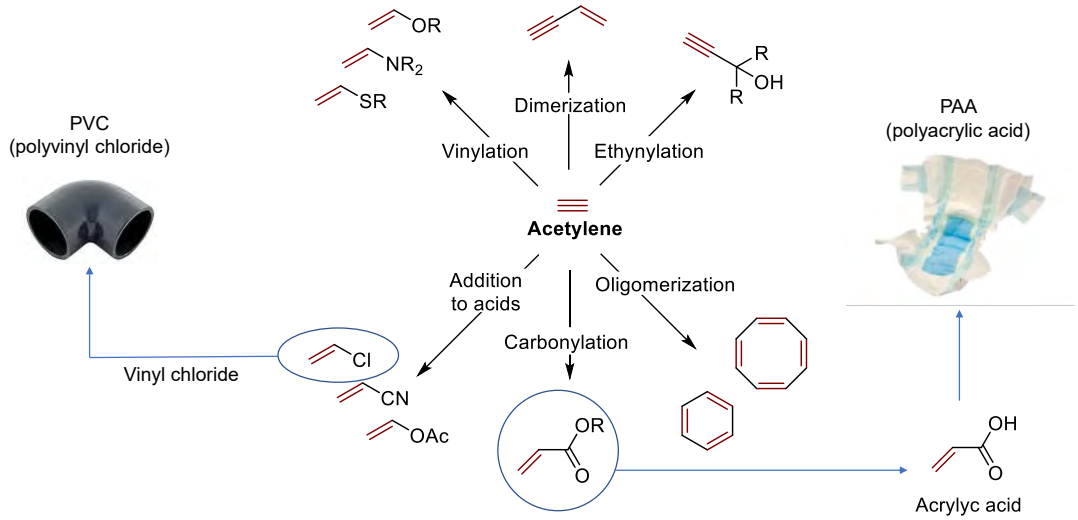

Figure 1.2.3. General overview of industrial transformations of acetylene and representative products.

1.2.2 Acetylene in fine chemistry

In sharp contrast with its industrial application, acetylene has been less used in fine chemistry. Homogeneous catalytic protocols leading to its direct functionalization (Scheme 1.2.3),[68] include Sonogashira-Castro reactions,[69-71] hydroamination,[72] hydrocarboxylation,[73] click-reactions[74-75] or conjugate additions.[76]

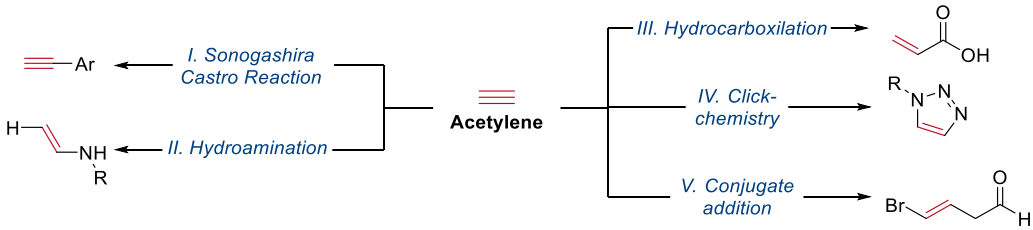

Scheme 1.2.1. I) Pd / Cu catalysis. II) Ti catalysis. III) Ni catalysis. IV) Cu catalysis. V) Pd catalysis.

Notably, the group of Prof. Shifa Zhu has recently contributed to a renaissance of the use of acetylene in catalytic processes. Zhu's team developed a series of catalytic methodologies for the transformation of acetylene into a diverse range of compounds. One of those procedures, published in 2021, is the 1,2-difunctionalization of acetylene *via* EnT by iridium-photocatalyzed radical thiol–yne coupling, enabling the use of acetylene as a C2 molecular glue (Scheme 1.2.2, a-b).[77] The protocol allowed macrocycles from 9 to 35 atoms in size to be ensembled in yields up to 42% (Scheme 1.2.2, a). Additionally, the intermolecular reaction, including phosphates as X-H donors, was also developed towards symmetric and unsymmetrical dihydrofunctionalization of the alkyne (Scheme 1.2.2, b). In the same year, the group of Zhu reported a similar strategy relying on a homolysis bond dissociation of α-oxocarboxylics with good reaction performance and broad scope (Scheme 1.2.2, c).[78] The C-C bond breaking driven by SET process leads to a ketyl radical that would attack acetylene. A second radical addition would then afford the desired saturated 1,4-diketone or the β-substituted heterocycle ketone. In addition to these 1,2-photocatalyzed difunctionalization reactions, Zhu reported a strategy for retaining the olefin, in contrast to previous works (Scheme 1.2.2, d).[79] The protocol was based on 4CzIPN photocatalysis and driven by Energy Transfer that promotes the homolytic cleavage of the S−X bond (X = S, O or Se).

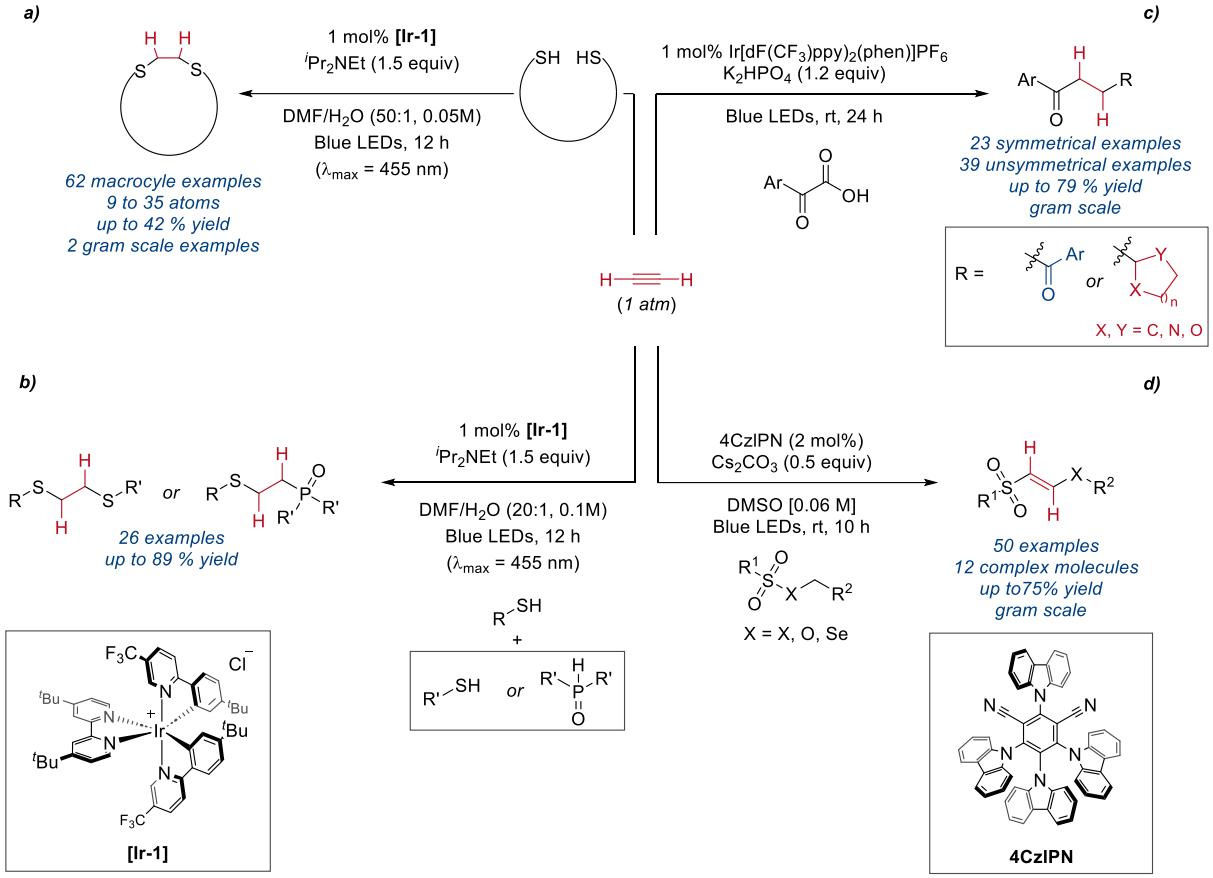

Scheme 1.2.2. Overview of photoredox catalysis for radical 1,2-difunctionalization of acetylene. a) Intramolecular Ir-photocatalyzed 1,2-dihydrofunctionalization of acetylene *via* EnT strategy. b) Intermolecular Ir-photocatalyzed 1,2-dihydrofunctionalization of acetylene *via* EnT strategy. c) Ir-photocatalyzed acetylene 1,2-dihydrofunctionalization via SET strategy. d) 4-CzIPN-photocatalyzed 1,2-difunctionalization of acetylene *via* EnT strategy.

Zhu's methodologies were successfully applied to the synthesis of tiamulin, an antibiotic for veterinary use; and Ombitasvir, an antiviral drug for hepatitis C virus infection (Scheme 1.2.3). Tiamulin was synthesized by using the thiol derivative of peuromutilin acid (a natural product from fungi Plerotus mutilus) as starting material, and the synthesis was accomplished in just a two-step sequence (Scheme 1.2.3, a). Regarding Ombitasvir, the reported synthetic pathway allowed to reach the target molecule in 6 steps (Scheme 1.2.3, b).

Alternatively, Zhu also developed organometallic catalyzed transformations of acetylene. One of those methodologies is the synthesis of vinyl alcohols using acetylene and aldehydes as starting materials, under nickel catalysis (Scheme 1.2.4, a).[80] The catalytic protocol yields allyl silyl ethers, which after a last step under mild TBAF conditions, the alcohol is obtained. Rh-based catalytic protocols were as well as developed to access polyenes (Scheme 1.2.4, b)[81] and of *E*-dienyl esters (Scheme 1.2.4, c)[82] Both methodologies involve the use of two acetylene molecules and were demonstrated to cover a diverse range of functionalities, including boronic esters, olefins, free alcohols, indoles, epoxides, phosphates or sulfones.

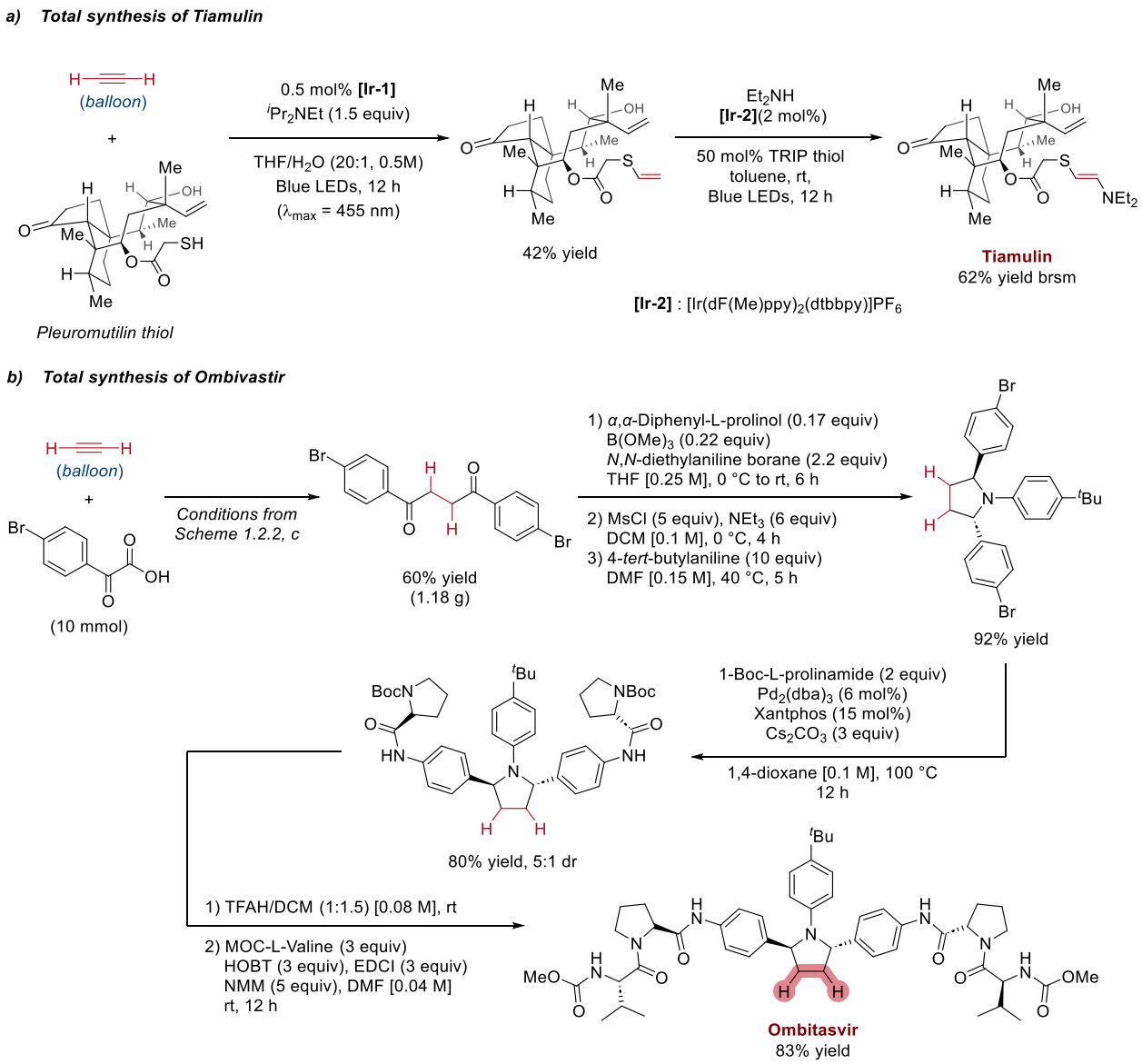

Scheme 1.2.3. Total synthesis of Tiamulin by Ir-catalyzed 1,2-dihydrofunctionalization of acetylene. BRSM = based on recovered starting material. TRIP thiol: 2,4,6-triisopropylbenzenethiol. b) Total synthesis of Ombitasvir. HOBT: 1-hydroxybenzotriazole hydrate. EDCI: *N*-(3-dimethylaminopropyl)-*N*'- ethylcarbodiimide hydrochloride. NMM: *N*-methylmorpholine.

Under conditions of acetylene trimerization with alkenes (Scheme 1.2.4, b), Shifa Zhu's group demonstrated the synthetic versatility through the formal synthesis of three natural polyenes such as FR252921, (+)-roxaticin and vitamin A (Scheme 1.2.5). The key step for all syntheses, after trimerization, is the cross-metathesis that leads directly to the desired polyene core from where, under already reported further transformations, the target products could be achieved. However, the requirement of using a large excess of the synthesized triene in the Grubbs I catalysis, could be considered as a major drawback in the synthetic route.

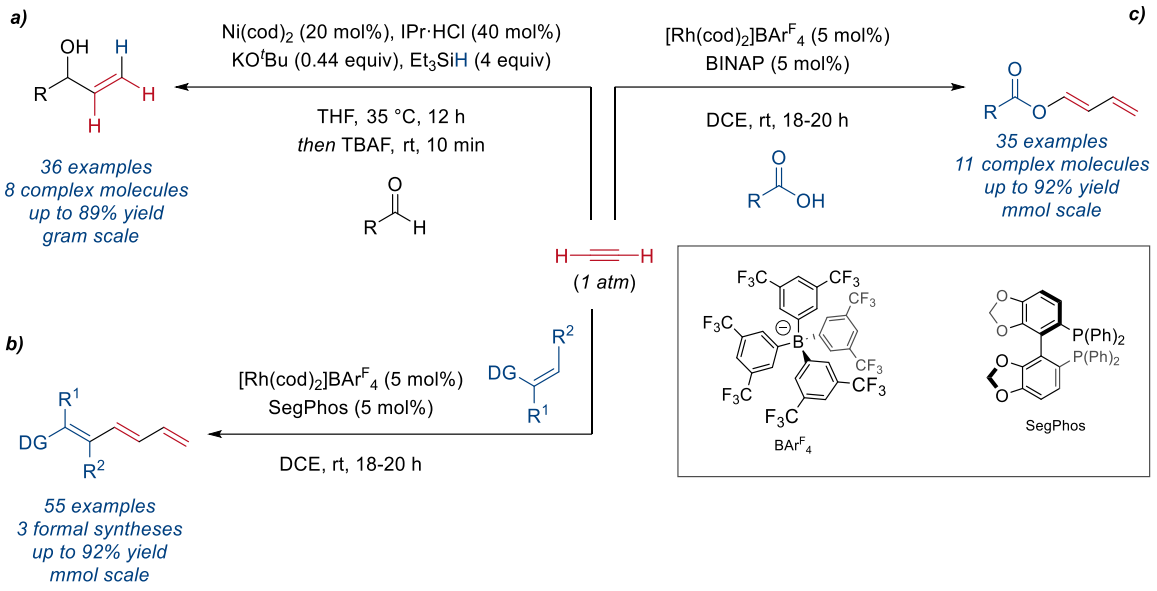

Scheme 1.2.4. Overview for organometallic catalyzed acetylene functionalizations. a) Ni-catalyzed synthesis of vinyl-substituted alcohols. b) Rh-catalyzed synthesis of trienes. c) Rh-catalyzed synthesis of *E*-dienyl esters.

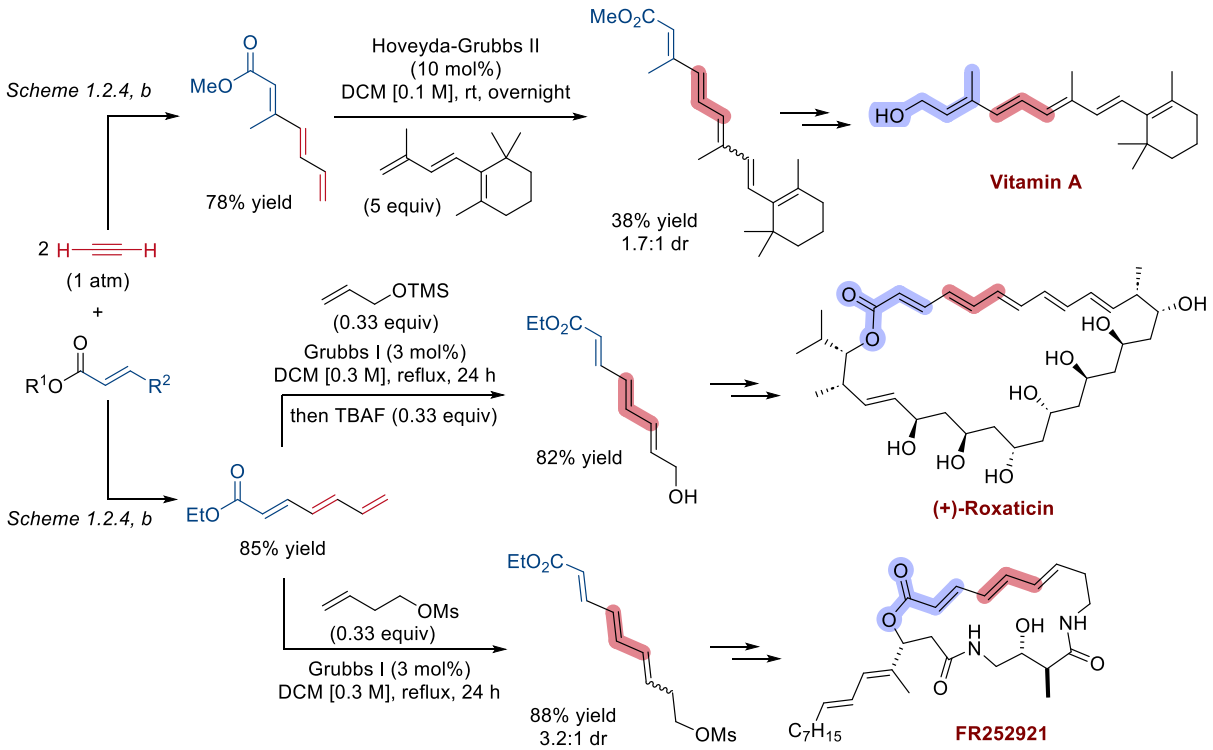

Scheme 1.2.5. Formal synthesis of Vitamin A, (+)-Roxaticin and FR252921 through Rh-catalyzed trimerization of acetylene and olefins.

On a different scenario, Zhu also reported a Cu-catalyzed carboboration of acetylene with Michael acceptors (Scheme 1.2.6).[83] The reaction was proposed to proceed via initial alkyne borylcupration (see section 1.1.1.3.1), followed by attack of the resulting alkenylcopper complex to the Michael acceptor, (see section 1.1.2), and final protonolysis of the σ-Cu intermediate. The above-described methodology has shown successful performing over a range

of substrates bearing internal and terminal alkynes (displaying excellent chemoselectivity), various heterocycles, free alcohols, and complex molecules such as Estrone or Indomethacin.

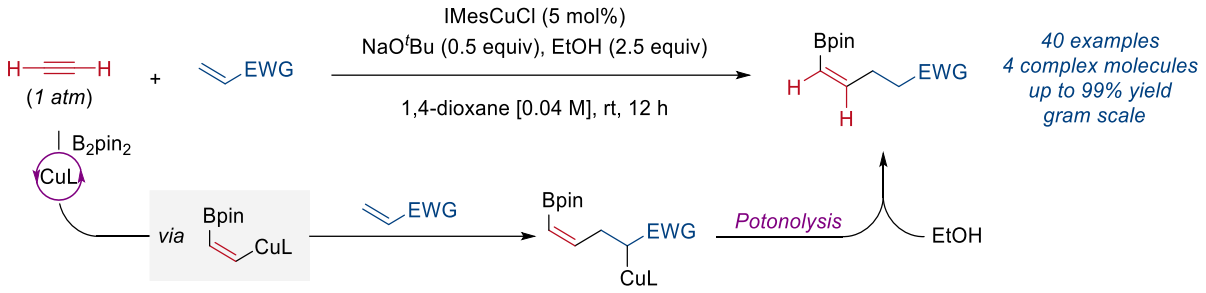

Scheme 1.2.6. Cu-catalyzed carboboration of acetylene with Michael acceptors.

In this field, it is also noteworthy to mention the contributions from the Echavarren group using acetylene in gold(I) catalysis. In 2020, they reported a gold-catalyzed coupling between acetylene and olefins that provideseither 1,3-dienes or biscyclopropyl compounds depending on the the gold catalyst that is used (Figure 1.2.7, a).[84] Acetylene is generated in situ by the reaction of calcium carbide with water, and directly bubbled into the reaction media. Moreover, the authors demonstrated the total synthesis of the natural product Waitziacuminone by reaction of acetylene with geranyl acetone (Figure 1.2.7, b).

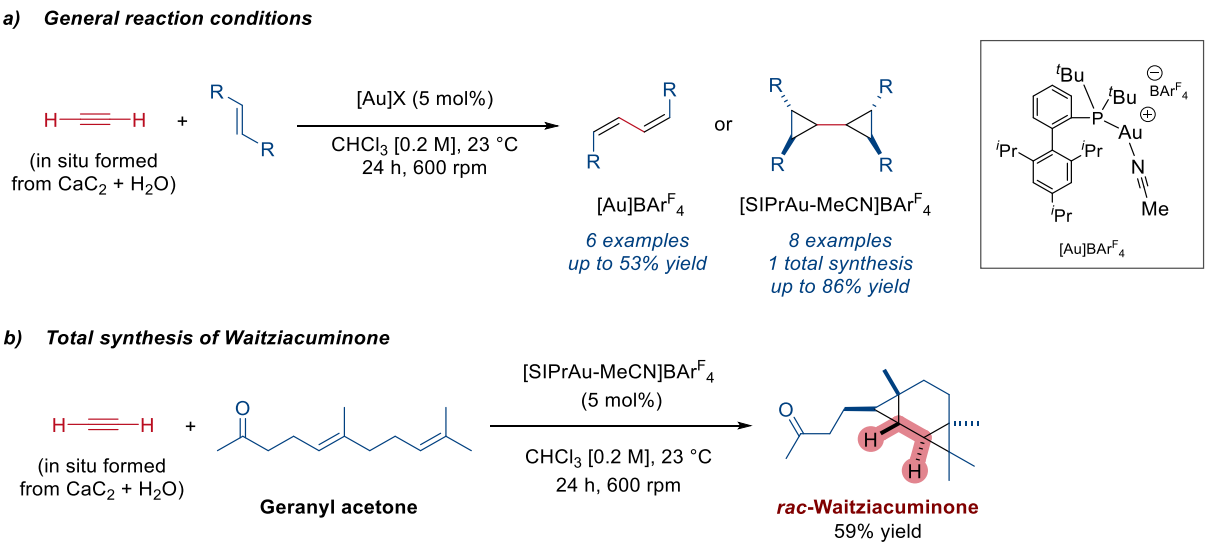

Scheme 1.2.7. Au-catalysis for acetylene usage as dicarbene. a) General reaction conditions. b) Total synthesis of *rac*-Waitziacuminone.

More recently, in 2024, Echavarren reported a three component reaction between acetylene, vinyl amides and alcohols that furnishes β-vinyl hemiaminals (Figure 1.2.8, a).[85] In the same work, they developed as well a complementary protocol to access *N*-heterocycles from amine-tethered alkenes (Figure 1.2.8, b). Those protocols are based on the formation of a gold(I)-carbene that later inserts into a double bond leading to complex scaffolds.

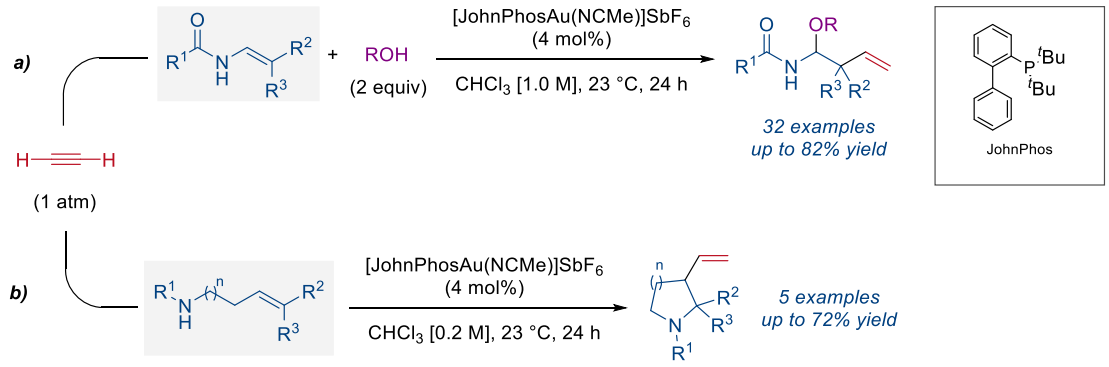

Scheme 1.2.8. Gold-catalyzed a) three-component alkoxyvynilation and b) amine cyclization.

1.2.2.1 Enantioselective catalytic protocols for acetylene functionalization

Despite the variety of catalytic functionalization reactions of acetylene, very few catalytic enantioselective transformations of acetylene gas have been described. In this field, the Krische group has contributed significantly. They developed the rhodium-catalyzed enantio- and diastereoselective reductive coupling of acetylene with aldehydes[86]or *N*-arylsulfonyl imines[87] (Scheme 1.2.9, a and b, repectively). Mechanistically, the reaction involves the formation of a 5-membered rhodacycle by acetylene dimerization. The catalyst would then coordinate the aldehyde (or imine). This coordination is required to discriminate between both faces of the coupling partner. Subsequent attack is therefore required to occur preferentially in one of the pro-*S* or pro-*R* faces, installing the configuration of the chiral center, forming through this process the new stereodefined 7-membered rhodacycle. At that point, carboxylic acid promotes a protonolytic cleavage of the X-Rh bond. Subsequent σ-bond metathesis with H_2 gas followed by reductive elimination, delivers the desired chiral diene and the starting rhodium(I) complex, to close the catalytic cycle.

This protocol was successfully applied to the synthesis of (+)-Trienomycims A and F, demonstrating the versatility and the opportunity that acetylene brings to the synthetic field.[88] In fact, that approach was useful to decrease the number of steps in the total synthesis of these compounds by enabling a new route for reaching carboxylic acid **Int27** in just 7 steps, in sharp contrast to the previously reported 12-step procedure (Scheme 1.2.9, c).

More recently, in 2023, the group of Prof. Echavarren reported a gold-catalyzed oxyvinylation reaction between ortho-allylphenols and acetylene gas (Scheme 1.2.10).[89] Although only moderate enantioselectivities were achieved, this work represented the first report of an enantioselective activation of acetylene under gold(I) catalysis. Regarding the reaction mechanism, the chiral gold catalyst would coordinate the acetylene and then the allylphenol with a preferential spatial orientation. Subsequent cyclopropanation would lead to a cyclopropyl gold(I)-carbene with defined stereochemistry, which reacts intramolecularly in a regioselective and stereospecific manner to form the 6-membered ring product.

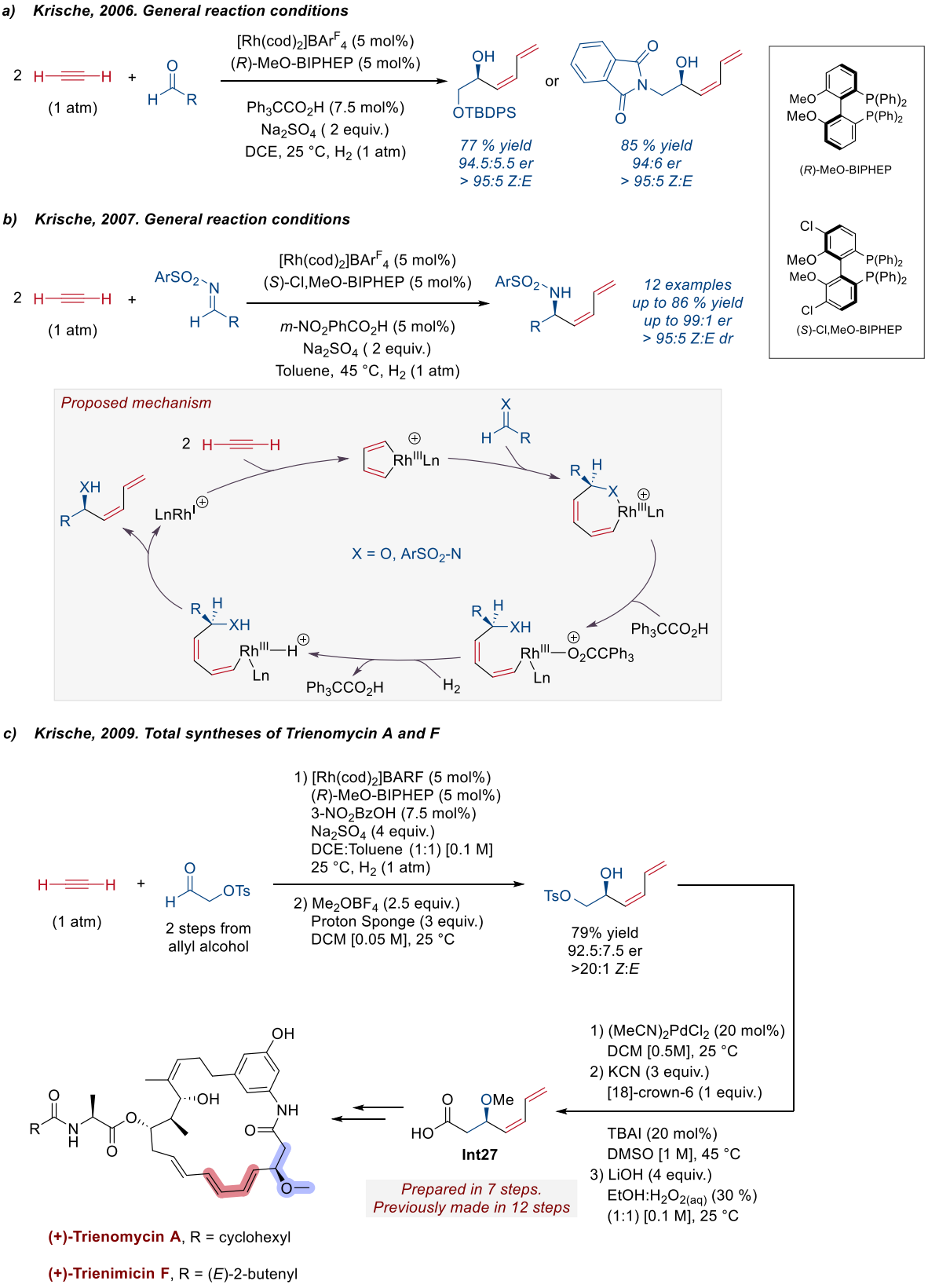

Scheme 1.2.9. Entioselective Rh-catalyzed reductive coupling of acetylene to a) aldehydes, b) *N*-arylsulfonyl imines and c) application in total synthesis.

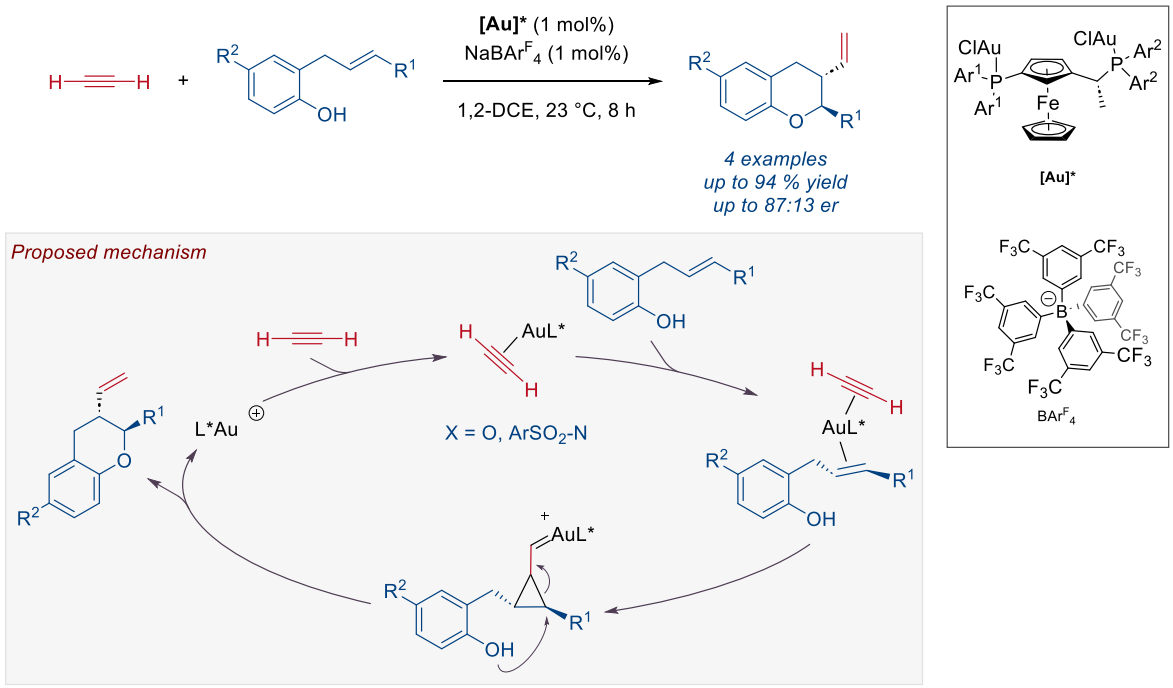

Scheme 1.2.10. Gold(I)-catalyzed intermolecular oxyvinylation between acetylene and o-allylphenols

1.3 ETHANE. GENERAL ASPECTS AND STATE-OF-THE-ART OF CATALYTIC FUNCTIONALIZATION REACTIONS.

Ethane (C_2H_6) is a naturally occurring hydrocarbon, present in many natural gas sources and in refinery gases, and it can be recovered for further industrial use.[90] After methane, is the second-largest component of natural gas and typically does not overcome the 10% in volume, varying this amount on the natural gas reservoir (Table 1.3.1).[91-93]

Table 1.3.1. Composition of Natural Gas from region.

	Groningen (Netherlands)	Arun (Indonesia)	Ekofisk (Norway)	Panhandle (USA, Texas)	Tenguiz (USSR)	Bidboland (Iran)
CH_4	81	75	85	73.2	42	85.0
C_2H_6	2.8	5.5	8.4	6.1	8.5	9.4
C_3H_8	0.4	2.3	5.9	3.2	5.2	3.5
C_3+	0.3	1.9	1.2	2.2	25.3	1.4
H_2S, N_2, CO_2	15.2	15.3	2.4	14.6	19.4	0.8

From a physical point of view, ethane is a colorless and odorless gas, slightly heavier than air, flammable, relatively inert and considered as nontoxic (Table 1.3.2).[90, 94] Chemically, due to their saturated character, nonpolar nature and lack of functional groups or any π-electrons, features a rather low reactivity. On basis on the Gibbs free energy formation energy (Table 1.3.1), ethane is thermodynamically stable.[90]

Table 1.3.2. Various physical properties of ethane.

Various physical properties of ethane	
Molecular mass	30.070 g/mol.
Density (gaseous C_2H_6 at 1 bar)	1.265 kg/m^3 (293.15 K)
Boiling point	-88.6 °C
Enthalpy of formation	-84.724 kJ/mol (298.15 K)
Gibbs free energy of formation	-32.908 kJ/mol (298.15 K)
Entropy of formation	229.646 J mol^{-1} K^{-1} (298.15 K)
Explosion limits	3.00 – 12.50 % volume of air (293.15 K)
Vapor pressure	3.750 MPa (294.25 K)
Bond dissociation energy (BDE)	101 kcal/mol

1.3.1 Industrial production and use of ethane

Ethane was first synthesized in 1834 by Michael Faraday,[95] and later in 1849 and 1850 by Hermann Kolbe[96] and Edward Frankland;[97] the three of them by electrolysis of aqueous acetates. However, the observed product was mistaken with methane (in Faraday's case) and methyl or ethyl radicals by Kolbe and Frankland. These errors were corrected in 1864 by Carl Schorlemmer by demonstrating that those reactions yielded, instead, ethane.[98]

Prior to the 1960s, ethane and the other larger molecules were typically not separated from methane in natural gas and simply burnt as a mixture for fuel purposes.[94] However, currently the trend has changed and ethane has become a relevant petrochemical feedstock and is separated from the other components For that, the main routes for ethane obtention are based on crude oil fractionation, thermal cracking of hydrocarbons, indirect liquefaction of coal and refining/gas processing.[90, 94]

1.3.1.1 Industrial applications

The far most important industrial use for ethane is the production of ethylene through steam-cracking process, which is then turned into plastics. However, due to ethane's stability, the process is endothermic and thermodynamically unfavorable and, therefore, cracking

temperatures typically are higher than for higher hydrocarbons (550–700 °C).[94, 99-100] The thermally-induced chlorination and oxychlorination of ethane is as well a highly commercialized process that can yield diverse chloroethanes or vinyl chloride, respectively.[99] The general availability of ethane from natural gas, has shifted the production of chlorinated C2 hydrocarbons from the classical carbide-acetylene-vinyl chloride route towards the ethylene route since World War II, however, since huge variations on gas natural prices over the last years, the old carbide route gained again some attention.[65, 99] Further application is found in the obtention of nitroethane and nitromethane via free-radical process by reacting ethane with nitrogen dioxide in the gas phase.[90, 101]

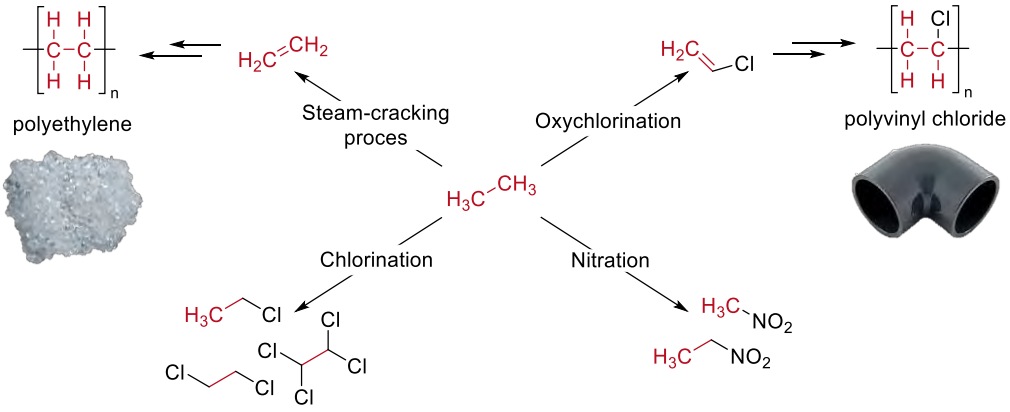

Figure 1.3.1. General overview of industrial transformations of ethane and representative products.

1.3.2 Homogeneous catalytic C−H functionalization of ethane

Due to the lack of functional groups and any π-electrons or vacant π* orbitals, reactions of saturated hydrocarbons are essentially limited to dehydrogenation or C-C cleavage (Figure 1.3.2).[90]

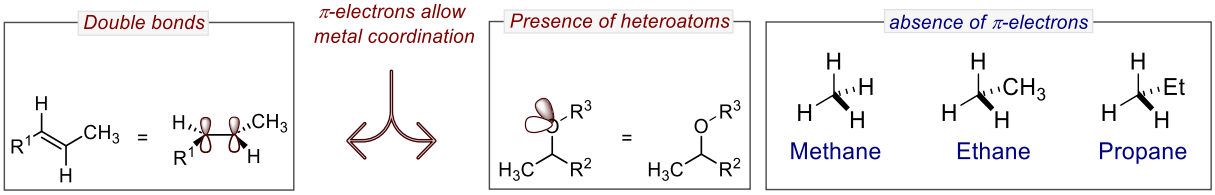

Figure 1.3.2. Key aspects to overcome in order to C-H functionalization of light alkanes.

However, from the first C−H activation of methane from Shilov by using Pt(II) catalyst for H/D exchange (1969), the field rapidly experimented a huge explosion during 70's to 90's decades with novel methodologies based on organometallic catalysts, where we can highlight the works from Bergmann, Wolczanski, Jones, Graham, Olah, Periana or Crabtree, among many other other relevant contributions.[102-104] Despite these groundbreaking advances, the finding of a suitable general methodology, or activation protocol, for gaseous alkanes has remained elusive for decades.

Carbon–carbon bond-forming reactions are central tools for the organic synthetic field since every organic molecule is made from them. One of the first reports forging Csp^3-$C_{sp}{}^3$ bonds with ethane, was the work developed by Asensio, Etienne and Pérez in 2011. The reported protocol takes advantage of the formation of carbene species whose later promotes the C−H activation (Scheme 1.3.1).[105] The methodology is based on a Ag catalyst that reacts with ethyl diazoacetate, leading to the silver carbene. The in situ formed complex reacts then with

ethane to deliver ethyl propionate, using supercritical CO_2 as solvent to avoid activation of solvent C–H bonds, by working in high-pressure reactors at 40 °C (total pressure = 250 bar). Moreover, catalytic loading is significantly low, with just 1 mol% of catalyst; at 1.5 mol scale and 35 bar of ethane.

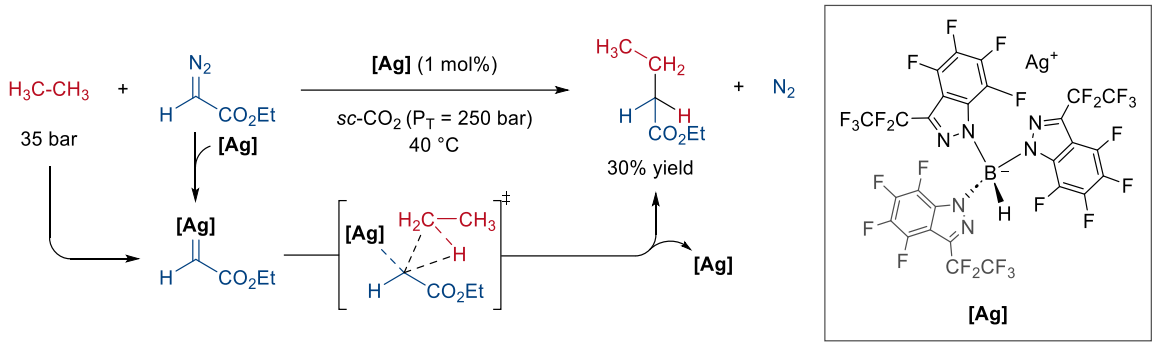

Scheme 1.3.1. Ethane C–H bond functionalization for C–C bond formation via carbene species under Ag-catalysis.

Another report was based on the direct borylation of its C–H bond. Borylation of liquid alkanes has previously reported under diverse conditions using Rh, Ru, Ir and even Re catalysis,[106-108] in 2016 the Sanford group reported the direct borylation of methane and ethane,[109] simultaneously with the group of Mindiola,[110] who just explored the reaction with methane. Sanford and coworkers demonstrated the excellent performance of the [Cp*Rh(η^4-C_6Me_6)] complex, in combination with B_2pin_2 in cyclohexane as solvent (Scheme 1.3.2). The direct borylation of ethane towards Et–Bpin was shown to display remarkable good yields and selectivity (solvent borylation constitutes almost negligible amounts), under 35 bar of pressure and 150 °C. It is noteworthy to highlight that choice of the catalyst was based on earlier computational studies by the group of Hall, proving the theoretical feasibility of the process.[111] Mechanistically, reaction would start with oxidative addition of the Rh^I-complex to the B_2pin_2, leading to a Rh^{III} bis(boryl) complex. Such 16-electron complex would promote a C–H agostic interaction, assisted by the unoccupied p-orbital on boron (**TS_{28}**), leading to the formation of the Rh^{III} ethyl boryl complex **Int28**, bearing a coordinated borane. This intermediate undergoes reductive elimination for B–C bond formation through multicentered transition state **$TS_{28\text{-}29}$** to release Et–Bpin, while subsequent oxidative addition of the coordinated borane takes place, leading to the Rh^{III} boryl hydride intermediate **Int29**. This species will then react with an additional B_2pin_2 molecule, releasing HBpin recovering Rh^{III} bis(boryl) complex.[107, 111]

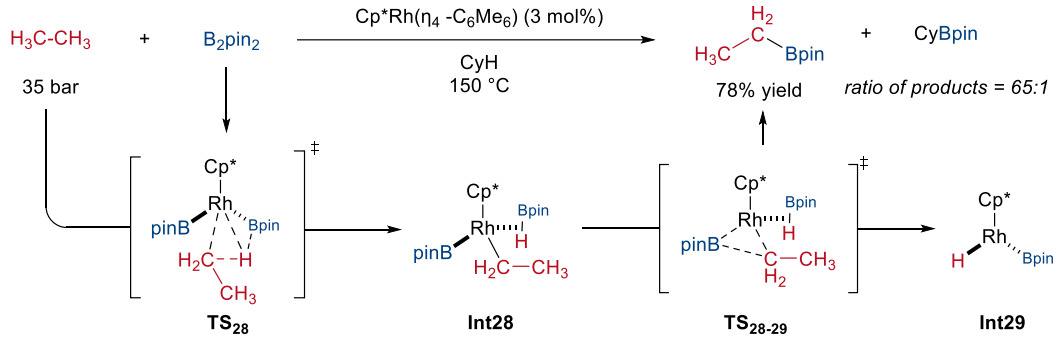

Scheme 1.3.2. Direct C–H borylation of ethane by Rh-catalysis.

Later on, in 2021, an extra protocol within the organometallic catalyzed functionalization of C–H bonds was published from Hong and Chang (Scheme 1.3.3).[112] The methodology was

based on a Co-catalyzed transformation of alkanes to *N*-alkyl carbamic acid ester derivatives. In the quest to assess the ethane activation, they reach the product albeit in poor yields, while requiring long reaction times, high catalyst loadings and 35 bar of pressure. Mechanistically, DFT calculations and EPR measurements illustrated that transformation evolves through a stepwise pathway involving cobalt-stabilized radical intermediates. Thus, it was found that two inter system crossing (ISC) events take place. Firstly (S_0-to-T) to promote the HAT, followed by a second (T-to-S_0) releasing the product and recovering the active catalyst.

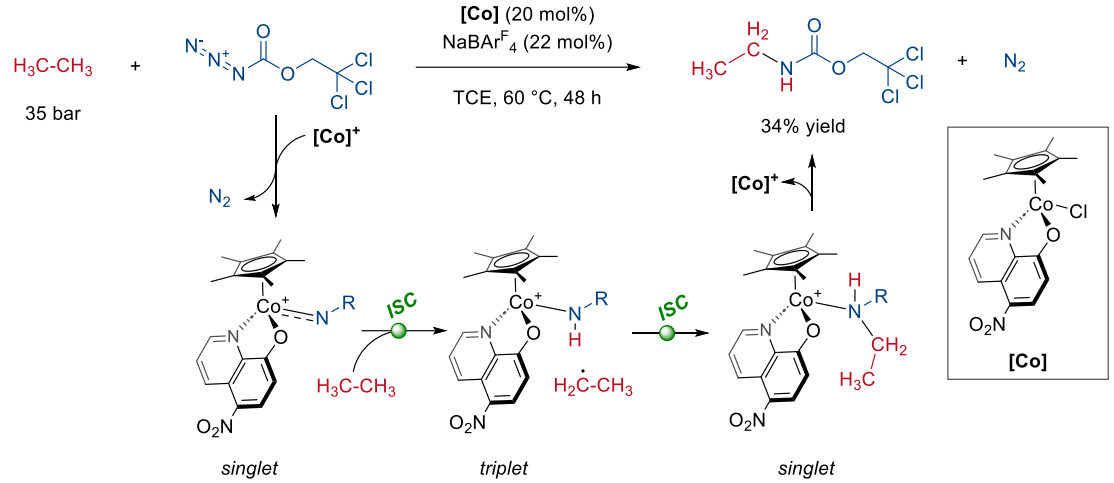

Scheme 1.3.3. Co-catalyzed C–H amination of ethane with *N*-alkyl carbamic acid ester.

Recently, in 2021, the groups of Hartwig and Pérez, reported a copper-catalyzed C–H amidation protocol based on the use of *tert*-butyl peroxide, both as oxidant and HAT reagent and CuI/Phenantroline complex as catalyst.[113] Ethane was susceptible to react under optimized conditions, requiring high temperatures in benzene (120 °C) and 35 bar of pressure. Alternatively, supercritical CO_2 could also be used in order to preclude side reactions derived from decomposition of the *tert*-butoxy radical, forming methyl radical which produces the *N*-methyl amide product. The amide nature was found to be critical for the reaction with amides bearing electron poor aryl rings being efficient in contrast to the ones featuring electron rich ones.

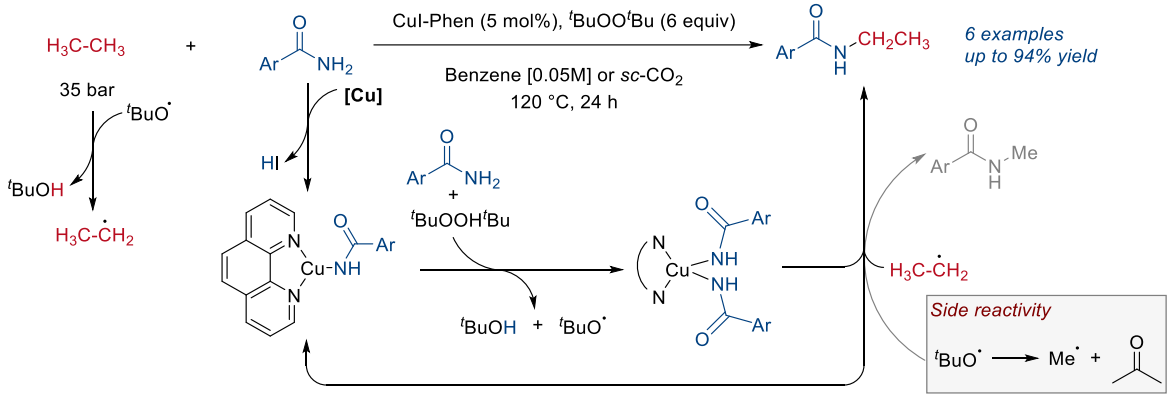

Scheme 1.3.4. C–H bond amidation of ethane by combination of Cu-catalysis and peroxides as HAT reagents.

Despite these great advances based on organometallic catalysis, a general and broadly applicable method for gaseous alkanes functionalization was still missing. However, some

years ago, photoredox HAT catalysis became extremely popular and a has also found its application in the functionalization of gaseous alkanes, via C−C bond formation.

1.3.2.1 Direct C−C bond formation via HAT photocatalysis

Since the first example by Crabtree and co-workers in 1993 by using Hg vapors,[114] several efforts have been made to develop catalytic and less hazardous protocols to promote C−C bond formation in alkanes. In this context, photocatalyzed HAT strategies have emerged as a potent methodology to abstract inactivated hydrogens atoms, leading to the formation of a C−centered radical.[115-117] Within this research field, two main methodologies to perform the HAT process can be defined: direct and indirect HAT.[118]

Direct HAT is based on the use of species that upon their excitation, they get the ability to abstract a hydrogen atom from the substrate, while indirect HAT are those that require an addition reagent, or catalyst, to their formation.[118] Molecules capable of promote direct HAT process are the polyoxometalate decatungstate (bearing well sodium or tetrabutyl ammonium as counter cation)[119-121] or benzophenone (and derivatives),[122-124] for instance (Figure 1.3.3, a). On the other hand, trichloromethyl or tribromomethyl radical (from SET of corresponding X_3CBr, X= Cl or Br),[125] quinuclidine radical-cation (from quinuclidine after oxidation via SET with an excited photocatalyst),[126] alkoxyl radicals (from LMCT with a metal)[127-128] and chlorine radicals (from LMCT with a metal or SET with an excited photocatalyst)[129] (Figure 1.3.3, b).

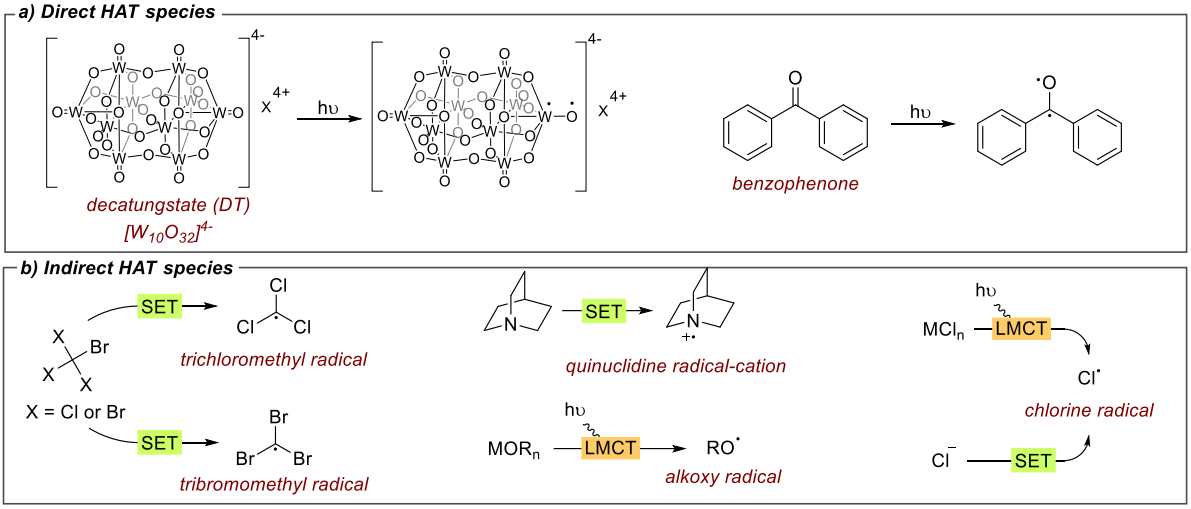

Figure 1.3.3. HAT species generated under photoredox conditions, classified in a) direct and b) indirect HAT species. X = tetrabutyl ammonium (TBA for TBADT) or Na (for NaDT).

1.3.2.1.1 Direct HAT photocatalysis

In 2020, Nöel reported the C−H functionalization of gaseous alkanes via a Giese radical addition to a range of Michael acceptors by combining TBADT photocatalysis with flow reactors (Scheme 1.3.5).[130] Regarding ethane activation, a pressure of 25 bar was necessary under irradiation by 60W 365 nm LEDs for a period of 8 h. Mechanistically, transformation was proposed to proceed as follows. Upon absorption of UV light, the decatungstate in the ground state is excited to the first singlet excited state (S_1). Subsequently, it rapidly undergoes a subsequent non-radiative transition by intersystem crossing reaching the first triplet excited state (T_1) − which would be the reactive species in the HAT step.[117, 120, 131] Therefore, the alkane reacts with TBADT(T_1) leading to the formation of the reduced photocatalyst and the

corresponding alkyl radical. This one would be trapped by the Michael acceptor forming the desired C−centered radical, that undergoes SET with the reduced photocatalyst affording the alkylated product (after protonation), leading to the regeneration of the active photocatalyst.

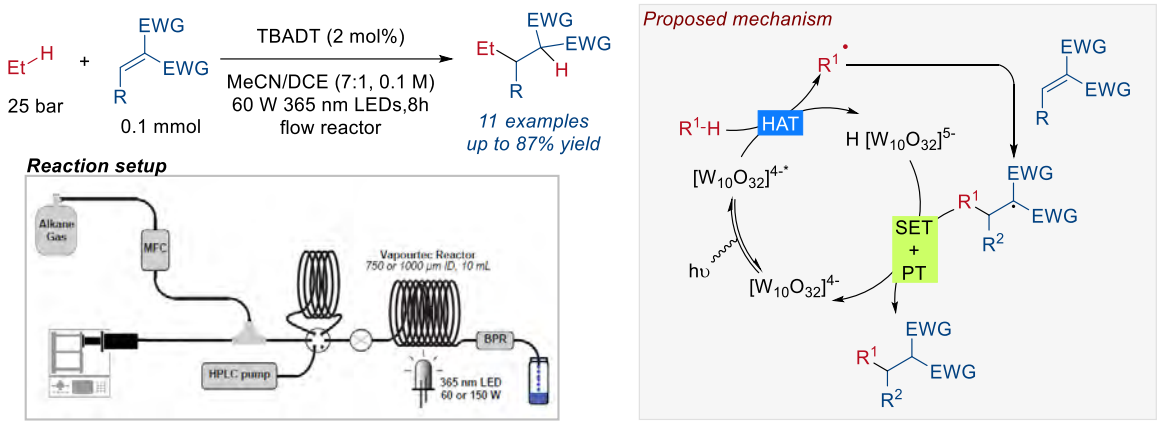

Scheme 1.3.5. TBADT catalyzed C-H functionalization of ethane with Michael acceptors under flow regime.

In a recent development, our group[132] and the one of Nöel[133] independently reported a cross-coupling of gaseous alkanes with aryl bromides via dual nickel/photoredox catalysis, under batch and flow regimes, respectively (Scheme 1.3.6). The two protocols illustrated the extensive applicability of the method to a diverse range of aryl and heteroaryl bromides. The group of Nöel performed kinetic isotope effect that reveal that HAT is not involved in the rate-determining step (RDS).[133] DFT calculations were performed to elucidate the actual RDS, which was identified as the oxidative addition step. Moreover, it was observed that smaller alkyl radicals led to higher activation barriers due to their lower donating ability, in comparison to higher alkyl moieties. Therefore, these last derived complexes would exhibit more stabilized orbital interactions (decreasing the HOMO-LUMO gap), enabling thereby a more efficient interaction with aryl bromides.[133]

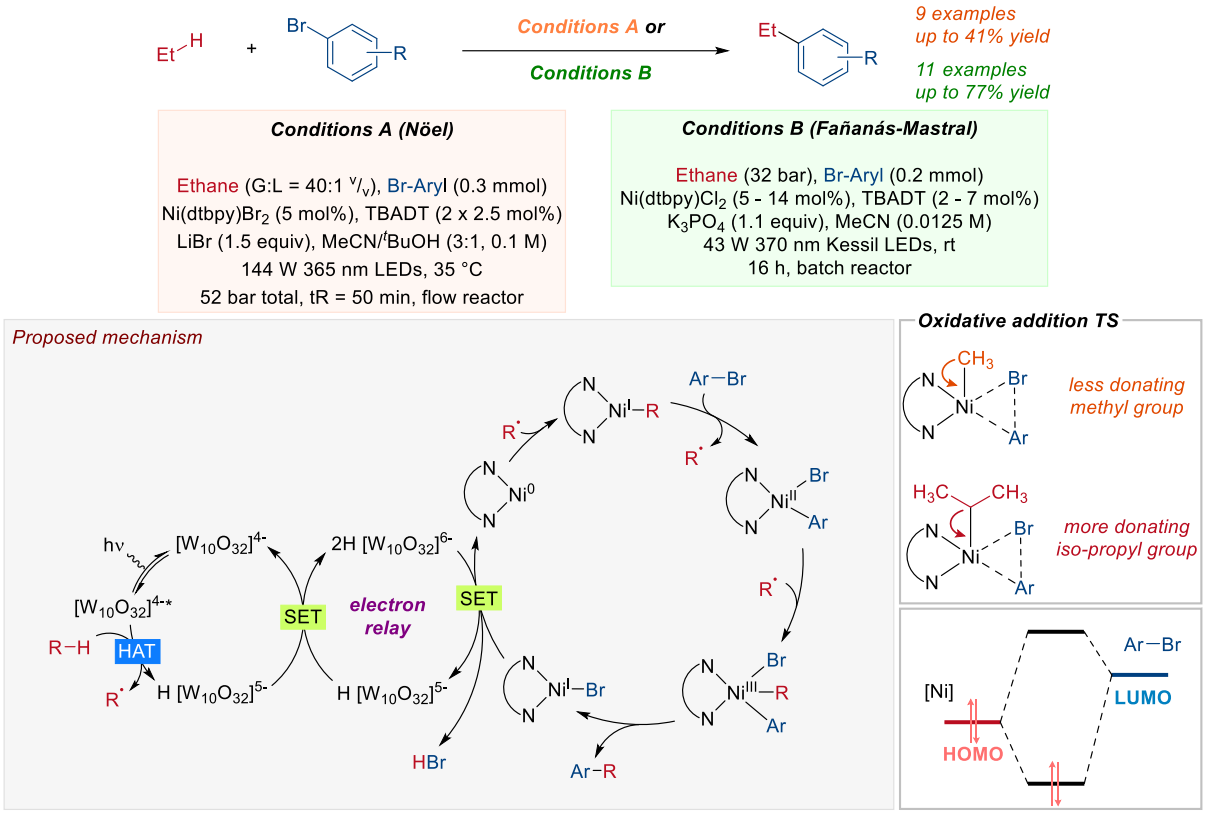

Scheme 1.3.6. Dual Ni/TBADT catalyzed C-H alkylation of (hetero)aryl bromides.

1.3.2.1.2 Indirect HAT photocatalysis

In 2018, the group of Zuo published a photocatalytic approach based on a combination of $CeCl_3$ catalyst and an alcohol, as co-catalyst, under 400 nm light irradiation.[134] Ethane was effectively used in Giese and Minisci-type reactions (Scheme 1.3.7, a) (Scheme 1.3.7, b) using Michael acceptors and isoquinolines as radical acceptors, respectively. The reaction was performed at 10 bar of pressure with a catalyst loading of just 5 mol% in a batch system. Similarly, the authors also reported a C–N bond formation by using diisopropyl azodicarboxylate as radical acceptor, resulting in the corresponding protected *N*-alkylated hydrazine in excellent yields. Mechanistically, after having conducted several thoroughly studies,[135] transformation was proposed to proceed by formation of a Ce(IV)-alkoxide complex ($[Ce(OR)Cl_5]^{2-}$), which then undergoes photoinduced LMCT. This leads to the selective formation of alkoxy radical (RO•), which is responsible for the rate-limiting alkane hydrogen atom abstraction. Subsequently, an alkyl radical addition to the Michael acceptor would form a new carbon centered radical, which would then react with the Ce(III) intermediate through a SET process, yielding the final product with concomitant regeneration of the active Ce(IV) catalyst.

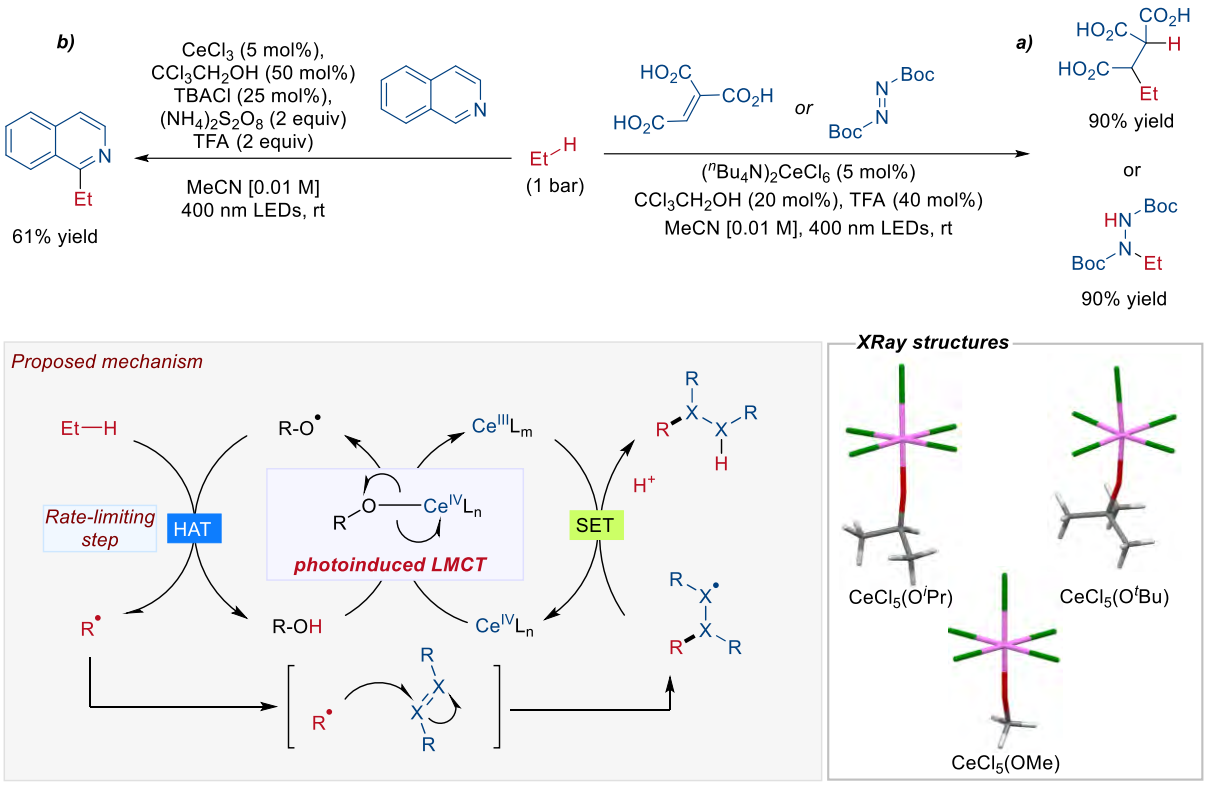

Scheme 1.3.7. Ce-catalyzed functionalization of ethane using alcohols as HAT reagents for C–C and C–N formation, and mechanistical proposal. Crystallographic data obtained free of charge from The Cambridge Crystallographic Data Centre.

Right after, Schelter and coworkers reported a similar approach, based on $CeCl_3$ catalyst, yet the use of alcohol as co-catalyst was not required at all.[136] Through the course of their investigation, the authors were quite critical with the mechanistical proposal from Zuo's group. The Schelter laboratory demonstrated that $[NEt_4]_2[CeCl_6]$ – in the absence of alcohol co-catalyst − was able to perform in excellent yields when reacting ethane with diisopropyl azodicarboxylate under 460 nm LEDs irradiation and 10 bar of pressure, after 48 h. According to their findings, HAT process is driven by Cl• and involvement of alcohol is completely dispensable. Furthermore, by performing severe and rigorous studies, in combination with DFT calculations, they attributed the role of alcohol to the formation of charge-transfer complexes such as [Cl−OHR]•. Nevertheless, later studies from the Zuo laboratory proved the actual involvement of the alkoxy radical due to the observed regioselectivity C−H activation onto diverse alkanes with and without the presence of alcohol.[135] It is worthy to note that, additionally, a combination of experimental and DFT mechanistic insights revealed that, while HAT process involving chlorine radicals occurs in a barrierless manner, when alkoxy radicals participate as HAT agents the elemental step becomes the rate-determining step (KIE = 5.5). Moreover, the researchers were also able to isolate and study different Ce-alkoxy complexes to further prove their involvement in the reaction (Scheme 1.3.7).

Additionally, in 2018, the group of Wu reported the functionalization of alkanes using HCl as a HAT catalyst precursor.[137] This reaction illustrated about the generation of new C–C bonds was demonstrated through a Giese-type reaction with Michael acceptors, using a stop-flow microtubing reactor (Scheme 1.3.8), requiring 20 bar of ethane. The generation of Cl• comes from reaction of Cl^- with the photoexcited Mes–Acr photocatalyst. The hydrogen atom abstraction resulted in the origin of a carbon centered radical which later reacts with the

Michael acceptor, leading to the generation of a new carbon radical. This undergoes SET with the reduced photocatalyst to regenerate the active species. The final protonation with HCl delivers the desired product and releases the chloride anion. The scope of electrophiles was limited to activated Michael acceptors with some installed functionality such as free carboxylic acids, phthalimides, alkyl chains or heterocycles.

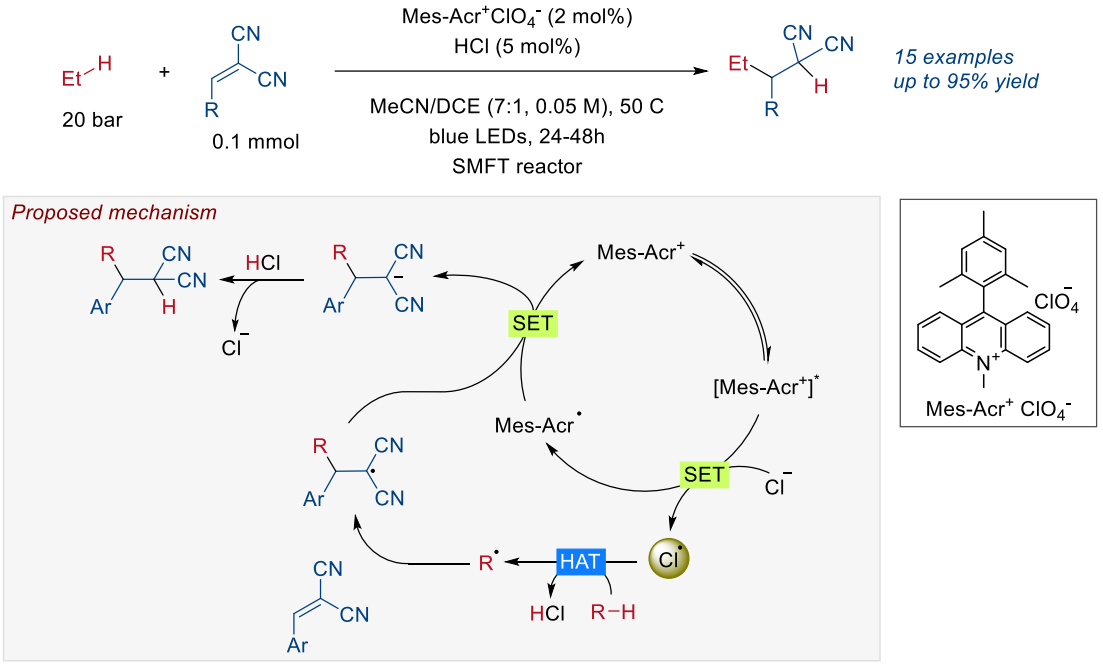

Scheme 1.3.8. Mesityl-acridinium catalyzed hydroalkylation driven by HCl as HAT catalyst in SFMT reactor.

Later, in 2022, the same group applied a similar protocol to perform Minisci-like reactions.[138] Reaction conditions required the use of [MesAcr+][ClO_4^-] together with diphenyl phosphate (Scheme 1.3.9). This transformation involves the participation of O-centered radicals, formed over the phosphate via SET with the excited photocatalyst, instead of the generation of Cl• as reported in previous work.[137] The presented methodology required higher catalyst loadings and longer reaction times. Furthermore, the use of a more potent LED light was also required for achieving optimal performance, and the transformation was shown to proceed with a variety of heteroaryl substrates (Scheme 1.3.9).

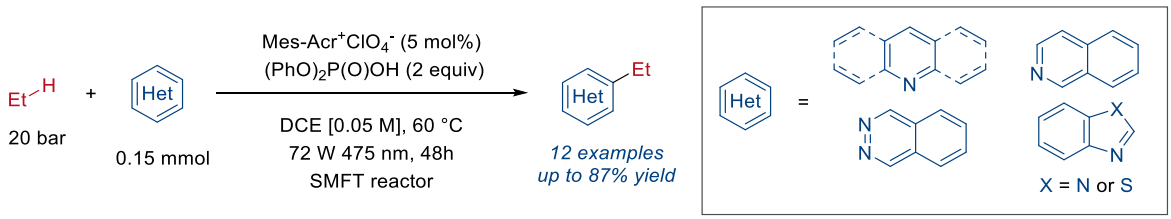

Scheme 1.3.9. Mesityl-acridinium catalyzed heteroarylation of ethane driven by $(PhO)_2P(O)OH$ as HAT reagent in SMFT reaction.

The group of Jin and Duan published in 2021 an iron-catalyzed functionalization of alkanes with Michael acceptors (Scheme 1.3.10, a),[139] and they subsequently expanded the methodology on a later work in 2022.[140] In the cases of ethane functionalization, a catalyst loading of 3 mol% was required, along with 800 rpm in MeCN at ambient temperature and pressure. However, some challenging substrates required the use of higher pressures (20 bar).

In terms of scope, the methodology was successfully applied to a variety of radical acceptors bearing pyridines, cyano groups, chlorines, amides and esters, as well as complex glycylglycine derivative, displaying good to excellent yields. Additionally, they provided examples of C–N formation with diazocarboxylates as coupling partners, including two discrete examples displaying excellent yields (Scheme 1.3.10, b).[139] Mechanistically, the transformation is initiated by the photoexcitation of the Fe(III)–Cl complex to [Fe(III)–Cl]* under UV-A irradiation. Subsequent homolysis of the Fe–Cl bond provides the Cl˙, which then reacts with the corresponding alkane to furnish the alkyl radical. This radical undergoes a Giese-type reaction to obtain a new C-centered radical which, after a SET process, provides the carbanion and regenerates the Fe–Cl active species. Finally, protonolysis gives rise to the desired product. DFT calculations identified the excitation of the photocatalyst as the rate-determining step, while radical trapping by the Michael acceptor occurs through a barrierless step.[140] Experimental measurements showed that the photocatalyst eventually degrades under continuous 365 nm irradiation, yet no further insight was gained.[139]

Moreover, the same research group also reported a direct alkynylation of alkanes using ethynyl phenyl sulfones (Scheme 1.3.11) based on the same LMCT strategy with $FeCl_3$.[141] The reaction was shown to proceed with ethane, but only one example was included, displaying a moderate yield. Regarding reaction mechanism, this process differs slightly from the previous (Scheme 1.3.10). The formed alkyl radical after the HAT reacts with the alkyne *via* α-addition, followed by a sulphonyl radical elimination to release the desired alkynylated product. The sulphonyl radical then reacts *via* a SET process with Fe(II) species, thereby restarting the iron catalytic cycle. The proposed mechanism was validated through a combination of experimental studies and DFT calculations.

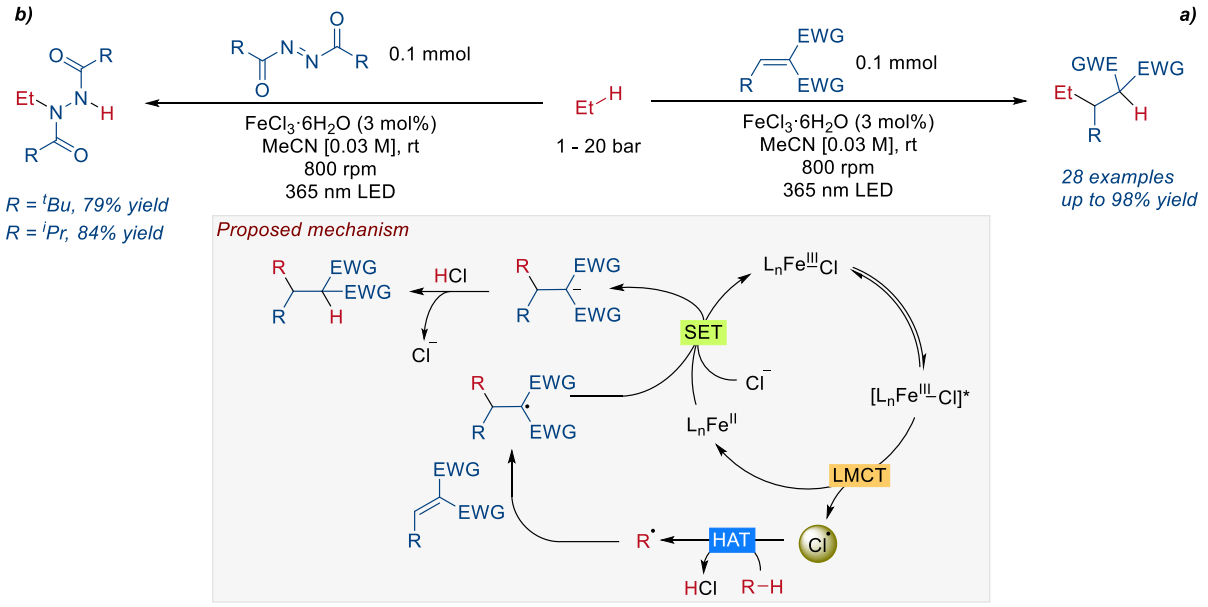

Scheme 1.3.10. Iron-catalyzed functionalization of alkanes enabled by LCMT Cl• generation for C–C and C–N formation, and mechanistic proposal.

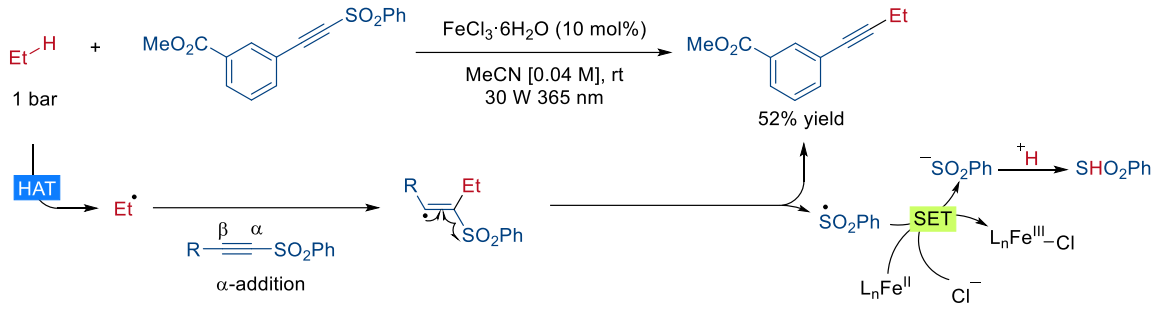

Scheme 1.3.11. Iron-catalysed alkynylation of alkanes enabled by LCMT Cl• generation for C–C bond formation

Schelter and co-workers reported the reactivity of dianionic species $Ti(IV)Cl_6^{2-}$ in $C(sp^3)$–H bond functionalization of light alkanes, including two examples of ethane (1 bar) with good yields (Scheme 1.3.12).[142] Moreover, it is noteworthy to highlight that $[PPh_4]_2TiCl_6$ was found to be significantly more air and moisture stable than current $TiCl_4$. UV-Vis experiments indicated that photoexcitation into the LMCT band of $Ti(IV)Cl_6^{2-}$ (390 nm, yellow solution) leads to the excited complex, which evolves towards a new species exhibiting an absorbance maximum at 685 nm, accounting for the blue color. The formed species $[Ti(III)Cl_4(MeCN)_2]^-$ could be fully characterized by X-ray diffraction. Additionally, an extra intermediate $[Ti(III)C_5(MeCN)]^{2-}$ that would be in equilibrium with the previous one, according to DFT calculations, could be isolated. Further measurements and computational results corroborated that irradiation of the complex at 390 nm leads to the excited complex. Upon vibrational relaxation, the formation of Cl• in combination with $Ti(III)Cl_5^{2-}$ takes place. Cl• promotes the HAT and after alkyl radical addition to the electron-deficient olefin, the resulting organoradical undergoes SET with $Ti(III)Cl_5^{2-}$, leading to $Ti(IV)Cl_5^-$ and the corresponding carbanion. The product is protonated with *in situ* formed HCl, yielding the product and photoactive $Ti(IV)Cl_6^{2-}$ catalyst regeneration.

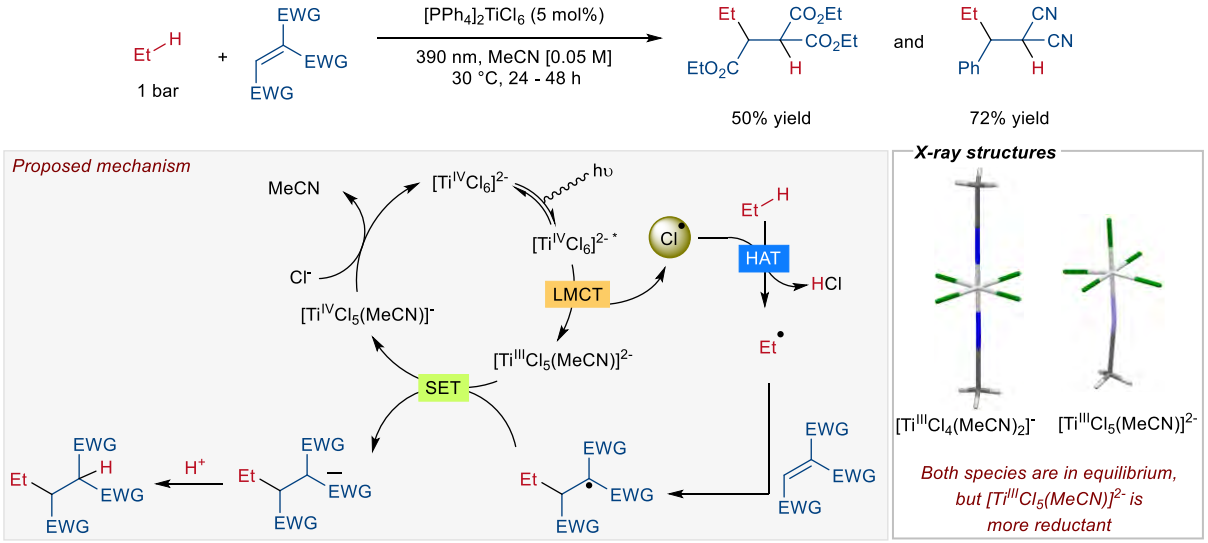

Scheme 1.3.12. $[PPh_4]_2TiCl_6$-catalysed functionalization of alkanes for C–C bond formation. Crystallographic data obtained free of charge from The Cambridge Crystallographic Data Centre.

In the same year, Gong and coworkers developed a methodology based the use of catalytic amounts of $FeCl_3$ and HCl as effective catalytic system towards activation of light and gaseous alkanes for their reaction with Michael acceptors.[143] Kinetic dependence of the [HCl]/[$FeCl_3$] ratio revealed that with a 20:1 ratio the reaction rate was enhanced by one order

of magnitude, due to increasing to the maximum the amount of photoactive $[FeCl_4]^-$. Regarding scope, ethane was just used for one example displaying moderate yield, while requiring 2 bar pressure (Scheme 1.3.13, a). Mechanistic studies of the transformation were conducted in order to gain deep insight into the reaction course. By competing between toluene and toluene-d_8, they observed a small, almost negligible, kinetic isotope effect, suggesting therefore that aliphatic C−H bond cleavage (HAT process) might not be involved in the rate-determining step (Scheme 1.3.13, b). Similar than Jin and Duan,[139] it was observed that under continuous irradiation in presence of cyclohexane, absorption spectra of $[FeCl_4]^-$ was gradually attenuated, being attributed to the formation of the chlorine radical and the reduced $[FeCl_3]^-$ species *via* the LMCT process. Thereby, radical C−H chlorination led to formation of chlorocyclohexane, detected by gas chromatography-mass spectrometry (GCMS) (Scheme 1.3.13, c).

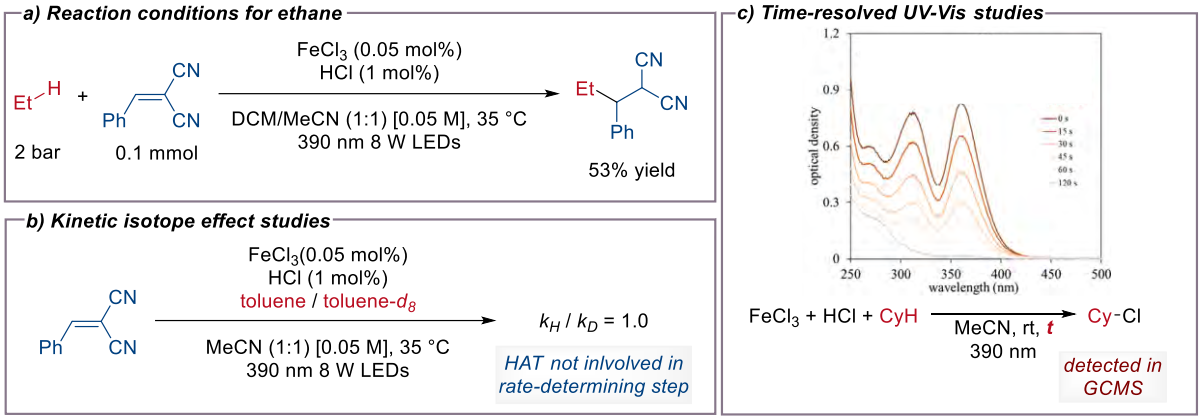

Scheme 1.3.13. $FeCl_3$/HCl catalyzed C–H functionalization of ethane with Michael acceptors and mechanistic studies. Time-resolved UV-Vis experiments graph were extracted with permission from ref [139]. © 2022 Elsevier Inc.

More recently, in 2024, our group reported a hydroalkylation of trifluoromethyl alkenes *via* photocatalytic coupling with alkanes, by using $FeCl_3 \cdot 6H_2O$ as HAT photocatalyst (Scheme 1.3.14).[144] The published protocol required the use of 30 bar of ethane while using very diluted reaction conditions – compared with previous examples – for achieving excellent performance, under 390 nm 52 W Kessil LED lamp irradiation. Mechanistically, it would perform through a similar pathway to previously exposed Giese additions. Radical attack to the olefin would form a tertiary stabilized C-centered radical. This undergoes SET with the reduced Fe(II) photocatalyst to regenerate the active Fe(III) species. The final protonation with HCl delivers the desired product and releases the chloride anion.

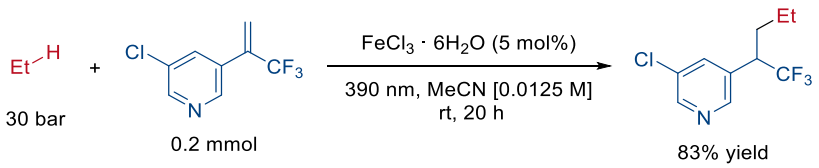

Scheme 1.3.14. $FeCl_3$-catalyzed ethane hydroalkylation of trifluoromethyl alkenes.

2 OBJECTIVES

The main objective of this thesis project is the development of new methodologies through metallic catalysis that allow the valorization of underutilized C2 gaseous molecules, such as acetylene and ethane. Such methodologies will combine the chemoselective activation of the C2 hydrocarbon towards reacting with an allylic substrate, either by homogeneous organometallic or photoredox catalysis, so molecules can react through an allylic substitution pathway to achieve functionalized olefins from simple building blocks.

In addition to reaction development, the thesis project also focused on study and understanding the reaction mechanisms of the developed transformations, as well as narrowly related reactions. Such studies will combine computational tools with experimental techniques, including DFT calculations and derived analysis, kinetic measurements and identification of the role of various involved species in the reaction.

To further achieve the proposed general objective, several subobjectives (**SO**) were identified and considered in the course of this thesis project:

- **SO1.** Study the reaction mechanism of Cu-catalyzed enantio-, diastereo-, regio- and chemoselective allylboration of alkynes and allenes with allylic *gem*-dichlorides. Current **SO1** would be focused on the establishment of relation between reaction outcomes and the effect of the ligand and base identity. For achieving the proposed **SO1**, DFT calculations and related analysis of the structures obtained would be performed.

- **SO2.** Development, application and mechanistic analysis of Cu-catalyzed enantio-, diastereo-, regio- and chemoselective acetylene allylboration reaction. Current **SO2** would seek for the upcycle of acetylene as C2 building block towards the access of complex densely functionalized molecules through a multicomponent reaction. Given the limited application found within the context of enantioselective transformations, open novel asymmetric routes for its transformation is highly desired. Moreover, obtained scaffolds would be undergone to synthetic modifications to reach high-value molecules such as natural products or advanced intermediates in total syntheses. Furthermore, DFT calculations based on **SO1** results would be performed to elucidate how the smaller size of acetylene gas determines reaction selectivity.

- **SO3.** Development, application and mechanistic analysis of $FeCl_3$ photorredox HAT catalyzed direct Csp^3-Csp^3 allylation of ethane. Proposed **SO3** would be oriented for the direct C−H functionalization of ethane under mild conditions for accessing synthetically attractive olefins. Due to the limitation of the showed methodologies to mainly Giese-type additions, enable new reactivity modes would promote its transformation in a wider range of substrates. Moreover, to prove the versatility of the obtained molecules, synthesis of added value would be performed. In addition, mechanistic studies would be performed in order to elucidate the reaction nature, and which are the main regulatory factors for reaction course.

3 RESULTS AND DISCUSSION

3.1 DFT MECHANISTIC ANALYSIS OF THE ENANTIO- AND DIASTEREOSELECTIVE COPPER-CATALYZED ALLYLBORATION OF ALKYNES AND ALLENES WITH ALLYLIC *GEM*-DICHLORIDES*

*The results from this section have already been published:

Andrea Chaves-Pouso,[a] Andrés. M. Álvarez-Constantino,[a] Martín Fañanás-Mastral.[a] Enantio- and Diastereoselective Copper-Catalyzed Allylboration of Alkynes with Allylic *gem*-Dichlorides. *Angew. Chem. Int. Ed.* **2022**, *61*, e202117696. (DOI: 10.1002/anie.202117696)

Martín Piñeiro-Suárez,[a] Andrés. M. Álvarez-Constantino,[a] Martín Fañanás-Mastral.[a] Copper-Catalyzed Enantioselective Borylative Allyl–Allyl Coupling of Allenes and Allylic *gem*-Dichlorides. *ACS Catal.* **2023**, *13*, 5578-5583. (DOI: 10.1021/acscatal.3c00536)

[a] Centro Singular de Investigación en Química Biolóxica e Materiais Moleculares (CiQUS), Universidade de Santiago de Compostela, 15782, Santiago de Compostela, Spain

The use of secondary 1,1-disubstituted allyl substrates has a limited presence in literature. In fact, few works have reported their use in copper-catalyzed allylic alkylation. Most of these examples focused on the use of Grignard reagents, while control over the diastereoselective formation of the resulting internal double bond represents a major issue. As depicted in Figure 3.1.1, the use of 1,1-disubstituted allyl substrates implies the presence of a racemic mixture and, therefore, multiple Cu-intermediates can be formed under reaction conditions, which can lead to (*Z*,*R*), (*Z*,*S*), (*E*,*R*) and (*E*,*S*) products. Selectivity towards Cu-coordination and subsequent oxidative addition might arise from steric interactions between the chiral ligand and allyl substituents. Therefore, controlling the reactivity of each pro-*Z* and pro-*R* substrates, as well as the face from where oxidative addition takes place, constitute a major challenge when dealing with this kind of allylic substrate.

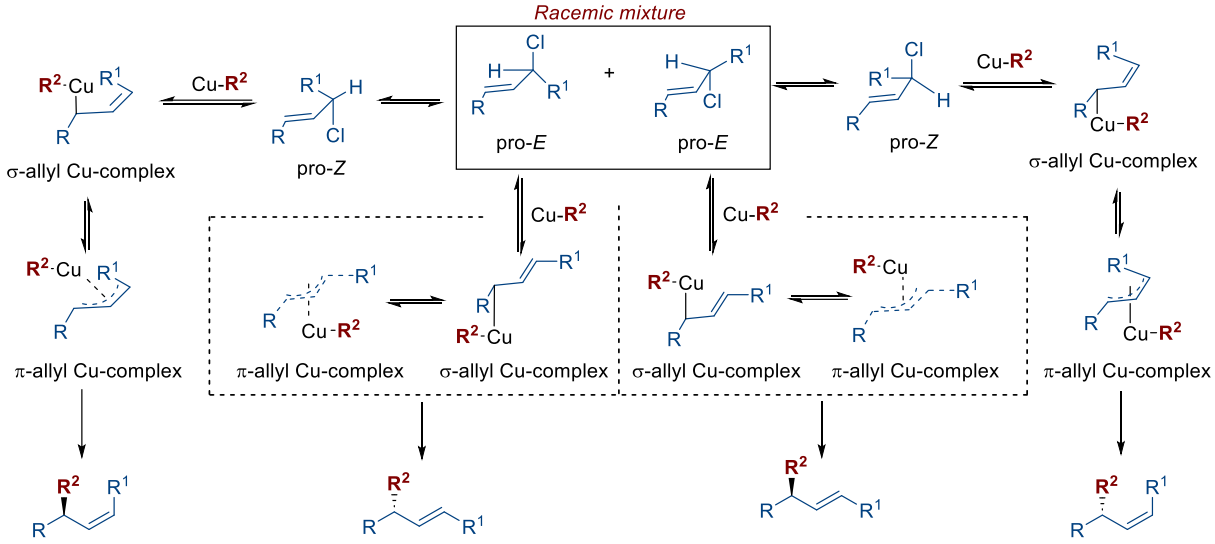

Figure 3.1.1. General reaction mechanism for copper-catalyzed allylic alkylation of secondary allylic leaving groups, involving all the isomerization routes and intermediates along the reaction pathway

Feringa and Fañanás-Mastral reported in 2010 a formal enantioselective conjugate addition of Grignard reagent to α,β-unsaturated aldehydes which was based on the in situ conversion of aldehydes into allylic α-haloacetates by using AcCl and $ZnCl_2$, followed by copper-catalyzed allylic alkylation in the presence of a Grignard and chiral phosphoramidite as ligand **L1***, leading to a chiral enol acetate (Scheme 3.1.1).[145] Very good enantioselectivity was generally observed, with good levels of *Z*-selectivity albeit it was compromised in some cases when using more challenging crotonaldehyde (66% *Z*) – preserving the high enantioselectivity (92% ee) – or MeMgBr (87% *Z*).

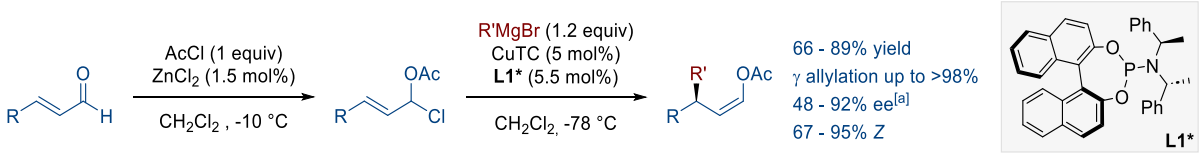

Scheme 3.1.1. Copper-catalyzed allylic alkylation of allylic α-haloacetates. a) Enantiomeric excess was measured in the corresponding aldehyde after hydrolysis of the AcO- in basic media.

One year later, Alexakis and colleagues published the use of secondary allylic chlorides in allylic alkylation under copper catalysis, along with a phosphoramidite ligand **L2***, using Grignard reagents as nucleophiles to reach branched chiral structures (Scheme 3.1.2).[146] However, despite the good to excellent enantioselectivity, almost equimolar amounts of *Z*:*E*

configuration was obtained. These results would be derived from the possibility of a parallel kinetic resolution, where Cu-complex only recognizes one of the faces (*Si* or *Re*) but has no preference towards coordination of pro-*E* or pro-*Z* intermediates.

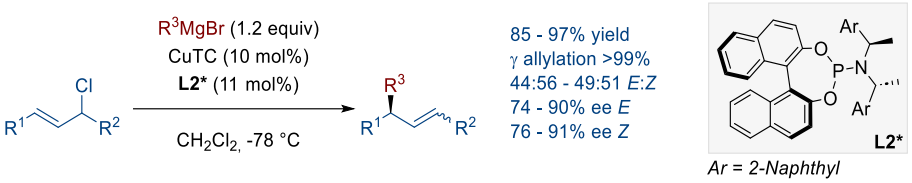

Scheme 3.1.2. Copper-catalyzed allylic alkylation of secondary allylic chlorides.

In addition to these works, in 2012, the Feringa group reported a new protocol involving allylic *gem*-dichlorides (Scheme 3.1.3).[147] Similar than previous works, reaction conditions consisted on the use of a copper catalyst featuring a chiral phosphoramidite **L3***, and Grignard reagents as nucleophiles. This new class of substrates afforded excellent *Z*-selectivity along with excellent enantioselectivities.

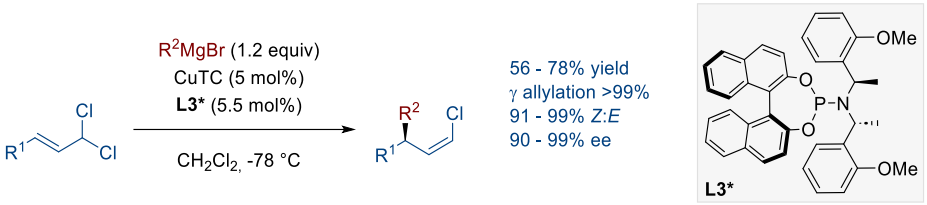

Scheme 3.1.3. Copper-catalyzed allylic alkylation of allylic *gem*-dichlorides.

The use of this new class of substrates provided chiral building blocks that were shown to be highly versatile substrates for subsequent functionalization reaction through Suzuki cross-coupling reactions, leading to optically active *Z*-alkyl- and aryl-substituted alkenes.[147]

Due to the excellent results obtained, we envisioned the use of allylic *gem*-dichlorides in a copper-catalyzed asymmetric borylative coupling with alkynes and allenes to efficiently provide chiral densely functionalized dienes bearing a *Z*-alkenyl chloride and a trisubstituted stereodefined alkenyl boronate. The fact that the C−C and C−B bond formation require high chemo-, regio-, enantio- and diastereoselectivity while establishing one stereocenter and two stereodefined internal olefins makes this method significantly challenging. Moreover, the successful realization of this idea would represent a new synthetic approach for the stereoselective synthesis of multifunctional acyclic and stereodefined building blocks.

3.1.1 DFT Analysis on Enantio- and Diastereoselective Copper-Catalyzed Allylboration of Alkynes with Allylic *gem*-Dichlorides

Following on our work on the asymmetric alkyne allylboration with allylic bromides,[55] in collaboration with Andrea Chaves-Pouso, we reported the enantio- and diastereoselective allylboration of alkynes using allylic *gem*-dichlorides (Scheme 3.1.4). It was found that the base played a non-innocent role since the nature of the cation had a notable effect, especially on the *Z*:*E* selectivity of the alkenyl chloride .

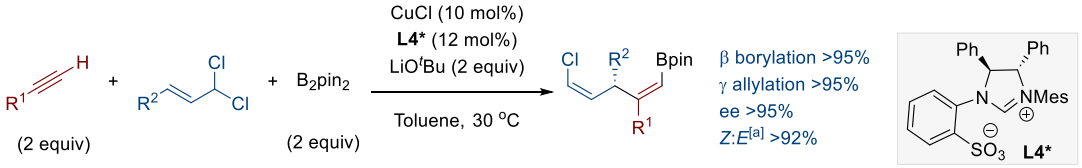

Scheme 3.1.4 Cu-catalyzed enantio- and diastereoselective allylboration alkynes with allylic *gem*-dichlorides. a) *Z*:*E* ratio refers to the alkenyl chloride unit. Alkenyl boronate was obtained as *E* isomer in all cases.

During the reaction optimization, it was found that further than the nature of the ligand, the base identity has a crucial role in the control over the stereochemistry of the newly formed alkenyl chloride (Scheme 3.1.5). When LiO^{t}Bu was used excellent levels of enantiomeric and diastereomeric ratios were obtained. In contrast, when moving towards the bigger Na cation, the *Z*:*E* ratio dropped from 92:8 to 85:15. Additionally, the use of a polar coordinating solvent like THF, with the optimal base, led to a drastic switch in steroselectivity (the *E* isomer became the major isomer) together with an erosion in enantioselectivity (82:18 er).

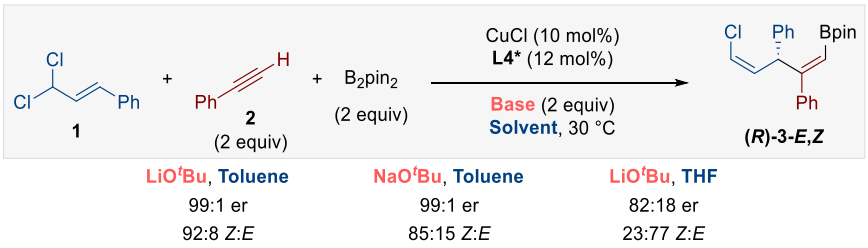

Scheme 3.1.5. Experimental mechanistic insights for Cu-catalyzed enantio- and diastereoselective allylboration of alkynes with allylic *gem*-dichlorides to yield skipped diene ***(R)*-3-*E*,*Z***. *Z*:*E* ratio refers to the alkenyl chloride unit. Alkenyl boronate was obtained as *E* isomer in all cases.

At this point, we asked ourselves several questions: (1) Which is the stereo-determining step? (2) How is enantioselectivity controlled? (3) Which are the factors that determine the Z-selectivity on the formation of the alkenyl chloride? (4) What is the effect of the cation nature? And (5) what is the effect of the solvent in the reaction outcome? To answer and rationalize all these factors, we have conducted a complete DFT analysis of the energy reaction profile.

3.1.1.1 Computational details

Calculations were performed at DFT level of theory using Gaussian16 software[148]. The structures of all the intermediates and transition states were optimized using the ωB97XD functional[149] with the 6-31G(d) basis set (BS1).[150-157] Single-point energies were calculated using the ωB97XD functional within the selfconsistent reaction field (SCRF) using the SMD model (toluene)[158] and a larger basis set *def2*-TZVPPD (BS2).[159-160] The final Gibbs energies were obtained adding the thermal and entropic corrections computed at the BS1 level to the electronic energy computed at BS2 level.

3.1.1.2 Gibbs free energy profile analysis

Based on our previous publication, we started our computational study from the NHC-Cu-Bpin **I** intermediate, which was then subjected to borylcupration event with α-selectivity from complex **II**, after association with the alkyne, to yield complex alkenylboryl Cu-complex **III**. Selectivity in the corresponding process was already studied and explained in our previous work.[55] Moreover, it is known that mentioned step is not involved in the rate-determining step.[55] Therefore, for the sake of clarity, corresponding energy profile stages were omitted in Figure 3.1.2. Analysis of the further profile revealed that the stereodetermining step is the coordination of the allylic substrate to the alkenyl-copper intermediate and subsequent oxidative addition, i.e. formation of intermediate **III** and the following $\mathbf{TS_{OA}^{IV-V}}$. That was the case for all the conformations and configurations studied (Figure 3.1.1). Oxidative addition process led to the formation of a π-allylcopper(III) from where reductive elimination ($\mathbf{TS_{RE}^{V-VI}}$) seemed to be almost barrierless for most of the intermediates **V**.

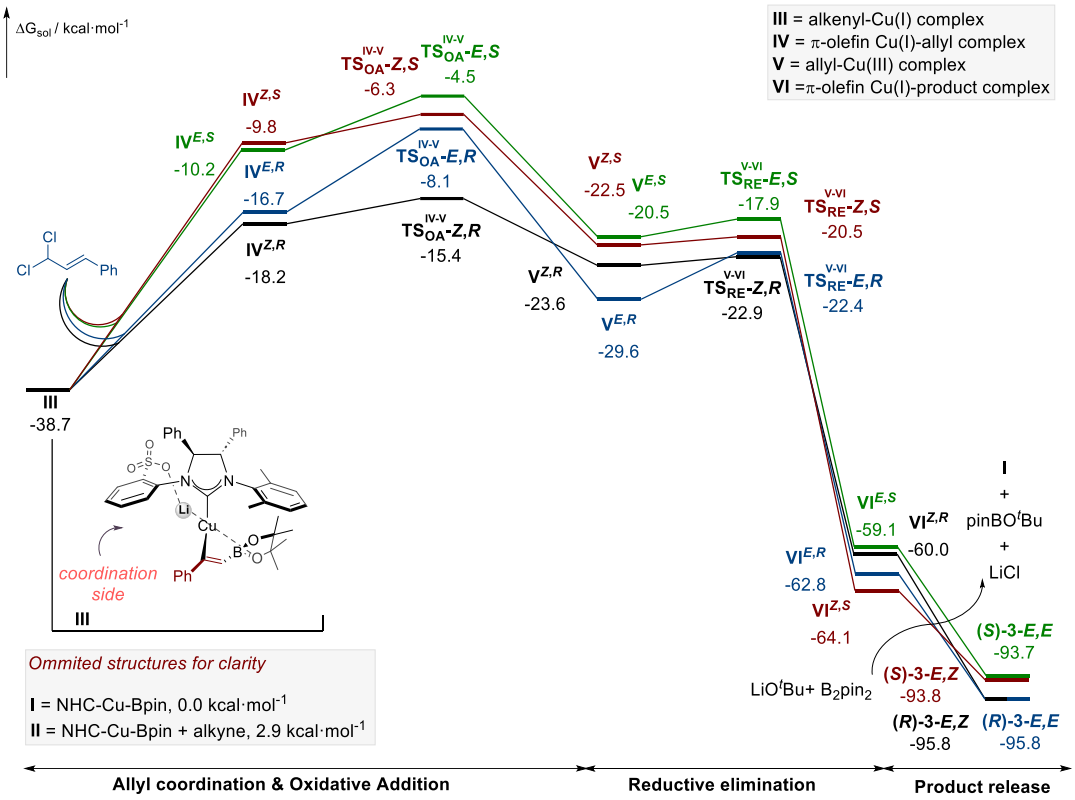

Figure 3.1.2. Complete Gibbs free energy profile for Cu-catalyzed enantio- and diastereoselective allylboration of alkynes with allylic *gem*-dichlorides with Li as metal cation for the pathways associated to the formation of both enantio- and diastereoisomers of product **3**. The numbers are relative Gibbs solvation energies in kcal·mol^{-1} to complex **I** combined with those of the relevant substrates. See Appendix B.I for optimized structures.

Optimized geometries for the transition state corresponding to the stereodetermining S_N2'-type oxidative addition step ($\mathbf{TS_{OA}^{IV-V}}$) show that the allylic *gem*-dichloride approaches the alkenylcopper intermediate opposite to the sizable *N*-aryl group while establishing a lithium cation bridge interaction between the NHC's sulfonate group and one (or both) of the chlorine atoms (Figure 3.1.3). Additional coordination modes of allyl substrate approaching from *N*-aryl group were previously studied but the routes were shown to be more energy demanding.[55]

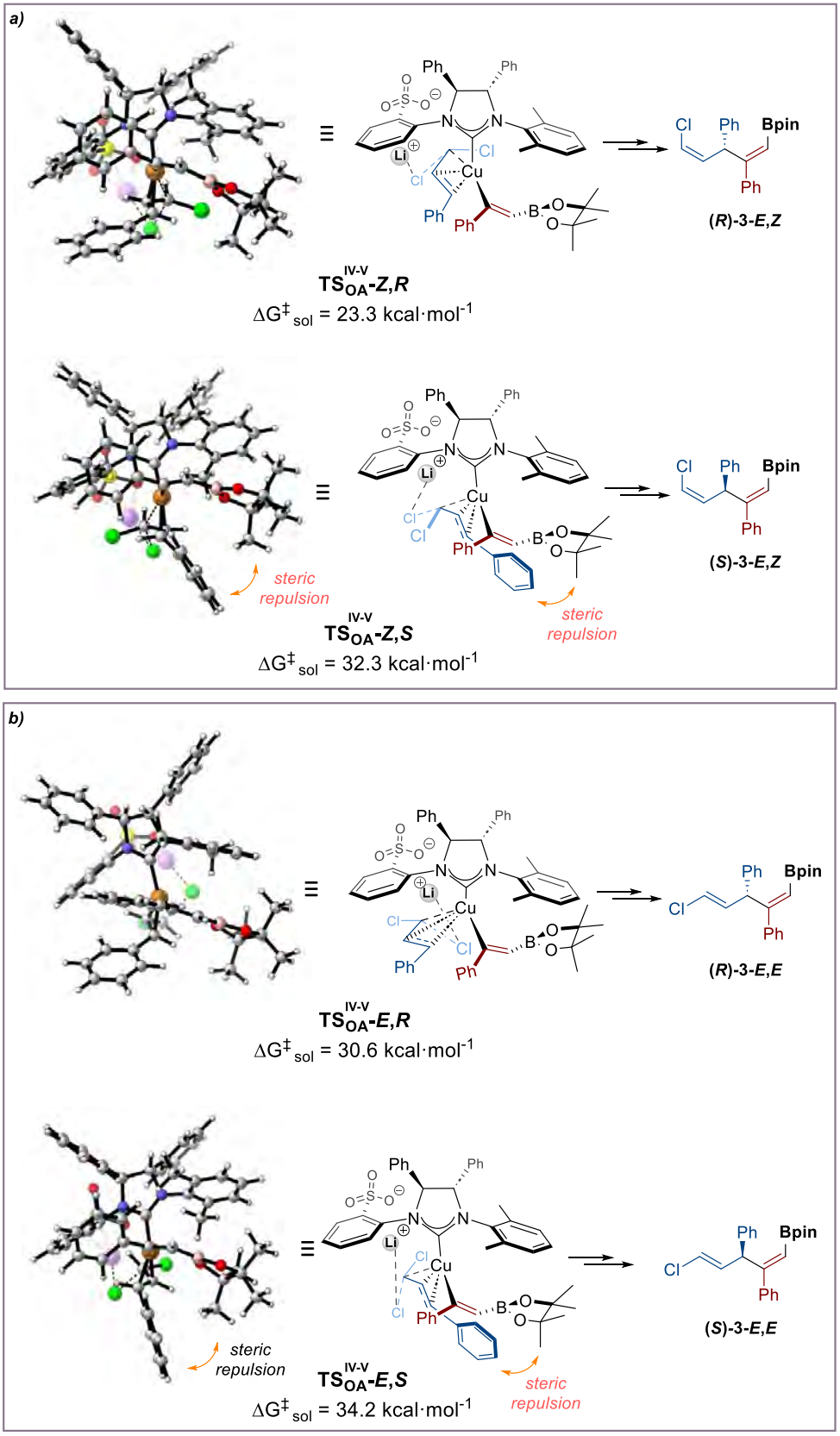

Figure 3.1.3. Optimized structures and energies for the stereochemistry-determining oxidative addition transition states.

Comparison between transition states $\mathbf{TS_{OA}^{IV-V}}$-***Z,R*** and $\mathbf{TS_{OA}^{IV-V}}$-***Z,S*** shows that the first is favored by $\Delta\Delta G^{\ddagger}$=9.0 kcal·mol^{-1}. Origin of enantioselectivity was suggested to arise from the repulsive steric interaction that is engendered between the Bpin unit and the phenyl substituent of the allylic substrate in transition state $\mathbf{TS_{OA}^{IV-V}}$-***Z,S***, disfavoring the formation of the minor *S* enantiomer (Figure 3.1.3, a). A similar model may apply for the transition states associated to the formation of the minor *E*,*E*-isomer (Figure 3.1.3, b). In accordance with the experimental results, both $\mathbf{TS_{OA}^{IV-V}}$-***E,R*** and $\mathbf{TS_{OA}^{IV-V}}$-***E,S*** resulted higher in energy than the preferred $\mathbf{TS_{OA}^{IV-V}}$-***Z,R*** ($\Delta\Delta G^{\ddagger}$=7.3 kcal·mol^{-1} *vs* $\Delta\Delta G^{\ddagger}$=10.9 kcal·mol^{-1}, respectively).

Another important aspect to elucidate was the effect of the metal cation in the diastereoselective formation of the *Z*-alkenyl chloride. To investigate this, the energy profile of the reaction was evaluated as using Na^+ cation instead of Li^+ (Figure 3.1.4). Similarly, the stereodetermining step was attributed to the allylic substrate coordination and S_N2'-type oxidative addition event. However, in this case, the energy difference between both $\mathbf{TS_{OA}^{IV-V}}$-***Z,R*-Na** and $\mathbf{TS_{OA}^{IV-V}}$-***E,R*-Na** was lower, accordingly to the experimental values ($\Delta\Delta G^{\ddagger}$=4.7 kcal·mol^{-1} *vs* $\Delta\Delta G^{\ddagger}$=7.3 kcal·mol^{-1}, Na^+ and Li^+ values respectively).

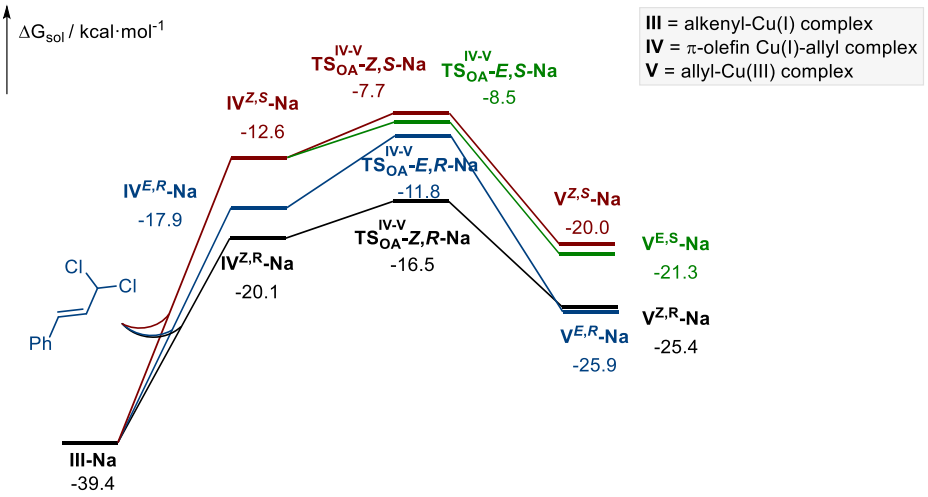

Figure 3.1.4. Gibbs free energy profile for oxidative addition step with Na as metal cation for the pathways associated to the formation of both enantio- and diastereoisomers of product **3**. The numbers are relative Gibbs solvation energies in kcal·mol^{-1} to complex **I-Na** combined with those of the relevant substrates. See Appendix B.I for optimized structures.

We noted that the agreement of the diastereoinduction levels computed by DFT ($\Delta\Delta G^{\ddagger}$ values), compared against the experimental data (Scheme 3.1.3), is not perfect; a result that might be associated to the low energy differences involved (Table 3.1.1). Nevertheless, the trend that lower diastereoselectivity is observed for Na compared to Li under similar conditions is reproduced. Moreover, mathematical comparison between expected (ΔG_{eq}, eq. 1) and calculated ΔG (ΔG_{DFT}) showed that energetic ratio (referred to Li values) is retained. These results suggest that the computational model is reasonable and allows us to propose a key relationship between the base and the *Z*/*E* ratio.

$$\Delta\Delta G_{eq} = -R \cdot T \cdot \ln(k) \qquad \textit{(eq. 1)}$$

Table 3.1.1. Compared experimental and computed ΔΔG for diastereoselectivity.

Base	*Z*	*E*	*K*	$\Delta\Delta G_{eq}$	$\Delta\Delta G_{DFT}$
Na	85	15	0.17	1.0	4.7
Li	92	8	0.09	1.5	7.3
		Energetic ratio		0.7	0.6

$\Delta\Delta G_{eq}$: R = 0.001987 kcal·mol·K^{-1}, T = 298.15 K, *k* = isomeric ratio.

Structural analysis for $\mathbf{TS_{OA}^{IV-V}}$-***Z,R*** and $\mathbf{TS_{OA}^{IV-V}}$-***E,R*** showed that the lithium bridge imposes a bigger C_{NHC}-Cu-C_α angle in $\mathbf{TS_{OA}^{IV-V}}$-***E,R*** (99.9º *vs* 93.0º in $\mathbf{TS_{OA}^{IV-V}}$-***Z,R***) (Figure 3.1.5, a). This angle opening pushes the allyl substrate closer to the Bpin unit leading to a bigger steric clash, that ends up with a stronger repulsive interaction. Moreover, when using sodium (Figure 3.1.5, b), structures showed that this cation causes a similar enlargement of the C_{NHC}-Cu-C_α angle in $\mathbf{TS_{OA}^{IV-V}}$-***E,R*-Na** with respect to $\mathbf{TS_{OA}^{IV-V}}$-***Z,R*-Na** (101.5º versus 92.0º). Additional analysis of the geometries, revealed that adopted position of the Cl atoms in $\mathbf{TS_{OA}^{IV-V}}$-***E,R*** and $\mathbf{TS_{OA}^{IV-V}}$-***E,R*-Na** may allow to stablish two Cl···M$^+$, which would result in an extra stabilizing interaction compared with the major diastereomers. Measurement of the distances revealed 3.25 Å in $\mathbf{TS_{OA}^{IV-V}}$-***E,R*** and 3.16 Å in in $\mathbf{TS_{OA}^{IV-V}}$-***E,R*-Na**.

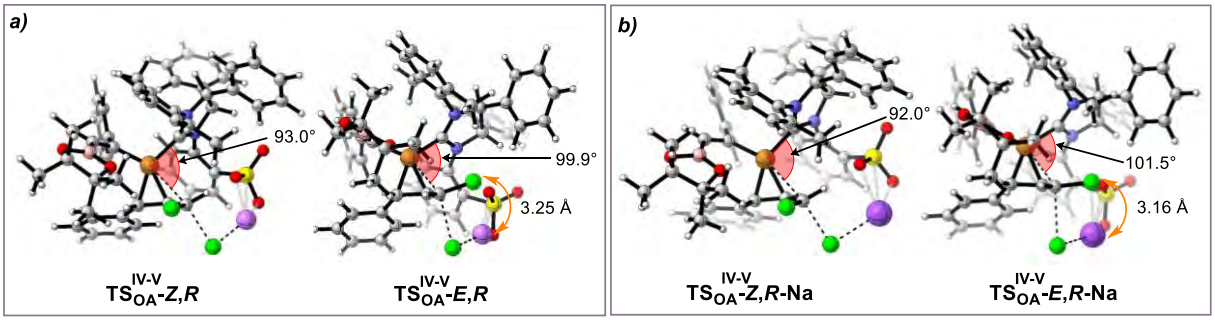

Figure 3.1.5. Optimized structures (back view) for the stereochemistry-determining oxidative addition transition states associated with the pathways leading to ***(R)*-3-*E,Z*** and ***(R)*-3-*E,E*** isomers using a) LiO^{t}Bu and b) NaO^{t}Bu. Geometrical parameters (C_{NHC}-Cu-C_α angle and Cl···M$^+$ distance) are indicated in the figure.

3.1.1.3 Distortion-Interaction Analysis

Given the structural similarities in both the lithium and the sodium systems, we performed a distortion-interaction analysis (DIA) [161-164] to gain further insight into the role of the cation. This model allows to dissect the activation energies as the sum of the required energies to distort the reactants to reach the geometries displayed in the transition state (**M***: distorted geometries for **M**; E_{dist} = activation strain or distortion energy) plus the interaction between the distorted species (E_{int} = interaction energy).

To perform the analysis in our system, which is based on a binuclear species (Figure 3.1.6, **A*---B***), the transition state is divided into both molecular components (**A*** + **B***) and single point calculation was performed for each pair of optimized and distorted geometries (**A**, **A*** and **B**, **B***). Distortion energy for each pair – $\Delta E^{\ddagger}_{dist}$(**A**) and $\Delta E^{\ddagger}_{dist}$(**B**) – was obtained as a rest of single point energies. Subsequent sum led to the total distortion energy ΔE_{dist}. Finally, by definition, interaction energy ΔE_{int} was obtained as the difference between the energy in the TS ($\Delta E^{\ddagger}$) and the distortion energy of the adduct (ΔE_{dist}). Translated to our system, **A** and **B** would be the allylic *gem*-dichloride **1** and complex **III** respectively, **A*---B*** would correspond

to $\mathbf{TS_{OA}^{IV-V}}$ and **C** to corresponding complexes **V**. Moreover, independent **A*** and **B*** structures would correspond with the distorted geometries of **1** (**1***) and **III** (**III***) in the transition state.

Following the explained procedure, transition state geometries were dissected into two parts: allylic *gem*-dichloride (**1***) and NHC-Cu-alkenylboronate (**III***). Once the dissection was done, a single point energy calculation at BS2 level was performed for each distorted part, obtaining the energies for both distorted geometries E(**1***) and E(**III***). E(**1**), E(**III**) and E($\mathbf{TS_{OA}^{IV-V}}$) refers to the corresponding electronic energy of optimized structures at BS2 level. Moreover, $\Delta E^{\ddagger}$ refers to the activation energy of the step in terms of electronic energy at BS2 level. To calculate the energy difference values for each pair of transition states, the mathematical procedure shown in equations 2 to 8 was followed.

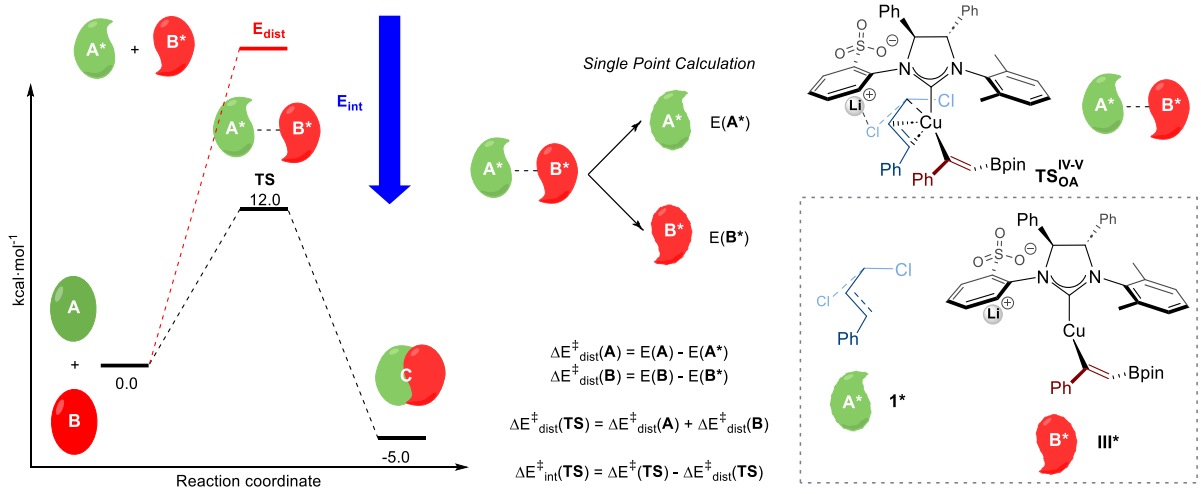

Figure 3.1.6. General schematic representation of distortion-interaction analysis workflow.

Distortion contributions:

$$\Delta E_{dist}^{\ddagger}(\boldsymbol{III}) = E(\boldsymbol{III}) - E(\boldsymbol{III}^{*}) \qquad \textit{(eq. 2)}$$

$$\Delta E_{dist}^{\ddagger}(\mathbf{1}) = E(\mathbf{1}) - E(\mathbf{1}^{*}) \qquad \textit{(eq. 3)}$$

$$\Delta E_{dist}^{\ddagger}(\boldsymbol{TS_{OA}^{IV-V}}) = \Delta E_{dist}^{\ddagger}(\boldsymbol{III}) - \Delta E_{dist}^{\ddagger}(\mathbf{1}) \qquad \textit{(eq. 4)}$$

$$\Delta\Delta E_{dist}^{\ddagger} = \Delta E_{dist}^{\ddagger}(\boldsymbol{TS_{OA}^{IV-V} - E,R}) - \Delta E_{dist}^{\ddagger}(\boldsymbol{TS_{OA}^{IV-V} - Z,R}) \qquad \textit{(eq. 5)}$$

Interaction contributions:

$$\Delta E^{\ddagger} = E\left(\boldsymbol{TS_{OA}^{IV-V}}\right) - [E(\mathbf{1}) + E(\boldsymbol{III})] \qquad \textit{(eq. 6)}$$

$$\Delta E_{int}^{\ddagger} = \Delta E^{\ddagger} - \Delta E_{dist}^{\ddagger} \qquad \textit{(eq. 7)}$$

$$\Delta\Delta E_{int}^{\ddagger} = \Delta E_{int}^{\ddagger}(\boldsymbol{TS_{OA}^{IV-V} - E,R}) - \Delta E_{int}^{\ddagger}(\boldsymbol{TS_{OA}^{IV-V} - Z,R}) \qquad \textit{(eq. 8)}$$

These studies revealed that $\mathbf{TS_{OA}^{IV-V}}$-***E,R*** distortion energy ($\Delta\Delta E^{\ddagger}_{dist}$) is 13.7 kcal·mol^{-1} higher than $\mathbf{TS_{OA}^{IV-V}}$-***Z,R***, while interaction energy ($\Delta\Delta E^{\ddagger}_{int}$) only favors $\mathbf{TS_{OA}^{IV-V}}$-***E,R*** by 5.3 kcal·mol^{-1} (Figure 3.1.7, a). Distortion energy of $\mathbf{TS_{OA}^{IV-V}}$-***E,R*-Na** related to $\mathbf{TS_{OA}^{IV-V}}$-***Z,R*-Na** (Figure 3.1.5, b; $\Delta\Delta E^{\ddagger}_{dist}$ = 13.9 kcal·mol^{-1}) is comparable with the value observed for the transition states bearing a lithium cation. However, stabilizing interaction energy is significantly higher for the sodium-containing system ($\Delta\Delta E^{\ddagger}_{int}$ = - 9.1 kcal·mol^{-1}), thus resulting

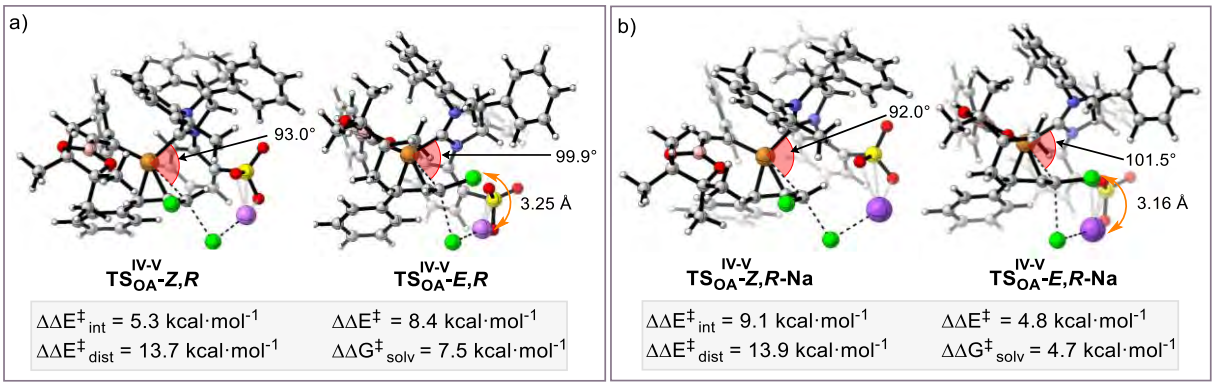

Figure 3.1.7. Optimized structures (back view) for the stereochemistry-determining oxidative addition transition states associated with the pathways leading to **(*R*)-3-*E*,*Z*** and **(*R*)-3-*E*,*E*** isomers using a) LiO^{t}Bu and b) NaO^{t}Bu. Energies from Distortion-Interaction Analysis are referenced to the corresponding $\boldsymbol{TS_{OA}^{IV-V}}$**-*Z*,*R*** in each pair. See section 5.2.1 for detailed dissected energies.

in a lower energy difference between both sodium-based transition states. This increment in the stabilizing interaction energy might be affected due to the larger size of the Na cation which might facilitate a more effective interaction with both chlorine atoms (3.16 Å vs 3.25 Å, in $\mathbf{TS_{OA}^{IV-V}}$**-*E*,*R*-Na** and $\mathbf{TS_{OA}^{IV-V}}$**-*E*,*R*** respectively). This would explain the slightly lower *Z*/*E* selectivity observed when NaO^{t}Bu is used instead of LiO^{t}Bu.

3.1.1.4 Non-Covalent Interaction (NCI) analysis

In order to further evaluate the effect of the aforementioned interactions that rule the *Z*-selectivity, analyses of the non-covalent interactions were carried out by using Multiwfn software with its NCIplot utility,[165] combined with VMD program for visualization.[166] NCI is a visualization index based on the electron density (ρ) and the reduced density gradient (s), that comes from the density and its first derivative (eq. 9), and produces isosurfaces of the reduced density gradient.[167] In order to differentiate between favorable and unfavorable interactions, the sign of the second density Hessian eigenvalue (sing(λ_2)) times the density (ρ) is implemented, whereas the density itself provides information about their strength. Bonding interactions can be identified by the negative sign of λ_2, as for the hydrogen bonds; or $\lambda_2 > 0$ if atoms are in nonbonded contact in the interatomic region.[167-168]

$$s \propto \frac{|\nabla\rho|}{\rho^{4/3}} \qquad \textit{(eq. 9)}$$

After performing the NCI analysis for both $\mathbf{TS_{OA}^{IV-V}}$**-*Z*,*R*** structures, NCI plots show that interaction between chlorine atoms and Bpin unit is governed by a combination of weak attractive and repulsive Van der Waals interactions. However, for both $\mathbf{TS_{OA}^{IV-V}}$**--*E*,*R*** more notorious differences were observed regarding repulsive interactions. Surfaces reveal a darker brown-to-red color between hydrogen and Bpin unit, what means that stronger repulsive interactions are present (Figure 3.1.8). It should be noted that for the case of Na-based system, the imposed larger angle (101.5° *vs* 99.9°) leads to a slightly redder surface between H and Bpin than Li-containing pair.

Based on the obtained data, we could also envision that a different mechanistic scenario may apply when THF is used as solvent. Given its more polar and coordinating nature, it may weaken (or completely disrupt) the supramolecular ligand-substrate interaction by cation

solvation, leading to a looser transition state, which would result in erosion in enantioselectivity and the preferential formation of the *E*-alkenyl chloride (Scheme 3.1.5).

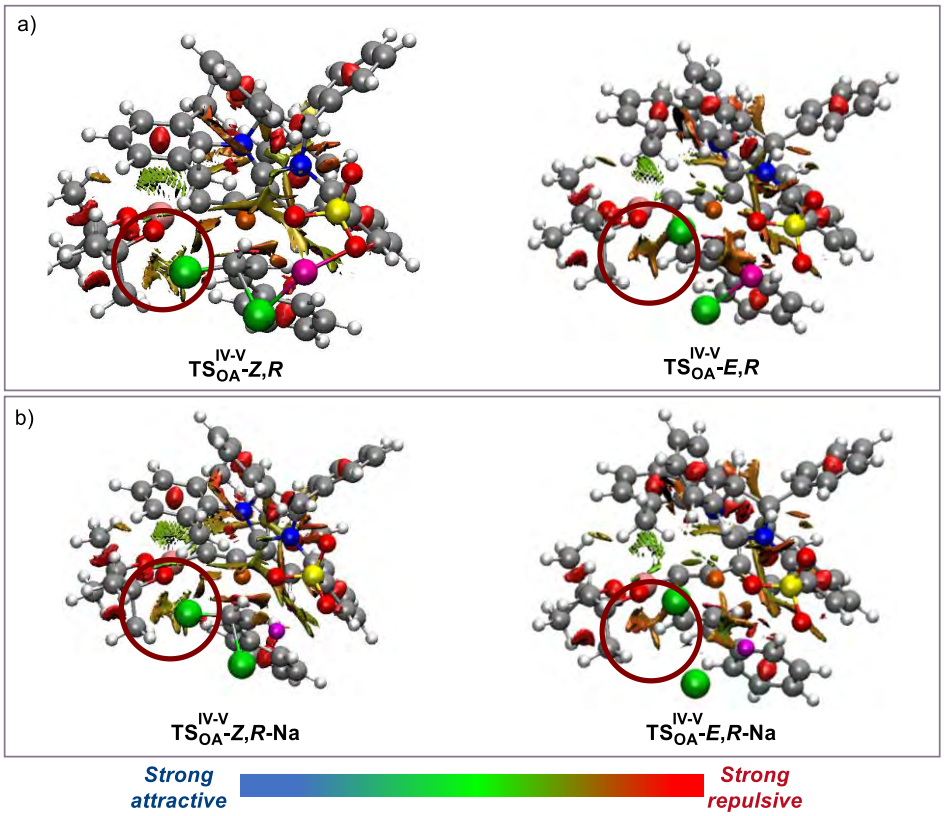

Figure 3.1.8. NCI plots for oxidative addition transition states using both a) Li cation and b) Na cation. For full set of NCI plots see Appendix C.I.

3.1.2 DFT Analysis on the Copper-Catalyzed Enantioselective Borylative Allyl–Allyl Coupling of Allenes and Allylic *gem*-Dichlorides

Following on the studies of the borylative coupling of alkynes and allylic *gem*-dichlorides, in collaboration with Martín Piñeiro-Suárez, we developed the enantio- and diastereoselective allylboration of allenes using allylic *gem*-dichlorides (Scheme 3.1.6). The transformation was observed to provide chiral internal 1,5-dienes bearing a (*Z*)-alkenyl boronate and (*Z*)-alkenyl chloride units, displaying high levels of chemo-, regio-, enantio-, and diastereoselectivity. The described protocol was found to tolerate a range of allenes (featuring aliphatic chains and cycles, heterocycles, silyl ethers, esters and amines), in sharp contrast to allyl substrates that was observed to be limited to aromatic rings, in order to keep the high stereoselectivities levels.

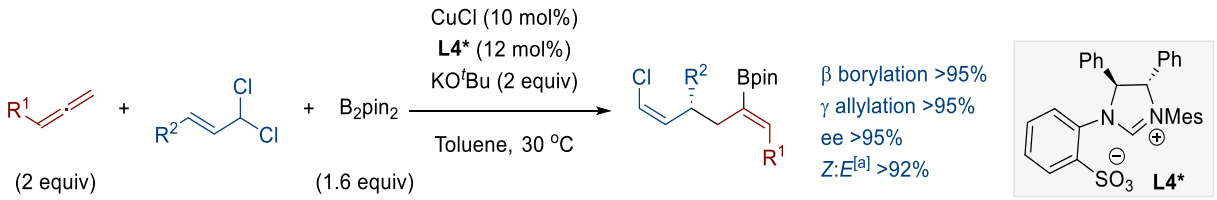

Scheme 3.1.6. Copper-catalyzed enantioselective borylative allyl-allyl coupling of allenes and allylic gem-dichlorides. a) *Z*:*E* ratio refers to the alkenyl chloride unit. Alkenyl boronate was obtained as *Z* isomer in all cases.

During the reaction optimization, a clear effect in the outcome was observed when the base identity was evaluated (Scheme 3.1.7). When KO^{t}Bu was used, in toluene, excellent levels of enantiomeric and diastereomeric ratios were obtained. In contrast, when moving towards the smaller Na and Li cations, enantiomeric ratios drastically dropped from 96:4 to 90:10 and 77:23 mixture. Moreover, the use of LiO^{t}Bu further erosioned the diastereomeric ratio from >20:1 to 5:1 mixture.

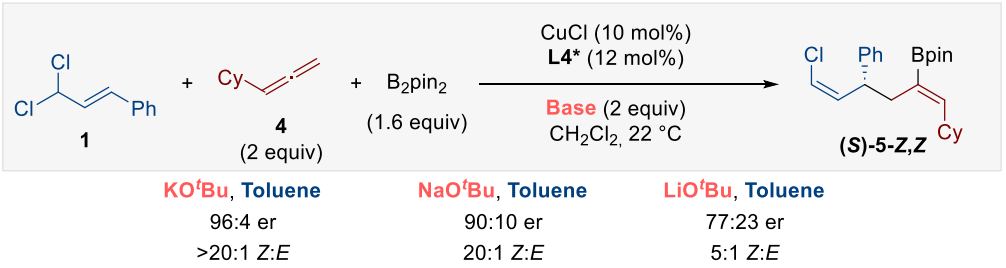

Scheme 3.1.7. Experimental mechanistic insights for Cu-catalyzed enantio- and diastereoselective allylboration alkynes with allylic *gem*-dichlorides to yield 1,5-diene ***(S)*-5-*Z*,*Z***. *Z*:*E* ratio refers to the alkenyl chloride unit. Alkenyl boronate was obtained as *Z* isomer in all cases.

Given the experimental results, computational studies were planned towards answering the most relevant aspects of the catalysis: which species are involved in the stereo-determining step, which (steric and/or electronic) factors are ruling the stereoselectivity and how the cation identity is affecting to the outcome reaction. We therefore decided to run a complete DFT analysis of the energy reaction profile.

3.1.2.1 Basis set and functional benchmarking to the experimental value and computational details

Since we previously found some discrepancy between the calculated activation energy barriers and the observed selectivity ratios, in order to find a suitable computational level for the system and reduce any possible energetic discrepancies, we firstly carried out the optimization of the structures for the oxidative addition step in the formation of product **(*S*)-5-*Z*,*Z*** and **(*R*)-5-*Z*,*Z*** using two different calculation levels (Table 3.1.2, **Lv1** and **Lv2**).

Table 3.1.2. Calculated single-point energies for benchmarking the BS1 to the experimental value.

Calculation level	$TS_{OA}^{VIII-IX}$-*Z*,*S*	$TS_{OA}^{VIII-IX}$-*Z*,*R*	$\Delta\Delta G^{\ddagger}_{sol}$ / kcal·mol^{-1}
	G_{sol} / Hartree	G_{sol} / Hartree	
Lv1	-6163.585434	-6163.57637	5.7
Lv2	-6163.604391	-6163.600132	2.7

- **Lv1** consists in the combination of wB97XD/*def2*-TZVP/*def2*-QZVP (Cu) (scrf=smd, toluene)//wB97XD/6-31G(d,p).
- **Lv2** consists in the combination of wB97XD/*def2*-TZVP/*def2*-QZVP (Cu) (scrf=smd, toluene)//wB97XD/6-31G(d,p)/SDD+f (Cu).

Compared to the experimental derived value (eq 1) $\Delta\Delta G^{\ddagger}$ = 1.9 kcal/mol (96:4 e.r.), **Lv2** in which Cu atom is treated apart with a larger basis set and including relativistic effects, provides a more accurate result.

Further exploration was focused on the selection of the single-point corrections with larger basis set. For this, **Lv2**, **Lv3**, **Lv4**, **Lv5** and **Lv6** were evaluated (Table 3.1.3):

Table 3.1.3. Calculated single-point energies for benchmarking the single-point correction to the experimental value.

Calculation level	$TS_{OA}^{VIII-IX}$-*Z*,*S*	$TS_{OA}^{VIII-IX}$-*Z*,*R*	$\Delta\Delta G^{\ddagger}_{sol}$ / kcal·mol^{-1}
	G_{sol} / Hartree	G_{sol} / Hartree	
Lv2	-6163.604391	-6163.600132	2.7
Lv3	-6163.956308	-6163.950756	3.5
Lv4	-6164.827151	-6164.821962	3.3
Lv5	-6163.586734	-6163.582406	2.7
Lv6	-6163.277975	-6163.27329	2.9

- **Lv2** consists in the combination of wB97XD/*def2*-TZVP/*def2*-QZVP (Cu) (srfc=smd, toluene)//wB97XD/6-31G(d,p)/SDD+f (Cu).
- **Lv3** consists in the combination of M06L/*def2*-TZVP/*def2*-QZVP (Cu) (srfc=smd, toluene)//wB97XD/6-31G(d,p)/SDD+f (Cu).
- **Lv4** consists in the combination of B3LYP-GD3(BJ)/*def2*-TZVP/*def2*-QZVP (Cu) (srfc=smd, toluene)//wB97XD/6-31G(d,p)/SDD+f (Cu).
- **Lv5** consists in the combination of wB97XD/*def2*-TZVPP (srfc=smd, toluene)//wB97XD/6-31G(d,p)/SDD+f (Cu).
- **Lv6** consists in the combination of wB97XD/6-311++G(d,p)/aug-cc-pVTZ (Cu) (srfc=smd, toluene)//wB97XD/6-31G(d,p)/SDD+f (Cu).

When other functionals were evaluated like M06L (**Lv3**) or B3LYP with D3(BJ) empirical dispersion correction (**Lv4**), moderate overestimation of $\Delta\Delta G^{\ddagger}_{sol}$ was observed. In the last case, it can be attributed to overstabilization of the complexes due to the empirical dispersion correction.[169] The use of other basis sets in combination with the wB97XD functional for the single-point calculation – **Lv5** and **Lv6** – led to similar energy differences than the one obtained with **Lv2**. Since our system has a transition metal (Cu), we decided to use the larger basis set combination **Lv2** for better description of its electrons (Figure 3.1.9).

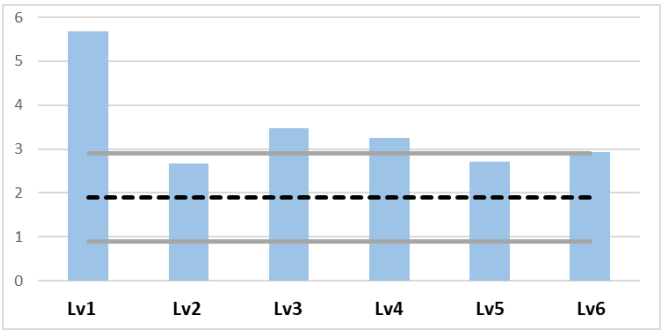

Figure 3.1.9. Comparison between calculated single-point energies (in blue) with the experimental derived value (1.9 kcal·mol^{-1}, black dotted line) considering an acceptable ± 1.0 kcal·mol^{-1} range (grey lines).

According to our benchmarking studies, the structures of all the intermediates and transition states were optimized using the wB97XD functional[149] in combination with basis set BS1. BS1 includes the 6-31G(d,p) basis set for the main group elements[151, 154] and the scalar relativistic Stuttgart-Dresden SDD pseudopotential and its associated double-ζ basis set,[170] complemented with a set of *f* polarization functions,[171] for the copper atom.

Single-point energies were calculated using the wB97XD functional within the self-consistent reaction field (SCRF) using the SMD model (toluene)[158] and a larger basis set BS2. BS2 consists in the *def2*-TZVP basis set for the main group elements and the quadruple-ζ *def2*-QZVP basis set for Cu.[159-160]

3.1.2.2 Gibbs free energy profile and NCI analysis for enantioselectivity

Once having identified the proper computational level, we computed the energy profiles for all the possible pathways leading to the four possible diastereomers. Based on previous works, borocupration step with NHC-Cu complexes is a well-stablished process that takes place at the more external C=C, leading to a (*Z*)-σ-allyl Cu-complex.[15, 22-23, 33] Therefore, we started our computational study from the mentioned structure. In the course of those studies, two lowest-energy structures (**VIIa** and **VIIb**), which can rapidly interconvert (ΔG_{sol} = 0.5 kcal·mol^{-1}), were found for the (*Z*)-σ-allyl-Cu(I) intermediate (Figure 3.1.10). From these intermediates, different modes of coordination with the allylic *gem*-dichloride were investigated to find the most favorable pathway.

Among all the binding modes, by comparing the activation energy barriers for the oxidative addition of the allylic *gem*-dichloride into the allyl-Cu(I) intermediate, the one featuring the allylic *gem*-dichloride opposite to the *N*-arylsulfonate group (i.e. coordination to **VIIa**), led to the most favorable oxidative addition process ($\Delta G^{\ddagger}_{sol}$=23.0 kcal·mol^{-1}, $\mathbf{TS_{OA}^{VIII-IX}}$-***Z,S***), pathway to the major *S* enantiomer. Reductive elimination from π-allyl-Cu(III) **IX-*Z,S*** intermediate ($\Delta G^{\ddagger}$=6.8 kcal·mol^{-1}, $\mathbf{TS_{RE}^{IX-X}}$-***Z,S***) revealed that the former is the stereodetermining step. This was assumed for the other pathways, and we thus focused on the

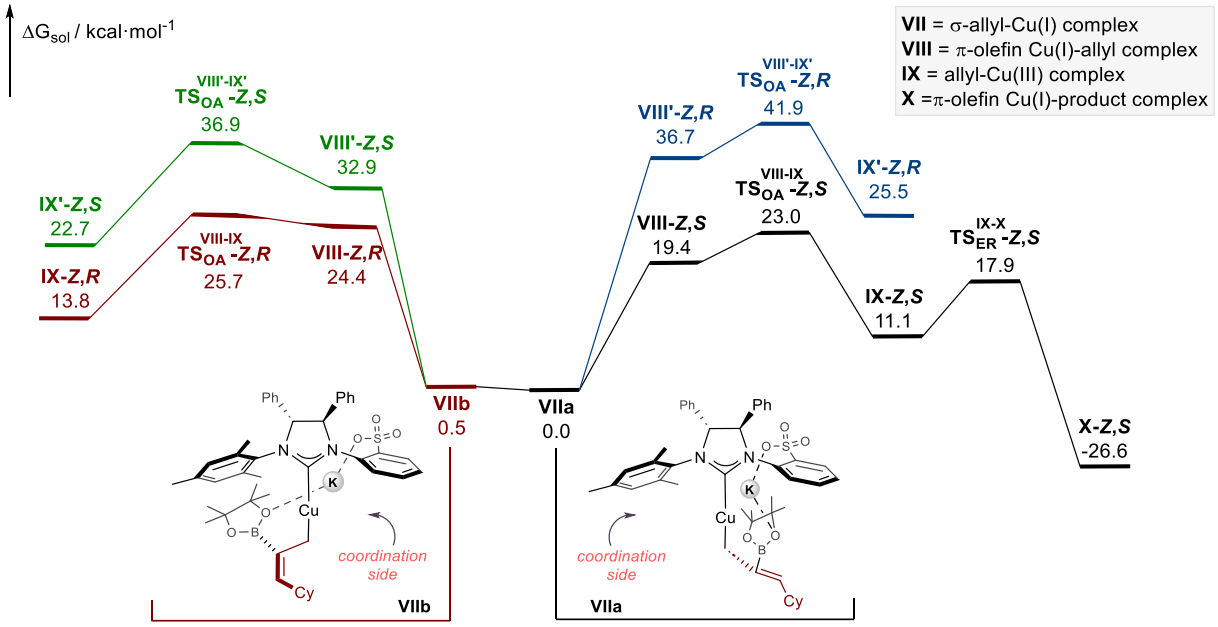

Figure 3.1.10. Complete Gibbs free energy profile for Cu-catalyzed enantio- and diastereoselective allylboration of allenes with allylic *gem*-dichlorides with K as metal cation for the pathways associated to the formation of both enantiomers of product **5-*Z*,*Z***. The numbers are relative Gibbs solvation energies in kcal·mol^{-1} to complex **VIIa** combined with those of the relevant substrates. See Appendix B.II for optimized structures.

study of the different transition states related to this step (Figure 3.1.10). Formation of the minor *R* enantiomer arises from coordination to **VIIb** where the allyl substrate is opposite to the NMes unit (Figure 3.1.10). The relative energy for transition state $\mathbf{TS_{OA}^{VIII-IX}}$***-Z,S*** was 2.7 kcal·mol^{-1} lower than for $\mathbf{TS_{OA}^{VIII-IX}}$***-Z,R***, in good agreement with the observed 96:4 er.

In order to account for this energy difference, analysis of Non-Covalent Interactions (NCI) was performed. NCI plots of both transition state structures showed no remarkable differences in terms of repulsive interactions (see Appendix C.II). However, analysis of the attractive interactions revealed that the coordination mode in $\mathbf{TS_{OA}^{VIII-IX}}$***-Z,S*** allows for establishing a double potassium cation bridge interaction between the NHC's sulfonate group and both chlorine atoms. In contrast, only one K···Cl interaction is present in $\mathbf{TS_{OA}^{VIII-IX}}$***-Z,R*** (Figure 3.1.11). This difference in attractive interactions may suggest that the origin of enantioselectivity arises from the extra stabilization in $\mathbf{TS_{OA}^{VIII-IX}}$***-Z,S*** which originates from the double substrate-ligand cation bridge interaction.

3.1.2.3 Gibbs free energy profile and NCI analysis for diastereoselectivity

To evaluate the factors governing the stereoselective formation of the *Z*-alkenyl chloride, we calculated the optimized structure for transition state $\mathbf{TS_{OA}^{VIII-IX}}$***-E,S*** and $\mathbf{TS_{OA}^{VIII-IX}}$***-E,R*** which would lead to the formation of minor diastereomer **5-*Z*,*E*** (Figure 3.1.12). In accordance with the experimental results, the lower $\mathbf{TS_{OA}^{VIII-IX}}$***-E,S*** resulted higher in energy than the preferred $\mathbf{TS_{OA}^{VIII-IX}}$***-Z,S*** ($\Delta G^{\ddagger}$=30.7 kcal·mol^{-1} *vs* $\Delta G^{\ddagger}$=23.0 kcal·mol^{-1}).

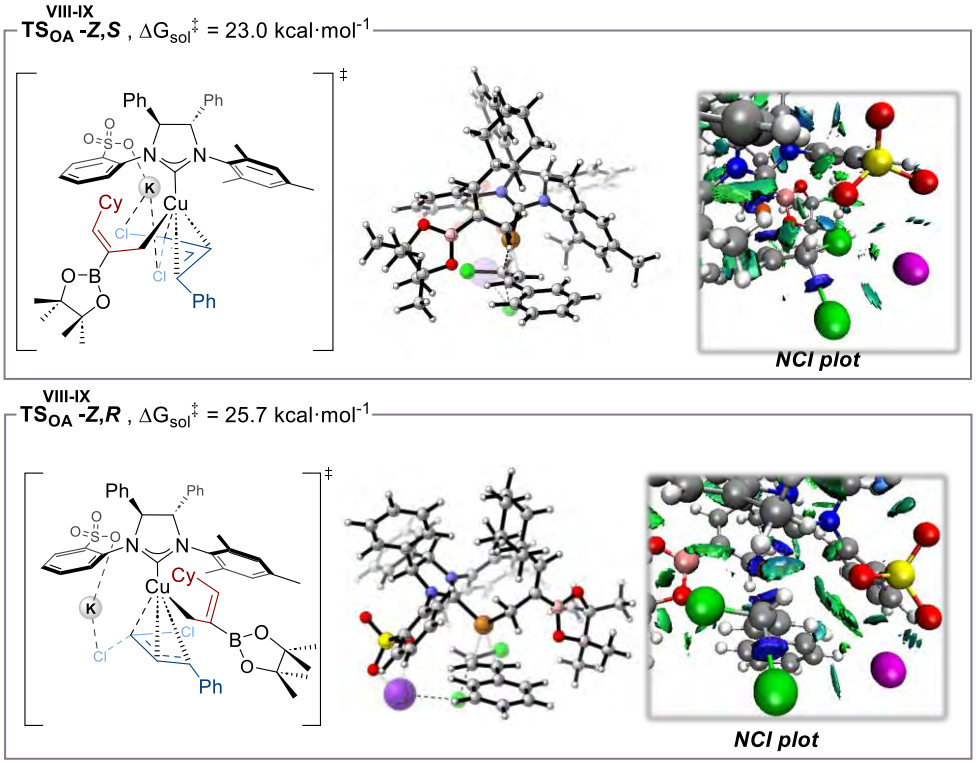

Figure 3.1.11. Optimized structures, Gibbs free energies and NCI analysis obtained from DFT calculations for the stereochemistry-determining oxidative-addition transition states associated with the most favored pathways leading to **(*S*)-5,*Z*,*Z*** and **(*R*)-5,*Z*,*Z*** using KO^{t}Bu. For full set of NCI plots see Appendix C.II.

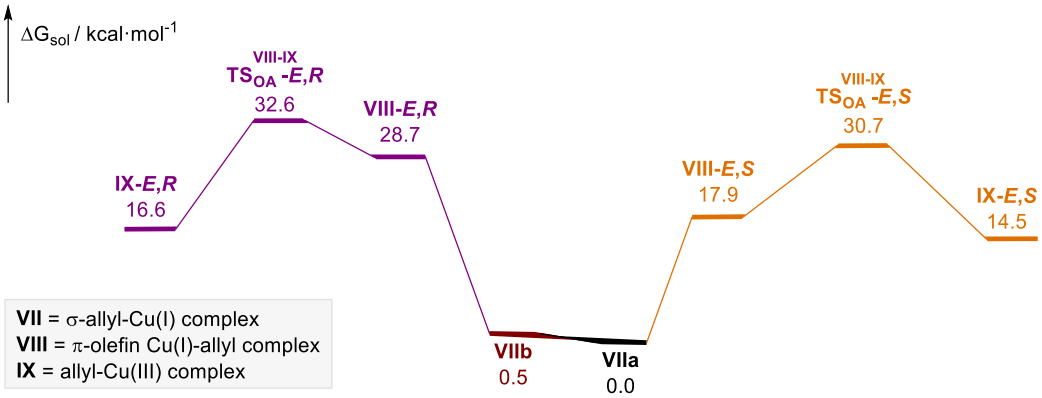

Figure 3.1.12. Complete Gibbs free energy profile for Cu-catalyzed enantio- and diastereoselective allylboration of allenes with allylic *gem*-dichlorides with K as metal cation for the pathways associated to the formation of both enantiomers of product **5-*Z*,*E***. The numbers are relative Gibbs solvation energies in kcal·mol^{-1} to complex **VIIa** combined with those of the relevant substrates. See Appendix B.II for optimized structures.

NCI plot analysis revealed that a new repulsive interaction between the Bpin unit and the *N*-arylsulfonate group appears in $\mathbf{TS_{OA}^{VIII-IX}}$-***E*,*S*** when compared to $\mathbf{TS_{OA}^{VIII-IX}}$-***Z*,*S*** (Figure 3.1.13). Moreover, repulsive interactions between the cyclohexyl ring and the phenyl and NMes units of the NHC ligand become larger in $\mathbf{TS_{OA}^{VIII-IX}}$-***E*,*S***. Analysis of the geometry of both structures shows that the stabilizing double cation-bridging interaction in $\mathbf{TS_{OA}^{VIII-IX}}$-***E*,*S*** imposes an structural reorganization which involves a decrease on the dihedral angle (Figure 3.1.13, orange marked angle) displayed between the C_{NHC} and C6 of the arylsulfonate ring (60.5º in $\mathbf{TS_{OA}^{VIII-IX}}$-***E*,*S*** vs 68.2º in $\mathbf{TS_{OA}^{VIII-IX}}$-***Z*,*S***). This angle modification pushes the *N*-arylsulfonate ring closer to the Bpin unit, causing a reorientation of the allyl substituent which

brings the cyclohexyl group towards the NMes and Ph units, and thus leading to larger repulsive interactions. Consequently, the σ-allyl substituent adopts a new spatial disposition that enhances the repulsive interactions between the cyclohexyl group and the NHC's phenyl and mesityl rings. This set of repulsive interactions would result in a higher-energy transition state and would explain the origin of the (*Z*)-selectivity.

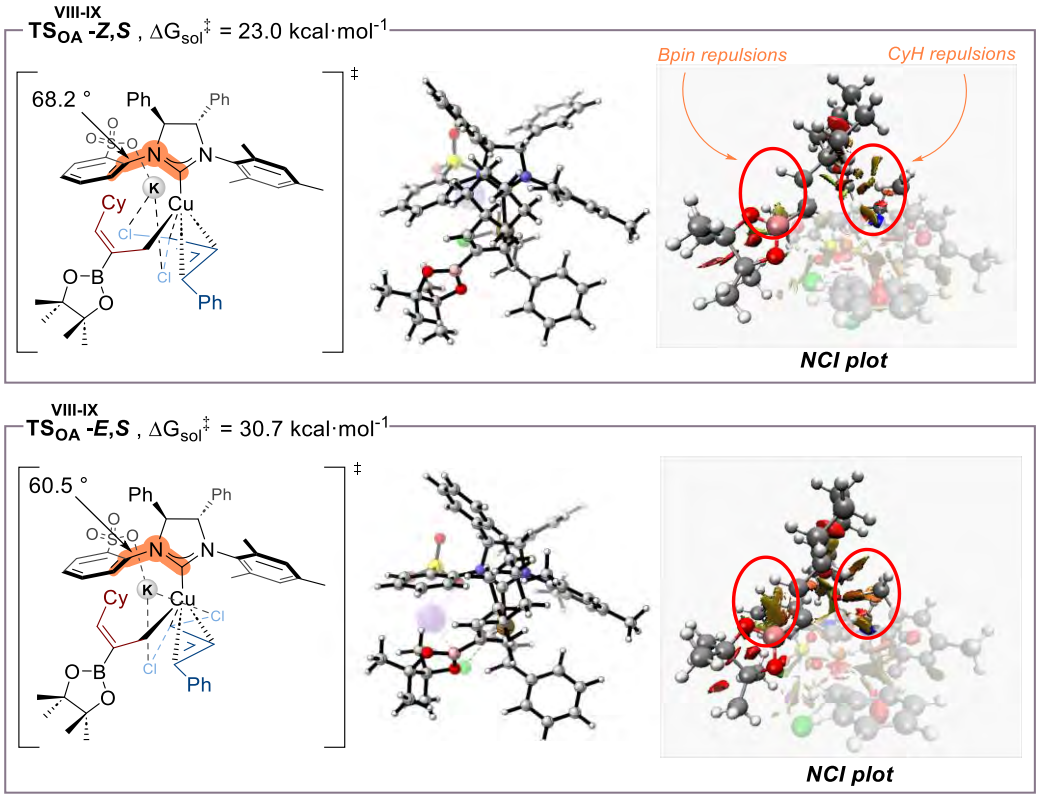

Figure 3.1.13. Optimized structures, Gibbs free energies and NCI analysis obtained from DFT calculations for the stereochemistry-determining oxidative-addition transition states associated with the most favored pathways leading to **(*S*)-5,*Z*,*Z*** and **(*S*)-5,*Z*,*E*** using KO^{t}Bu. For full set of NCI plots see Appendix C.II.

3.1.2.4 Gibbs free energy profile and NCI analysis for Li^+ effect on enantioselectivity

Similarly, since experimental results showed that enantioselectivity was influenced for the cation nature (Scheme 3.1.4), we explored the potential energy surface using a lithium cation, instead of potassium, for the both lower energy pathways associated with the formation of both **(*S*)-5-*Z*,*Z*** and **(*R*)-5-*Z*,*Z*** enantiomers (Figure 3.1.14). As expected from experimental studies, we observed a lower energy difference between both oxidative additions processes compared with the observed when potassium was used ($\Delta\Delta G^{\ddagger}_{sol}$ = 2.1 kcal·mol^{-1} vs 2.7 kcal·mol^{-1}, for Li^+ and K^+ respectively).

Analysis of the optimized structures for the transition states $\mathbf{TS_{OA}^{VIII-IX}}$**-*Z*,*S*-Li** and $\mathbf{TS_{OA}^{VIII-IX}}$**-*Z*,*R*-Li**, showed that the extra stabilization given by the second cation bridge interaction of the second chlorine atom is missing in $\mathbf{TS_{OA}^{VIII-IX}}$**-*Z*,*S*-Li** (Figure 3.1.15), in contrast to the observed with potassium (Figure 3.1.11). This lack of the second coordination leads to a higher-energy transition state and, thus, to a smaller energy difference with $\mathbf{TS_{OA}^{VIII-IX}}$**-*Z*,*R*-Li**. The absence of the second stabilizing interaction may be due to the smaller size of the Li cation and might explain the lower enantioselectivity (Scheme 3.1.4).

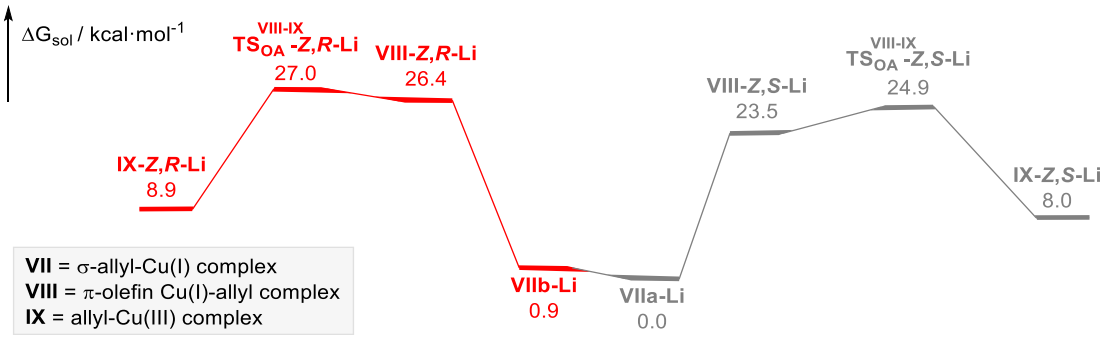

Figure 3.1.14. Gibbs free energy profiles for Cu-catalyzed enantio- and diastereoselective allylboration of allenes with allylic *gem*-dichlorides with Li as metal cation for the pathways associated to the formation of both enantiomers of product **5-*Z*,*Z***. The numbers are relative Gibbs solvation energies in kcal·mol^{-1} to complex **VIIa-Li** combined with those of the relevant substrates. See Appendix B.II for optimized structures.

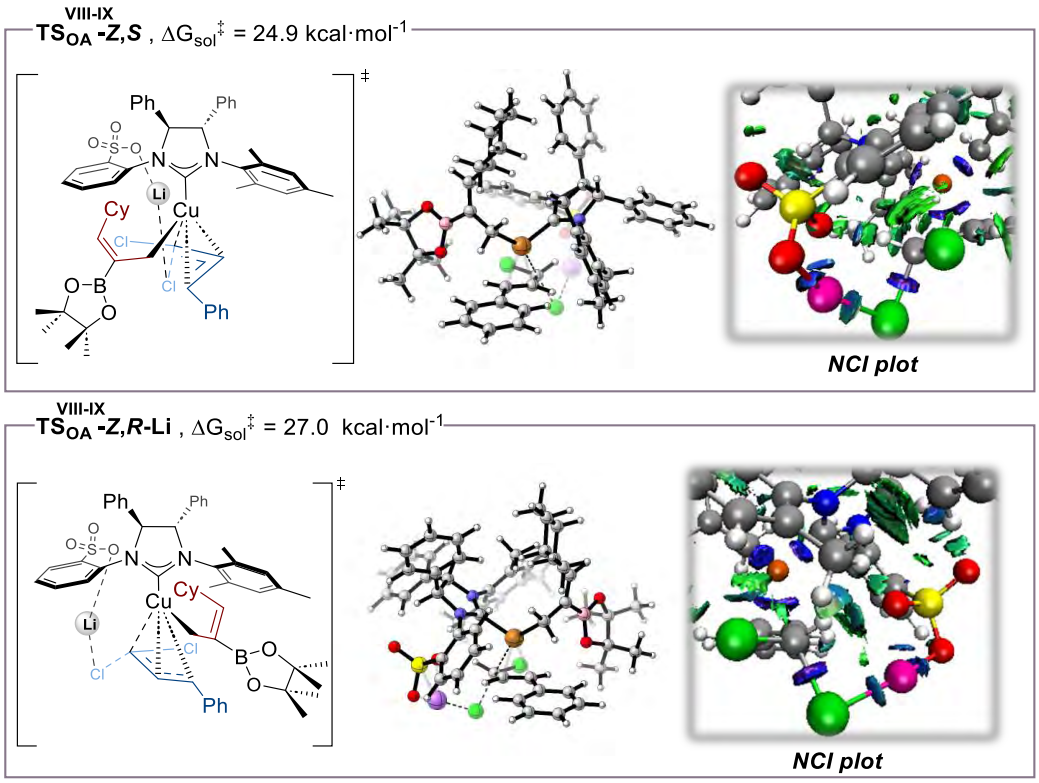

Figure 3.1.15. Optimized structures, Gibbs free energies and NCI analysis obtained from DFT calculations for the stereochemistry-determining oxidative-addition transition states associated with the most favored pathways leading to **(*S*)-5,*Z*,*Z*** and **(*S*)-5,*Z*,*E*** using LiO^{t}Bu. For full set of NCI plots see Appendix C.II.

3.2 ENANTIOSELECTIVE ALLYLBORATION OF ACETYLENE: A VERSATILE TOOL FOR THE STEREODIVERGENT SYNTHESIS OF NATURAL PRODUCTS*

*The results from this section have already been published:

Andrés. M. Álvarez-Constantino,[a] Andrea Chaves-Pouso,[a] Martín Fañanás-Mastral.[a] Enantioselective Allylboration of Acetylene: A Versatile Tool for the Stereodivergent Synthesis of Natural Products. *Angew. Chem. Int. Ed.* **2024**, *63*, e202407813. (DOI: 10.1002/anie.202407813)

[a] Centro Singular de Investigación en Química Biolóxica e Materiais Moleculares (CiQUS), Universidade de Santiago de Compostela, 15782, Santiago de Compostela, Spain

In the context of these efficient transformations within the framework of our ongoing research, and the continuous need to capitalize on simple and abundant chemical feedstocks, we considered whether this simple C2 hydrocarbon feedstock could be efficiently engaged in an asymmetric allylboration reaction. The envisioned multicomponent reaction represents an important synthetic target since it would give straightforward access to a chiral skipped diene structure with a stereogenic sp^3 carbon at the central position, an ubiquitous structural motif in a range of biologically active natural products (Figure 3.2.1).[172-174] Despite significant advances in the field,[55, 175-179] the stereoselective preparation of chiral skipped dienes still remains a significant challenge in organic synthesis. Indeed, few methodologies combine features such as access to proper diene substitution pattern and modifiable double bond stereochemistry, making them broadly applicable to the enantioselective synthesis of skipped diene natural products.[177] Ideally, such a method should be stereoselective, but also stereodivergent in order to allow access from the same starting material to the four possible stereoisomers derived from the two olefins.

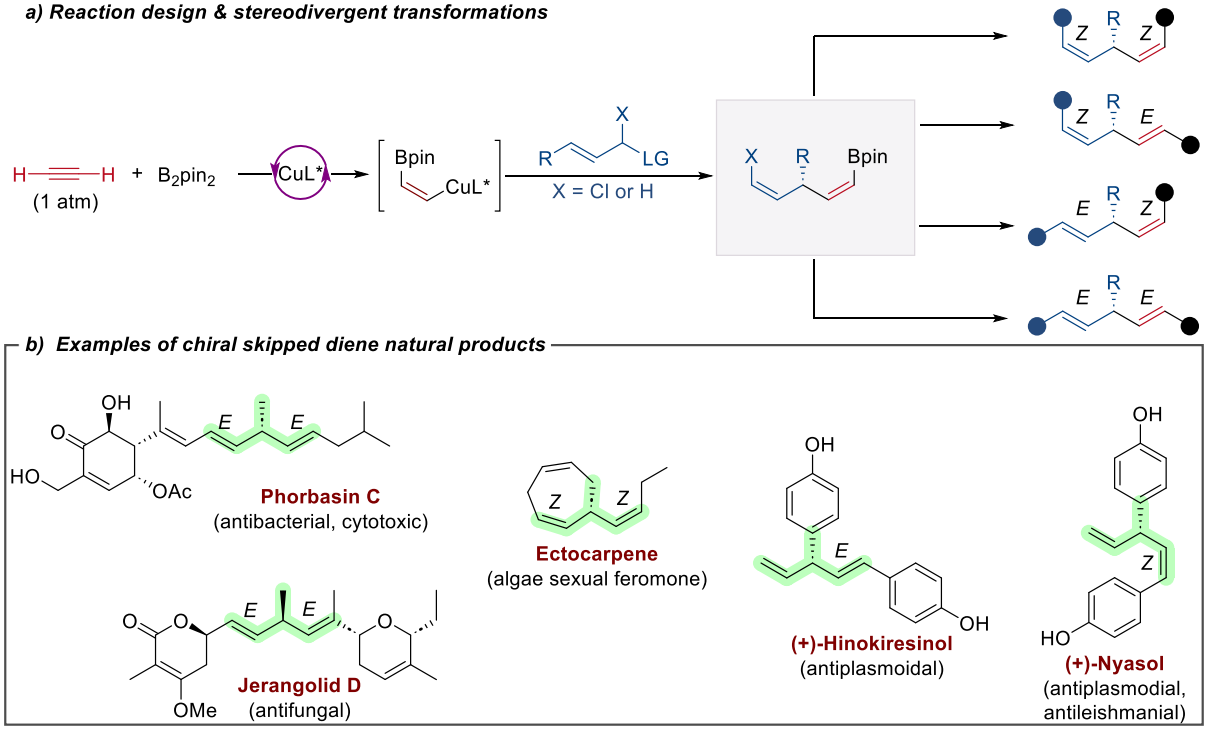

Figure 3.2.1. Reaction design and representantive example of chiral skipped diene natural products.

3.2.1 Reaction Optimization and Scope

We began our investigations by exploring the reaction of acetylene gas **6** (1 atm), *trans*-cinnamyl bromide **7** and B_2pin_2 (Table 1). Given the high efficiacy demonstrated by Hoveyda's sulfonate-bearing NHC chiral ligands in enantioselective allylic substitutions,[57, 59, 177, 180-182] as well as their optimal performance in previous reactions involving asymmetric allylboration of substituted alkynes,[18, 55, 179, 183] we centered our study on this type of ligand. In the copper-catalyzed enantioselective allylboration of substituted alkynes with allylic bromides,[55] we found that the use of ligand **L5** using NaO^{t}Bu as base and toluene as solvent was optimal to achieve high efficiency and high levels of enantioselectivity. However, when acetylene was tested under those conditions skipped diene product **8** was obtained in moderate yield and with almost negligible enantioselectivity (entry 1). The use of chiral ligand **L6** bearing a bulkier *tert*-

butyl group in the *para* position of the *N*-aryl unit did not lead to any significant improvement (entry 2). A slight increase in the enantiomeric ratio was observed when **L7** bearing a different 5-(*tert*-butyl)-2-methyl substitution pattern was used although selectivity was far from satisfactory (entry 3). Considering that the nature of the leaving group has been shown to significantly influence the outcome of the allylic substitution step, particularly in copper catalysts featuring an anionic group capable of establishing a cation-bridge ligand-substrate interaction,[55, 57, 59, 179, 183-184] we evaluated different allylic substrates. The use of *trans*-cinnamyl chloride **9** did not bring any improvement (entry 4). In sharp contrast, when *trans*-cinnamyl diethylphosphate **10** was employed product **8** was obtained with a promising 85:15 enantiomeric ratio, albeit with diminished conversion and yield (entry 5). The use of different solvent did not improve the reaction outcome (entries 6-8). Gratifyingly, the use of ligand **L8** which features a bulkier phenyl group at the *ortho*-position of the *N*-aryl ring in combination with the allylic phosphate led to the exclusive formation of product **8** with an improved enantioselectivity (96:4 er; entry 9). Interestingly, product yield was further enhanced by increasing the reaction stirring rate (entries 10-11), likely due to the improved acetylene mass transfer between the gas/liquid phases.[185] The effect of other *tert*-butoxides was evaluated but erosion in both enantiomeric ratio and yield was observed (entries 12-13). Thus, by using Cu/**L8** as catalyst at a reaction stirring rate of 1000 rpm under a 1 atm of acetylene atmosphere, product **8** was isolated as a single product in 74% yield with 96:4 enantiomeric ratio (entry 11).

Table 3.2.1. Optimization of the reaction conditions.

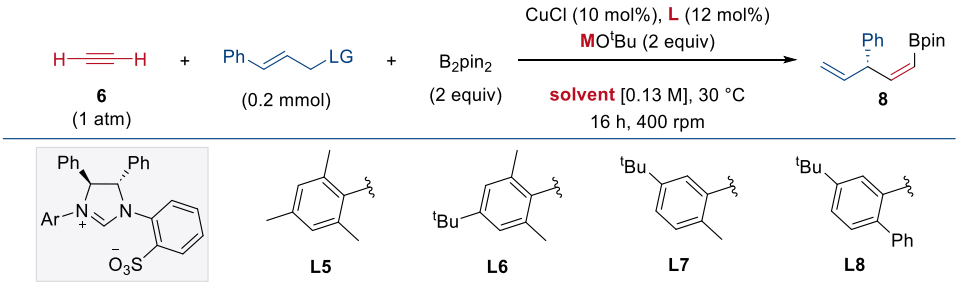

Entry[a]	LG	L*	Solvent	Conversion / %[b]	Yield / %[c]	e.r.[d]
1	Br	L5	Toluene	Full	54	60:40
2	Br	L6	Toluene	Full	63	59:41
3	Br	L7	Toluene	Full	49	66:34
4	Cl	L7	Toluene	51	49	57:43
5	$OP(O)(OEt)_2$	L7	Toluene	71	30	85:15
6	$OP(O)(OEt)_2$	L7	Hexane	64	33	73:27
7	$OP(O)(OEt)_2$	L7	THF	41	10	80:20
8	$OP(O)(OEt)_2$	L7	Dioxane	31	traces	n.d.
9	$OP(O)(OEt)_2$	L8	Toluene	Full	46	96:4
10[e]	$OP(O)(OEt)_2$	L8	Toluene	Full	64	96:4
11[f]	$OP(O)(OEt)_2$	L8	Toluene	Full	74	96:4
12[f] [g]	$OP(O)(OEt)_2$	L8	Toluene	75	35	90:10
13[f] [h]	$OP(O)(OEt)_2$	L8	Toluene	49	40	94:6

[a] Reaction conditions: allylic substrate (0.2 mmol), 6 (1 atm), B_2pin_2 (0.4 mmol), CuCl (10 mol%), ligand (12 mol%), NaO^{t}Bu (0.4 mmol), toluene (1.5 mL) at 30 °C and 400 rpm, unless otherwise noted. [b] Conversion (consumption of allylic substrate) was measured by ^{1}H-NMR analysis of the reaction crude using 1,3,5-trimethoxy benzene as internal standard. [c] Yield of isolated product. [d] Enantiomeric ratio was measured by chiral uHPLC analysis. [e] Reaction stirred at 800 rpm. [f] Reaction stirred at 1000 rpm. [g] Reaction conducted with LiO^{t}Bu instead of NaO^{t}Bu. [h] Reaction conducted with KO^{t}Bu instead of NaO^{t}Bu.

Once having identified the optimal reaction conditions for primary allylic substrates, we proceeded to study the reaction with the more challenging allylic *gem*-dichloride **11** (Table 3.2.2). We started adapting the obtained conditions in Table 3.2.1 by changing the base for LiO^{t}Bu – since we previously reported the excellent combination of Li^+ with this family of allylic substrates.[179] However, when using acetylene, moderate diastereoselectivity for **12** was observed (entry 1). This could be improved up to an excellent >20:1 ratio by using NaO^{t}Bu (entry 2). Further improvement was obtained by increasing temperature from 30 °C to 40 °C. Under these conditions, **12** was obtained in an excellent 86% yield with 96.5:3.5 e.r. and perfect *Z* selectivity (entry 3).

Table 3.2.2. Optimization of the reactions for allylic gem-dichlorides.

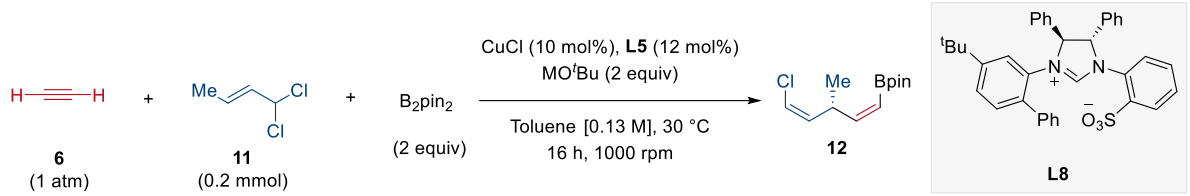

Entry[a]	M	T / °C	Conversion (%) [b]	Yield (%) [c]	e.r. [d]	d.r. [e]
1	Li	30	full	43	n.d.	87:13
2	Na	30	full	60	n.d.	> 20:1
3 [f]	Na	40	full	86	96.5:3.5	> 20:1

[a] Reaction conditions: 11 (0.2 mmol), 6 (1 atm), B_2pin_2 (0.4 mmol), CuCl (10 mol%), ligand (12 mol%), NaO^{t}Bu (0.4 mmol), toluene (1.5 mL) and 1000 rpm. [b] Conversion (consumption of starting material 11 was measured by ^{1}H-NMR analysis of the reaction crude using 1,3,5-trimethoxy benzene as internal standard. [c] Yield of isolated product. [d] Enantiomeric ratio was measured by chiral uHPLC analysis. [e] Diastereomeric ratio was by ^{1}H-NMR analysis on the reaction crude. [f] Enantiomeric ratio was measured by chiral uHPLC analysis in (*S*,*Z*,*Z*)-23 derivatization.

Scalability of the reaction was demonstrated although it required a slight modification of the reaction conditions (Table 3.2.3). When the reaction was performed on a 1 mmol scale under optimal conditions for lower scale (see above) product **8** was obtained in a moderate 47% yield, even after running the reaction for longer time, (entry 5). Nevertheless, since we were using a lower catalyst loading, we reasoned that a higher concentration may help to recover the efficiency of the reaction. Indeed, when the allylic substrate concentration was increased from 0.13 M to 0.26 M allylboration product was isolated in a good 65% yield (entry 6).

Once the optimized conditions were identified for both families of allylic substrates, we next explored the substrate scope for this reaction (Scheme 3.2.1). The methodology proved to be effective with a range of allylic phosphates. Phosphates bearing aromatic (**8, 13**, **14**) or heteroaromatic (**15**) substituents were well tolerated and provided the corresponding borylated skipped dienes with excellent chemo-, regio- and enantioselectivity in all cases. Notably, allylic phosphates bearing cyclic and acyclic alkyl units (**16**, **17**) were also efficient for the enantioselective allylboration of acetylene gas. Interestingly, the allylic phosphate derived from (−)-citronellal which bears a stereogenic center and an extra double bond was used with complete chemo- and diastereoselectivity (**18**). Allylic *gem*-dichlorides with aromatic substituents also proved to be efficient and furnished difunctionalized skipped dienes **19** and **20** with excellent diastereoselectivity and good enantioselectivity.

Table 3.2.3. Up-scaling studies.

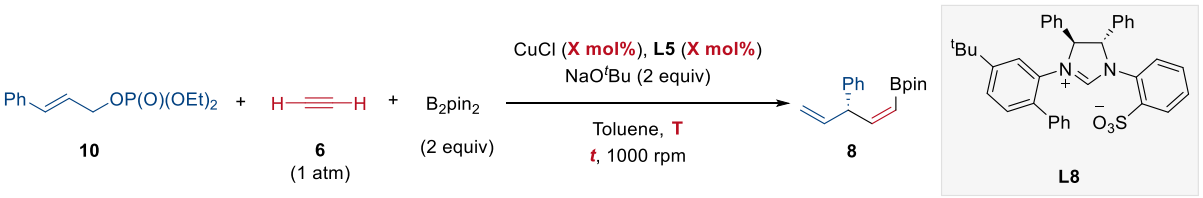

Entry[a]	Scale / mmol	CuL*/ mol%	T / °C	t / h	Conversion / % [b]	Yield /% [c]
1	0.5	10	30	16	full	74
2	0.5	5	30	16	80	40
3	0.5	5	40	16	full	48
4	0.5	5	30	30	full	73
5	1	5	30	30	73	47
6 [f]	1	5	30	30	full	65

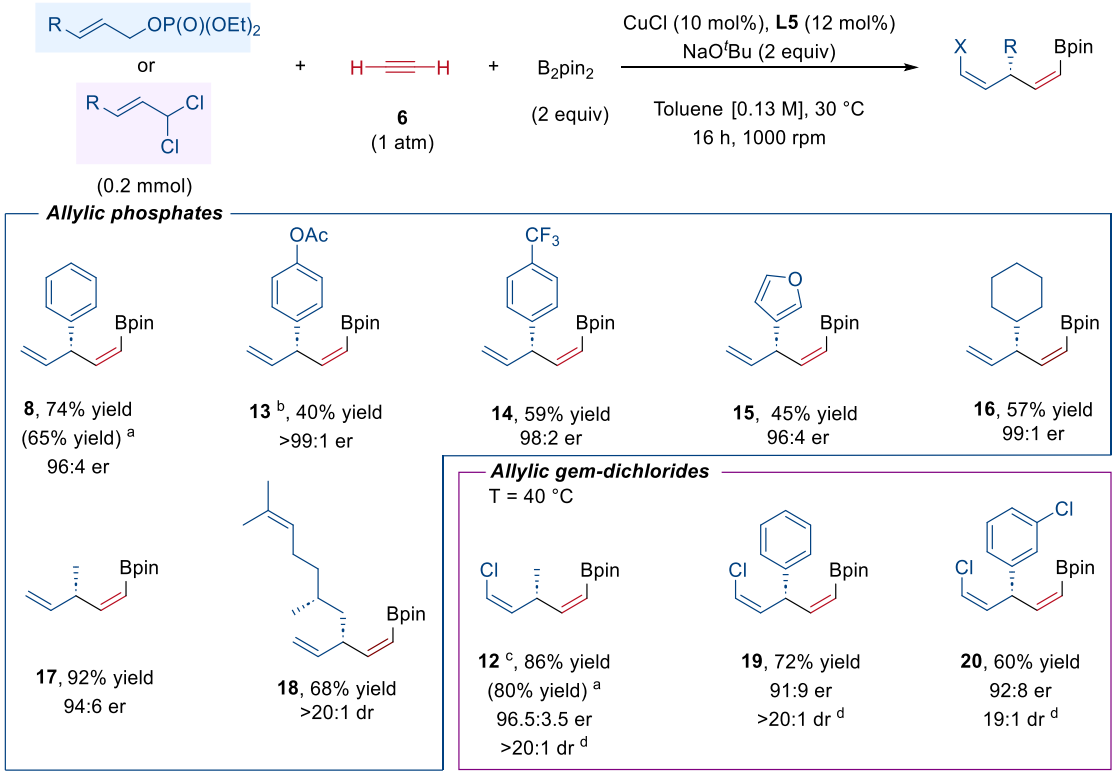

Scheme 3.2.1. Reaction scope. Unless otherwise noted, all reactions were performed on a 0.2 mmol scale under optimized conditions (Table 1, entry 8). Yield values refer to isolated products. [a] Reaction run on a 1 mmol scale using 5 mol% of the catalyst in toluene [0.27 M] during 30 h. [b] Reaction run at 20 °C. Allyl phosphate was added via syringe pump over 5 h. [c] Obtained from a 0.8:1 mixture of the allylic 1,1- and 1,3-dichlorides. Yield is referred to the 1,1-isomer. [d] *Z*:*E* ratio refers to the alkenyl chloride unit. Alkenyl boronate was obtained as *Z* isomer in all cases.

Absolute configuration of products was established by converting **13**, **17** and **12** into known compounds (see section 3.2.4), followed by comparison with the reported specific rotations. Importantly, we could extend the scalability of the reaction to the 1 mmol-scale synthesis of products **17** and **12**, in addition to **8**. These functionalized skipped dienes were isolated without erosion in yield or stereoselectivity, without the need of employing higher acetylene pressures.

3.2.2 DFT Mechanistic analysis

3.2.2.1 Gibbs free energy profile analysis

The origins of the high levels of enantio- and *Z*-selectivity were studied by DFT calculations using the formation of **12** as model reaction (see Section 5.3.5 for full computational details).

Given the high flexibility of the alkenylcopper complex arising from acetylene borylcupration (compared to phenylacetylene), different conformations arising from different orientation of the β-Bpin-alkenyl moiety were studied. First, we evaluated the formation of the major product **(*R*)-12-*Z*,*Z*** (Figure 3.2.2, right side). Here, two intermediates (**XII-*Z*,*R*** and **XII'-*Z*,*R***) similar in energy were found by modification of the β-Bpin-alkenyl unit orientation. Both pathways (black and blue pathways) proved to be viable ($\Delta G^{\ddagger}_{sol}$ = 21.1 kcal·mol^{-1} and 22.2 kcal·mol^{-1}, for $\mathbf{TS_{OA}^{XII-XIII}}$**-*Z*,*R*** and $\mathbf{TS_{OA}^{XII'-XIII'}}$**-*Z*,*R*** respectively), with the former being slightly more favorable. In this preferred pathway associated with the formation of product **(*R*)-12-*Z*,*Z*** (black pathway), comparison of the activation energy barriers for the oxidative addition of the allylic *gem*-dichloride into **XII-*Z*,*R*** ($\Delta G^{\ddagger}_{sol}$ = 21.1 kcal·mol^{-1}) and reductive elimination from allyl-Cu(III) intermediate **XIII-*Z*,*R*** ($\Delta G^{\ddagger}_{sol}$ = 0.8 kcal·mol^{-1}) revealed that the former is the stereodetermining step. This was assumed for the other pathways, and we thus focused on the study of the different transition states related to this step. In agreement with the experimental observations, pathways found for the formation of the minor enantiomer **(*S*)-12-*Z*,*Z*** (Figure 3.2.2, left side; orange and green pathways) proved to be higher in energy ($\Delta G^{\ddagger}_{sol}$ =22.5 kcal·mol^{-1} and 23.2 kcal·mol^{-1}, $\mathbf{TS_{OA}^{XII-XIII}}$**-*Z*,*S*** and $\mathbf{TS_{OA}^{XII'-XIII'}}$**-*Z*,*S***, respectively). The calculated $\Delta\Delta G^{\ddagger}_{sol}$ between the lowest-energy pathways for each enantiomer ($\mathbf{TS_{OA}^{XII-XIII}}$**-*Z*,*R*** *vs* $\mathbf{TS_{OA}^{XII-XIII}}$**-*Z*,*S***) is 1.4 kcal·mol^{-1}, which is in good agreement the value derived from the experimental result (96.5:3.5 er, $\Delta\Delta G^{\ddagger}_{eq}$ = 1.9 kcal·mol^{-1}).

We then evaluated the different pathways for the formation of the minor *Z* diastereomer **(*R*)-12-*Z*,*E*** and compared its energy with the formation of the major product **(*R*)-12-*Z*,*Z*** (Figure 3.2.3). Both pathways associated with the lowest-energy conformations (red and purple pathways) feature higher activation energy barriers ($\Delta G^{\ddagger}_{sol}$ =25.6 kcal·mol^{-1} and 31.6 kcal·mol^{-1}, $\mathbf{TS_{OA}^{XII-XIII}}$**-*E*,*R*** and $\mathbf{TS_{OA}^{XII'-XIII'}}$**-*E*,*R*** respectively) which support the observed selectivity for the formation of the *Z*-alkenyl chloride. In both cases the corresponding allyl-Cu(III) intermediate could not be found, resulting in direct collapse of transition states $\mathbf{TS_{OA}^{XII-XIII}}$**-*E*,*R*** and $\mathbf{TS_{OA}^{XII'-XIII'}}$**-*E*,*R*** into the coordinated product. This is likely due to an insignificant energy barrier for the reductive elimination step.

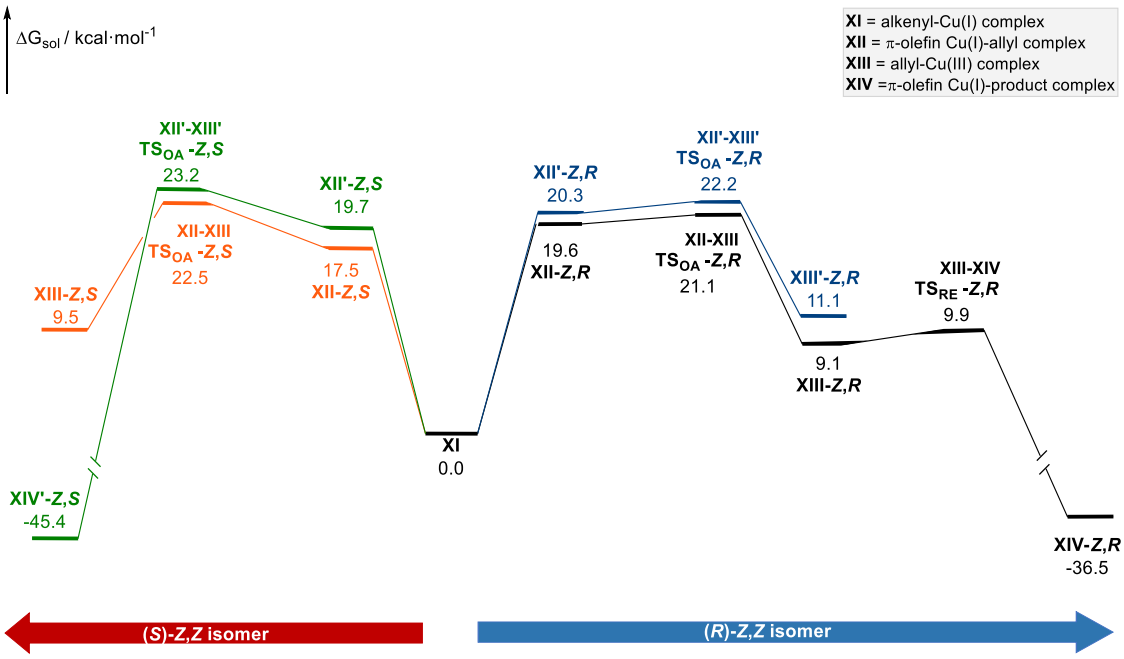

Figure 3.2.2. Free energy profile computed at the ωB97XD/def2-TZVP/def2-QZVP (Cu) (scrf=smd, toluene) //ωB97XD/6-31G(d,p)/SDD+f (Cu) level for the pathways associated to the formation of **(*R*)-12-*Z*,*Z*** (black and blue profiles) and **(*S*)-12-*Z*,*Z*** (orange and green profiles). Energies are relative to complex **I** combined with those of the relevant substrates. Subscripts OA and RE in transition state labels refer to oxidative additions and reductive elimination, respectively. See Appendix B.III for optimized structures.

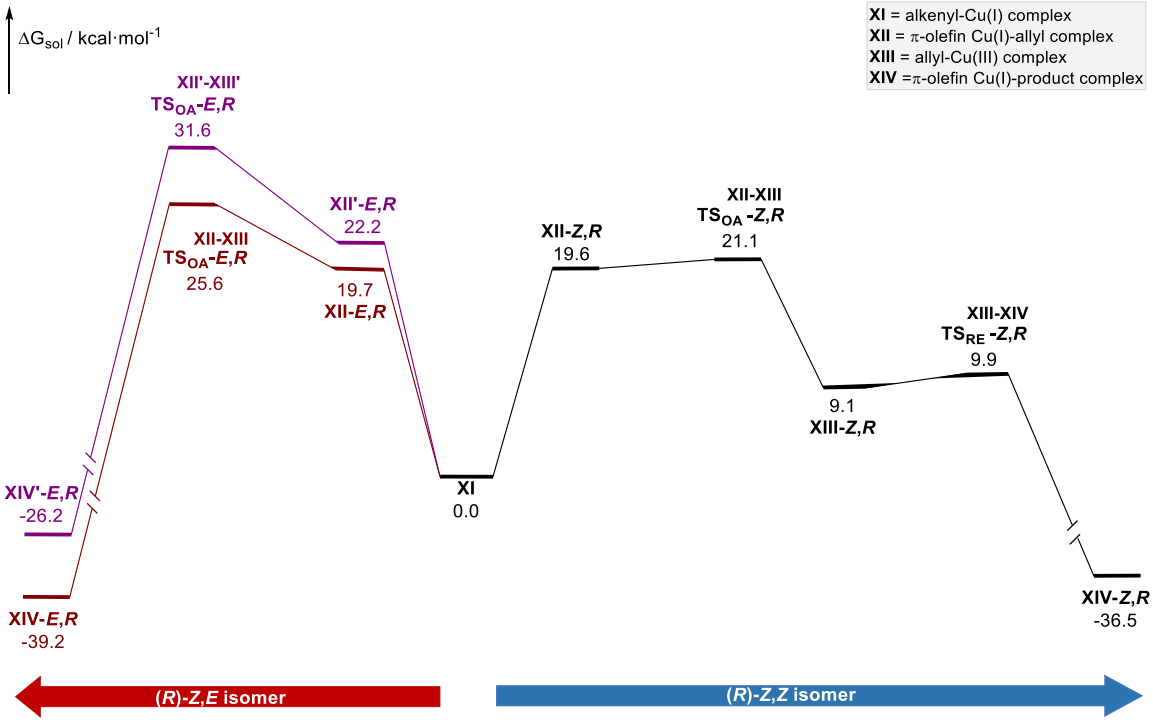

Figure 3.2.3. Free energy profile computed at the ωB97XD/def2-TZVP/def2-QZVP (Cu) (scrf=smd, toluene) //ωB97XD/6-31G(d,p)/SDD+f (Cu) level for the pathways associated to the formation of both enantiomers of product **(*R*)-12-*Z*,*Z*** (black profile, right) and **(*R*)-12-*Z*,*E*** (red and purple profiles, left). Energies are relative to complex I combined with those of the relevant substrates. OA and RE refer to oxidative addition and reductive elimination, respectively. See Appendix B.III for optimized structures.

3.2.2.2 Non-covalent interactions analysis.

Non-Covalent Interactions (NCI) analysis on the stereodetermining transition states revealed that this energy difference mainly accounts for repulsive interactions that are engendered between the methyl substituent of the allyl fragment and the Bpin unit (Figure 3.2.4, blue box), and between the allylic C_α and the sulfonate moiety of the ligand (Figure 3.2.4, red box) which are larger in $\mathbf{TS_{OA}^{XII-XIII}}$-***Z,S***. Regarding the *Z* selectivity in the formation of the alkenyl chloride, the Cl··Na··sulfonate interaction in $\mathbf{TS_{OA}^{XII-XIII}}$-***E,R*** imposed by the chlorine atoms orientation promotes a rotation over the C_{NHC}–Cu bond which brings the *N*-aryl ring closer to the Bpin unit, thus creating a steric clash between the ^{t}Bu group and the Bpin unit (Figure 3.2.5, blue box). This new spatial disposition also enhances the repulsive interaction between the allyl fragment and the sulfonate aryl ring in $\mathbf{TS_{OA}^{XII-XIII}}$-***E,R*** (Figure 3.2.5, red box). This set of repulsive interactions result in a higher energy transition state and would explain the origin of the *Z* selectivity.

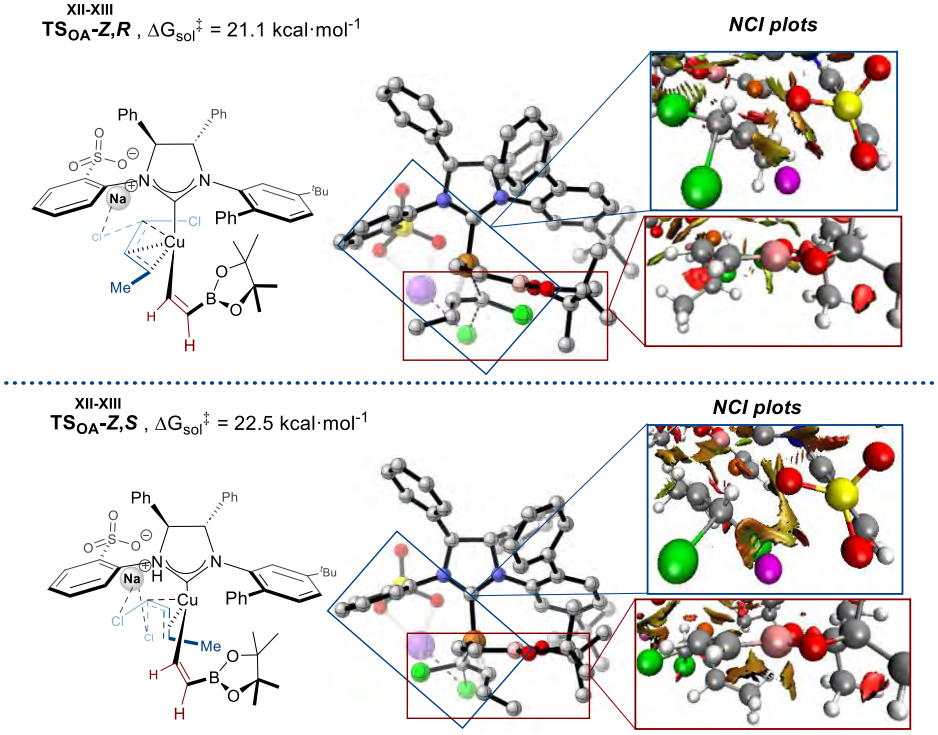

Figure 3.2.4. Optimized structures and energies obtained from DFT calculations performed at the ωB97XD/*def2*-TZVP/*def2*-QZVP (Cu) (scrf = smd, toluene) // ωB97XD/6-31G(d,p)/SDD+f (Cu) level for the stereochemistry-determining oxidative-addition transition states associated with the most favored pathways leading to (a) **(*R*)-12-*Z*,*Z*** and **(*S*)-12-*Z*,*Z***. For full set of NCI plots see Appendix C.III.

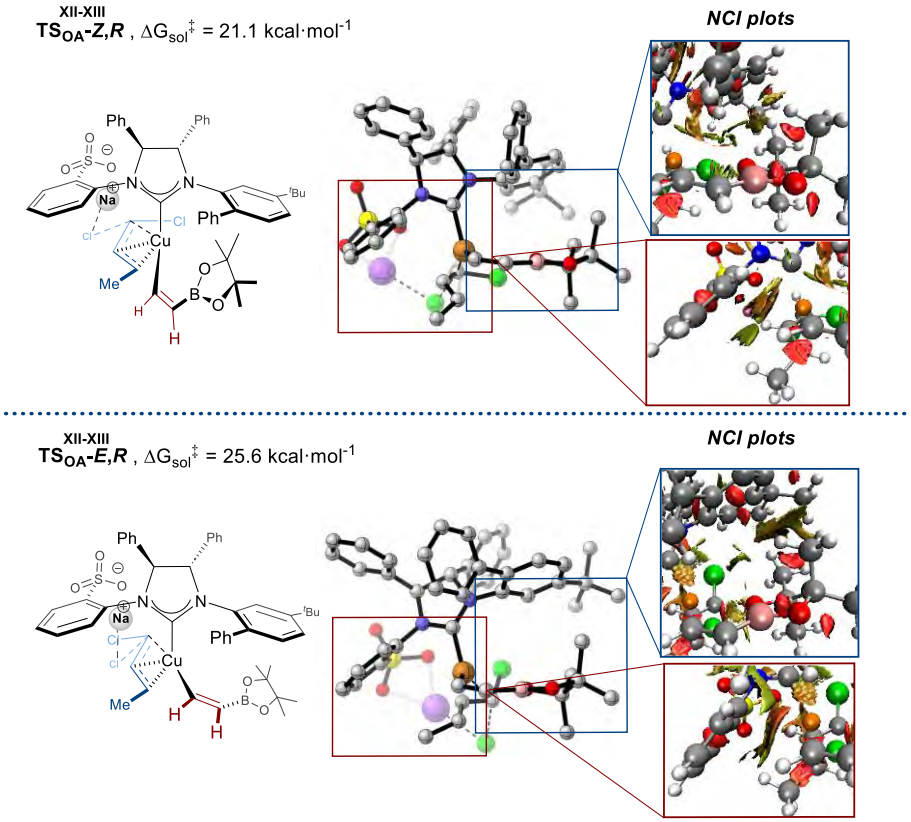

Figure 3.2.5. Optimized structures and energies obtained from DFT calculations performed at the ωB97XD/*def2*-TZVP/*def2*-QZVP (Cu) (scrf = smd, toluene) // ωB97XD/6-31G(d,p)/SDD+f (Cu) level for the stereochemistry-determining oxidative-addition transition states associated with the most favored pathways leading to **(*R*)-12-*Z*,*Z*** and **(*R*)-12-*E*,*Z***. For full set of NCI plots see Appendix C.III.

3.2.3 Enantio- and Diastereodivergence

An important challenge in asymmetric synthesis is the ability to access the complete set of possible stereoisomers of a molecule with full stereocontrol from the same substrate.[186-189] A very interesting structural feature of the skipped diene products that arise from the enantioselective allylboration of acetylene gas with allylic *gem*-dichlorides is the presence of two orthogonally functionalized disubstituted olefins having equal stereochemistry. We reasoned that a simple two-step sequence involving Suzuki coupling with an organic halide and a boronic acid in which the structure of those reagents is switched would provide enantiodivergent access to both enantiomers of the coupled product. We sought to demonstrate this idea by the enantiodivergent transformation of compound **12** which was converted into enantiomeric products **(*S*,*Z*,*Z*)-23** and **(*R*,*Z*,*Z*)-23** in good yields (Scheme 3.2.2).

The vast reactivity of alkenyl boronate[190] and alkenyl chloride[191] units also offered the possibility to explore the diastereodivergent transformation of compound **12** into the four possible stereoisomers derived from the two olefins of the skipped diene core. Beyond the synthesis of **(*S*,*Z*,*Z*)-23**, combination of stereoretentive and stereoinvertive cross-couplings allowed access to the other three diastereomers (Scheme 3.2.3). A reaction sequence based on initial Suzuki-Miyaura coupling followed by alkenyl chloride conversion into the corresponding alkyne by LDA-mediated dehydrochlorination, alkyne hydroboration and final Suzuki coupling afforded product **(*S*,*E*,*Z*)-23** without erosion of the enantiomeric ratio. The Zweifel olefination in which addition of an organometallic reagent to an alkenyl boronic ester

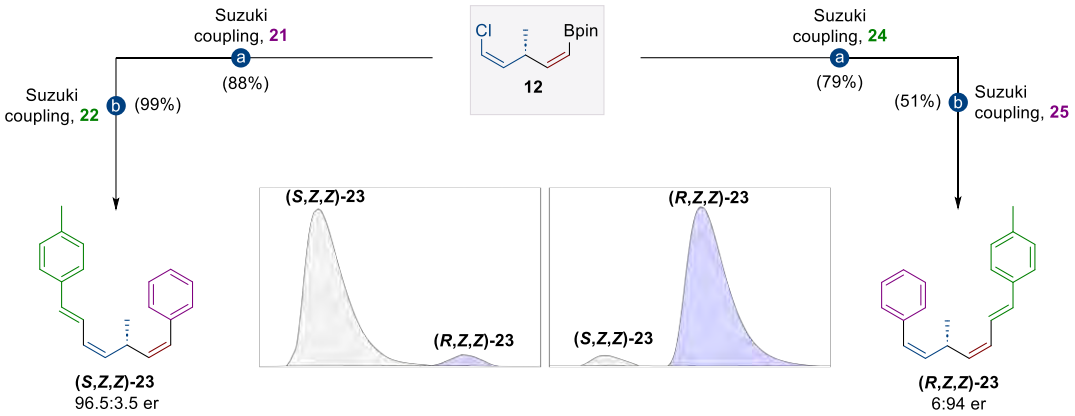

Scheme 3.2.2. Enantiodivergent modifications of chiral skipped diene **12**. a) **21** or **24**, $Pd(PPh_3)_4$ (10 mol%), $NaOH_{(aq)}$ [2 M], Dioxane, 40 °C, 16 h. b) **22** or **25**, $Pd_2(dba)_3$ (5 mol%), XPhos (10 mol%), CsF, 100 °C, 2 h. See the Section 5.3 for detailed experimental conditions. **21** = iodobenzene **22** = (*E*)-(4-methylstyryl)boronic acid. **24** = (*E*)-1-(2-bromovinyl)-4-methylbenzene. **25** = phenylboronic acid.

generates an alkenyl boron-ate complex which is subsequently treated with iodine and sodium hydroxide is an appealing method for the stereoinvertive synthesis of alkenes.[192] Based on this methodology, the alkenyl-Bpin unit in **12** was converted through a stereoinvertive coupling into a *Z*,*E*-configured skipped dienyl chloride which by Suzuki coupling led to the formation of isomer **(*S*,*Z*,*E*)-23** with retention of the enantioselectivity. Finally, a sequence involving Zweifel olefination, dehydrochlorination, hydroboration an final Suzuki cross-coupling furnished the remaining diastereomer **(*S*,*E*,*E*)-23** with excellent levels of selectivity (Scheme 3.2.3).

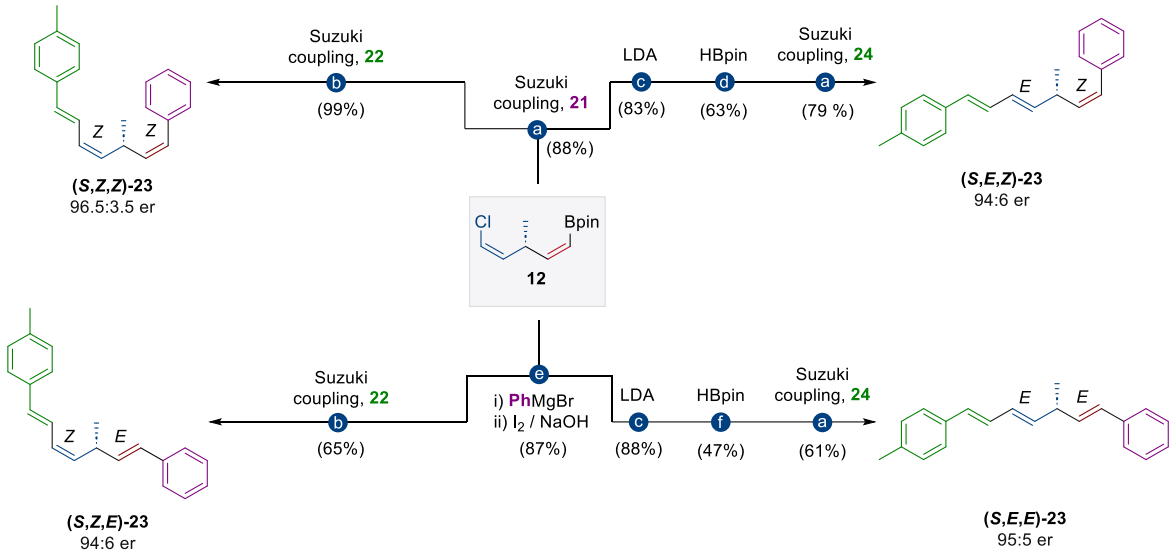

Scheme 3.2.3. Diastereodivergent modifications of chiral skipped diene **10**. Reaction conditions: **a**) **21** or **24**, $Pd(PPh_3)_4$ (10 mol%), $NaOH_{(aq)}$ [2 M], Dioxane, 40 °C, 16 h. **b**) **22**, $Pd_2(dba)_3$ (5 mol%), XPhos (10 mol%), CsF, 100 °C, 2 h. **c**) ^{n}BuLi, $^i Pr_2NH$, THF, 30 min, -78 °C, 45 min. **d)** HBpin, Et_3N, Cp_2ZrHCl (10 mol%), THF, 60 °C, 48 h. **e**) (i) PhMgBr, Et_2O, 30 min, -78 °C, then 1 h, 0 °C; (ii) I_2, MeOH, 0 °C to rt, 3 h; (iii) $NaOH_{(aq)}$ [3 M], rt, 15 min. **f**) HBpin, $BH_3{\cdot}SMe_2$ [2 M in THF] (10 mol%), 60 °C, 20 min. See the Section 5.3 for detailed experimental conditions. **21** = iodobenzene **22** = (*E*)-(4-methylstyryl)boronic acid. **24** = (*E*)-1-(2-bromovinyl)-4-methylbenzene. LDA = lithium diisopropylamide.

3.2.4 Synthetic Utility

3.2.4.1 Stereodivergent enantioselective total syntheses of (+)-Nyasol and (+)-Hinokiresinol.

The synthetic transformations outlined in Scheme 3.2.3 underscore the potential of our method to access chiral skipped dienes in a stereodivergent manner. Application of such processes to the synthesis of natural bioactive compounds would be a clear indicator of the utility of this catalytic enantioselective methodology. We first targeted the enantioselective synthesis of the natural products (+)-Nyasol and (+)-Hinokiresinol which are stereoisomeric naturally occurring norlignans, firstly isolated by Brown[193] and Nakatsuka,[194] with antiplasmoidal and antileishmanial properties, respectively (Figure 3.2.6). We envisioned a stereodivergent strategy from chiral borylated skipped diene **13** which is accessed from the copper-catalyzed enantioselective allylboration of acetylene with excellent enantioselectivity (>99:1 er) and complete regiocontrol and *Z*-selectivity.

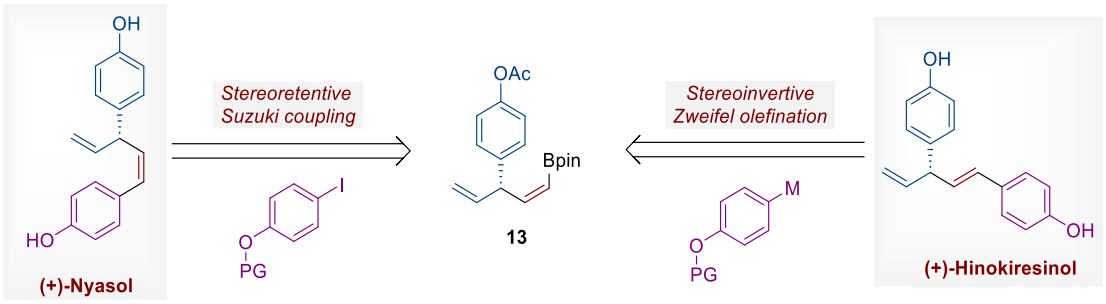

Figure 3.2.6. Retrosynthetic plan for accessing (+)-Nyasol and (+)-Hinokiresinol natural products.

For Suzuki coupling optimization (Table 3.2.4), we explored different palladium sources and ligands, as well as bases. $Pd(PPh_3)_4$ performed poorly (entry 1), but $Pd_2(dba)_3$ combined with XPhos allowed to increase the yield of **26** from 13% to 50% (entry 2). The use of dppf was detrimental (entry 3). When CsF was used as based instead of NaOH, the yield of the reaction dropped while ester hydrolysis did not occur, and AcO-protected product (**27**) was obtained instead (entry 5). Finally, increase of the equivalents of base (which plays a double role in the activation of the boronic ester and promoting the hydrolysis of the acetate group) led to a slight increase in the yield (54%).

Table 3.2.4. Optimization for Suzuki coupling reaction over diene **13.**

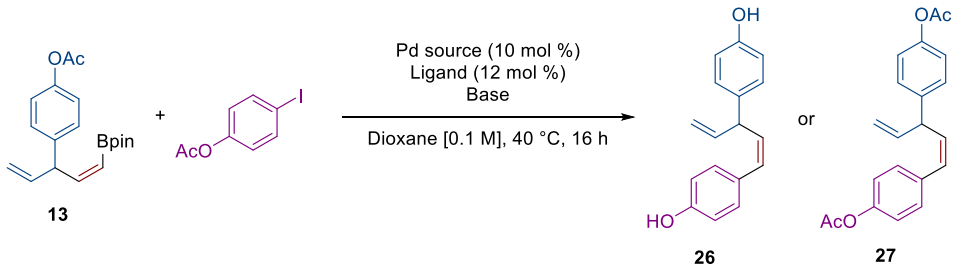

Entry	Pd source	Ligand	Base	Yield / % (27)
1	$Pd(PPh_3)_4$	-	NaOH [2 M] (2 equiv)	13
2	$Pd_2(dba)_3$	XPhos	NaOH [2 M] (2 equiv)	50
3	$Pd_2(dba)_3$	dppf	NaOH [2 M] (2 equiv)	32
4	$Pd_2(dba)_3$	XPhos	CsF (3 equiv)	(30)
5	$Pd_2(dba)_3$	XPhos	NaOH [2 M] (4 equiv)	54

The results show in Scheme 3.2.8 illustrate how, (+)-Nyasol could be easily obtained from **13** by a stereoretentive Suzuki cross-coupling with 4-iodophenyl acetate in which both phenol units would be deprotected under reaction conditions (Scheme 3.2.4). On the other hand, stereoinvertive Zweifel coupling with (4-methoxyphenyl)magnesium bromide-LiCl complex and subsequent MeO-deprotection provided (+)-Hinokiresinol in good overall yield (Scheme 3.2.4). It is important to note that the present method does not require the preparation and isolation of a stereodefined alkenylboron compound prior to the enantioselective step, allowing access to both natural products from the same precursor obtained from a simple and abundant chemical feedstock such as acetylene gas.

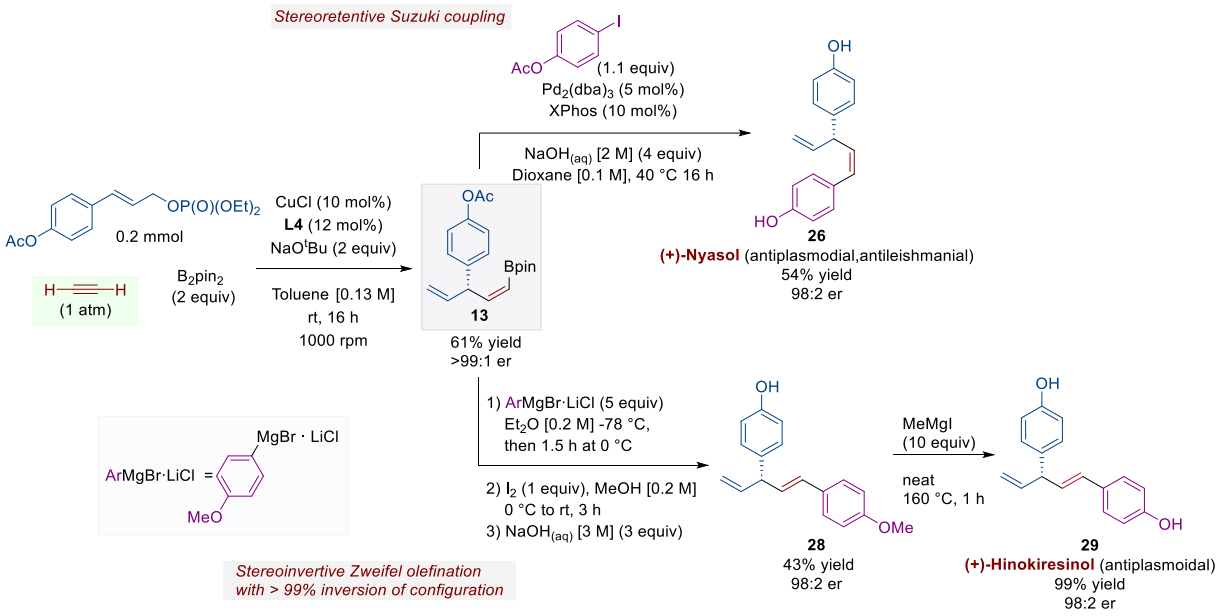

Scheme 3.2.4. Stereodivergent total syntheses of (+)-Nyasol and (+)-Hinokiresinol from chiral borylated skipped diene 13.

3.2.4.2 Enantioselective formal synthesis of Phorbasin C

We next devised the formal synthesis of (+)-Phorbasin C, a diterpene isolated from a southern Australian marine sponge (Phorbas sp.),[195] which has shown cytotoxic activity against lung, colorectal and breast cancer cell lines (Figure 3.2.7).[196] Our strategy was based on the synthesis of compound **30**, a key intermediate in the total synthesis of Phorbasin C.[197] We first devised a two-step route towards **30** involving a stereoinvertive Zweifel olefination followed by Ru-catalyzed cross-metathesis, using diene **17** as the starting point.

When we tried the first route (Figure 3.2.7, upper route), Zweifel coupling with **17** surprisingly failed despite using different solutions of ^{i}BuLi. Analysis of reaction crude suggested an overreactivity of the Zweifel-derived substrate and its transformation into an epoxide at the terminal olefin (Table 3.2.5, entries 1 and 2).

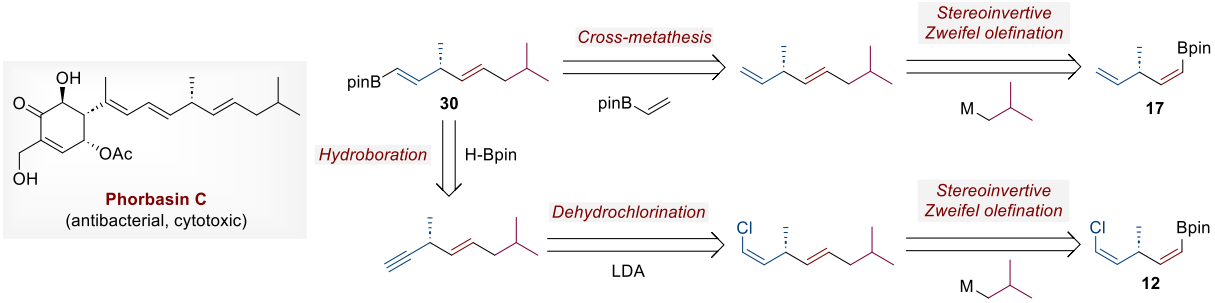

Figure 3.2.7. Retrosynthetic plan for accessing borylated skipped diene **30**.

We then focused on an alternative route involving a first Zweifel olefination using **12** instead of **17**, followed by a dehydrochlorination of the resulting skipped diene, and a final hydroboration reaction. Satisfactorily, when we moved towards the alternative plan based on skipped diene **12**, we could isolate the desired product in 42% yield (Table 3.2.5, entry 3), and it could be improved up to 60% after a slight modification on I_2 addition step (entry 4). Conditions for subsequent steps were based on the diastereodivergent protocols, with minor adaptations.

Table 3.2.5. Optimization for Zweifel olefination reaction over dienes **17** and **12.**

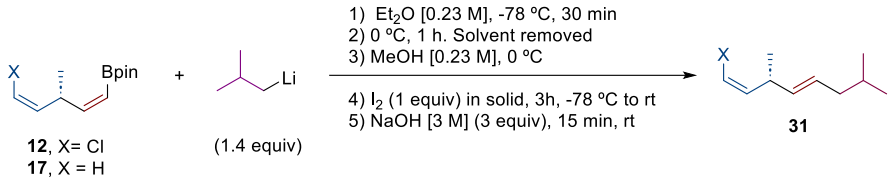

12, X= Cl
17, X = H

Entry	X	RLi [X M]	Yield / %
1	H	1.7 M in heptane	-
2 [a]	H	0.67 M in Et_2O	-
3 [a]	Cl	0.67 M in Et_2O	42 [b]
4 [a,c]	Cl	0.67 M in Et_2O	60

a) *In situ* prepared ^{i}BuLi from ^{i}BuBr and ^{t}BuLi. b) Yield after two columns. c) I_2 added in solid form after MeOH.

In summary, **30** could be prepared from difunctionalized skipped diene **12** following a protocol involving a Zweifel olefination with ^{i}BuLi, subsequent LDA-promoted dehydrochlorination and a final zirconium-catalyzed alkyne hydroboration (Scheme 3.2.5). It is important to highlight that this skipped diene skeleton is present in most of the members of the Phorbasin family (Phorbasins B–K).[198] Thus, the present methodology also represents a new simple and efficient synthetic avenue towards the enantioselective synthesis of these bioactive compounds.

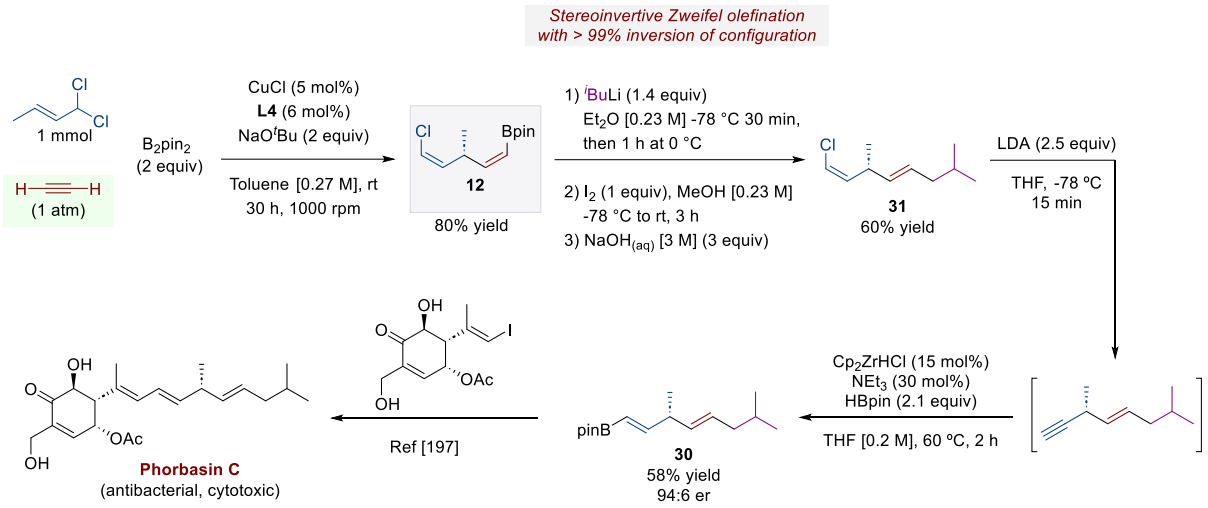

Scheme 3.2.5. Formal synthesis of Phorbasin C from chiral difunctionalized skipped diene **12.**

3.2.4.3 Enantioselective synthesis of other relevant chiral molecules

The copper-catalyzed enantioselective allylboration of acetylene described herein not only offers the possibility of synthesizing skipped diene products. For instance, the dehydrochorination of the alkenyl chloride unit provides a chiral skipped enyne structure that also serves as important reaction intermediate in the synthesis of bioactive compounds.

We sought to demonstrate this by the enantioselective synthesis of product **34** which was reported as an advanced intermediate for the total synthesis of gonadotropin-releasing hormone (GnRH) antagonist **35** (Scheme 3.2.6).[199] Retrosynthetic analysis led us to envision two key disconnections (Sonogashira coupling and Zweifel olefination) and one functional group modification (dehydrochlorination), starting from difunctionalized skipped diene **12**. Synthetic route was evaluated, and the designed pathway rendered chiral skipped enyne **25** in 29% overall yield (Scheme 3.2.6, a). Synthetically relevant chiral small molecules can also be targeted by applying the enantioselective allylboration of acetylene. Chiral alcohol **36** has been reported as a key intermediate for the synthesis of several natural and bioactive products.[200-205] Despite its apparent simplicity, its enantioselective synthesis relies on the use of stoichiometric chiral auxiliaries,[206-207] chiral pool strategies (i.e. enantiopure citronellene multistep transformation)[200-201] or Ru-catalyzed hydrogenation at 100 bar dihydrogen pressure.[204] Since alkenyl boronic esters are easily oxidized to aldehydes, we could synthesize product **36** in very good yield and with very high enantioselectivity from borylated skipped diene **17** through a straightforward, mild and simple oxidation-reduction protocol (Scheme 3.2.6, b).

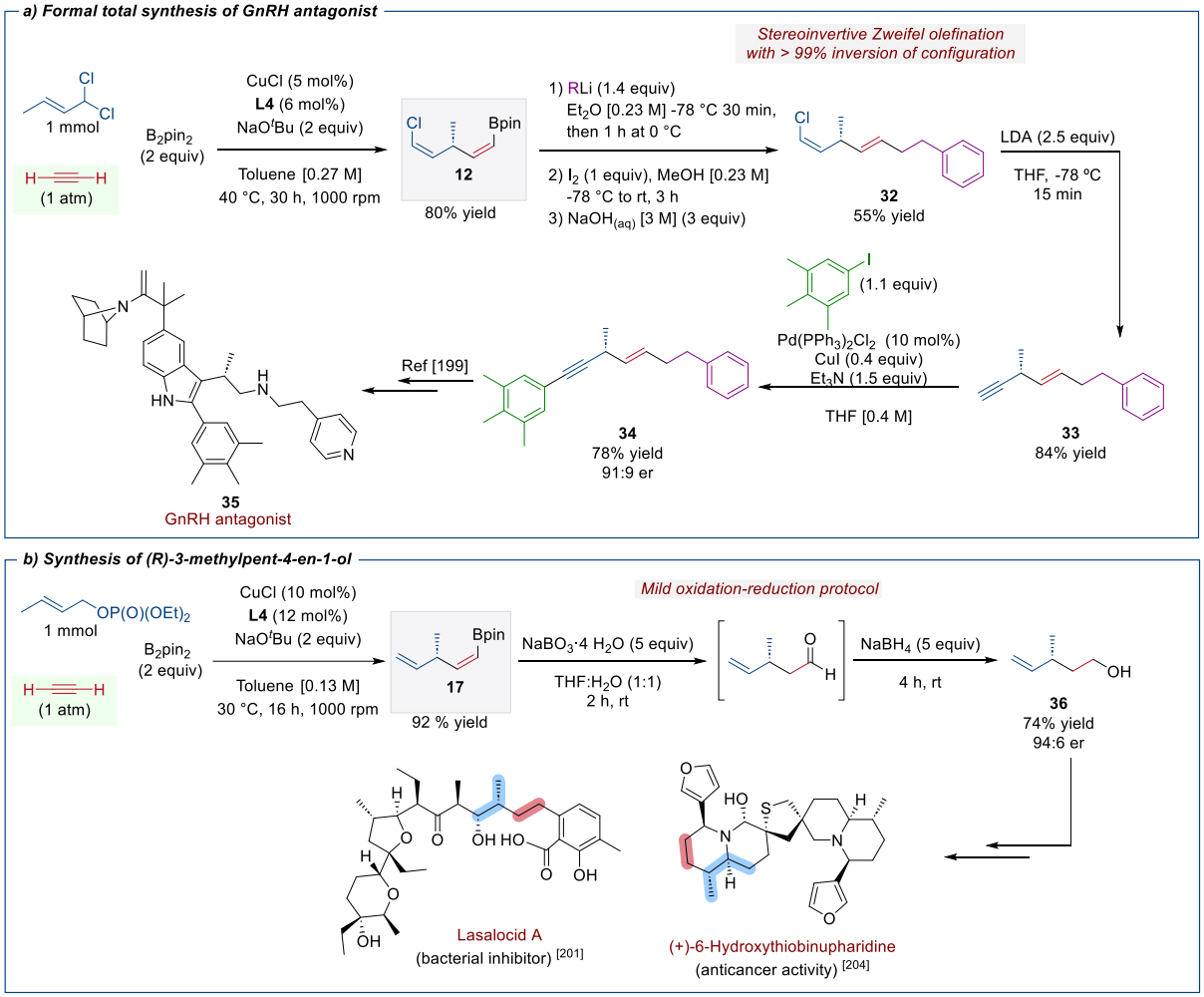

Scheme 3.2.6. Enantioselective synthesis of other relevant chiral molecules.

3.2.4.4 Comparative analysis of synthetic applications

The synthetic strategies outlined above demonstrate how the enantioselective acetylene allylboration serves as an effceint tool for the stereodivergent synthesis of chiral skipped dienes and related molecules. In its application to the synthesis of natural products, and compared with previous methodologies, the allylboration of acetylene avoids the necessity of pre-synthesizing stereodefined olefins for subsequent coupling and the preparation of enantiopure allylic substrates for later stereospecific allylation. These features represent a significant shortcut in the synthetic pathways, reducing the number of steps, enhancing atom efficiency and avoiding the (super)stoichiometric utilization of organometallic or harmful reagents (e.g. dibal-H, $Pb(OAc)_2$ or HF). Moreover, the high stereoselectivity displayed for the reaction improves methodologies relying on procedures that leads to diastereomeric mixtures of olefins (*E*:*Z* and branch:linear) or mixtures of dienes (1,4:1,3). To illustrate the advantages of our protocol over the previously reported strategies, a summary of the most important features in each case are depicted in Table 3.2.6.

Table 3.2.6. Comparison between previous methodologies and the ones based on acetylene allylboration for the total synthesis of the natural products mentioned in this chapter.

Product	Nº steps (Overall yield)	Comments
Nyasol	6 [182] (42%)	Conversion of trimethylsilylacetylene into internal alkyne via Sonogashira coupling; formation of alkenylaluminum reagent via a hydroalumination with dibal-H (2 equiv); Cu-catalyzed enantioselective allylic substitution; three protection/deprotection steps.
	2 [176] (58%)	Ir-catalyzed enantioselective allylic substitution with *cis-para*-methoxystyryl trifluoroborate salt (branched:linear 3.8:1). Use of HF (2 equiv); final deprotection of the methoxy groups with MeMgI.
	4 [177] (50%)	Formation of a *cis*-alkenyl-Bpin reagent via *Z*-selective Mo-catalyzed cross-metathesis; Cu-catalyzed enantioselective allylic substitution, -OTs deprotection under basic conditions and final deprotection of the methoxy group with MeMgI.
	2 (33%)	*This work*
Hinokiresinol	2 [176] (67%)	Ir-catalyzed enantioselective allylic substitution with *trans-para*-methoxystyryl trifluoroborate salt (branched:linear 18:1). Use of HF (2 equiv); final deprotection of the methoxy groups with MeMgI.
	3 (26%)	*This work*
Advanced intermediate **22** (formal synthesis of Phorbasin C)	6 [197] (16%)	Multistep procedure from (2*S*)-2-methyl-3-(tetrahydro-*2H*-pyran-2-oxy)propan-1-ol[c] involving oxidation, Julia-Kocienski olefination, THP deprotection, oxidation, Takai olefination (1,4:1,3 diene 5:1) and lithium halogen exchange/borylation.
	4 (28%)	*This work*
Advanced intermediate **25** (formal synthesis of GnRH inhibitor)	6 [199, 208] (23%)	Ru-catalyzed enantioselective reduction of 1-phenyl-4-hexyn-3-one; protection of resulting alcohol with TBDMSCl; *Z*-selective reduction of alkyne with Pd/$BaSO_4$; TBS deprotection, phosphate formation and Cu-catalyzed stereospecific allylic substitution.
	4 (29%)	*This work*
3-methylpent-4-en-1-ol (**27**)	4 [200] (25%)	Chiral pool strategy from (+)-citronellene involving monepoxidation of internal olefin and isomerization to ketone. Autoxidative degradation led to mixture of aldehyde and carboxylic acid, that was then reduced to alcohol **27** with $LiAlH_4$.
	5 [201] (38%)	Chiral pool strategy from (-)-citronellene involving hydroboration of terminal alkene with 9-BBN, oxidation to alcohol and acylation; oxidative cleavage of trisubstituted olefin by ozonolysis to the carboxylic acid; Kochi decarboxylative oxidation ($Pb(OAc)_2$/$Cu(OAc)_2$) to install the vinyl group and final basic hydrolysis.
	3 [204] (79%)	Ru-catalyzed asymmetric hydrogenation of 2-methylene-γ-butyrolactone (H_2, 100 bar); lactone reduction with *i*Bu_2Al-H (1.1 equiv) to give crude lactol; Wittig reaction with methyltriphenylphosphonium bromide.
	3 (67%)	*This work*

3.3 $FeCl_3$ PHOTORREDOX HAT CATALYZED DIRECT Csp^3-Csp^3 ALLYLATION OF ETHANE

As outlined in section 1.3.2, several transformations have been described in the past years for the functionalization of gaseous alkanes. However, these transformations were mainly limited to Giese type reactions, while research mainly focused on developing different HAT photocatalyst to promote the C−H activation. Radical Giese type reactions are characterized by ending up with a carbon-centered radical that is the responsible for reoxidizing the reduced photocatalyst, restarting the catalytic cycle. However, radical allylation reactions using gaseous alkanes were not reported. These kinds of reactions, following a S_H2 or S_H2' mechanism, are much more challenging since no carbon-centered radical is formed and, therefore, compromises the photocatalyst oxidation step.

Kamijo and co-workers, in 2016, reported the direct C−H allylation of cyclic alkanes with activated allyl sulfones, by using 5,7,12,14-pentacenetetrone (PT) as a HAT photocatalyst (Scheme 3.3.1, a).[209] The use of this arylketone as the HAT photocatalyst enabled the reaction to be efficiently conducted both under 365 nm (UV-A) and even 425 nm visible light irradiation. Furthermore, the group of Wu, along with the reported Giese additions (Scheme 1.3.8), also included examples of radical allylations under the same reaction conditions (Scheme 3.3.1, b).[137] The two protocols rely on the use of activated allyl substrates, in combination with a well-known leaving group capable of undergoing SET with the reduced photocatalyst, promoting its reoxidation and consequent regeneration. However, the atom economy of the transformation is significantly low.

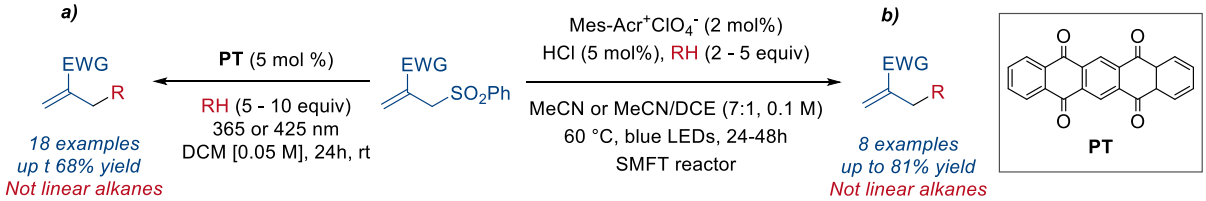

Scheme 3.3.1. Radical C−H allylation of cyclic alkanes a) catalyzed by arylketone PT and b) by acridinium photocatalyst.

In a recent publication, the group of Gong reported the dual use of nickel/TBADT catalysis for the allylation of alkanes with branched allylic carbonates bearing aromatic groups (Scheme 3.3.2).[210] The reaction provides linear products and was shown to work efficiently for cyclic alkanes. When linear alkanes were used, reaction was observed to proceed in low yield and regioselectivity. Mechanistic studies by DFT calculations suggest that the reaction goes through the formation of an alkyl–Ni(I) by combining the alkyl radical with the catalytically active Ni(0) complex. Subsequently, an oxidative addition of the allylic carbonate leads to an allyl–Ni(III) intermediate. This intermediate reacts with the doubly reduced decatungstate $2H[W_{10}O_{32}]^{6-}$ *via* SET to generate an allyl–Ni(II) complex that provides, after being subjected to a reductive elimination, the desired product and while recovering the active Ni(0) species.

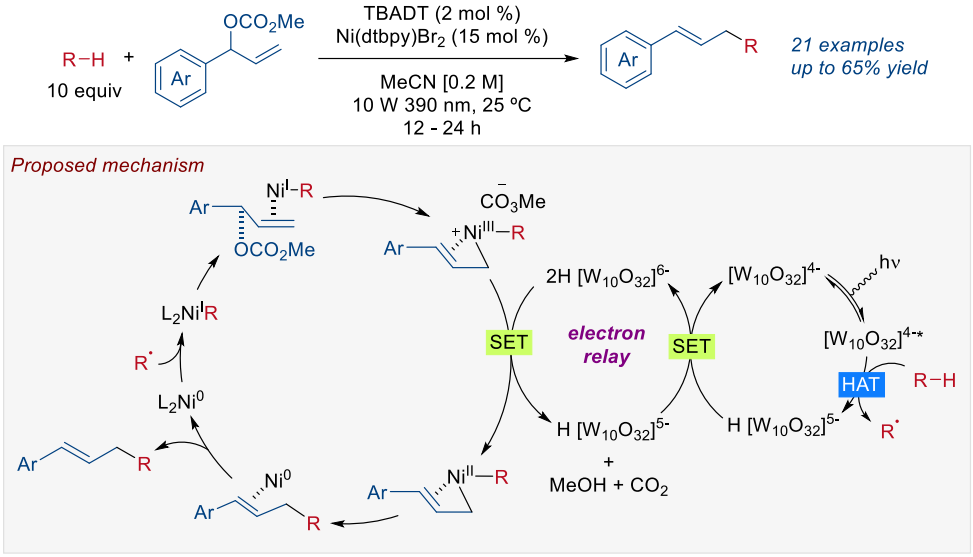

Scheme 3.3.2. Dual Ni/TBADT photocatalyzed C-H allylation of alkanes.

Simultaneously, our research group described a photocatalytic approach that allowed alkanes to be directly coupled with allylic chlorides (Scheme 3.3.3).[211] This process was based on a cooperative effect between TBADT and a Cu(I) co-catalyst. In this transformation, the alkyl radical generated after photocatalyzed HAT undergoes to a S_H2' reaction with an activated allylic π-olefin-Cu(I) complex. This step results in the formation of the product together with a $LCu(II)Cl_2$ complex, which engages in a SET with the reduced decatungstate anion to regenerate both catalytic species. The results of mechanistic experiments based on NMR and UV measurements supported the mechanism and the activating role of the copper complex. This synergistic catalysis allowed the direct C–H functionalization of a range of simple cyclic and linear alkanes. Moreover, allylic chlorides were found to be efficient for this transformation when bearing both aromatic and aliphatic substituents on the 2-position.

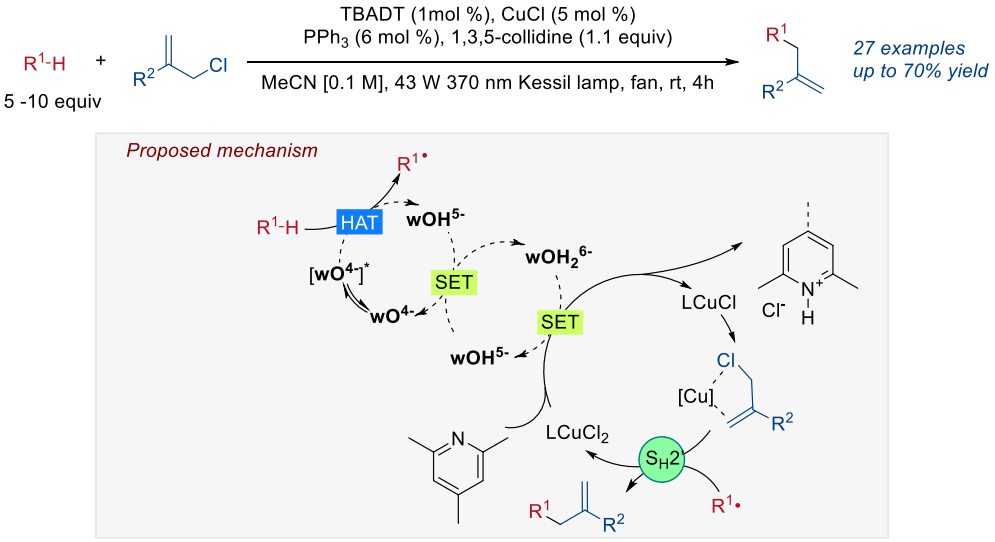

Scheme 3.3.3. Dual Cu/TBADT photocatalyzed C-H allylation of alkanes. For simplicity, wO = $W_{10}O_{32}$.

Encouraged by these results and the lack of methodologies for allylation of gaseous alkanes, we studied and developed a photoredox HAT strategy for direct Csp^3-Csp^3 allylation of gaseous alkanes.

3.3.1 Reaction optimization

We began our investigation by running the reaction between the allylic chloride **37** and ethane in the presence of different HAT photocatalysts (Table 3.3.1). However, all the attempts led to insignificant conversions, an absence of product formation, or a combination of both (entries 1-6). Notably, only the Fe-based HAT photocatalytic systems (entries 5,6) afforded the desired product **39** despite poor yields. Therefore, further exploration of these promising results was conducted. Remarkably, the use of 2,4,6-collidine as an additive resulted in the obtention of good conversion and yield (Entry 7). The use of the anhydrous $FeCl_3$ did not afford better results (entry 8). In the quest for increasing the yield, the combination with lithium chloride (entry 9) or performed $[FeCl_4]TBA$ (entry 10) was observed to perform less effectively. Indeed, a further boost was observed when increasing the collidine equivalents to 2 (entry 11). Further increase in collidine amount was not beneficial (entry 12).

Table 3.3.1. Screening of HAT photocatalytic systems.

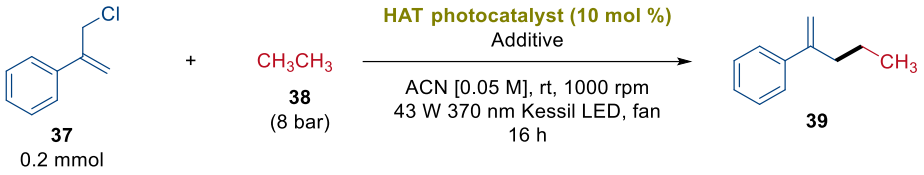

Entry	Photocatalyst	Additive	Conv.[a] / %	Yield [b] / %
1	TBADT (1 mol%)	-	-	-
2	TBADT (1 mol%)	Collidine (1.1 equiv), CuCl (5 mol%), PPh_3 (6 mol%)	71	-
3 [c]	$[NEt_4]_2CeCl_6$	-	-	-
4 [d]	$(PPh_3)_2TiCl_6$	-	-	traces
5 [d]	$FeCl_3$	HCl (5 mol%)	11	7
6	$FeCl_3 \cdot 6H_2O$	-	8	5
7	$FeCl_3 \cdot 6H_2O$	Collidine (1.1 equiv)	47	48
8	$FeCl_3$	Collidine (1.1 equiv)	64	47
9	$FeCl_3 \cdot 6H_2O$	Collidine (1.1 equiv), LiCl (3 equiv)	30	30
10	$[FeCl_4]TBA$	Collidine (1.1 equiv)	56	38
11	$FeCl_3 \cdot 6H_2O$	Collidine (2 equiv)	70	70
12	$FeCl_3 \cdot 6H_2O$	Collidine (3 equiv)	82	51

Conv. = consumed starting material **37**. a) Values given by ^{1}H-NMR analysis using 1,3,5-trimethoxy benzene or trimethyl benzene-1,3,5-tricarboxylate as internal standard b) Values calculated after isolation by column chromatography. c) 44 W 467 nm Kessil LED. d) 52 W 390 nm Kessil LED. TBA = tetrabutyl ammonium.

We then studied the performance of various bases under reaction conditions (Table 3.3.2). When we used pyridinic bases (Entries 2-3) the yield was eroded, and similar observation have been done when using inorganic K_2HPO_4 (Entries 4-5). In the last entry, the absence of conversion was attributed to the formation of a heterogeneous mixture resulting from the high load of base, which may interfere with the reaction's light absorption through light scattering processes.

Table 3.3.2. Screening of base identity.

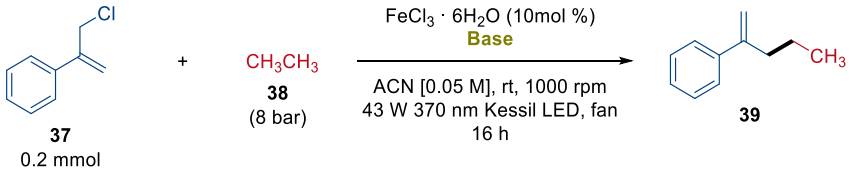

Entry	Bases	Conv. [a] / %	Yield [b] / %
1	Collidine (2 equiv)	70	69
2	2,6-Di-*tert*-butyl-4-methylpyridine (2 equiv)	51	45
3	Pyridine (2 equiv)	25	29
4	K_2HPO_4 (1 equiv)	59	36
5	K_2HPO_4 (2 equiv)	-	traces

Conv. = consumed starting material **37**. a) Values given by ^{1}H-NMR analysis using 1,3,5-trimethoxy benzene or trimethyl benzene-1,3,5-tricarboxylate as internal standard b) Values calculated after isolation by column chromatography

Given the pronounced drop in reactivity when different bases were used, we postulated that collidine might have some additional role beyond acting merely as a base. Accordingly, we explored the effect of diverse inorganic bases when collidine was used in catalytic amounts as ligand (Table 3.3.3). When using K_2HPO_4 and 20 mol% of collidine, yield increases in nearly 20%, compared to the reaction run in the absence of collidine (entry 1 *vs* 2). When other bases (entries 3-5) or combination of them (entry 6), were evaluated in the reaction better results were not obtained. Moreover, we tried to increase the amount of K_2HPO_4 but we found a similar effect as observed before (Table 3.3.2, Entry 7). These results suggested an extra role of collidine besides indicating that it is the best base for this transformation (Table 3.3.2, Entry 8).

Table 3.3.3. Screening of inorganic bases with collidine as ligand

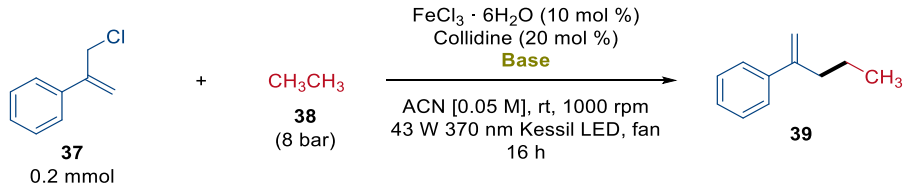

Entry	Bases	Conv. [a] / %	Yield [b] / %
1 [c]	K_2HPO_4 (1 equiv)	59	36
2	K_2HPO_4 (1 equiv)	57	55
3	K_3PO_4 (1 equiv)	24	-
4	KH_2PO_4 (1 equiv)	55	49
5	Na_2HPO_4 (1 equiv)	89	54
6	K_2HPO_4 (1 equiv) / $Na_2WO_4 \cdot 2H_2O$ (0.5 equiv)	39	35
7	K_2HPO_4 (2 equiv)	7	-
8 [d]	Collidine (1.8 equiv)	70	70

Conv. = consumed starting material **37**. a) Values given by ^{1}H-NMR analysis using 1,3,5-trimethoxy benzene or trimethyl benzene-1,3,5-tricarboxylate as internal standard. b) Values calculated after isolation by column chromatography. c) Reaction without collidine. d) Reaction with 1 equiv of collidine.

Based on this observation regarding the ligand-like properties of collidine, we decided to study the performance of different ligands and iron complexes in the presence of K_2HPO_4, the best inorganic base performing under catalytic conditions (Table 3.3.4). Different *N,N'*-chelating ligands like bipyridine (Bpy), phenanthroline (Phen) or 4,4'-di-*tert*-butyl-2,2'-

dipyridyl (4,4'-dtbbpy), led to low to moderate yields (20–46%) (entries 1-4). 2,6-dichloro pyridine – more electrodeficient than collidine – provided higher conversions but the desired product was obtained in low yields (entry 5). In fact, analysis of the reaction at shorter time 2.5 h revealed that decomposition of starting material was faster than product formation (entry 6). The use of phosphines like triphenyl phosphine or XantPhos did not lead to higher yield (entries 7-9). We decided then to choose $FeCl_3 \cdot 6H_2O$ (10 mol%)/collidine (2 equiv) as the best combination for ethane allylation.

Table 3.3.4. Iron complex screening with inorganic K_2HPO_4 base.

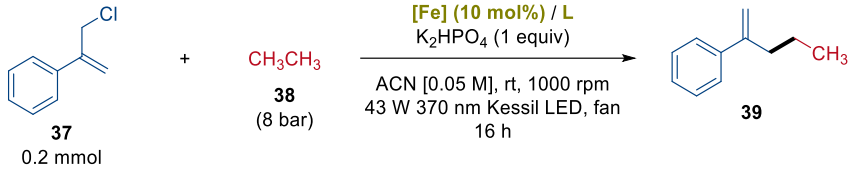

Entry	Iron source / Ligand [a]	Conv. [b] / %	Yield [c] / %
1	Bpy (10 mol%)	52	27
2	$Fe(Bpy)Cl_3$	54	21
3	$Fe(Phen)Cl_3$	69	43
4	$Fe(4,4'\text{-dtbbpy})Cl_3$	76	46
5	2,6-dichloro pyridine (20 mol%)	>99	(35)
6 [d]	2,6-dichloro pyridine (20 mol%)	40	(30)
7	PPh_3 (20 mol%)	65	45
8	XantPhos (10 mol%)	>99	(38)
9 [e]	XantPhos (10 mol%)	74	(39)

Conv. = consumed starting material **37**. a) Unless otherwise noted, the iron source is $FeCl_3 \cdot 6H_2O$ (10 mol%), and was used along with corresponding ligand. b) Values given by ^{1}H-NMR analysis using 1,3,5-trimethoxy benzene or trimethyl benzene-1,3,5-tricarboxylate as internal standard. c) Values calculated after isolation by column chromatography. Values given in brackets were obtained from ^{1}H-NMR analysis. d) Reaction analyzed at 2.5 h. e) Reaction analyzed at 4 h.

Having set the catalytic system, we evaluated different leaving groups in the allylic substrate (Table 3.3.5). It was found that allylic chloride is the substrate of choice group (entry 1) while the use of a bromide led to decomposition of the starting material and an allylic sulfone provided low yield and conversion.

Table 3.3.5. Leaving group identity screening

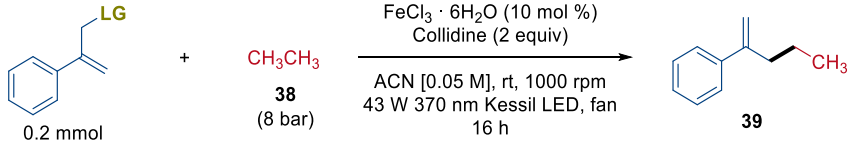

Entry	Leaving group (LG)	Conv. [a] / %	Yield [b] / %
1	Cl	70	70
2	Br	(>99)	-
3	SO_2Ph	36	20

Conv. = consumed starting material **37**. a) Values given by ^{1}H-NMR analysis using 1,3,5-trimethoxy benzene or trimethyl benzene-1,3,5-tricarboxylate as internal standard. b) Values calculated after isolation by column chromatography.

To complete the optimization screening, different catalyst loadings were evaluated (Table 3.3.6). When increasing to 15 mol%, reaction showed a yield drop with a slight increment in conversion (Entry 2). The reaction outcome was also analyzed after 7 h, in order to preclude

product degradation, but the same yield as after 16 h was observed along with lower starting material conversion, revealing degradation of the allyl chloride (Entry 3). Finally, we tried to decrease the Fe-loading to 5 mol% but reaction efficiency was compromised (Entry 4).

Table 3.3.6. Catalyst loading screening.

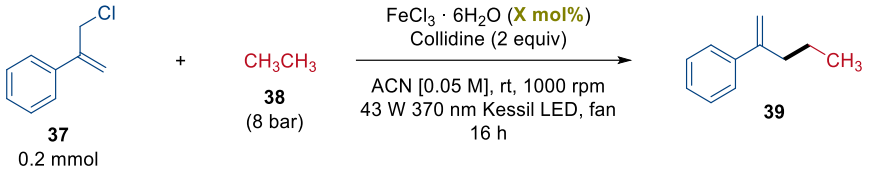

Entry	Catalyst loading	Conv. [a] / %	Yield [b] / %
1	10 mol %	70	70
2	15 mol %	75	52
3 [c]	15 mol %	68	52
4	5 mol %	52	23

Conv. = consumed starting material **37**. a) Values given by ^{1}H-NMR analysis using 1,3,5-trimethoxy benzene or trimethyl benzene-1,3,5-tricarboxylate as internal standard. b) Values calculated after isolation by column chromatography. c) Reaction analyzed at 7 h.

Further screening of parameters, like light source, stirring rate, dilution or ethane pressure were evaluated (Table 3.3.7). Decreasing the light power from 43 W to 32 W led to a detriment on the reaction yield (Entry 2). The use of other wavelengths, like 390 and 427 nm, did not improve either (Entry 3) or just not promote any reactivity towards desired allylation product (Entry 4). When the 370 nm 44 W Gen 2 Kessil lamps were used instead, a similar conversion was obtained but a slight drop in the yield was observed (Entry 5). This could be motivated, probably, because photon flux is presumed to be higher than the first-generation models. More diluted conditions were evaluated expecting a better ethane diffusion into the solvent (Entry 6), and higher stirring rate for enhancing mass transfer from gas atmosphere to solution (Entry 7), but no improvement could be achieved. Similarly, lowering ethane concentrations by decreasing stirring rate to 800 rpm (Entry 8) or using lower pressure (Entry 9), did not yield better reaction performance.

Table 3.3.7. Further conditions screening.

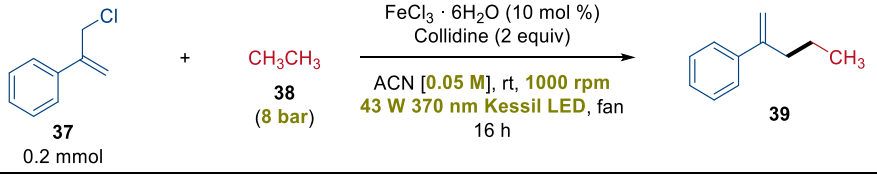

Entry	Variation	Conv. [a] / %	Yield [b] / %
1	none	70	70
2	32 W 370 nm Kessil LED	29	27
3	52 W 390 nm Kessil LED	70	36
4	45 W 427 nm Kessil LED	52	-
5	44 W Gen 2 370 nm Kessil LED	72	51
6	[0.033 M]	63	42
7	1300 rpm	69	48
8	800 rpm	74	37
9	5 atm	65	31

Conv. = consumed starting material. a) Values given by ^{1}H-NMR analysis using 1,3,5-trimethoxy benzene or trimethyl benzene-1,3,5-tricarboxylate as internal standard. b) Values calculated after isolation by column chromatography.

3.3.2 Scope of the reaction & synthesis of valuable products

Once the optimized conditions were identified (Table 3.3.6, Entry 1), we set out to explore the substrate scope for this reaction (Scheme 3.3.4). The methodology proved to be effective with a range of allylic chlorides. Chlorides bearing aromatic (**39-49**) or heteroaromatic (**50**) substituents were well tolerated and provided the corresponding alkylated substrate independently of the electronic properties and position of the substituents on the aromatic ring. It is important to note that allyl chlorides bearing electrowithdrawing substituents render better yields than when electrodonating are used. Notably, allylic chlorides bearing plenty of alkyl C−H bonds (**40**,**41**) could be selectively coupled with ethane. Aromatic rings bearing electron-withdrawing substituents (**42**,**43**) exhibited excellent performance leading to almost quantitative yields. Gratifyingly, the presence of α-oxy C−H bonds (**44**,**45**) was well tolerated, including even more sensitive benzylic/α-oxy C−H bonds (**46**) which led to moderate yields. The presence of amide bonds (**47**) showed to be not sensitive to reaction conditions, and even the use of more conjugated substrates (**48**,**49**) and thiophene derivative (**50**) engaged in the transformation to provide the ethane allylation. Furthermore, dienyl systems (**51**,**52**) could be used with complete selectivity, even bearing a long alkyl chain (**52**), without observing functionalization of other C–H bonds of the structure.

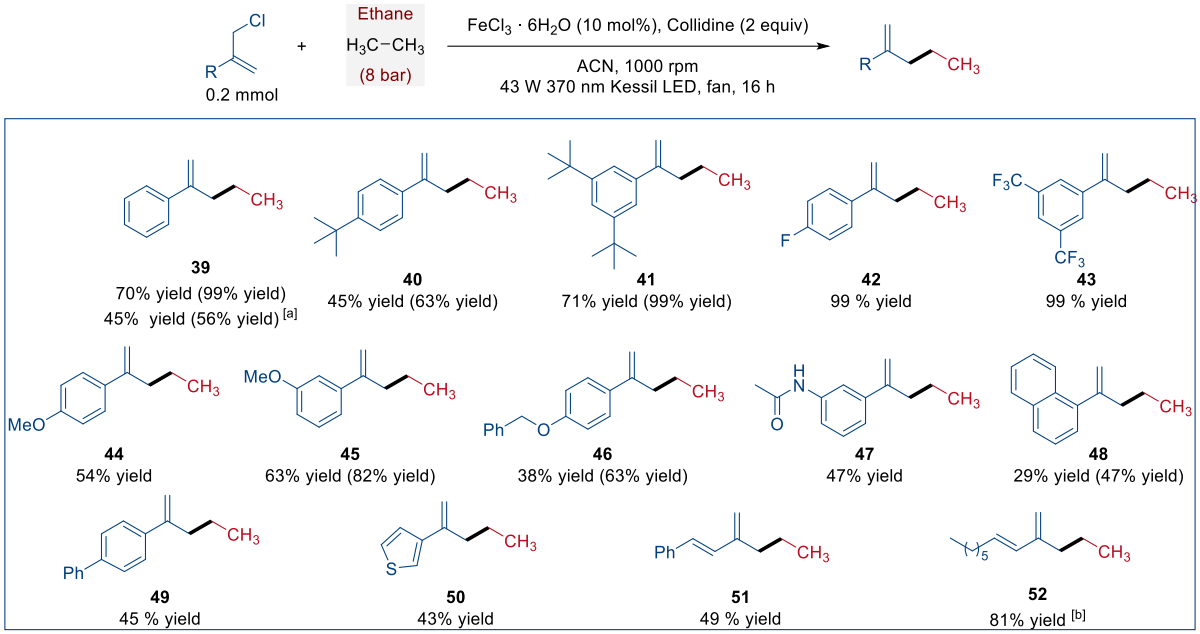

Scheme 3.3.4. Unless otherwise noted, reactions were performed as described: allylic chloride (0.2 mmol), collidine (2 equiv), MeCN (4 mL) and indicated pressure. [a] Reaction run on a 3 mmol scale with 2 lamps. [b] Reaction run under Kessil 75% light intensity (32 W).

One of the claimed goals of the methodology is to enable new reactivity further than Giese additions in order to unlock new reactivities and synthetic applications. In order to illustrate the synthetic potential of the methodology, we performed the synthesis of a relevant carboxylic acid **54** that found several applications along the literature as intermediate for preparing alpha-amino acids,[212] bromodomain and extra-terminal motif (BET) protein inhibitors[213] or stimulator of interferon genes (STING) inhibitors for cancer therapies.[214] The designed route involves alkylation of allyl chloride **37**, followed by regioselective *anti*-Markonikov hydroboration of the terminal olefin, and final oxidation of the alkyl-Bpin to corresponding carboxylic acid, with an overall 31% yield and three steps (Scheme 3.3.5).

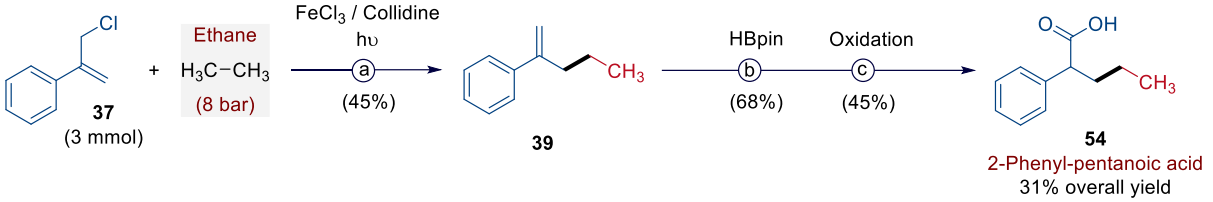

Scheme 3.3.5. Synthesis of 2-Phenyl-pentanoic acid. Conditions: a) $FeCl_3$ (10 mol%), Collidine (2 equiv), CH_3CH_3 (8 bar), MeCN, 370 nm 43 W Kessil lamp, rt, 16 h. b) ^{n}BuLi (10 mol%), HBpin, toluene, 130 °C, 12 h. c) $NaOH_{(aq)}$ 20%, $H_2O_{2(aq)}$ 30%, MeOH, rt, 2 h, then PCC (2 mol%), H_5IO_6, MeCN, 0 °C, 3 h. See Section 5.4.3.4 for detailed experimental conditions.

3.3.3 Mechanistic studies of the transformation.

As explained above, the use of collidine was essential to achieve an efficient ethane C−H allylation. Indeed, in its absence the catalyst barely performs one turnover. We therefore conducted a series of experiments to gain some mechanistic insight.

First, we evaluated the radical nature of the transformation by running the reaction in the presence of TEMPO. As we expected, the reaction did not yield the corresponding allylation product. In this case, we could detect (and characterize by HRMS) the ethyl-TEMPO adduct while no formation of any allyl-TEMPO adduct was observed (Scheme 3.3.6).

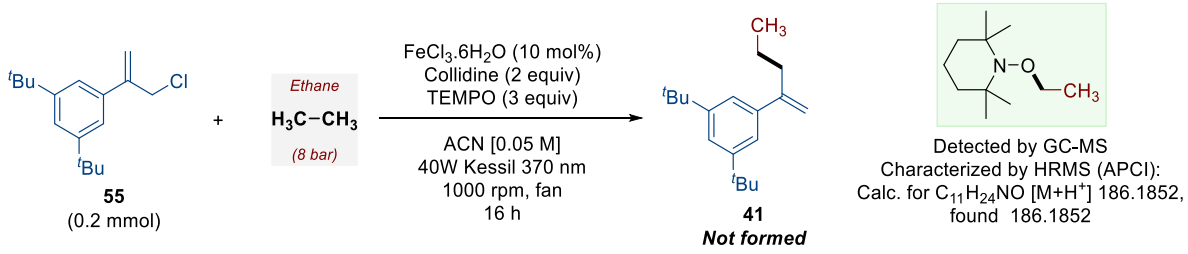

Scheme 3.3.6. Radical trapping experiment with TEMPO.

Then, we analyzed the reaction pathway. When deuterated allylic chloride **37-*d*$_2$** was used under optimal conditions, product **39-*d*$_2$** was obtained as a 94:6 mixture of deuterated isomers (Scheme 3.3.7, a). This deuterium labeling experiment supports an S_H2' mechanism, while the formation of minor product could be explained by a minimal chlorine scrambling promoted by radical chlorine (Scheme 3.3.7, b).

To further confirm the S_H2' mechanism, we synthesized a secondary allylic chloride **56** in an inseparable mixture with corresponding isomer **56**'. When a 1:2 mixture was used, excellent yields of **57** were obtained together with complete control over the stereochemistry of the olefin formed (Scheme 3.3.7, c). These results suggest that both structures are in equilibrium and only the terminal olefin is reactive towards the radical addition. Therefore, as **56** is consumed, the equilibrium would be shifted towards its own formation.

Moreover, quantum yield of the reaction was measured in order to discard chain propagation mechanisms – since the Cl• that is released after allylation could engage in further HAT processes. A determined quantum yield of 0.028 suggests that a chain mechanism is unlikely, thus confirming a closed photoredox catalytic cycle.[215-216]

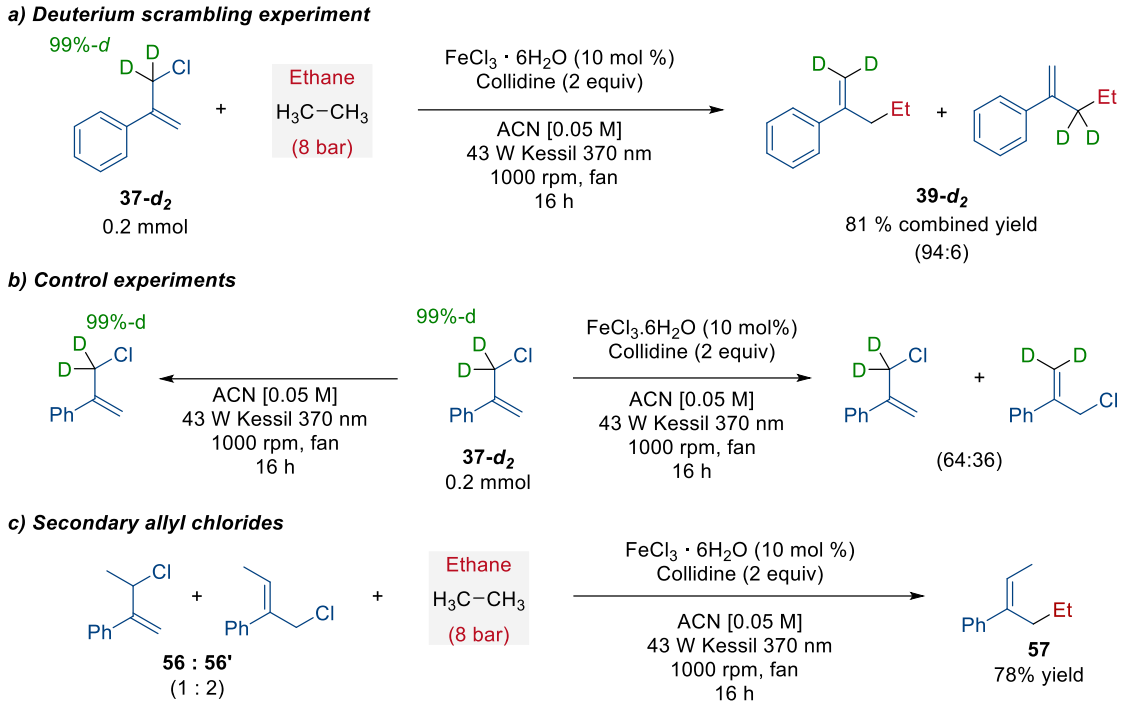

Scheme 3.3.7. Mechanistic experiments to confirm the S_H2' nature of the reaction.

Having achieved basic understanding about the mechanim, we turned to the central question about the role of collidine. To better determine potential side products, the reaction was run with cyclohexane in the presence and absence of collidine. Formation of chlorocyclohexane (CyCl) was detected by GCMS in both reactions. Nevertheless, a rather different outcome was observed in each case. Similarly to the reaction to ethane, in the absence of collidine allylation product was obtained in a low 8%. In contrast, in the presence of collidine allylation product was obtained in 45% yield together with a minor amount of CyCl (Scheme 3.3.8, a). Therefore, the reactivity problem was not derived from the gaseous nature of ethane or the high BDEs but was most likely due to catalyst deactivation. In fact, the relative ratios between CyCl and product were determined to be 7:93 and 56:44, with and without collidine, respectively.

Accordingly, a time-course analysis of stoichiometric chlorination reactions of cyclohexane in the absence of allylic substrate was conducted. We could clearly observe that in absence of collidine, the CyCl yield rapidly achieved a yield of nearly 70% in just 15 minutes. Conversely, when collidine was used, the reaction rate was dramatically slowed down, resulting in a yield of only 9% in the same period (Scheme 3.3.8, b).

In view of the evidence from previous observations suggesting the rapid quenching of $FeCl_3$ under continuous irradiation,[143, 217] To further evaluate differences in both catalytic systems ($FeCl_3$ vs $FeCl_3$/collidine) we recorded the UV-Vis spectra of both systems (Figure 3.3.1, a). In the presence of collidine, absorption spectrum displays lower absorptivity and almost negligible blue shifted LMCT band (from 361 to 357 nm). Lambert-Beer Law plot was constructed for $FeCl_3$ in acetonitrile, with and without collidine (Figure 3.3.1, b-c), centered in the LMCT band. Linear regression for both samples confirmed the linear relationship between absorbance and concentration at the chose concentration levels. Both samples were therefore subjected to continuous irradiation at 370 nm.

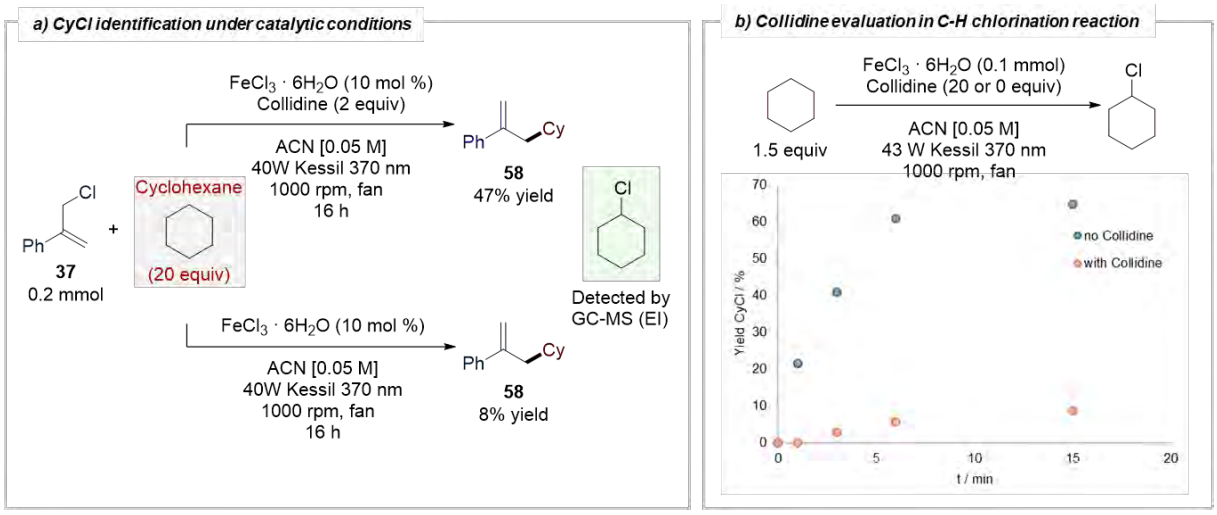

Scheme 3.3.8. Studies concerning side reactivity of C-H chlorination of alkanes.

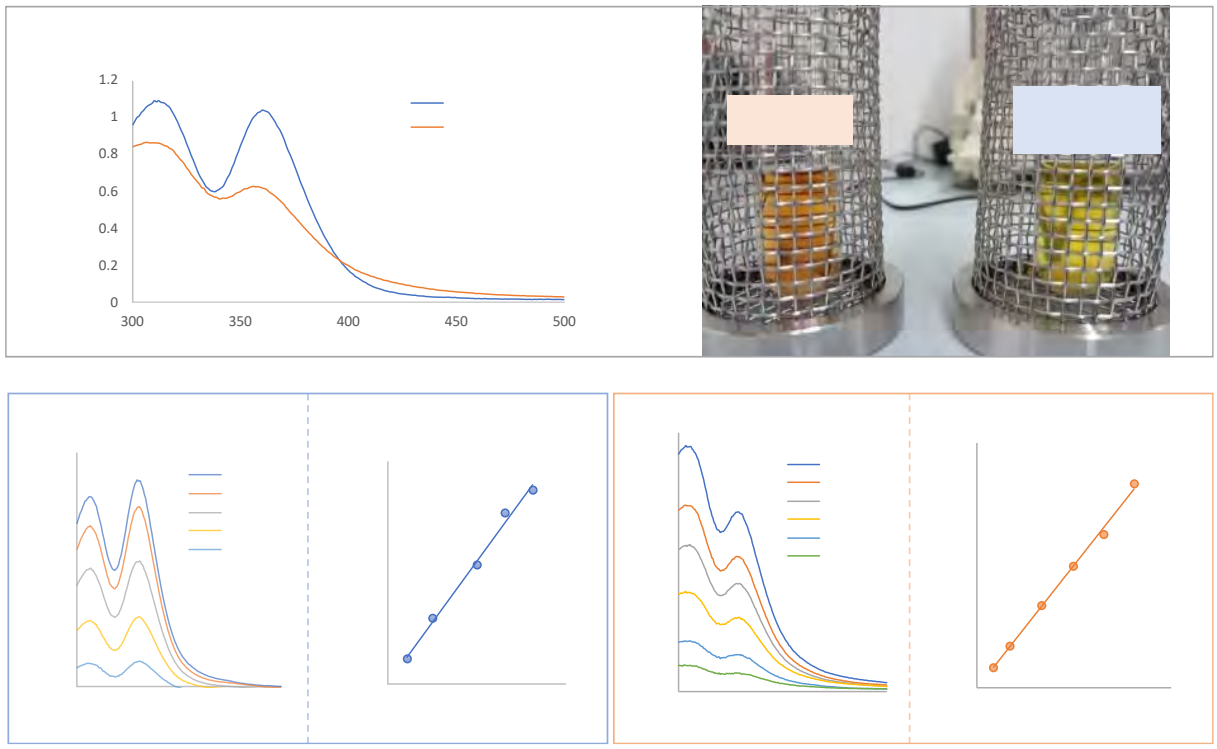

Figure 3.3.1. Comparative of UV-Vis spectra of reaction with and without collidine plus Lambert-Beer Law plots for both samples.

We then perfomed time-resolved UV-Vis spectroscopy experiments. The presence of collidine was once more observed to display a pronounced effect. In its absence, the reaction color changed from yellow to colorless in less than a minute, resulting in a rapid drop in the absorbance (Figure 3.3.2). In sharp contrast, the presence of collidine permitted the maintenance of the intense orange color of the reaction for more than an hour, and absorbance decay followed a much smoother kinetic profile. As demonstrated by Schelter,[136] when $[CeCl_6]^-$ was irradiated in acetonitrile its absorption was observed to diminish progressively. This was most probably due to the generated Cl• engaging in HAT processes with the solvent. Considering the similar process occurring in our system, and since acetonitrile is present in a

large excess, the variation in the concentration is negligible. Consequently, the reaction order and the observed rate constant could be calculated through the graphical method (Figure 3.3.2, a-c).[218]

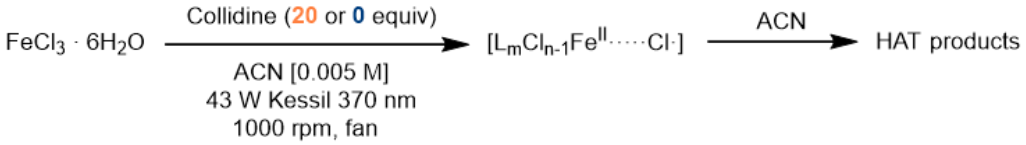

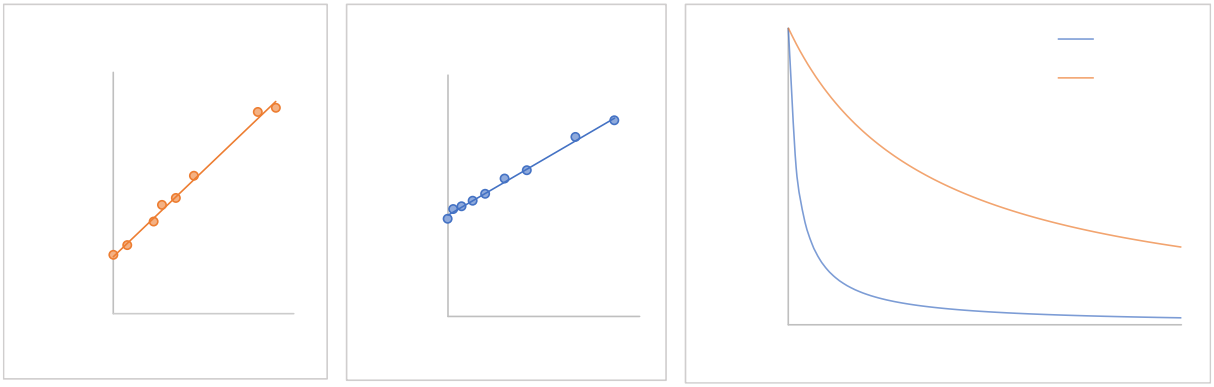

Figure 3.3.2. General reaction scheme illustrates photodegradation of catalyst. a) Time-course data fitted to second order reaction using 20 equiv. of collidine. b) Time-course data fitted to second order reaction in absence of collidine. c) Comparative plot for both kinetic profiles.

The data obtained from kinetic studies suggest that depletion by Cl• formation via LMCT for naked $FeCl_3$ is approximately one order of magnitude higher than the $FeCl_3$ / collidine system (Figure 3.3.2, c). Consequently, higher concentrations of Cl• would be rapidly and easily achieved when no collidine is present in the media. This finding also brings to light that once Cl• is formed, in the absence of radical trap, it readily reacts with the solvent to promote HAT products formation. Its consumption would hamper the $[Fe(II)Cl_3]^-$ reoxidation, what would led to the quenching of the photocatalyst.

To further confirm the transformation of Fe(III) into inactive Fe(II), we perform electron paramagnetic resonance (EPR) spectroscopy measurements (Figure 3.3.3). The two samples showed a spin state of $S = {}^1/_2$ S, with a single peak near a *g*-factor of 2.0, typical signal for organic radicals or transition metals with an unpaired electron (Figure 3.3.3, a).[219-220] The Fe(III) sample without collidine was then subjected to 370 nm irradiation for a period of 3 minutes and measured immediately. As can be observed in spectrum, signal intensity decreased around 90%. This suggests a change in the electronic state of the Fe(III), possibly by forming paramagnetic Fe(II) species. The sample with collidine provided a similar EPR signal (Figure 3.3.3, b). Nevertheless, when the $FeCl_3$/collidine was exposed to irradiation, intensity signal was only observed to decay a 10%. This is in excellent agreement with the UV-Vis measurements (Figure 3.3.2). The different behavior between both samples under irradiation could be explained for a different environment, in the second sample, that may enhance the photostability of Fe(III) ions.

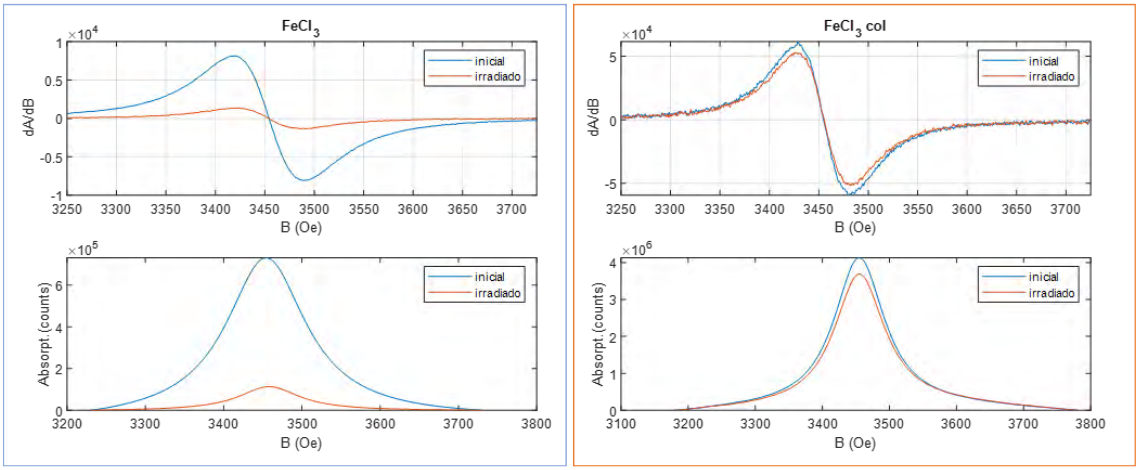

Figure 3.3.3. EPR spectra for $FeCl_3$ (at room temperature) in a) absence of collidine and b) in presence of collidine. Samples were measured before and after irradiation. Upper spectra show the measurement and bottom shows the integral.

To consolidate the relevance of these findings, an X-ray quality crystal of $FeCl_3$ in collidine could be obtained by Pol Martínez-Balart (Figure 3.3.4). The formed crystal allowed to characterize the presumed formed species in the reaction media. The molecular structure is composed of a $[Fe^{III}Cl_4]^-$ anion core, which is surrounded by three collidinium cations $[Collidine{\cdot}H]^+$, and two free chlorides ions in the crystal lattice. The supramolecular structure is stabilized by a dense network of H-bonds, leading to a total of 9 supramolecular interactions. H-bonds established with the collidine methyl groups ($CH_3\cdots Cl$) display distances of 2.360 Å and 2.398 Å, in the strongest region considered to be almost covalent interactions; while protonated nitrogen ($N{-}H\cdots Cl$) bond gets 2.810 Å, accounting for mostly electrostatic interactions.[221] Thus, each iron center sits in tetrahedral coordination geometry. Furthermore, the isolated structure was subjected to reaction conditions in order to assess the capability of the isolated Fe-complex to undergo HAT and catalyzed the C−H allylation of gaseous alkanes, observing a 33% yield of ethane allylation.

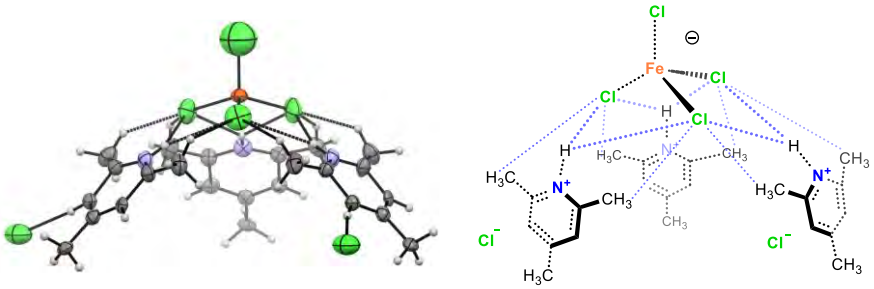

Figure 3.3.4. X-ray structure of isolated Fe(III) complex and ChemDraw structure.

We proved therefore its ability to catalyze the transformation. It is noteworthy to mention that acetonitrile solutions of $FeCl_3{\cdot}6H_2O$ in presence of nitrogenated bases are known to hydrolyze due to moisture, leading to the formation of different species. Therefore, according to the experimental results, and the literature,[222-224] despite not having isolated any other Fe-complexes, we cannot discard the concurrent presence of additional active Fe-species under reaction conditions.

Finally, a last question regarding the observed requirement of base in the reaction remained still unresolved. As illustrated in the Table 3.3.3 (Entry 1), C−H allylation product was obtained

with K_2HPO_4, albeit the poor yield. It was reported that Cl• can interact with HCl to form a charge transfer complex such as [Cl−ClH]• which is known to promote C−H chlorination reactions.[225] Therefore, despite K_2HPO_4 does not presents the ability to forming the observed H-bonds network, we could presume it is working as a base, removing HCl from the media and slowing down the side C−H chlorination. According to this, reaction would furnish a certain amount of product, higher than in the absence of base.

In conclusion, the transformation should ideally be mechanistically working as follows. The formed $L_nCl_2Fe^{III}$-Cl complex (L = collidine) undergoes excitation under light irradiation. Excited [$L_nCl_2Fe^{III}$-Cl]* would undergo [Fe^{III}←Cl] LMCT process promoting homolytic cleavage to provide the reduced $L_nFe^{II}Cl_2$ and Cl•. The formed Cl• undergoes HAT to furnish the alkyl radical, which will react with the allylic substrate. The Cl• leaving group would then recombine with the reduced Fe(II) to regenerate the active photocatalyst $L_nCl_2Fe^{III}$-Cl (Figure 3.3.5, a). However, as we demonstrated along the mechanistical studies, multiple side processes are taking place in parallel. We demonstrated by the deuterium scrambling experiments (Scheme 3.3.7) that Cl• is involved in isomerization of the allylic substrates (Figure 3.3.5, b). Also, through the GCMS analyses by using cyclohexane as alkane (Scheme 3.3.8), we could leverage that alkane C−H chlorination is responsible for deactivation of catalyst and inhibition of the allylation since the consumption of Cl• would forbid Fe(II)-to-Fe(III) reoxidation. This process could take place right after the LMCT with a present R• (Figure 3.3.5, c) or after allylation between the Cl• leaving group and a newly generated alkyl radical (Figure 3.3.5, d). We proved that the presence of any kind of base is capable to boost the reaction by removing the formed HCl, which is involved as well in alkane chlorination by forming charge transfer complexes (Figure 3.3.5, e). And finally, the role of the collidine was demonstrated by UV-Vis, EPR and GCMS measurements, and further consolidated after reaching the X-ray structure (Figure 3.3.4). Moreover, we cannot discard some further role of the collidine since it is well reported the ability of nitrogenated bases to coordinate and stabilize Cl• by forming Cl•∴N complexes (2 centers–3 electron complex) (Figure 3.3.5, f).[226-228]

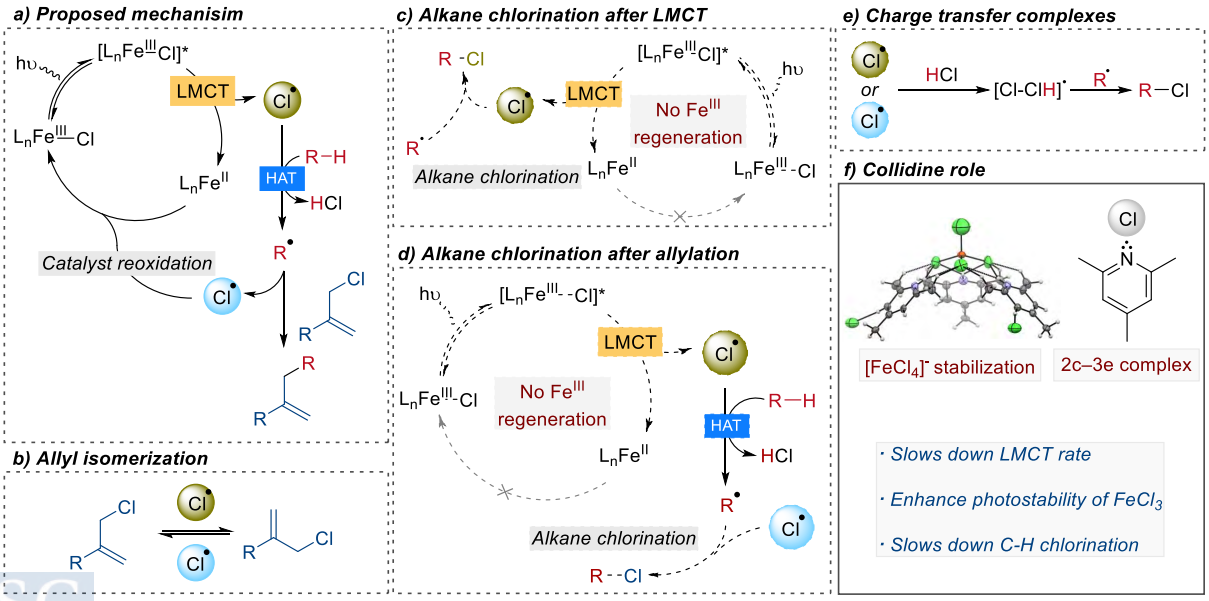

Figure 3.3.5. Mechanistic proposal and key insights into side reactions happening under reaction conditions.

4 CONCLUSIONS

In section 3.1 we have tackled the **SO1** by studying the reaction mechanism of Cu-catalyzed enantio-, diastereo-, regio- and chemoselective allylboration of alkynes and allenes with allylic *gem*-dichlorides. We have demonstrated that both reactions involve oxidative addition and reductive elimination steps, being the first the rate- and stereodetermining stage. We have combined different computational analyses to enlighten factors controlling stereoselectivity. We have demonstrated that factors regulating alkyne enantioselectivity rely on steric repulsions engendered between the Bpin unit and the allylic substituent in the oxidative addition step. NCI plots and DIAs proved that stereoselectivity is ruled by coordination of the chlorine atoms to the metal cation, enhancing the *Z*-selectivity when smaller Li cation is involved. Regarding allenes, we have found that two Cu-allylboryl complexes are formed. Enantioselectivity was found to arise from the coordination mode of the allyl substrate, where NCI plots clearly revealed that pro-*S* displays two cation-bridge interactions (major enantiomer) while pro-*R* just one (minor enantiomer). We have also proved that enantiodiscriminating ability is highly dependent on the cation nature. *Z*-selectivity was found to be regulated by repulsive interactions engendered between *N*-aryl sulfonate ring and Bpin unit when pro-*E* conformation is adopted.

In section 3.2 we have developed an efficient methodology for the stereodefined synthesis of borylated 1,4-dienes *via* NCH-Cu catalysis addressing the **SO2**. We have reported that acetylene can be used in a simple setup and under mild reaction conditions to yield functionalized building blocks, bearing orthogonal substitution. We also demonstrate the synthetically versatility of the resulting dienes by designing a stereodivergent reaction scheme. This strategy was further applied to the total synthesis of (+)-Hinokiresinol and (+)-Nyasol, to the formal synthesis of (+)-Phorbasin C and a GnRH inhibitor, and to the synthetically versatile (*R*)-3-methylpent-4-en-1-ol. DFT calculations revealed, similarly to previous systems from section 3.1, that oxidative addition is the rate- and stereodetermining step. NCI plots have revealed that enantioselectivity arises from repulsive interactions between the allyl substituent and Bpin moiety. *Z*-selectivity was found to be controlled by steric repulsions between Bpin and sizable *N*-aryl group from the ligand when pro-*E* conformation is adopted.

Finally, in section 3.3 we developed the direct C-H allylation of ethane, elusive in the literature, as proposed in the **SO3**. This reaction represents the first example of allylation of gaseous alkanes. The use of $FeCl_3$ / Collidine as catalytic system enabled the efficient alkylation of allylic chlorides, allowing the use of a variety of substituents. Furthermore, the methodology was applied to the synthesis of 2-phenyl-pentanoic acid, a versatile molecule with several synthetic applications in medicinal chemistry. Mechanistic studies involving deuterium scrambling reactions, radical trapping experiments, time-coursed UV-Vis and GCMS measurements, EPR and X-ray analyses revealed the crucial role of the collidine for enabling the reactivity towards allylation while slowing down side reactivities.

In summary, we have conducted an extensive study regarding reactivity of multiple Cu and Fe-catalyzed systems which enable the access of multifunctional building blocks that can be further used in the synthesis of added value molecules. We have conducted a detailed mechanistic study by means of DFT calculations on Cu-catalyzed allylboration reactions involving alkynes and allenes. Moreover, we have developed efficient methodologies for the upcycling of acetylene and ethane based on Cu and Fe catalysis, taking advantage of homogeneous organometallic and photoredox catalysis, respectively. Furthermore, we have studied the reaction mechanism of developed reactions, and we apply the obtained products in the synthesis of natural products, advanced intermediates of drugs, and synthetically relevant molecules.

5 EXPERIMENTAL PART

5.1 GENERAL METHODS

- All reactions were performed under argon atmosphere using oven dried glassware and using standard Schlenk techniques. Solvents were dried using an MBraun SPS 800 system. All chemicals were purchased from Acros Organics Ltd., Aldrich Chemical Co. Ltd., Alfa Aesar, Apollo, Strem Chemicals Inc., Fluorochem Ltd. or TCI Europe N.V., BLD Pharmatec or Eurisotop chemical companies and used without further purification, unless otherwise noted.

- In order to preclude side hydroboration reactions, B_2pin_2 was dried over Na_2SO_4 prior to being used. In order to preclude the presence of 2,4,6-collidine *N*-oxide or any other impurity, commercial 2,4,6-collidine was distilled and stored under argon in the fridge.

- Acetylene (99.5% purity) and ethane (99.5% purity) gases were purchased from Nippon Gases company. Acetylene is dissolved in acetone or dimethylformamide within a gas container which in the inside is made of a porous solid material. Traces of solvent may be released to the reaction, although solvent vapor concentration in the gas is less than concentration limits that would require a change in the classification of acetylene.

- The LED light sources used are Kessil PR 160L 370, 390, 427 nm.

- Analytical thin layer chromatography was carried out on silica-coated aluminum plates (silica gel 60 F254 Merck) and components were visualized by UV light and $KMnO_4$ staining. Flash column chromatography was performed on silica gel 60 (Merck, 230-400 mesh) without previous deactivation, unless otherwise stated.

- ^{1}H, ^{13}C, ^{11}B and ^{19}F NMR experiments were carried out using a Varian Inova 500MHz or a Varian Mercury 300MHz NMR spectrometer. Chemical shift values are reported in ppm with the solvent resonance as the internal standard ($CHCl_3$: δ 7.26 for ^{1}H, δ 77.16 for ^{13}C). Coupling constants (*J*) are given in Hertz (Hz). Multiplicities are reported as follows: s = singlet, d = doublet, t = triplet, q = quartet, m = multiplet or as a combination of them.

- Because of quadrupolar relaxation, in all cases the carbon directly attached to the boron atom was not detected by ^{13}C NMR technique.

- Diastereomeric ratios were analyzed by GC-MS analyses were performed in an Agilent instrument GC-6890N equipped with Chemical Ionization (CI) MS-5973 detector.

- High Resolution Mass spectrometry was carried out on a Bruker microTOF or Bruker Impact II spectrometers using ESI or APCI.

- Enantiomeric ratios were determined by Supercritical Fluid Chromatography (SFC) analysis in a Jasco Series 4000 instrument or by High Performance Liquid Chromatography (HPLC) analysis using a WATERS ACQUITY Arc System, consisting of a quaternary pump, column oven and auto-sampler coupled with a 2998 PDA detector.

- Optical rotation was determined in a Jasco P-2000 Polarimeter.

- ATR spectra were recorded in solid, using a Spectrum Two FT-IR/Perkin Elmer UART-TWO Spectrometer equipped with a KBr window and a LiTaO3 detector.

- EPR measurements were carried out in a Bruker EMX spectrometer operating at 9.7 GHz with 100 kHz modulation.

- UV-Vis absorbance spectra were recorded using a JASCO V-630 spectrophotometer coupled to a Jasco ETC-717 temperature controller, using a standard Hellman semi-micro cuvette (108.002-QS) with a light path of 10 mm. Measurements were made at 20 °C. Acquisition parameters were: 300-500 nm range, scan speed of 100 nm/min, resolution of 0.2 nm.

- The cartesian coordinates for the structures associated with sections 3.1.1, 3.1.2 and 3.2 have been deposited in the Zenodo repository, which has been named as "*Data related to Catalytic methodologies for the valorization of C2 hydrocarbons and mechanistic studies*" assigned with the DOI: 10.5281/zenodo.14105393. Uploaded files can be consulted in the following [link].

5.2 DFT MECHANISTIC ANALYSIS OF THE ENANTIO- AND DIASTEREOSELECTIVE COPPER-CATALYZED ALLYLBORATION OF ALKYNES AND ALLENES WITH ALLYLIC *GEM*-DICHLORIDES

Calculations were performed at DFT level of theory using Gaussian16 software[148]. The structures of all the intermediates and transition states were optimized using the ωB97XD functional.[149]

Structures from section 3.1.1 were optimized using 6-31G(d) basis set (BS1). Single-point energies were calculated using the ωB97XD functional within the selfconsistent reaction field (SCRF) using the SMD model (toluene)[158] and a larger basis set *def2*-TZVPPD (BS2).[159-160]

Structures from sections 3.1.2 were optimized using basis set BS3. BS3 includes the 6-31G(d,p) basis set for the main group elements[150-157] and the scalar relativistic Stuttgart-Dresden SDD pseudopotential and its associated double-ζ basis set,[170] complemented with a set of *f* polarization functions,[171] for the copper atom.

Frequency calculations were performed at the same level to evaluate the zero-point vibrational energy and thermal corrections at 298 K and to confirm the nature of the stationary points, yielding one imaginary frequency for the transition states and none for the minima. It was confirmed that transition states connect with the corresponding intermediates by usual intrinsic reaction coordinate (IRC) calculations and subsequent optimization to minima.

Single-point energies for structures from section 3.1.1 were calculated using the wB97XD functional within the self-consistent reaction field (SCRF) using the SMD model (toluene)[158] and a larger basis set BS2. BS2 level consist in *def2*-TZVPP basis set.[159-160] The final Gibbs energies were obtained adding the thermal and entropic corrections computed at the BS1 level to the electronic energy computed at BS2 level. The reaction profiles were built up in terms of ΔG_{sol}.

Single-point energies for structures from sections 3.1.2 were calculated using the wB97XD functional within the self-consistent reaction field (SCRF) using the SMD model (toluene)[158] and a larger basis set BS4. BS4 consists in the *def2*-TZVP basis set for the main group elements and the quadruple-ζ *def2*-QZVP basis set for Cu.[159-160] The final Gibbs energies were obtained adding the thermal and entropic corrections computed at the BS1 level to the electronic energy computed at BS4 level. The reaction profiles were built up in terms of ΔG_{sol}.

All 3D chemical structures were prepared using CYLview20.[229]

5.2.1 Dissected energies for DIAs analysis by structure

Table S1. Calculated energies for each pair of stereodetermining oxidative addition transition states to yield *R* enantiomer.

	TS_{OA}-*Z*,*R*	**TS_{OA}-*E*,*R***	**TS_{OA}-*Z*,*R*-Na**	**TS_{OA}-*E*,*R*-Na**
$\Delta E^{\ddagger}$ / kcal·mol^{-1}	3.3	11.7	2.3	7.1
E^{*}(**2**) / Hartree	-1268.151324	-1268.131156	-1268.150628	-1268.128202
E^{*}(**III**) / Hartree	-4221.598812	-4221.597128	-4376.353408	-4376.353648
$\Delta E^{\ddagger}_{dist}$ (**2**) / kcal·mol^{-1}	30.6	43.2	31.0	45.1
$\Delta E^{\ddagger}_{dist}$ (**III**) / kcal·mol^{-1}	38.5	39.5	35.8	35.7
$\Delta E^{\ddagger}_{dist}$ / kcal·mol^{-1}	69.0	82.7	66.8	80.8
$\Delta E^{\ddagger}_{int}$ / kcal·mol^{-1}	-65.7	-71.0	-64.6	-73.7
$\Delta\Delta E^{\ddagger}_{dist}$ / kcal·mol^{-1}	0	13.7	0	13.9
$\Delta\Delta E^{\ddagger}_{int}$ / kcal·mol^{-1}	0	-5.3	0	-9.1
$\Delta\Delta E^{\ddagger}$ / kcal·mol^{-1}	0	8.4	0	4.8

5.3 ENANTIOSELECTIVE ALLYLBORATION OF ACETYLENE: A VERSATILE TOOL FOR THE STEREODIVERGENT SYNTHESIS OF NATURAL PRODUCTS

5.3.1 List of Starting Materials

Allylic phosphates (Figure 5.3.1) **1**,[230] **59**,[182] **60**,[231] **61**,[180] and **62-63**,[182] allylic *gem*-dichlorides (Figure 5.3.2) **11**,**1** and **65**[179] and ligands (Figure 5.3.3) **L5**,[232] **L6-L7**,[233] **L8**[234] were prepared according to literature procedures. The synthesis of allylic phosphate **64** is reported in section 5.3.3.

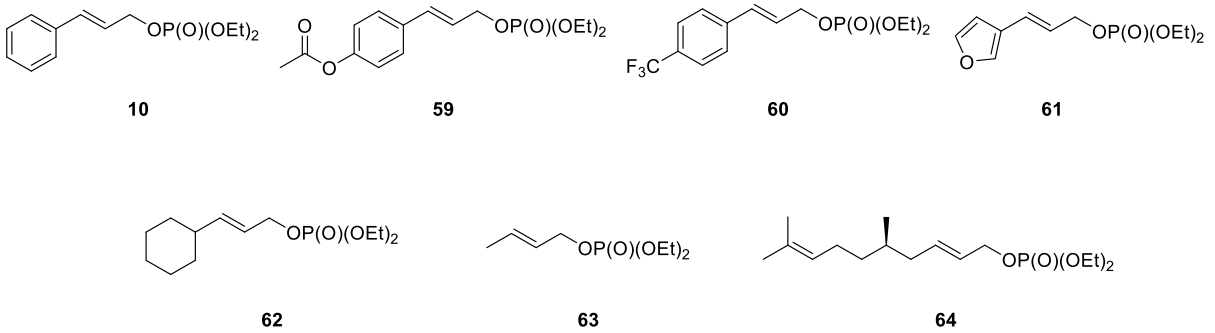

Figure 5.3.1. List of allylic phosphates used as starting materials in Cu-catalyzed allylboration of acetylene

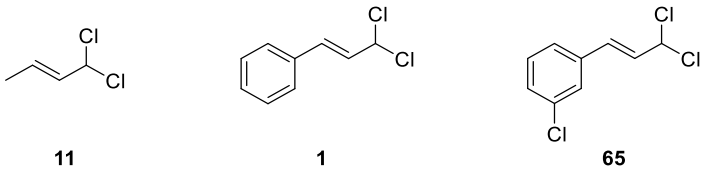

Figure 5.3.2. List of allylic *gem*-dichlorires used as starting materials in Cu-catalyzed allylboration of acetylene

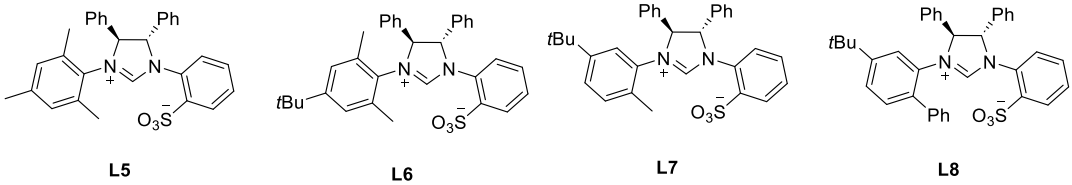

Figure 5.2.3. List of NHC chiral ligands used in the Cu-catalyzed allylboration of acetylene

5.3.2 General Procedures

5.3.2.1 General procedure for the Cu-catalyzed enantioselective allylboration of acetylene (General procedure A)

A screw cap vial equipped with a magnetic stirring bar was charged with CuCl (2 mg, 10 mol%, 0.02 mmol) and NaO^{t}Bu (9.6 mg, 0.1 mmol) in a glovebox. The vial was removed from the glovebox, ligand **L8** (14 mg, 12 mol%, 0.024 mmol) was added, and the mixture was dissolved in dry toluene (0.5 mL) and stirred during 15 min at room temperature (solution 1). A separate flame-dried tube equipped with a magnetic stirring bar and charged with B_2pin_2 (101.6 mg, 2.0 equiv, 0.4 mmol) and NaO^{t}Bu (28.8 mg, 0.3 mmol, from the glovebox) was filled with acetylene atmosphere (3x vacuum/acetylene cycles). Solution 1 was added to the tube to afford an orange-to-red mixture. The vial was rinsed with extra dry toluene (0.5 mL) and added to the reaction tube. The allylic substrate (1.0 equiv, 0.2 mmol) was dissolved in dry toluene (0.5 mL) and added to the tube. The acetylene was then gently bubbled directly to the mixture during 5 min with a stirring rate of 800 rpm and reaction turned garnet red. The tube was sealed, and the mixture was stirred at 1000 rpm over 18 h at the corresponding temperature.

After this time, reaction was quenched with water (10 mL) and extracted with CH_2Cl_2 (3 x 10 mL). Combined organic layers were dried over anhydrous $MgSO_4$, filtered, and solvent was removed under reduced pressure. Crude product was purified through flash column chromatography using the indicated mixture of solvents as eluent.

Note 1: Volatile allylic substrates **63** and **11** were added after bubbling the acetylene in the reaction.

Note 2: Racemic products were synthesized by reaction at 30 °C in toluene using chloro[1,3-bis(2,4,6-trimethylphenyl)imidazol-2-ylidene]copper(I) (IMesCuCl) (8.1 mg, 10 mol%, 0.02 mmol) or CuCl (10 mol%)/*rac*-**L5** (11.9 mg, 12 mol%, 0.024 mmol) as catalyst and NaO^{t}Bu as base.

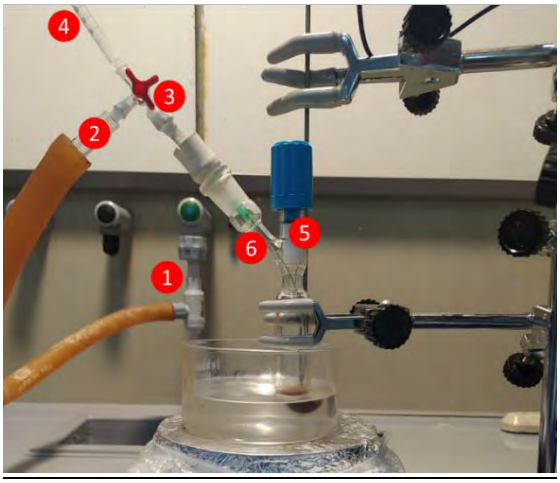

Figure 5.3.1. Reaction setup. Sealed tube with a homemade selector system connected to a trompe and a gas inlet line. Parts: 1) trompe, 2) vacuum line, 3) homemade selector, 4) gas inlet line, 5) sealed tube, 6) needle. Solutions of chemicals are added through the septum with a separate needle.

5.3.2.2 General procedures for synthetic modifications of skipped dienes (General procedures B-E)

Suzuki-Miyaura cross-coupling of alkenyl boronic esters (General Procedure B):

$Pd(PPh_3)_4$ (10 mol%) was added to a Schlenk flask equipped with a stirring bar. Then, the corresponding substrate (1.0 equiv) was added in 1,4-dioxane [0.1 M], followed by the addition of the corresponding organic halide (1.1 equiv) and aq. NaOH (2.0 M, 2.0 equiv). The reaction was stirred at 40 °C for 16 h. After this time, the resulting crude was diluted with Et_2O (15 mL) and washed with H_2O (2 x 10 mL). The organic layer was dried over anhydrous Na_2SO_4, filtered, and 1,4-dioxane removed in vacuo by steam distillation (600 mBar, 40 ºC). The residue was purified by column chromatography (pentane).

Suzuki-Miyaura cross-coupling of alkenyl chlorides (General Procedure C):

A dry Schlenk flask equipped with a magnetic stirring bar was charged with tris(dibenzylideneacetone)dipalladium(0) (5 mol%) and cesium fluoride (3 equiv) in a glovebox. Out of the glovebox, dicyclohexylphosphino-2',4',6'-triisopropylbiphenyl (XPhos) (10 mol%), and The corresponding boronic acid (1.1 equiv) were added to the Schlenk. The corresponding starting material (1 equiv) was diluted in 1,4-dioxane [0.1 M] and added to the

mixture which was then heated at 100 ºC for 2 h. The mixture was allowed to cool to room temperature, diluted with ether (5 mL) and washed with aqueous NaOH (1.0 M, 5 mL). The layers were separated, and the aqueous phase was extracted with ether (5 mL). The combined organic layers were dried over anhydrous Na_2SO_4, filtered, and concentrated in vacuo. The crude mixture was purified by column chromatography (pentane).

LDA-mediated dehydrochlorination of alkenyl chlorides (General Procedure D):

In an Ar-filled vial equipped with a stirring bar, the corresponding alkenyl chloride (1 equiv) was dissolved in THF [0.1 M] (Solution 1). In a separate oven dried Schlenk equipped with a magnetic stirring bar, a solution of *n*BuLi (2.5 M in hexanes; 1.5 equiv) was added to a solution of *i*Pr$_2$NH (1.7 equiv) in THF (same volume as solution 1) at -78 °C, and was stirred for 30 min. Then, solution 1 was added to the preformed LDA at -78 °C, and the reaction was stirred for 10 min. The reaction was then quenched with saturated aqueous solution of NH_4Cl (5 mL) and allowed to get to room temperature. The mixture was extracted with CH_2Cl_2 (2 x 5 mL). Combined organic layers were dried over Na_2SO_4, filtered, and concentrated in vacuo (600 mBar, 40 ºC). The crude product was purified through flash column chromatography (pentane).

Zweifel olefination (General Procedure E):

In a Schlenk dry flask equipped with a stirring bar, the corresponding alkenyl boronic ester was diluted in Et_2O [0.2 M] and cooled to -78 °C. Then, the corresponding Grignard reagent (1.4 equiv) was added, and the reaction was warmed to 0 °C and stirred for 1.5 h. In cases where organolithium reagent is used (1.4 equiv), mixture is stirred 30 min at -78 °C and 1 h at 0 °C. After this time, solvents were evaporated under vacuum and a solution of I_2 (1 equiv) in dry MeOH (0.4 mL) was added at -78 °C, allowing to reach room temperature. After 3 hours, a solution of aq. NaOH (3.0 M, 3 equiv) was added and stirred for 15 min. The resulting mixture was then diluted with Et_2O (15 mL). The organic layer was dried over Na_2SO_4 and filtered. The residue was purified by column chromatography (pentane).

Note: Homemade organolithium reagents were prepared from the corresponding halogenated precursor by lithium-halogen exchange using the following procedure. In a Schlenk tube equipped with a magnetic stirring bar, the organic halide was dissolved in Et_2O [0.6 M] and cooled at -78 ˚C. Then, *t*BuLi (2 equiv) was added dropwise and the mixture was stirred at -78 ˚C for 20 minutes before being used.

5.3.3 Characterization Data

5.3.3.1 Synthesis of starting material **64**

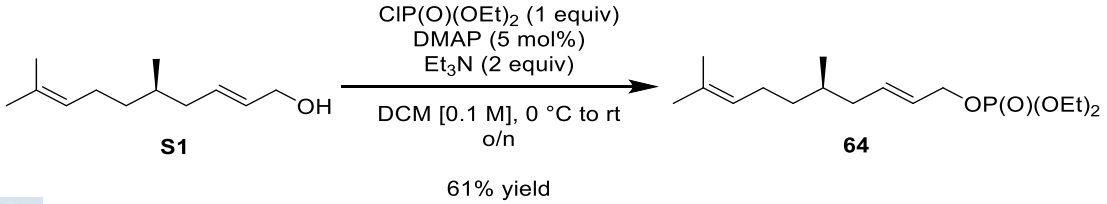

(*R*,*E*)-4,8-Dimethylnona-2,7-dien-1-ol (**S1**) was prepared according to a literature procedure.[235]

To an Ar-filled round bottom flask, allylic alcohol **S1** (814.2 mg, 4.47 mmol), DMAP (20.2 mg, 0.2 mmol), Et_3N (1.3 mL, 8.94 mmol) and CH_2Cl_2 (40 mL) were added. The mixture was cooled down to 0 °C using an ice-water bath and was stirred for 30 min. Then, $ClP(O)(OEt)_2$ (0.63 mL, 4.47 mmol) was added dropwise over the reaction. The mixture was allowed to get to room temperature and was stirred overnight. Reaction was diluted with 10 mL of water, carefully quenched with 10 mL of $HCl_{(aq)}$ [1 M] solution and extracted with CH_2Cl_2 (3x20 mL). Combined organic layers were dried over anhydrous $MgSO_4$, filtered, and solvent was removed under reduced pressure. Crude product was purified through flash column chromatography (Hexane/AcOEt, 9:1 to 1:1) yielding **33** as a colorless oil in 61% yield (874.7 mg).

^{1}H NMR (300 MHz, $CDCl_3$) δ 5.82 – 5.71 (m, 1H), 5.59 (dt, *J* = 14.9, 6.1 Hz, 1H), 5.07 (ddd, *J* = 8.3, 4.8, 2.0 Hz, 2H), 4.48 (t, *J* = 7.4 Hz, 2H), 4.10 (p, *J* = 7.2 Hz, 4H), 2.08 (dt, *J* = 13.1, 6.3 Hz, 1H), 1.93 (tq, *J* = 14.0, 7.3 Hz, 2H), 1.67 (s, 3H), 1.59 (s, 3H), 1.51 (td, *J* = 12.9, 6.3 Hz, 1H), 1.33 (t, *J* = 7.1 Hz, 9H), 1.20 – 1.07 (m, 1H), 0.86 (d, *J* = 6.6 Hz, 3H) ppm. **^{13}C NMR** (75 MHz, $CDCl_3$) δ 135.2, 131.4, 125.9, 125.8, 124.8, 68.3 (d, *J* = 5.7 Hz), 63.8 (d, *J* = 5.8 Hz), 39.7, 36.8, 32.5, 25.8 (d, *J* = 11.3 Hz), 19.5, 17.8, 16.3 (d, *J* = 6.6 Hz) ppm. **^{31}P NMR** (202 MHz, $CDCl_3$) δ 0.25 ppm. **HRMS (APCI)** Calc. for $C_{16}H_{32}O_4P$ [$M+H^+$] 319.2033, found 319.2033. **Specific rotation:** $[\alpha]_D^{21}$ -16.1 (c= 0.51, $CHCl_3$).

5.3.3.2 Products derived from the enantioselective allylboration of acetylene.

(*S*,*Z*)-4,4,5,5-Tetramethyl-2-(3-phenylpenta-1,4-dien-1-yl)-1,3,2-dioxaborolane (8)

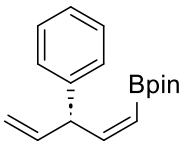

Synthesized from **10** (54.0 mg, 0.2 mmol), **6** and B_2pin_2 according to general procedure A. Yellow oil obtained in 74% yield with 96:4 er after column chromatography (hexane:CH_2Cl_2, 100:0 to 90:10). **^{1}H NMR** (300 MHz, $CDCl_3$) δ 7.36 – 7.27 (m, 4H), 7.24 – 7.16 (m, 1H), 6.52 (dd, *J* = 13.2, 10.0 Hz, 1H), 6.12 – 5.99 (m, 1H), 5.44 (d, *J* = 13.3 Hz, 1H), 5.17 (dt, *J* = 6.6, 1.7 Hz, 1H), 5.12 (d, *J* = 1.5 Hz, 1H), 5.00 (ddt, *J* = 9.8, 6.5, 1.6 Hz, 1H), 1.30 (s, 12H) ppm. **^{13}C NMR** (75 MHz, $CDCl_3$) δ 154.7, 143.5, 140.5, 128.6, 127.9, 126.4, 115.3, 83.2, 50.9, 25.1, 25.0 ppm. **^{11}B NMR** (160 MHz, $CDCl_3$) 29.4 ppm. **HRMS (APCI)** Calc. for $C_{17}H_{23}BO_2$ [$M+H^+$] 271.1867, found 271.1872. **Specific rotation:** $[\alpha]_D^{21}$ +147.3 (c= 0.6, $CHCl_3$).

Enantiomeric purity was determined by chiral uHPLC analysis [Lux i-cellulose-5, T_{oven}: 40 °C, flow: 1.0 mL/min; 100% *n*-hexane, λ = 227 nm, minor enantiomer t_R = 4.71 min, major enantiomer t_R = 5.04 min].

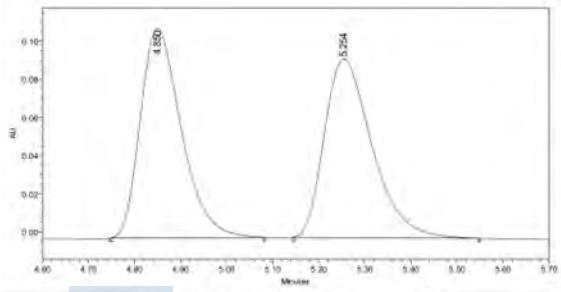

Unknown Peak Results

	Peak Type	RT	Area	% Area	Height
1	Unknown	4.850	678889	50.14	109892
2	Unknown	5.254	675040	49.86	93872

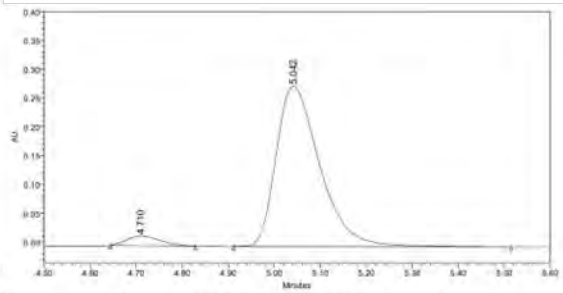

Unknown Peak Results

	Peak Type	RT	Area	% Area	Height
1	Unknown	4.710	83216	4.35	16467
2	Unknown	5.042	1829813	95.65	278226

(*S*,*Z*)-4-(1-(4,4,5,5-Tetramethyl-1,3,2-dioxaborolan-2-yl)penta-1,4-dien-3-yl)phenyl acetate (13)

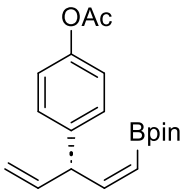

Synthesized from **59** (65.7 mg, 0.2 mmol), **6** and B_2pin_2 according to a modified general procedure A, where **28** was added via syringe pump during 5 h in 0.5 mL of toluene, and reaction was kept at 20 °C inside of a water bath. Colorless oil obtained in 61% yield with >99:1 er after column chromatography in previously deactivated SiO_2 with hexane:NEt_3 (95:5) (hexane:CH_2Cl_2, 100:0 to 80:20). **^{1}H NMR** (300 MHz, $CDCl_3$) δ 7.27 (d, *J* = 7.6 Hz, 2H), 7.01 (d, *J* = 8.6 Hz, 2H), 6.48 (dd, *J* = 13.3, 9.9 Hz, 1H), 6.09 – 5.95 (m, 1H), 5.44 (d, *J* = 13.3 Hz, 1H), 5.20 – 5.09 (m, 2H), 4.99 (t, *J* = 8.1 Hz, 1H), 2.28 (s, 3H), 1.29 (s, 12H) ppm. **^{13}C NMR** (75 MHz, $CDCl_3$) δ 154.3, 149.4, 141.0, 140.1, 128.8, 121.5, 115.5, 83.2, 50.2, 25.0, 21.2 ppm. **^{11}B NMR** (160 MHz, $CDCl_3$) δ 30.5 ppm. **HRMS (APCI)** Calc. for $C_{19}H_{26}BO_4$ [M+H$^+$] 329.1919, found 329.1929. **Specific rotation:** [α] $^{22}_{D}$ +181.8 (c= 0.59, $CHCl_3$).

Enantiomeric purity was determined by chiral uHPLC analysis [Lux i-cellulose-5, T_{oven}: 40 °C, flow: 1.0 mL/min; 99% *n*-hexane, λ = 220 nm, minor enantiomer t_R = 7.23 min, major enantiomer t_R = 7.61 min].

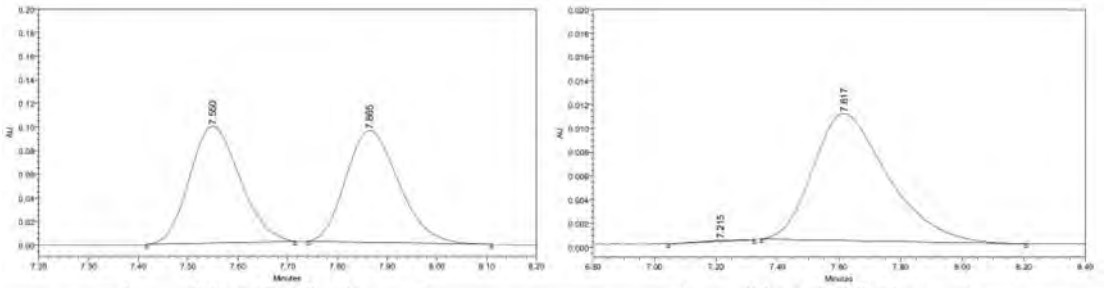

Unknown Peak Results

	Peak Type	RT	Area	% Area	Height
1	Unknown	7.550	697036	49.90	98889
2	Unknown	7.865	699791	50.10	94714

Unknown Peak Results

	Peak Type	RT	Area	% Area	Height
1	Unknown	7.215	651	0.36	85
2	Unknown	7.617	180724	99.64	10688

(*S*,*Z*)-4,4,5,5-Tetramethyl-2-(3-(4-(trifluoromethyl)phenyl)penta-1,4-dien-1-yl)-1,3,2 dioxaborolane (14)

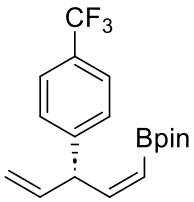

Synthesized from **60** (67.6 mg, 0.2 mmol), **6** and B_2pin_2 according to general procedure A. Colorless oil obtained in 59% yield with 98:2 er after column chromatography (hexane:CH_2Cl_2, 100:0 to 90:10). **^{1}H NMR** (300 MHz, $CDCl_3$) δ 7.56 (d, *J* = 8.1 Hz, 2H), 7.39 (d, *J* = 8.0 Hz, 2H), 6.49 (dd, *J* = 13.2, 9.9 Hz, 1H), 6.03 (ddd, *J* = 16.9, 10.5, 6.4 Hz, H), 5.54 – 5.43 (m, 1H), 5.20 (s, 1H), 5.15 (d, *J* = 9.6 Hz, 1H), 5.06 (dd, 9.9, 6.5 Hz, 1H), 1.29 (s, 12H) ppm. **^{13}C NMR** (75 MHz, $CDCl_3$) δ 153.5, 147.6, 139.5, 128.7 (d, *J* = 32.1 Hz), 128.3, 125.5 (q, *J* = 3.8 Hz), 124.5 (q, *J* = 271.9 Hz), 119.1, 116.1, 83.4, 50.7, 25.0 ppm. **^{11}B NMR** (160 MHz, $CDCl_3$) δ 29.7 ppm. **^{19}F NMR** (282 MHz, $CDCl_3$) δ -62.40 ppm. **HRMS (APCI)** Calc. For $C_{18}H_{22}BF_3O_2$ [M+H$^+$] 339.1741, found 339.1730. **Specific rotation:** [α] $^{21}_{D}$ +115.6 (c=0.66, $CHCl_3$).

Enantiomeric purity was determined by chiral uHPLC analysis [Lux i-cellulose-5, T_{oven}: 40 °C, flow: 0.5 mL/min; 100% *n*-hexane, λ = 215 nm, minor enantiomer t_R = 7.32 min, major enantiomer t_R = 7.52 min].

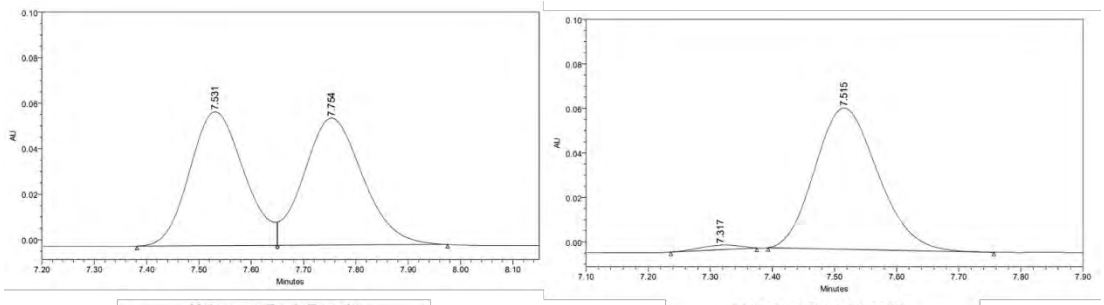

Unknown Peak Results

	Peak Type	RT	Area	% Area	Height
1	Unknown	7.531	423927	49.22	58817
2	Unknown	7.754	437302	50.78	55788

Unknown Peak Results

	Peak Type	RT	Area	% Area	Height
1	Unknown	7.317	9142	2.00	2035
2	Unknown	7.515	447649	98.00	63447

(*S*,*Z*)-2-(3-(Furan-3-yl)penta-1,4-dien-1-yl)-4,4,5,5-tetramethyl-1,3,2-dioxaborolane (15)

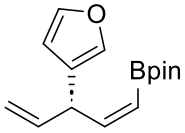

Synthesized from **61** (52.0 mg, 0.2 mmol), **6** and B_2pin_2 according to general procedure A. Colorless oil obtained in 45% yield with 96:4 er after column chromatography (hexane:CH_2Cl_2, 100:0 to 90:10). **^{1}H NMR** (300 MHz, $CDCl_3$) δ 7.40 – 7.33 (m, 1H), 7.25 – 7.20 (m, 1H), 6.44 (dd, *J* = 13.4, 9.8 Hz, 1H), 6.32 (s, 1H), 5.97 (ddd, *J* = 17.0, 10.2, 6.8 Hz, 1H), 5.46 (d, *J* = 13.2 Hz, 1H), 5.17 (dt, *J* = 17.1, 1.6 Hz, 1H), 5.11 (dt, *J* = 10.1, 1.4 Hz, 1H), 4.88 – 4.79 (m, 1H), 1.30 (s, 12H) ppm. **^{13}C NMR** (75 MHz, $CDCl_3$) δ 153.8, 142.9, 139.6, 139.0, 127.2, 115.1, 110.4, 83.2, 42.5, 25.0 ppm. **^{11}B NMR** (160 MHz, $CDCl_3$) δ 29.7 ppm **HRMS (APCI)** Calc. for $C_{15}H_{22}BO_3$ [M+H$^+$] 261.1657, found 261.1670. **Specific rotation:** [α] $^{22}_{D}$ +41.2 (c=0.95, $CHCl_3$)

Enantiomeric purity was determined by chiral uHPLC analysis [Lux i-amylose-3, T_{oven}: 40 °C, flow: 1 mL/min; 100% *n*-hexane, λ = 234 nm, minor enantiomer t_R = 3.29 min, major enantiomer t_R = 3.37 min].

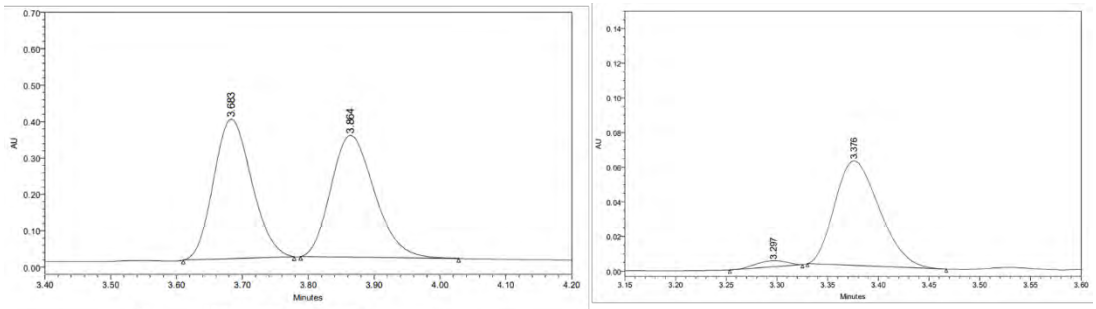

Unknown Peak Results

	Peak Type	RT	Area	% Area	Height
1	Unknown	3.683	1540961	50.02	383143
2	Unknown	3.864	1540022	49.98	334472

Unknown Peak Results

	Peak Type	RT	Area	% Area	Height
1	Unknown	3.297	7336	3.82	3451
2	Unknown	3.376	184953	96.18	60328

(*R*,*Z*)-2-(3-Cyclohexylpenta-1,4-dien-1-yl)-4,4,5,5-tetramethyl-1,3,2-dioxaborolane (16)

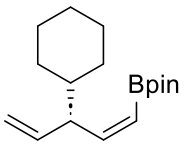

Synthesized from **62** (55.2 mg, 0.2 mmol), **6** and B_2pin_2 according to general procedure A. Colorless oil obtained in 57% yield with 99:1 er after column chromatography (hexane:CH_2Cl_2, 100:0 to 90:10). **^{1}H NMR** (300 MHz, $CDCl_3$) δ 6.28 (dd, *J* = 13.5, 10.2 Hz, 1H), 5.72 (ddd, *J* = 17.2, 10.2, 8.0 Hz, 1H), 5.36 (d, *J* = 13.5 Hz, 1H), 5.08 – 4.93 (m, 2H), 3.40 (dt, *J* = 10.3, 7.8 Hz, 1H), 1.79 – 1.57 (m, 6H), 1.26 (s, 12H), 1.21 – 1.11 (m, 3H), 0.94 (m, 2H) ppm. **^{13}C NMR** (75 MHz, $CDCl_3$) δ 155.6, 140.7, 114.7, 83.0, 52.1, 41.9, 30.8, 30.5, 26.8, 26.6, 25.1, 24.9 ppm. **^{11}B NMR** (160 MHz, $CDCl_3$) δ 29.8 ppm. **HRMS (APCI)** Calc. for $C_{17}H_{29}BO_2$ [M+H$^+$] 277.2337, found 277.2330. **Specific rotation:** [α] $^{21}_{D}$ -23.3 (c=0.64, $CHCl_3$).

Enantiomeric purity was determined by chiral uHPLC analysis [Lux i-cellulose-5, T_{oven}: 40 °C, flow: 1.0 mL/min; 100% *n*-hexane, λ = 215 nm, minor enantiomer t_R = 5.07 min, major enantiomer t_R = 4.75 min].

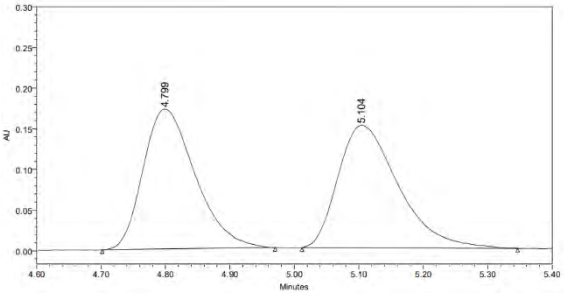

Unknown Peak Results

	Peak Type	RT	Area	% Area	Height
1	Unknown	4.799	966144	49.62	171958
2	Unknown	5.104	980941	50.38	150704

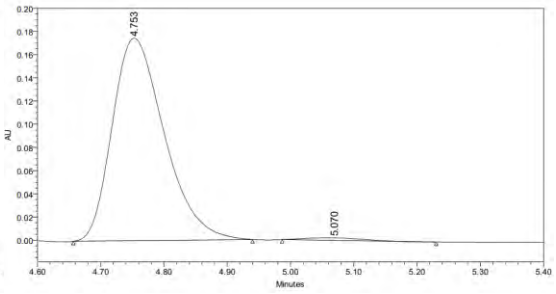

Unknown Peak Results

	Peak Type	RT	Area	% Area	Height
1	Unknown	4.753	998862	98.61	174612
2	Unknown	5.070	14116	1.39	2230

(*S*,*Z*)-4,4,5,5-Tetramethyl-2-(3-methylpenta-1,4-dien-1-yl)-1,3,2-dioxaborolane (17)

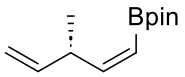

Synthesized from **63** (41.6 mg, 0.2 mmol), **6** and B_2pin_2 according to general procedure A. Colorless oil obtained in 92% yield with 94:6 er after column chromatography (pentane:CH_2Cl_2, 100:0 to 95:5). **^{1}H NMR** (300 MHz, $CDCl_3$) δ 6.22 (t, *J* = 11.3 Hz, 1H), 5.80 (ddd, *J* = 17.3, 10.4, 6.3 Hz, 1H), 5.30 (d, *J* = 13.5 Hz, 1H), 5.01 (d, *J* = 15.7 Hz, 1H), 4.94 (d, *J* = 10.2 Hz, 1H), 3.68 (q, *J* = 7.3 Hz, 1H), 1.26 (s, 12H), 1.08 (d, *J* = 6.8 Hz, 3H) ppm. **^{13}C NMR** (75 MHz, $CDCl_3$) δ 157.9, 143.0, 112.8, 83.0, 39.9, 25.0, 24.9, 20.2 ppm. **^{11}B NMR** (160 MHz, $CDCl_3$) δ 29.7 ppm. **HRMS (APCI)** Calc. for $C_{12}H_{21}BO_2$ [M+H$^+$] 209.1710, found 209.1703. **Specific rotation:** [α] $^{20}_{D}$ -133.0 (c=0.68, $CHCl_3$).

Enantiomeric purity was measured on derivatization product **S2.**

(*S*,*Z*)-4-(3-Methylpenta-1,4-dien-1-yl)phenyl propionate (S2)

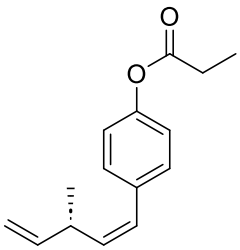

Synthesized from **17** (37.5 mg, 0.18 mmol) and 4-iodophenyl propionate (54.6 mg, 0.2 mmol) according to general procedure B. Colorless oil obtained in 73% yield with 94:6 er after column chromatography (pentane:CH_2Cl_2, 100:0 to 80:20). **^{1}H NMR** (300 MHz, $CDCl_3$) δ 8.00 (d, *J* = 8.5 Hz, 2H), 7.33 (d, *J* = 8.4 Hz, 2H), 6.47 (d, *J* = 11.6 Hz, 1H), 5.87 (ddd, *J* = 17.3, 10.3, 5.7 Hz, 1H), 5.66 – 5.53 (m, 1H), 5.13 – 4.97 (m, 2H), 4.37 (q, *J* = 7.1 Hz, 2H), 3.48 – 3.32 (m, 1H), 1.39 (t, *J* = 7.1 Hz, 3H), 1.13 (d, *J* = 6.7 Hz, 3H) ppm. **^{13}C NMR** (75 MHz, $CDCl_3$) δ 198.0, 166.6, 142.2, 137.9, 129.6, 128.8, 128.6, 127.6, 113.6, 61.0, 36.4, 21.1, 14.5 ppm. **HRMS (APCI)** Calc. for $C_{15}H_{19}O_2$ [M+H$^+$] 231.1380, found 231.1376. **Specific rotation:** [α] $^{21}_{D}$ -94.5 (c=0.82, $CHCl_3$).

Enantiomeric purity was determined by chiral SFC [Lux i-cellulose-1, T_{oven}: 40 °C, flow: 2.0 mL/min; 1% MeOH, λ = 250 nm, minor enantiomer t_R = 6.99 min, major enantiomer t_R = 7.59 min].

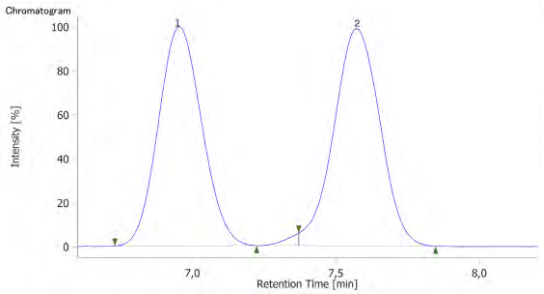

Peak Information

#	Peak Name	CH	tR [min]	Area [µV·sec]	Area%
1	Unknown	11	6,953	1714798	48,743
2	Unknown	11	7,570	1803241	51,257

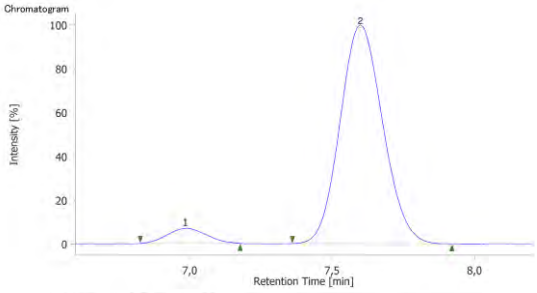

Peak Information

#	Peak Name	CH	tR [min]	Area [µV·sec]	Area%
1	Unknown	11	6,990	90249	5,851
2	Unknown	11	7,597	1452301	94,149

2-((3*S*,5*R*,*Z*)-5,9-Dimethyl-3-vinyldeca-1,8-dien-1-yl)-4,4,5,5-tetramethyl-1,3,2-dioxaborolane (18)

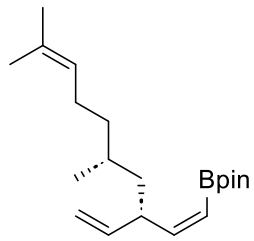

Synthesized from **64** (63.7 mg, 0.2 mmol), **6** and B_2pin_2 according to general procedure A. Colorless oil obtained in 68% yield with >20:1 dr after column chromatography (pentane:CH_2Cl_2, 100:0 to 90:10). **^{1}H NMR** (300 MHz, $CDCl_3$) δ 6.27 – 6.18 (m, 1H), 5.68 (ddd, *J* = 17.4, 9.9, 7.3 Hz, 1H), 5.30 (d, *J* = 13.5 Hz, 1H), 5.15 – 4.88 (m, 3H), 3.73 (p, *J* = 7.1 Hz, 1H), 1.95 (td, *J* = 14.9, 7.6 Hz, 2H), 1.67 (s, 3H), 1.59 (s, 3H), 1.48 – 1.35 (m, 3H), 1.26 (s, 12H), 1.19 – 1.06 (m, 2H), 0.89 (d, *J* = 6.8 Hz, 3H) ppm. **^{13}C NMR** (75 MHz, $CDCl_3$) δ 157.4, 141.8, 130.9, 125.3, 113.9, 83.0, 44.0, 42.4, 37.0, 30.1, 25.8, 25.5, 25.0, 19.7, 17.8 ppm. **^{11}B NMR** (160 MHz, $CDCl_3$) δ 29.8 ppm**. HRMS (APCI)** Calc. for $C_{20}H_{35}BO_2$ [M+H$^+$] 319.2801, found 319.2806. **Specific rotation:** [α] $^{22}_{D}$ -16.0 (c=0.60, $CHCl_3$).

2-((*R*,1*Z*,4*Z*)-5-Chloro-3-methylpenta-1,4-dien-1-yl)-4,4,5,5-tetramethyl-1,3,2-dioxaborolane (12)

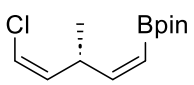

Synthesized from **11** (25.0 mg, 0.2 mmol), **6** and B_2pin_2 according to general procedure A. Colorless oil obtained in 86% yield with 96.5:3.5 er and >20:1 dr after column chromatography (pentane:CH_2Cl_2, 100:0 to 90:10). **^{1}H NMR** (300 MHz, $CDCl_3$) δ 6.27 – 6.13 (m, 1H), 5.95 (d, *J* = 8.1 Hz, 1H), 5.64 (dd, *J* = 9.0, 7.1 Hz, 1H), 5.31 (d, *J* = 13.6 Hz, 1H), 4.23 (h, *J* = 6.7 Hz, 1H), 1.27 (s, 12H), 1.09 (d, *J* = 6.8 Hz, 3H) ppm. **^{13}C NMR** (75 MHz, $CDCl_3$) δ 155.4, 135.5, 117.0, 83.3, 35.5, 25.1, 24.9, 20.9 ppm. **^{11}B NMR** (160 MHz, $CDCl_3$) δ 31.1 ppm. **HRMS (APCI)** Calc. for $C_{12}H_{20}BClO_2$ [M+H$^+$] 243.1320, found 243.1325. **Specific rotation:** [α] $^{23}_{D}$ +1.90 (c=0.91, $CHCl_3$)

Enantiomeric purity was measured on derivatization product **(*S*,*Z*,*Z*)-23.**

2-((*R*,1*Z*,4*Z*)-5-Chloro-3-phenylpenta-1,4-dien-1-yl)-4,4,5,5-tetramethyl-1,3,2-dioxaborolane (19)

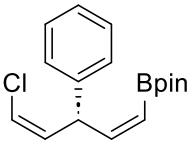

Synthesized from **1** (37.4 mg, 0.2 mmol), **6** and B_2pin_2 according to general procedure A. Yellow oil obtained in 72% yield with 91:9 er and >20:1 dr after column chromatography (hexane:CH_2Cl_2, 100:0 to 90:10). **^{1}H NMR** (300 MHz, $CDCl_3$) δ 7.28 (s, 2H), 7.23 – 7.13 (m, 2H), 6.40 (dd, *J* = 13.0, 10.0 Hz, 1H), 6.17 – 6.11 (m, 1H), 6.01 – 5.94 (m, 1H), 5.53 (t, *J* = 9.7 Hz, 1H), 5.44 (d, *J* = 13.1 Hz, 1H), 1.26 (s, 12H) ppm. **^{13}C NMR** (75 MHz, $CDCl_3$) δ 152.4, 142.4, 132.7, 128.7, 127.5, 126.5, 118.9, 83.4, 45.5, 25.1, 25.0 ppm.**^{11}B NMR** (160 MHz, $CDCl_3$) δ 29.4 ppm**. HRMS (APCI)** Calc. for $C_{17}H_{22}BClO_2$ [M+H$^+$] 305.1474, found 305.1490. **Specific rotation:** [α] $^{21}_{D}$ + 64.5 (c= 0.56, $CHCl_3$).

Enantiomeric purity was determined by chiral uHPLC analysis [Lux i-cellulose-5, T_{oven}: 40 °C, flow: 1.0 mL/min; 100% *n*-hexane, λ = 221 nm, minor enantiomer t_R = 8.39 min, major enantiomer t_R = 9.05 min].

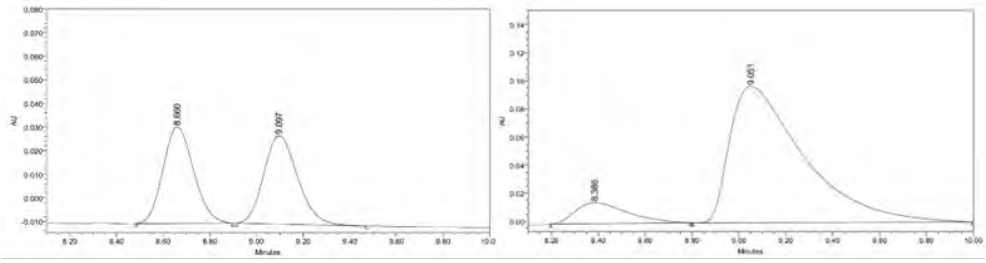

Unknown Peak Results

	Peak Type	RT	Area	% Area	Height
1	Unknown	8.660	373870	49.75	40920
2	Unknown	9.097	377576	50.25	37456

Unknown Peak Results

	Peak Type	RT	Area	% Area	Height
1	Unknown	8.386	230605	9.81	14935
2	Unknown	9.051	2121142	90.19	96861

2-((*R*,1*Z*,4*Z*)-5-Chloro-3-(3-chlorophenyl)penta-1,4-dien-1-yl)-4,4,5,5-tetramethyl-1,3,2-dioxaborolane (20)

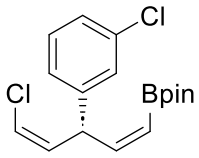

Synthesized from **65** (44.3 mg, 0.2 mmol), **6**, and B_2pin_2 according to general procedure A. Yellowish oil obtained in 60% yield with 92:8 er and 19:1 dr after column chromatography (hexane:CH_2Cl_2, 100:0 to 90:10). **^{1}H NMR** (300 MHz, $CDCl_3$) δ 7.29 (td, *J* = 1.5, 0.8 Hz, 1H), 7.24 – 7.15 (m, 3H), 6.39 (dd, *J* = 13.2, 9.9 Hz, 1H), 6.19 (dt, *J* = 7.1, 0.7 Hz, 1H), 5.96 (ddd, *J* = 9.3, 7.1, 0.6 Hz, 1H), 5.54 (t, *J* = 9.6 Hz, 1 H), 5.51 (d, *J* = 13.3 Hz, 1H), 1.30 (s, 12H) ppm. **^{13}C NMR** (75 MHz, $CDCl_3$) δ 151.6, 144.5, 132.0, 129.9, 127.9, 126.7, 125.7, 119.6, 83.5, 45.1, 25.1, 25.0 ppm. **^{11}B NMR** (160 MHz, $CDCl_3$) δ 29.5 ppm **HRMS (APCI)** Calc. for $C_{17}H_{21}BCl_2O_2$ [M+H$^+$] 339.1084, found 339.1067. **Specific rotation:** $[\alpha]_D^{21}$ + 54.8 (c= 0.56, $CHCl_3$).

Enantiomeric purity was determined by chiral uHPLC analysis [Lux i-cellulose-5, T_{oven}: 40 °C, flow: 1.0 mL/min; 100% *n*-hexane, λ = 231 nm, minor enantiomer t_R = 7.07min, major enantiomer t_R = 7.62 min].

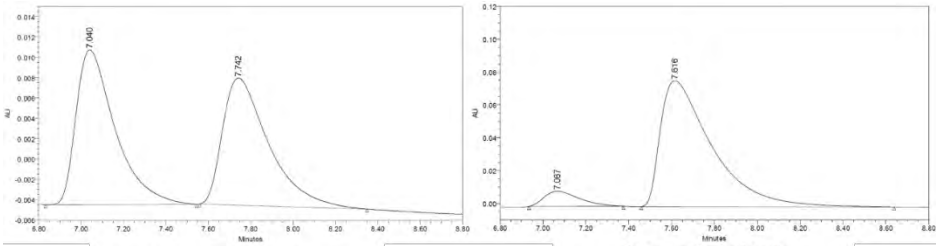

	Peak Type	RT	Area	% Area	Height
1	Unknown	7.040	195765	50.83	15243
2	Unknown	7.742	189382	49.17	12497

	Peak Type	RT	Area	% Area	Height
1	Unknown	7.067	104352	7.54	9166
2	Unknown	7.616	1280215	92.46	76593

5.3.3.2.1 Products derived from enantiodivergent transformations of chiral skipped diene **12**

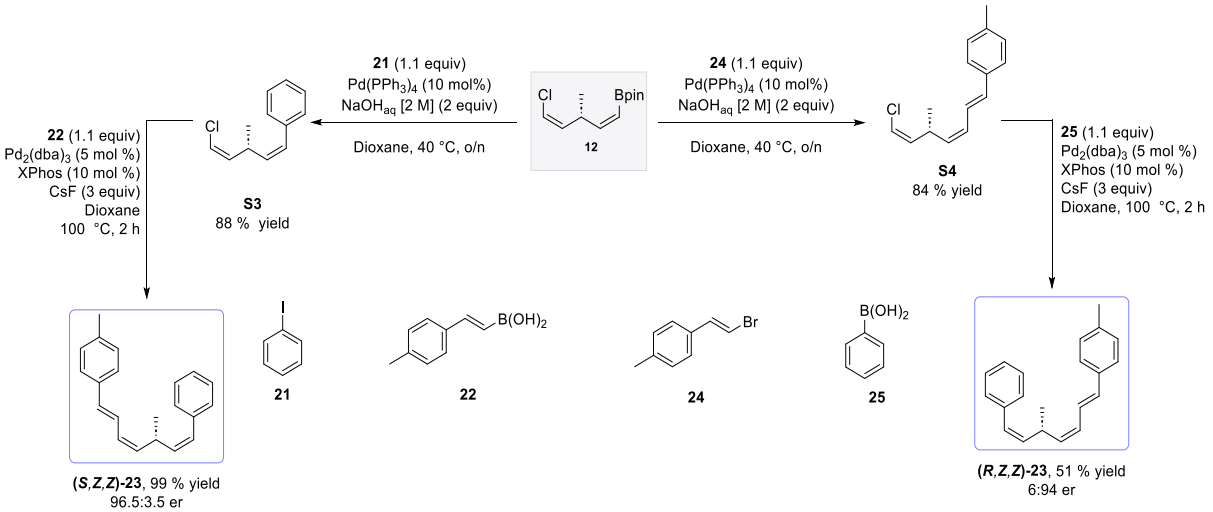

((*R*,1*Z*,4*Z*)-5-Chloro-3-methylpenta-1,4-dien-1-yl)benzene (S3)

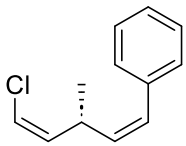

Synthesized from **10** (138.3 mg, 0.57 mmol) and iodobenzene **12** (127.9 mg, 0.63 mmol), using $Pd(PPh_3)_4$ (65.7 mg, 0.057 mmol), 1,4-Dioxane (5.7 mL) and $NaOH_{aq}$ [2 M] (0.57 mL) according to general procedure B. Colorless oil obtained in 88% yield after column chromatography. **^{1}H NMR** (300 MHz, $CDCl_3$) δ 7.40 – 7.21 (m, 5H), 6.43 (d, *J* = 11.5 Hz, 1H), 6.00 (d, *J* = 7.0 Hz, 1H), 5.74 (dd, *J* = 9.0, 7.1 Hz, 1H), 5.53 (t, *J* = 10.8 Hz, 1H), 3.99 (q, *J* = 9.0 Hz, 1H), 1,14 (d, *J* = 6.8 Hz, 3H) ppm. **^{13}C NMR** (126 MHz, $CDCl_3$) δ 137.2, 135.5, 134.8, 128.9, 128.9, 128.4, 126.9, 116.9, 31.7, 21.0 ppm. **HRMS (APCI)** Calc. for $C_{12}H_{14}Cl$ $[M+H^+]$ 193.0779, found 193.0773. **Specific rotation:** $[\alpha]_D^{18}$ +3.0 (c=0.87, $CHCl_3$).

1-Methyl-4-((*S*,1*E*,3*Z*,6*Z*)-5-methyl-7-phenylhepta-1,3,6-trien-1-yl)benzene ((*S*,*Z*,*Z*)-23)

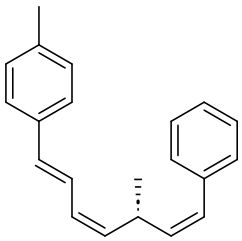

Synthesized from **S3** (96.3 mg, 0.50 mmol) and (*E*)-(4-methylstyryl)boronic acid **22** (89.1 mg, 0.55 mmol), using $Pd_2(dba)_3$ (22.9 mg, 0.025 mmol), XPhos (23.8 mg, 0.05 mmol), CsF (227.9 mg, 1.5 mmol) and 1,4-Dioxane (5.0 mL) according to general procedure C. Colorless oil obtained in 99% yield with 96.5:3.5 er after column chromatography. **^{1}H NMR** (300 MHz, $CDCl_3$) δ 7.42 – 7.27 (m, 5H), 7.11 – 7.03 (m, 4H), 6.72 (dd, *J* = 15.5, 11.1 Hz, 1H), 6.50 – 6.39 (m, 2H), 6.10 (t, *J* = 10.8 Hz, 1H), 5.58 (t, *J* = 10.8 Hz, 1H), 5.45 (t, *J* = 10.0 Hz, 1H), 4.01 (h, *J* = 6.7 Hz, 1H), 2.35 (s, 3H), 1.22 (d, *J* = 6.7 Hz, 3H) ppm. **^{13}C NMR** (75 MHz, $CDCl_3$) δ 137.8, 137.4, 136.7, 135.9, 134.7, 132.8, 129.3, 128.9, 128.5, 127.9, 127.3, 126.8, 126.5, 123.7, 32.1, 22.1, 21.4 ppm. **HRMS (APCI)** Calc. for $C_{21}H_{23}$ $[M+H^+]$ 275.1794, found 275.1785. **Specific rotation:** $[\alpha]_D^{18}$ +63.4 (c=1.09, $CHCl_3$).

Enantiomeric purity was determined by chiral uHPLC analysis [Lux i-cellulose-5, T_{oven}: 40 °C, flow: 1.0 mL/min; 99% *n*-hexane, λ = 220 nm, minor enantiomer t_R = 6.36 min, major enantiomer t_R = 5.90 min].

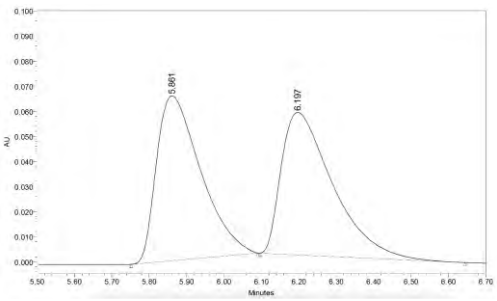

Unknown Peak Results

	Peak Type	RT	Area	% Area	Height
1	Unknown	5.861	539520	49.86	65674
2	Unknown	6.197	542567	50.14	56760

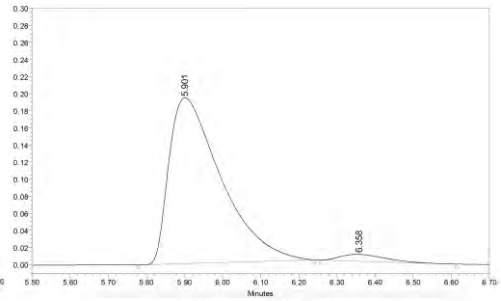

Unknown Peak Results

	Peak Type	RT	Area	% Area	Height
1	Unknown	5.901	1847055	96.59	193964
2	Unknown	6.358	65155	3.41	8051

1-((*R*,1*E*,3*Z*,6*Z*)-7-Chloro-5-methylhepta-1,3,6-trien-1-yl)-4-methylbenzene (S4)

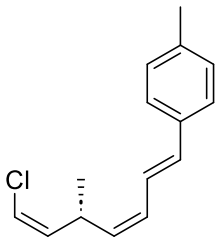

Synthesized from **12** (84.9 mg, 0.35 mmol) and (*E*)-1-(2-bromovinyl)-4-methylbenzene **24** (75.9 mg, 0.38 mmol), using $Pd(PPh_3)_4$ (40.4 mg, 0.035 mmol), 1,4-Dioxane (3.5 mL) and $NaOH_{aq}$ [2 M] (0.35 mL) according to general procedure B. Yellow oil obtained in 84% yield after column chromatography. **^{1}H NMR** (300 MHz, $CDCl_3$) δ 7.33 (d, *J* = 8.3 Hz, 2H), 7.13 (d, *J* = 7.6 Hz, 2H), 6.52 (d, *J* = 15.7 Hz, 1H), 6.12 (t, *J* = 10.8 Hz, 1H), 5.97 (d, *J* = 7.0 Hz, 1H), 5.67 (dd, *J* = 9.3, 7.0 Hz, 1H), 5.33 (t, *J* = 9.7 Hz, 1H), 4.07 – 3.96 (m, 1H), 2.34 (s, 3H), 1.15 (d, *J* = 6.8 Hz, 3H) ppm. **^{13}C NMR** (75 MHz, $CDCl_3$) δ 137.6, 135.7, 134.8, 134.1, 133.3, 129.5, 129.0, 126.5, 123.7, 116.3, 31.5, 21.4, 20.8 ppm. **HRMS (APCI)** Calc. for $C_{15}H_{17}$ [$M+H^+$-HCl] 197.1325, found 197.1318. **Specific rotation:** $[\alpha]_D^{18}$ -62.5 (c=0.88, $CHCl_3$).

1-Methyl-4-((*R*,1*E*,3*Z*,6*Z*)-5-methyl-7-phenylhepta-1,3,6-trien-1-yl)benzene ((*R*,*Z*,*Z*)-23)

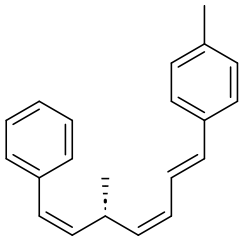

Synthesized from **S4** (67.5 mg, 0.29 mmol) and phenyl boronic acid **25** (38.9 mg, 0.32 mmol), using $Pd_2(dba)_3$ (12.8 mg, 0.014 mmol), XPhos (13.8 mg, 0.029 mmol), CsF (132.1 mg, 0.87 mmol) and 1,4-Dioxane (2.9 mL) according to general procedure C. Colorless oil obtained in 51% yield with 6:94 er after column chromatography. NMR data matches **(*S*,*Z*,*Z*)-23)**. **Specific rotation:** $[\alpha]_D^{21}$ -22.2 (c=0.59, $CHCl_3$).

Enantiomeric purity was determined by chiral uHPLC analysis [Lux i-cellulose-5, T_{oven}: 40 °C, flow: 1.0 mL/min; 99% *n*-hexane, 1% *i*PrOH, λ = 220 nm, minor enantiomer t_R = 5.65 min, major enantiomer t_R = 6.00 min].

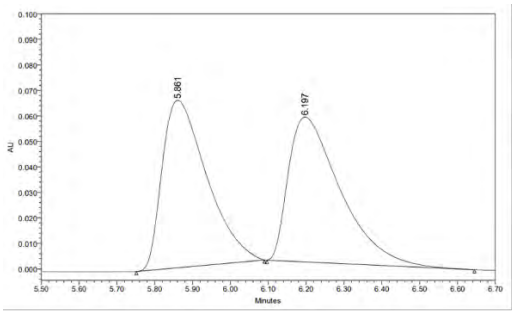

Unknown Peak Results

	Peak Type	RT	Area	% Area	Height
1	Unknown	5.861	539520	49.86	65674
2	Unknown	6.197	542567	50.14	56760

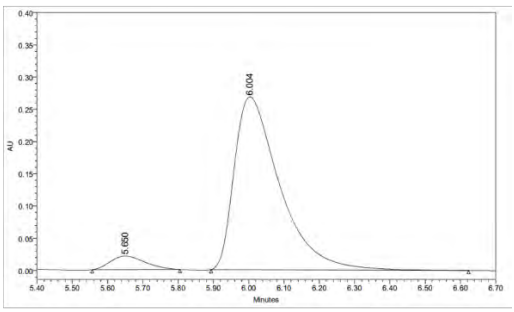

Unknown Peak Results

	Peak Type	RT	Area	% Area	Height
1	Unknown	5.650	143474	5.64	21063
2	Unknown	6.004	2401833	94.36	267987

5.3.3.3 Products derived from diastereodivergent transformations of chiral skipped diene **12**

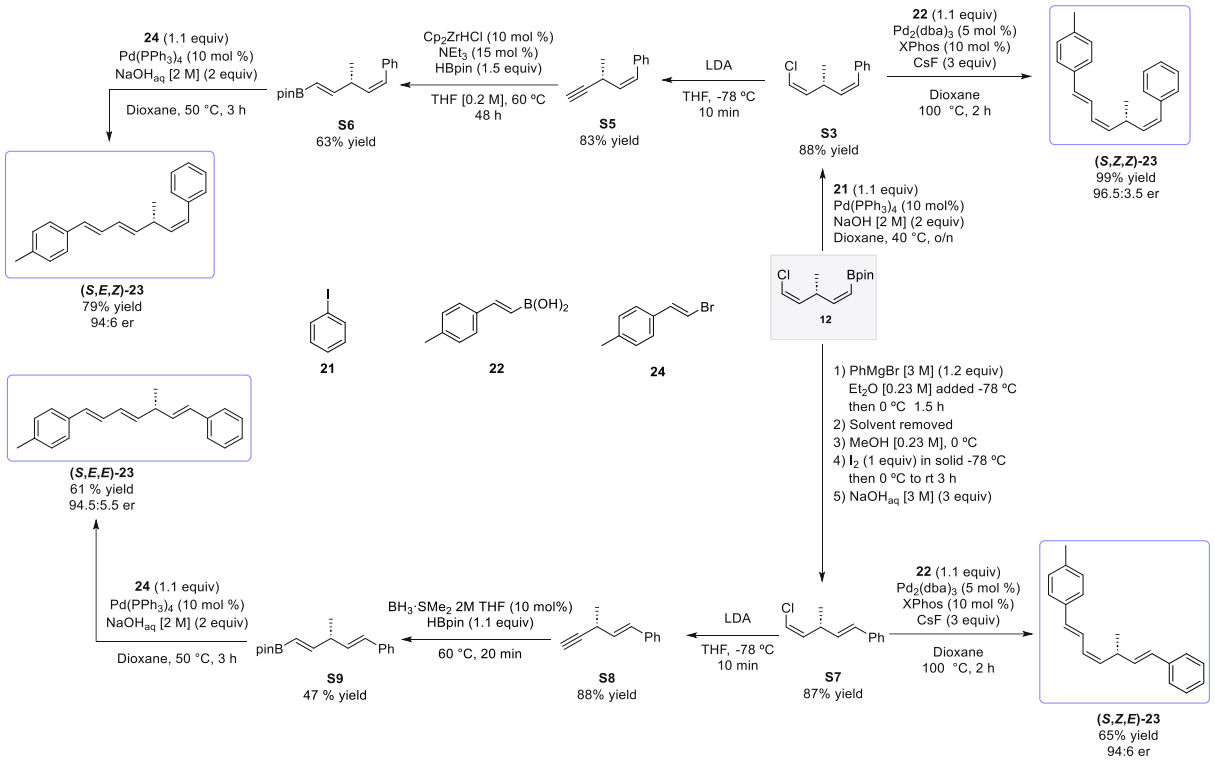

(*R*,*Z*)-(3-Methylpent-1-en-4-yn-1-yl)benzene (S4)

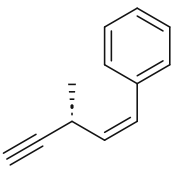

Synthesized from **S3** (79.0 mg, 0.41 mmol), using *i*Pr$_2$NH (70.5 mg, 98 µL, 0.70 mmol), *n*BuLi [2.5 M] in hexanes (0.25 mL, 0.62 mmol) and THF (8.2 mL) according to general procedure D. Colorless oil obtained in 83% yield after column chromatography. **^{1}H NMR** (300 MHz, $CDCl_3$) δ 7.42 – 7.23 (m, 5H), 6.49 (d, *J* = 11.3 Hz, 1H), 5.72 – 5.57 (m, 1H), 3.73 – 3.58 (m, 1H), 2.17 (d, *J* = 2.4 Hz, 1H), 1.33 (d, *J* = 6.9 Hz, 3H) ppm. **^{13}C NMR** (75 MHz, $CDCl_3$) δ 136.8, 133.2, 129.1, 128.8, 128.5, 127.2, 87.5, 68.8, 24.7, 22.0 ppm. **HRMS (APCI)** Calc. for $C_{12}H_{13}$ [M+H$^+$] 157.1012, found 157.1008. **Specific rotation:** [α] $^{21}_{D}$ -226.5 (c=0.98, $CHCl_3$).

4,4,5,5-Tetramethyl-2-((*S*,1*E*,4*Z*)-3-methyl-5-phenylpenta-1,4-dien-1-yl)-1,3,2-dioxaborolane (S5)

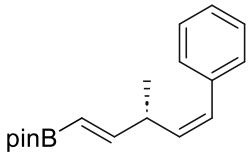

In an Ar-filled glove box, a tube vial equipped with a stirring bar was charged with Cp_2ZrHCl (3.1 mg, 0.012 mmol, 10 mol%). The tube was sealed and taken out of the glove box. Then, **S4** (18.7 mg, 0.12 mmol, 1 equiv), Et_3N (3 µL, 0.018 mmol, 15 mol%) and THF (0.6 mL) were added through a septum. To this mixture HBpin (26 µL, 0.18 mmol, 1.5 equiv) was added. The mixture was stirred at 60 °C during 48 h, after which the mixture was allowed to cool to room temperature. The reaction was quenched with saturated aqueous solution of NH_4Cl (5 mL), and the mixture was extracted with CH_2Cl_2 (2 x 5 mL). The combined organic layers were dried over Na_2SO_4, filtered, and concentrated in vacuo (600 mBar, 40 ºC). Crude

product was purified by flash column chromatography (pentane) and **S5** was obtained as yellow oil obtained in 63% yield after column chromatography. **^{1}H NMR** (300 MHz, $CDCl_3$) δ 7.36 – 7.18 (m, 5H), 6.67 (dd, *J* = 18.1, 5.5 Hz, 1H), 6.47 (d, *J* = 11.5 Hz, 1H), 5.58 – 5.42 (m, 2H), 3.59 – 3.43 (m, 1H), 1.28 (s, 12H), 1.14 (d, *J* = 6.8 Hz, 3H) ppm. **^{13}C NMR** (75 MHz, $CDCl_3$) δ 157.2, 137.5, 135.3, 128.7, 128.3, 126.8, 83.3, 38.0, 25.0, 20.6 ppm. **^{11}B NMR** (160 MHz, $CDCl_3$) δ 30.1 ppm. **HRMS (APCI)** Calc. for $C_{18}H_{26}BO_2$ $[M+H^+]$ 285.2020, found 285.2013. **Specific rotation:** $[\alpha]_D^{20}$ -151.5 (c=0.94, $CHCl_3$).

1-Methyl-4-((*S*,1*E*,3*E*,6*Z*)-5-methyl-7-phenylhepta-1,3,6-trien-1-yl)benzene ((*S*,*E*,*Z*)-23)

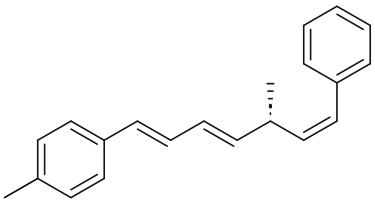

Synthesized from **S6** (17.1 mg, 0.06 mmol) and (*E*)-1-(2-bromovinyl)-4-methylbenzene **24**[236] (13.0 mg, 0.066 mmol), using $Pd(PPh_3)_4$ (6.9 mg, 0.006 mmol), 1,4-Dioxane (0.6 mL) and $NaOH_{aq}$ [2 M] (60 µL) according to general procedure B. The reaction was stirred 2 h at 40 ºC. Yellow oil obtained in 79% yield after column chromatography. **^{1}H NMR** (300 MHz, $CDCl_3$) δ 7.42 – 7.23 (m, 7H), 7.13 (d, *J* = 8.0 Hz, 2H), 6.77 (dd, *J* = 15.4, 10.9 Hz, 1H), 6.54 – 6.44 (m, 2H), 6.27 (dd, *J* = 15.3, 10.2 Hz, 1H), 5.87 (dd, *J* = 15.3, 5.8 Hz, 1H), 5.55 (t, *J* = 10.9 Hz, 1H), 3.64 – 3.49 (m, 1H), 2.36 (s, 3H), 1.20 (d, *J* = 6.8 Hz, 3H) ppm. **^{13}C NMR** (75 MHz, $CDCl_3$) δ 138.5, 137.6, 137.2, 136.0, 134.9, 131.1, 129.4, 128.8, 128.5, 128.4, 128.3, 126.9, 126.3, 35.5, 21.5, 21.3 ppm. **HRMS (APCI)** Calc. for $C_{21}H_{23}$ $[M+H^+]$ 275.1794, found 275.1785. **Specific rotation:** $[\alpha]_D^{19}$ -322.2 (c=0.34, $CHCl_3$).

Enantiomeric purity was determined by chiral uHPLC analysis [Lux i-amylose-3, T_{oven}: 40 °C, flow: 0.5 mL/min; 100% *n*-hexane, λ = 284 nm, minor enantiomer t_R = 17.50 min, major enantiomer t_R = 14.20 min].

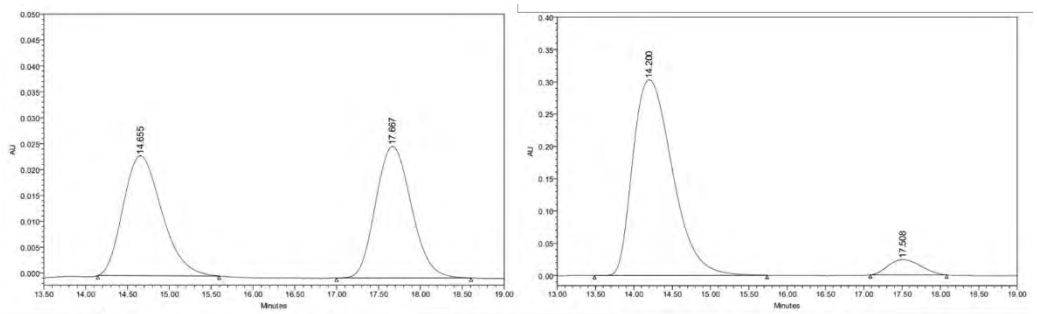

Unknown Peak Results

	Peak Type	RT	Area	% Area	Height
1	Unknown	14.655	745237	49.71	23156
2	Unknown	17.667	754047	50.29	25403

Unknown Peak Results

	Peak Type	RT	Area	% Area	Height
1	Unknown	14.200	10882969	94.00	303158
2	Unknown	17.508	694291	6.00	23681

((*R*,1*E*,4*Z*)-5-Chloro-3-methylpenta-1,4-dien-1-yl)benzene (S6)

Synthesized from **12** (92.2 mg, 0.38 mmol) and phenyl magnesium bromide [3.0 M] in Et_2O (0.15 mL, 0.46 mmol), using Et_2O (1.6 mL), MeOH (1.6 mL), I_2 (47.0 mg, 0.38 mmol) and $NaOH_{aq}$ [3 M] (0.38 mL) according to general procedure E. Yellow oil obtained in 87% yield after column chromatography. **^{1}H NMR** (300 MHz, $CDCl_3$) δ 7.38 – 7.26 (m, 4H), 7.24 – 7.17 (m, 1H), 6.42 (dd, *J* = 16.0, 1.6 Hz, 1H), 6.15 (dd, *J* = 16.0, 6.5 Hz, 1H), 6.06 (dd, *J* = 7.1, 0.9 Hz, 1H), 5.71 (dd, *J* = 9.1, 7.0 Hz, 1H), 3.65 (dq, *J* = 14.6, 6.7 Hz, 1H), 1.22 (d, *J* = 6.9 Hz, 3H)

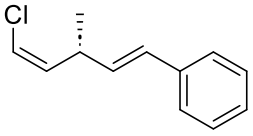

ppm. **^{13}C NMR** (75 MHz, $CDCl_3$) δ 137.6, 135.1, 132.7, 129.1, 128.7, 127.3, 126.3, 117.6, 35.1, 19.9 ppm. **HRMS (APCI)** Calc. for $C_{12}H_{14}Cl$ [M+H$^+$] 193.0779, found 193.0772. **Specific rotation:** [α] $^{20}_{D}$ +203.3 (c=0.7, $CHCl_3$).

1-Methyl-4-((*S*,1*E*,3*Z*,6*E*)-5-methyl-7-phenylhepta-1,3,6-trien-1-yl)benzene ((*S*,*Z*,*E*)-23)

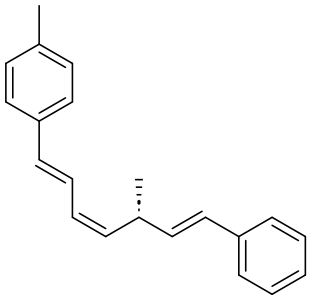

Synthesized from **S6** (21.2 mg, 0.11 mmol) and (*E*)-(4-methylstyryl)boronic acid **22** (19.6 mg, 0.12 mmol), using $Pd_2(dba)_3$ (5.0 mg, 0.0055 mmol), XPhos (5.2 mg, 0.011 mmol), CsF (50.1 mg, 0.33 mmol) and 1,4-Dioxane (1.1 mL) according to general procedure C. Colorless oil obtained in 65% yield and 94:6 er after column chromatography. **^{1}H NMR** (500 MHz, $CDCl_3$) δ 7.30 – 7.18 (m, 7H), 7.05 (d, *J* = 8.1 Hz, 2H), 6.99 (dd, *J* = 15.7, 11.4 Hz, 1H), 6.47 (d, *J* = 15.5 Hz, 1H), 6.34 (d, *J* = 17.3 Hz, 1H), 6.17 – 6.07 (m, 2H), 5.33 (t, *J* = 10.1 Hz, 1H), 3.56 (h, *J* = 6.7 Hz, 1H), 2.27 (s, 3H), 1.17 (d, *J* = 6.9 Hz, 3H) ppm. **^{13}C NMR** (126 MHz, $CDCl_3$) δ 136.6, 136.4, 134.4, 133.7, 133.4, 131.9, 128.3, 127.5, 127.3, 127.1, 126.0, 125.3, 125.1, 122.3, 34.5, 20.2, 20.0 ppm. **HRMS (APCI)** Calc. for $C_{21}H_{23}$ [M+H$^+$] 275.1794, found 275.1787. **Specific rotation:** [α] $^{21}_{D}$ +621.2 (c=0.56, $CHCl_3$).

Enantiomeric purity was determined by chiral uHPLC analysis [Lux i-cellulose-5, T_{oven}: 40 °C, flow: 1.0 mL/min; 100% *n*-hexane, λ = 320 nm, minor enantiomer t_R = 9.69 min, major enantiomer t_R = 11.89 min].

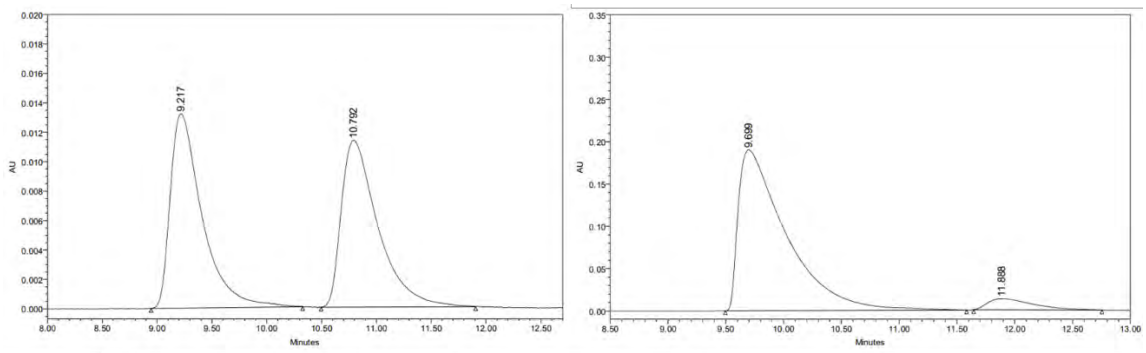

Unknown Peak Results

	Peak Type	RT	Area	% Area	Height
1	Unknown	9.217	266527	50.27	13212
2	Unknown	10.792	263696	49.73	11329

Unknown Peak Results

	Peak Type	RT	Area	% Area	Height
1	Unknown	9.699	5472416	93.90	190107
2	Unknown	11.888	355361	6.10	13169

(*R*,*E*)-(3-Methylpent-1-en-4-yn-1-yl)benzene (S7)

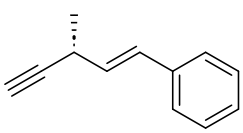

Synthesized from **S6** (92.5 mg, 0.48 mmol), using *i*Pr$_2$NH (82.6 mg, 112 µL, 0.82 mmol), *n*BuLi [2.5 M] in hexanes (0.29 mL, 0.72 mmol) and THF (9.6 mL) according to general procedure D. Colorless oil obtained in 88% yield after column chromatography. **^{1}H NMR** (300 MHz, $CDCl_3$) δ 7.43 – 7.36 (m, 2H), 7.36 – 7.28 (m, 2H), 7.27 – 7.20 (m, 1H), 6.66 (d, *J* = 15.9 Hz, 1H), 6.17 (dd, *J* = 15.7, 6.1 Hz, 1H), 3.42 – 3.29 (m, 1H), 2.28 (t, *J* = 2.6 Hz, 1H), 1.39 (d, *J* = 7.1 Hz, 3H) ppm. **^{13}C NMR** (75 MHz, $CDCl_3$) δ 137.1, 130.6, 129.8, 128.7, 127.5, 126.5, 86.3, 70.5, 28.9, 21.7

ppm. **HRMS (APCI)** Calc. for $C_{12}H_{13}$ [M+H$^+$] 157.1012, found 157.1012. **Specific rotation:** $[\alpha]_D^{20}$ -2.8 (c=0.93, $CHCl_3$).

4,4,5,5-Tetramethyl-2-((*S*,1*E*,4*E*)-3-methyl-5-phenylpenta-1,4-dien-1-yl)-1,3,2-dioxaborolane (S9)

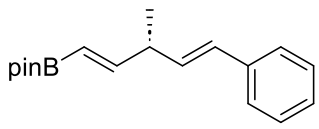

An oven-dried sealed tube equipped with a magnetic stirring bar under argon atmosphere was charged with **S7** (17.2 mg, 0.11 mmol, 1 equiv), HBpin (17 µL, 0.12 mmol, 1.1 equiv) and a solution of $BH_3{\cdot}SMe_2$ in THF [2.0 M] (6 µL. 0.011 mmol, 0.1 equiv). The reaction mixture was stirred for 20 minutes at 60 °C. Reaction was cooled down to room temperature and quenched with H_2O (5 mL) and was extracted with CH_2Cl_2 (2x5 mL). The solvents were removed under reduced pressure and the residue was purified by flash column chromatography (pentane: CH_2Cl_2 80:20), to give the product **S7** in 47% yield as a colorless oil. **^{1}H NMR** (300 MHz, $CDCl_3$) δ 7.37 – 7.25 (m, 5H), 7.19 (t, *J* = 6.3 Hz, 1H), 6.65 (dd, *J* = 18.1, 6.3 Hz, 1H), 6.38 (d, *J* = 16.0 Hz, 1H), 6.14 (dd, *J* = 15.9, 7.3 Hz, 1H), 5.50 (d, *J* = 17.9 Hz, 1H), 3.11 (q, *J* = 7.1 Hz, 1H), 1.27 (s, 12H), 1.22 (d, *J* = 7.0 Hz, 3H) ppm. **^{13}C NMR** (75 MHz, $CDCl_3$) δ 157.2, 137.8, 133.5, 129.3, 128.6, 127.2, 126.3, 83.3, 42.6, 24.9, 19.4 ppm. **^{11}B NMR** (160 MHz, $CDCl_3$) δ 29.9 ppm. **HRMS (APCI)** Calc. for $C_{18}H_{26}BO_2$ [M+H$^+$] 285.2020, found 285.2016. **Specific rotation:** $[\alpha]_D^{20}$ +9.2 (c=0.7, $CHCl_3$).

1-Methyl-4-((*S*,1*E*,3*E*,6*E*)-5-methyl-7-phenylhepta-1,3,6-trien-1-yl)benzene ((*S*,*E*,*E*)-23)

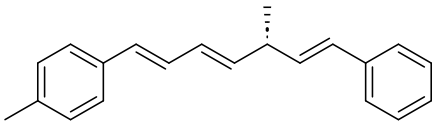

Synthesized from **S9** (0.04 mmol) and (*E*)-1-(2-bromovinyl)-4-methylbenzene **24**[12] (8.7 mg, 0.044 mmol), using $Pd(PPh_3)_4$ (4.6 mg, 0.004 mmol), 1,4-Dioxane (0.4 mL) and $NaOH_{aq}$ [2 M] (40 µL) according to general procedure B. Colorless oil obtained in 61% yield and 95:5 er after column chromatography. **^{1}H NMR** (500 MHz, $CDCl_3$) δ 7.30 (d, *J* = 7.7 Hz, 2H), 7.25 – 7.18 (m, 5H), 7.04 (d, *J* = 8.0 Hz, 2H), 6.67 (dd, *J* = 15.6, 10.4 Hz, 1H), 6.40 (d, *J* = 15.5 Hz, 1H), 6.33 (d, *J* = 16.0 Hz, 1H), 6.21 – 6.09 (m, 2H), 5.75 (dd, *J* = 15.3, 6.9 Hz, 1H), 3.07 (h, *J* = 7.0 Hz, 1H), 2.26 (s, 3H), 1.18 (d, *J* = 6.9 Hz, 4H) ppm. **^{13}C NMR** (126 MHz, $CDCl_3$) δ 138.3, 137.8, 137.2, 134.9, 134.4, 131.1, 129.7, 129.4, 128.9, 128.6, 128.4, 127.2, 126.3, 126.3, 40.0, 21.4, 20.4 ppm. **HRMS (APCI)** Calc. for $C_{21}H_{23}$ [M+H$^+$] 275.1794, found 275.1785. **Specific rotation:** $[\alpha]_D^{20}$ +19.7 (c=0.27, $CHCl_3$).

Enantiomeric purity was determined by chiral uHPLC analysis [Lux i-amylose-3, T_{oven}: 40 °C, flow: 0.1 mL/min; 100% *n*-hexane, λ = 263 nm, minor enantiomer t_R = 52.69 min, major enantiomer t_R = 48.23 min].

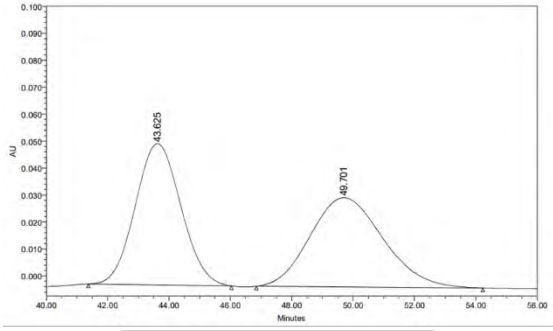

Unknown Peak Results

	Peak Type	RT	Area	% Area	Height
1	Unknown	43.625	5429292	49.83	52435
2	Unknown	49.701	5466867	50.17	33124

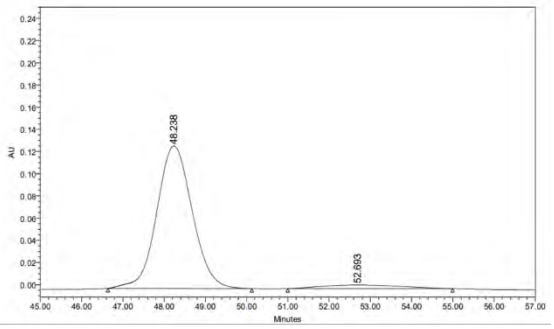

Unknown Peak Results

	Peak Type	RT	Area	% Area	Height
1	Unknown	48.238	7678906	94.65	128474
2	Unknown	52.693	433840	5.35	3160

5.3.3.4 Products derived from natural product syntheses

5.3.3.4.1 Total synthesis of (+)-Nyasol (**26**)

(+)–Nyasol (26)

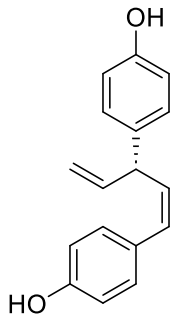

A dry Schlenk flask equipped with a magnetic stirring bar was charged with tris(dibenzylideneacetone)dipalladium(0) (6.9 mg, 0.0075 mmol, 5 mol%) in a glovebox. Out of the glovebox, the Schlenk was charged with dicyclohexylphosphino-2',4',6'-triisopropylbiphenyl (XPhos) (7.2 mg, 0.015 mmol, 10 mol%), $NaOH_{(aq)}$ 2M (0.3 mL, 0.6 mmol, 4 equiv) and 4-iodophenyl acetate (43.2 mg, 0.17 mmol, 1.1 equiv). Compound **13** (49.2 mg, 0.15 mmol, 1 equiv) was diluted in 1,4-dioxane (1.5 mL) and added to the mixture which was then heated at 40 ºC for 16 h. The mixture was allowed to cool to room temperature, diluted with ethyl acetate (5 mL) and washed with 1 M aqueous HCl (5 mL). The layers were separated, and the aqueous phase was extracted with ethyl acetate (5 mL). The combined organic layers were dried over Na_2SO_4, filtered, and concentrated in vacuo (*Note: protection from light is necessary to avoid product decomposition*). [237] The crude mixture was purified by column chromatography (covered with aluminum foil) (pentane:acetone 90:10) obtaining the product as a yellow oil in 54% yield and with 98:2 er. **^{1}H NMR** (300 MHz, $CDCl_3$) δ 7.17 (d, *J* = 8.8 Hz, 2H), 7.10 (d, *J* = 8.6 Hz, 2H), 6.85 – 6.69 (m, 1H), 6.52 (d, *J* = 11.4 Hz, 1H), 6.13 – 5.88 (m, 1H), 5.74 – 5.61 (m, 1H), 5.18 (dt, *J* = 6.2, 1.6 Hz, 1H), 5.14 (d, J = 1.7 Hz, 1H), 4.96 (br s, 2H), 4.77 (s, 1H), 4.52 – 4.47 (m, 1H) ppm. **^{13}C NMR** (75 MHz, $CDCl_3$) δ 154.7, 154.2, 140.9, 135.7, 131.8, 130.2, 129.9, 129.0, 128.7, 115.6, 115.3, 115.2, 47.0 ppm. **HRMS (APCI)** Calc. for $C_{17}H_{17}O_2$ $[M+H^+]$ 253.1223, found 253.1216. **Specific rotation:** $[\alpha]_D^{20}$ +96.4 (c=0.26, $CHCl_3$).

Spectroscopic and physical data were in accordance with those previously reported.[176]

Enantiomeric purity was determined by chiral SFC analysis [Lux i-cellulose-1, 100 bar, Toven: 40 °C, flow: 2 mL/min; 12% MeOH, λ = 250 nm, minor enantiomer t_R = 32.72 min, major enantiomer t_R = 34.64 min].

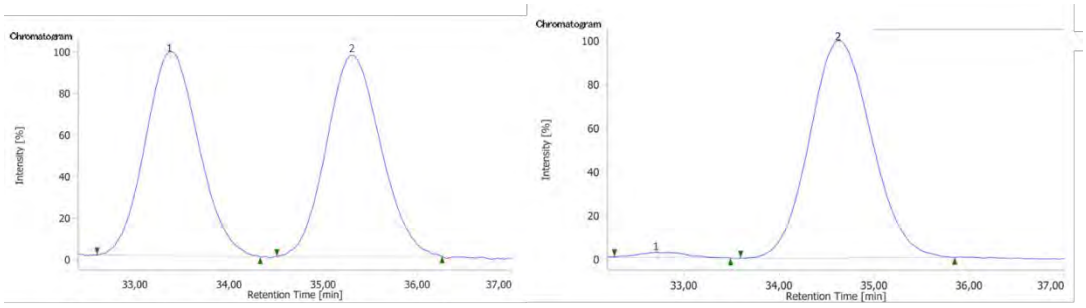

Peak Information

#	Peak Name	CH	tR [min]	Area [µV·sec]	Area%
1	Unknown	11	33,383	974119	49,904
2	Unknown	11	35,303	977850	50,096

Peak Information

#	Peak Name	CH	tR [min]	Area [µV·sec]	Area%
1	Unknown	11	32,723	67452	1,759
2	Unknown	11	34,637	3768174	98,241

5.3.3.4.2 Total synthesis of (+)-Hinokiresinol (**29**)

(*S*,*E*)-4-(1-(4-Methoxyphenyl)penta-1,4-dien-3-yl)phenol (28)

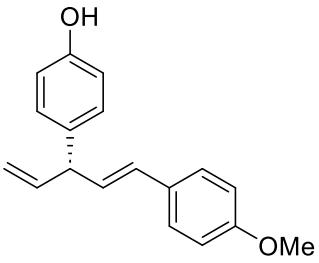

Synthesized from **13** (49.2 mg, 0.15 mmol, 1 equiv) and freshly prepared (4-methoxyphenyl) magnesium bromide-lithium chloride adduct [1.2 M] in THF[238] (0.9 mL, 0.75 mmol, 5 equiv), using Et_2O (1 mL), MeOH (1 mL), I_2 (56.2 mg, 0.20 mmol, 1.3 equiv) and $NaOH_{aq}$ [3 M] (0.15 mL) according to a modified general procedure E. Colorless oil obtained in 43% yield with 98:2 er after column chromatography in Pure C-815 Flash system from Buchi (hexane/CH_2Cl_2, 4 g SiO_2 EcoFlex cartridge, flow = 15 mL/min, gradient: 0 min (100% hexane), 0.5 min (100% hexane), 2 min (60% hexane), 7 min (28% hexane), 9.5 min (28% hexane), 9.6 min (0% hexane), 11 min (0% hexane), 11.1 min (100% hexane)). **^{1}H NMR** (500 MHz, $CDCl_3$) δ 7.30 (d, *J* = 8.7 Hz, 2H), 7.13 (d, *J* = 8.6 Hz, 2H), 6.84 (d, *J* = 8.8 Hz, 2H), 6.79 (d, *J* = 8.6 Hz, 2H), 6.35 (d, *J* = 16.0 Hz, 1H), 6.23 (dd, *J* = 15.9, 6.9 Hz, 1H), 6.07 (ddd, *J* = 17.1, 10.2, 6.7 Hz, 1H), 5.17 – 5.07 (m, 2H), 4.78 (br. s, 1 H) 4.14 (t, *J* = 6.8 Hz, 1H), 3.80 (s, 3H) ppm. **^{13}C NMR** (126 MHz, $CDCl_3$) δ 159.1, 154.3, 140.7, 135.2, 130.4, 130.0, 129.9, 129.4, 127.5, 115.5, 115.4, 114.1, 55.5, 51.6 ppm. **HRMS (ESI-)** Calc. for $C_{18}H_{17}O_2$ [M-H$^-$] 265.1234, found 265.1234. **Specific rotation:** $[\alpha]_D^{22}$ +2.9 (c=0.65, $CHCl_3$).

Enantiomeric purity was determined by chiral uHPLC analysis [Lux i-amylose-3, T_{oven}: 40 °C, flow: 1 mL/min; 100% *n*-hexane, λ = 210 nm, minor enantiomer t_R = 17.21 min, major enantiomer t_R = 20.59 min].

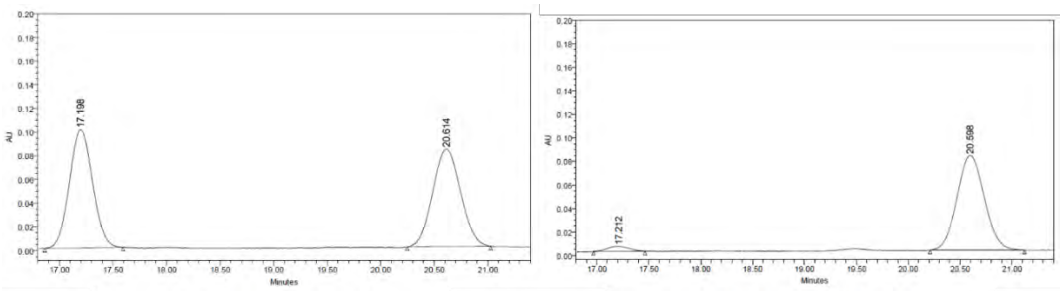

Unknown Peak Results

	Peak Type	RT	Area	% Area	Height
1	Unknown	17.198	1505691	50.25	100029
2	Unknown	20.614	1490890	49.75	82476

Unknown Peak Results

	Peak Type	RT	Area	% Area	Height
1	Unknown	17.212	61052	3.97	4290
2	Unknown	20.598	1478153	96.03	80609

(+)-Hinokiresinol (29)

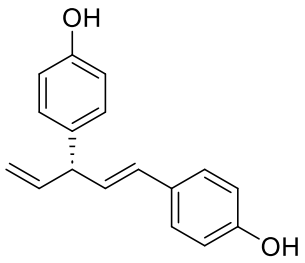

Compound **28** (16.0 mg, 0.06 mmol, 1 equiv) was added to an oven-dried sealed tube equipped with a magnetic stirring bar under argon atmosphere. Freshly prepared methyl magnesium iodide [1.66 M] in Et_2O (0.36 mL, 0.6 mmol, 10 equiv)[239] was added and solvent was carefully removed under vacuum at room temperature. Neat mixture was heated at 160 °C in an oil bath during 1 h. After being cooled to room temperature, EtOAc (3 mL) was added, and the resulting solution was quenched by addition of a saturated aqueous NH_4Cl solution (3 mL). The mixture was extracted with EtOAc (3 × 5 mL). Combined organic layers were washed with brine (5 mL), dried over anhydrous $MgSO_4$, filtered and solvent was removed under reduced pressure. Crude product was purified through flash column chromatography in Pure C-815 Flash system from Buchi (hexane/AcOEt, 4 g SiO_2 EcoFlex cartridge, flow = 15 mL/min, gradient: 0 min (100% hexane), 1.8 min (83% hexane), 14.5 min (83% hexane), 15.6 min (70% hexane), 15.7 min (0% hexane), 19 min (0% hexane), 19.1 min (100% hexane)) as a colorless oil in 99% yield with 98:2 er which over time turned red.[240] **^{1}H NMR** (500 MHz, $CDCl_3$) δ 7.25 (d, *J* = 8.6 Hz, 2H), 7.12 (d, *J* = 8.6 Hz, 4H), 6.78 (dd, *J* = 15.1, 8.6 Hz, 4H), 6.33 (d, *J* = 15.2 Hz, 1H), 6.22 (dd, *J* = 15.9, 7.0 Hz, 1H), 6.07 (ddd, *J* = 17.0, 10.2, 6.8 Hz, 1H), 5.15 (dd, *J* = 10.2, 1.4 Hz, 1H), 5.10 (d, *J* = 17.2 Hz, 1H), 4.76 (br s, 2H), 4.13 (t, *J* = 6.7 Hz, 1H) ppm. **^{13}C NMR** (126 MHz, $CDCl_3$) δ 155.0, 154.3, 140.6, 135.2, 130.6, 130.1, 129.9, 129.4, 127.7, 115.5, 115.5, 115.4, 51.6 ppm. **Specific rotation:** $[\alpha]_D^{21}$ +1.1 (c=0.30, $CHCl_3$).

Spectroscopic and physical data were in accordance with those previously reported.[241]

Enantiomeric purity was determined by chiral SFC analysis [Lux i-cellulose-1, 100 bar, Toven: 40 °C, flow: 1.5 mL/min; 15% MeOH, λ = 250 nm, major enantiomer t_R = 32.00 min, minor enantiomer t_R = 33.37 min].

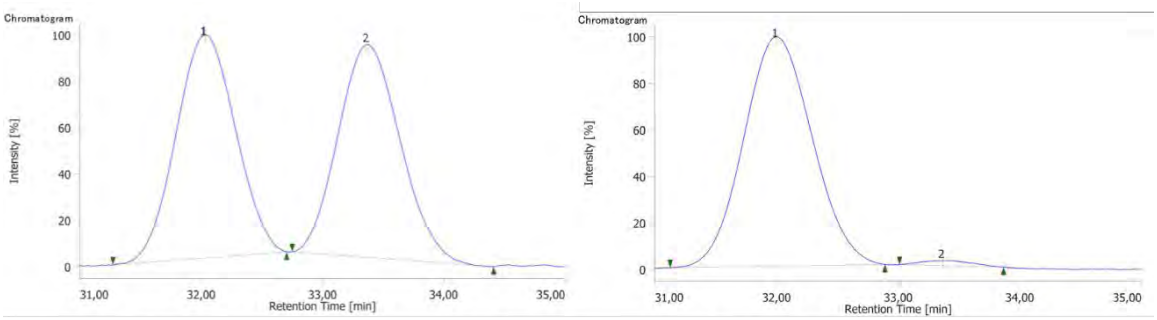

Peak Information

#	Peak Name	CH	tR [min]	Area [µV·sec]	Area%
1	Unknown	11	32.033	1611748	50.059
2	Unknown	11	33.373	1607968	49.941

Peak Information

#	Peak Name	CH	tR [min]	Area [µV·sec]	Area%
1	Unknown	11	32.000	4615534	98.403
2	Unknown	11	33.367	74886	1.597

5.3.3.4.3 Formal total synthesis of Phorbasin C

(*R*,1*Z*,4*E*)-1-Chloro-3,7-dimethylocta-1,4-diene (31)

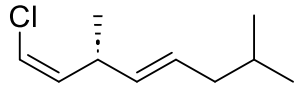

Synthesized from **12** (172.2 mg, 0.71 mmol) and an *in situ* generated solution of *i*BuLi [0.4 M] in Et_2O (2.49 mL, 0.99 mmol),[242] using Et_2O (3 mL), MeOH (3 mL), I_2 (199.5 mg, 0.20 mmol, 1 equiv) and $NaOH_{aq}$ [3 M] (0.71 mL) according to general procedure E. Colorless oil obtained in 60% yield after column chromatography in pentanes. **^{1}H NMR** (300 MHz, $CDCl_3$) δ 5.98 (d, *J* = 7.0 Hz, 1H), 5.61 (dd, *J* = 8.9, 6.9 Hz, 1H), 5.49 – 5.29 (m, 2H), 3.43 (h, *J* = 6.9 Hz, 1H), 1.88 (t, *J* = 6.8 Hz, 2H), 1.60 (dq, *J* = 13.6, 6.8 Hz, 1H), 1.09 (d, *J* = 7.2 Hz, 3H), 0.87 (d, *J* = 6.9 Hz, 6H) ppm. **^{13}C NMR** (75 MHz, $CDCl_3$) δ 136.1, 133.6, 128.6, 116.7, 42.0, 34.9, 28.6, 22.4, 20.2 ppm. **HRMS (APCI)** Calc. for $C_{10}H_{18}Cl$ [M+H$^+$] 173.1092, found 173.1093. **Specific rotation:** $[\alpha]_D^{20}$ +205.2 (c=0.68, $CHCl_3$).

2-((*S*,1*E*,4*E*)-3,7-Dimethylocta-1,4-dien-1-yl)-4,4,5,5-tetramethyl-1,3,2-dioxaborolane (30)

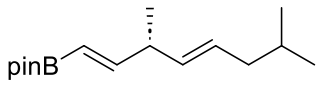

In a Ar-filled Schlenk tube equipped with a magnetic stirring bar, a solution of *n*BuLi [2.5 M] in hexanes (0.4 mL, 1.0 mmol, 2.5 equiv) was added to a solution of *i*Pr$_2$NH (0.15 mL, 1.1 mmol, 2.7 equiv) in THF (4.2 mL) at -78 °C and stirred for 30 min. Then, a solution of **31** (70.8 mg, 0.42 mmol, 1 equiv) in THF (4.2 mL) was added to the previous mixture at -78 °C, and the reaction was stirred for 15 min. The reaction was quenched with HCl [4 M] in dioxane (0.6 mL, 2.5 mmol, 6 equiv) and allowed to reach room temperature, getting a white residue. The Schlenk tube was connected to a vigreux vacuum jacketed micro distillation head and carefully heated to 85 °C while stirring to carefully evacuate THF. Once the solvent was removed, the remaining white mixture was allowed to reach room temperature. The residue was dissolved in H_2O and washed with Et_2O (3 x 10 mL). Combined organic layers were dried over anhydrous $MgSO_4$, filtered, and carefully concentrated in vacuo (600 mbar, 40 ºC), yielding a yellowish oil (**S10**) which was used without further purification.

In an Ar-filled glove box, a tube vial equipped with a stirring bar was charged with Cp_2ZrHCl (16.2 mg, 0.063 mmol, 15 mol%). The tube was sealed and taken out of the glove box. Then, **S10**, Et_3N (17.6 µL, 0.13 mmol, 30 mol%) and THF (2.1 mL) were added through a septum. To this mixture HBpin (0.13 mL, 0.88 mmol, 2.1 equiv) was added. The mixture was stirred at 60 °C during 2 h, after which the mixture was allowed to cool to room temperature. The reaction was quenched with saturated aqueous solution of NH_4Cl (5 mL), and the mixture was extracted with CH_2Cl_2 (2 x 5 mL). The combined organic layers were dried over Na_2SO_4, filtered, and concentrated in vacuo (600 mbar, 40 ºC). Crude product was purified by flash column chromatography (pentane) and **22** was obtained as a yellow oil in 58% yield with 94:6 er. **^{1}H NMR** (500 MHz, $CDCl_3$) δ 6.59 (dd, *J* = 18.0, 6.1 Hz, 1H), 5.46 – 5.29 (m, 3H), 2.89 (h, *J* = 6.5 Hz, 1H), 1.87 (td, *J* = 6.7, 2.6 Hz, 2H), 1.62 – 1.56 (m, 2H), 1.26 (s, 12H), 1.09 (d, *J* = 7.0 Hz, 4H), 0.87 (d, *J* = 6.6 Hz, 6H) ppm. **^{13}C NMR** (126 MHz, $CDCl_3$) δ 158.4, 134.3, 128.8, 83.2, 42.3, 42.1, 28.6, 24.9, 22.5, 22.4, 19.7 ppm. **^{11}B NMR** (160 MHz, $CDCl_3$) δ 30.0 ppm. **HRMS (APCI)** Calc. for $C_{16}H_{29}BO_2$ [M+H$^+$] 264.2251, found 264.2255. **Specific rotation:** $[\alpha]_D^{22}$ +8.1 (c=0.79, $CHCl_3$).

Spectroscopic and physical data were in accordance with those previously reported.[197]

Enantiomeric purity was determined by chiral uHPLC analysis [Lux i-cellulose-5, T_{oven}: 40 °C, flow: 1 mL/min; 100% *n*-hexane, λ = 221 nm, major enantiomer t_R = 4.16 min, minor enantiomer t_R = 4.38 min].

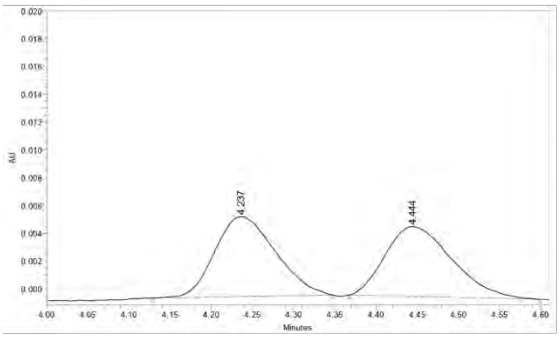

Unknown Peak Results

	Peak Type	RT	Area	% Area	Height
1	Unknown	4.237	29304	50.94	5751
2	Unknown	4.444	28218	49.06	5021

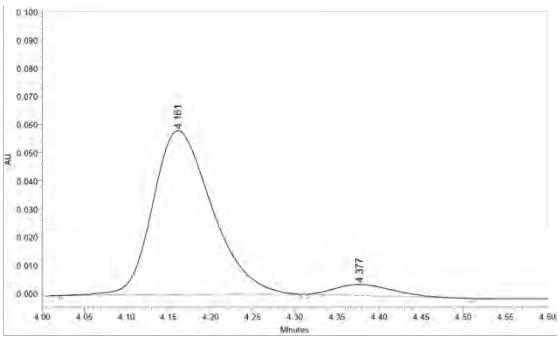

Unknown Peak Results

	Peak Type	RT	Area	% Area	Height
1	Unknown	4.161	285857	93.91	58231
2	Unknown	4.377	18534	6.09	3871

5.3.3.4.4 Formal total synthesis of GnRH antagonist (**35**)

((*R*,3*E*,6*Z*)-7-Chloro-5-methylhepta-3,6-dien-1-yl)benzene (32)

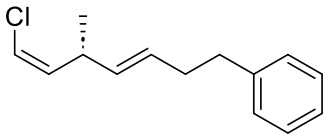

Synthesized from **12** (121.2 mg, 0.5 mmol) and an *in situ* generated solution of (2-phenylethyl)lithium [0.35 M] in Et_2O (2 mL, 0.7 mmol)[16] (from 2-phenethyl iodide), using Et_2O (2.3 mL), MeOH (2.3 mL), I_2 (127.8 mg, 0.5 mmol) and $NaOH_{aq}$ [3 M] (0.5 mL) according to general procedure E. Colorless oil obtained in 55% yield after column chromatography in pentanes, in combination with unreacted 2-phenethyl iodide. **^{1}H NMR** (500 MHz, $CDCl_3$) δ 7.31 – 7.25 (m, 2H), 7.21 – 7.14 (m, 3H), 5.98 (dd, *J* = 7.0, 1.0 Hz, 1H), 5.59 (dd, *J* = 9.2, 7.0 Hz, 1H), 5.51 (dtd, *J* = 15.4, 6.6, 1.3 Hz, 1H), 5.37 (ddt, *J* = 15.4, 6.3, 1.3 Hz, 1H), 3.48 – 3.36 (m, 1H),), 2.67 (dd, J = 8.9, 6.7 Hz, 2H), 2.31 (dtt, *J* = 8.9, 6.6, 1.1 Hz, 2H), 1.07 (d, *J* = 6.9 Hz, 3H) ppm. **^{13}C NMR** (126 MHz, $CDCl_3$) δ 142.1, 135.8, 133.2, 128.9, 128.7, 128.4, 125.9, 116.8, 36.1, 34.8, 34.6, 20.0 ppm. **HRMS (APCI)** Calc. for $C_{14}H_{18}Cl$ [M+H$^+$] 221.1092, found 221.1093. **Specific rotation:** [α] $^{22}_{D}$ -110.3 (c=1, $CHCl_3$).

(*R*,*E*)-(5-Methylhept-3-en-6-yn-1-yl)benzene (33)

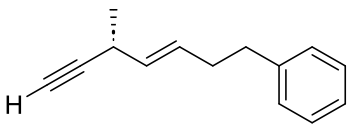

Synthesized from **32** (92.7 mg, 0.42 mmol). using *i*Pr_2NH (97 µL, 0.71 mmol), *n*BuLi [2.5 M] in hexanes (0.25 mL, 0.63 mmol) and THF (8.4 mL) according to general procedure D. Colorless oil obtained in 84% yield after column chromatography in pentanes. **^{1}H NMR** (300 MHz, $CDCl_3$) δ 7.36 – 7.29 (m, 2H), 7.26 – 7.20 (m, 3H), 5.78 (dt, *J* = 15.0, 6.7 Hz, 1H), 5.47 (dd, *J* = 15.3, 6.1 Hz, 1H), 3.24 – 3.08 (m, 1H), 2.74 (m, 2H), 2.39 (q, *J* = 7.3 Hz, 2H), 2.22 (dq, *J* = 1.6 Hz, 1H), 1.29 (d, *J* = 7.1 Hz, 3H) ppm .**^{13}C NMR** (75 MHz, $CDCl_3$)

δ 142.1, 131.3, 129.8, 128.6, 128.4, 125.9, 87.1, 69.7, 35.9, 34.2, 28.5, 21.8 ppm. **HRMS (APCI)** Calc. for $C_{14}H_{17}$ [M+H$^+$] 185.1325, found 185.1320. **Specific rotation:** $[\alpha]_D^{21}$ -21.8 (c=0.54, $CHCl_3$).

(*R*,*E*)-1,2,3-Trimethyl-5-(3-methyl-7-phenylhept-4-en-1-yn-1-yl)benzene (34)

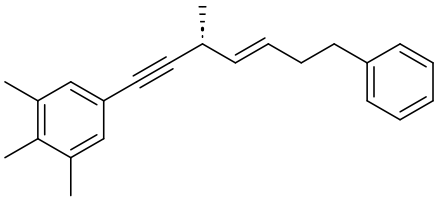

An Ar-filled dry Schleck tube equipped with a magnetic stirring bar was charged with **33** (29.5 mg, 0.16 mmol, 1.0 equiv), 5-iodo-1,2,3-trimethylbenzene (54.1 mg, 0.22 mmol, 1.1 equiv), $Pd(PPh_3)_2Cl_2$ (11.2 mg, 0.016 mmol, 10 mol%), and CuI (15.2 mg, 0.08 mmol, 0.4 equiv,). Solids were dissolved in THF (0.4 mL) and Et_3N (42 uL, 0.3 mmol, 1.5 equiv) was then added. The mixture was stirred at r.t. for 1.5 h. After that time, the reaction was quenched with water (10 mL) and extracted with CH_2Cl_2 (3 x 10 mL). Combined organic layers were dried over anhydrous $MgSO_4$, filtered, and solvent was removed under reduced pressure. Crude was purified through flash column chromatography in silica (hexane: CH_2Cl_2, 100:0 to 95:5) affording the product as a colorless oil in 78% yield with 91:9 er. **^{1}H NMR** (300 MHz, $CDCl_3$) δ 7.36 – 7.30 (m, 2H), 7.28 – 7.20 (m, 3H), 7.12 (s, 2H), 5.83 (dtd, *J* = 14.9, 6.7, 1.3 Hz, 1H), 5.54 (ddtd, *J* = 15.2, 6.0, 1.4, 0.7 Hz, 1H), 3.43 – 3.27 (m, 1H), 2.76 (dd, *J* = 9.1, 6.6 Hz, 2H), 2.45 – 2.36 (m, 2H), 2.29 (s, 6H), 2.20 (s, 3H), 1.35 (d, *J* = 7.1 Hz, 3H) ppm. **^{13}C NMR** (75 MHz, $CDCl_3$) δ 142.2, 136.5, 135.2, 132.1, 130.8, 129.4, 128.7, 128.4, 125.9, 120.5, 91.2, 82.5, 36.0, 34.2, 29.4, 22.1, 20.5, 15.5 ppm. **Specific rotation:** $[\alpha]_D^{20}$ -21.8 (c=0.9, $CHCl_3$).

Spectroscopic and physical data were in accordance with those previously reported.[199]

Enantiomeric purity was determined by chiral uHPLC analysis [Lux i-amylose-3, T_{oven}: 40 °C, flow: 0.5 mL/min; 99% *n*-hexane, λ = 254 nm, major enantiomer t_R = 6.97 min, minor enantiomer t_R = 7.35 min].

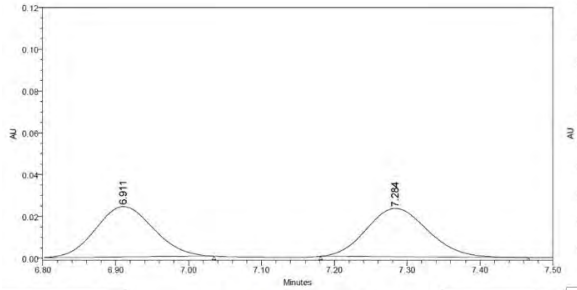

Unknown Peak Results

	Peak Type	RT	Area	% Area	Height
1	Unknown	6.911	132706	49.53	24063
2	Unknown	7.284	135205	50.47	23120

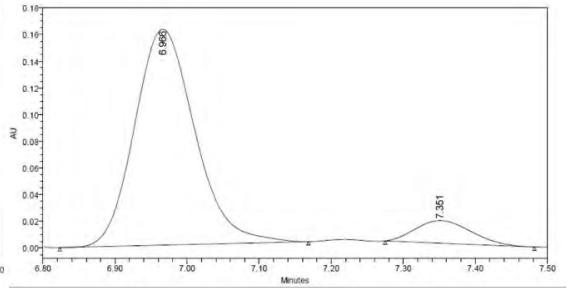

Unknown Peak Results

	Peak Type	RT	Area	% Area	Height
1	Unknown	6.966	938455	91.20	161686
2	Unknown	7.351	90550	8.80	16913

5.3.3.4.5 Synthesis of (*R*)-3-methylpent-4-en-1-ol (**36**)

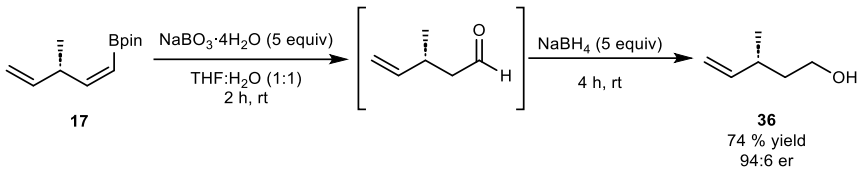

(*R*)-3-Methylpent-4-en-1-ol (36)

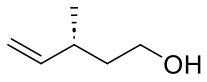

In a Schenck tube equipped with a magnetic stirrer, **17** (104.0 mg, 0.5 mmol, 1 equiv) and $NaBO_3 \cdot 4H_2O$ (384.7 mg, 2.5 mmol, 5 equiv) were dissolved in a THF:H_2O mixture (1:1, 1 mL) and the resulting solution was stirred at r.t. for 2 h. After that time, the mixture was diluted with Et_2O (3 mL) and the organic layer was decantated. $NaBH_4$ (94.6 mg, 2.5 mmol, 5 equiv) was added to the organic layer and the resulting mixture was stirred for 4 h. Reaction was quenched with 5 mL of $HCl_{(aq)}$ [1 M] and extracted with Et_2O (3x5 mL). Combined organic layers were dried over anhydrous $MgSO_4$, filtered, and solvent was removed carefully under reduced pressure (600 mBar, 40 ºC). Crude was filtered through a short path of silica (pentane:Et_2O, 100:0 to 1:1) obtaining the product as a colorless oil in 74% yield with 94:6 er assuming the enantiomeric purity is kept the same as compound **8** (see above). **^{1}H NMR** (300 MHz, $CDCl_3$) δ 5.72 (ddd, *J* = 17.2, 10.2, 7.8 Hz, 1H), 5.01 (d, *J* = 17.2 Hz, 1H), 4.95 (d, *J* = 9.3 Hz, 1H), 3.74 – 3.60 (m, 2H), 2.32 (dq, *J* = 13.8, 6.7 Hz, 1H), 1.58 (q, *J* = 6.5 Hz, 3H), 1.31 (bs, 1H), 1.03 (d, *J* = 6.8 Hz, 3H) ppm. **^{13}C NMR** (75 MHz, $CDCl_3$) δ 144.4, 113.2, 61.4, 39.5, 35.0, 20.5 ppm. **Specific rotation:** $[\alpha]_D^{20}$ -7.0 (c=0.34, $CHCl_3$).

Spectroscopic and physical data were in accordance with those previously reported.[243]

5.3.4 ^{1}H-NMR, ^{13}C-NMR, ^{11}B-NMR and ^{19}F-NMR Spectra

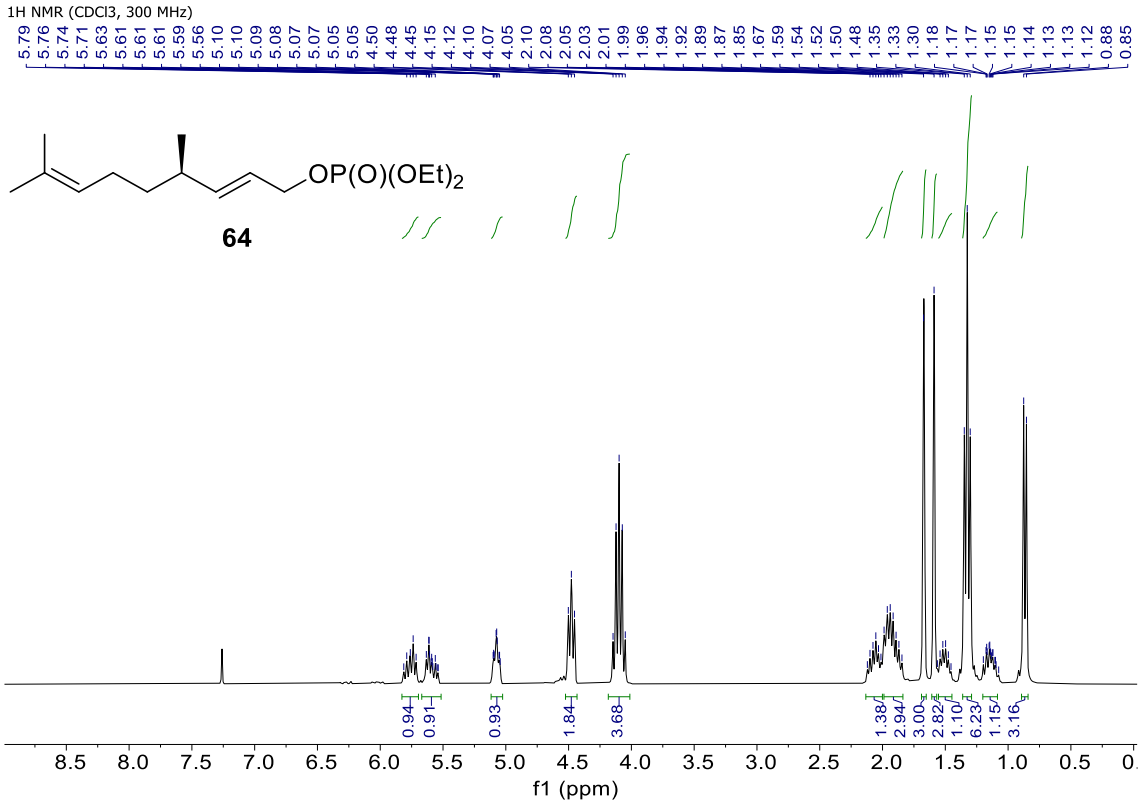

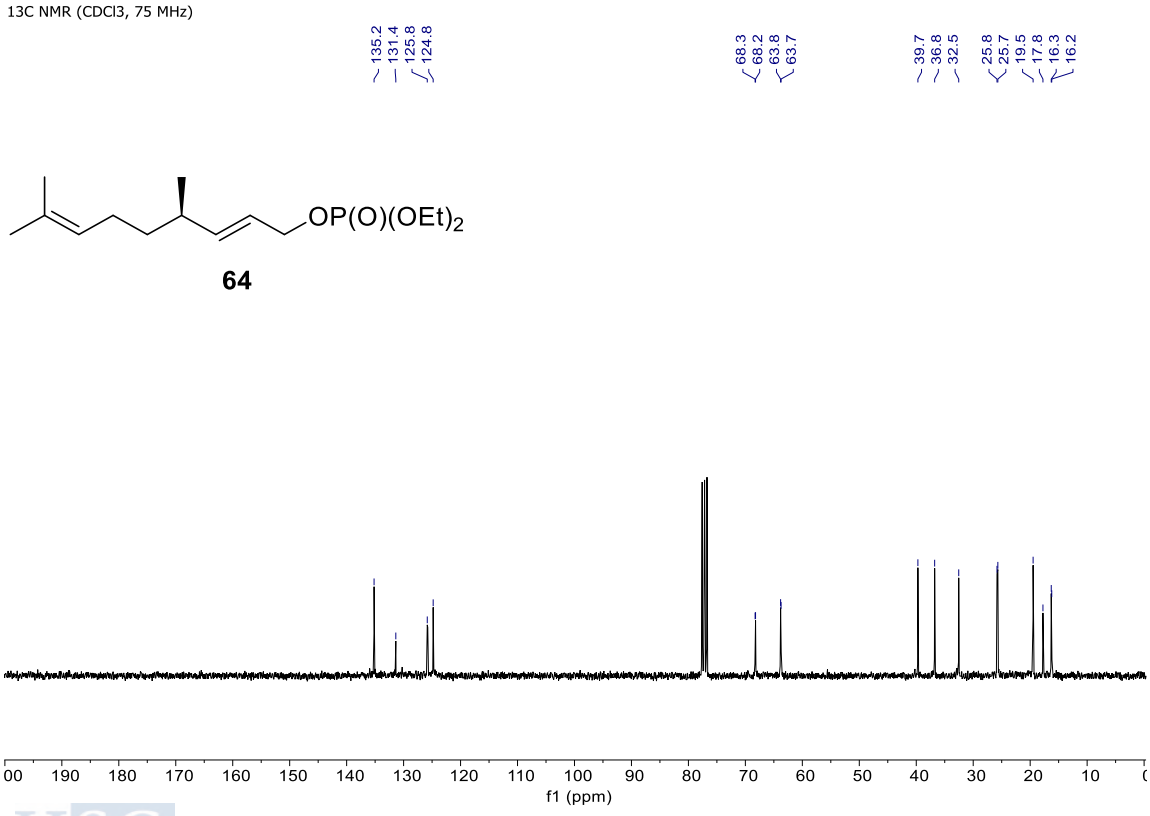

31P NMR (CDCl3, 202 MHz)

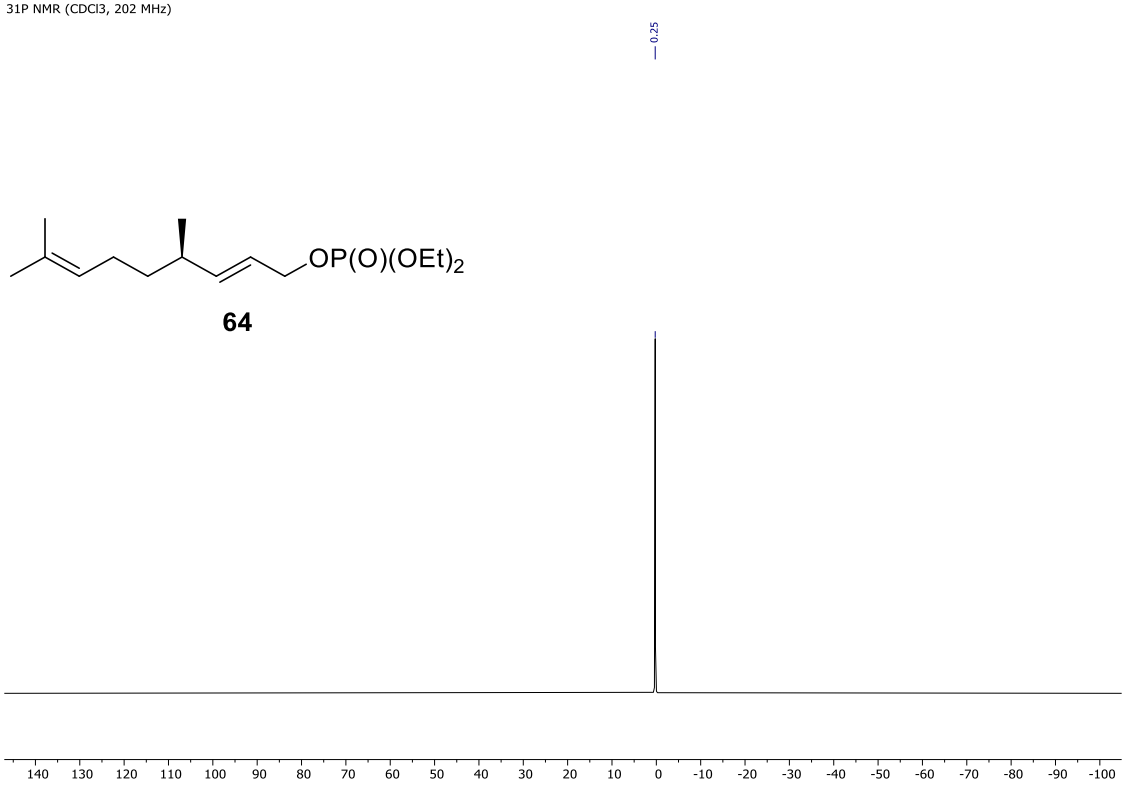

64

1H NMR (CDCl3, 300 MHz)

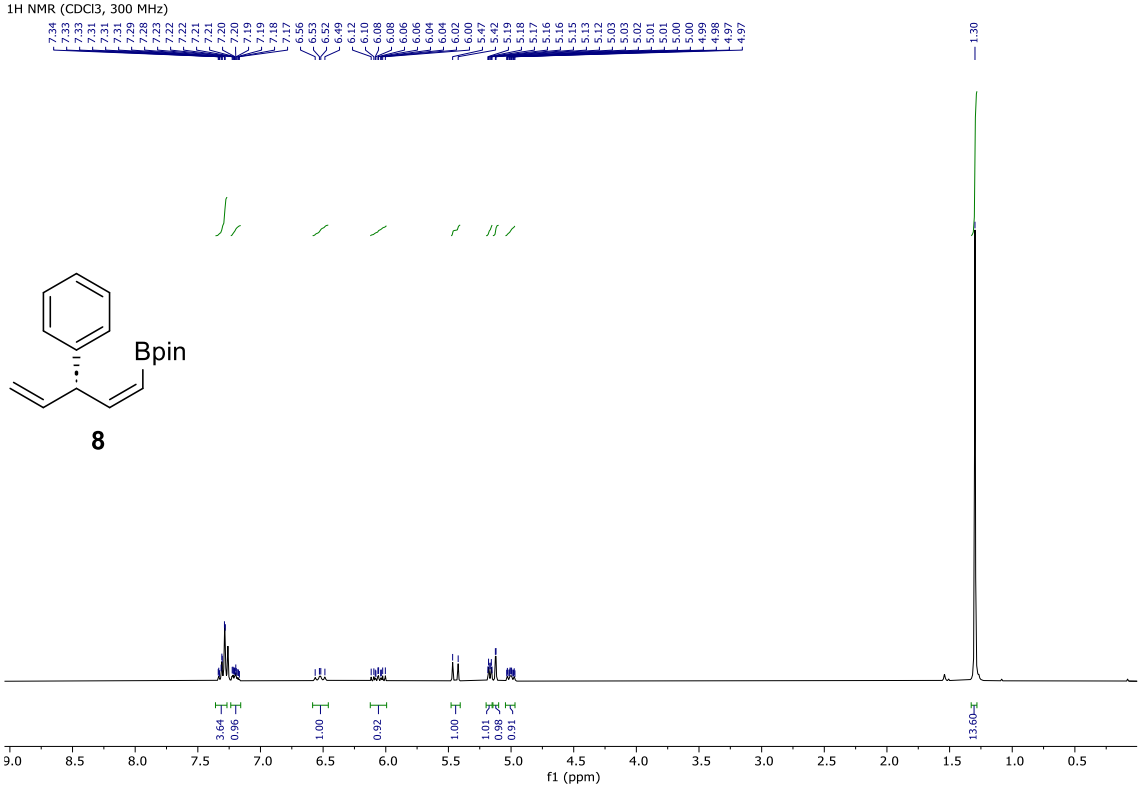

13C NMR (CDCl3, 75 MHz)

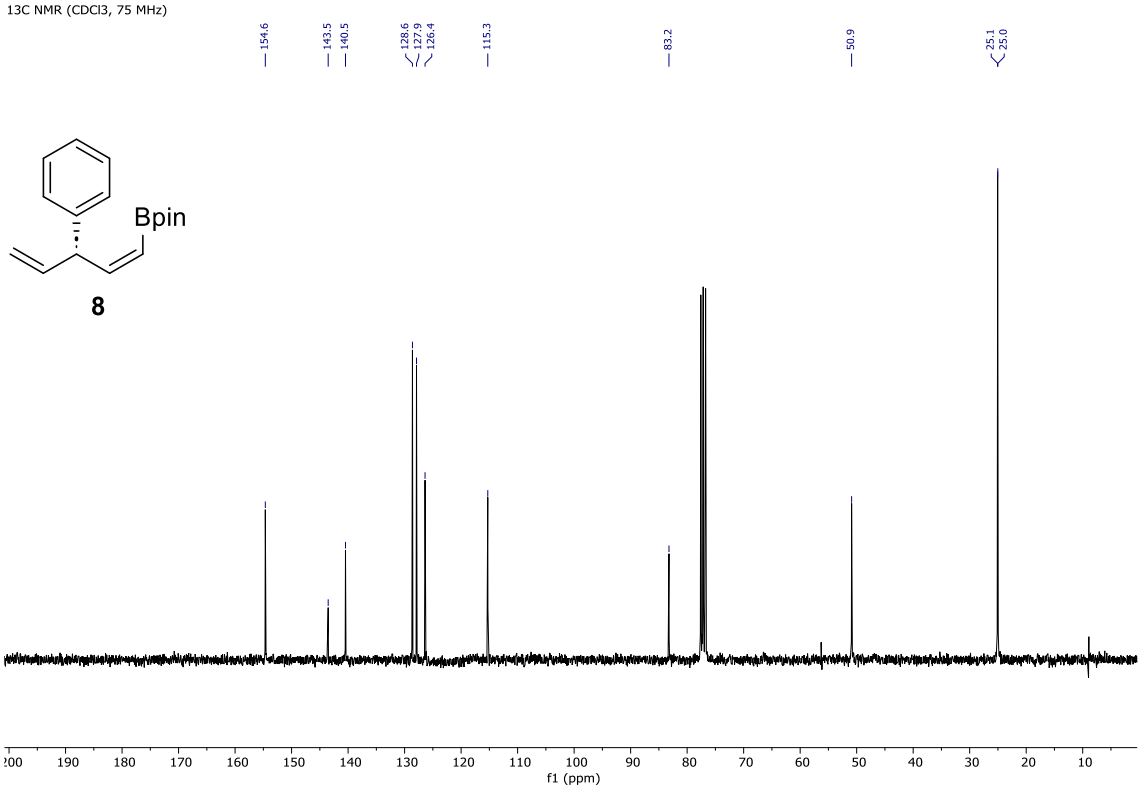

11B NMR (CDCl3, 160 MHz)

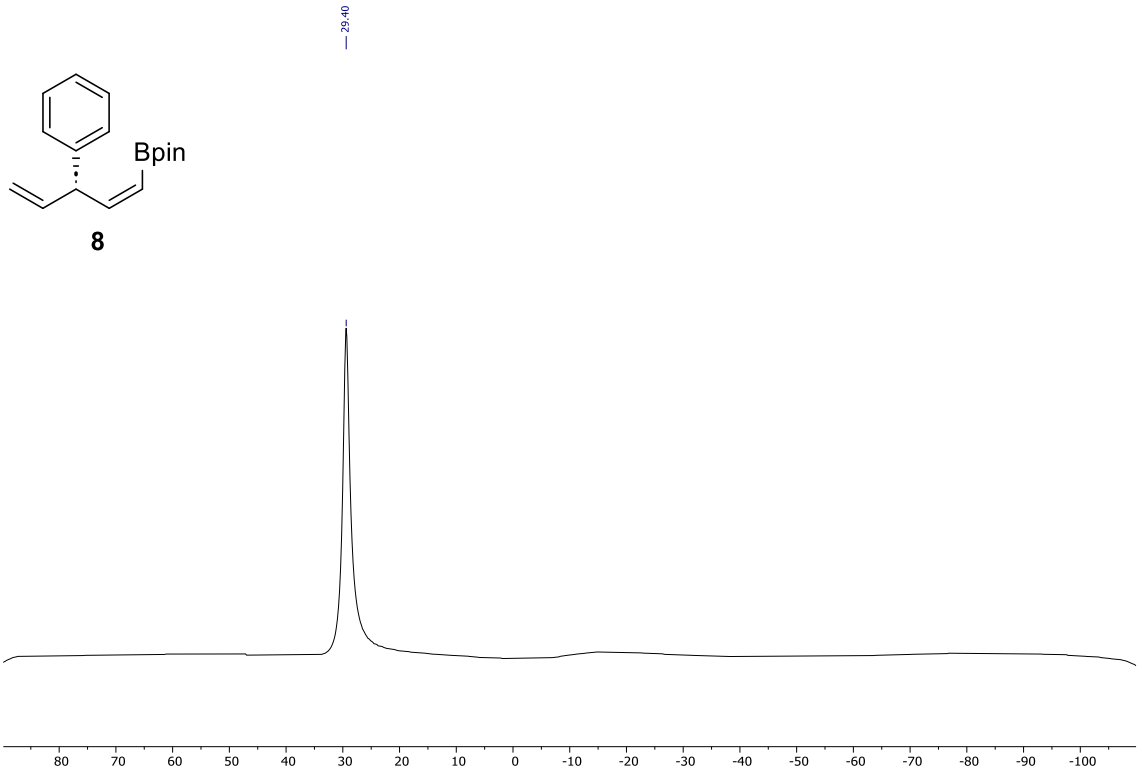

1H NMR (CDCl3, 300 MHz)

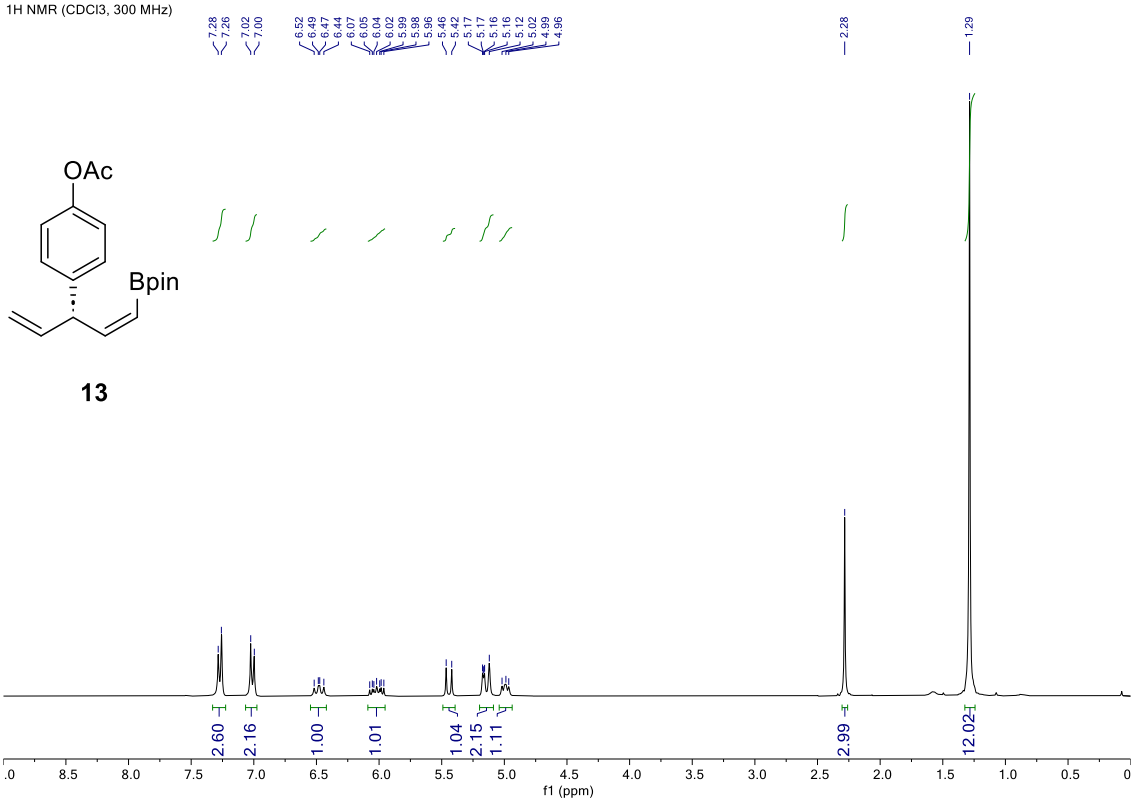

13

13C NMR (CDCl3, 75 MHz)

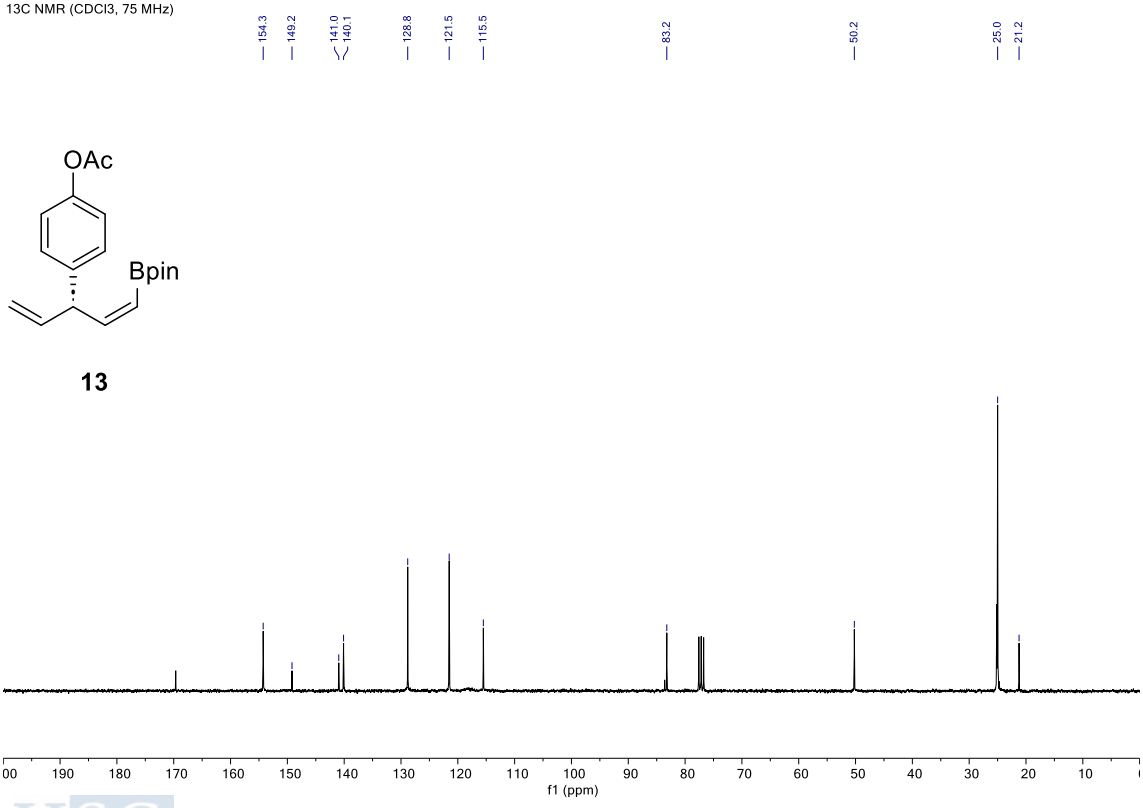

13

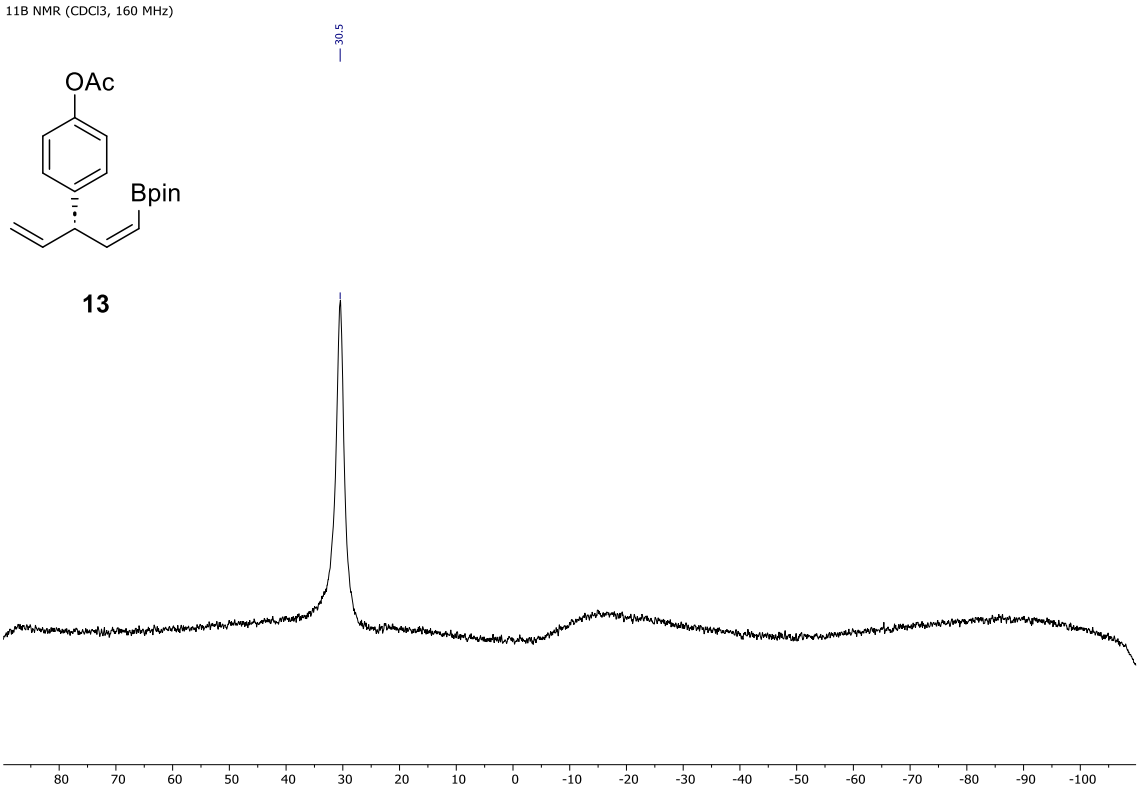

1H NMR (CDCl3, 300 MHz)

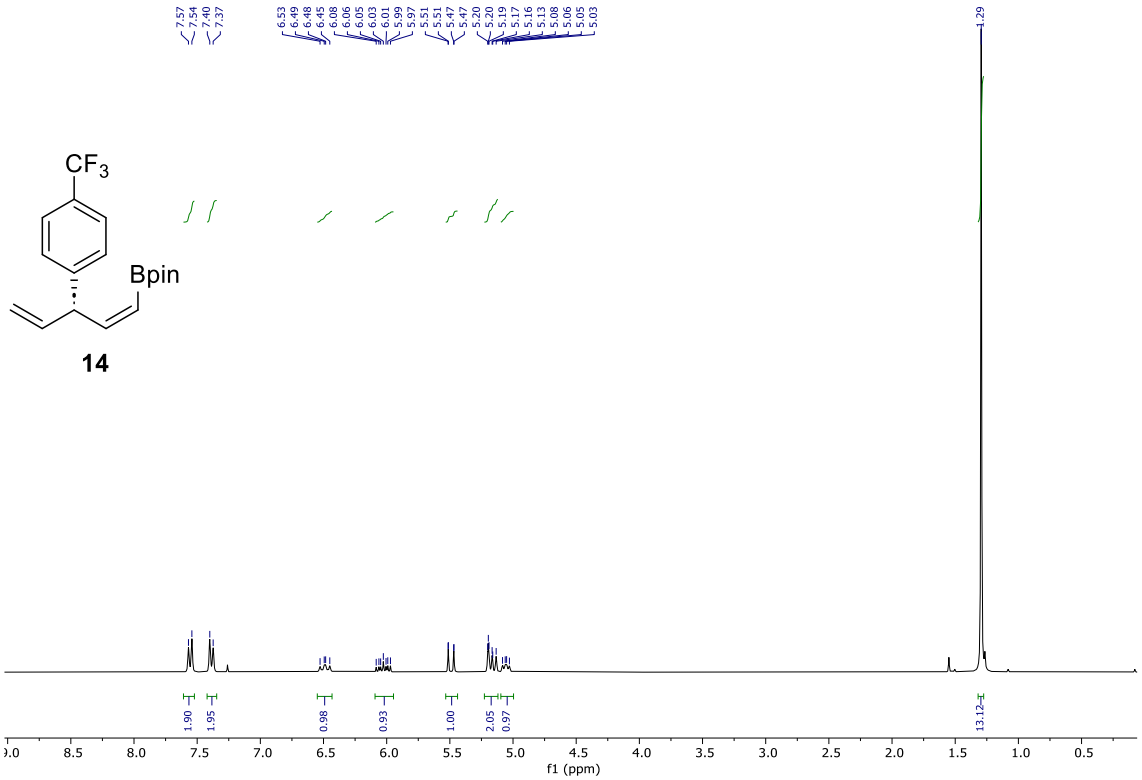

14

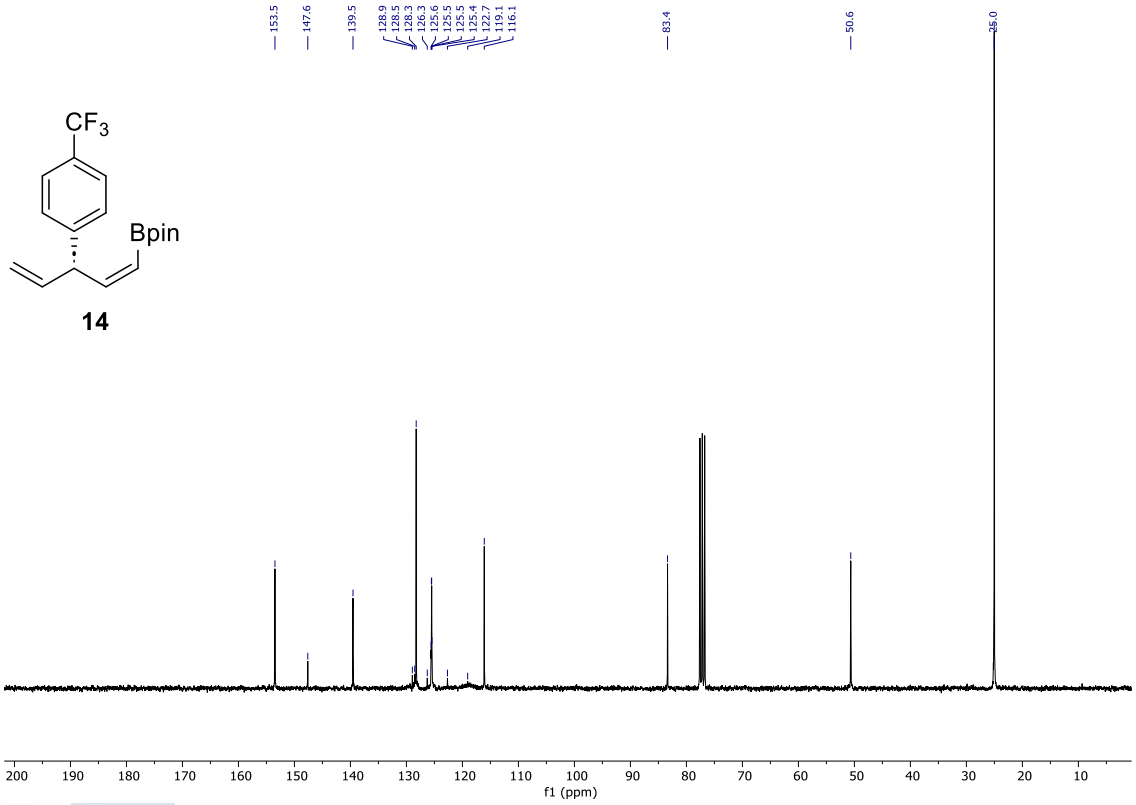

14

11B NMR (CDCl3, 160 MHz)

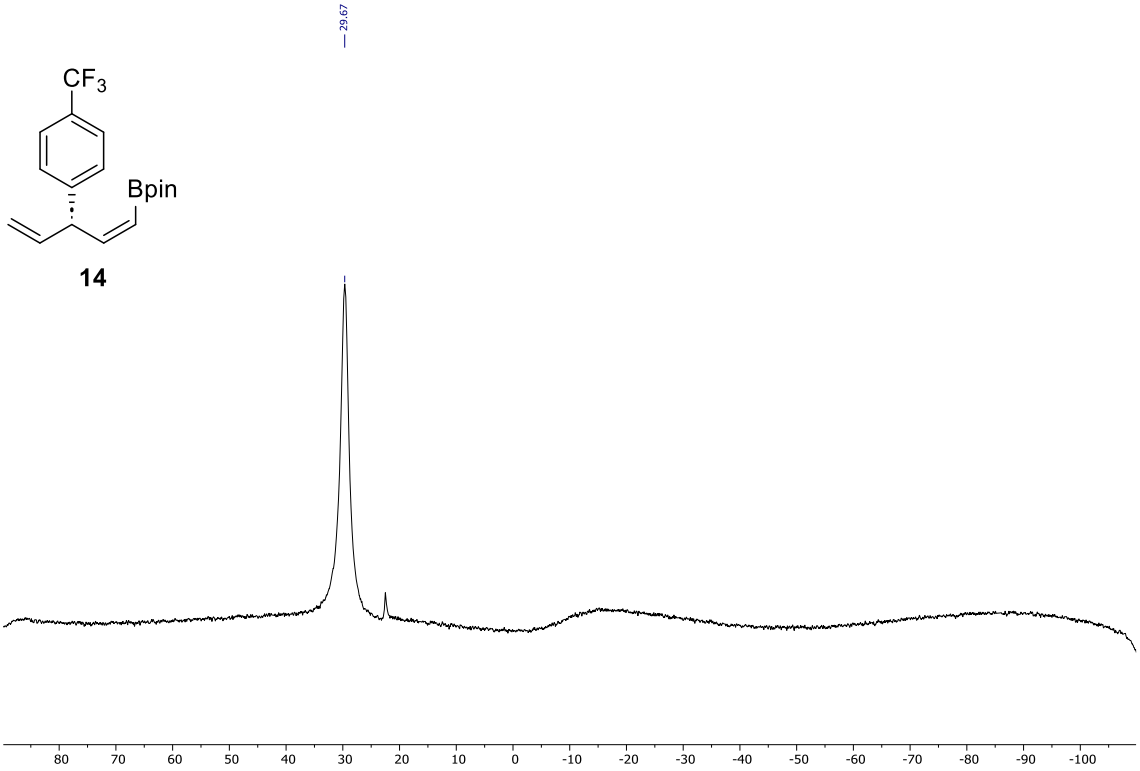

Note: signal at 22.5 ppm corresponds to B_2pin_2 (< 5%; not detected in ^{1}H-NMR nor ^{13}C-NMR)

19F NMR (CDCl3, 282 MHz)

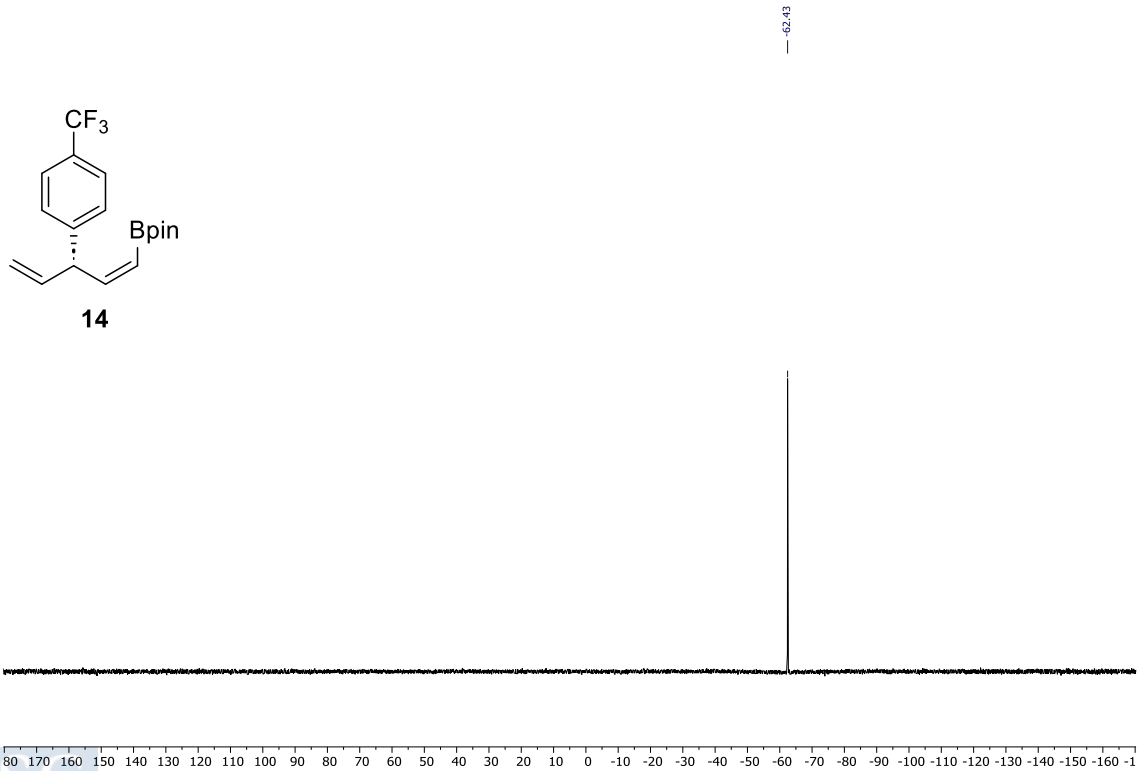

1H NMR (CDCl3, 300 MHz)

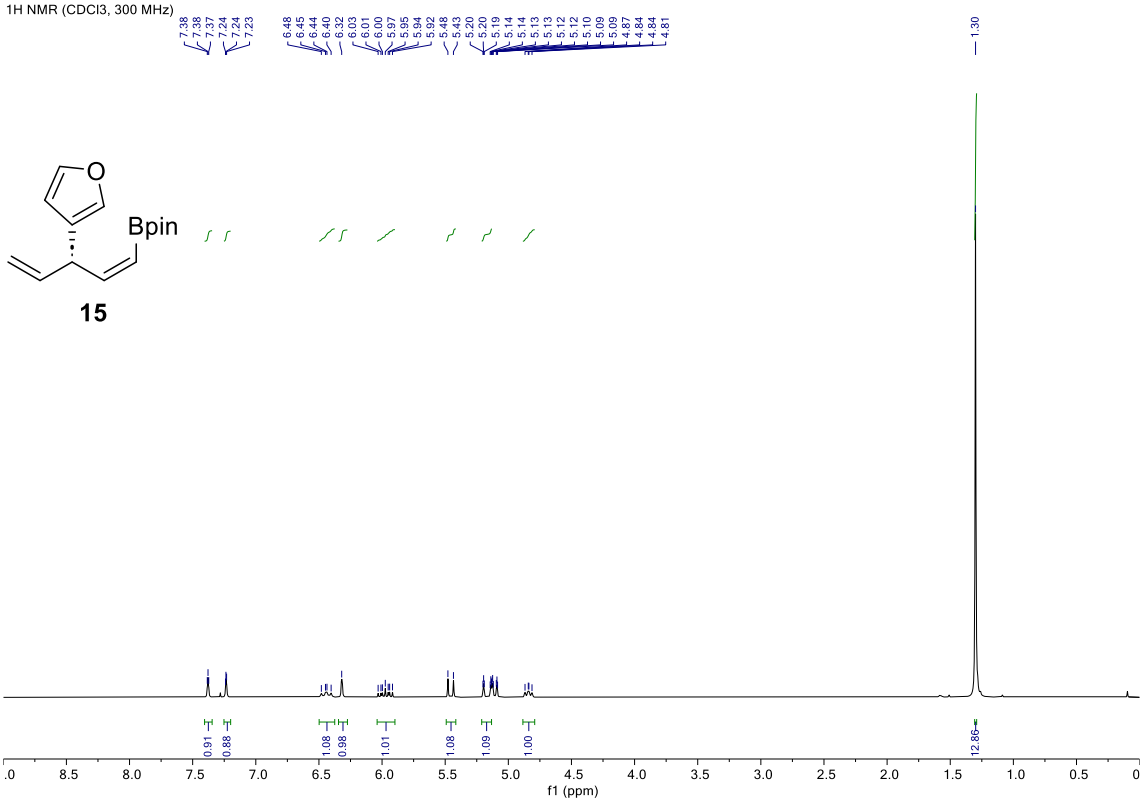

15

13C NMR (CDCl3, 75 MHz)

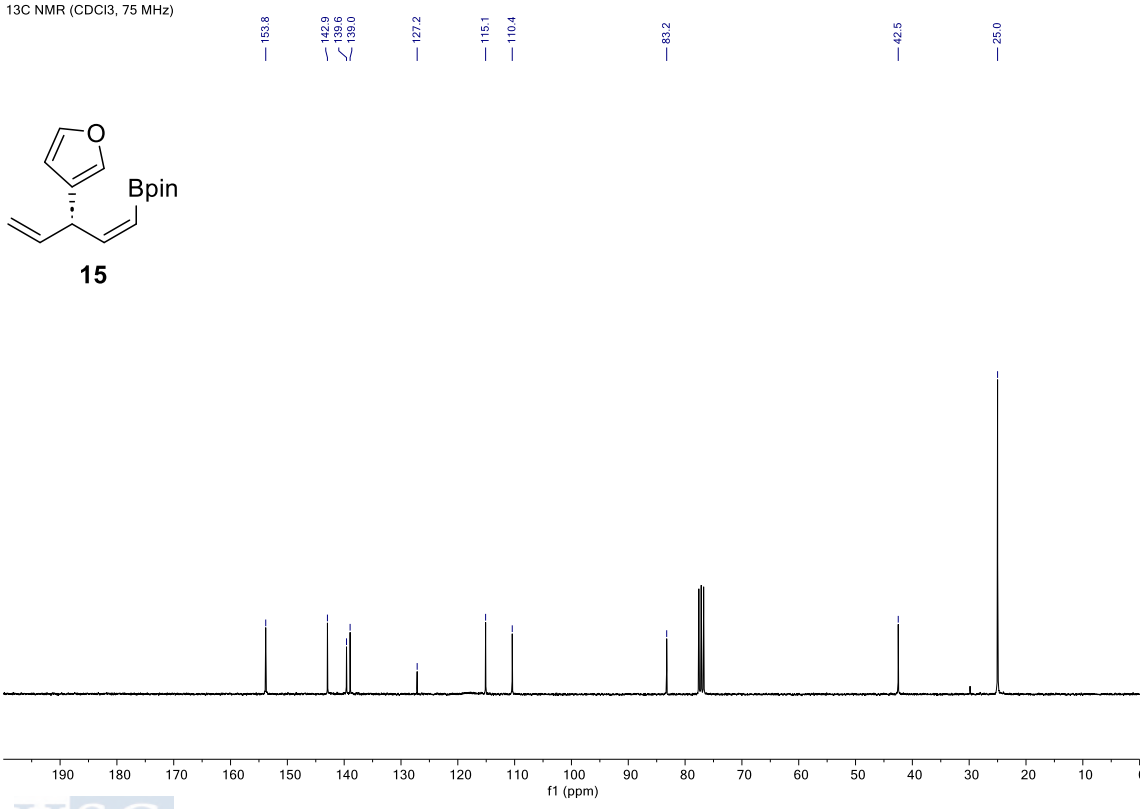

15

11B NMR (CDCl3, 160 MHz)

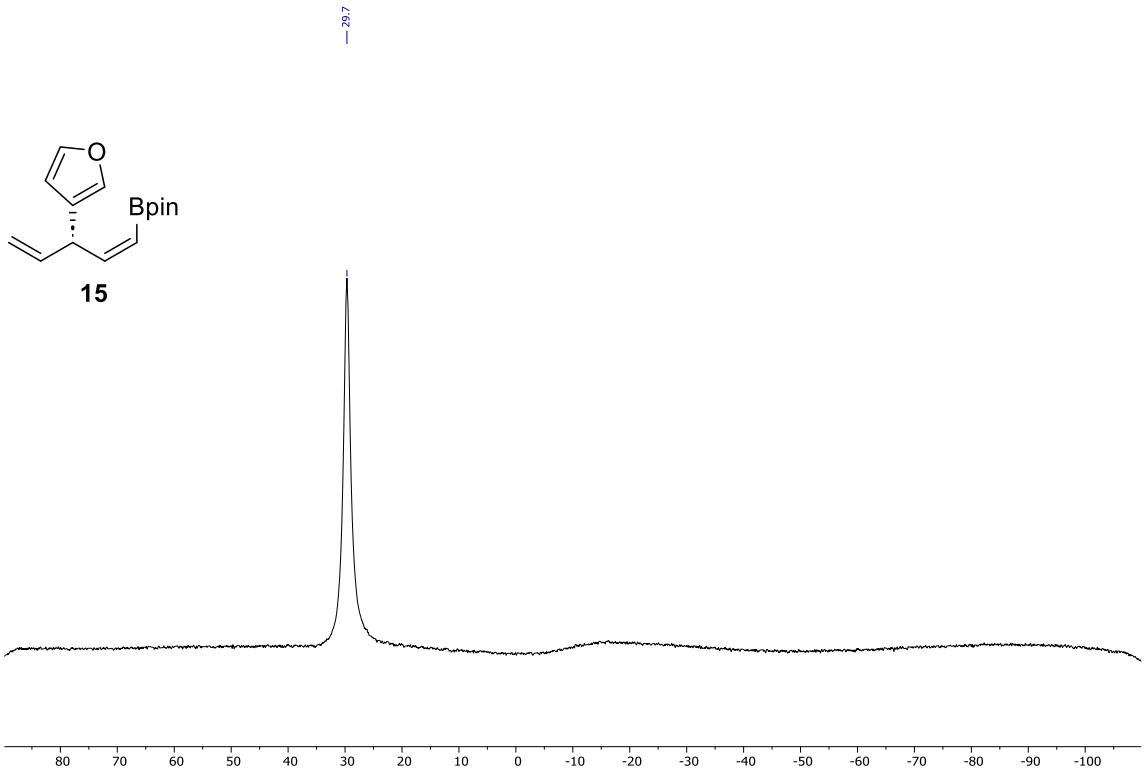

15

1H NMR (CDCl3, 300 MHz)

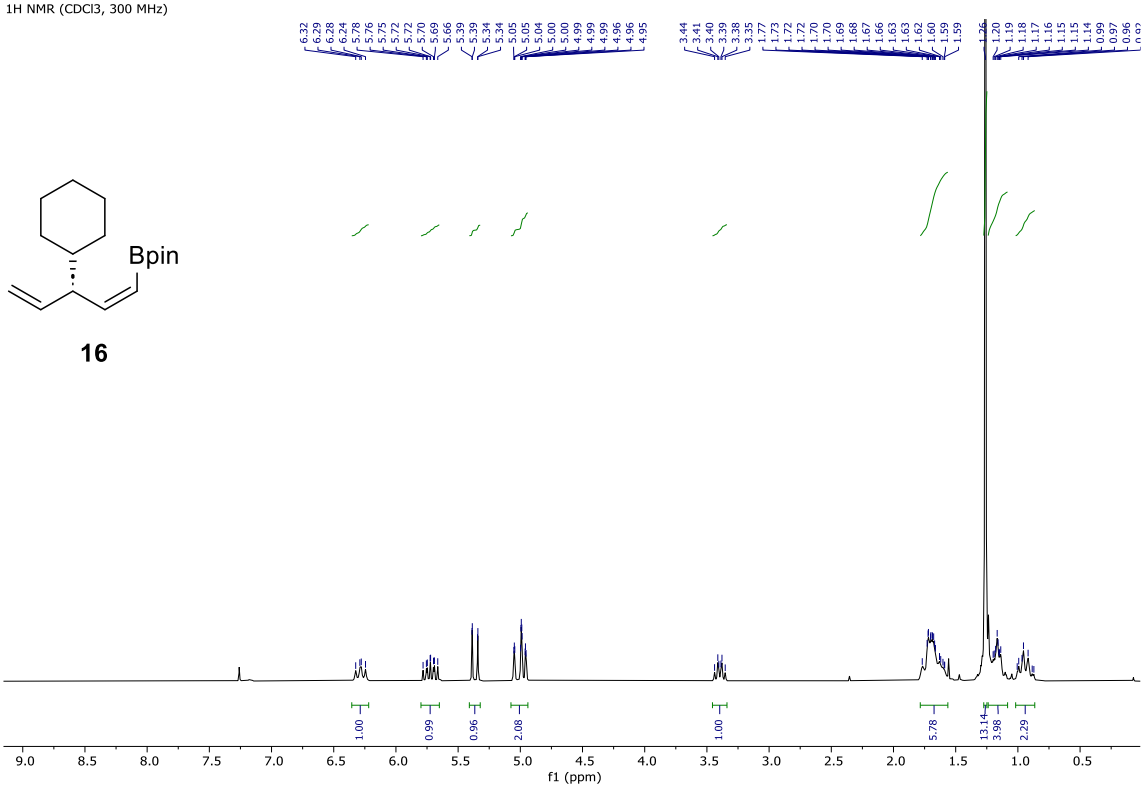

13C NMR (CDCl3, 75 MHz)

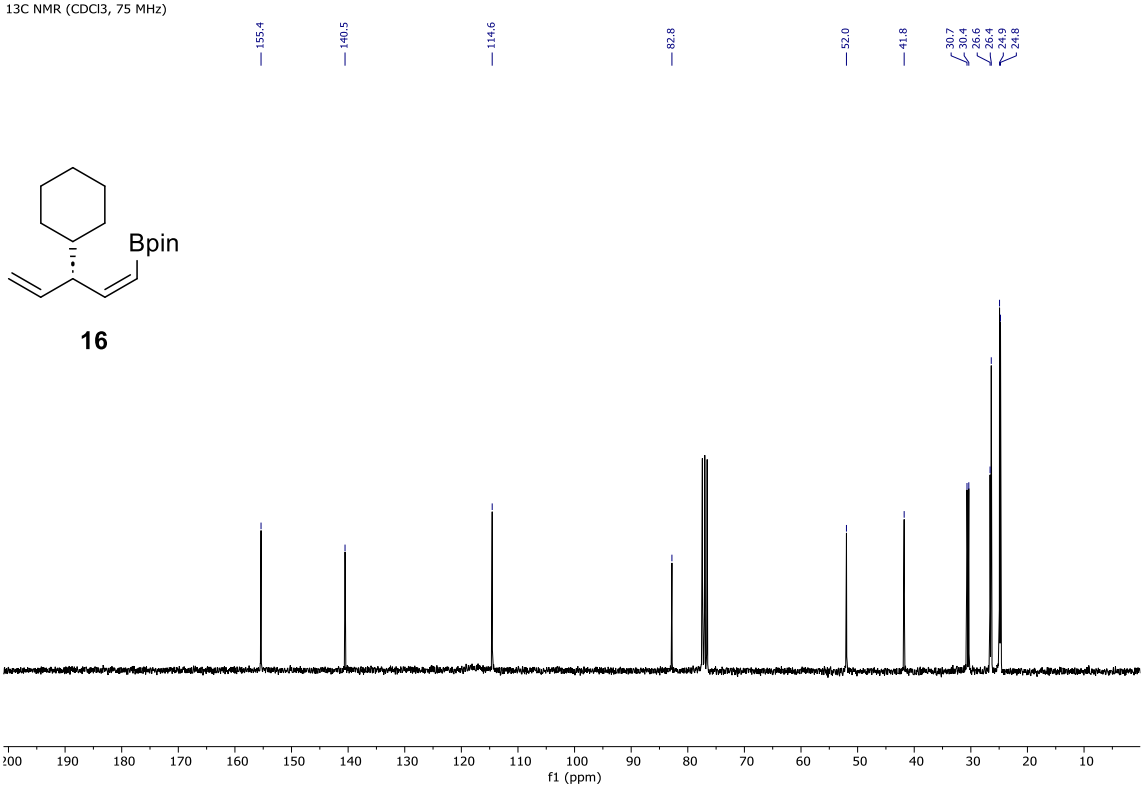

11B NMR (CDCl3, 160 MHz)

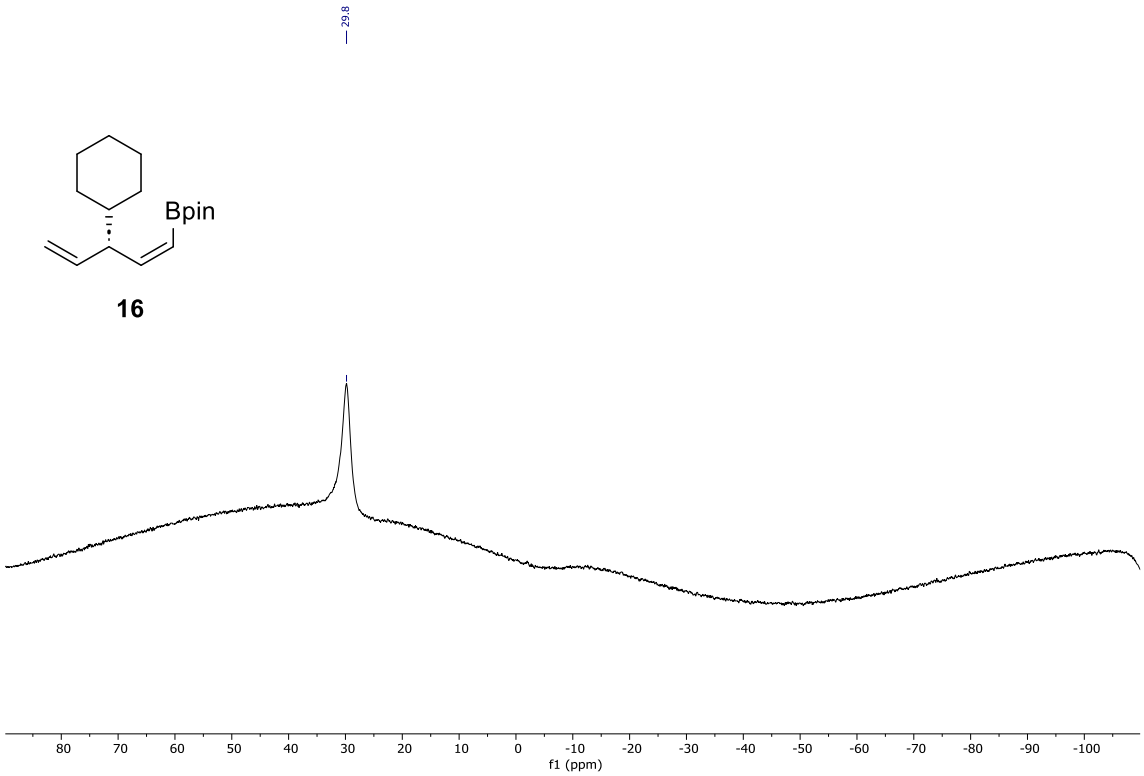

16

1H NMR (CDCl3, 300 MHz)

17

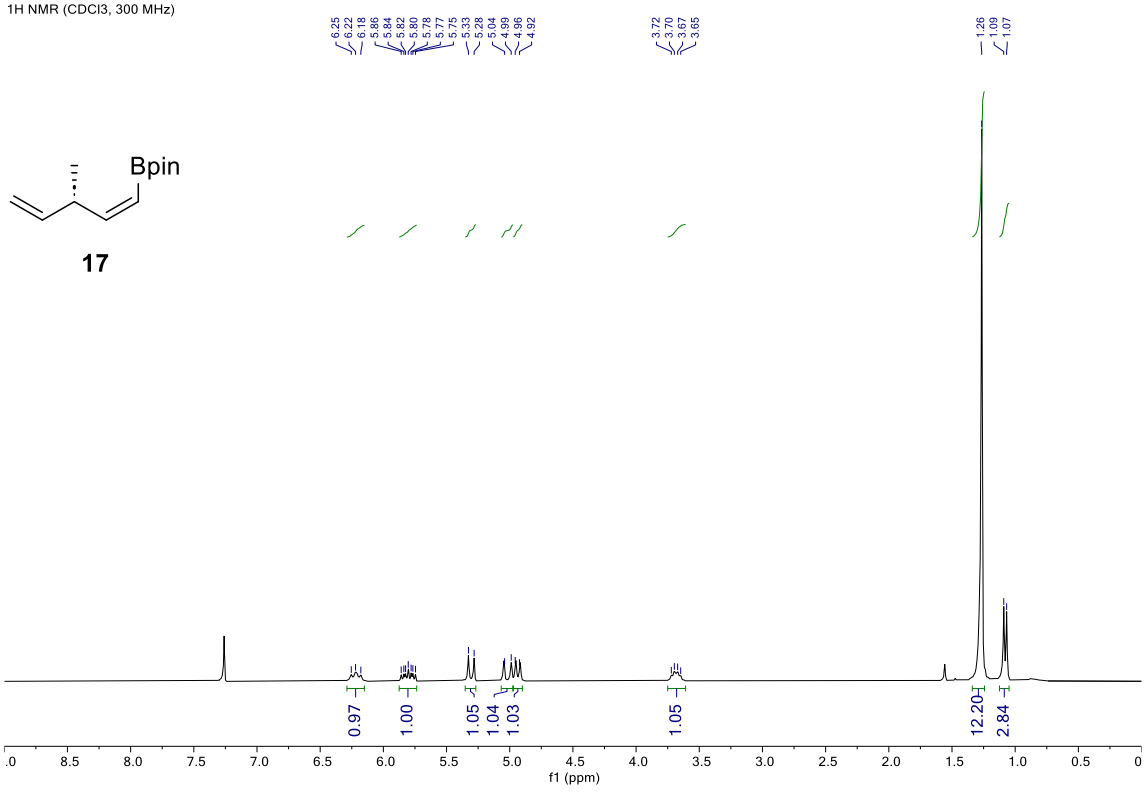

13C NMR (CDCl3, 75 MHz)

17

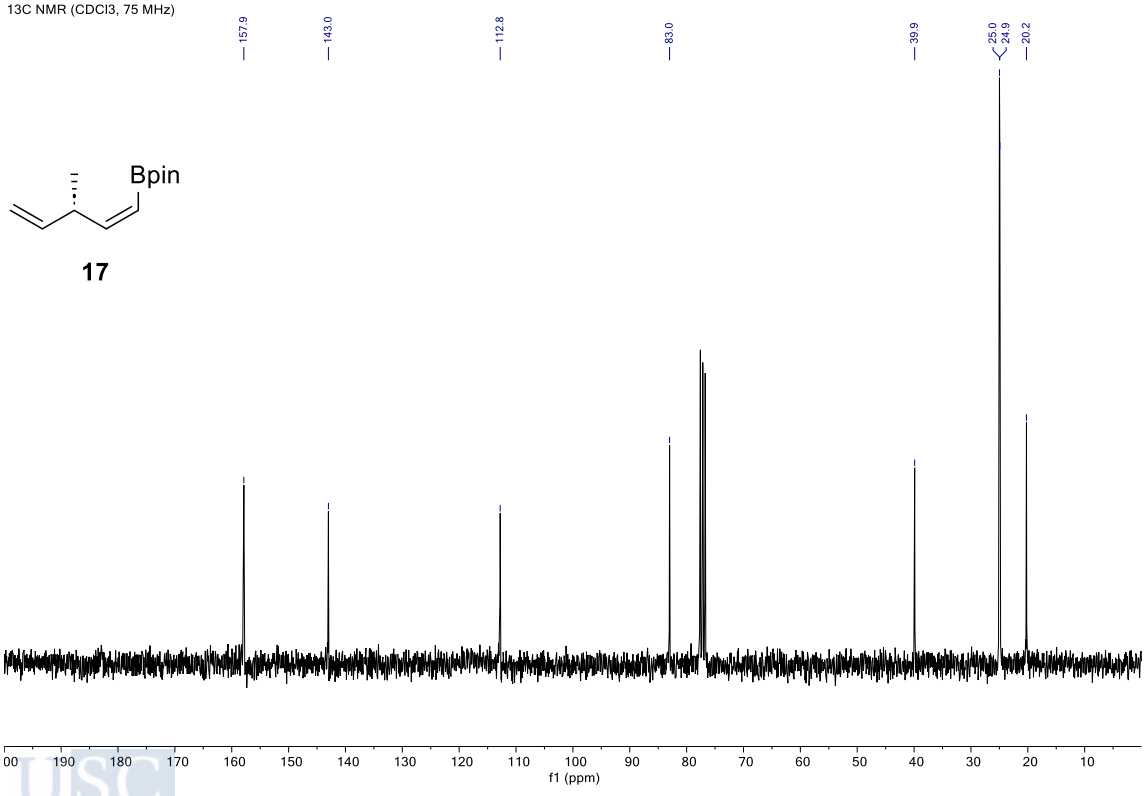

11B NMR (CDCl3, 160 MHz)

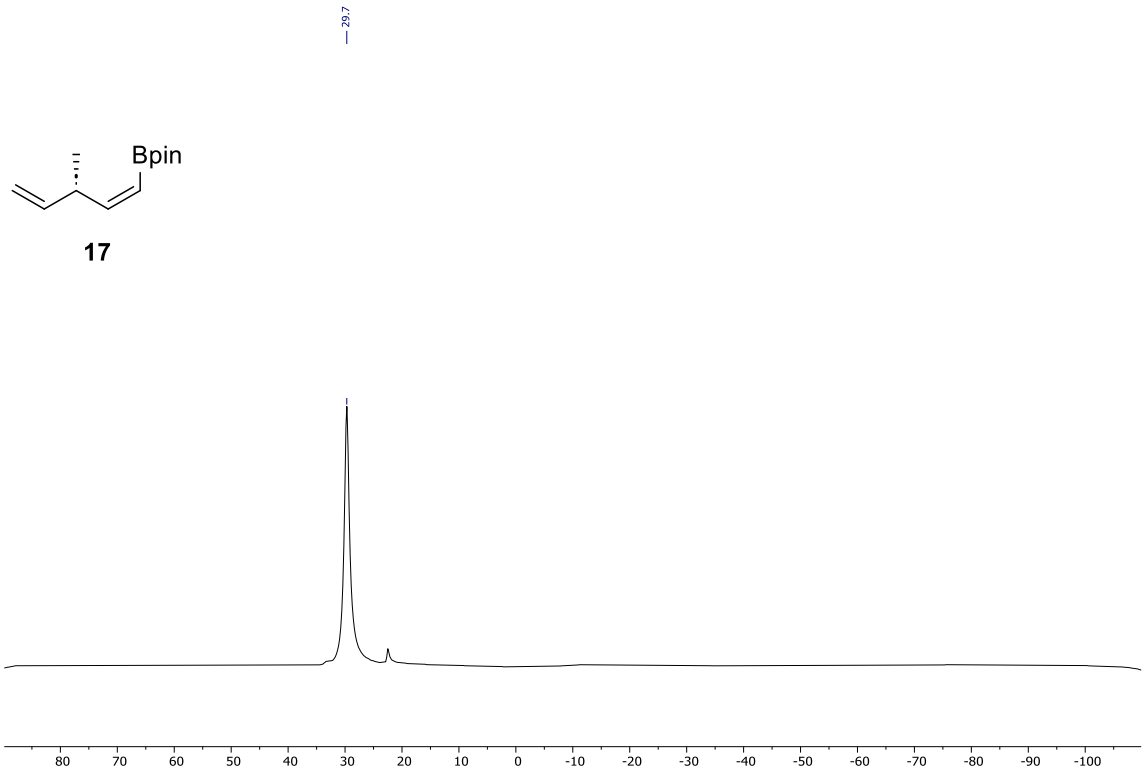

17

Note: signal at 22.5 ppm corresponds to B_2pin_2 (< 5%; not detected in ^{1}H-NMR nor ^{13}C-NMR)

1H NMR (CDCl3, 300 MHz)

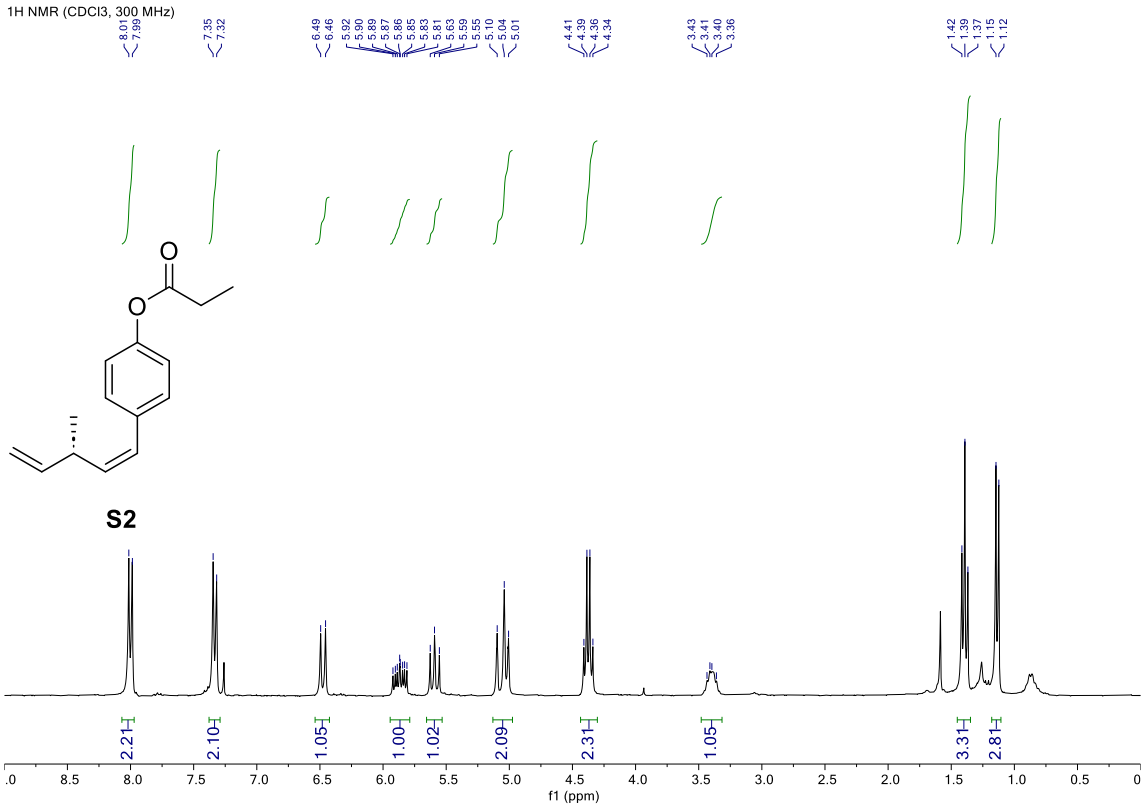

13C NMR (CDCl3, 75 MHz)

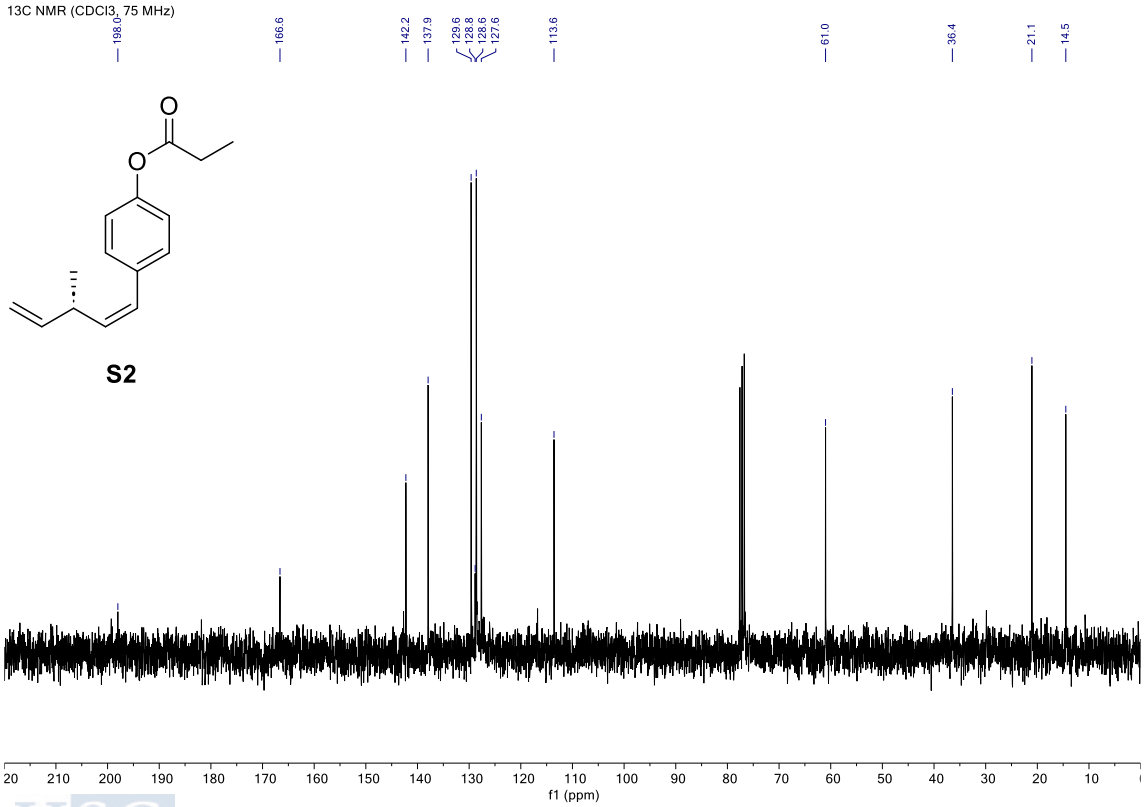

1H NMR (CDCl3, 300 MHz)

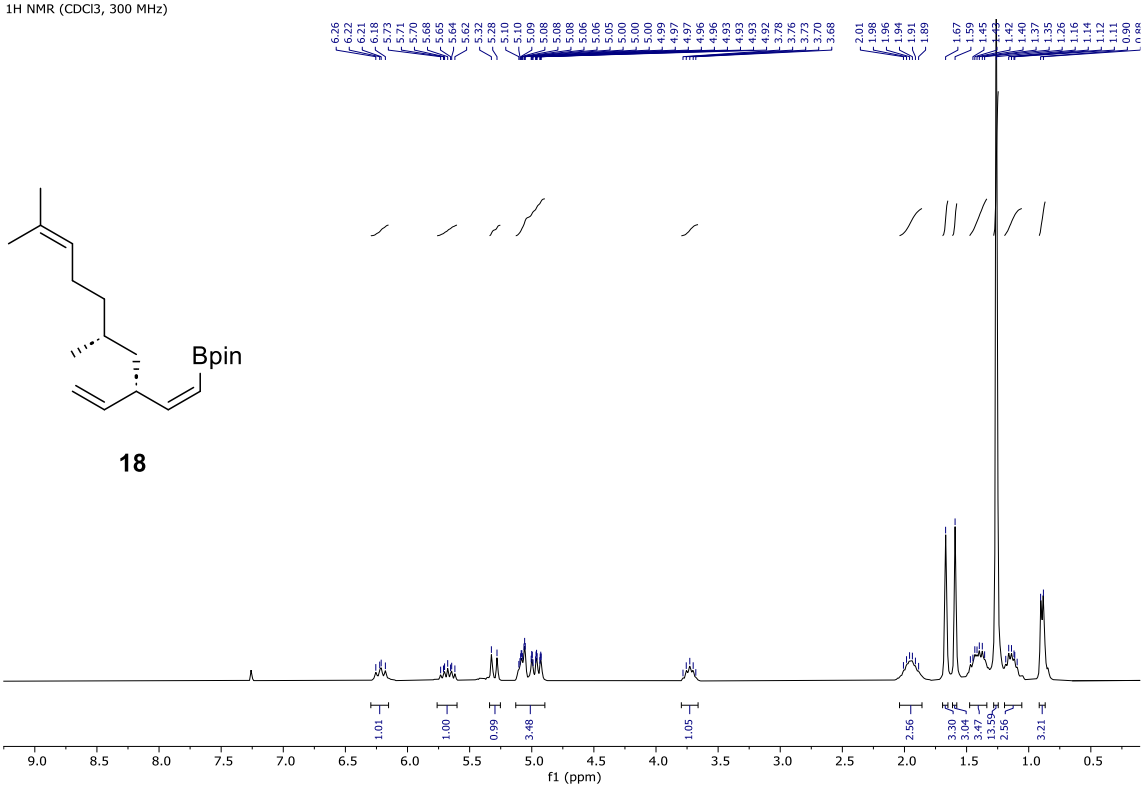

13C NMR (CDCl3, 75 MHz)

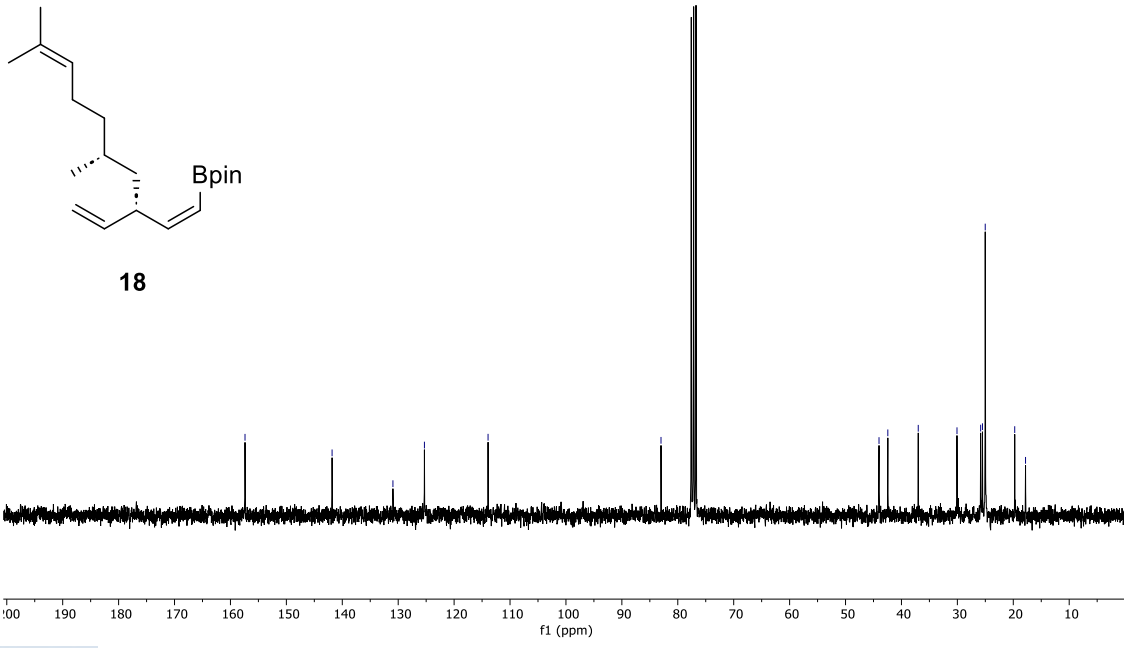

11B NMR (CDCl3, 160 MHz)

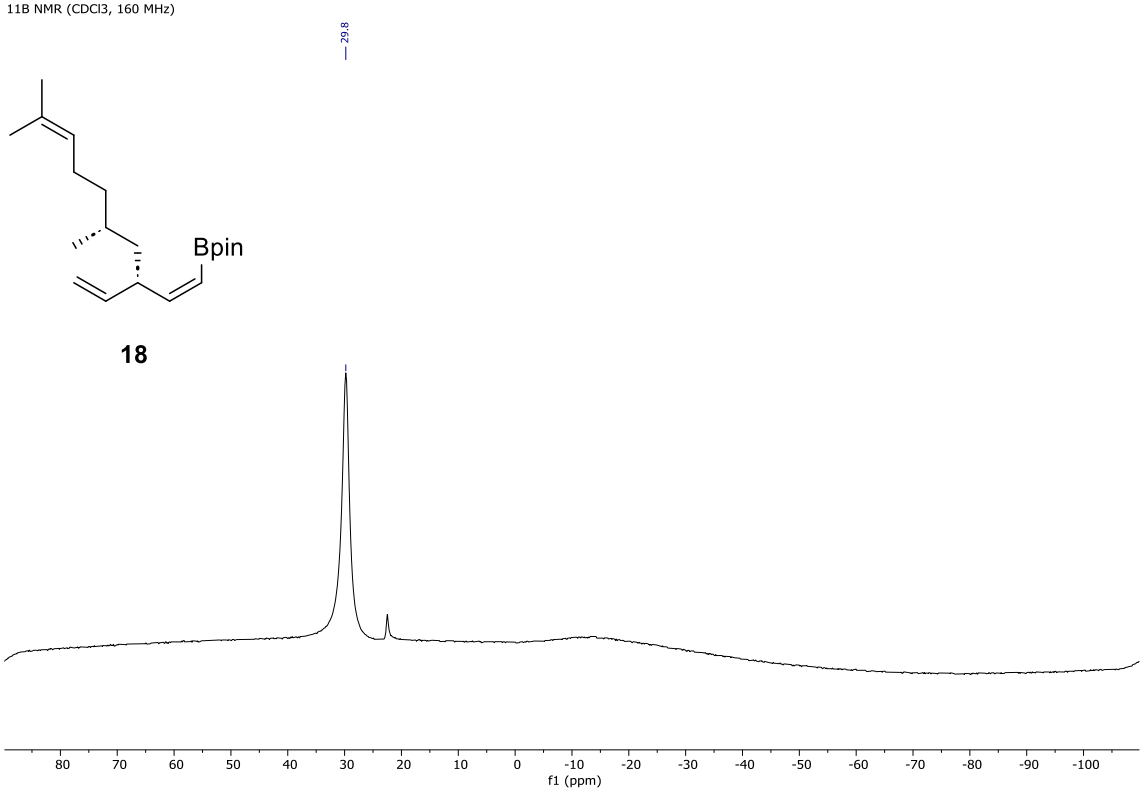

18

Note: signal at 22.5 ppm corresponds to B_2pin_2 (< 5%; not detected in ^{1}H-NMR nor ^{13}C-NMR)

1H-NMR (300 MHz)

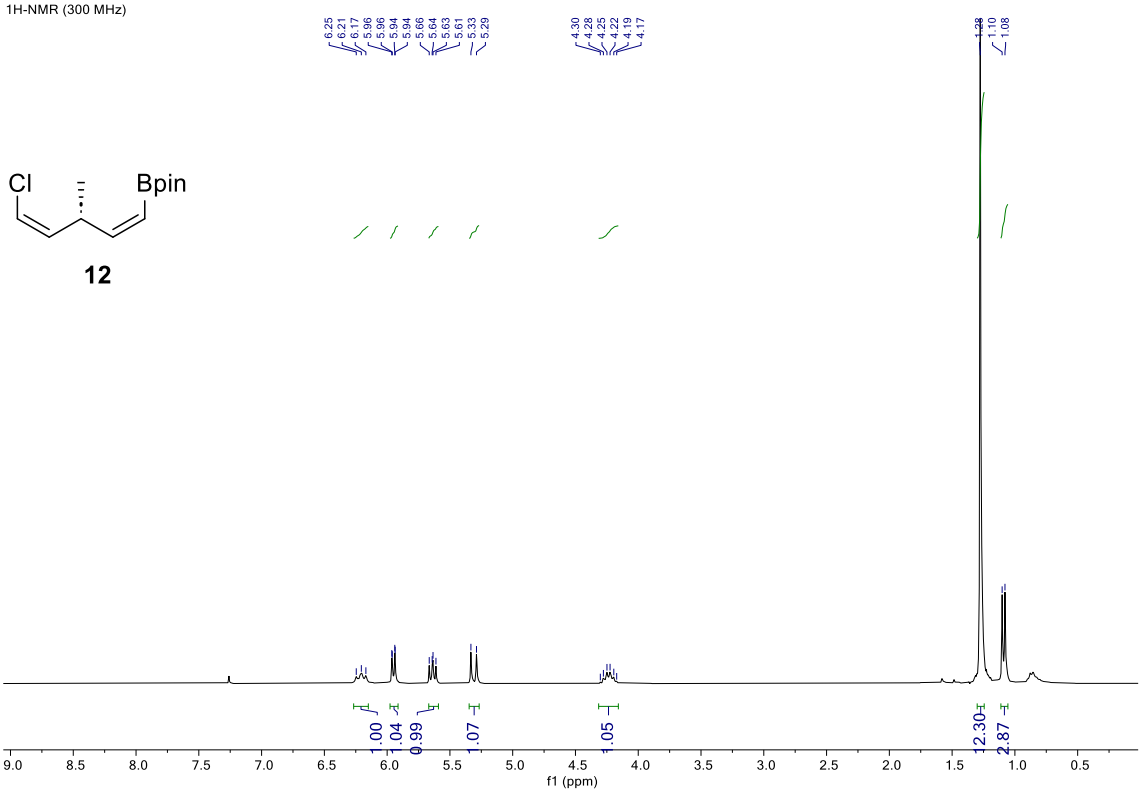

13C NMR (CDCl3, 75 MHz)

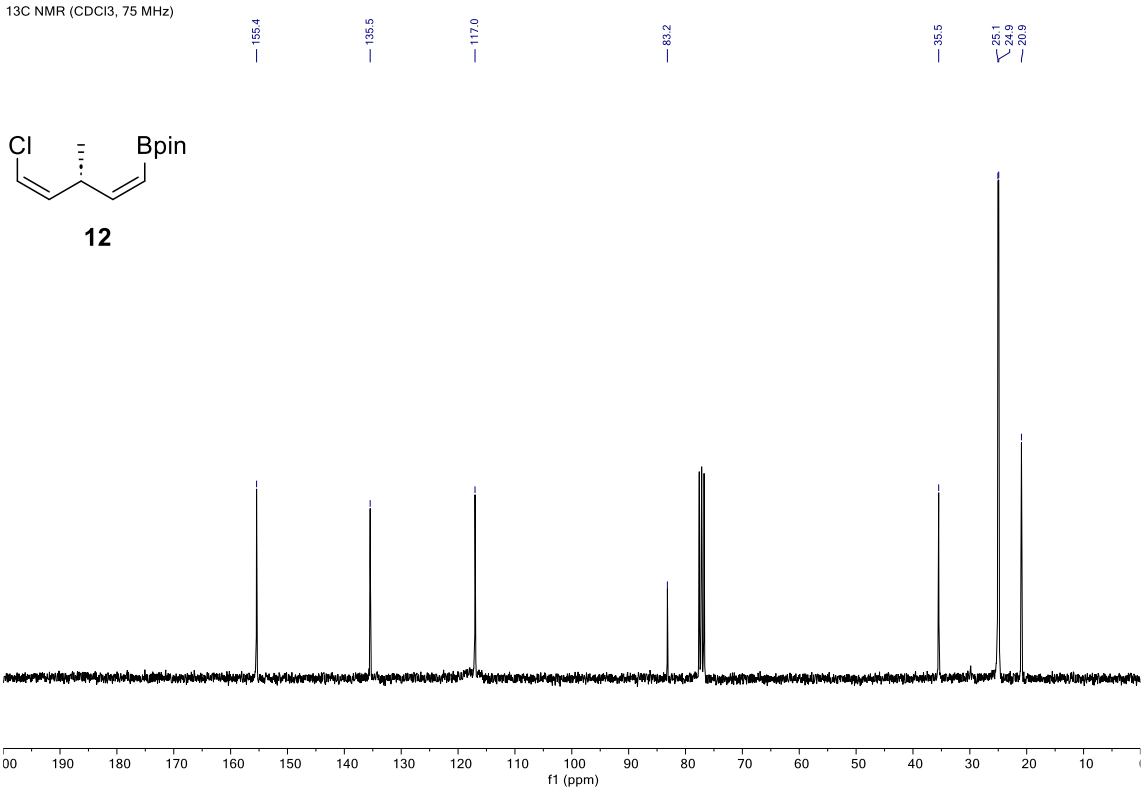

11B NMR (CDCl3, 160 MHz)

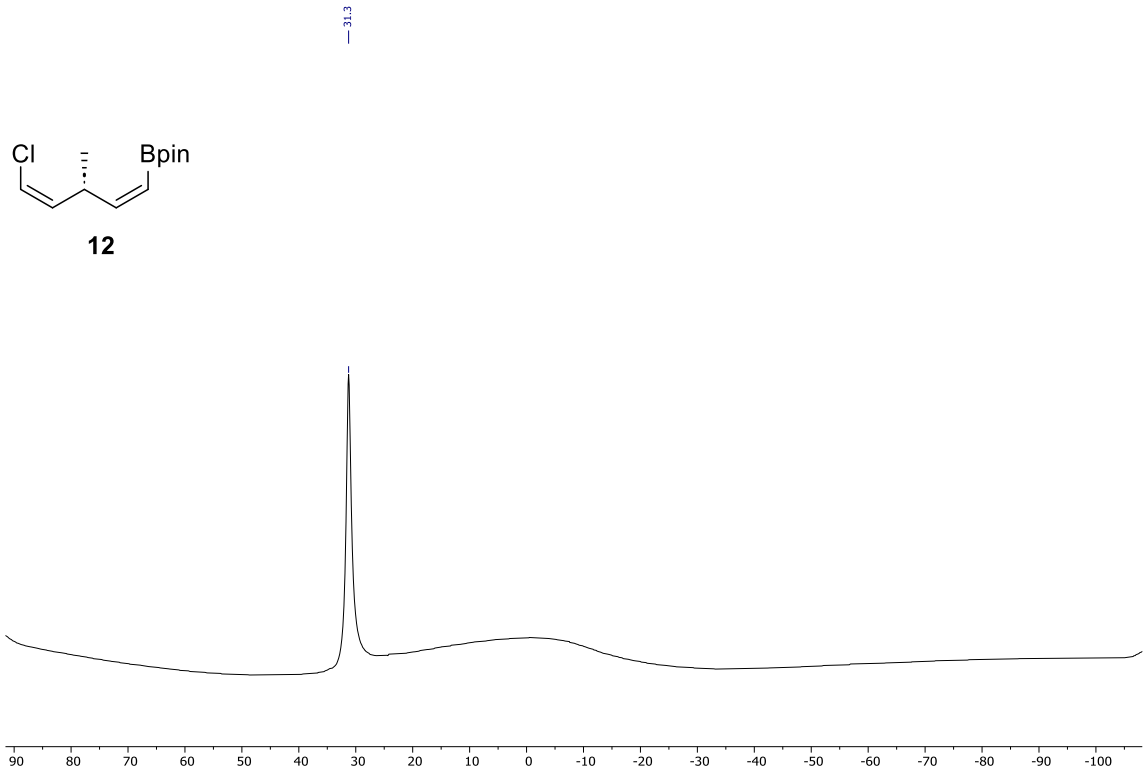

12

1H NMR (CDCl3, 300 MHz)

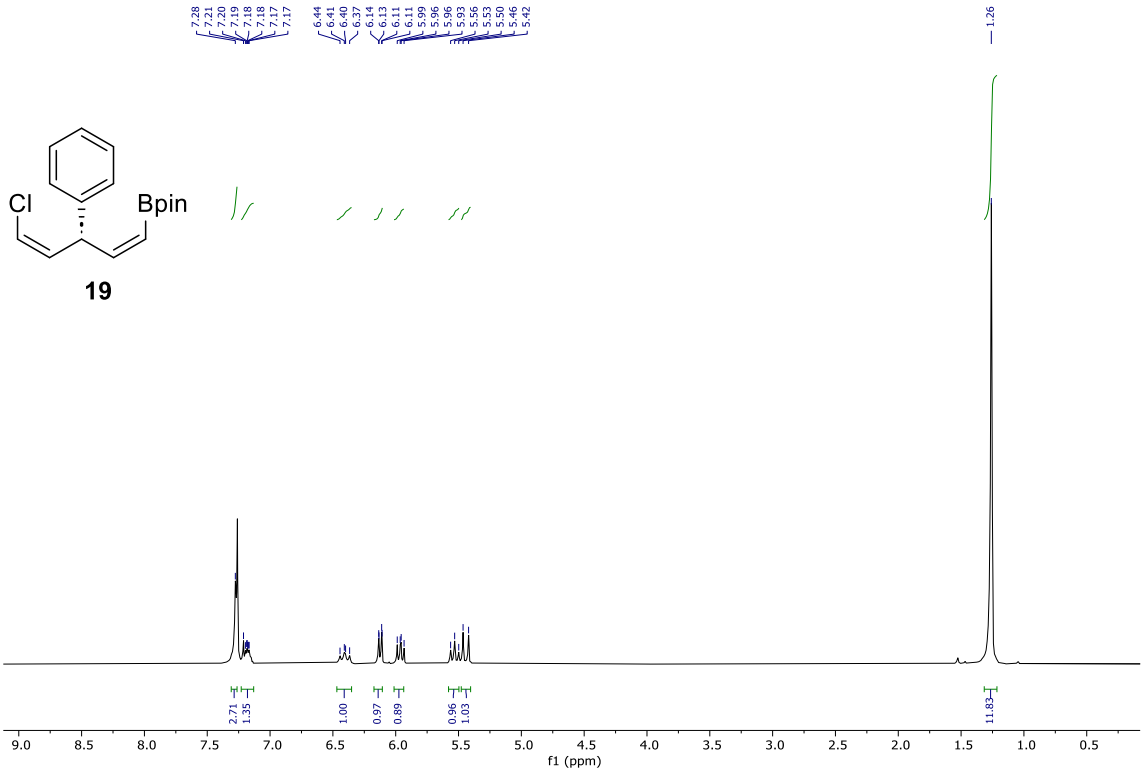

1H NMR (CDCl3, 300 MHz)

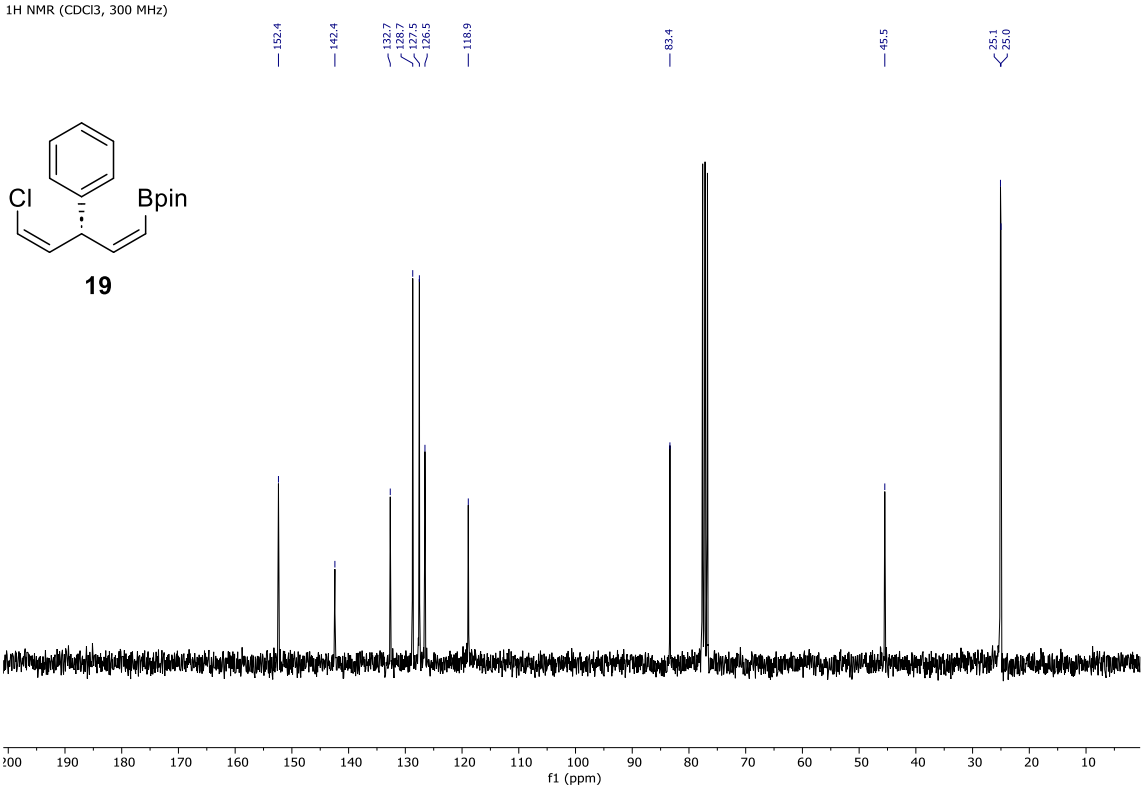

11B NMR (CDCl3, 160 MHz)

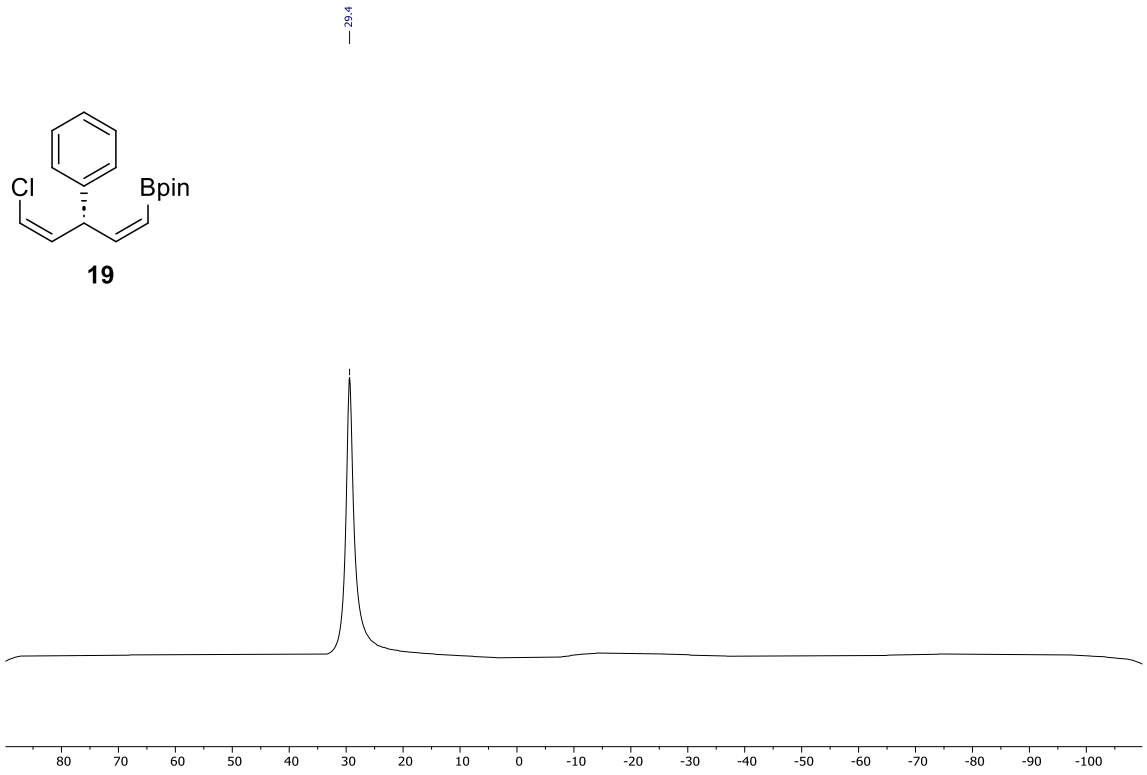

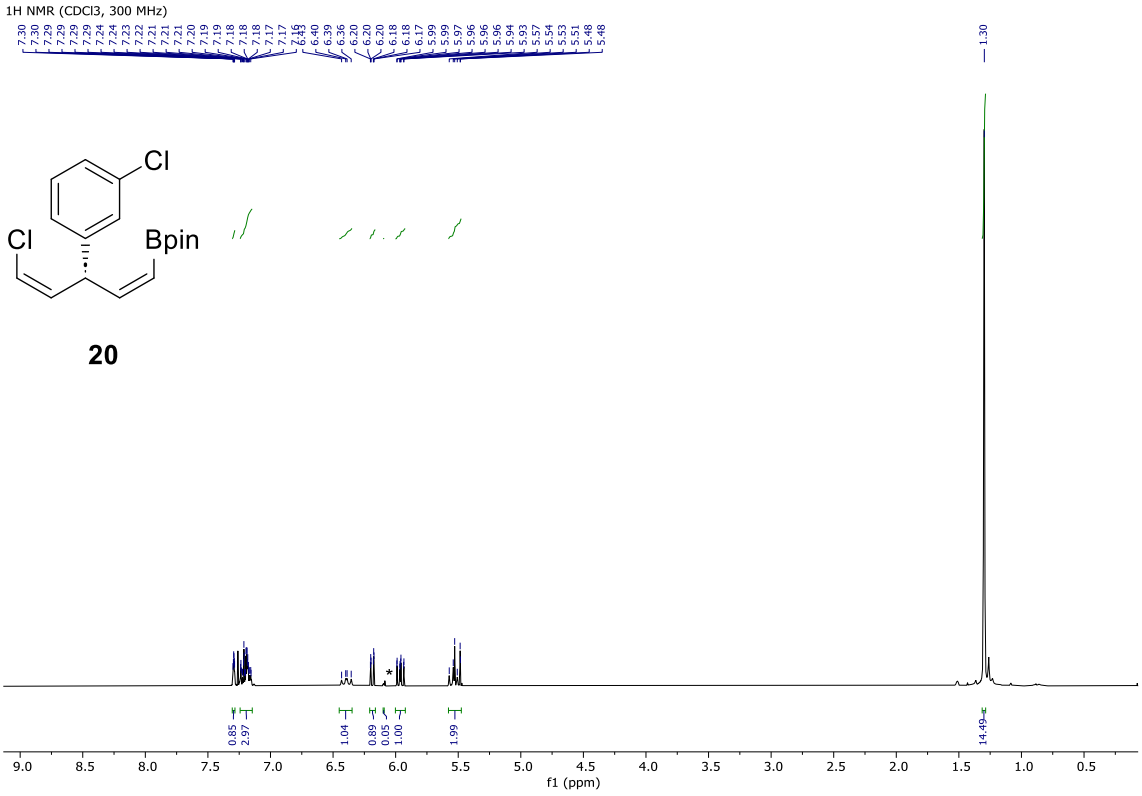

Marked signals (*) correspond to (*Z*,*E*) isomer

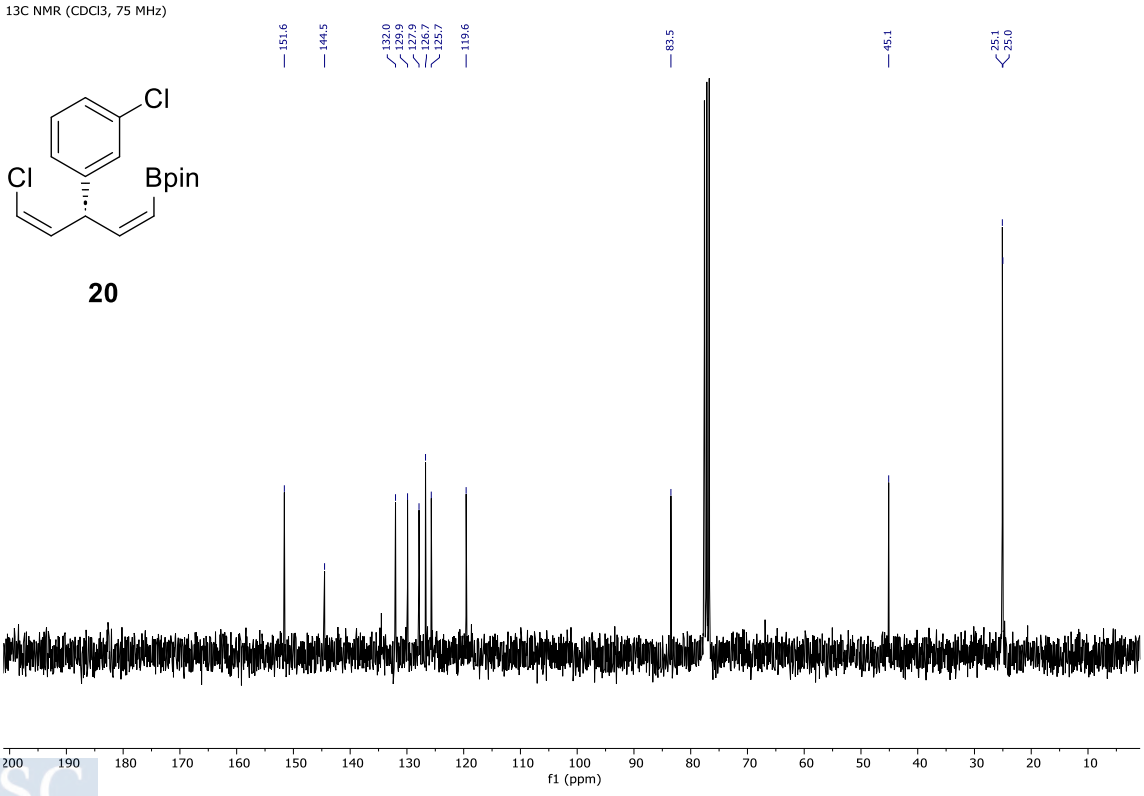

11B NMR (CDCl3, 160 MHz)

20

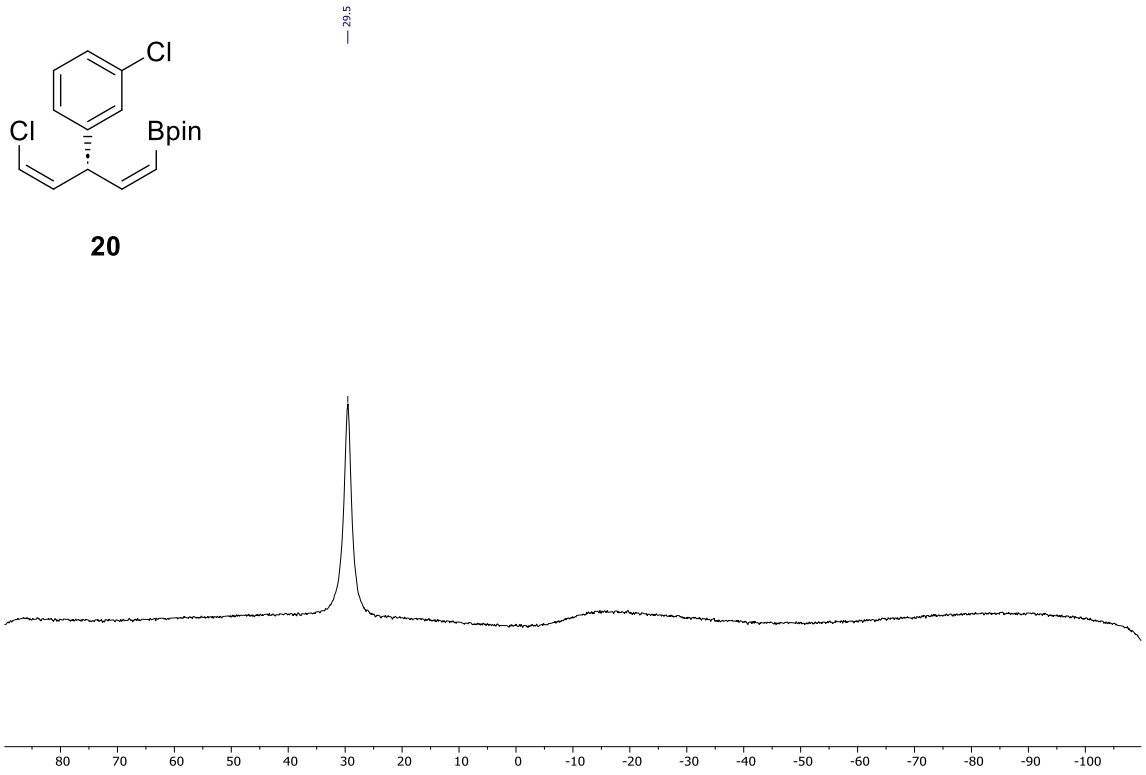

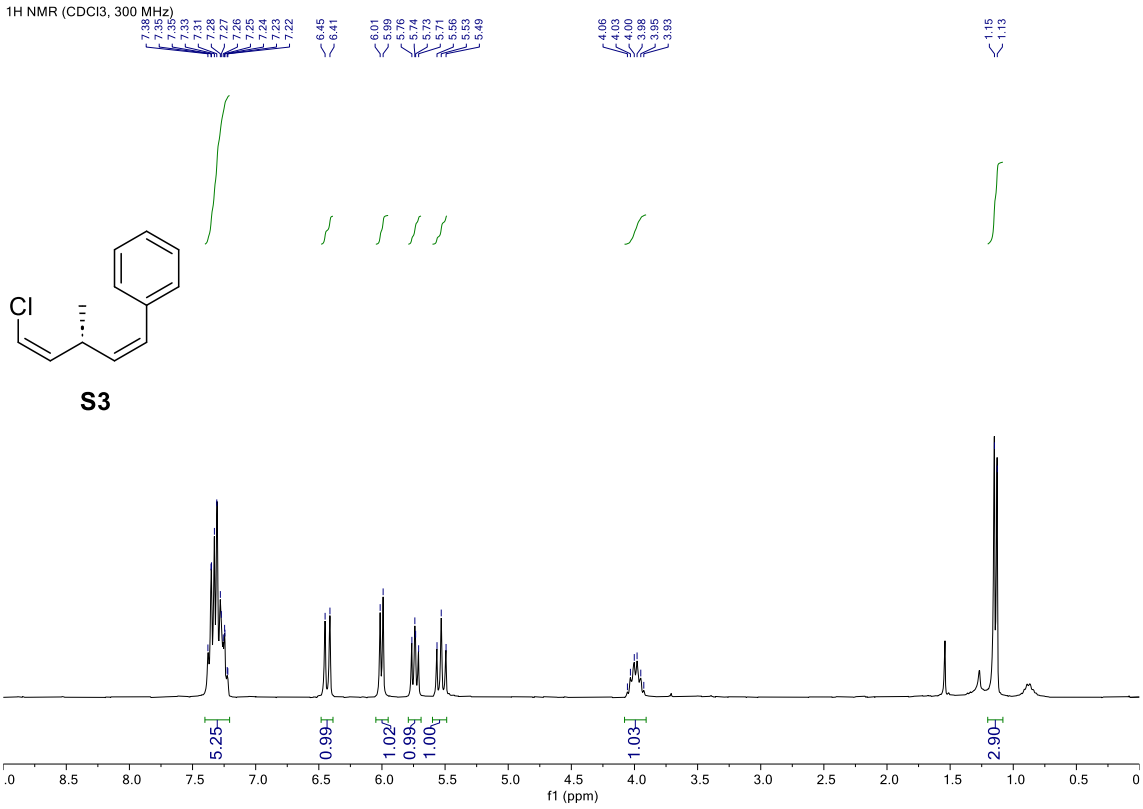
1H NMR (CDCl3, 300 MHz)
7.38
7.35
7.35
7.33
7.31
7.28
7.27
7.26
7.25
7.24
7.23
7.22
6.45
6.41
6.01
5.99
5.76
5.74
5.73
5.71
5.56
5.53
5.49
4.06
4.03
4.00
3.98
3.95
3.93
1.15
1.13
Cl
S3
5.25
0.99
1.02
0.99
1.00
1.03
2.90
f1 (ppm)

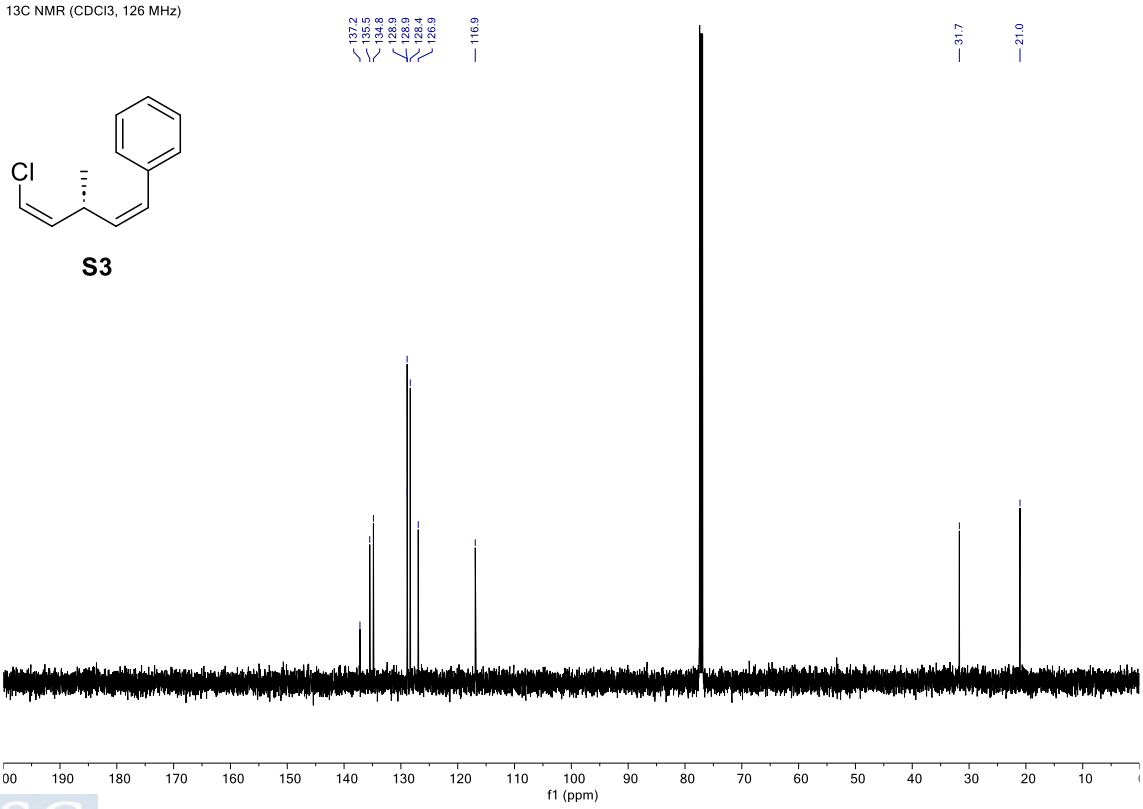
13C NMR (CDCl3, 126 MHz)
137.2
135.5
134.8
128.9
128.9
128.4
126.9
116.9
31.7
21.0
Cl
S3
f1 (ppm)

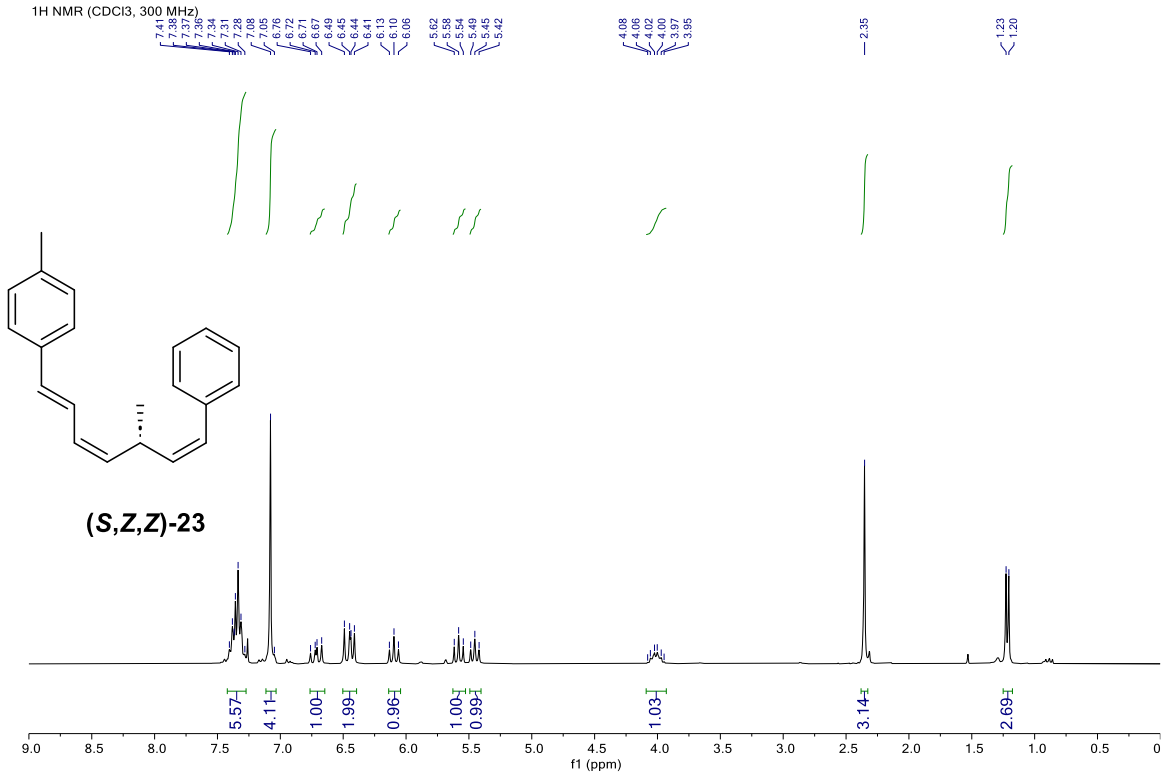
1H NMR (CDCl3, 300 MHz)
(S,Z,Z)-23
f1 (ppm)

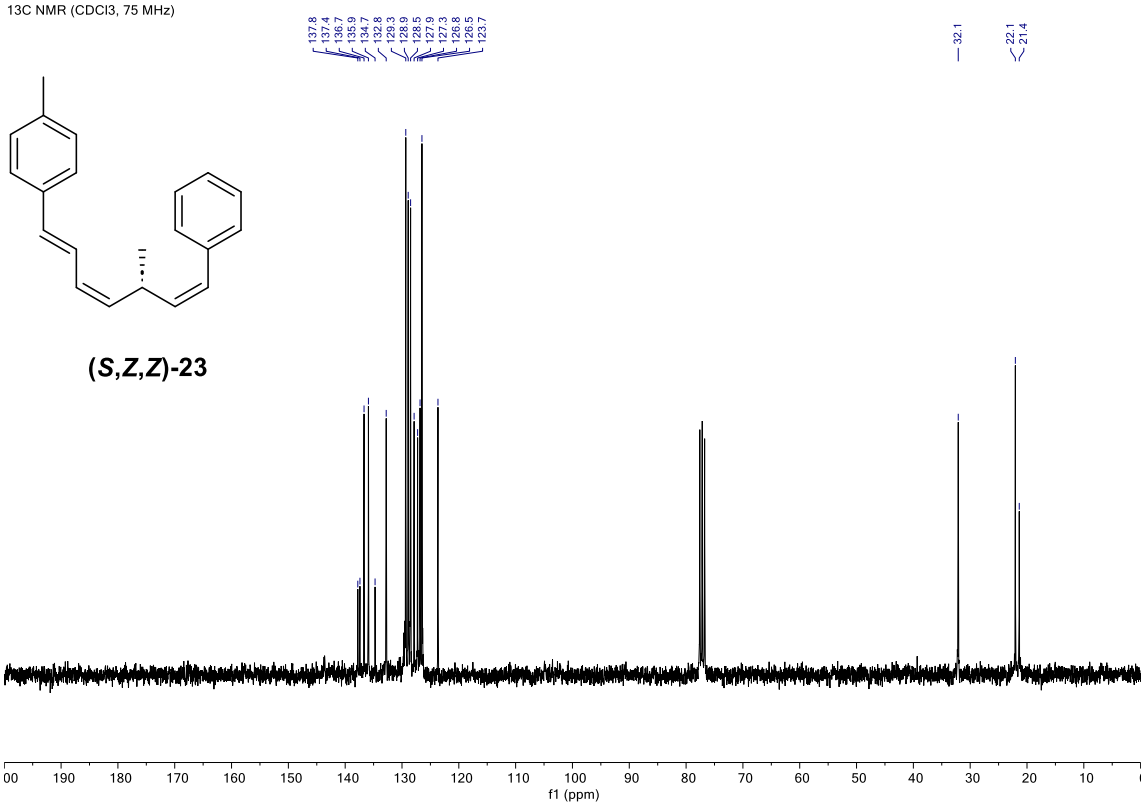
13C NMR (CDCl3, 75 MHz)
(S,Z,Z)-23
f1 (ppm)

1H NMR (CDCl3, 300 MHz)

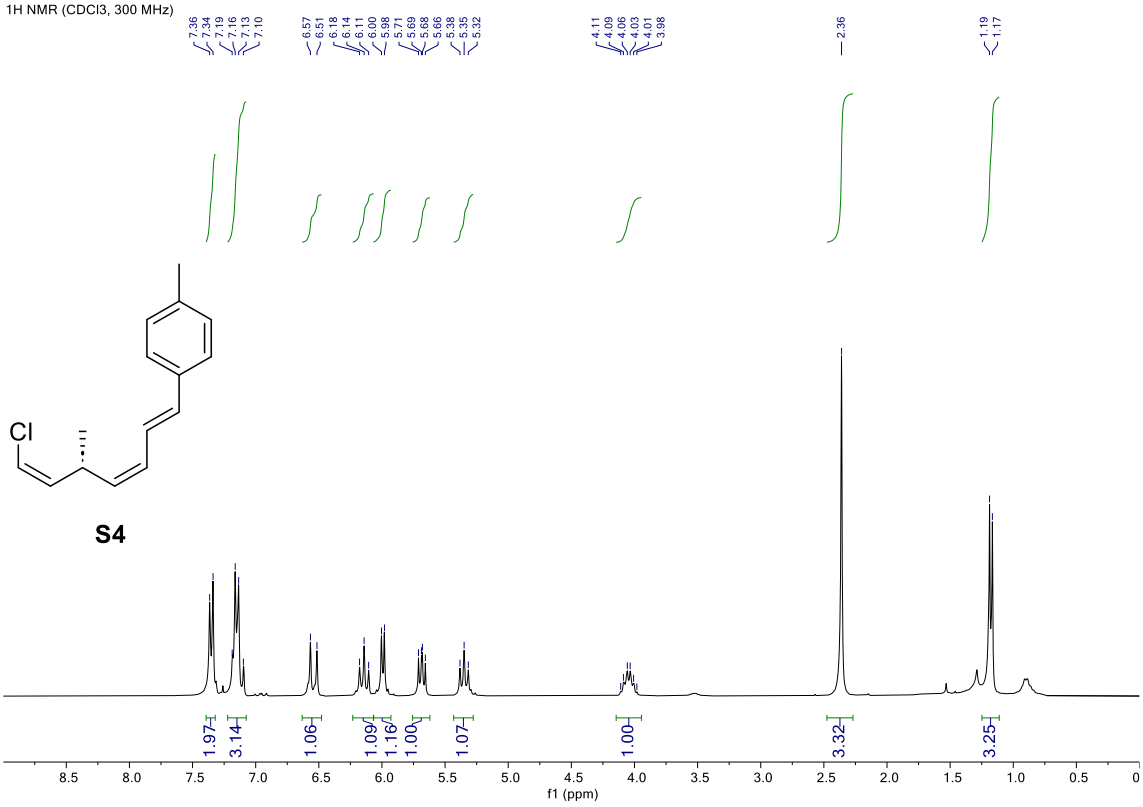

S4

13C NMR (CDCl3, 75 MHz)

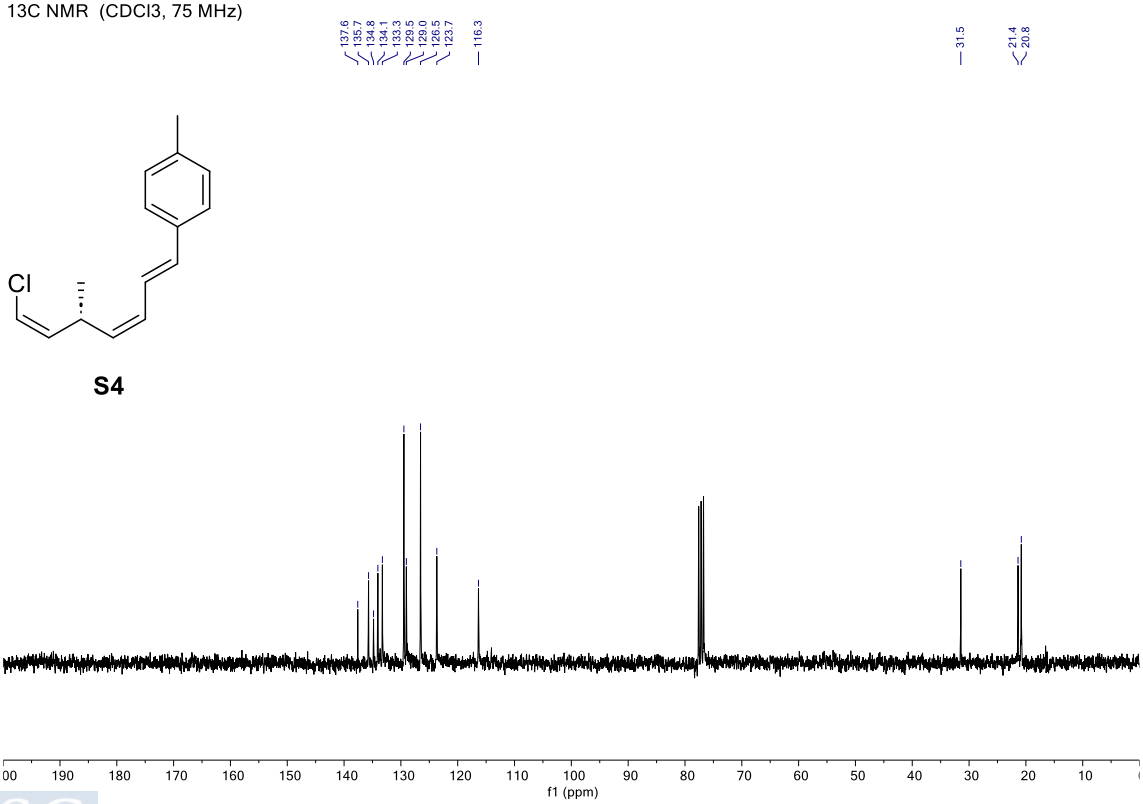

S4

1H NMR (CDCl3, 300 MHz)

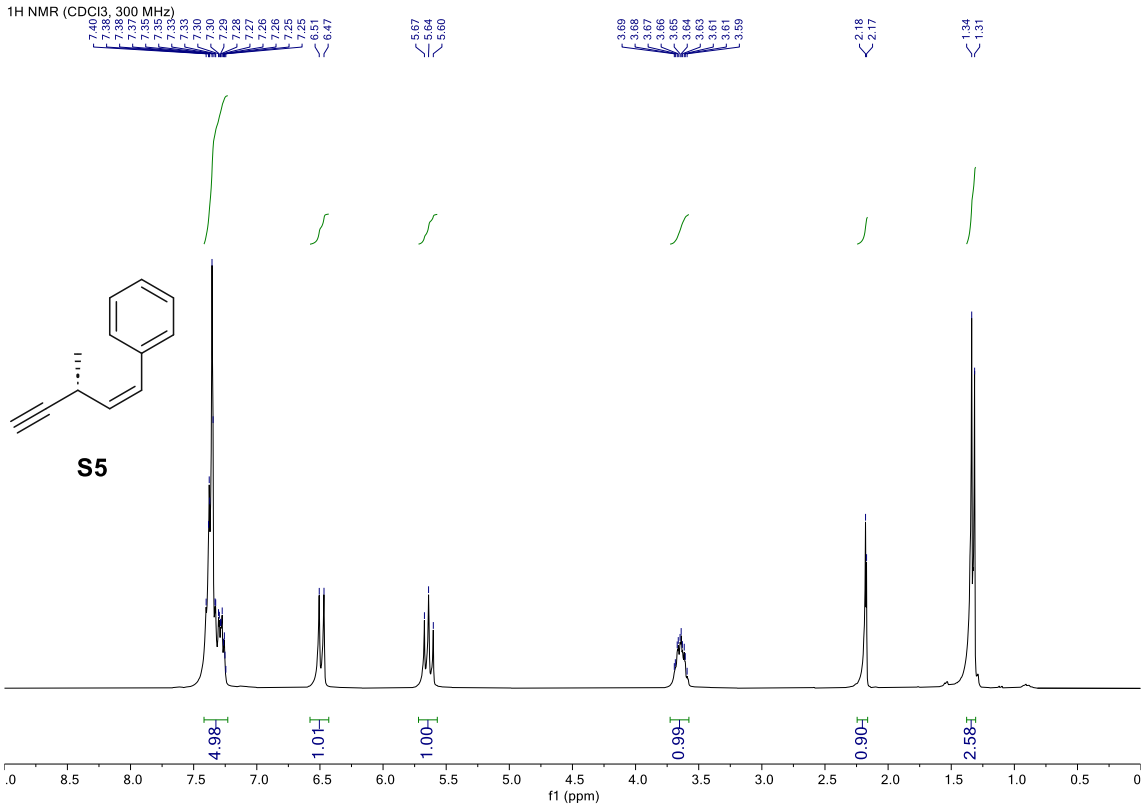

S5

13C NMR (CDCl3, 75 MHz)

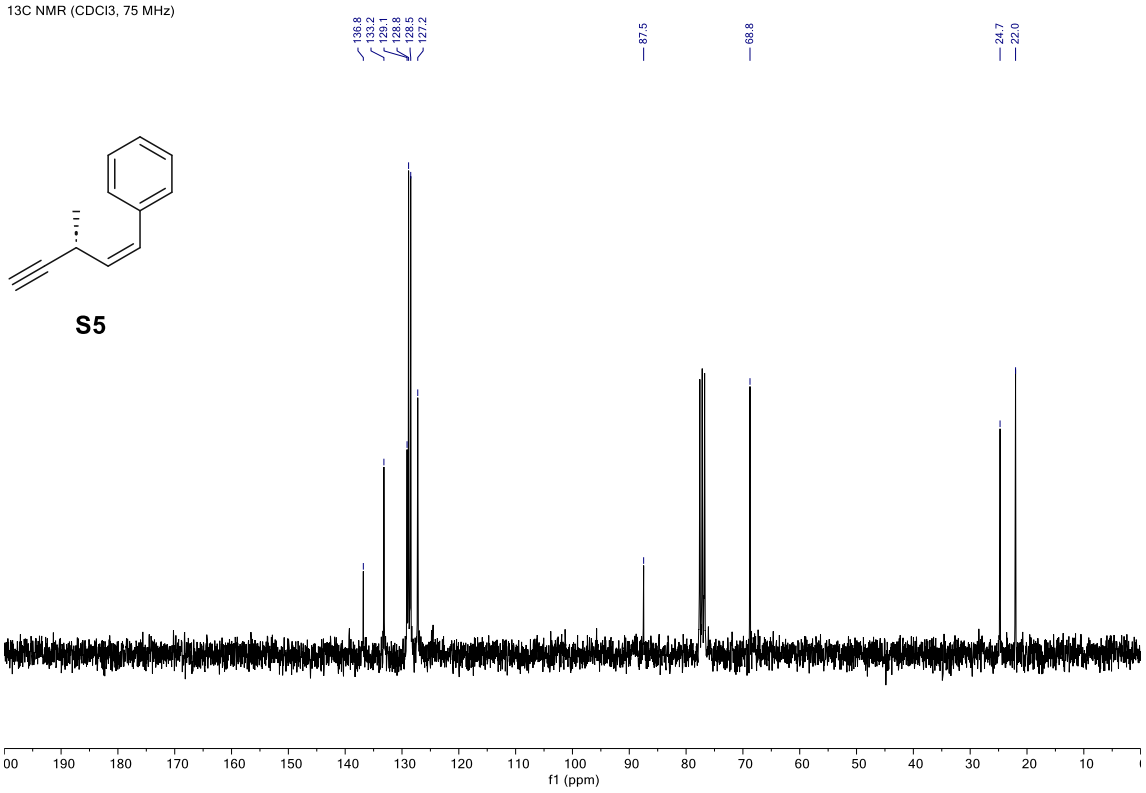

S5

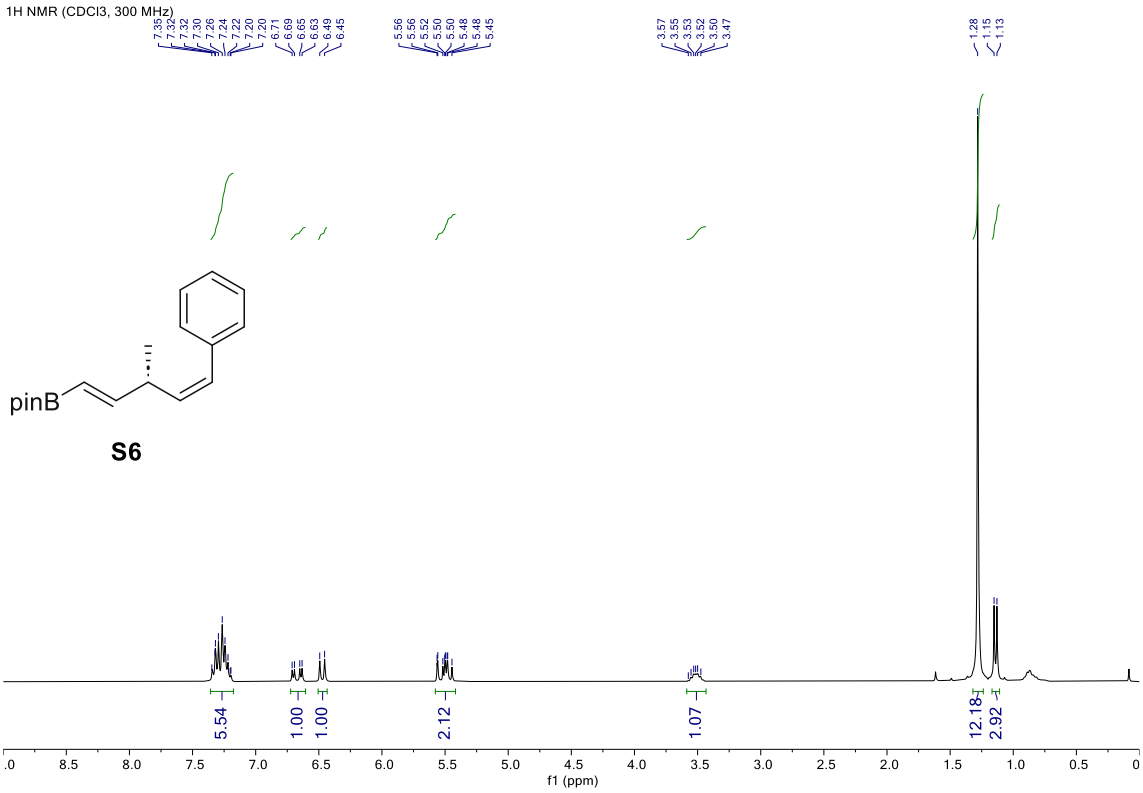
1H NMR (CDCl3, 300 MHz)
7.35
7.32
7.32
7.30
7.26
7.24
7.22
7.20
7.20
6.71
6.69
6.65
6.63
6.49
6.45
5.56
5.56
5.52
5.50
5.50
5.48
5.48
5.45
3.57
3.55
3.53
3.52
3.50
3.47
1.28
1.15
1.13
pinB
S6
5.54
1.00
1.00
2.12
1.07
12.18
2.92
f1 (ppm)

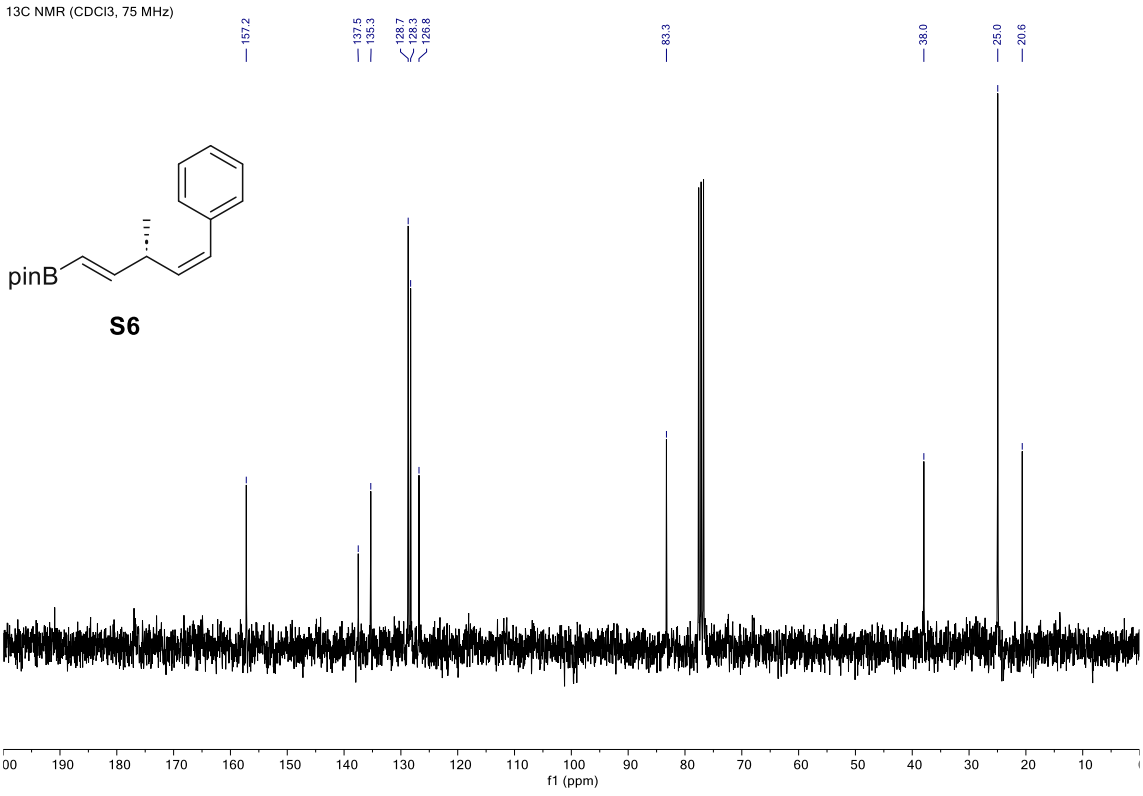
13C NMR (CDCl3, 75 MHz)
157.2
137.5
135.3
128.7
128.3
126.8
83.3
38.0
25.0
20.6
pinB
S6
f1 (ppm)

11B-NMR (CDCl3, 160 MHz)

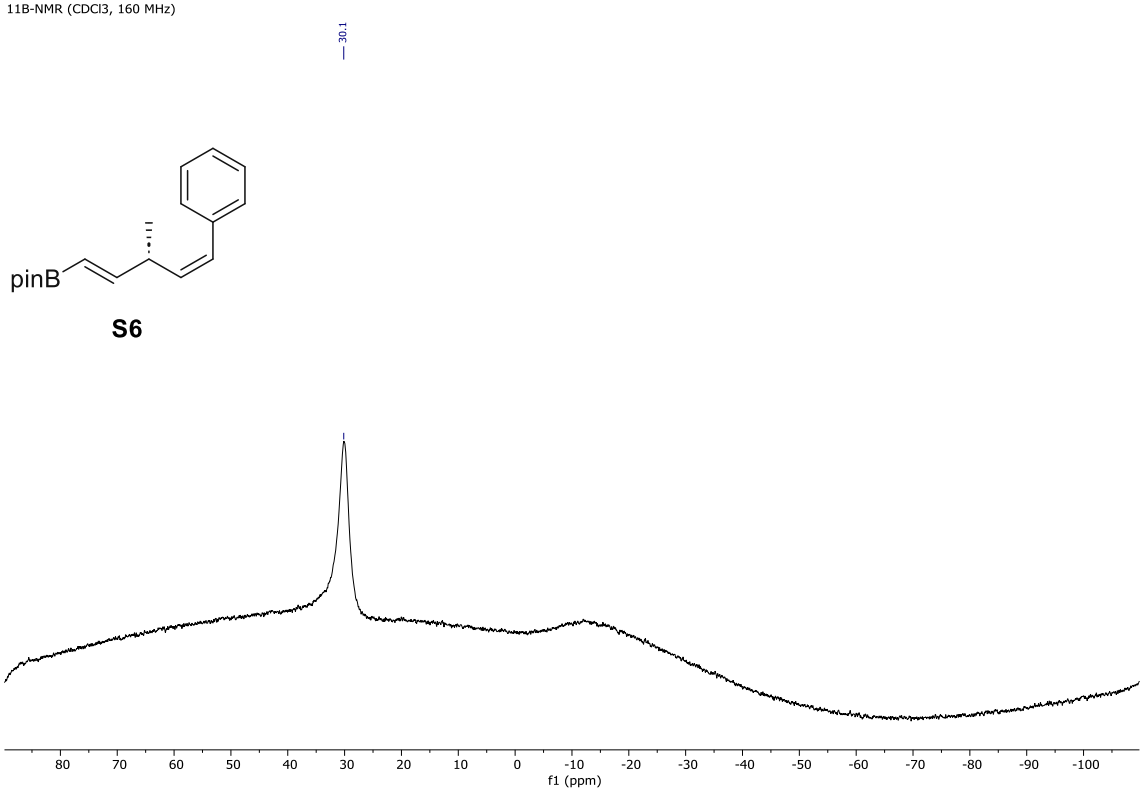

S6

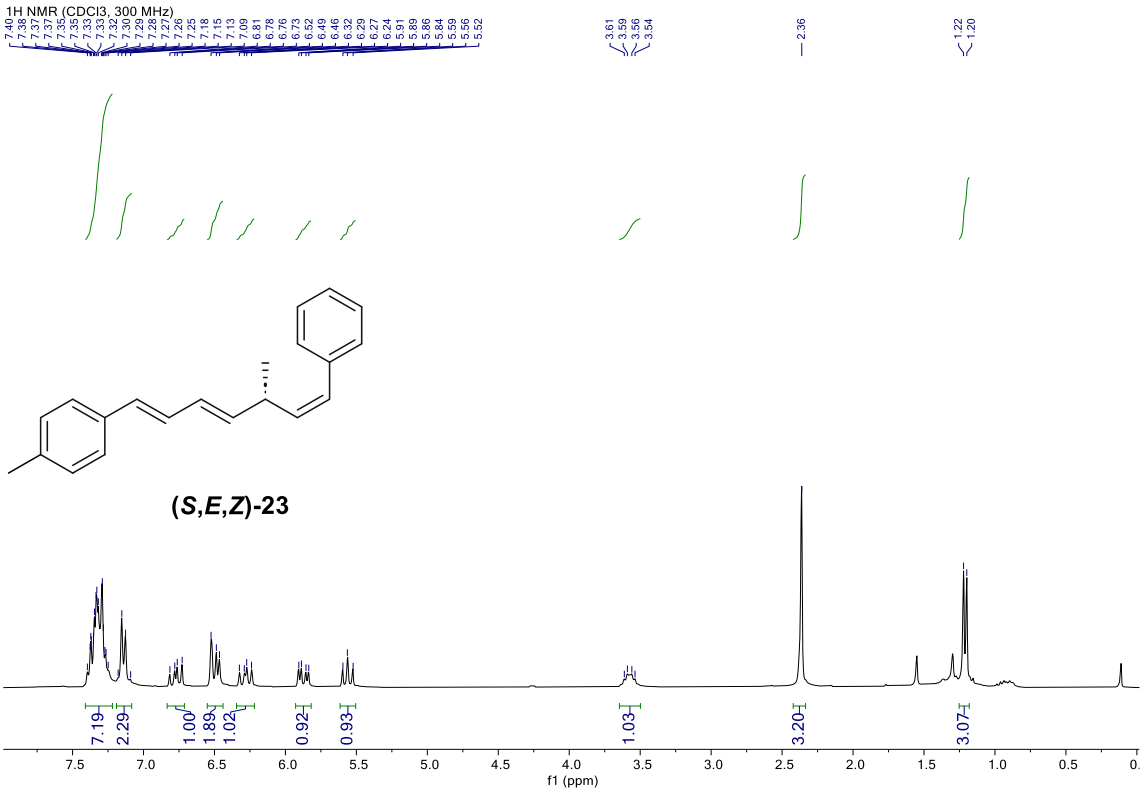
1H NMR (CDCl3, 300 MHz)
(S,E,Z)-23
7.19
2.29
1.00
1.89
1.02
0.92
0.93
1.03
3.20
3.07
f1 (ppm)

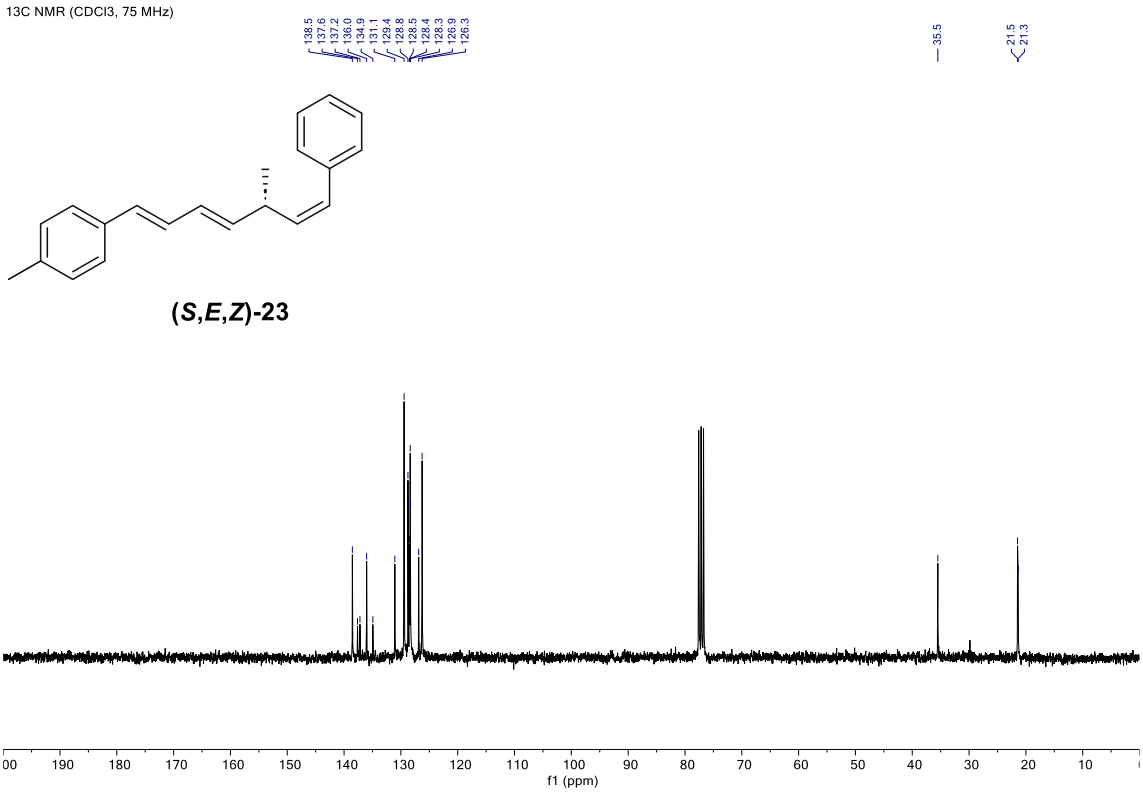
13C NMR (CDCl3, 75 MHz)
(S,E,Z)-23
f1 (ppm)

1H NMR (CDCl3, 300 MHz)

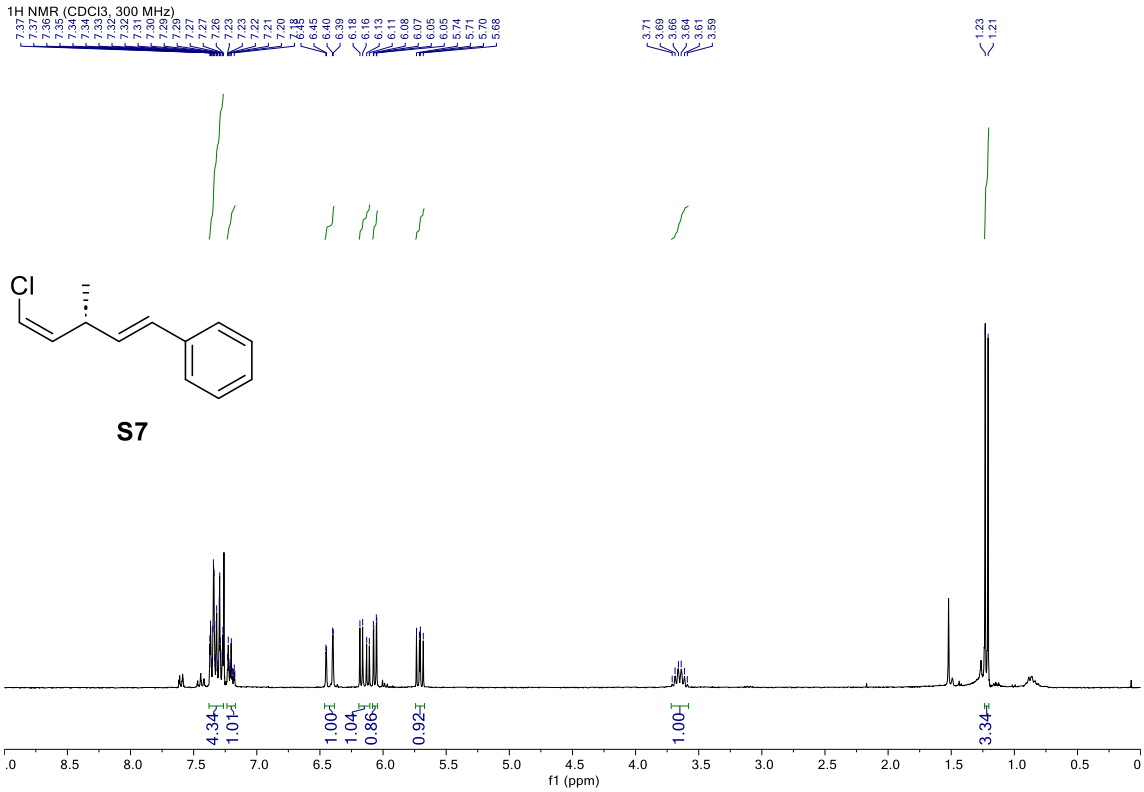

S7

13C NMR (CDCl3, 75 MHz)

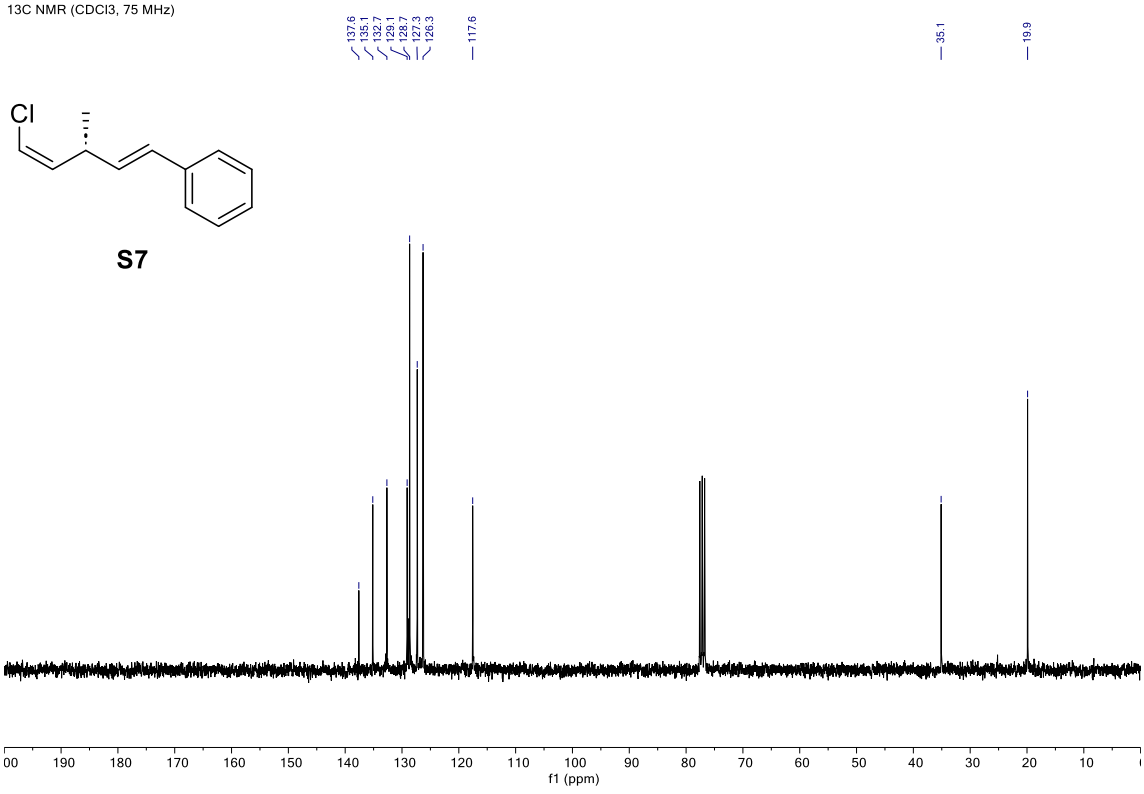

S7

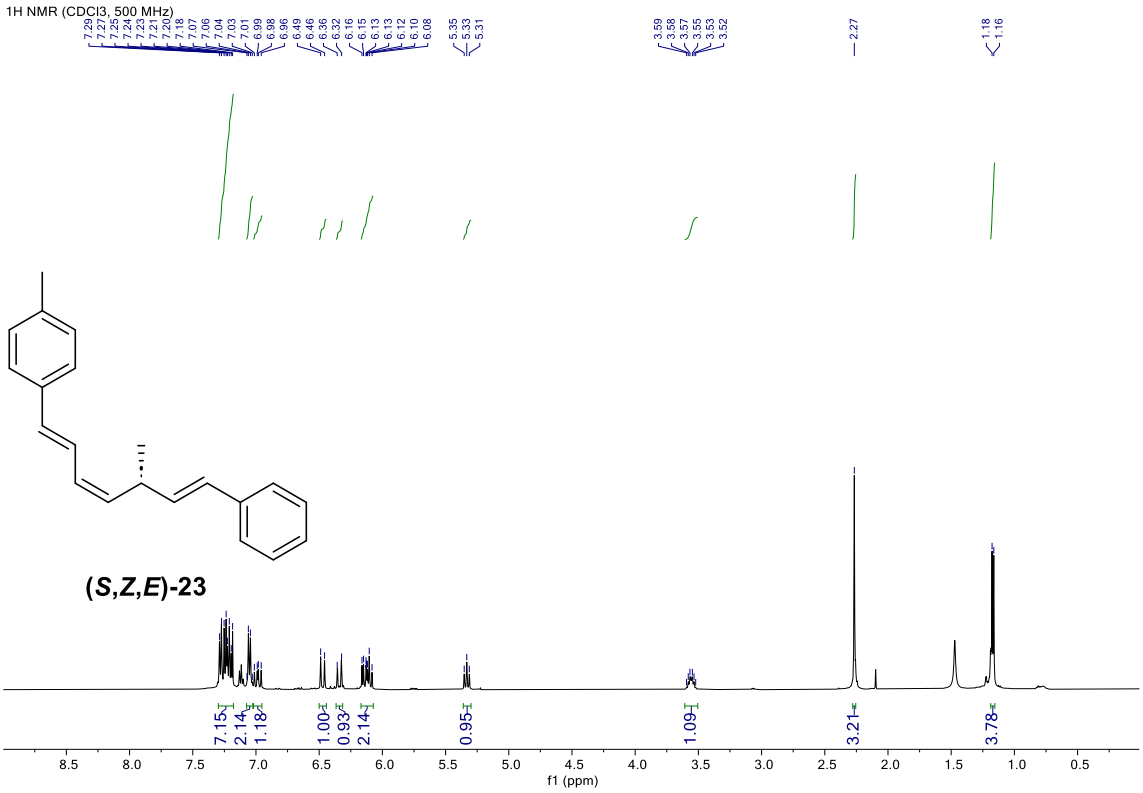

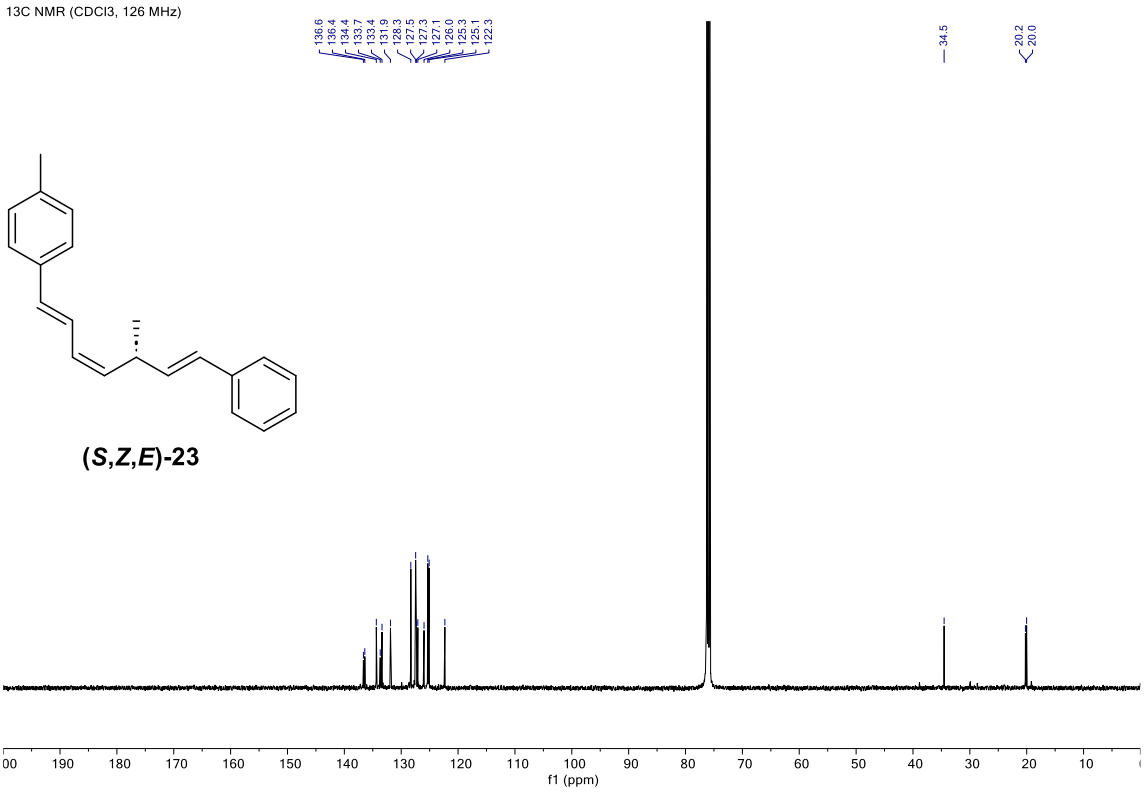

1H NMR (CDCl3, 300 MHz)

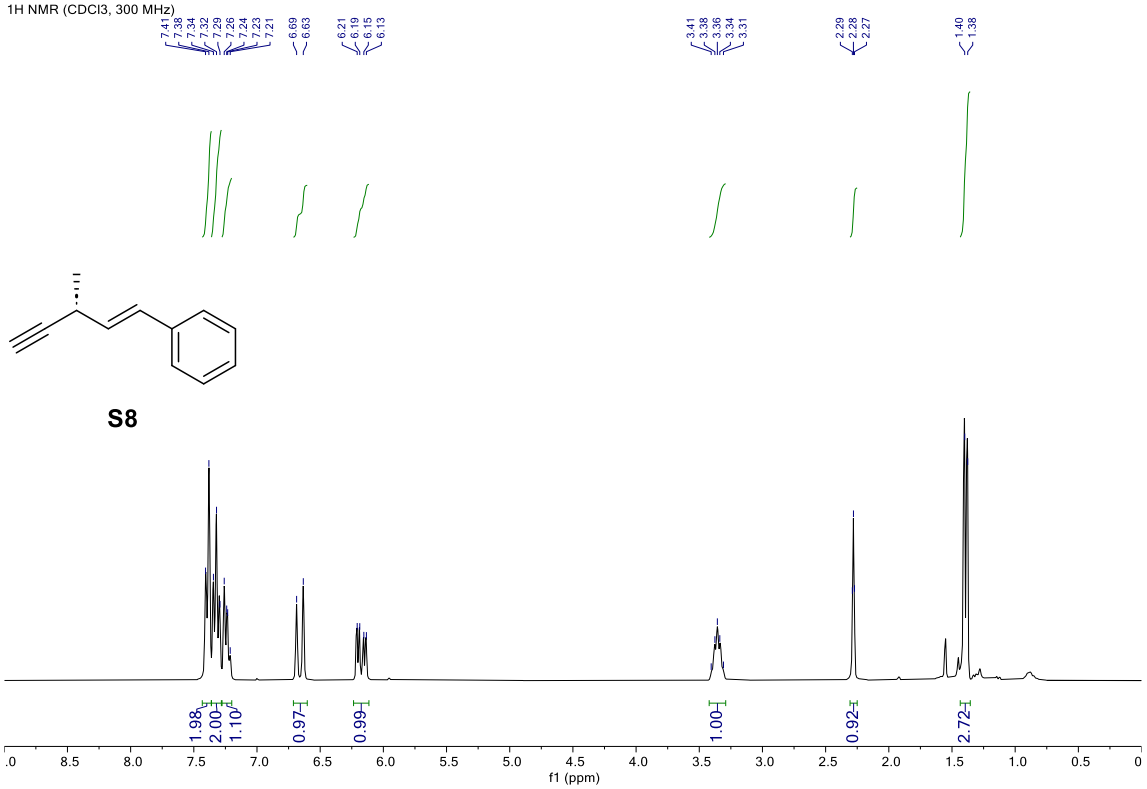

S8

13C NMR (CDCl3, 75 MHz)

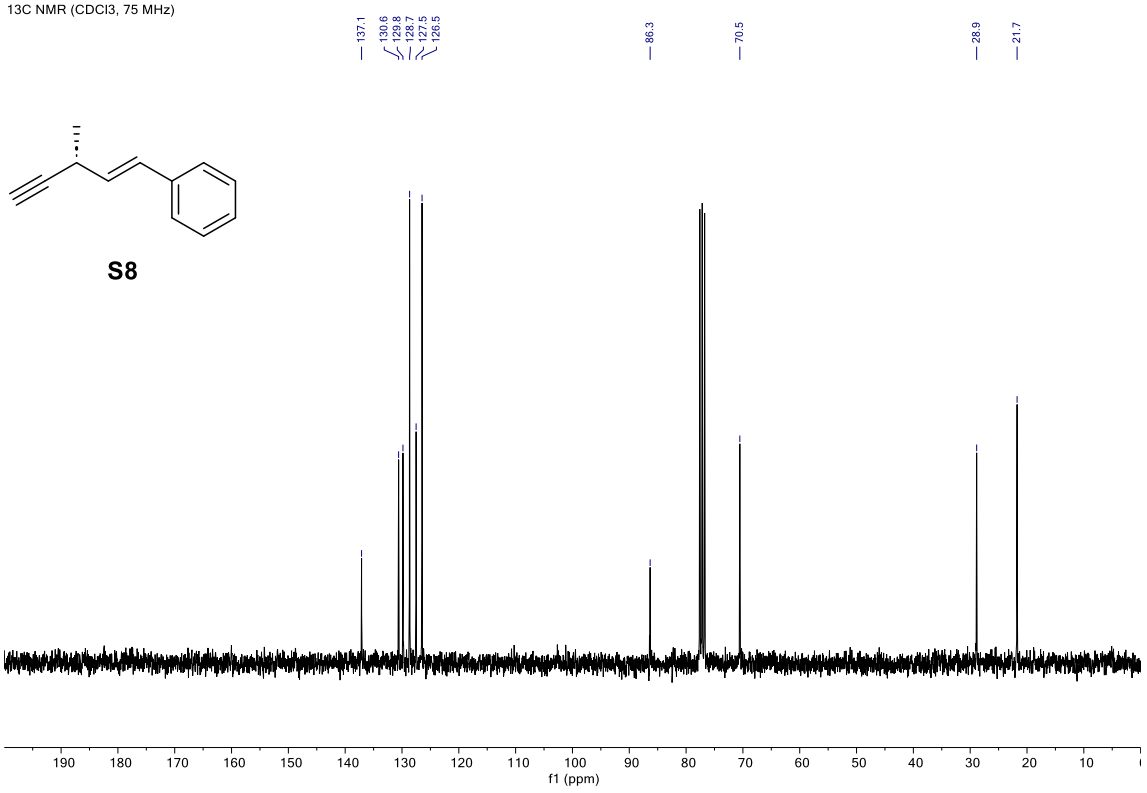

S8

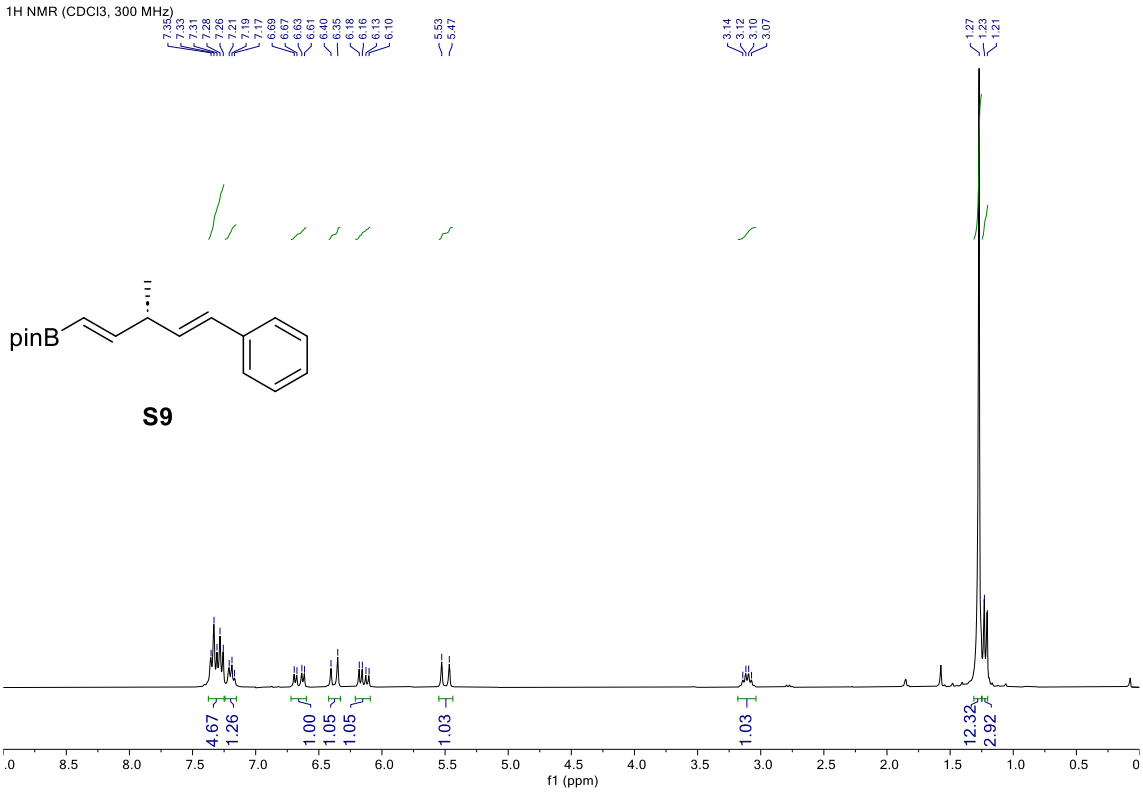
1H NMR (CDCl3, 300 MHz)
7.35
7.33
7.31
7.28
7.26
7.21
7.19
7.17
6.69
6.67
6.63
6.61
6.40
6.35
6.18
6.16
6.13
6.10
5.53
5.47
3.14
3.12
3.10
3.07
1.27
1.23
1.21
pinB
S9
4.67
1.26
1.00
1.05
1.05
1.03
1.03
12.32
2.92
f1 (ppm)

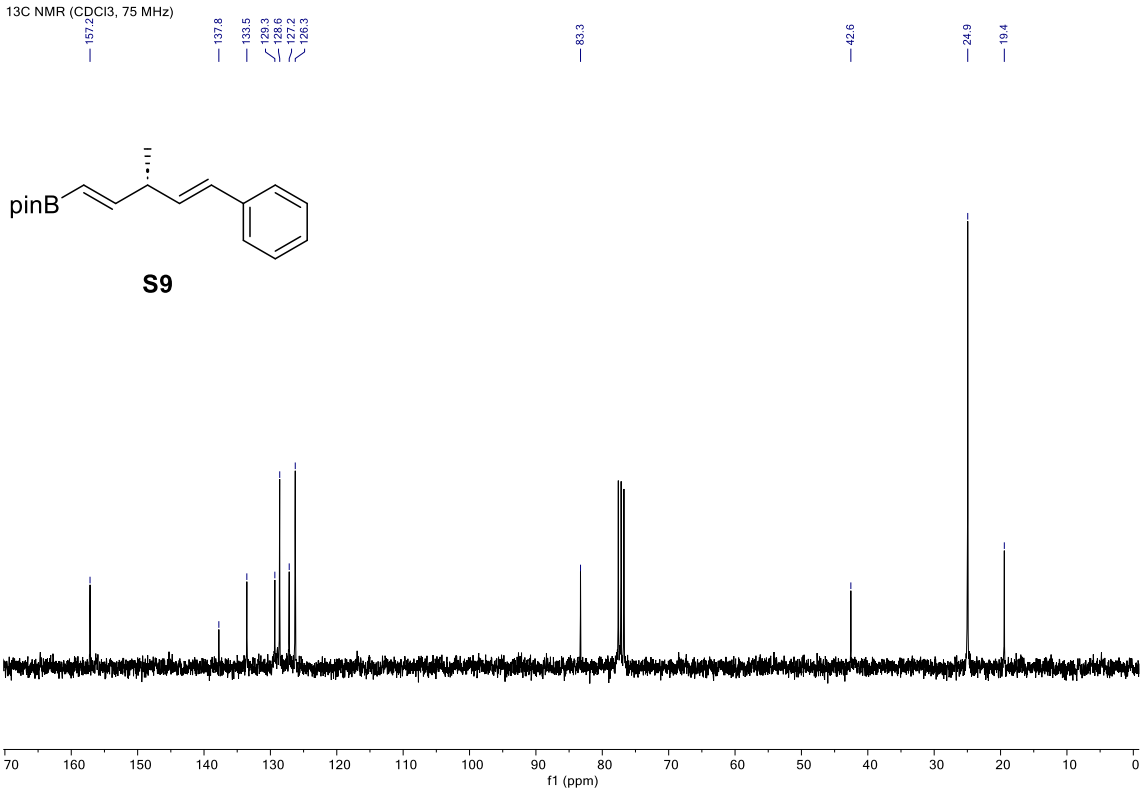
13C NMR (CDCl3, 75 MHz)
157.2
137.8
133.5
129.3
128.6
127.2
126.3
83.3
42.6
24.9
19.4
pinB
S9
f1 (ppm)

11B NMR (CDCl3, 160 MHz)

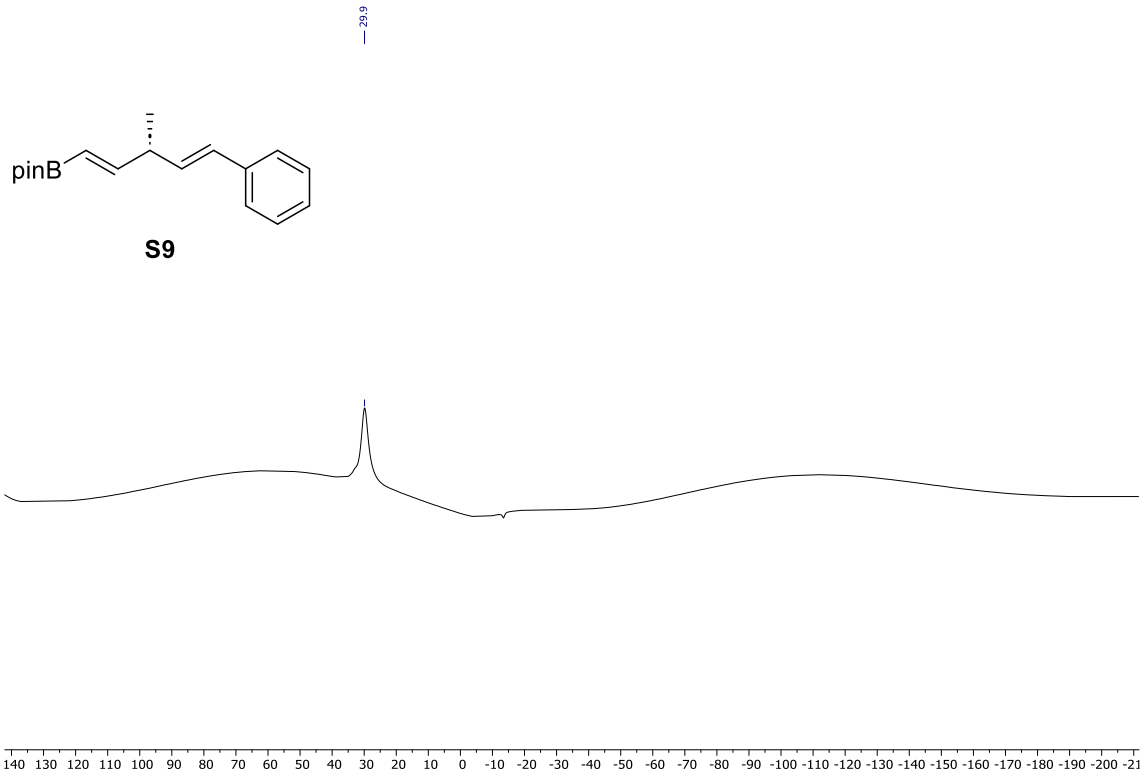

S9

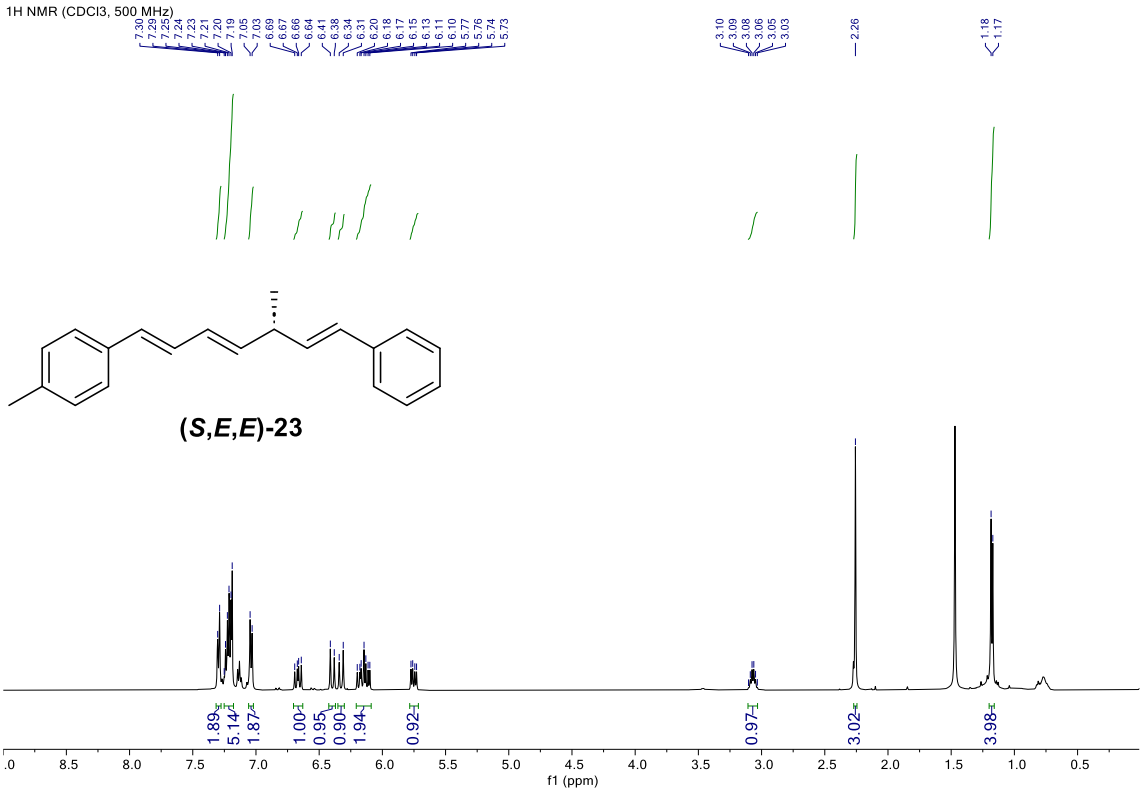
1H NMR (CDCl3, 500 MHz)
7.30
7.29
7.25
7.24
7.23
7.21
7.20
7.19
7.05
7.03
6.69
6.67
6.66
6.64
6.41
6.38
6.34
6.31
6.20
6.18
6.17
6.15
6.13
6.11
6.10
5.77
5.76
5.74
5.73
3.10
3.09
3.08
3.06
3.05
3.03
2.26
1.18
1.17
(S,E,E)-23
1.89
5.14
1.87
1.00
0.95
0.90
1.94
0.92
0.97
3.02
3.98
f1 (ppm)

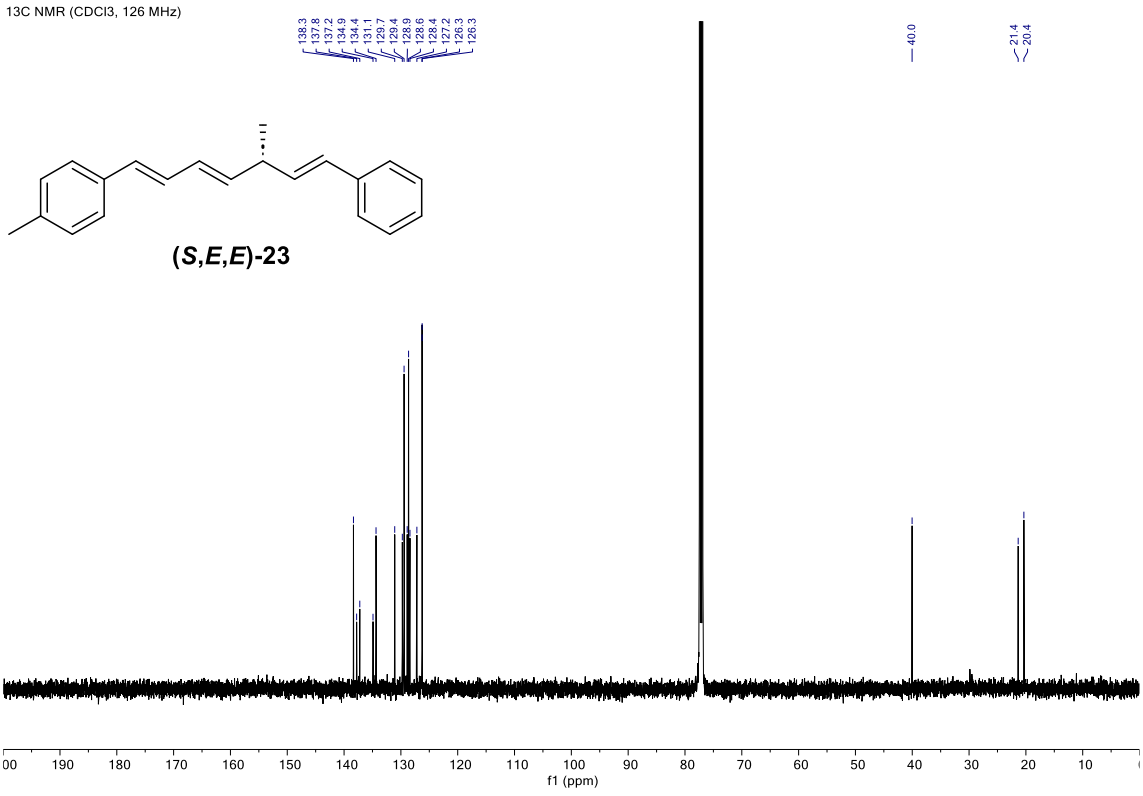
13C NMR (CDCl3, 126 MHz)
138.3
137.8
137.2
134.9
134.4
131.1
129.7
129.4
128.9
128.6
128.4
127.2
126.3
126.3
40.0
21.4
20.4
(S,E,E)-23
f1 (ppm)

1H NMR (CDCl3, 300 MHz)

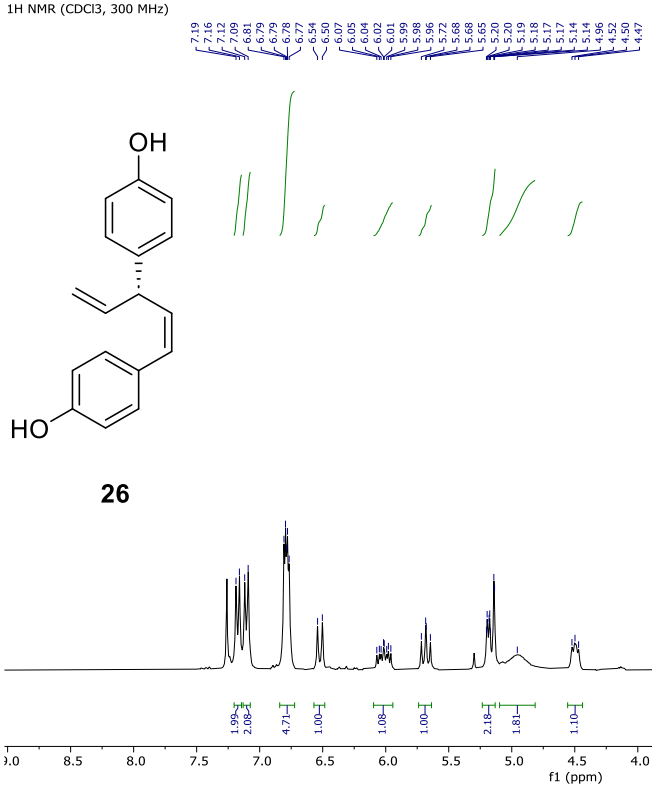

26

13C NMR (CDCl3, 75 MHz)

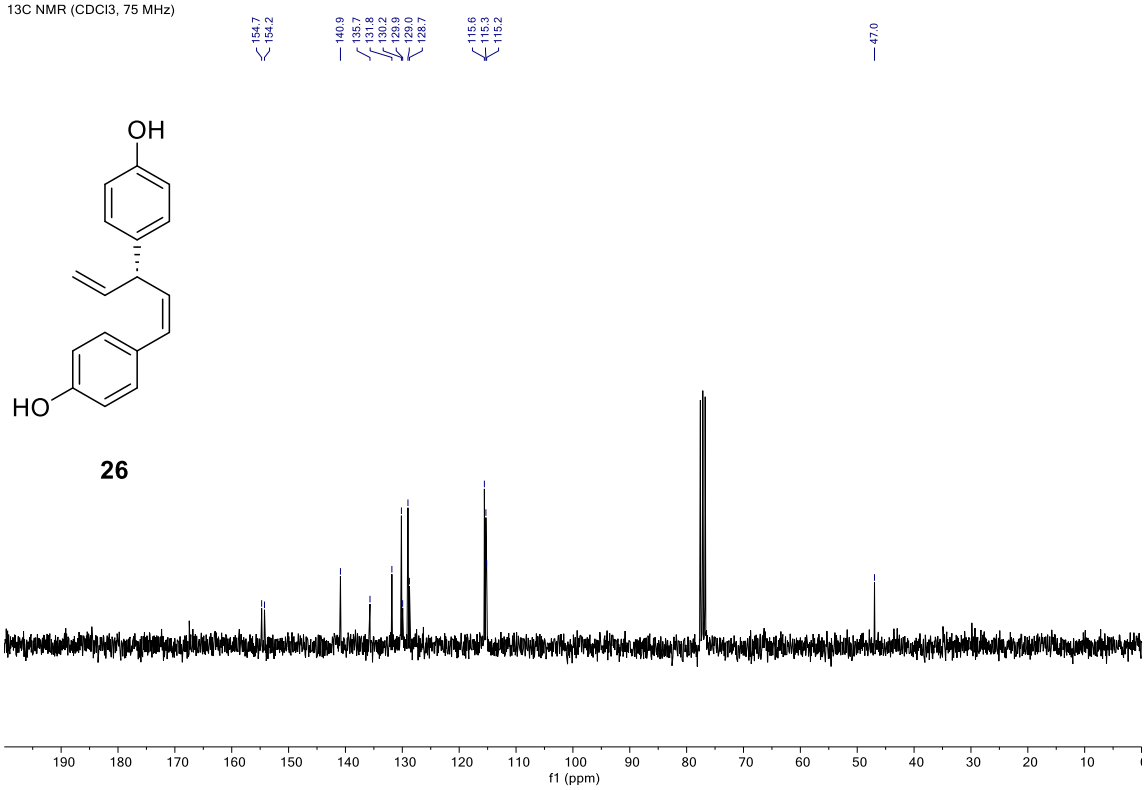

26

1H NMR (CDCl3, 300 MHz)

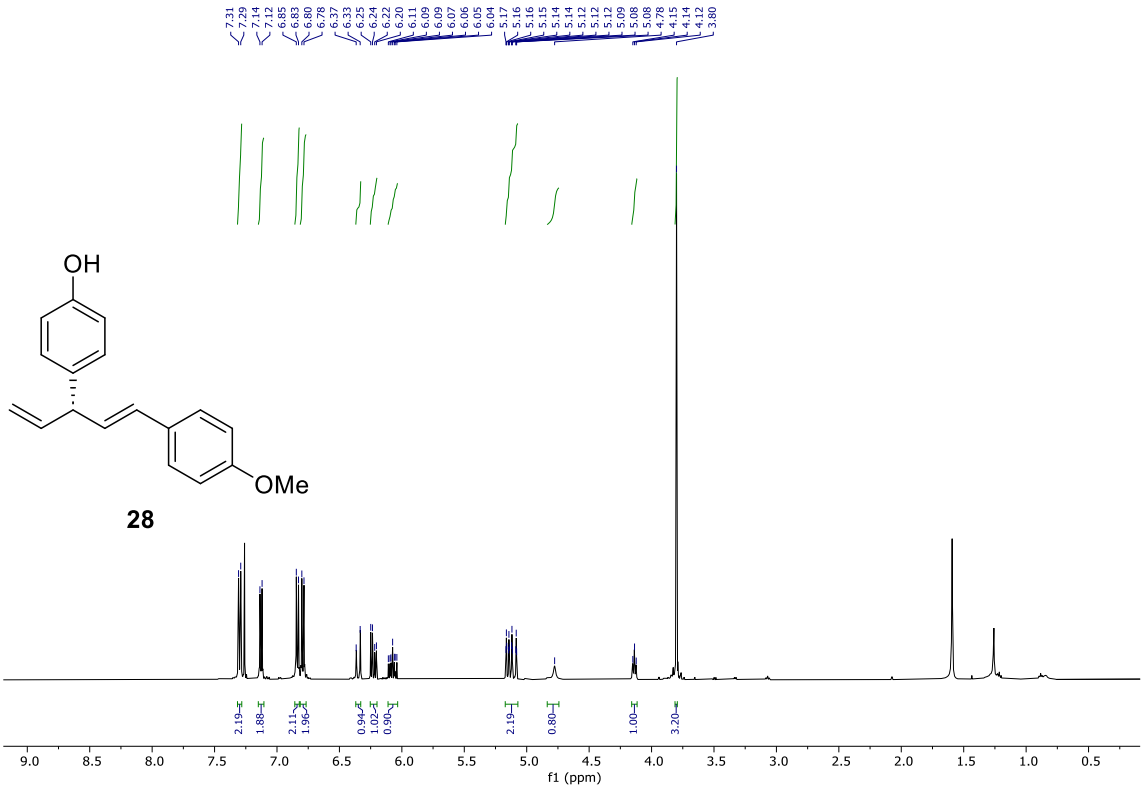

13C NMR (CDCl3, 126 MHz)

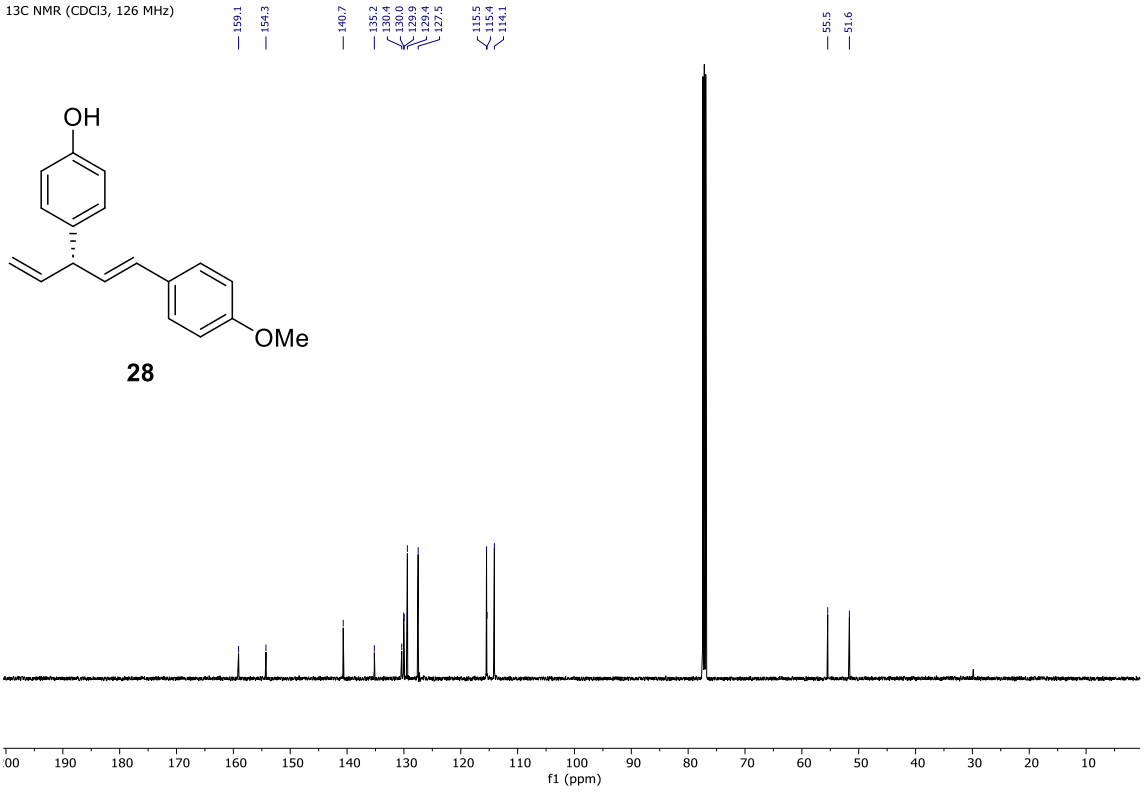

1H NMR (CDCl3, 500 MHz)

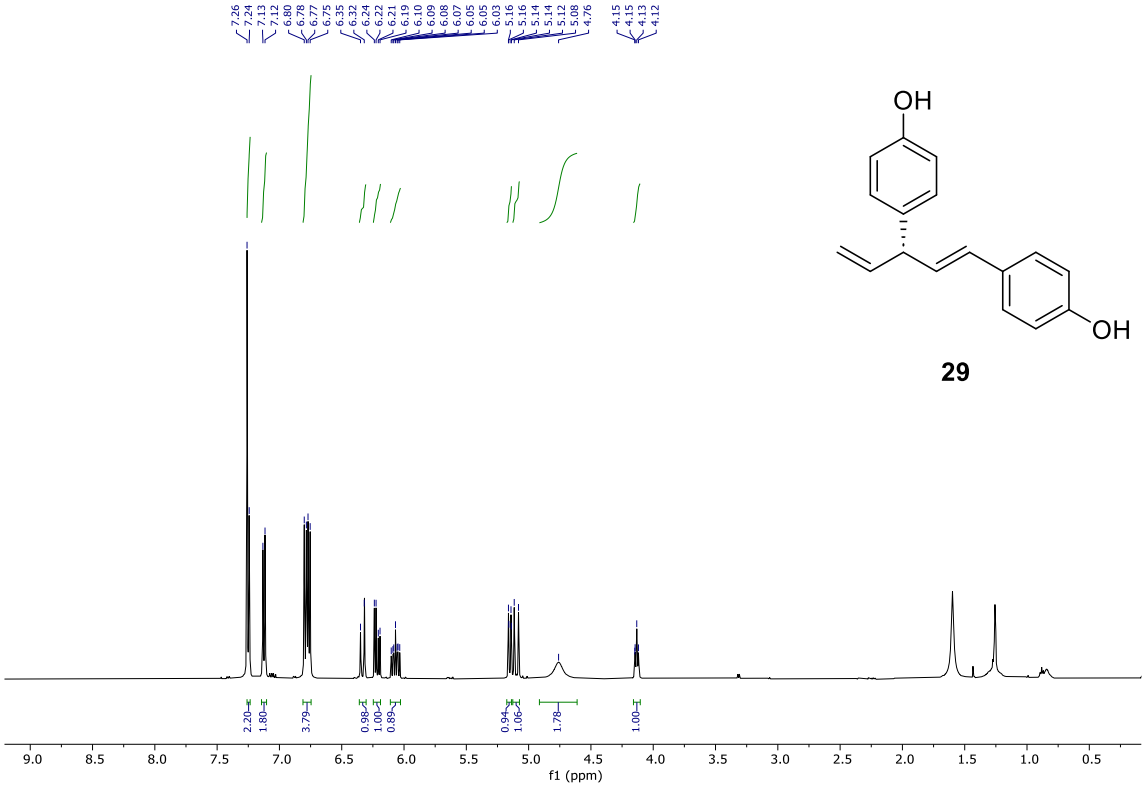

29

13C NMR (CDCl3, 126 MHz)

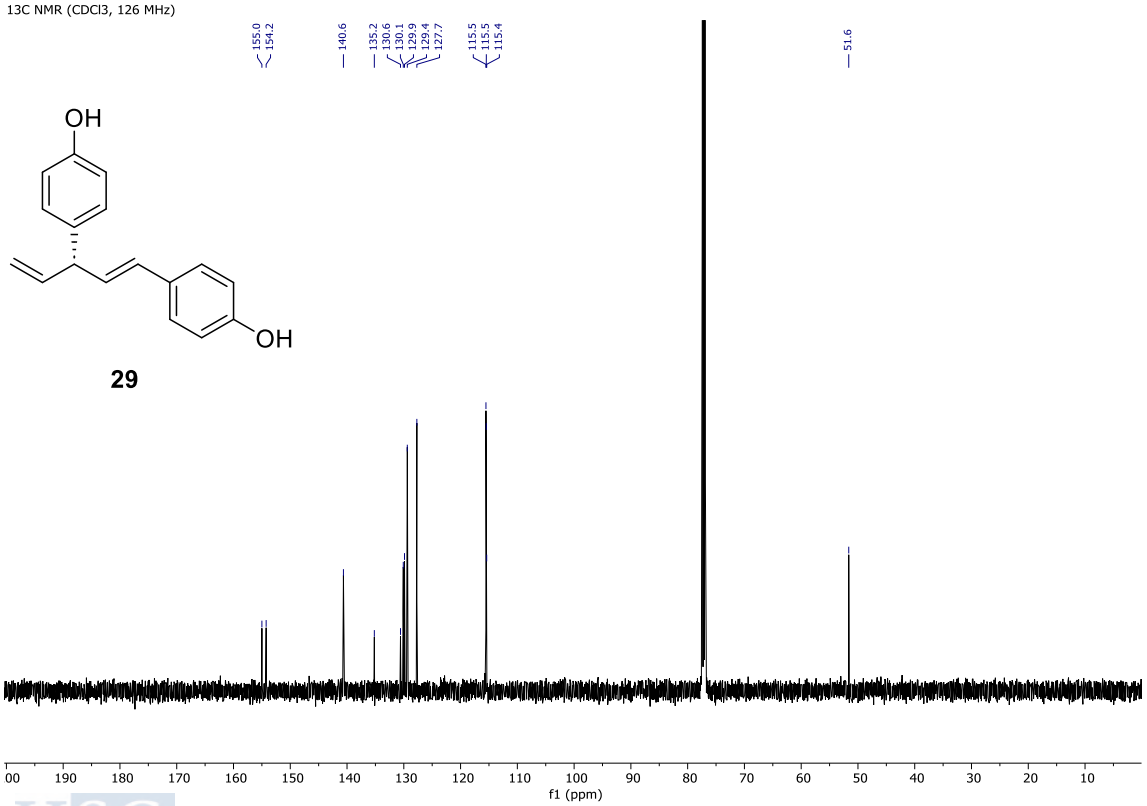

29

1H NMR (CDCl3, 300 MHz)

31

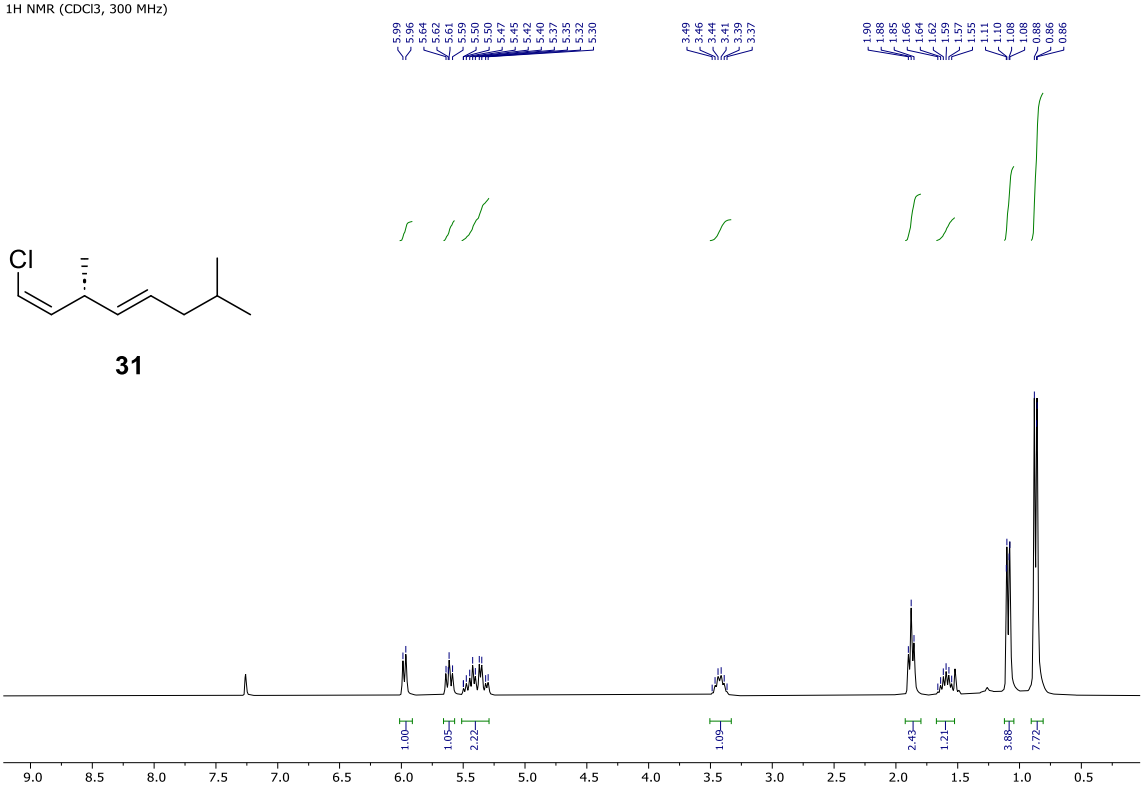

13C NMR (CDCl3, 75 MHz)

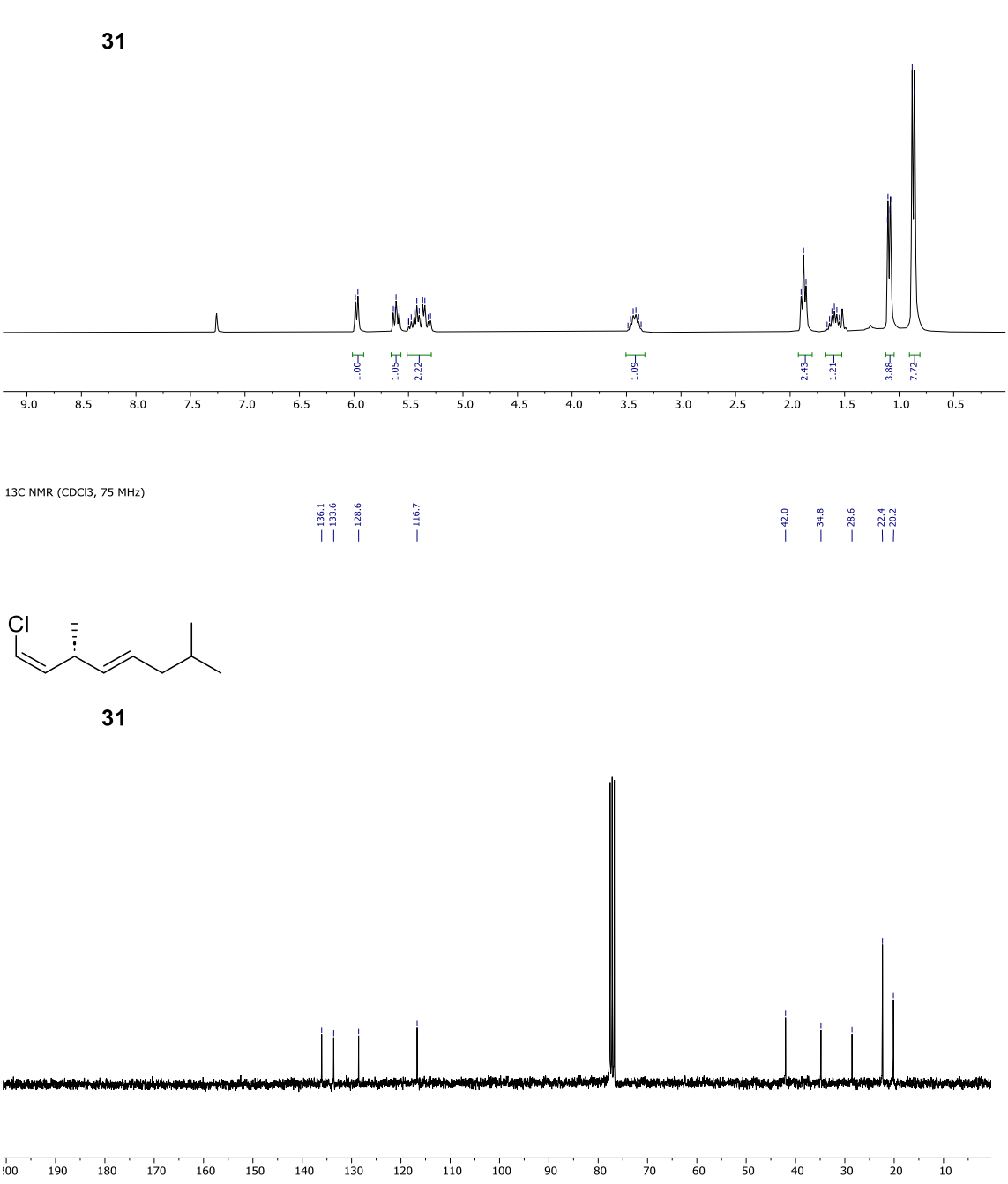

31

1H NMR (CDCl3, 500 MHz)

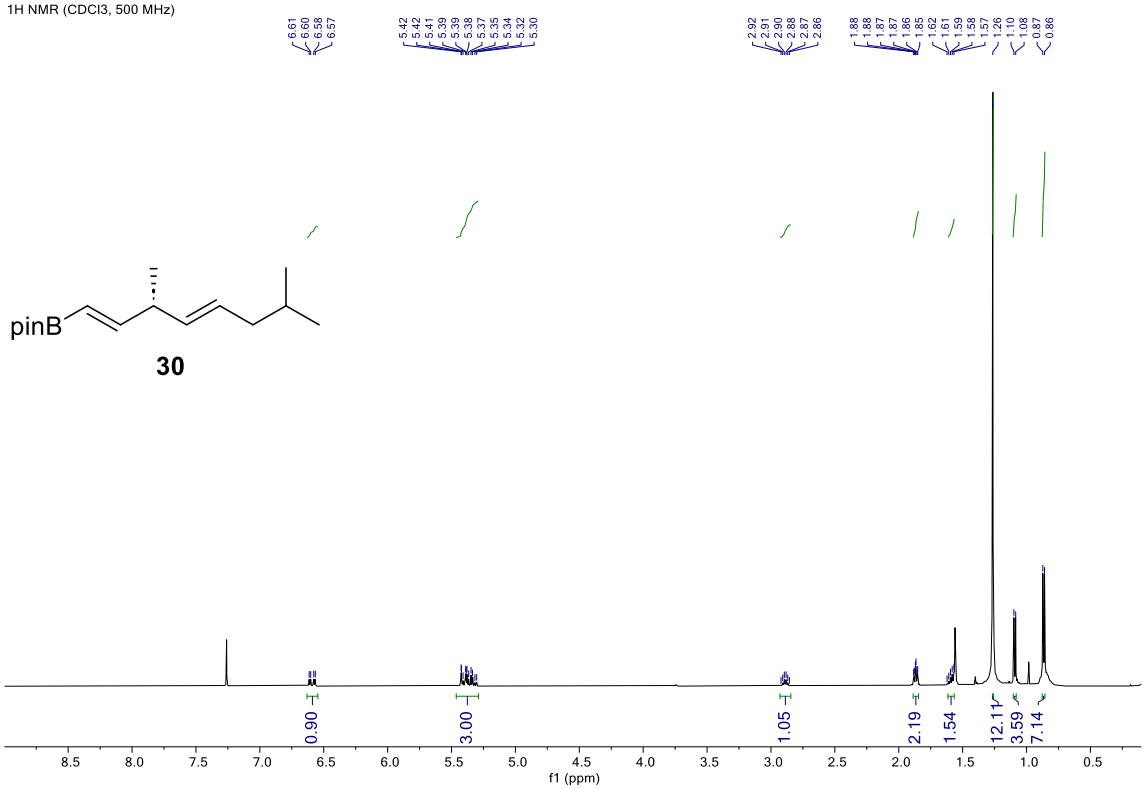

13C NMR (CDCl3, 126 MHz)

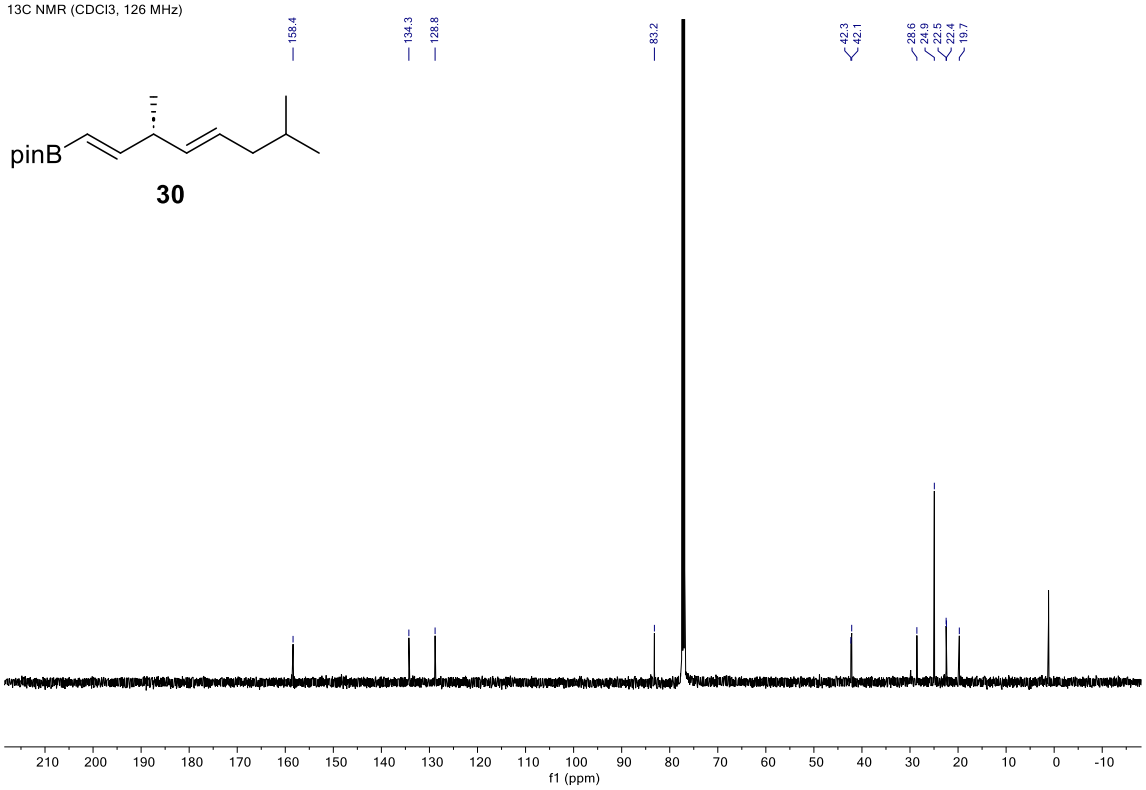

11B NMR (CDCl3, 160 MHz)

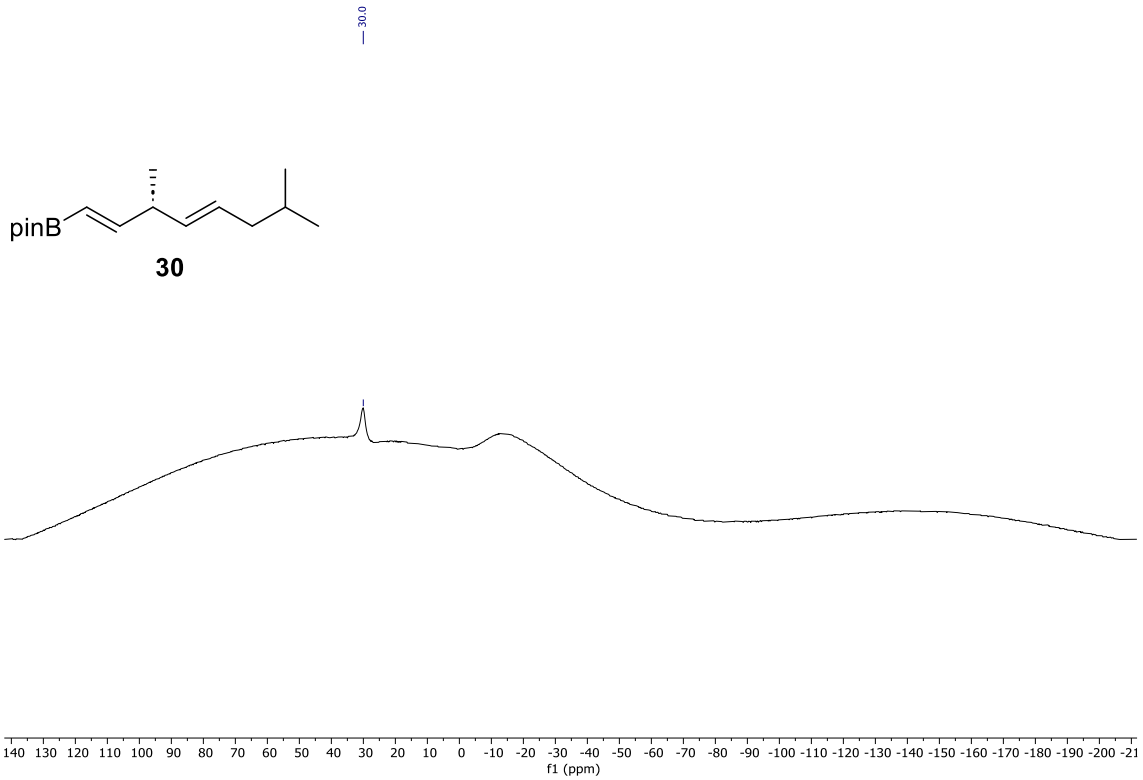

30

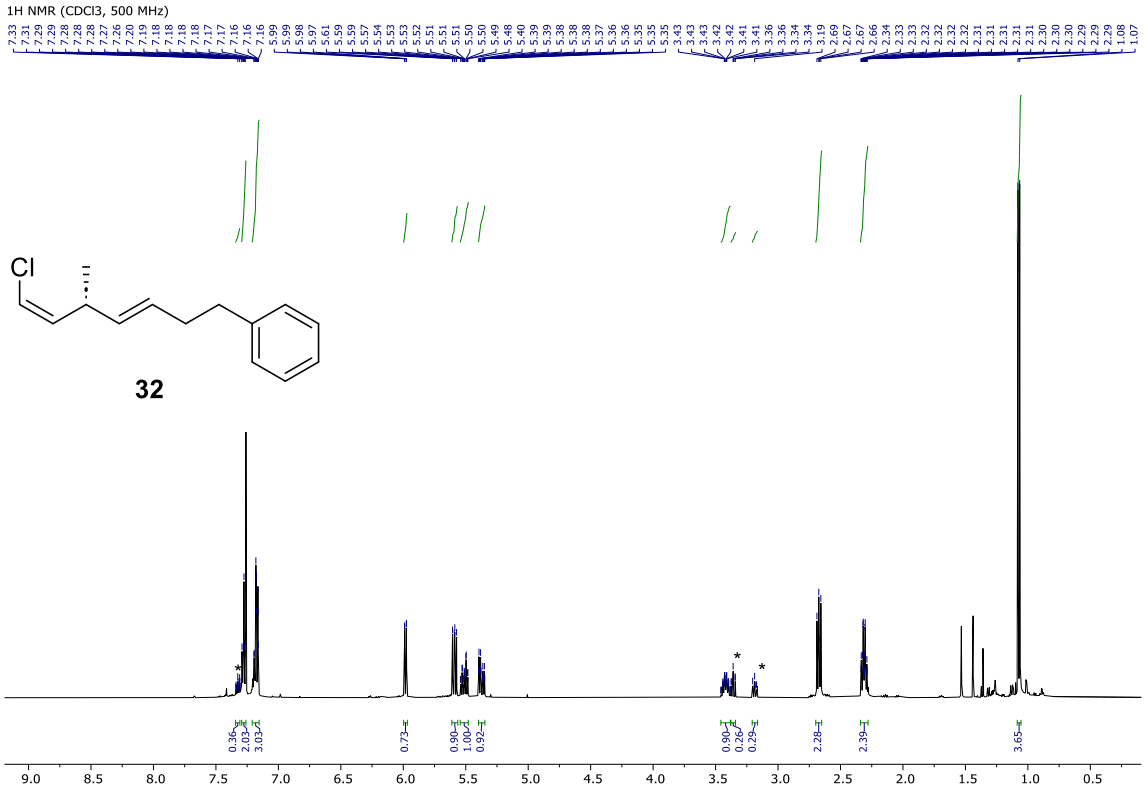

Marked signals (*) correspond to unreacted phenethyl iodide

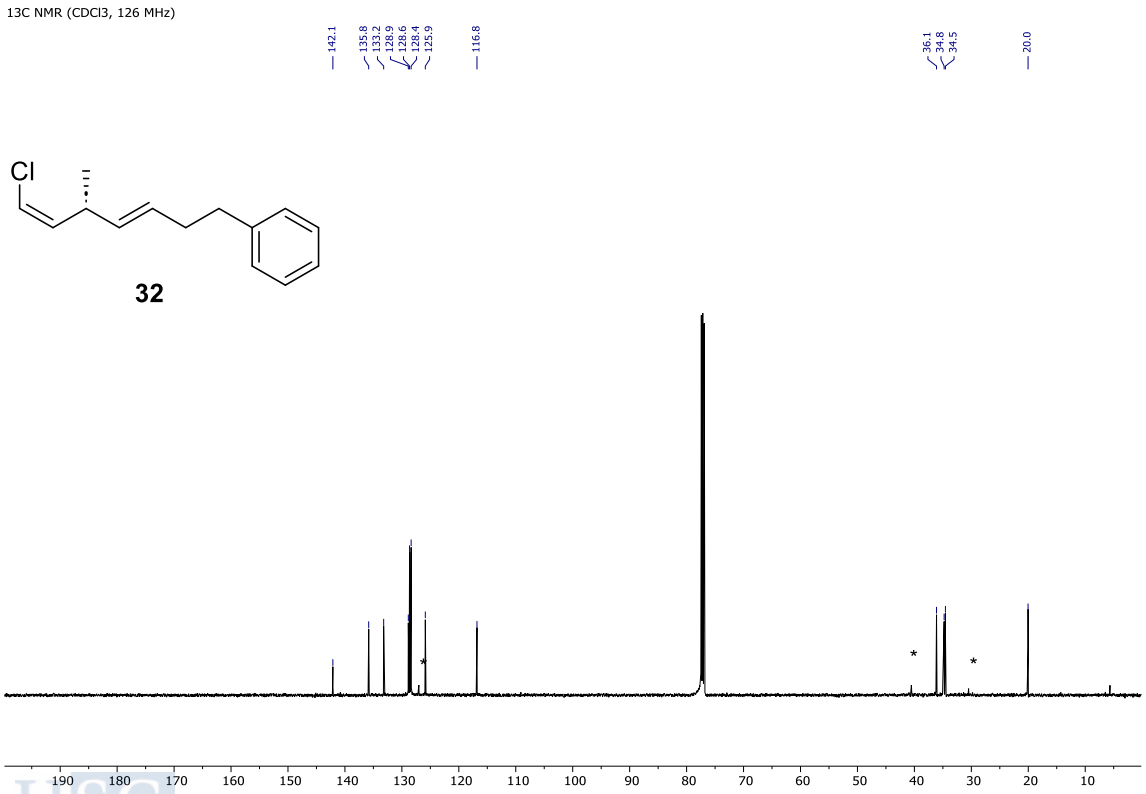

Marked signals (*) correspond to unreacted phenethyl iodide

1H NMR (CDCl3, 300 MHz)

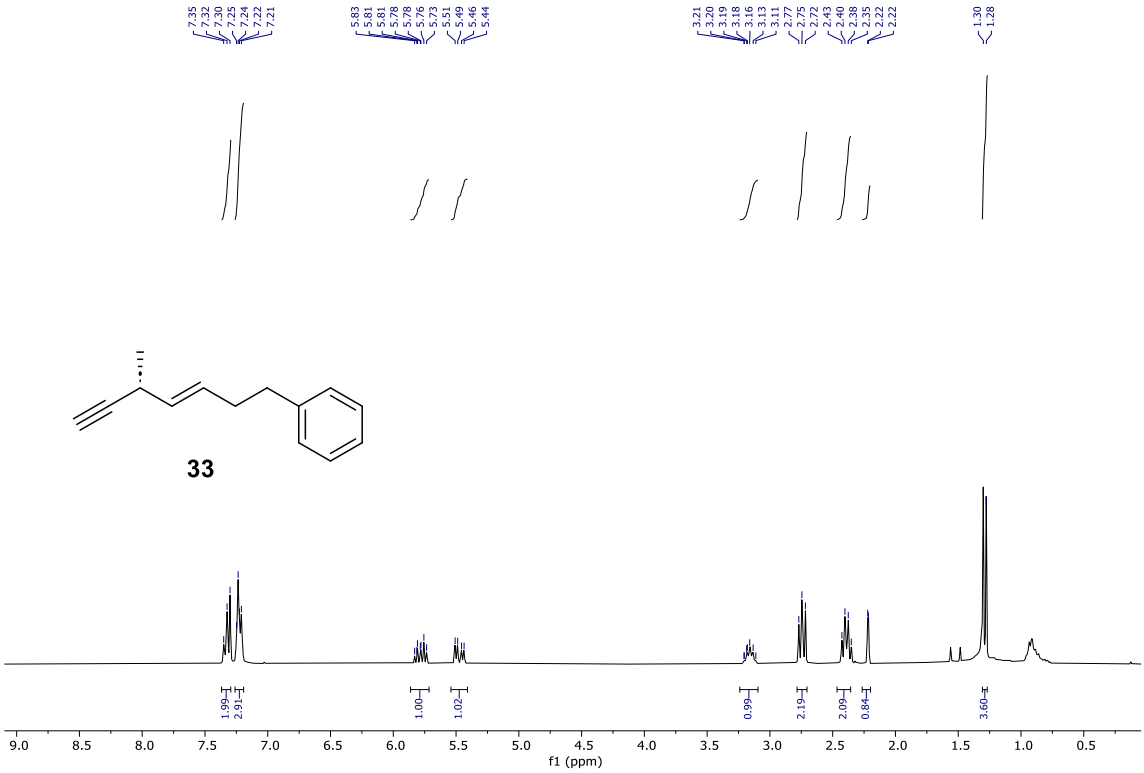

13C NMR (CDCl3, 75 MHz)

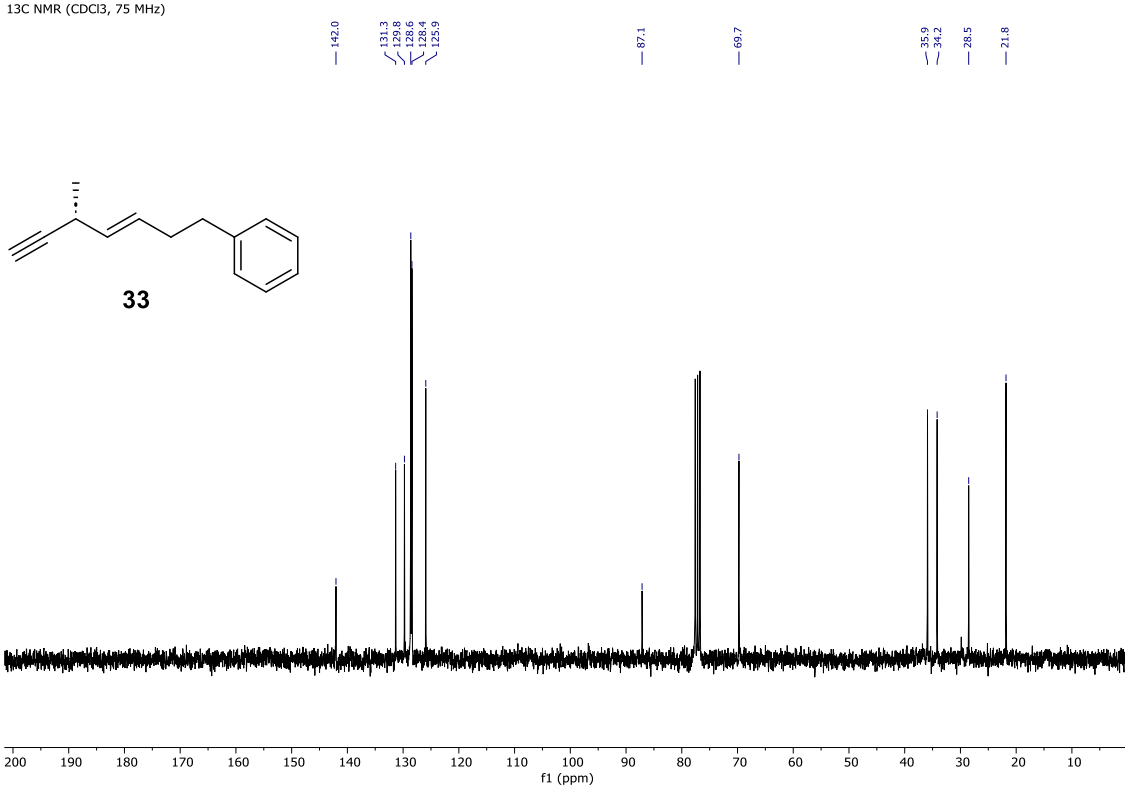

1H NMR (CDCl3, 300 MHz)

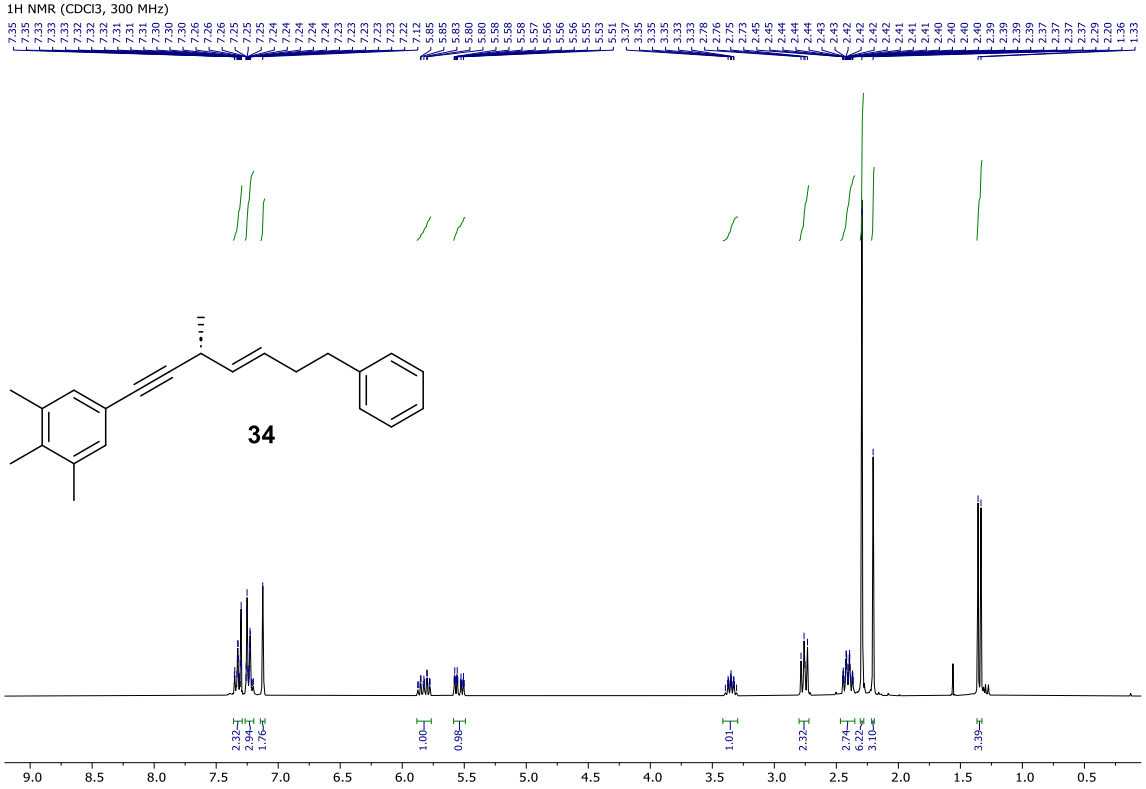

13C NMR (CDCl3, 75 MHz)

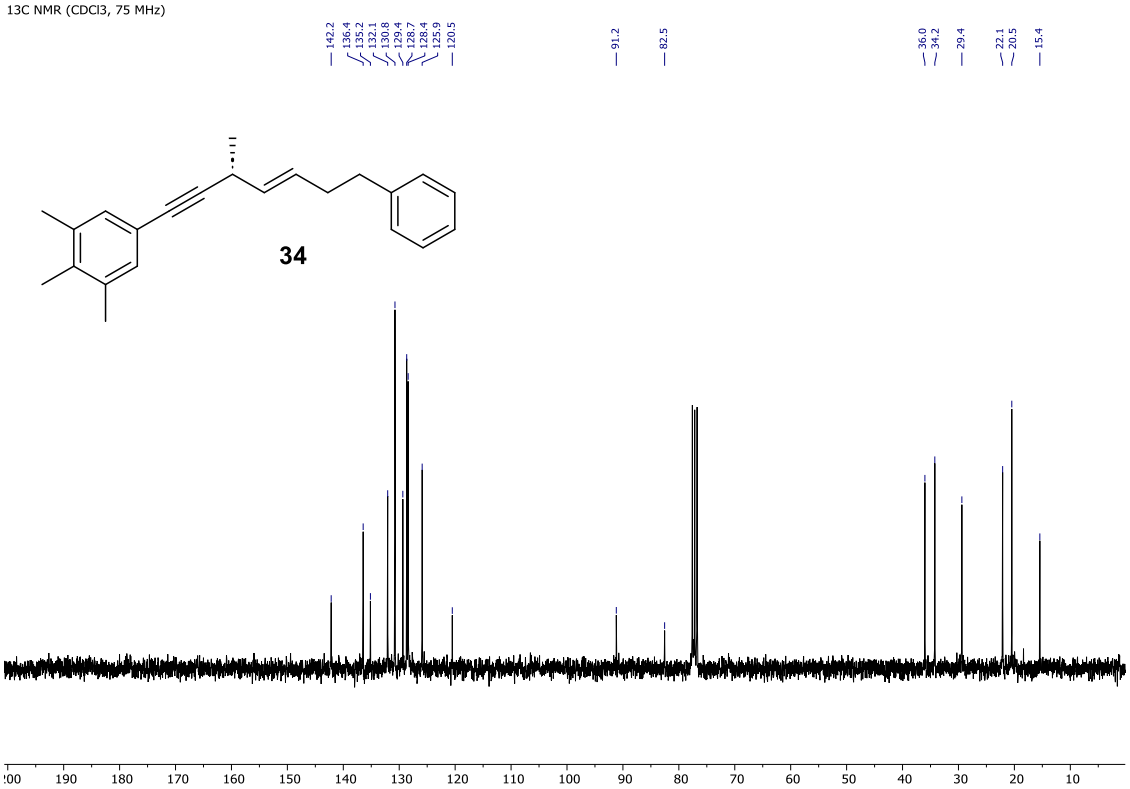

1H NMR (CDCl3, 300 MHz)

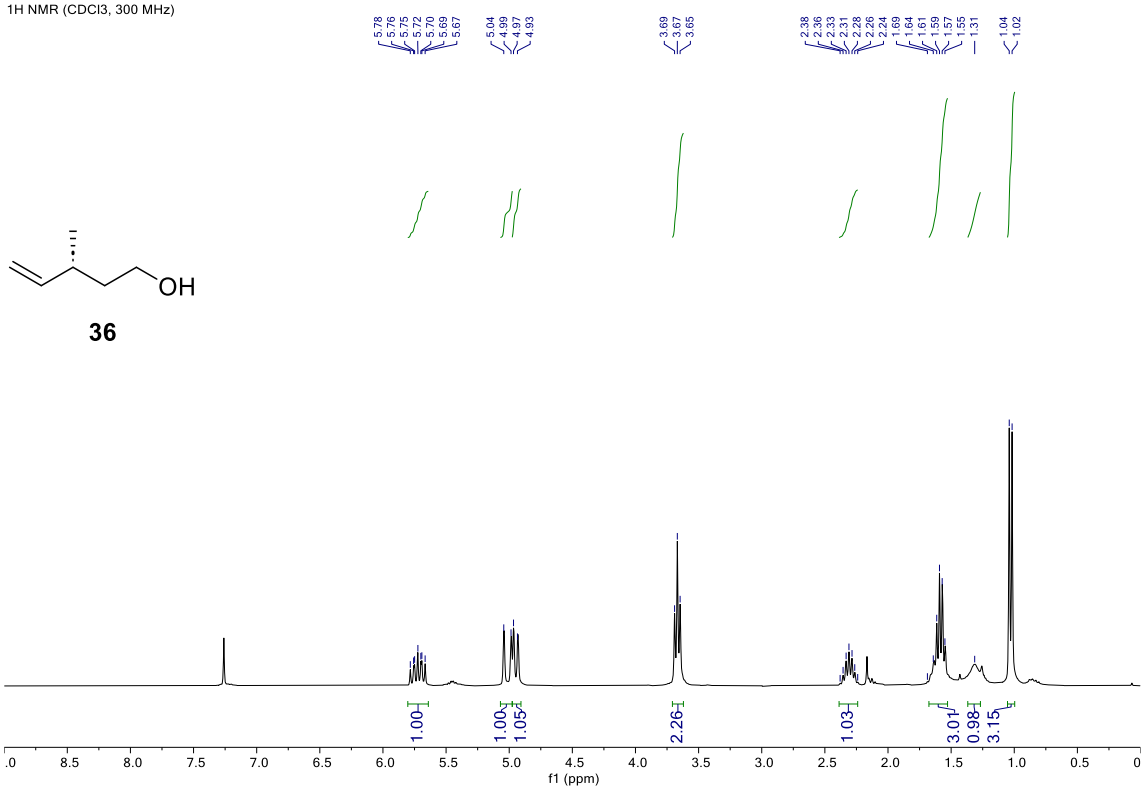

36

13C NMR (CDCl3, 75 MHz)

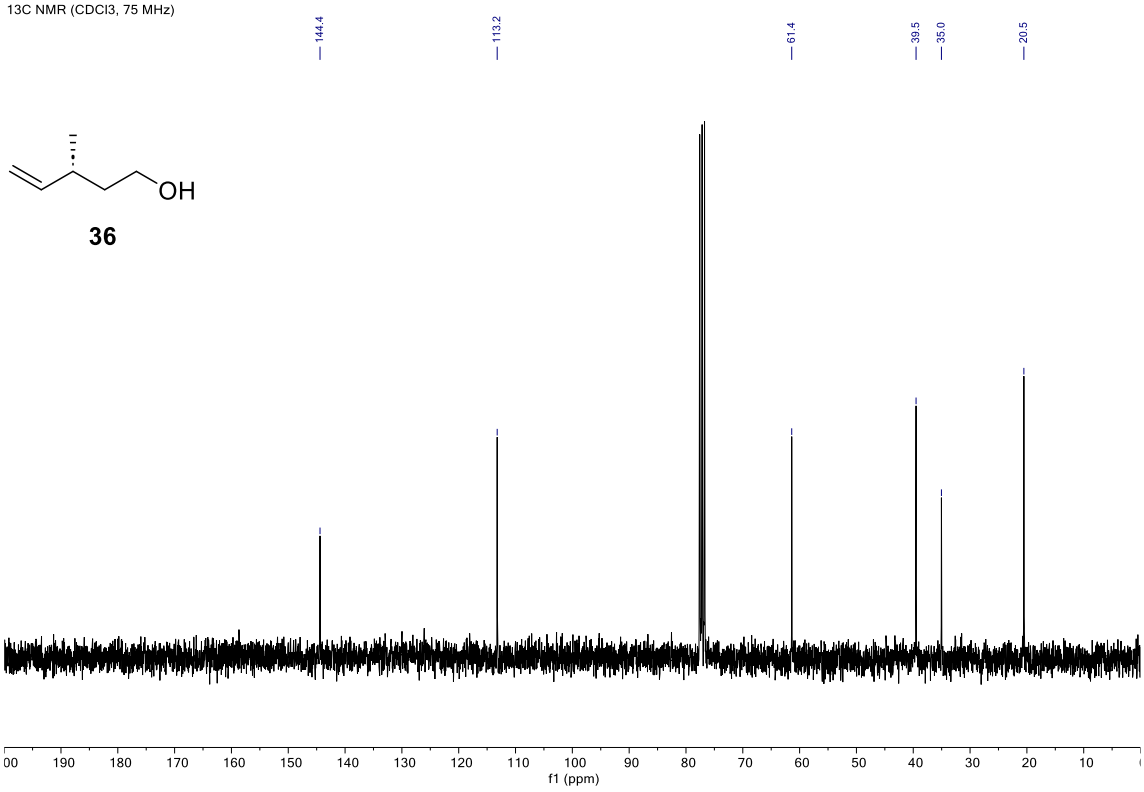

36

5.3.5 Computational Details

Calculations were performed at DFT level of theory using Gaussian16 software[148]. The structures of all the intermediates and transition states were optimized using the ωB97XD functional.[149]

Structures from sections 3.1.2 were optimized using basis set BS3. BS3 includes the 6-31G(d,p) basis set for the main group elements[150-157] and the scalar relativistic Stuttgart-Dresden SDD pseudopotential and its associated double-ζ basis set,[170] complemented with a set of *f* polarization functions,[171] for the copper atom.

Frequency calculations were performed at the same level to evaluate the zero-point vibrational energy and thermal corrections at 298 K and to confirm the nature of the stationary points, yielding one imaginary frequency for the transition states and none for the minima. It was confirmed that transition states connect with the corresponding intermediates by usual intrinsic reaction coordinate (IRC) calculations and subsequent optimization to minima.

Single-point energies for structures from sections 3.1.2 were calculated using the wB97XD functional within the self-consistent reaction field (SCRF) using the SMD model (toluene)[158] and a larger basis set BS4. BS4 consists in the *def2*-TZVP basis set for the main group elements and the quadruple-ζ *def2*-QZVP basis set for Cu.[159-160] The final Gibbs energies were obtained adding the thermal and entropic corrections computed at the BS1 level to the electronic energy computed at BS4 level. The reaction profiles were built up in terms of ΔG_{sol}.

All 3D chemical structures were prepared using CYLview20.[229]

5.4 $FeCl_3$ PHOTORREDOX HAT CATALYZED DIRECT Csp^3-Csp^3 ALLYLATION OF ETHANE

5.4.1 List of Starting Materials

Allylic chlorides (Figure 5.2.4) **1**,[244] **53-54**,[211] **55**,[244] **57**,[211] **56**,[245] **59**,[211] **60**,[211] **65**[244] and **64**[211] were prepared according to literature procedures. Allylic chlorides **74** and **75** were purchased from Aldrich Chemical Co. Ltd.

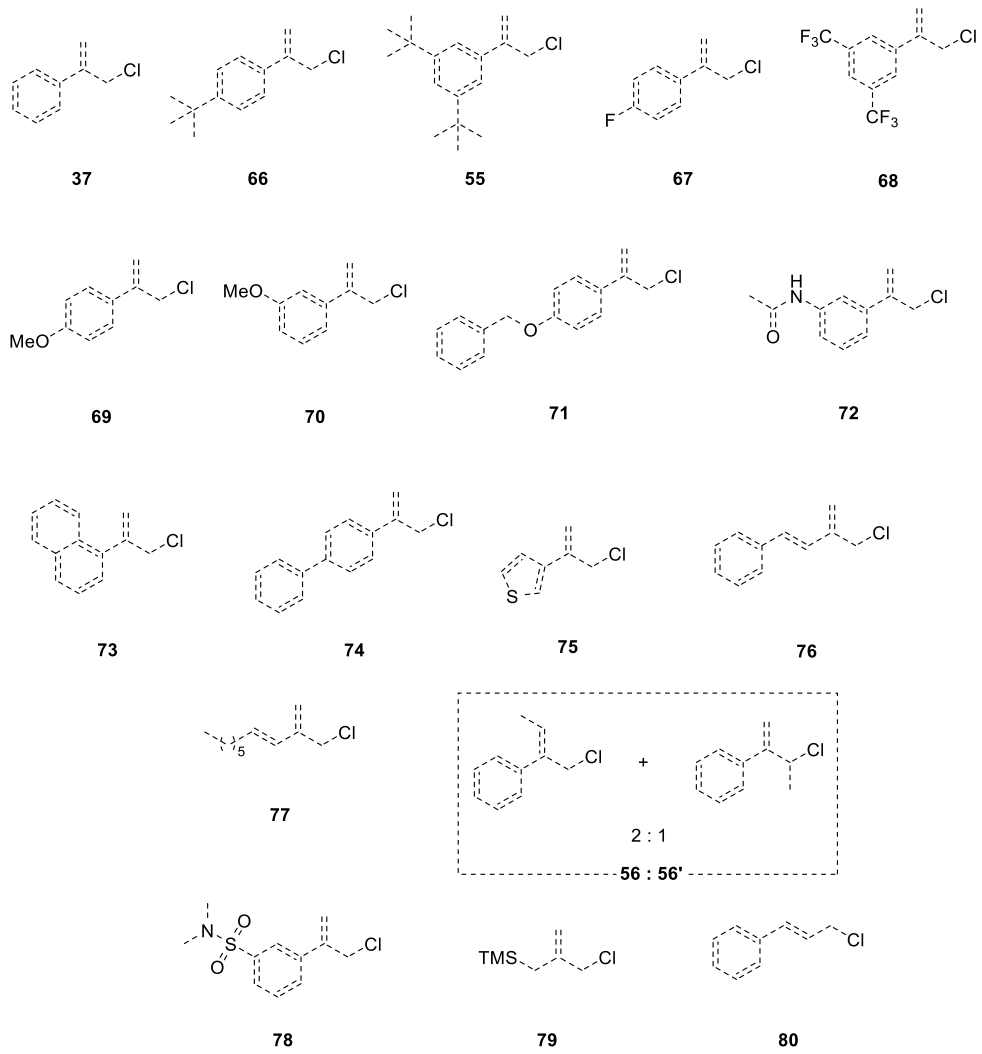

Figure 5.4.1. List of allylic chlorides used in the $FeCl_3$ photorredox HAT catalyzed direct Csp3-Csp3 allylation of ethane

5.4.2 General Procedures

5.4.2.1 General procedures for the synthesis of starting materials involved in $FeCl_3$ photorredox HAT catalyzed direct Csp^3-Csp^3 allylation of ethane (General procedure F-G)

Suzuki-Miyaura cross-coupling of boronic acids with 2-bromoallyl alcohol (General procedure F):

An oven dried two-neck round bottom flask equipped with a magnetic stirring bar, was charged with corresponding boronic acid (1 equiv), $Pd(PPh_3)_4$ (10 mol%) and K_3PO_4 (3 equiv). The reaction flask was equipped with a reflux condenser and purged with argon. Solids were dissolved in dioxane:THF (1:1) mixture and then 2-bromoallyl alcohol (1.2 equiv) was added. Reaction was heated and stirred at 100 °C for 16 h. The mixture was allowed to cool to room temperature, and quenched wih HCl_{aq} 1M. The mixture was extracted with AcOEt. Combined organic layers were dried over anhydrous Na_2SO_4, filtered and solvent removed under reduced pressure. Crude product was purified through flash column chromatography in silica (hexane:AcOEt, 100:0 to 60:40) to yield the corresponding allylic alcohol.

Apple reaction (General procedure G):

An oven dried round bottom flask equipped with a magnetic stirring bar, was charged with corresponding allylic alcohol (1 equiv) and PPh_3 (1 equiv). The reaction flask was purged with argon and solids were dissolved in DCM and allowed to stir for 15 min at room temperature. Then, mixture was cooled down to 0 °C in an ice-water bath, and NCS (0.98 equiv) was added portion wise along 1 h. Once addition was completed, the reaction was allowed to warm up to room temperature and stirred for an additional 3 h. Reaction was quenched with $NH_4Cl_{(sat.\ aq.)}$ and the mixture was extracted with DCM. Combined organic layers were dried over anhydrous Na_2SO_4, filtered and solvent removed under reduced pressure. Crude product was purified though flash column chromatography in silica to yield the corresponding allylic chloride.

5.4.2.2 General procedure for the synthetis of Fe(III) complexes bearing bidentate nitrogen ligands (General Procedure H)

Bidentate iron complexes were synthesized from $FeCl_3 \cdot 6H_2O$ according to a modified reported procedure:[246] $FeCl_3 \cdot 6H_2O$ (100 mg, 0.37 mmol) and corresponding complexing ligand were dissolved in 5 mL of methanol. After stirring for 15 min at room temperature, Et_2O was added to precipitate the complex, filtered off and dried under vacuum. The resulting solid, was redissolved in anhydrous MeCN and recrystallized to yield the final complex after dried under reduced pressure.

5.4.2.3 General procedure for the $FeCl_3$ photorredox HAT catalyzed direct Csp^3-Csp^3 allylation of ethane (General Procedure I-J)

0.2 mmol scale reaction (General Procedure I):

An opened to air 10 mL glass pressure vessel from Buchiglasüster® company inside the corresponding protective mesh, was equipped with a magnetic stirring bar and charged with $FeCl_3 \cdot 6H_2O$ (5.4 mg, 0.02 mmol, 10 mol%). The solid was then dissolved in MeCN (2 mL), leading to a yellow solution. While stirring, 2,4,6-collidine (58 µL, 0.4 mmol, 2 equiv.) was added and the solution acquired a dark orange color. Mixture was allowed to stir for 15 min. After that time, corresponding allylic chloride (0.2 mmol, 1 equiv.) dissolved in an additional MeCN volume (2 mL) was added over the mixture. Then, the reactor head, bearing a rupture disc pressure gauge and a gas-liquid inlet, was firmly screwed. Through the inlet connection, reaction was filled with ethane atmosphere while stirring at 1000 rpm (4x vacuum/ethane 5 bar cycles + 1 ethane 8 bar final). The mixture was irradiated (43 W Kessil 370 nm) and allowed to react for 16 h. After this time, the reaction was quenched with water (10 mL) and extracted with pentane (3 x 10 mL). Combined organic layers were dried over anhydrous $MgSO_4$, filtered, and solvent was removed under reduced pressure. Crude product was purified through flash column chromatography using the indicated mixture of solvents as eluent.

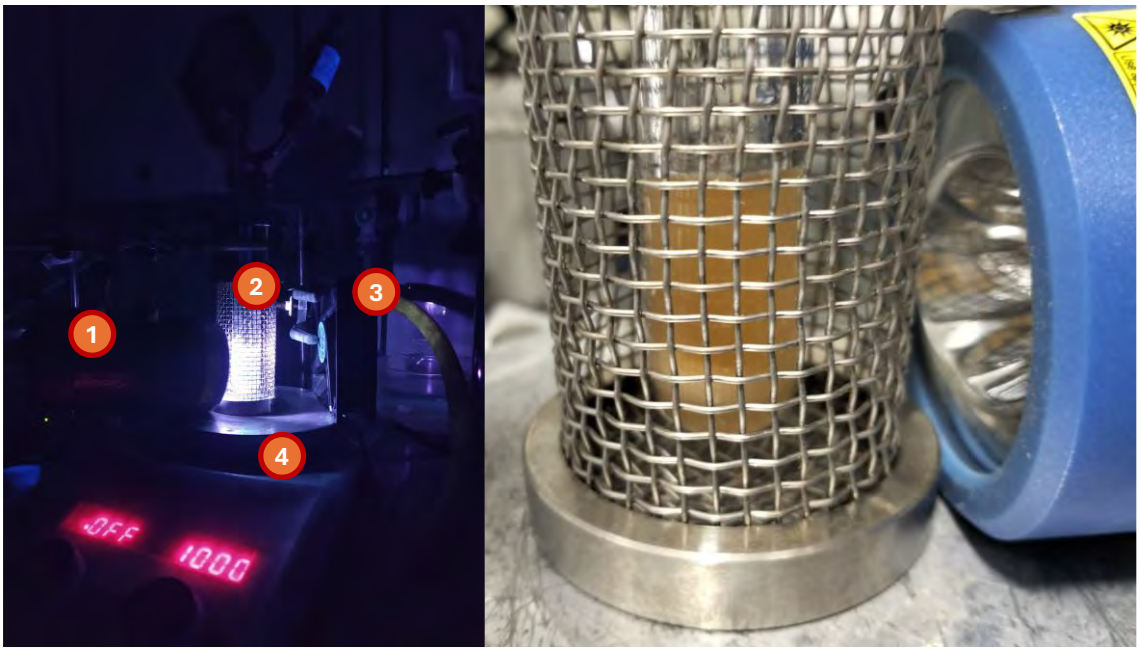

Figure 5.4.2. Reaction setup. Left: Buchiglasüster® tinyclave - small pressure reactor equipped with a 10 mL glass pressure vessel and corresponding protective mesh. 1) Kessil lamp, 2) pressure reaction, 3) fan and 4) stir plate. Right: illustrating picture for lamp-reaction distance.

3 mmol scale reaction (General Procedure J):

An opened to air 150 mL glass pressure vessel from Buchiglasüster® company inside the corresponding protective mesh, was equipped with a magnetic stirring bar and charged with $FeCl_3 \cdot 6H_2O$ (81 mg, 0.3 mmol, 10 mol%). The solid was then dissolved in MeCN (30 mL), leading to a yellow solution. While stirring, 2,4,6-collidine (0.9 mL, 6 mmol, 2 equiv.) was added and the solution acquired a dark orange color. Mixture was allowed to stir for 20 min. After that time, corresponding allylic chloride (3 mmol, 1 equiv.) dissolved in an additional

MeCN volume (30 mL) was added over the mixture. Then, the reactor head, bearing a rupture disc pressure gauge and a gas-liquid inlet, was firmly screwed. Through the inlet connection, the reaction was filled with ethane atmosphere while stirring at 1000 rpm (4x vacuum/ethane 5 bar cycles + 1 ethane 8 bar final). When propane was used, the reactor was filled with propane atmosphere while stirring at 1000 rpm (5x vacuum/ propane 1.5 bar cycles). The mixture was irradiated with two lamps (43 W Kessil 370 nm) and allowed to react during 42 h. After this time, the reaction was quenched with water (50 mL) and extracted with pentane (3 x 30 mL). Combined organic layers were dried over anhydrous $MgSO_4$, filtered, and solvent was removed under reduced pressure. Crude product was purified through flash column chromatography using the indicated mixture of solvents as eluent.

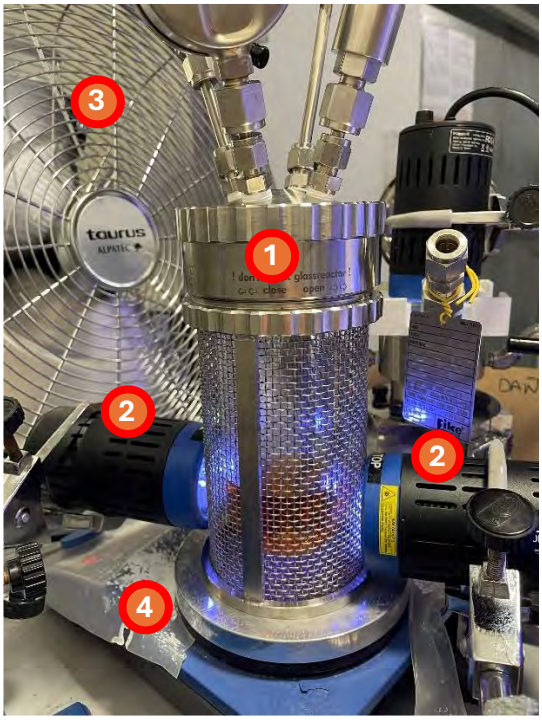

Figure 5.4.3. Reaction setup. Buchiglasüster® miniclave - small pressure reactor equipped with a 150 mL glass pressure vessel and corresponding protective mesh. 1) Pressure reaction, 2) Kessil lamp, 3) fan and 4) stir plate.

5.4.3 Characterization data

5.4.3.1 Products derived from starting material synthesis

(*E*)-2-Methylene-4-phenylbut-3-en-1-ol (S11)

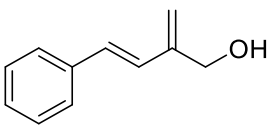

Synthesized from (*E*)-styrylboronic acid (443.9 mg, 3 mmol) and 2-bromoallyl alcohol (0.29 mL, 3.6 mmol, 1.2 equiv), by using $Pd(PPh_3)_4$ (346.7 mg, 0.3 mmol, 10 mol%) and K_3PO_4 (1.9 g, 9 mmol, 3 equiv) in dioxane:THF (30 mL, 1:1) according to general procedure A. After purification, **S5** was obtained as a pale-yellow semisolid in 51% yield. **^{1}H NMR (300 MHz, $CDCl_3$)** δ 7.48 (d, *J* = 7.6 Hz, 2H), 7.37 (t, *J* = 6.8 Hz, 2H), 7.30 (d, *J* = 6.3 Hz, 1H), 6.86 (d, *J* = 16.6 Hz, 1H), 6.72 (d, *J* = 16.6 Hz, 1H), 5.40 (s, 1H), 5.33 (s, 1H), 4.51 (d, *J* = 5.7 Hz, 2H), 1.54 (t, *J* = 5.9 Hz, 1H) ppm. **^{13}C NMR (75 MHz, $CDCl_3$)** δ 129.0, 128.8, 128.3, 127.9, 126.6, 116.3, 63.4 ppm. **HRMS (APCI)** Calc. for $C_{11}H_{13}O$ [$M+H^+$] 161.0961, found 161.0966

Spectroscopic and physical data were in accordance with those previously reported.[247]

(*E*)-2-Methylenedec-3-en-1-ol (S12)

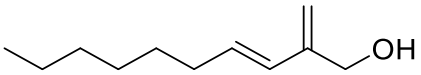

Synthesized from (*E*)-oct-1-en-1-ylboronic acid (780.2 mg, 5 mmol) and 2-bromoallyl alcohol (0.48 mL, 6 mmol, 1.2 equiv), by using Pd(PPh$_3$)$_4$ (577.8 mg, 0.5 mmol, 10 mol%) and K$_3$PO$_4$ (3.2 g, 15 mmol, 3 equiv) in dioxane:THF (50mL, 1:1) according to general procedure A. After purification, **S13** was obtained as a pale yellow oil in 48% yield. **^{1}H NMR (300 MHz, CDCl$_3$)** δ 6.07 (d, *J* = 16.1 Hz, 1H), 5.77 (dt, *J* = 15.9, 6.9 Hz, 1H), 5.13 (s, 1H), 5.02 (s, 1H), 4.31 (s, 2H), 2.10 (q, *J* = 7.1 Hz, 3H), 1.45 – 1.36 (m, 3H), 1.35 – 1.24 (m, 7H), 0.88 (t, *J* = 6.1 Hz, 3H) ppm. **^{13}C NMR (75 MHz, CDCl$_3$)** δ 145.4, 131.5, 129.4, 113.2, 63.5, 33.2, 31.9, 29.4, 29.1, 22.7, 14.2 ppm. **HRMS (APCI)** Calc. for C$_{11}$H$_{21}$O [M+H$^+$] 169.1587, found 169.1590.

***N*-(3-(3-Hydroxyprop-1-en-2-yl)phenyl)acetamide (S13)**

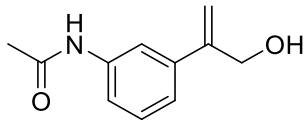

Synthesized from (3-acetamidophenyl)boronic acid **S14**[248] (1.0 g, 6 mmol) and 2-bromoallyl alcohol (0.58 mL, 7.2 mmol, 1.2 equiv), by using Pd(PPh$_3$)$_4$ (693.3 mg, 0.6 mmol, 10 mol%) and K$_3$PO$_4$ (3.8 g, 18 mmol, 3 equiv) in dioxane:THF (60 mL, 1:1) according to general procedure A. After purification, **S7** was obtained as a pale-yellow oil in 17 % yield. **^{1}H NMR (300 MHz, CDCl$_3$)** δ 7.56 (s, 1H), 7.47 (d, *J* = 7.5 Hz, 1H), 7.38 (t, *J* = 7.5 Hz, 1H), 7.31 – 7.25 (m, 1H), 7.19 (d, *J* = 7.4 Hz, 1H), 5.46 (s, 1H), 5.35 (s, 1H), 4.50 (s, 2H), 2.16 (s, 3H), 1.84 (s, 1H) ppm. **^{13}C NMR (75 MHz, CDCl$_3$)** δ 168.6, 147.0, 139.6, 138.3, 129.3, 122.3, 119.6, 117.8, 113.4, 65.2, 24.7 ppm. **HRMS (APCI)** Calc. for C$_{11}$H$_{14}$NO$_2$ [M+H$^+$] 192.1019, found 192.1024.

3-(3-hydroxyprop-1-en-2-yl)-*N*,*N*-dimethylbenzenesulfonamide (S16)

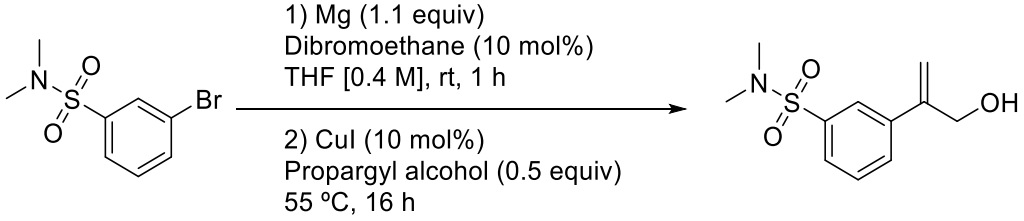

S15 **S16**

An oven dried Schlenk equipped with a magnetic stirring bar, was charged with activated Mg turnings (256 mg, 10.7 mmol, 1.1 equiv) and purged with argon. Then, dibromoethane (0.1 mL, 0.98 mmol, 10 mol%) was added diluted in THF (2 mL), and the mixture was allowed to stir at room temperature for 10 min. Reaction changes from colorless to greyish color. After that time, aryl bromide **S15** (2.6 g, 9.8 mmol) was carefully added diluted in THF (22 mL). Reaction was stirred at room temperature for 1 h, until complete consumption of Mg turnings. Titration with I$_2$ revealed the obtention of corresponding ArMgBr (0.40 M in THF).

A separate oven dried two-neck round bottom flask equipped with a magnetic stirring bar, was charged with CuI (182.8 mg, 0.96 mmol, 10 mol %). The reaction flask was equipped with a

reflux condenser and purged with argon. The previously freshly prepared ArMgBr was added over the solid and stirred for 30 min at room temperature. Then, the mixture was cooled down in an ice-water bath, and propargyl alcohol (0.28 mL, 4.8 mmol, 0.5 equiv) was dropwise added over the mixture. Once completed, the reaction was stirred at 55 °C for 16 h. The mixture was allowed to cool to room temperature, and quenched wih HCl_{aq} 1M (10 mL). The mixture was extracted with AcOEt (3 x 15 mL). Combined organic layers were dried over anhydrous Na_2SO_4, filtered and solvent removed under reduced pressure. Crude product was purified though flash column chromatography in silica (hexane:AcOEt, 100:0 to 30:70) to yield **S14** in 13% yield. **^{1}H NMR (300 MHz, $CDCl_3$)** δ 7.85 (s, 1H), 7.73 – 7.66 (m, 2H), 7.53 (t, *J* = 7.8 Hz, 1H), 5.57 (s, 1H), 5.48 (s, 1H), 4.57 (s, 2H), 2.77 (s, 1H), 2.72 (s, 6H) ppm. **^{13}C NMR (75 MHz, $CDCl_3$)** δ 145.9, 139.9, 135.9, 130.5, 129.3, 126.9, 125.3, 115.0, 64.8, 38.0.ppm **HRMS (APCI)** Calc. for $C_{11}H_{16}NO_3S$ [M+H$^+$] 242.0845, found 242.0843.

1-(Benzyloxy)-4-(3-chloroprop-1-en-2-yl)benzene (71)

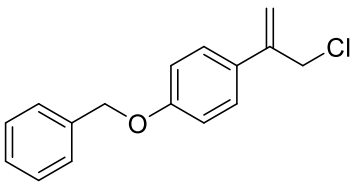

Synthesized from 2-(4-(benzyloxy)phenyl)prop-2-en-1-ol **S17**[249] (555.9 mg, 2.31 mmol) by using PPh_3 (605.9 mg, 2.31 mmol, 1 equiv) and NCS (301.7 mg, 2.26 mmol, 0.98 equiv) in DCM (5.2 mL) according to general procedure B. After purification through flash column chromatography in silica (Hexane:Et_2O 9:1), **71** was obtained as a colorless oil in 39% yield. **^{1}H NMR (300 MHz, $CDCl_3$)** δ 7.52 – 7.32 (m, 7H), 7.00 (d, *J* = 8.7 Hz, 2H), 5.51 (s, 1H), 5.39 (s, 1H), 5.10 (s, 2H), 4.46 (s, 2H) ppm. **^{13}C NMR (75 MHz, $CDCl_3$)** δ 159.0, 143.4, 137.0, 130.4, 128.7, 128.1, 127.6, 127.5, 115.3, 115.0, 70.2, 46.8 ppm. **HRMS (APCI)** Calc. for $C_{16}H_{16}ClO$ [M+H$^+$] 259.0884, found 259.0882.

***N*-(3-(3-Chloroprop-1-en-2-yl)phenyl)acetamide (72)**

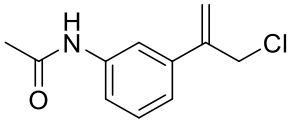

Synthesized from **S13** (184.7 mg, 0.97 mmol) by using PPh_3 (254.4 mg, 0.97 mmol, 1 equiv) and NCS (127.7 mg, 0.95 mmol, 0.98 equiv) in DCM (2.4 mL) according to general procedure B. After purification through flash column chromatography in silica (Hexane:AcOEt 9:1 to 1:1), **72** was obtained as a yellow oil in 62% yield. **^{1}H NMR (300 MHz, $CDCl_3$)** δ 8.25 (s, 1H), 7.64 (s, 1H), 7.49 (d, *J* = 7.9 Hz, 1H), 7.26 (t, *J* = 7.8 Hz, H), 7.18 (d, *J* = 7.7 Hz, 1H), 5.50 (s, 1H), 5.40 (s, 1H), 4.39 (s, 2H), 2.13 (s, 3H) ppm. **^{13}C NMR (75 MHz, $CDCl_3$)** δ 169.3, 143.6, 138.5, 129.1, 122.12, 120.1, 117.9, 117.3, 46.6, 24.5 ppm. **HRMS (APCI)** Calc. for $C_{11}H_{13}ClNO$ [M+H$^+$] 210.0680, found 210.0683.

(*E*)-(3-(Chloromethyl)buta-1,3-dien-1-yl)benzene (76)

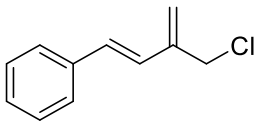

Synthesized from **S11** (245.1 mg, 1.53 mmol) by using PPh_3 (401.3 mg, 1.53 mmol, 1 equiv) and NCS (200.2 mg, 1.49 mmol, 0.98 equiv) in DCM (3 mL) according to general procedure B. After purification, **76** was obtained as a colorless oil in 23% yield. **^{1}H NMR (300 MHz, $CDCl_3$)** δ 7.49 (d, *J* = 7.7 Hz, 2H), 7.38 (t, *J* = 7.5 Hz, 2H), 7.33 – 7.29 (m, 1H), 6.80 (dd, *J* = 19.2, 2.5 Hz, 2H), 5.46 (s, 1H), 5.41 (s, 1H), 4.37 (s, 3H) ppm. **^{13}C NMR (75 MHz, $CDCl_3$)** δ 142.2, 136.9, 130.4, 128.8, 128.1, 127.3, 126.8, 120.0, 44.3 ppm. **HRMS (APCI)** Calc. for $C_{11}H_{12}Cl$ [M+H$^+$] 179.0622, found 179.0627.

(*E*)-2-(Chloromethyl)deca-1,3-diene (77)

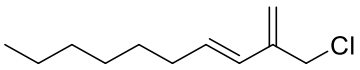

Synthesized from **S12** (201.8 mg, 1.20 mmol) by using PPh_3 (314.7 mg, 1.20 mmol, 1 equiv) and NCS (157.2 mg, 1.17 mmol, 0.98 equiv) in DCM (2.4 mL) according to general procedure A. After purification, **70** was obtained as a colorless oil in 49% yield. **^{1}H NMR (300 MHz, $CDCl_3$)** δ 6.05 (d, *J* = 16.0 Hz, 1H), 5.86 (dt, *J* = 15.9, 6.7 Hz, 1H), 5.21 (s, 1H), 5.11 (s, 1H), 4.19 (s, 2H), 2.13 (q, *J* = 7.0 Hz, 2H), 1.45 – 1.37 (m, 2H), 1.34 – 1.24 (m, 6H), 0.93 – 0.83 (m, 3H) ppm. **^{13}C NMR (75 MHz, $CDCl_3$)** δ 142.2, 133.1, 128.5, 117.2, 44.6, 33.1, 31.9, 29.3, 29.0, 22.7, 14.2 ppm. **HRMS (APCI)** Calc. for $C_{11}H_{20}Cl$ [M+H$^+$] 187.1248, found 187.1241.

3-(3-Chloroprop-1-en-2-yl)-*N*,*N*-dimethylbenzenesulfonamide (78)

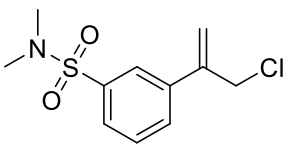

Synthesized from **S16** (164.1 mg, 0.68 mmol) by using PPh_3 (178.3 mg, 0.68 mmol, 1 equiv) and NCS (87.7 mg, 0.66 mmol, 0.98 equiv) in DCM (2 mL) according to general procedure B. After purification, **79** was obtained as a yellow oil in 34% yield. **^{1}H NMR (300 MHz, $CDCl_3$)** δ 7.84 (s, 1H), 7.71 (d, *J* = 7.8 Hz, 2H), 7.54 (t, *J* = 7.8 Hz, 1H), 5.64 (s, 1H), 5.55 (s, 1H), 4.48 (s, 2H), 2.70 (s, 6H) ppm. **^{13}C NMR (75 MHz, $CDCl_3$)** δ 142.7, 138.7, 136.0, 130.5, 129.4, 127.3, 125.4, 118.8, 46.2, 38.0 ppm. **HRMS (APCI)** Calc. for $C_{11}H_{15}ClNO_2S$ [M+H$^+$] 260.0507, found 260.0506.

(*Z*)-(1-Chlorobut-2-en-2-yl)benzene (56)// (3-Chlorobut-1-en-2-yl)benzene (56')

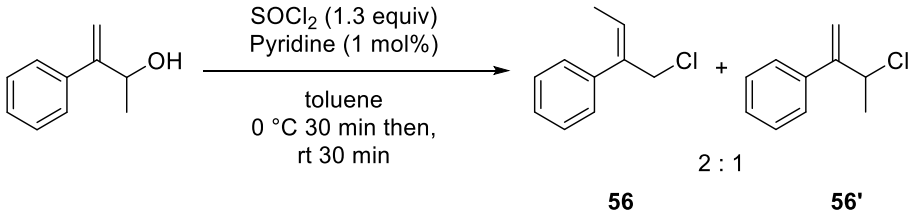

An oven dried round bottom flask equipped with a magnetic stirring bar was purged with argon and 3-phenylbut-3-en-2-ol **S17**[250] (436.9 mg, 2.95 mmol, 1 equiv.) was added dissolved in toluene (3.6 mL). Mixture was cooled down to 0 °C in an ice-water bath and then pyridine (2 μL, 0.003 mmol, 1 mol%) was added over the solution. $SOCl_2$ (0.28 mL, 3.8 mmol, 1.3 equiv.) was carefully added dissolved in an additional volume of toluene (0.9 mL). Once addition was completed, the reaction was allowed to stir at 0 °C for 30 min. Then, the reaction was allowed to warm up to room temperature and stirred for additional 30 min, when observed full conversion by TLC (hexane:AcOEt, 4:1). Reaction was poured into a small amount of ice and the mixture was extracted with DCM (3 x 10 mL). Combined organic layers were dried over anhydrous $MgSO_4$, filtered and solvent removed under reduced pressure. Crude product was purified through a flash column chromatography in a short path of silica (hexane) to yield the corresponding mixture of allylic chlorides as a yellow oil in a 53% yield. **^{1}H NMR (300 MHz, $CDCl_3$)** δ 7.50 – 7.23 (m, 5H, **56**; 5H, **56'**), 5.98 (q, *J* = 6.9 Hz, 1H, **56**), 5.50 (s, 1H, **56'**), 5.39 (s, 1H, **56'**), 5.02 (q, *J* = 6.8 Hz, 1H, **56'**), 4.32 (s, 2H, **56**), 1.71 (d, *J* = 6.8 Hz, 3H, **56'**), 1.65 (d, *J* = 6.9 Hz, 3H, **56**) ppm. **^{13}C NMR (126 MHz, $CDCl_3$)** δ 150.0, 139.7, 138.0, 137.8, 131.9,

128.9, 128.5, 128.4, 128.1, 127.5 (**56**), 127.1, 115.3 (**56'**), 58.1 (**56'**), 50.8 (**56**), 24.3 (**56'**), 15.0 (**56**) ppm. **HRMS (APCI)** Calc. for $C_{10}H_{12}Cl$ [$M+H^+$] 167.0622, found 167.0629.

5.4.3.2 Fe(III) complexes bearing bidentate nitrogen ligands

$[Fe(bpy)_2Cl_2][FeCl_4]$

Prepared as described above by using 2,2'-bypiridine (57.8 mg, 0.37 mmol, 1 equiv) as ligand. Complex isolated as a brown solid in 78% yield. **UV/Vis (MeCN)** λ_{max} = 301 nm (ε = 7554 M^{-1} cm^{-1}) and 361 nm (ε = 3041 M^{-1} cm^{-1}). **ATR (solid)** *v* 3107 (w), 3063 (w), 1574 (w), 1599 (m), 1495 (w), 1470 (m), 1442 (s), 1314 (m), 1245 (w), 1173 (w), 1024 (m), 1015 (m), 766 (s), 729 (m), 655 (m), 635 (w) cm^{-1}. **HRMS (ESI+)** Calc. for $C_{20}H_{16}Cl_2FeN_4$ $[M]^+$ 438.0096, found 438.0097. **HRMS (ESI-)** Cl_4Fe $[M]^-$ 195.8109, found 195.8114.

$[Fe(4,4'\text{-}dtbbpy)_2Cl_2][FeCl_4]$

Prepared as described above using 4,4'-di-*tert*-butyl-2,2'-dipyridyl (99.3 mg, 0.37 mmol, 1 equiv) as ligand. Complex isolated as dark red solid in 93% yield. **UV/Vis (MeCN)** λ_{max} = 301 nm (ε = 12220 M^{-1} cm^{-1}) and 360 nm (ε = 4741 M^{-1} cm^{-1}). **ATR (solid)** *v* 2967 (m), 2871 (w), 1611 (s), 1547 (m), 1486 (m), 1410 (s), 1367 (m), 1250 (m), 1203 (w), 1122 (w), 1203 (m), 1122 (w), 1023 (m), 898 (m), 849 (s), 739 (m), 719 (m), 606 (s), 550 (m) cm^{-1}. **HRMS (ESI+)** Calc. for $C_{36}H_{48}Cl_2FeN_4$ $[M]^+$ 662.2600, found 662.2607. **HRMS (ESI-)** Cl_4Fe $[M]^-$ 195.8109, found 195.8116.

$[Fe(phen)_2Cl_2][FeCl_4]$

Prepared as described above using 1,10-phenantroline (66.7 mg, 0.37 mmol, 1 equiv) as ligand. Complex isolated as dark red solid in 84% yield. **UV/Vis (MeCN)** λ_{max} = 361 nm (ε = 3776 M^{-1} cm^{-1}). **ATR (solid)** *v* 3059 (m), 1626(w), 1579 (m), 1518 (s), 1494 (m), 1424 (s), 1341 (m), 1309 (w), 1224 (w), 1143 (m), 1105 (m), 846 (s), 721 (s), 645 (m) cm^{-1}. **HRMS (ESI+)** Calc. for $C_{24}H_{16}Cl_2FeN_4$ $[M]^+$ 486.0096, found 486.0096. **HRMS (ESI-)** Cl_4Fe $[M]^-$ 195.8109, found 195.8113.

5.4.3.3 Products derived from Fe-catalyzed allylation of ethane

Pent-1-en-2-ylbenzene (39)

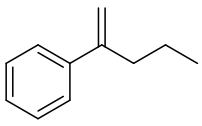

Synthesized from **37** (30.5 mg, 0.2 mmol, 1 equiv) and ethane (8 bar) according to general procedure C. Colorless oil obtained in 69% yield after column chromatography (pentane). **^{1}H NMR (300 MHz, $CDCl_3$)** δ 7.46 – 7.40 (m, 2H), 7.38 – 7.26 (m, 3H), 5.30 (d, *J* = 1.6 Hz, 1H), 5.09 (q, *J* = 1.5 Hz, 1H), 2.52 (td, *J* = 7.5, 1.3 Hz, 2H), 1.52 (dq, *J* = 14.7, 7.3 Hz, 2H), 0.96 (t, *J* = 7.3 Hz, 3H) ppm. **^{13}C NMR (75 MHz, $CDCl_3$)** δ 148.6, 141.5, 128.2, 127.2, 126.1, 112.2, 37.5, 21.4, 13.7 ppm. **HRMS (APCI)** Calc. for $C_{11}H_{15}$ $[M+H^+]$ 147.1168, found 147.1174.

1-(*Tert*-butyl)-4-(pent-1-en-2-yl)benzene (40)

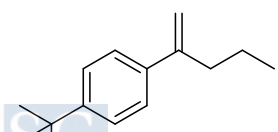

Synthesized from **66** (41.7 mg, 0.2 mmol, 1 equiv) and ethane (8 bar) according to general procedure C. Colorless oil obtained in 45% yield after column chromatography (pentane). **^{1}H NMR (300 MHz, $CDCl_3$)** δ 7.35 (s, 4H), 5.27 (d, *J* = 1.6 Hz, 1H), 5.02 (q, *J* = 1.4 Hz, 1H), 2.48 (td, *J* = 7.6, 1.2 Hz, 2H), 1.50 (h, *J* = 7.2 Hz, 2H), 1.33 (s, 9H), 0.94 (t,

J = 7.3 Hz, 3H) ppm. **^{13}C NMR (75 MHz, CDCl$_3$)** δ 150.3, 148.3, 138.6, 125.9, 125.3, 111.6, 37.6, 34.6, 31.5, 21.6, 14.0 ppm. **HRMS (APCI)** Calc. for $C_{15}H_{23}$ [M+H$^+$] 203.1794, found 203.1800.

1,3-Di-*tert*-butyl-5-(pent-1-en-2-yl)benzene (41)

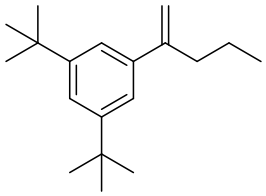

Synthesized from **55** (53.0 mg, 0.2 mmol, 1 equiv) and ethane (8 bar) according to general procedure C. Colorless oil obtained in 71% yield after column chromatography (pentane).**^{1}H NMR (300 MHz, CDCl$_3$)** δ 7.35 (t, *J* = 1.8 Hz, 1H), 7.25 (d, *J* = 1.8 Hz, 2H), 5.26 (d, *J* = 1.8 Hz, 1H), 5.03 (d, *J* = 1.6 Hz, 1H), 2.49 (t, *J* = 7.5 Hz, 2H), 1.61 – 1.43 (m, 2H), 1.35 (s, 18H), 0.95 (t, *J* = 7.3 Hz, 3H) ppm. **^{13}C NMR (75 MHz, CDCl$_3$)** δ 150.5, 149.8, 141.0, 121.5, 120.5, 111.7, 37.8, 35.0, 31.7, 21.6, 14.0. **HRMS (APCI)** Calc. for $C_{19}H_{31}$ [M+H$^+$] 259.2421, found 259.2420.

1-Fluoro-4-(pent-1-en-2-yl)benzene (42)

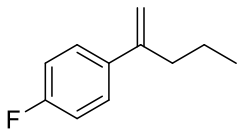

Synthesized from **67** (34.1 mg, 0.2 mmol, 1 equiv) and ethane (8 bar) according to general procedure C. Colorless oil obtained in 99% yield after column chromatography (pentane). **^{1}H NMR (300 MHz, CDCl$_3$)** δ 7.41 – 7.33 (m, 1H), 7.05 – 6.96 (m, 1H), 5.21 (d, *J* = 1.6 Hz, 0H), 5.04 (d, *J* = 1.5 Hz, 0H), 2.45 (t, *J* = 7.4 Hz, 1H), 1.46 (h, *J* = 7.4 Hz, 0H), 0.92 (t, *J* = 7.3 Hz, 1H). **^{13}C NMR (75 MHz, CDCl$_3$)** δ 162.34 (d, *J* = 245.5 Hz), 147.6, 137.63 (d, *J* = 3.1 Hz), 127.8 (d, *J* = 7.8 Hz), 115.1 (d, *J* = 21.2 Hz) 112.3, 37.7, 21.4, 13.9 ppm. **^{19}F NMR (282 MHz, CDCl$_3$)** -115.7 ppm. **HRMS (APCI)** Calc. for $C_{11}H_{14}F$ [M+H$^+$] 165.1074, found 165.1077.

1-(Pent-1-en-2-yl)-3,5-bis(trifluoromethyl)benzene (43)

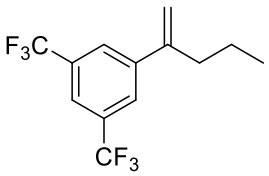

Synthesized from **68** (57.7 mg, 0.2 mmol, 1 equiv) and ethane (8 bar) according to general procedure C. Colorless oil obtained in 99% yield after column chromatography (pentane). **^{1}H NMR (300 MHz, CDCl$_3$)** δ 7.81 (s, 2H), 7.77 (s, 1H), 5.39 (s, 1H), 5.25 (s, 1H), 2.51 (t, *J* = 7.5 Hz, 2H), 1.48 (m, 2H), 0.95 (t, *J* = 7.3 Hz, 3H) ppm. **^{13}C NMR (75 MHz, CDCl$_3$)** 146.3, 143.9, 131.8 (q, *J* = 33.1 Hz), 126.3 (d, *J* = 2.9 Hz), 123.6 (d, *J* = 272.8 Hz), 121.1 (dt, *J* = 7.6, 3.7 Hz), 115.6, 37.17, 21.23, 13.76 ppm. **^{19}F NMR (282 MHz, CDCl$_3$)** -62.9 ppm. **HRMS (APCI)** Calc. for $C_{13}H_{13}F_6$ [M+H$^+$] 283.0916, found 283.0917.

1-Methoxy-4-(pent-1-en-2-yl)benzene (44)

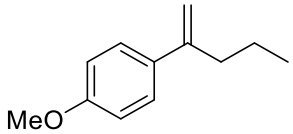

Synthesized from **69** (36.5 mg, 0.2 mmol, 1 equiv) and ethane (8 bar) according to general procedure C. Colorless oil obtained in 54% yield after column chromatography (pentane:Et$_2$O, 100:0 to 99.5:0.5). **^{1}H NMR (300 MHz, CDCl$_3$)** δ 7.38 – 7.32 (m, 2H), 6.92 – 6.79 (m, 1H), 5.20 (d, *J* = 1.7 Hz, 1H), 4.97 (q, *J* = 1.5 Hz, 1H), 3.81 (s, 3H), 2.45 (td, *J* = 7.8, 1.4 Hz, 2H), 1.52 – 1.41 (m, 2H), 0.92 (t, *J* = 7.3 Hz, 3H) ppm. **^{13}C NMR (75 MHz, CDCl$_3$)** δ 165.5, 159.1, 147.9, 127.3, 113.7, 110.8, 55.4, 37.7, 21.6, 13.9 ppm. **HRMS (APCI)** Calc. for $C_{12}H_{17}O$ [M+H$^+$] 177.1274, found 177.1278.

1-Methoxy-3-(pent-1-en-2-yl)benzene (45)

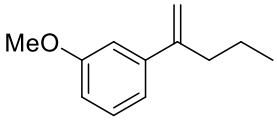

Synthesized from **70** (36.5 mg, 0.2 mmol, 1 equiv) and ethane (8 bar) according to general procedure C. Colorless oil obtained in 63% yield after column chromatography (pentane:Et$_2$O, 100:0 to 99.5:0.5). **^{1}H NMR (300 MHz, CDCl$_3$)** δ 7.24 (t, *J* = 7.9 Hz, 1H), 7.00 (ddd, *J* = 7.7, 1.6, 0.9 Hz, 1H), 6.99 – 6.91 (m, 1H), 6.82 (ddd, *J* = 8.3, 2.7, 1.0 Hz, 1H), 5.27 (d, *J* = 1.7 Hz, 1H), 5.05 (q, *J* = 1.4 Hz, 1H), 3.83 (s, 3H), 2.46 (td, *J* = 7.5, 1.4 Hz, 2H), 1.48 (h, *J* = 7.4 Hz, 2H), 0.92 (t, *J* = 7.3 Hz, 3H). **^{13}C NMR (75 MHz, CDCl$_3$)** δ 159.7, 148.6, 143.3, 129.3, 118.9, 112.6, 112.5, 112.4, 55.4, 37.7, 21.5, 13.9 ppm. **HRMS (APCI)** Calc. for $C_{12}H_{17}O$ [M+H$^+$] 177.1274, found 177.1280.

1-(Benzyloxy)-4-(pent-1-en-2-yl)benzene (46)

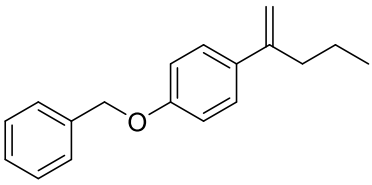

Synthesized from **71** (51.7 mg, 0.2 mmol, 1 equiv) and ethane (8 bar) according to general procedure C. Amorphous solid obtained in 38% yield after column chromatography (pentane:Et$_2$O, 100:0 to 99.5:0.5). **^{1}H NMR (300 MHz, CDCl$_3$) δ** 7.49 – 7.31 (m, 7H), 6.94 (d, *J* = 8.8 Hz, 2H), 5.21 (d, *J* = 1.3 Hz, 1H), 5.08 (s, 2H), 5.03 – 4.88 (d, *J* = 1.1 Hz, 1H), 2.46 (t, *J* = 7.5 Hz, 2H), 1.48 (h, *J* = 7.4 Hz, 2H), 0.92 (t, *J* = 7.3 Hz, 3H) ppm. **^{13}C NMR (75 MHz, CDCl$_3$)** δ 158.4, 147.9, 137.3, 134.3, 128.7, 128.1, 127.6, 127.4, 114.7, 110.9, 70.2, 37.6, 21.6, 13.9 ppm. **HRMS (APCI)** Calc. for $C_{18}H_{21}O$ [M+H$^+$] 253.1587, found 253.1583.

***N*-(3-(pent-1-en-2-yl)phenyl)acetamide (47)**

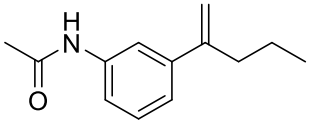

Synthesized from **72** (41.9 mg, 0.2 mmol, 1 equiv) and ethane (8 bar) according to general procedure C. Colorless oil obtained in 47% yield after column chromatography (hexane:Et$_2$O, 100:0 to 70:30). **^{1}H NMR (300 MHz, CDCl$_3$)** δ 7.59 (s, 1H), 7.50 (s, H), 7.46 (d, *J* = 8.0 Hz, 01H), 7.25 (t, *J* = 7.8 Hz, 1H), 7.14 (d, *J* = 7.6 Hz, 1H), 5.24 (s, 1H), 5.04 (s, 1H), 2.44 (t, *J* = 7.4 Hz, 12H), 2.15 (s, H), 1.46 (h, *J* = 7.3 Hz, 2H), 0.90 (t, *J* = 7.3 Hz, 2H) ppm. **^{13}C NMR (75 MHz, CDCl$_3$)** δ 168.7, 148.2, 142.6, 138.1, 128.9, 122.3, 119.1, 117.9, 112.7, 37.5, 24.6, 21.4, 13.8 ppm. **HRMS (APCI)** Calc. for $C_{13}H_{18}NO$ [M+H$^+$] 204.1383, found 204.1380.

1-(Pent-1-en-2-yl)naphthalene (48)

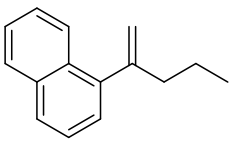

Synthesized from **73** (40.5 mg, 0.2 mmol, 1 equiv) and ethane (8 bar) according to general procedure C. Colorless oil obtained in 29% yield after column chromatography (pentane). **^{1}H NMR (300 MHz, CDCl$_3$)** δ 8.04 (dd, *J* = 6.3, 3.6 Hz, 1H), 7.89 – 7.80 (m, 1H), 7.76 (d, *J* = 8.2 Hz, 1H), 7.52 – 7.37 (m, 3H), 7.28 (d, *J* = 1.3 Hz, 1H), 5.39 (d, *J* = 2.2 Hz, 1H), 5.07 (d, *J* = 2.2 Hz, 1H), 2.49 (t, *J* = 7.3 Hz, 2H), 1.45 (h, *J* = 7.4 Hz, 2H), 0.93 (t, *J* = 7.3 Hz, 3H) ppm. **^{13}C NMR (75 MHz, CDCl$_3$)** δ 149.1, 141.7, 133.9, 131.5, 128.4, 127.2, 126.0, 125.8, 125.7, 125.3, 125.1, 115.3, 40.9, 21.4, 14.0 ppm. **HRMS (APCI)** Calc. for $C_{15}H_{17}$ [M+H$^+$] 197.1325, found 197.1330.

4-(Pent-1-en-2-yl)-1,1'-biphenyl (49)

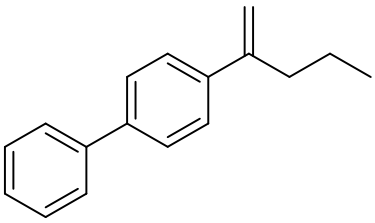

Synthesized from **74** (45.7 mg, 0.2 mmol, 1 equiv) and ethane (8 bar) according to general procedure C. Colorless oil obtained in 45% yield after column chromatography (pentane). **^{1}H NMR (300 MHz, $CDCl_3$)** δ 7.64 – 7.55 (m, 4H), 7.51 – 7.42 (m, 4H), 7.40 – 7.29 (m, 1H), 5.35 (s, 1H), 5.09 (s, 1H), 2.53 (t, *J* = 7.5 Hz, 2H), 1.60 – 1.47 (m, 2H), 0.96 (t, *J* = 7.4 Hz, 3H) ppm. **^{13}C NMR (75 MHz, $CDCl_3$)** δ 148.1, 141.0, 140.5, 140.2, 128.9, 127.4, 127.1, 127.1, 126.7, 112.4, 37.5, 21.6, 13.9 ppm. **HRMS (APCI)** Calc. for $C_{17}H_{19}$ [M+H$^+$] 223.1481, found 223.1486.

3-(pent-1-en-2-yl)thiophene (50)

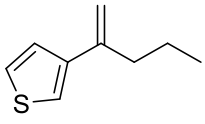

Synthesized from **75** (31.7 mg, 0.2 mmol, 1 equiv) and ethane (8 bar) according to general procedure C. Colorless oil obtained in 43% yield after column chromatography (pentane). **^{1}H NMR (300 MHz, $CDCl_3$)** δ 7.29 – 7.25 (m, 2H), 7.22 (d, *J* = 1.6 Hz, 1H), 5.37 (d, *J* = 1.4 Hz, 1H), 5.03 (q, *J* = 1.4 Hz, 1H), 2.45 (td, *J* = 7.5, 1.4 Hz, 2H), 1.58 (h, *J* = 7.4 Hz, 2H), 0.97 (t, *J* = 7.4 Hz, 3H) ppm. **^{13}C NMR (126 MHz, $CDCl_3$)** δ 143.0, 142.9, 126.0, 125.4, 120.3, 111.0, 37.7, 21.6, 14.0 ppm. **HRMS (APCI)** Calc. for $C_9H_{13}S$ [M+H$^+$] 153.0732, found 153.0739.

(*E*)-(3-methylenehex-1-en-1-yl)benzene (51)

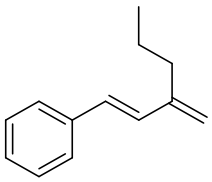

Synthesized from **76** (35.7 mg, 0.2 mmol, 1 equiv) and ethane (8 bar) according to general procedure C. Yellowish oil obtained in 49% yield after column chromatography (pentane). **^{1}H NMR (300 MHz, $CDCl_3$)** δ 7.42 (d, *J* = 7.5 Hz, 3H), 7.32 (t, *J* = 7.5 Hz, 3H), 7.25 – 7.19 (m, 2H), 6.81 (d, *J* = 16.3 Hz, 1H), 6.58 (d, *J* = 16.3 Hz, 1H), 5.14 (s, 1H), 5.06 (s, 1H), 2.31 (t, *J* = 7.5 Hz, 3H), 1.60 (dt, *J* = 15.0, 7.4 Hz, 3H), 0.98 (t, *J* = 7.3 Hz, 3H) ppm. **^{13}C NMR (126 MHz, $CDCl_3$)** δ 146.3, 131.3, 128.7, 128.0, 127.5, 126.6, 116.3, 34.3, 21.6, 14.2 ppm. **HRMS (APCI)** Calc. for $C_{13}H_{17}$ [M+H$^+$] 173.1325, found 173.1326.

(*E*)-4-methylenedodec-5-ene (52)

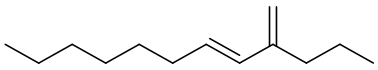

Synthesized from **77** (37.3 mg, 0.2 mmol, 1 equiv) and ethane (8 bar), by using Kessil lamp at 75% of power, according to general procedure C. Colorless oil obtained in 81% yield after column chromatography (pentane). **^{1}H NMR (500 MHz, $CDCl_3$)** δ 6.05 (d, *J* = 15.8 Hz, 1H), 5.70 (dt, *J* = 15.6, 6.9 Hz, 1H), 4.88 (s, 1H), 4.83 (s, 1H), 2.20 – 2.14 (m, 2H), 2.09 (q, *J* = 7.2 Hz, 2H), 1.51 (h, *J* = 7.3 Hz, 2H), 1.39 (p, *J* = 7.2 Hz, 2H), 1.35 – 1.24 (m, 6H), 0.93 (t, *J* = 7.3 Hz, 3H), 0.89 (t, *J* = 6.8 Hz, 3H) ppm. . **^{13}C NMR (125 MHz, $CDCl_3$)** δ 132.2, 130.4, 113.0, 34.6, 33.0, 31.9, 29.6, 29.1, 22.8, 21.6, 14.2, 14.2 ppm. **HRMS (APCI)** Calc. for $C_{13}H_{25}$ [M+H$^+$] 181.1951, found 181.1953.

(*E*)-Hex-2-en-3-ylbenzene (57)

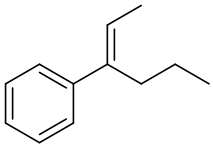

Synthesized from **56**/**56' mixture** (33.3 mg, 0.2 mmol, 1 equiv) and ethane (8 bar) according to general procedure C. Colorless oil obtained in 78% yield after column chromatography (pentane). **^{1}H NMR (300 MHz, $CDCl_3$)** δ 7.35 – 7.28 (m, 4H), 7.22 – 7.20 (m, 1H), 5.75 (q, *J* = 6.8 Hz, 1H), 2.48 (t, *J* = 7.6 Hz, 2H), 1.79 (d, *J* = 6.8 Hz, 3H), 1.38 1.38 (td, *J* = 14.6, 7.1 Hz, 2H), 0.89 (t, *J* = 7.3 Hz, 3H) ppm. **^{13}C NMR (125 MHz, $CDCl_3$)** δ 143.7, 141.0, 128.3, 126.5, 126.4, 123.1, 31.5, 21.7, 14.3, 14.1 ppm. **HRMS (APCI)** Calc. for $C_{12}H_{17}$ [M+H$^+$] 161.1325, found 161.1328.

5.4.3.4 Products derived from 2-phenyl pentanoic acid synthesis

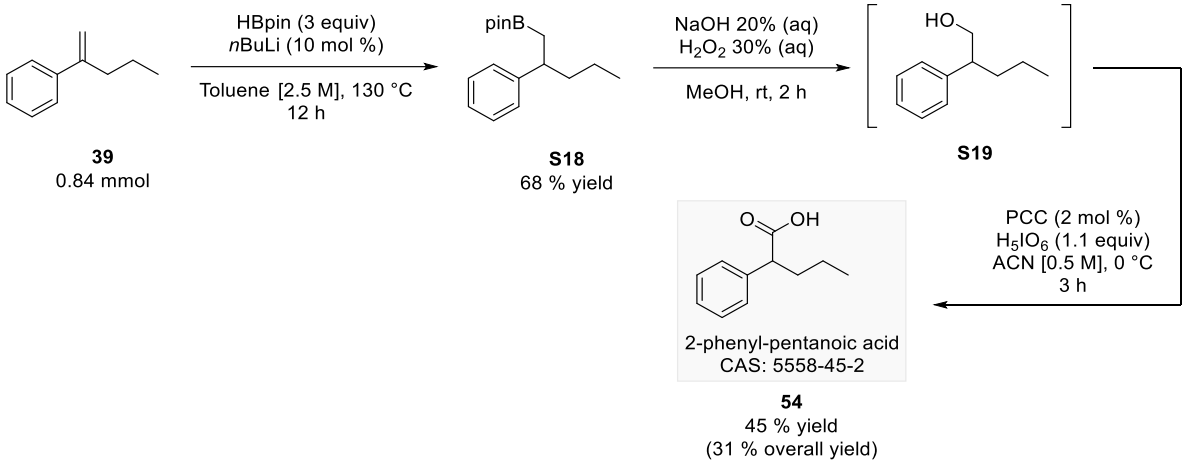

4,4,5,5-tetramethyl-2-(2-phenylpentyl)-1,3,2-dioxaborolane (S18)

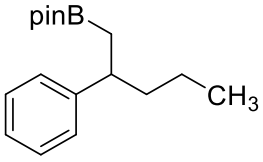

Synthesized from **39** (122.8 mg, 0.84 mmol) according to a modified procedure from literature:[251] In an argon-filled sealed tube containing a magnetic stirring bar, toluene (0.23 mL), HBpin (145 µL, 1.0 mmol, 1.2 equiv) and *n*BuLi (2.5 M in hexane, 33 µL, 0.084 mmol, 10 mol %) were added sequentially. Then the mixture was stirred for 5 min at room temperature. Then, **39** (0.84 mmol) was added dropwise in toluene (0.1 mL) and the mixture stirred at 130 °C for 12 h. After completion of the reaction, the reaction mixture was allowed to cool to r.t. and quenched by HCl_{aq} 1.0 M. After an aqueous workup with EtOAc (3 x 10 mL), combined organic layers were dried over anhydrous $MgSO_4$ and solvent removed under reduced pressure. Product was purified by chromatography on silica gel (hexane:DCM, 100:0 to 70:30) to yield **S18** as a colorless oil (156.6 mg, 68% yield). **^{1}H NMR (300 MHz, $CDCl_3$)** δ 7.31 – 7.07 (m, 5H), 2.85 (p, *J* = 7.6 Hz, 1H), 1.63 – 1.54 (q, *J* = 7.6 Hz, 2H), 1.29 – 1.16 (m, 4H), 1.11 (s, 12H), 0.86 (t, *J* = 7.3 Hz, 3H) ppm. **^{13}C NMR (75 MHz, $CDCl_3$)** δ 147.7, 128.2, 127.6, 125.8, 83.0, 42.0, 41.4, 24.8, 20.9, 14.3 ppm. **^{11}B NMR (160 MHz, $CDCl_3$)** δ 33.8 ppm. **HRMS (APCI)** Calc. for $C_{17}H_{28}BO_2$ [M-H$^+$] 275.2177, found 275.2180.

2-phenyl pentanoic acid (54)

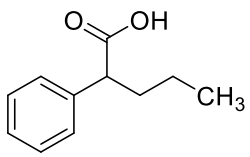

In a 10 mL round bottom flask equipped with a magnetic stirring bar, **S18** (156.3 mg, 0.57 mmol) was dissolved in MeOH (0.6 mL) and then NaOH 20% (aq) (0.18 mL) and H_2O_2 30 % $^{v}/_{v}$ (aq) (0.18 mL) were sequentially added. Mixture was vigorous stirred at room temperature for 2 h. After that time, the reaction was quenched with 5 mL of HCl_{aq} 1.0 M and mixture extracted with Et_2O (3 x 10 mL). Combined organic layers were dried over anhydrous $MgSO_4$ and solvent removed under reduced pressure. Alcohol **A** was used without further purification.

Alcohol **S19** was further oxidized to the carboxylic acid **54** by means of a modified reported procedure:[252] in a 10 mL round bottom flask equipped with a magnetic stirring bar, H_5IO_6 (133 mg, 0.6 mmol, 1.05 equiv) was dissolved in MeCN (4 mL) and the mixture was stirred vigorously at r.t. for 15 min. After that time, mixture was cooled down in an ice-water bath and alcohol **S19** was then added in MeCN solution (1 mL), followed by addition of PCC (2 mg, 0.01 mmol, 2 mol%). Reaction mixture was stirred for 3 h and quenched with HCl_{aq} 1 M until reach pH = 2 - 3, diluted with EtOAc (10 mL) and washed with brine (10 mL), sat. aq. $NaHSO_3$ solution (10 mL), and brine (10 mL), respectively, dried over anhydrous Na_2SO_4 and concentrated to yield the clean carboxylic acid **54** (45.7 mg, 45% yield 2 steps). **^{1}H NMR (300 MHz, $CDCl_3$)** δ 7.35 – 7.27 (m, 5H), 3.57 (t, *J* = 7.7 Hz, 1H), 2.06 (td, *J* = 13.9, 7.5 Hz, 1H), 1.77 (dq, *J* = 13.8, 7.6 Hz, 1H), 1.38 – 1.21 (m, 4H), 0.91 (t, *J* = 7.3 Hz, 3H) ppm. **^{13}C NMR (75 MHz, $CDCl_3$)** δ 180.5, 138.7, 128.8, 128.2, 127.5, 51.5, 35.3, 20.8, 13.9 ppm. **HRMS (ESI-)** Calc. for $C_{11}H_{13}O_2$ [M-H^+] 177.0921, found 177.0925.

5.4.4 Atenuated Total Reflectance (ATR) Spectra

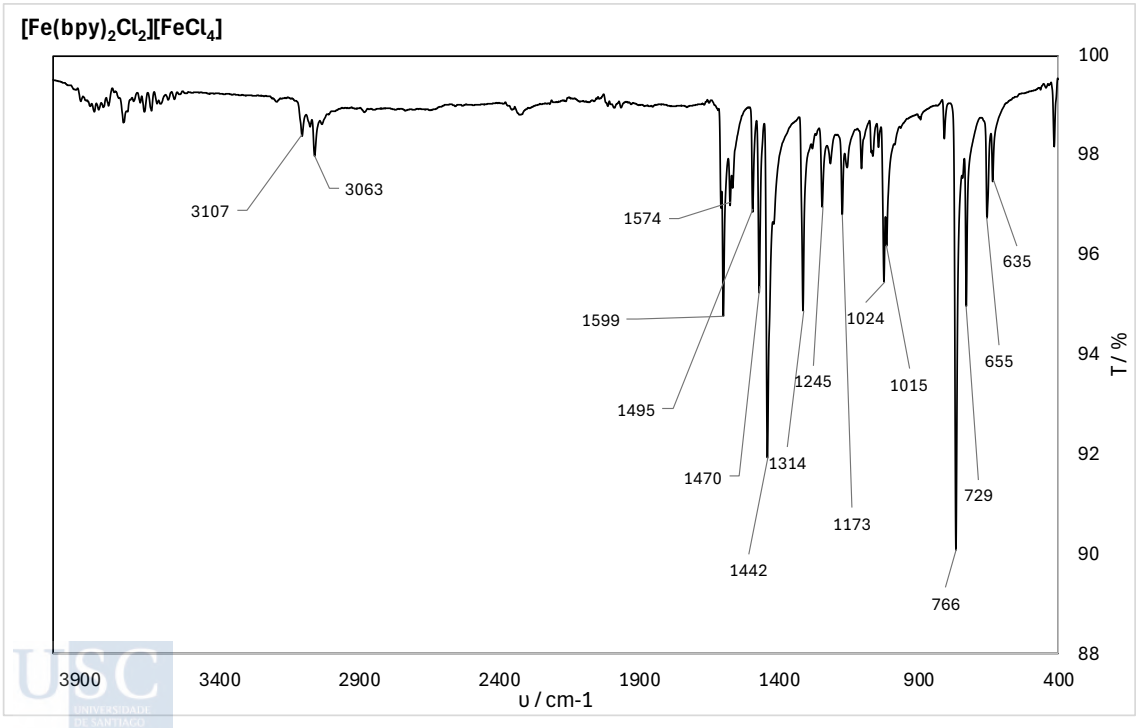

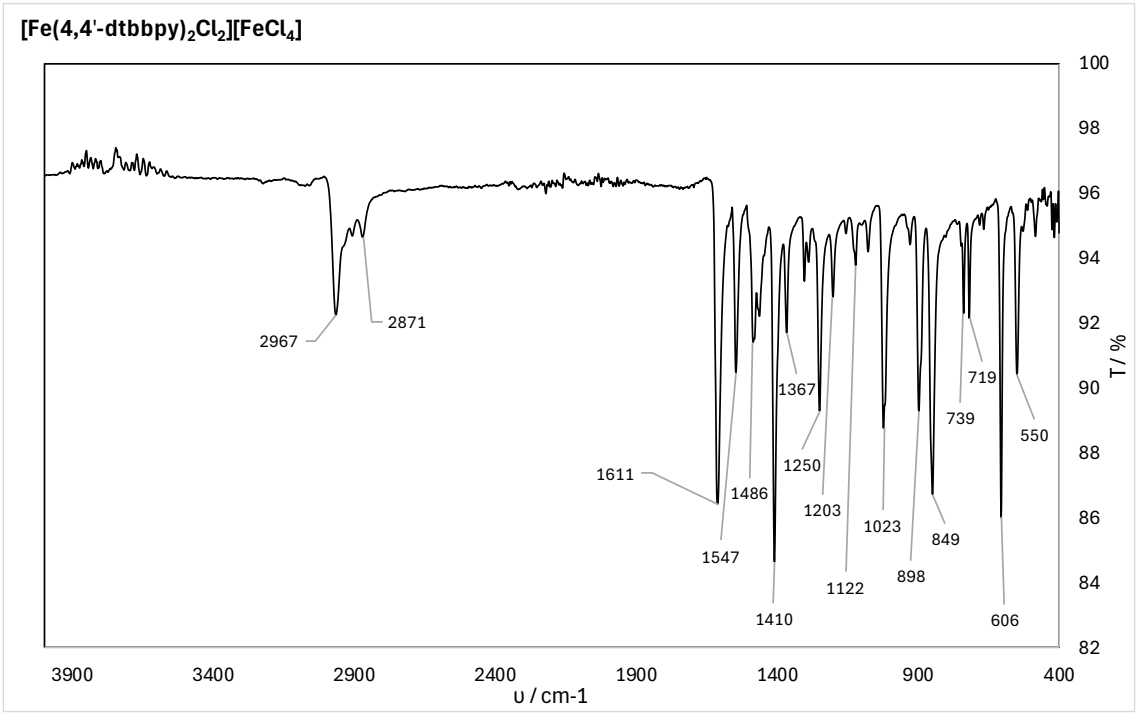
[Fe(4,4'-dtbbpy)2Cl2][FeCl4]
2967
2871
1611
1547
1486
1410
1367
1250
1203
1122
1023
898
849
739
719
606
550
T / %
υ / cm-1

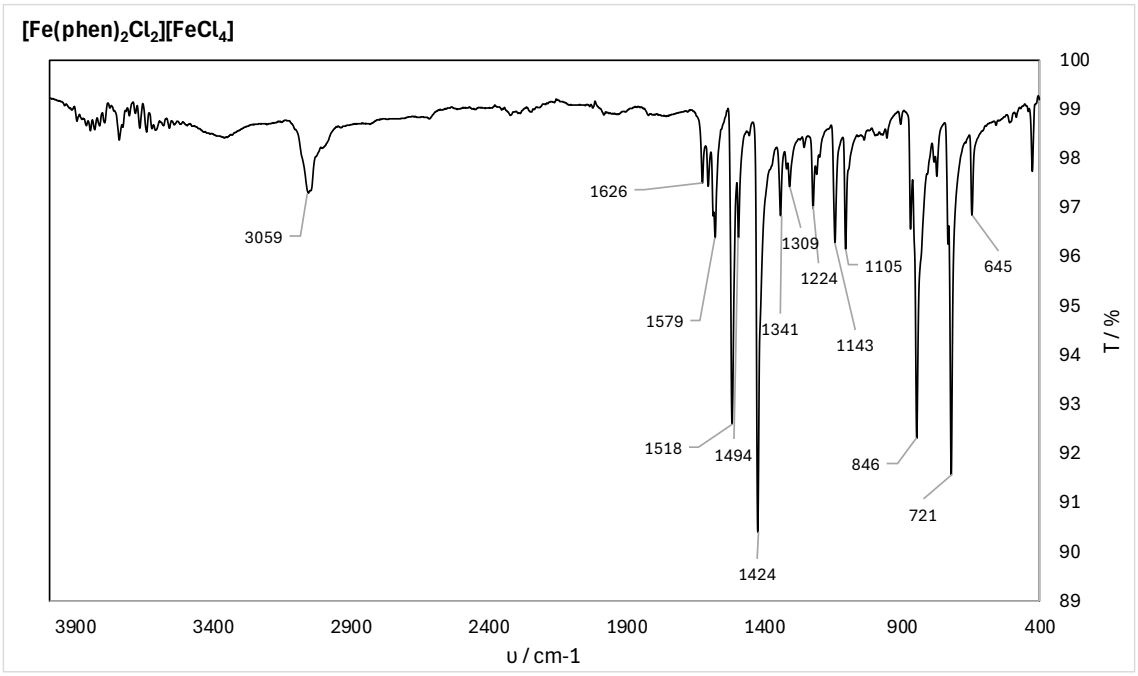
[Fe(phen)2Cl2][FeCl4]
3059
1626
1579
1518
1494
1424
1341
1309
1224
1143
1105
846
721
645
T / %
υ / cm-1

5.4.5 ^{1}H-NMR, ^{13}C-NMR, ^{11}B-NMR and ^{19}F-NMR Spectra

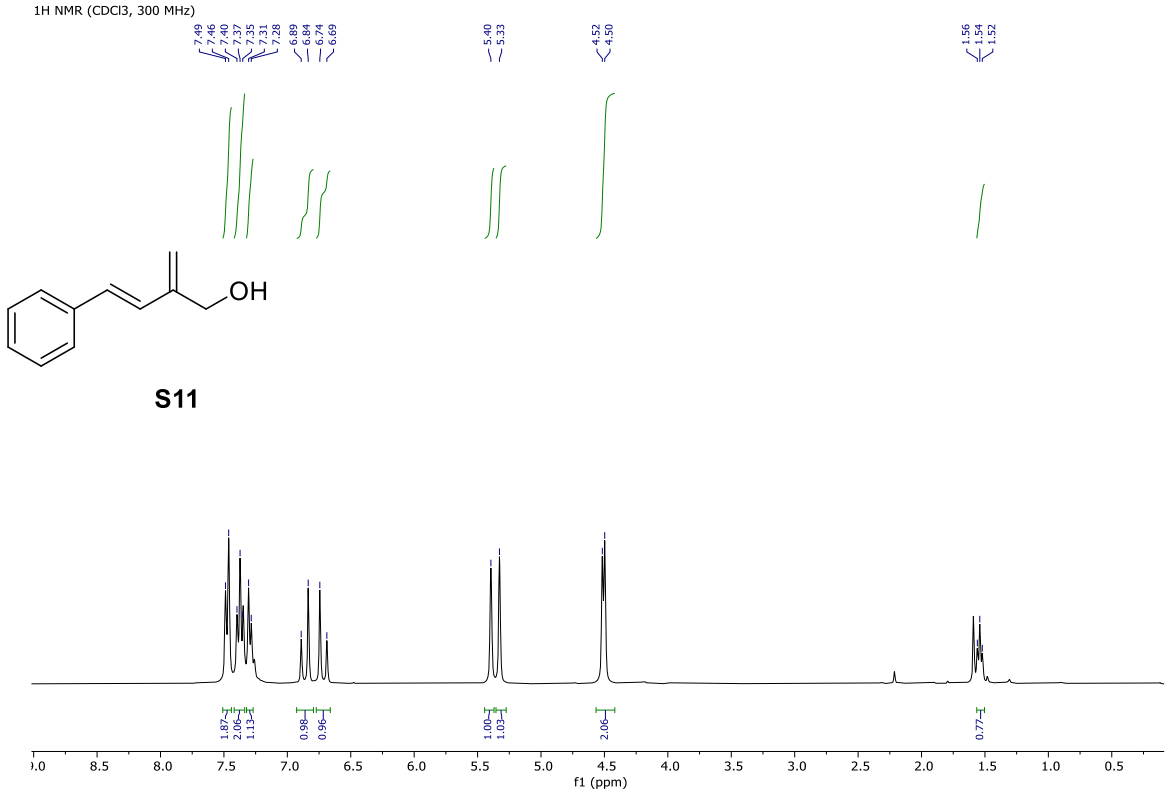

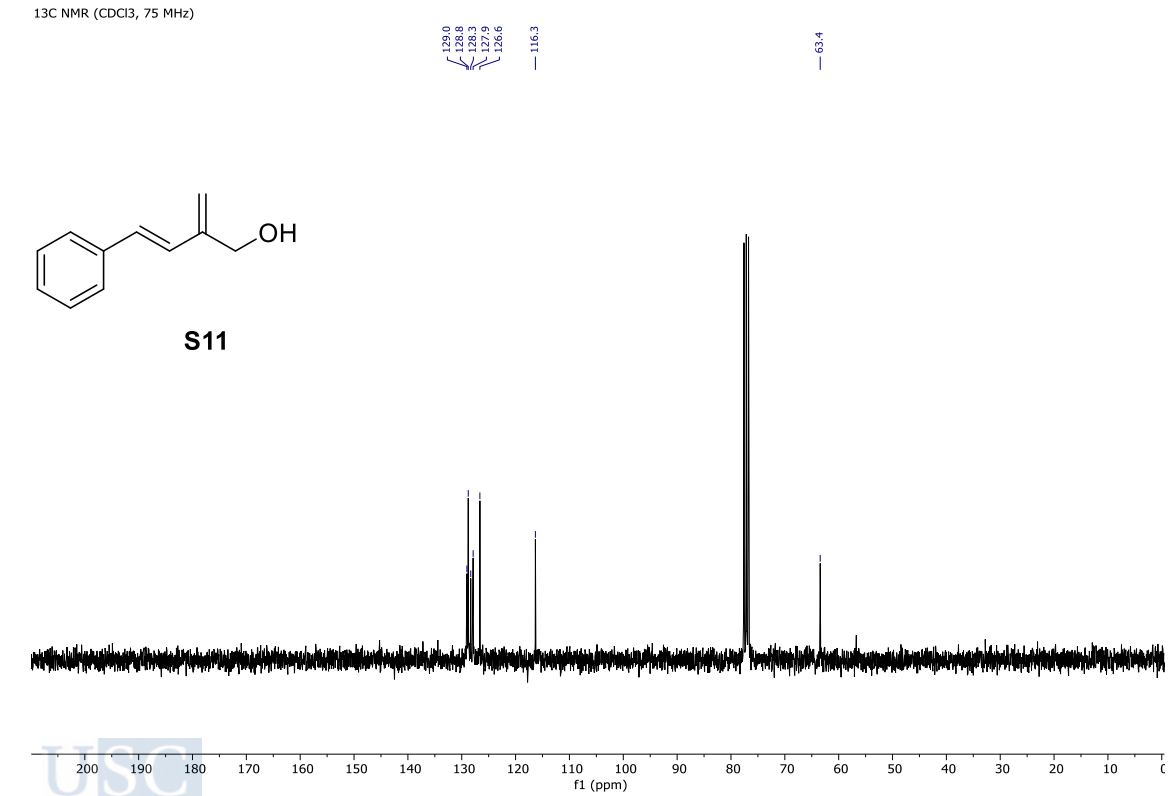

1H NMR (CDCl3, 300 MHz)

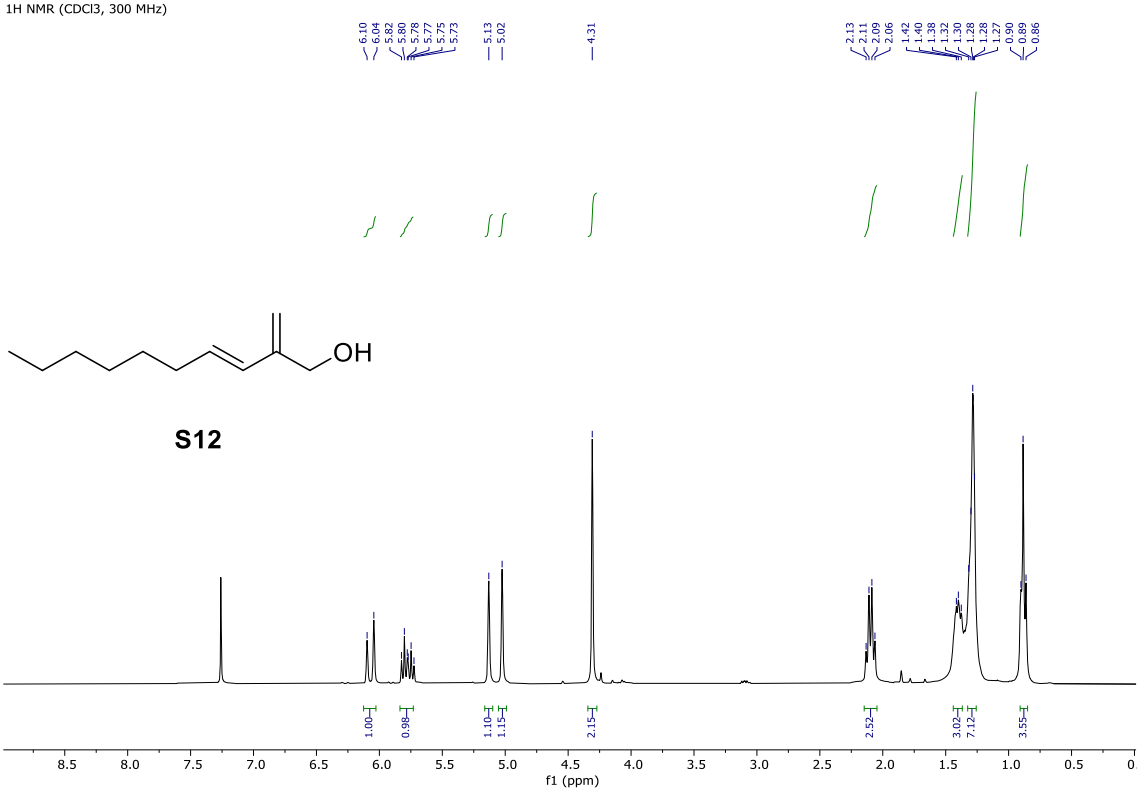

13C NMR (75 MHz)

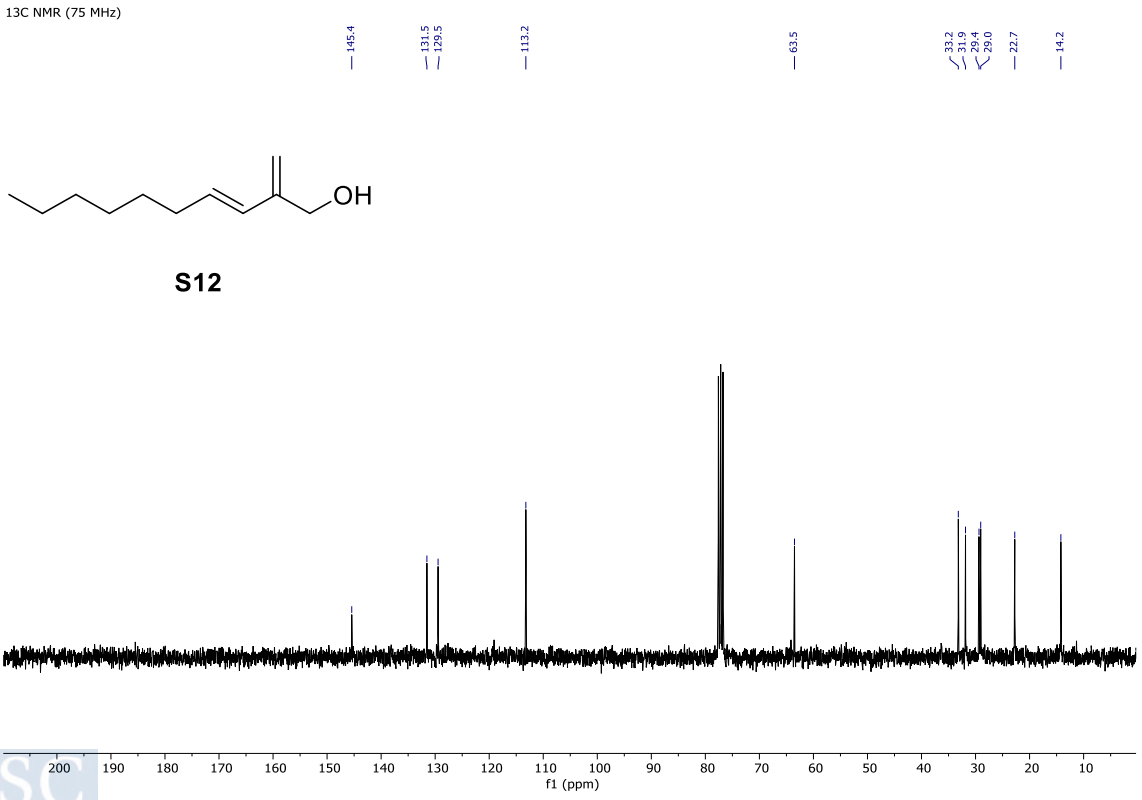

1H NMR (CDCl3, 300 MHz)

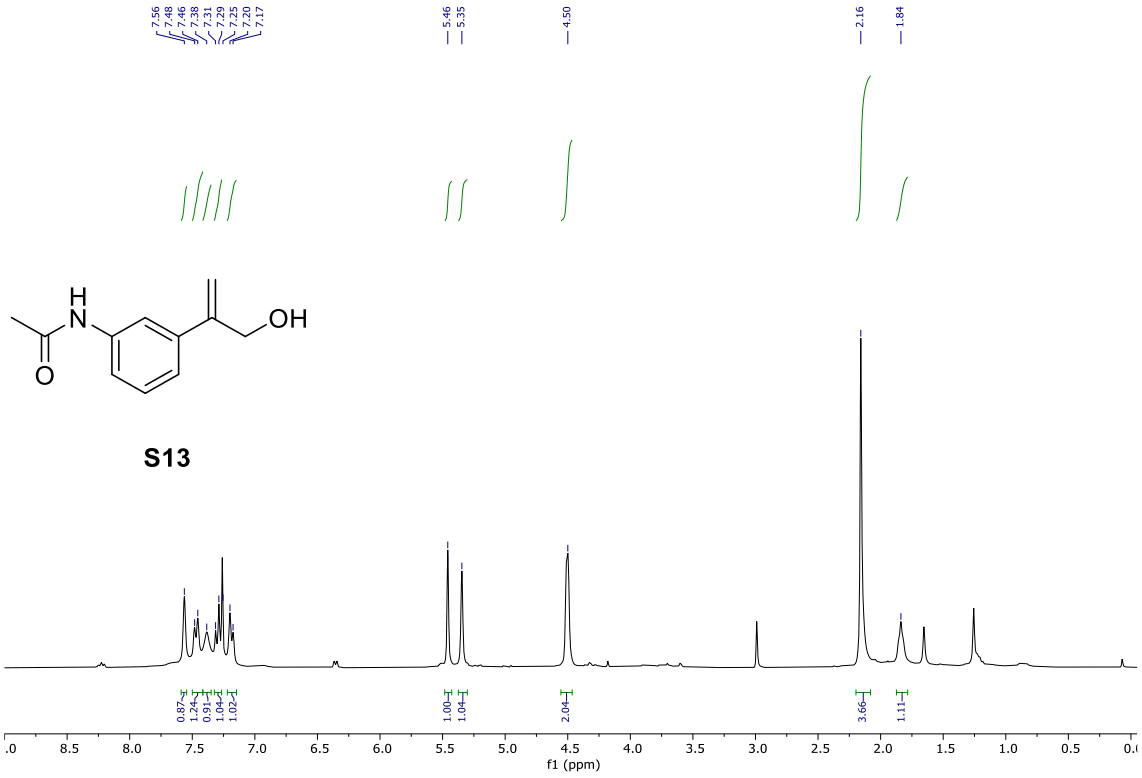

S13

13C NMR (CDCl3, 75 MHz)

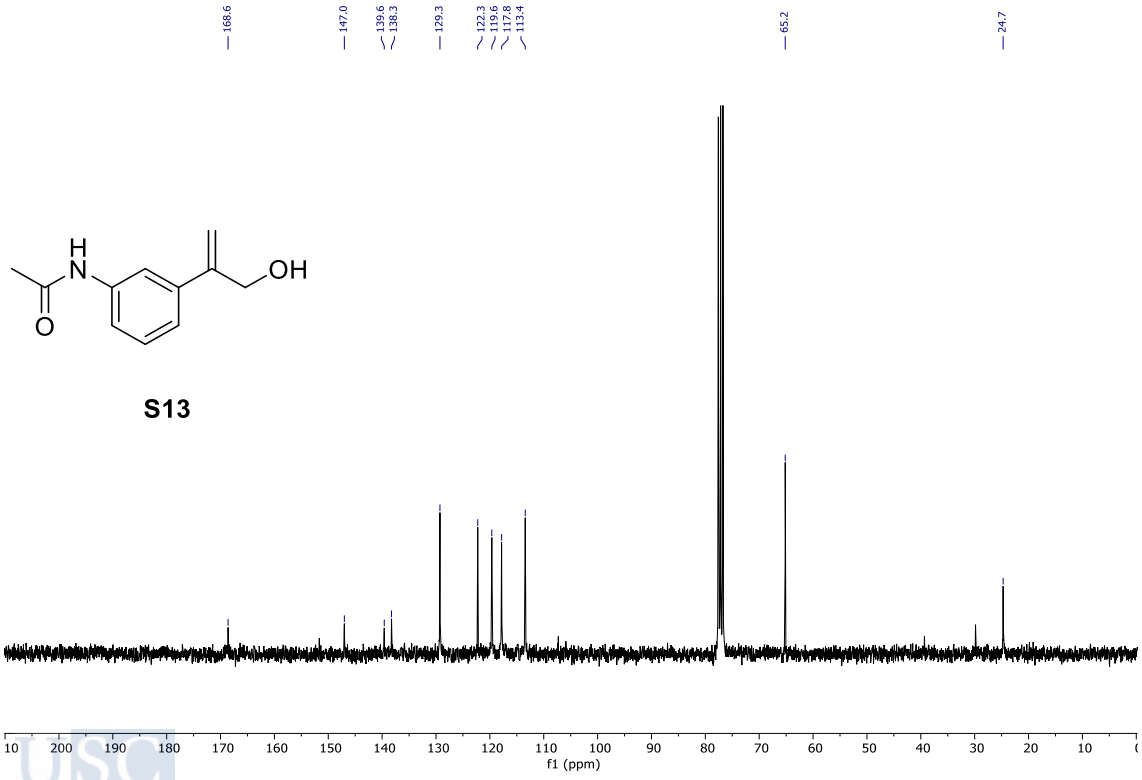

S13

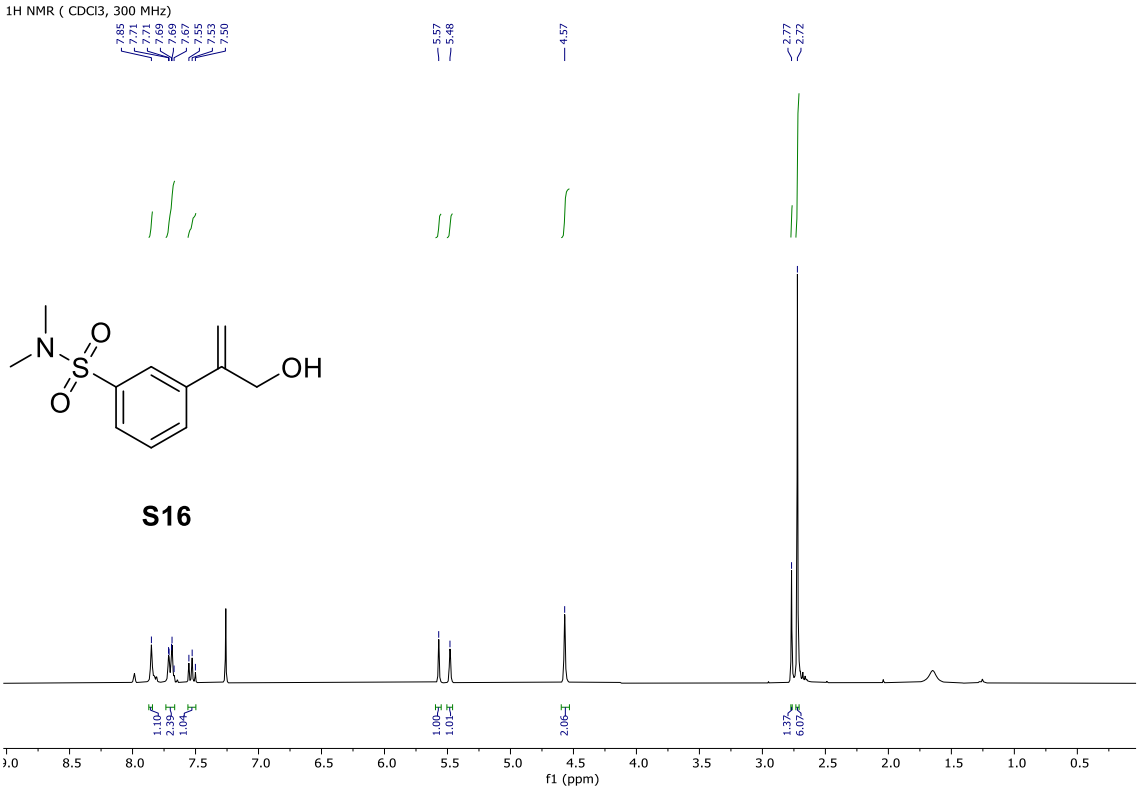

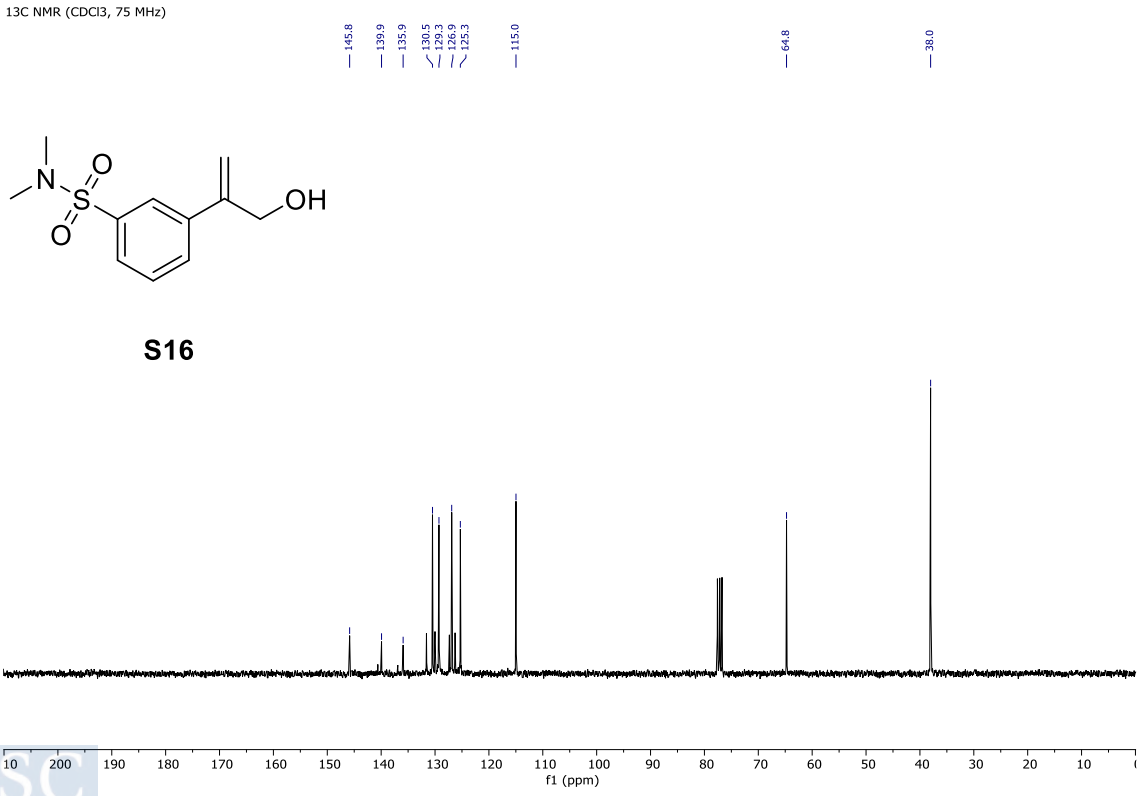

1H NMR (CDCl3, 300 MHz)

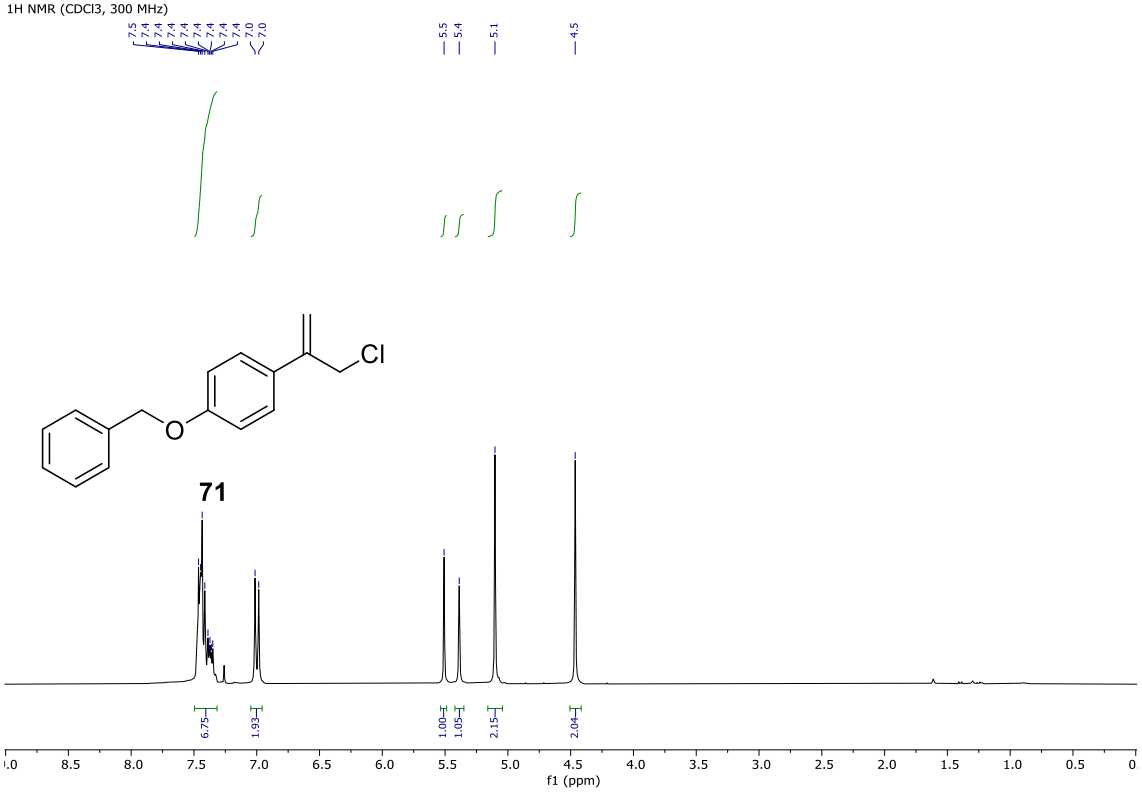

13C NMR (CDCl3, 75 MHz)

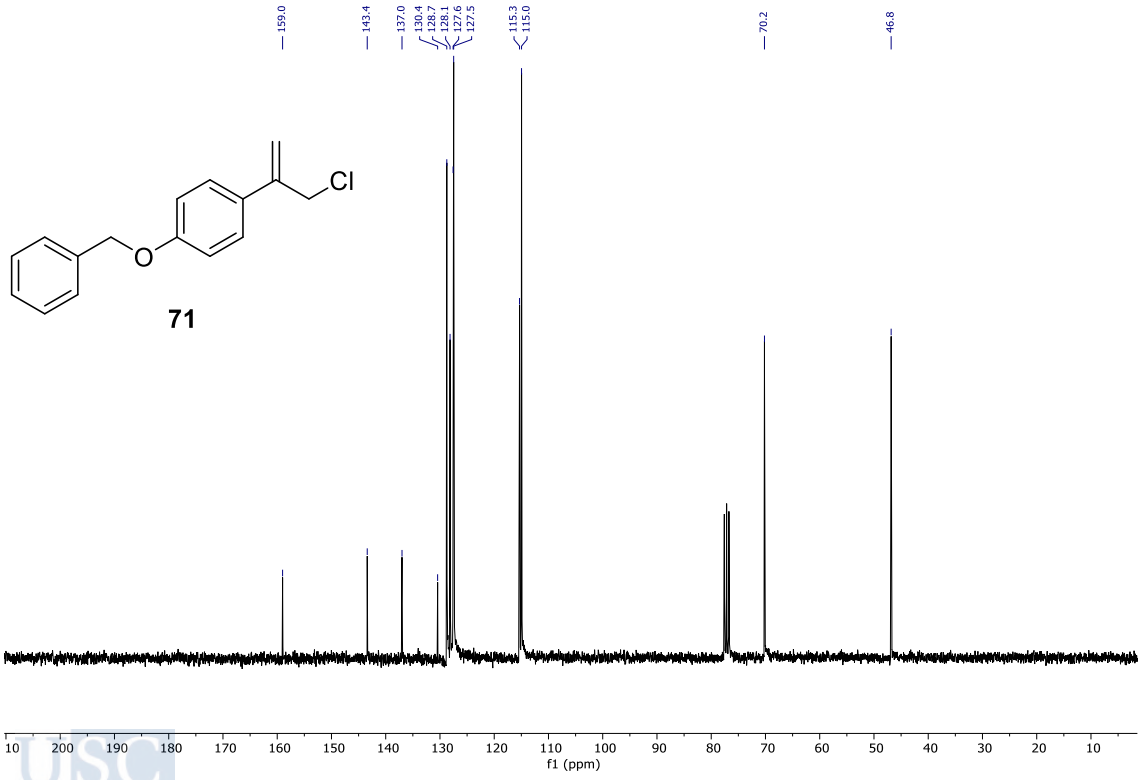

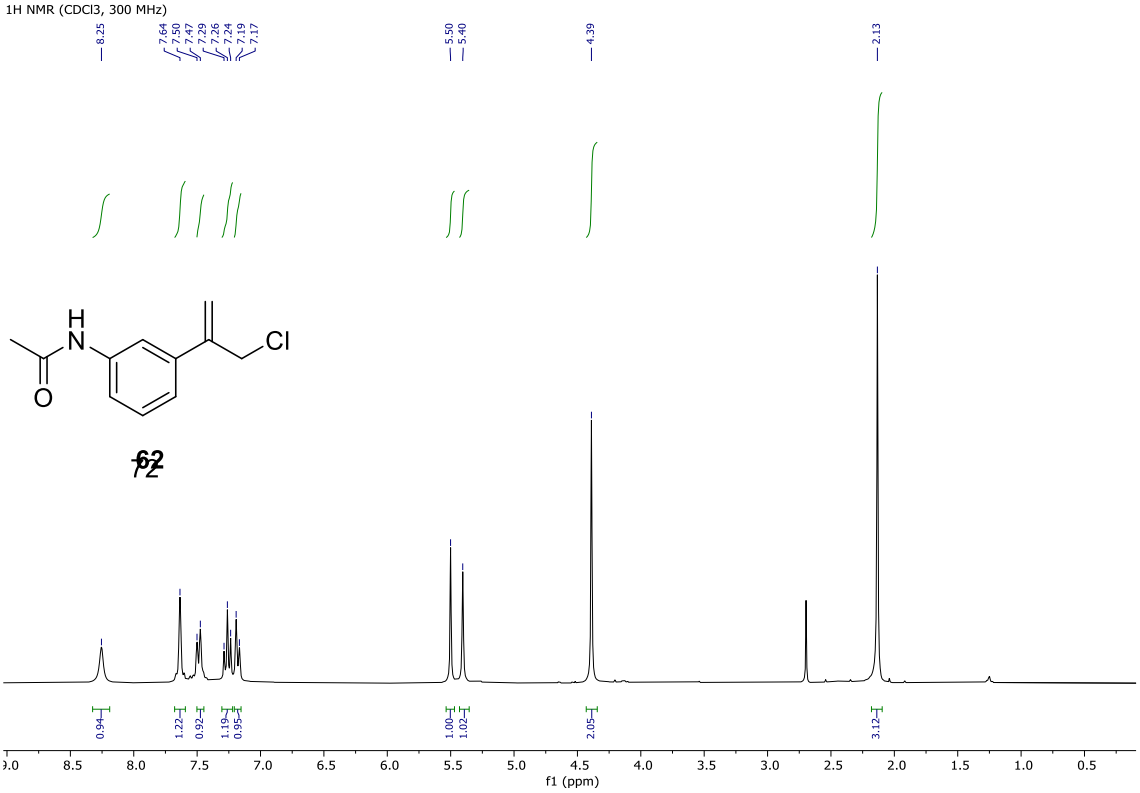
1H NMR (CDCl3, 300 MHz)
8.25
7.64
7.50
7.47
7.29
7.26
7.24
7.19
7.17
5.50
5.40
4.39
2.13
H
N
O
Cl
62
0.94
1.22
0.92
1.19
0.95
1.00
1.02
2.05
3.12
f1 (ppm)

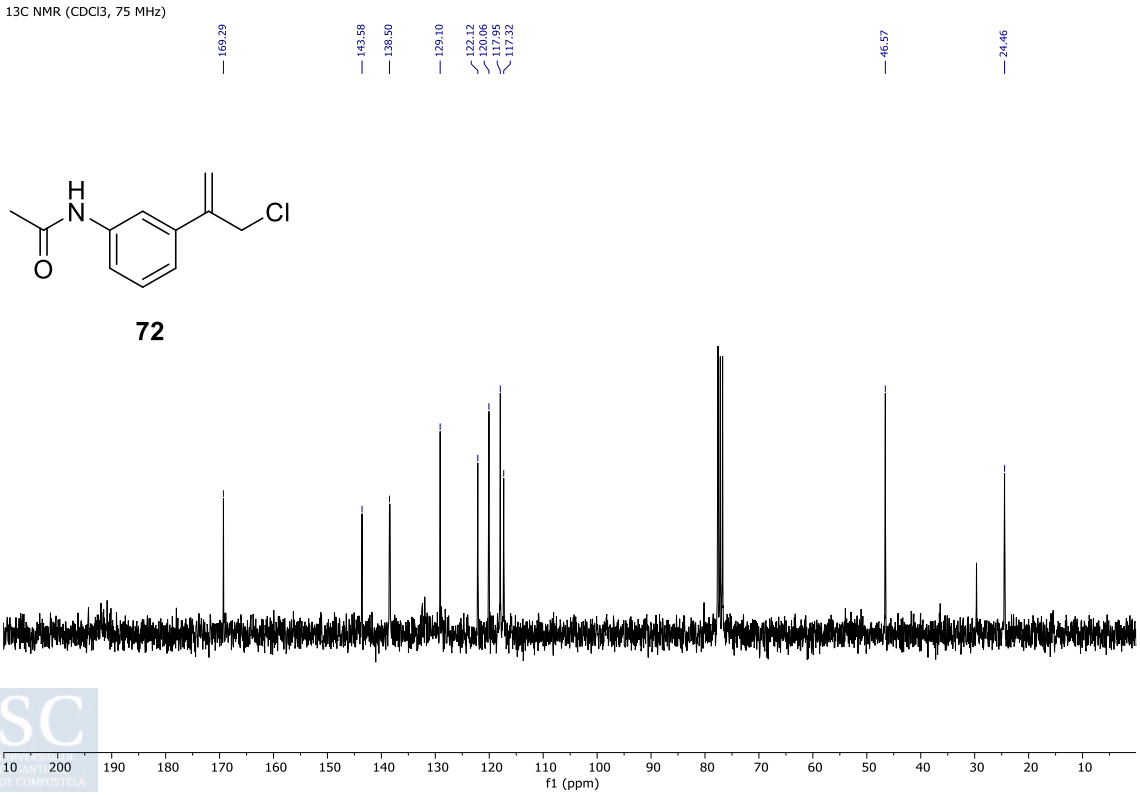
13C NMR (CDCl3, 75 MHz)
169.29
143.58
138.50
129.10
122.12
120.06
117.95
117.32
46.57
24.46
H
N
O
Cl
72
f1 (ppm)

1H NMR (CDCl3, 300 MHz)

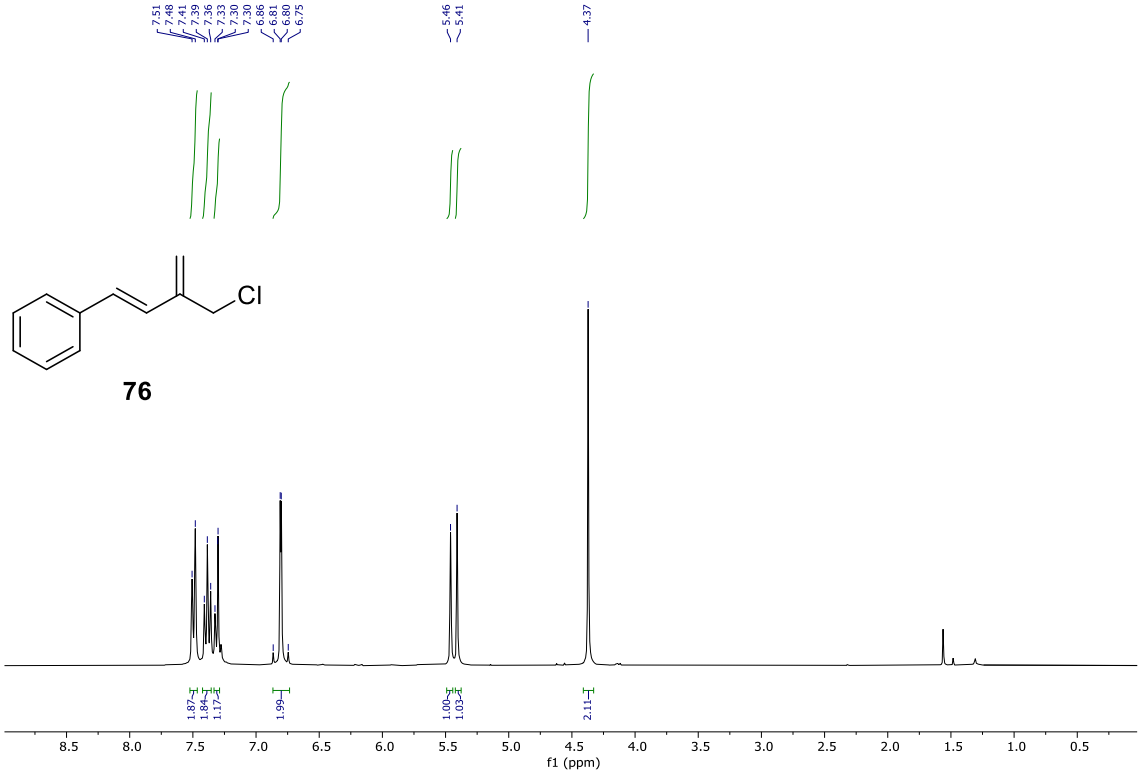

76

13C NMR (CDCl3, 75 MHz)

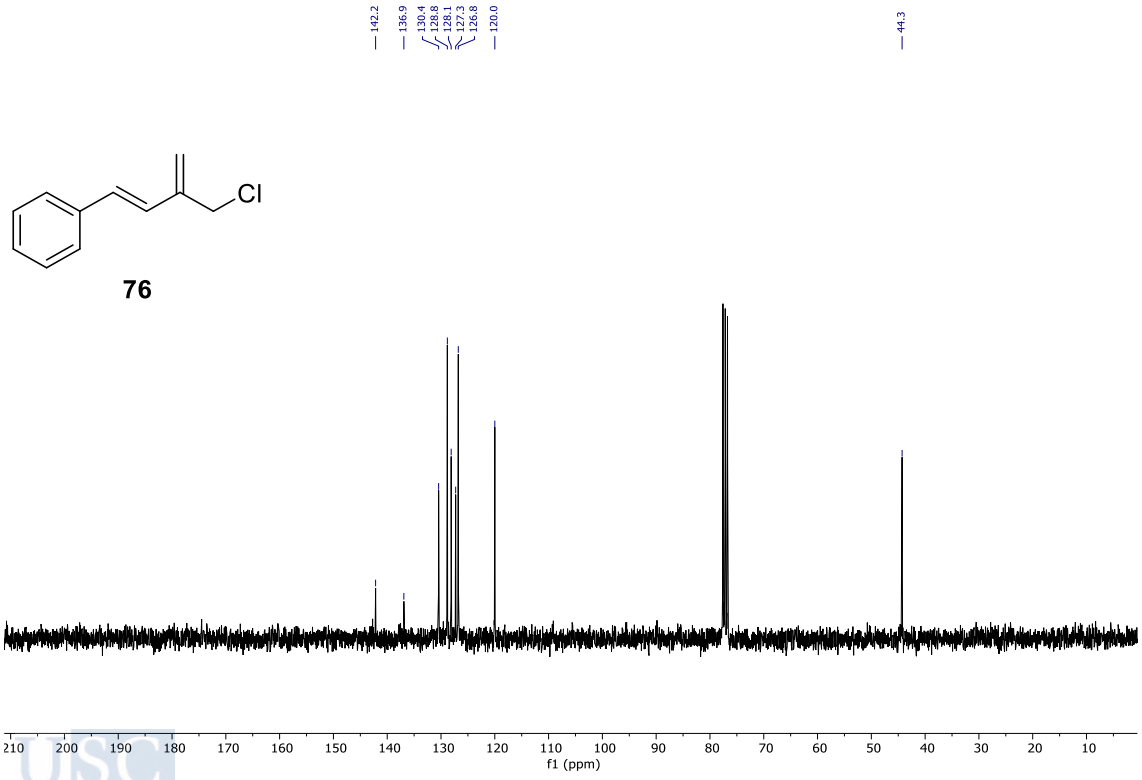

76

1H NMR (CDCl3, 300 MHz)

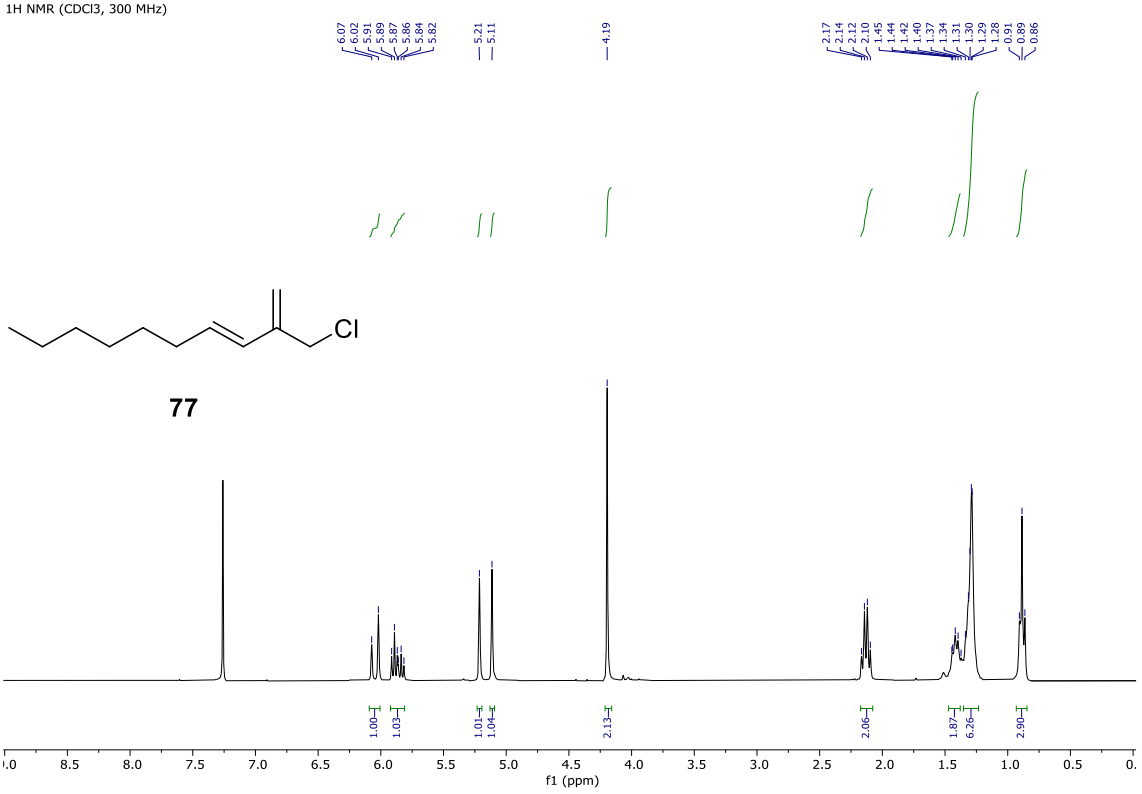

13C NMR (CDCl3, 75 MHz)

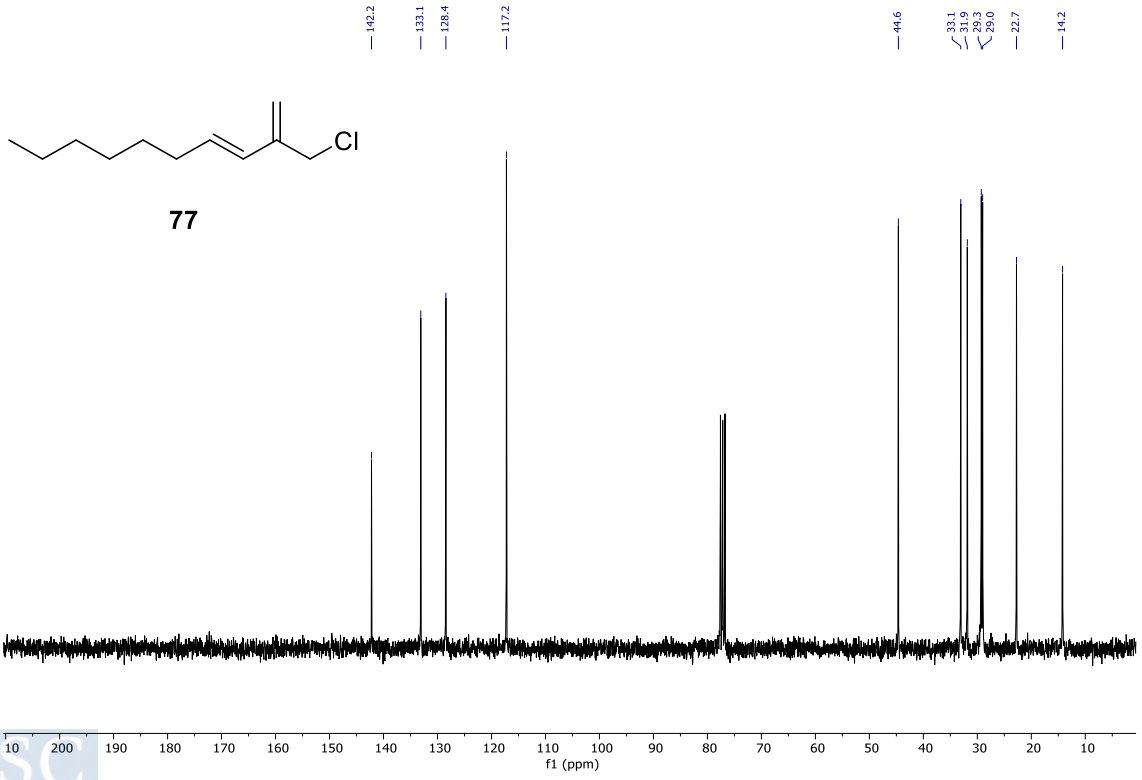

1H NMR (CDCl3, 300 MHz)

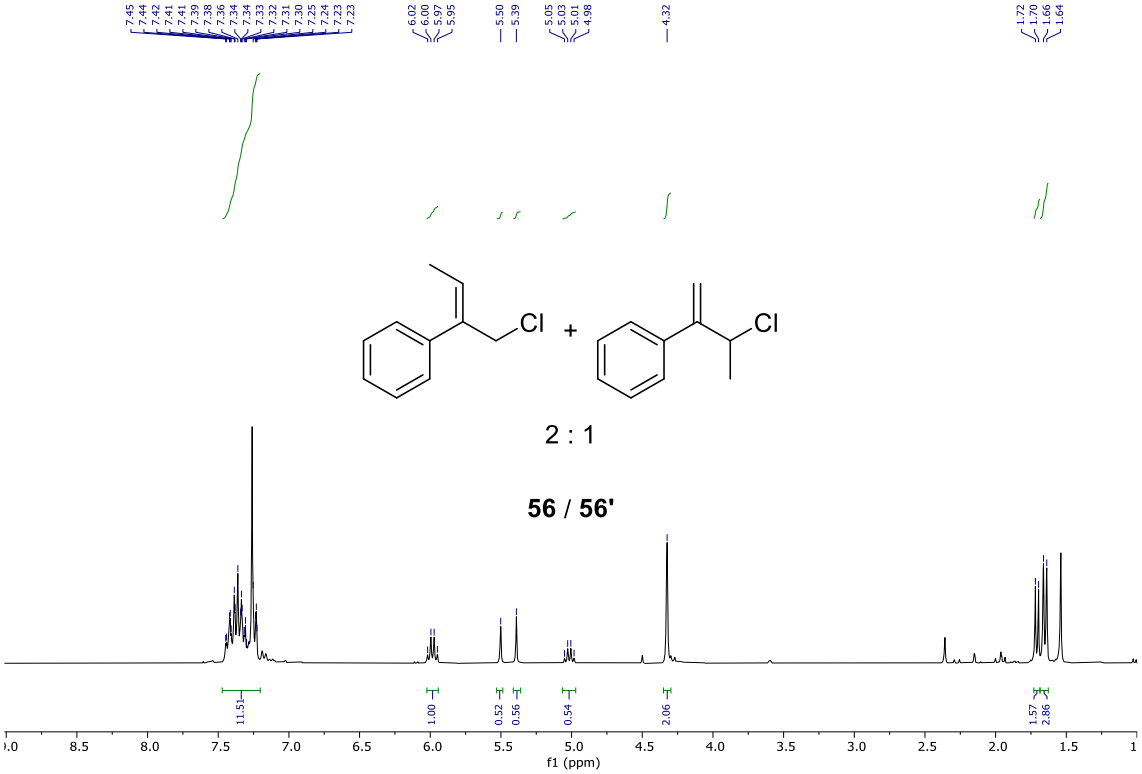

13C NMR (CDCl3, 500 MHz)

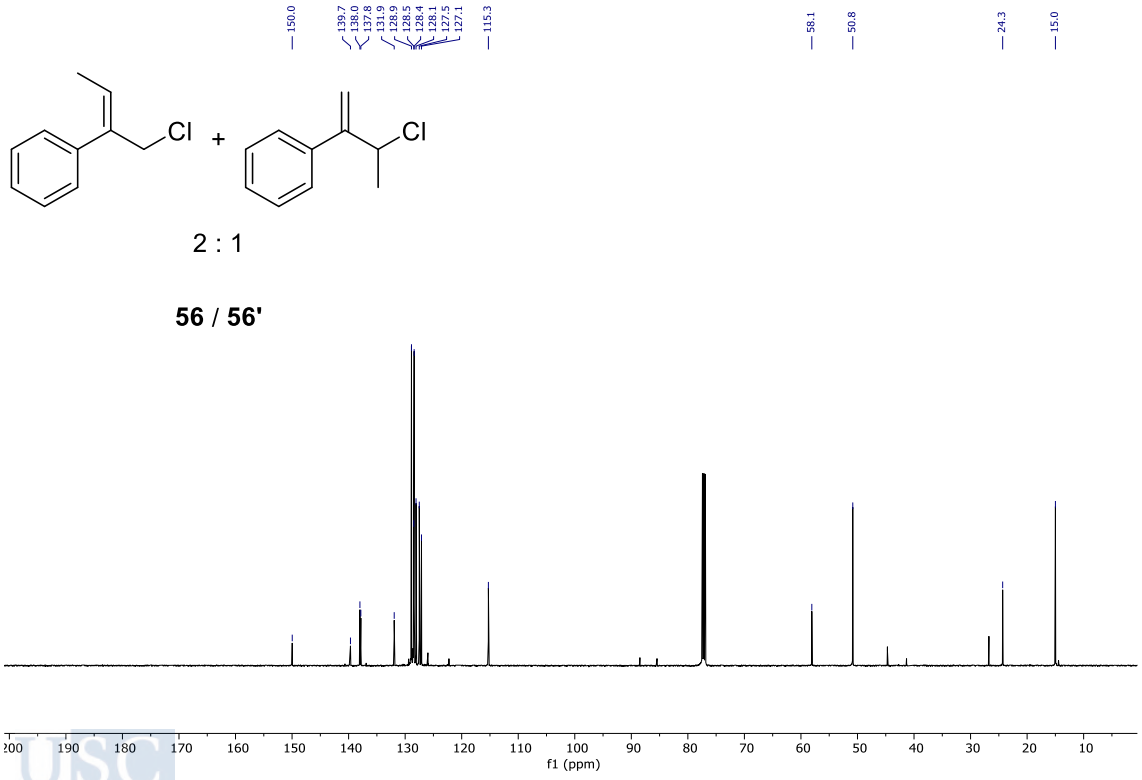

NOESY (CDCl3, 500 MHz)

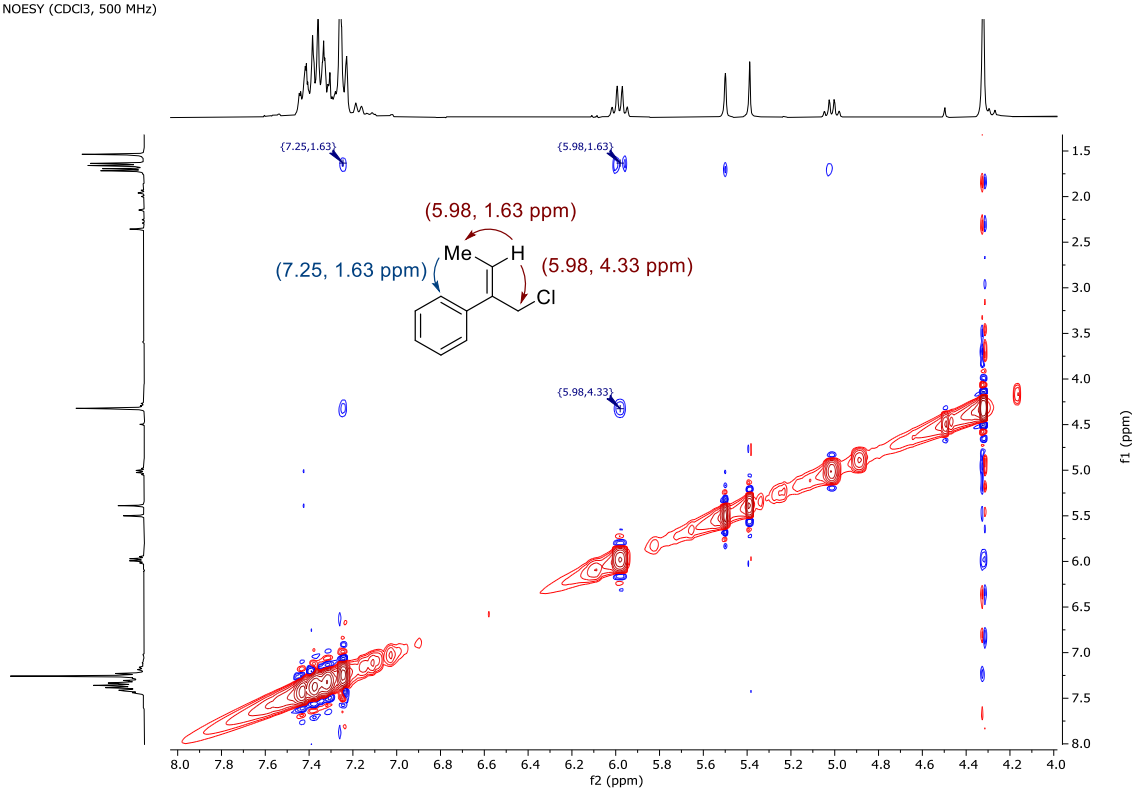

HSQC (CDCl3, 500 MHz)

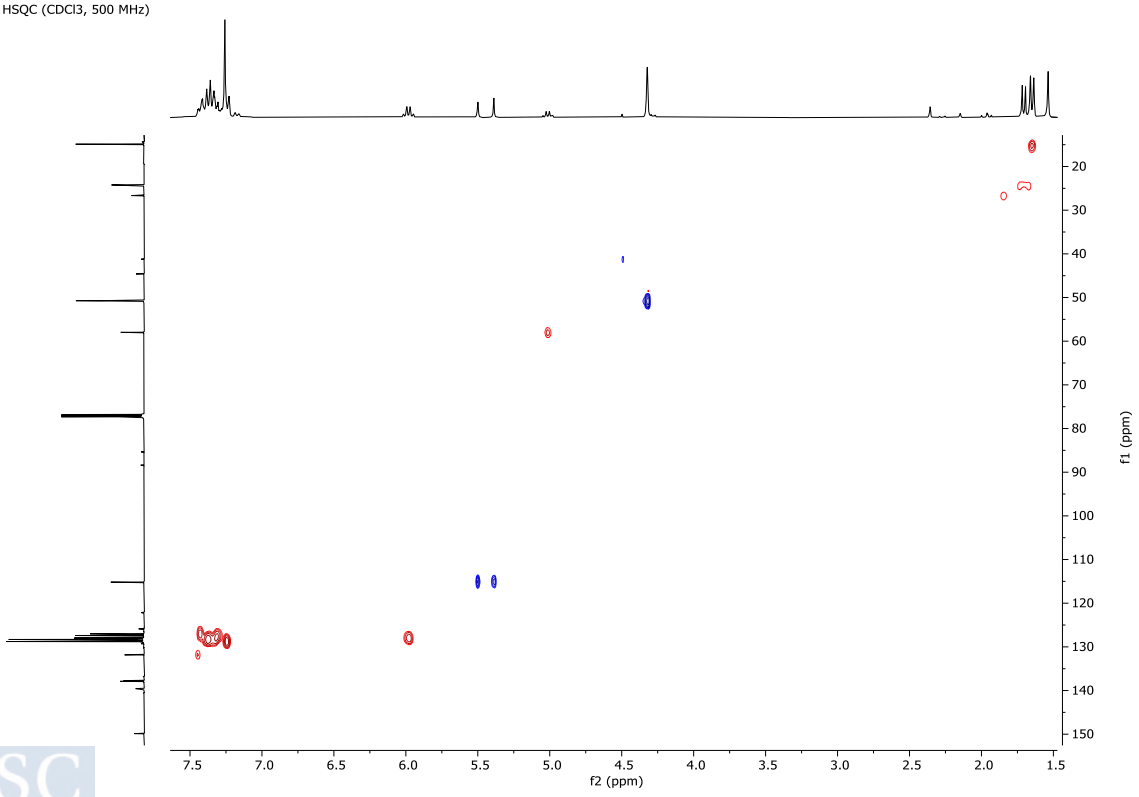

1H NMR (CDCl3, 300 MHz)

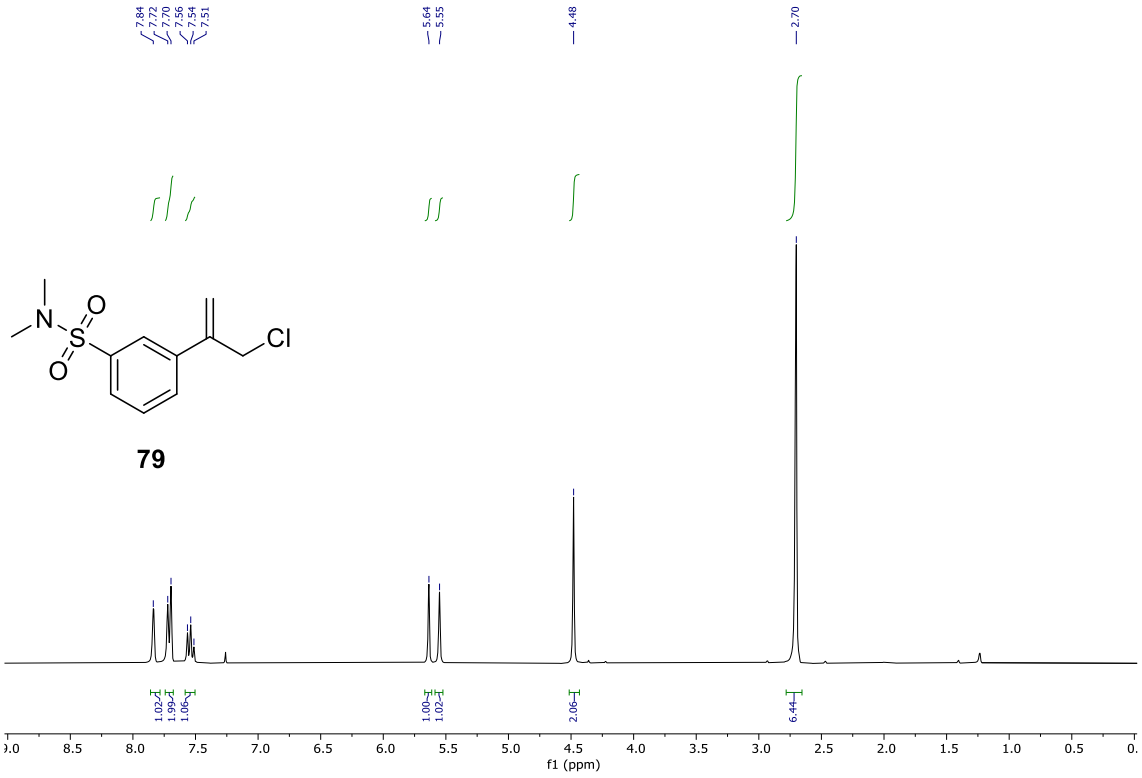

79

13C NMR (CDCl3, 75 MHz)

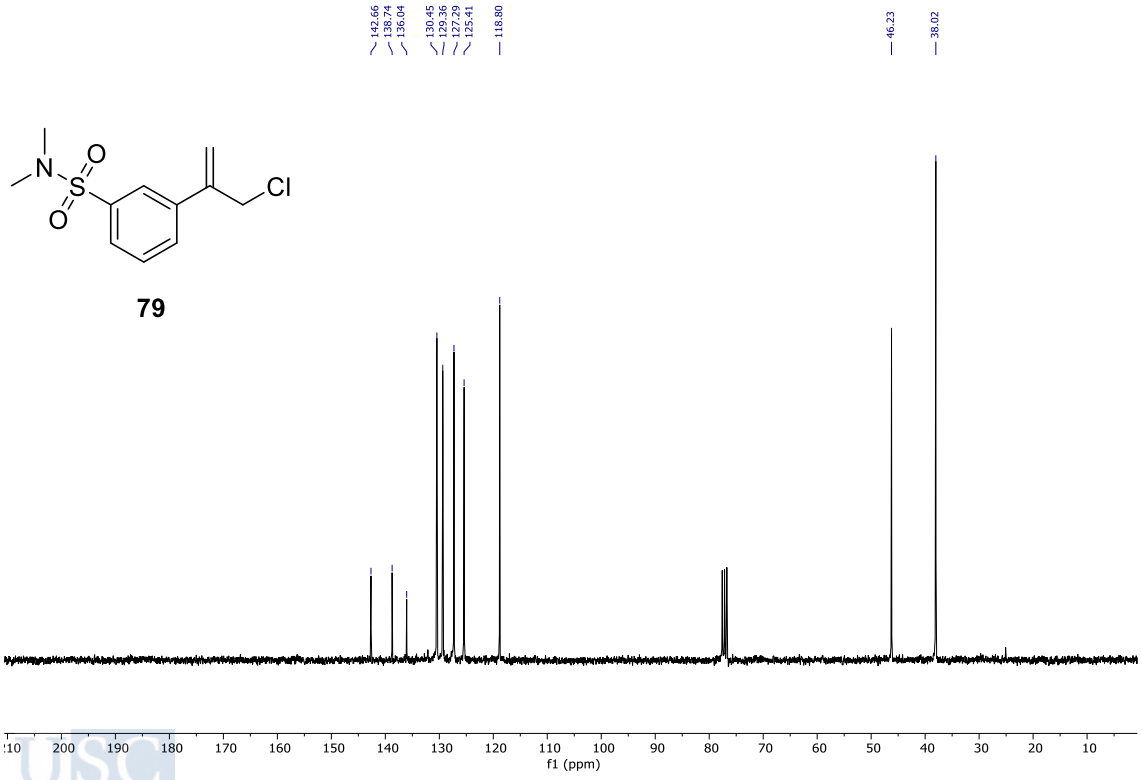

79

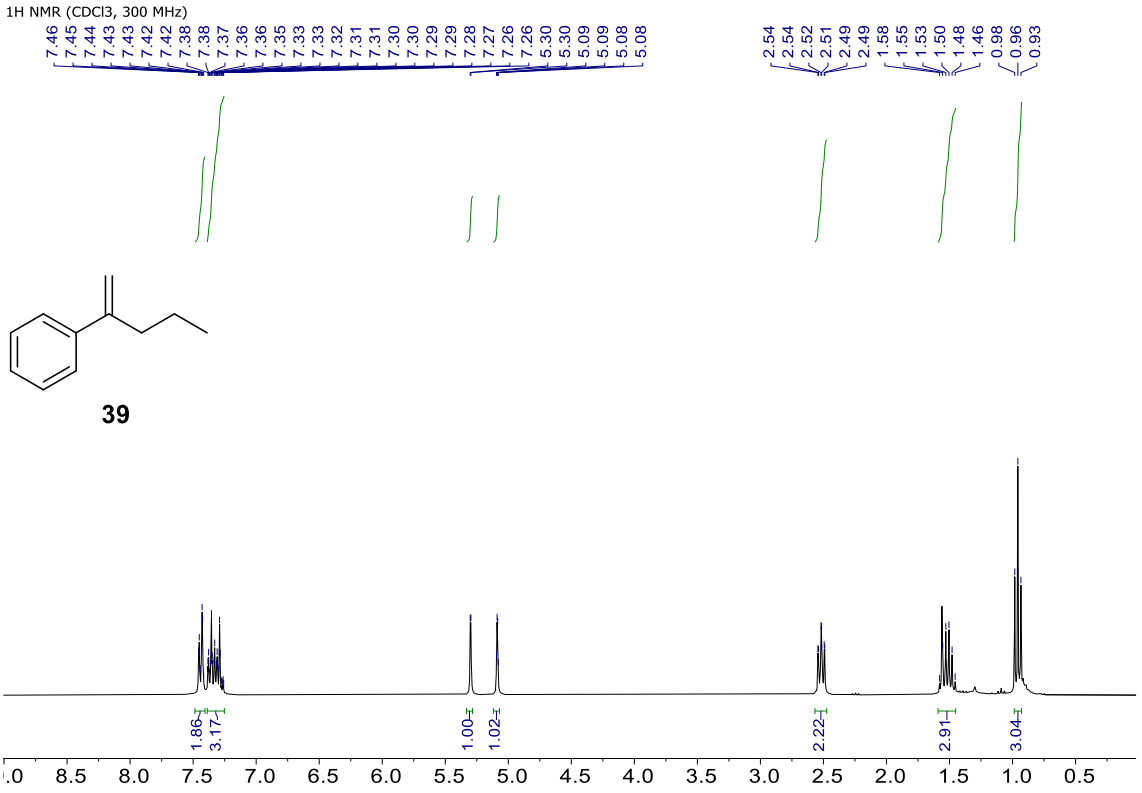

1H NMR (CDCl3, 300 MHz)

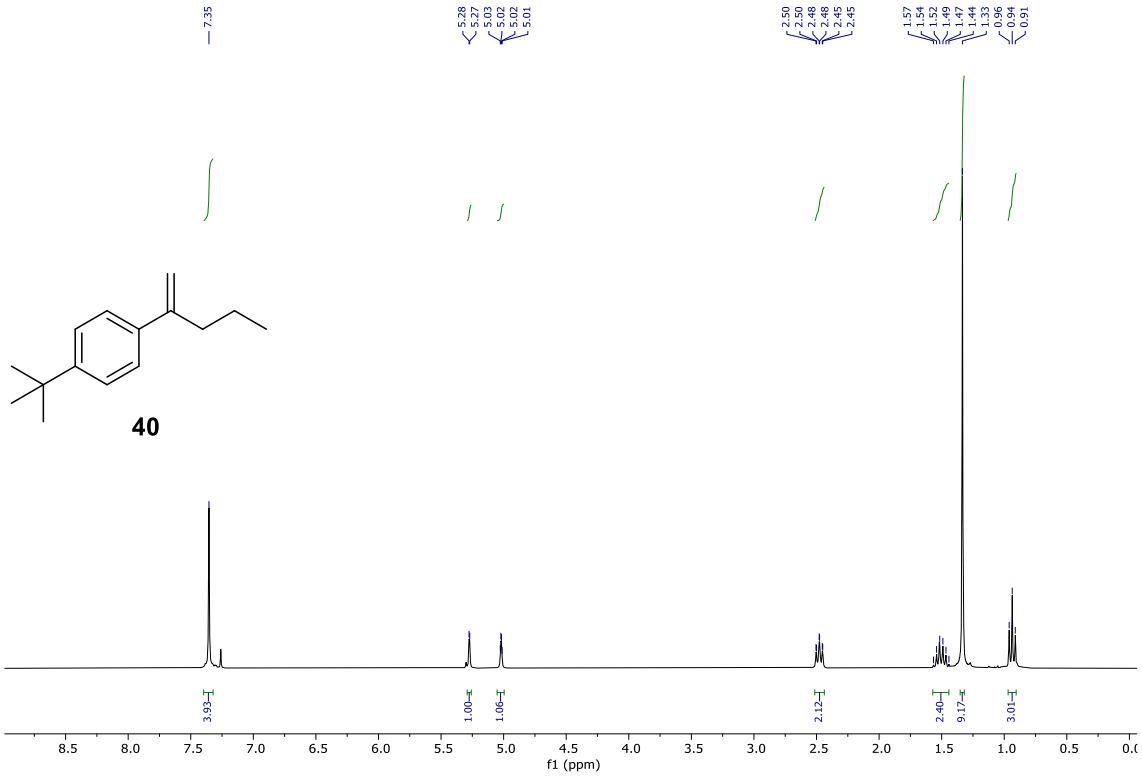

40

13C NMR (CDCl3, 75 MHz)

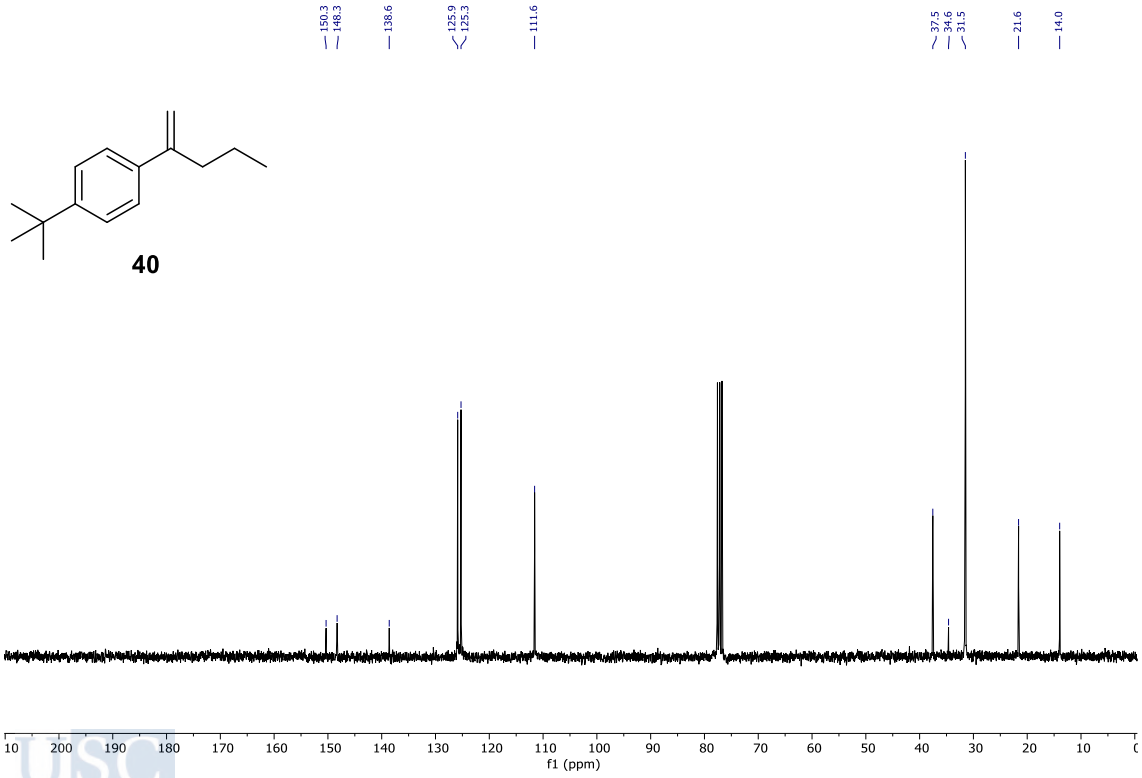

40

1H NMR (CDCl3, 300 MHz)

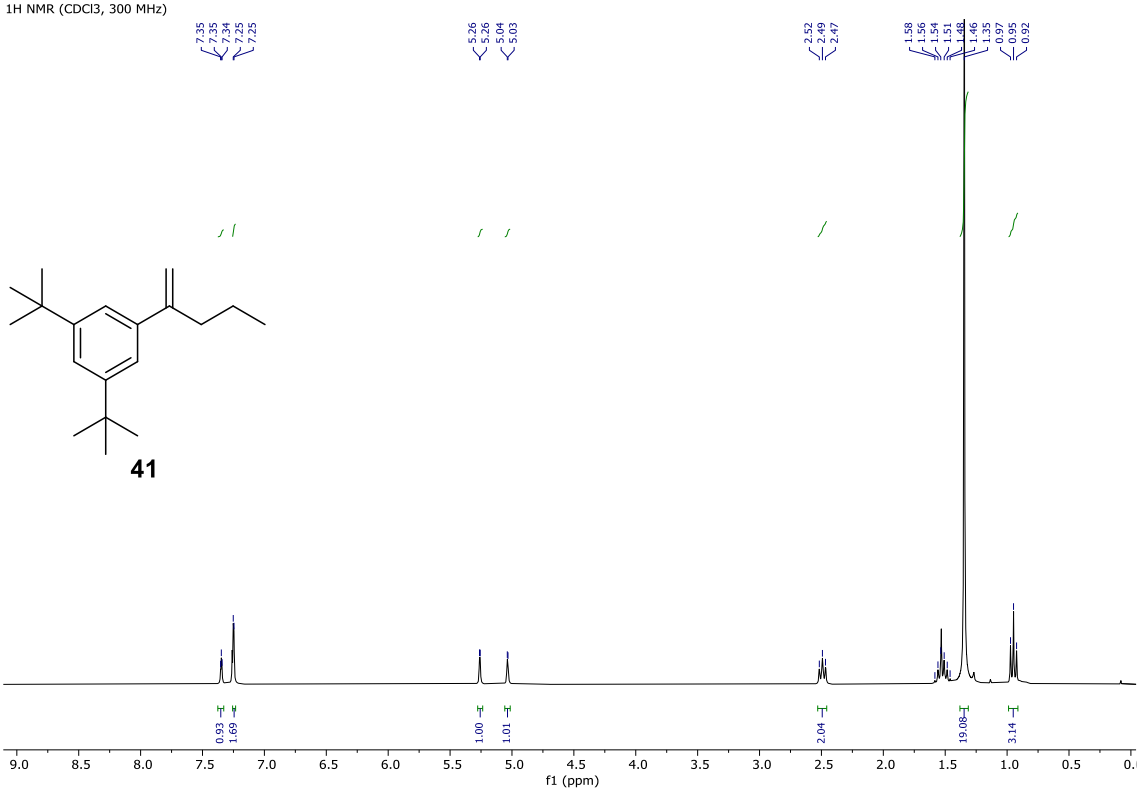

13C NMR (CDCl3, 75 MHz)

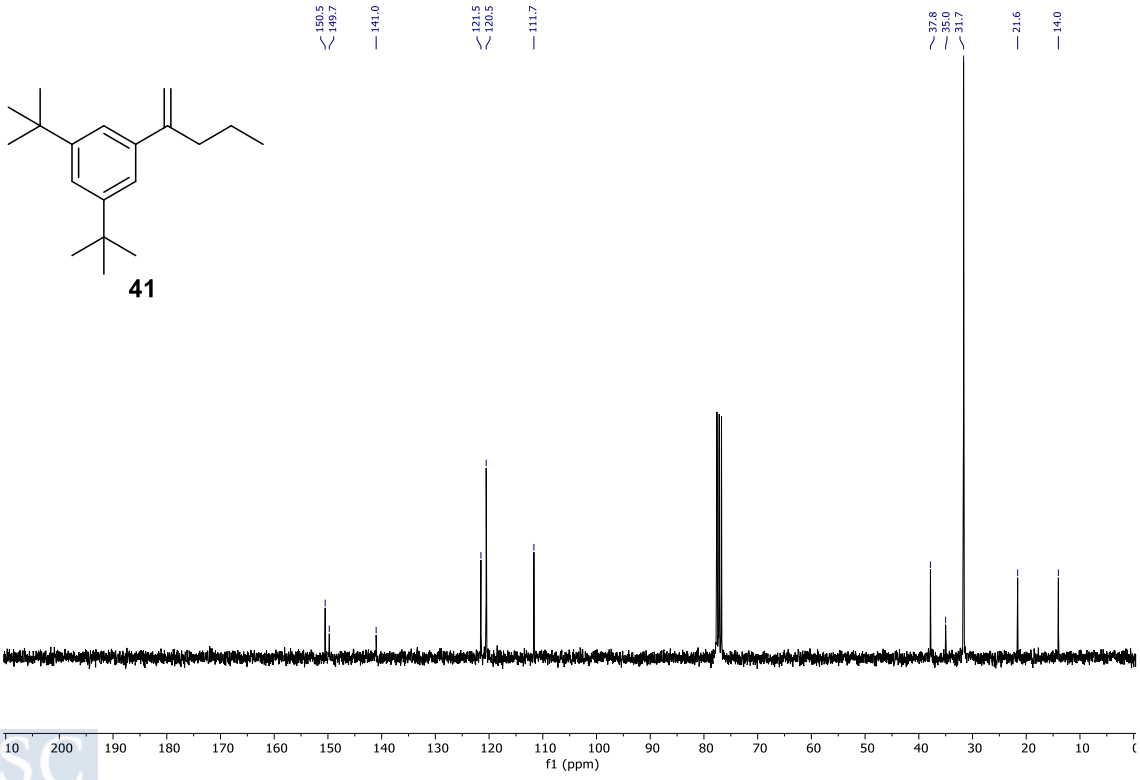

1H NMR (CDCl3, 300 MHz)

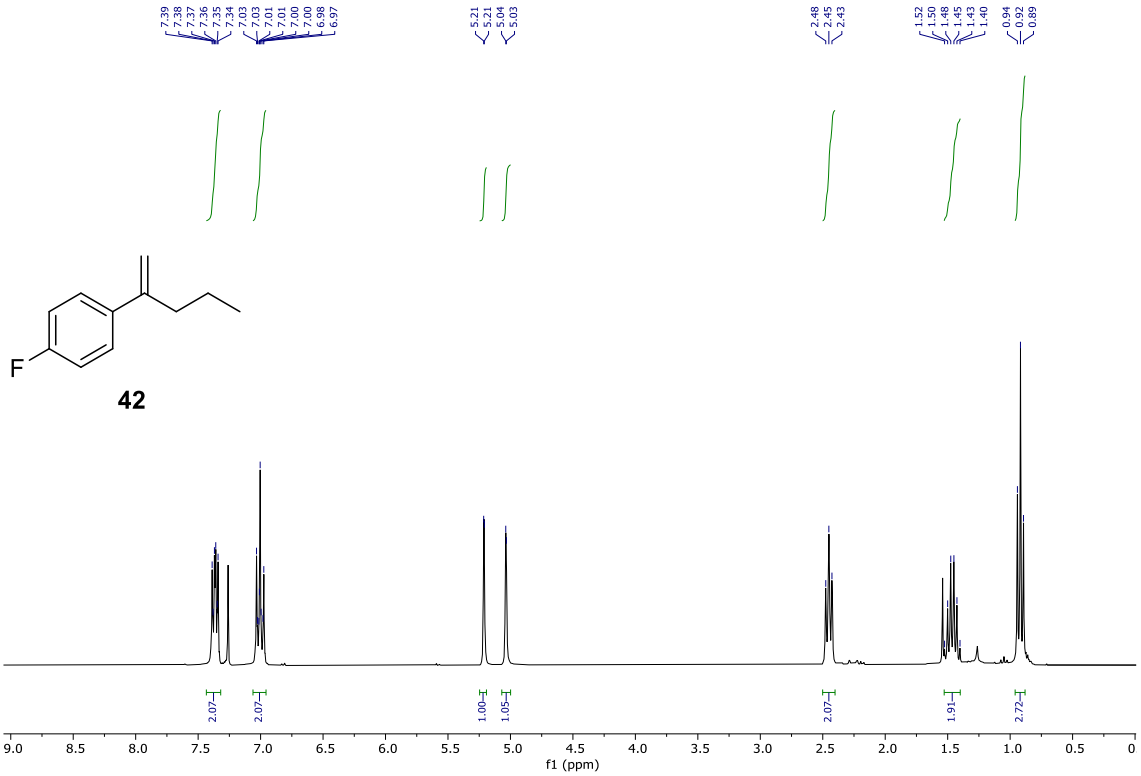

42

13C NMR (CDCl3, 75 MHz)

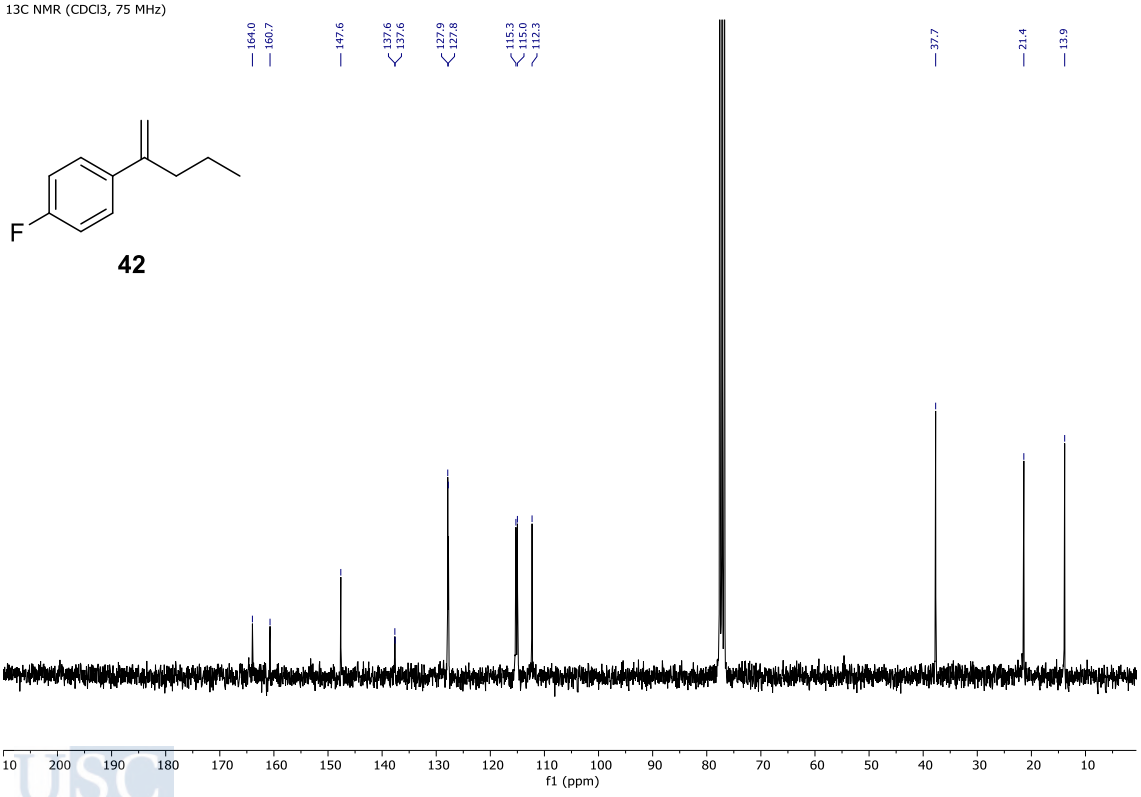

42

19F NMH (CDCl3, 282 MHz)

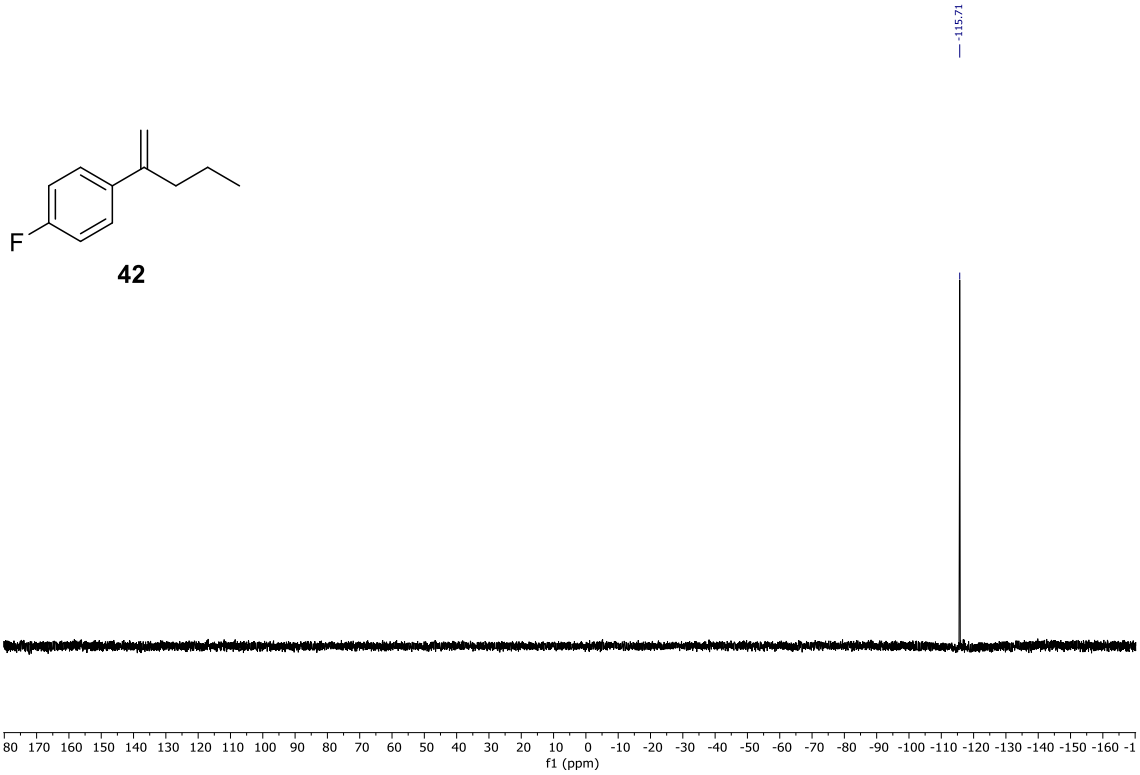

42

1H NMR (CDCl3, 300 MHz)

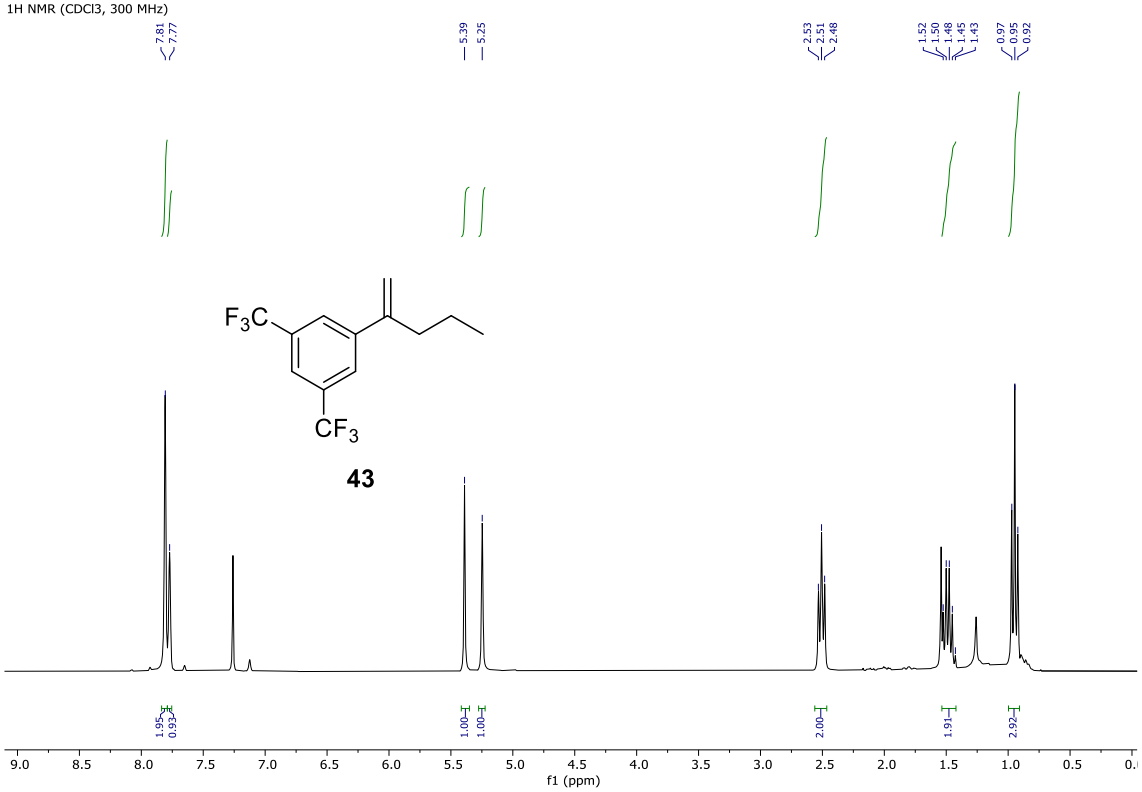

43

13C NMR (CDCl3, 75 MHz)

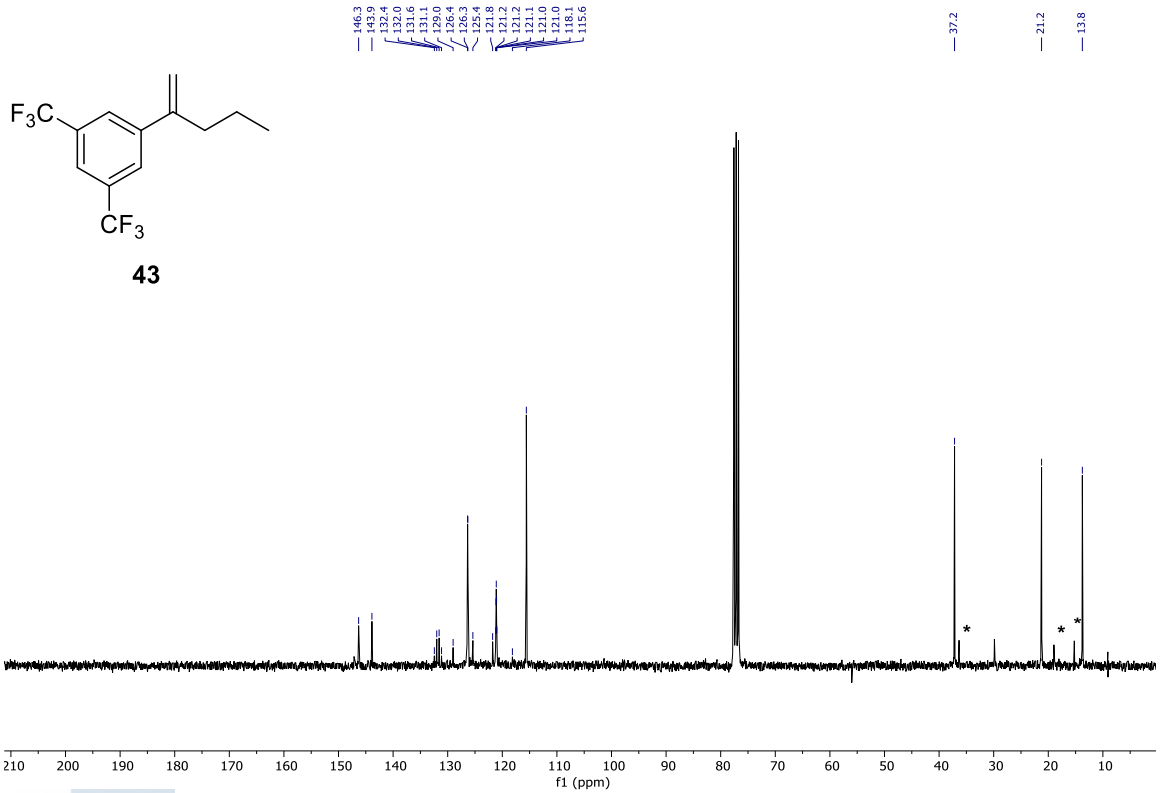

43

Pentane could not be completely removed due to volatility of compound. Marked (*) signals correspond to pentane.

19F NMR (CDCl3, 282 MHz)

43

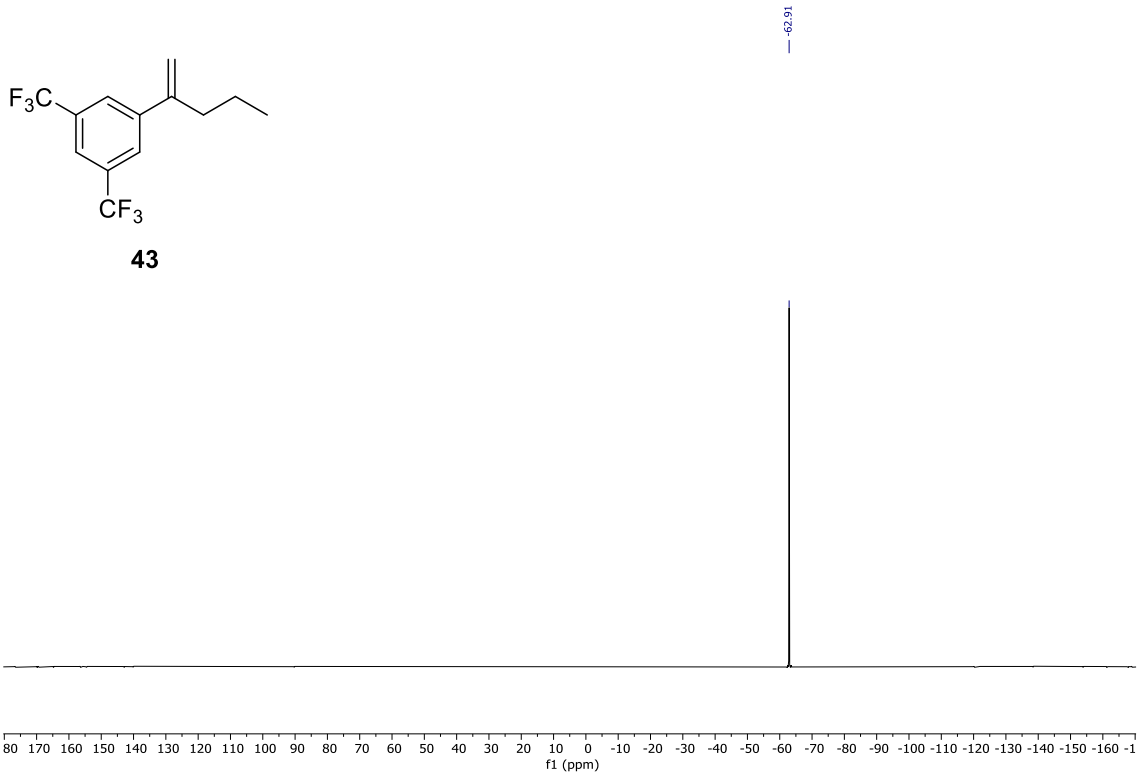

1H NMR (CDCl3, 300 MHz)

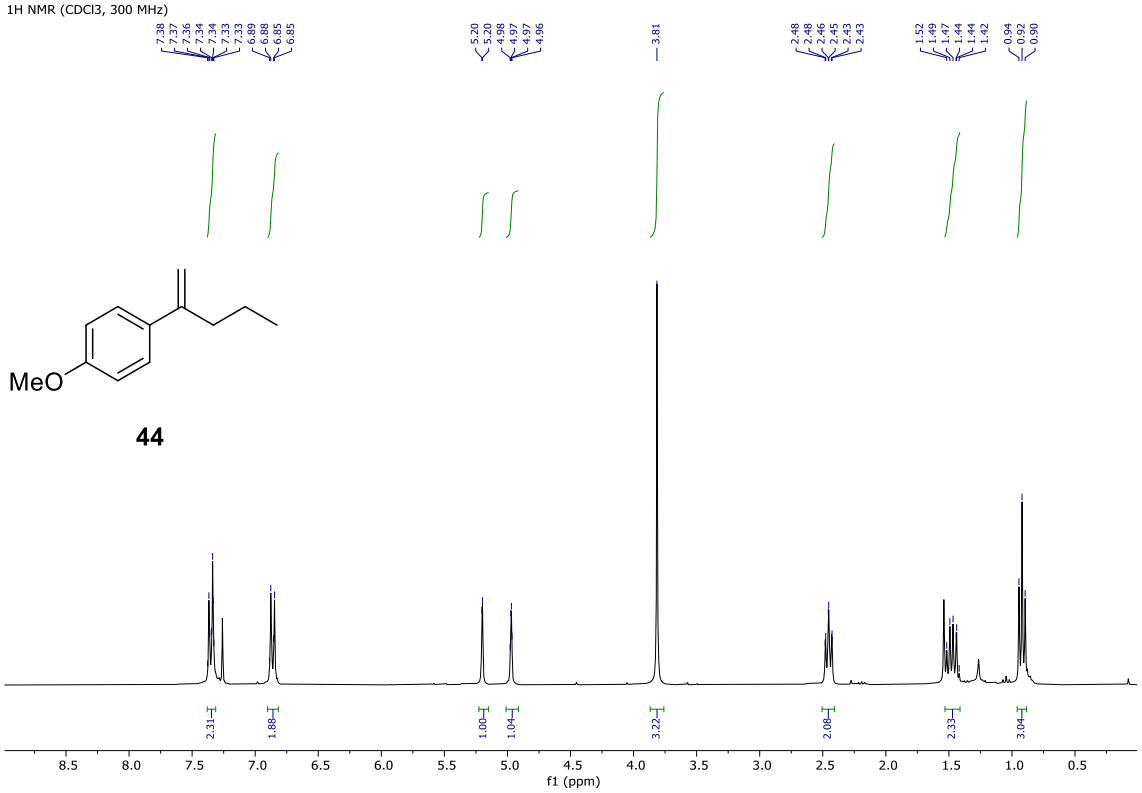

44

13C NMR (CDCl3, 75 MHz)

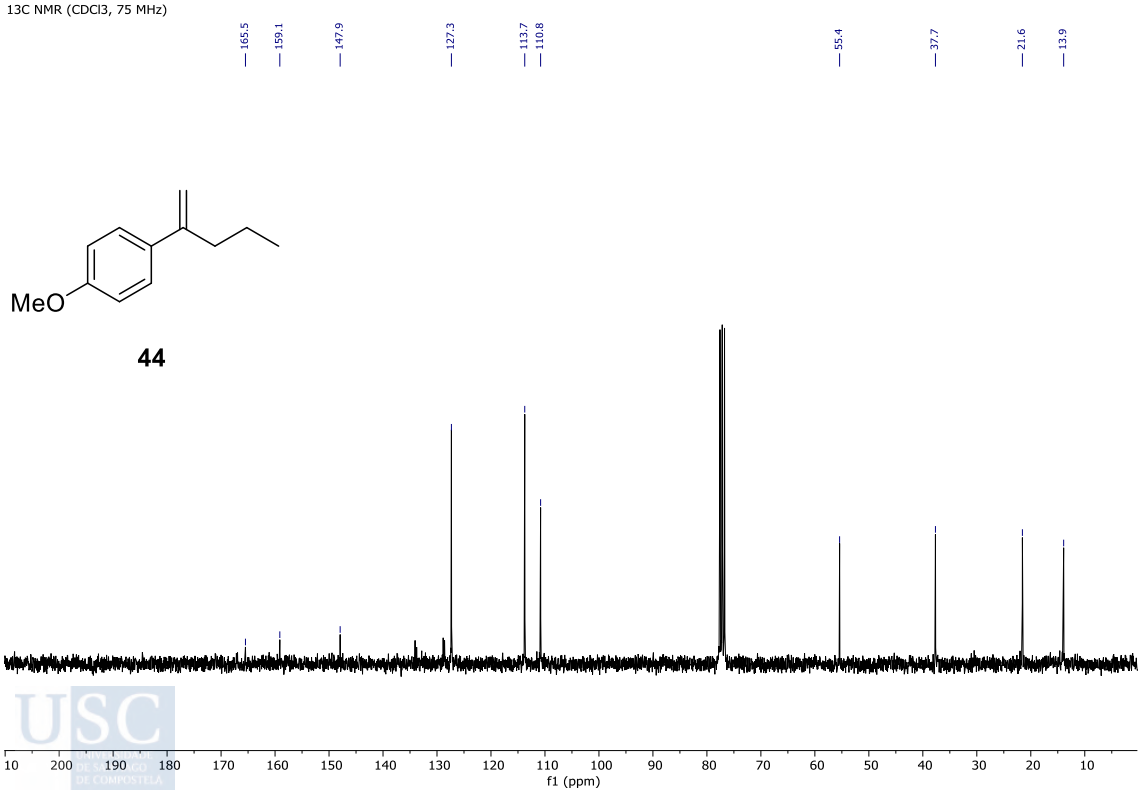

44

1H NMR (CDCl3, 300 MHz)

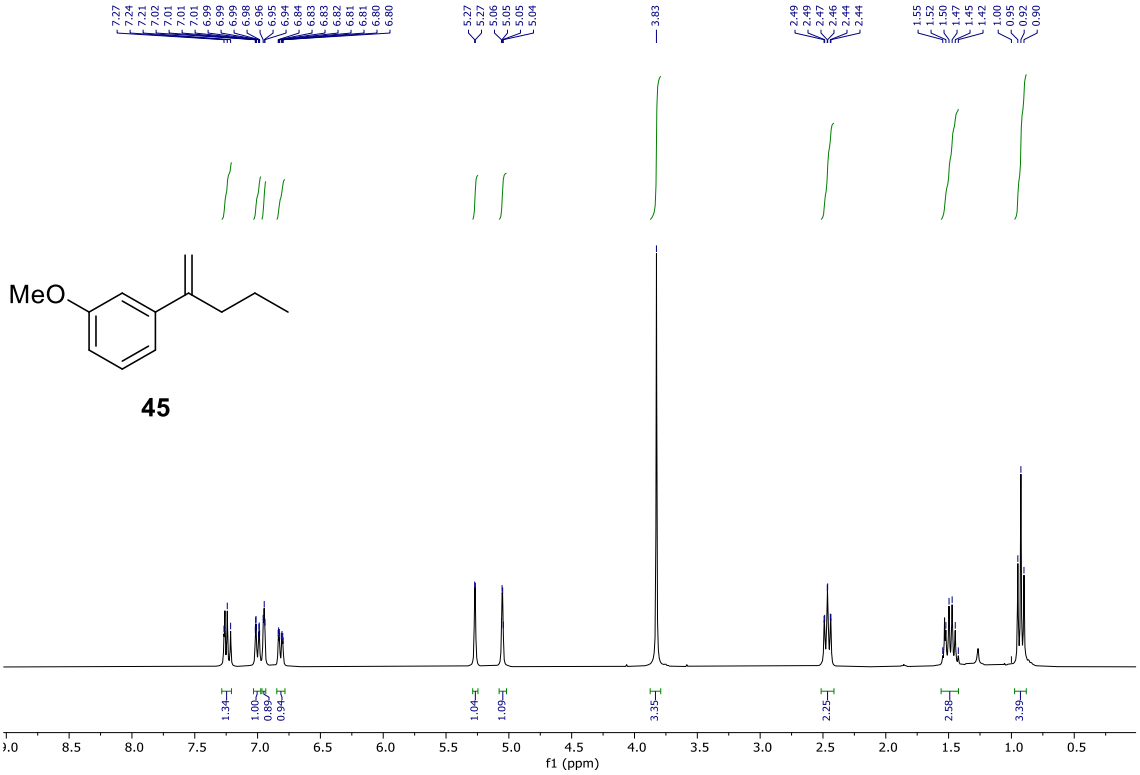

45

13C NMR (CDCl3, 75 MHz)

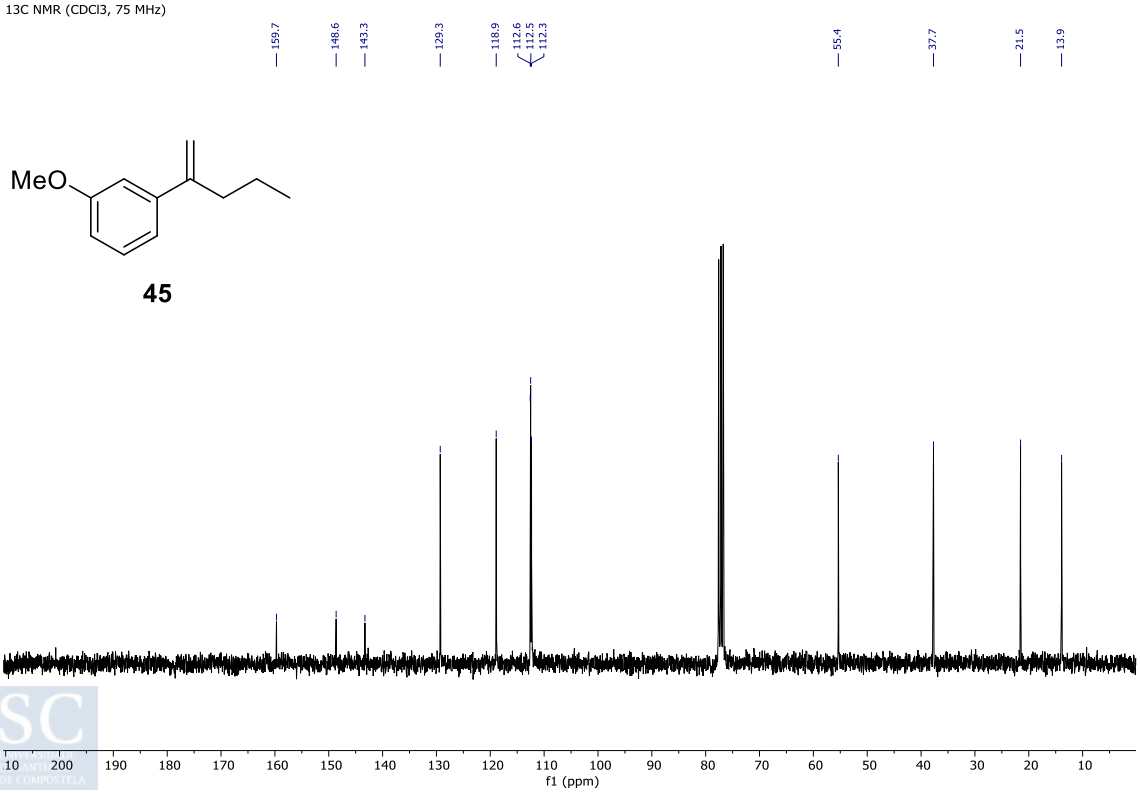

45

1H NMR (CDCl3, 300 MHz)

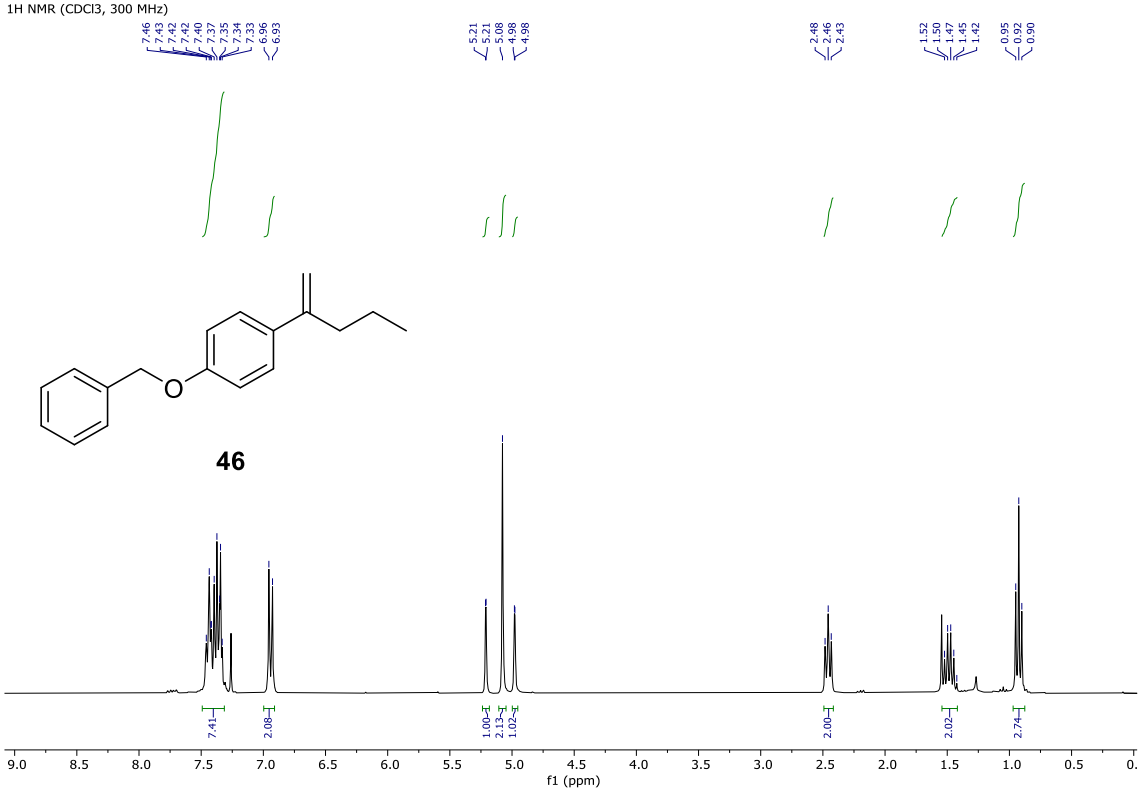

46

13C NMR (CDCl3, 75 MHz)

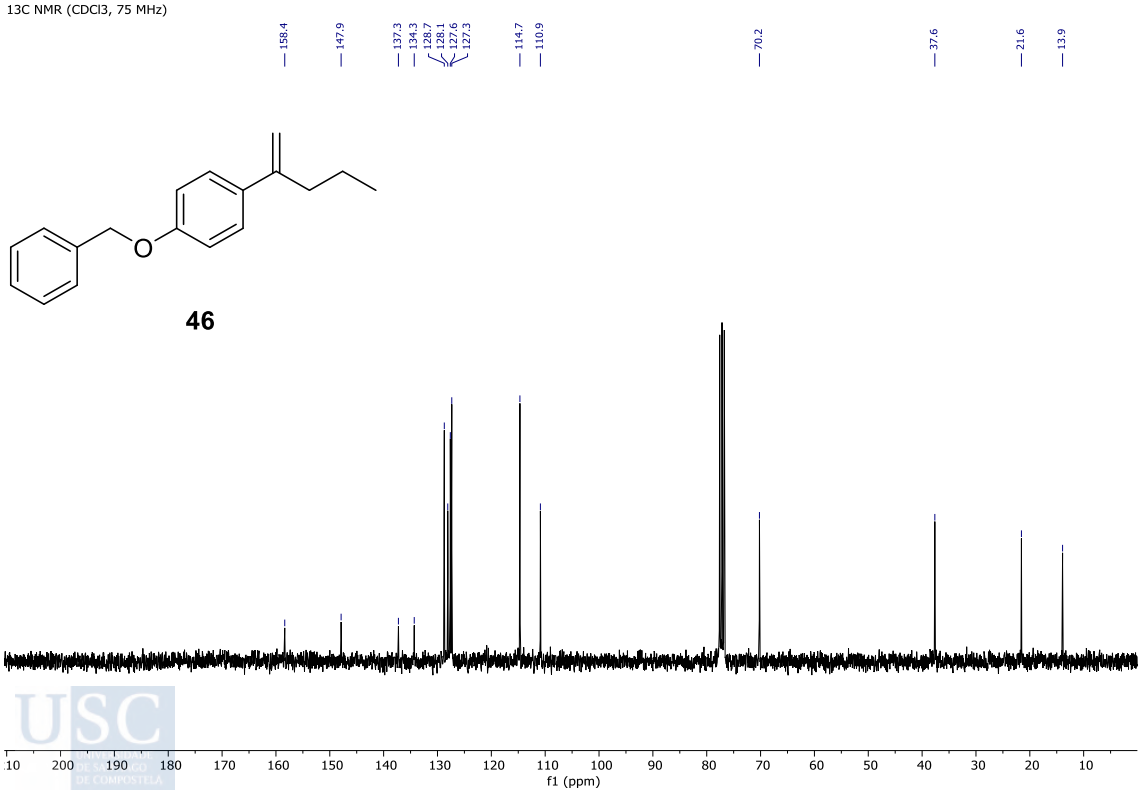

46

1H NMR (300 MHz)

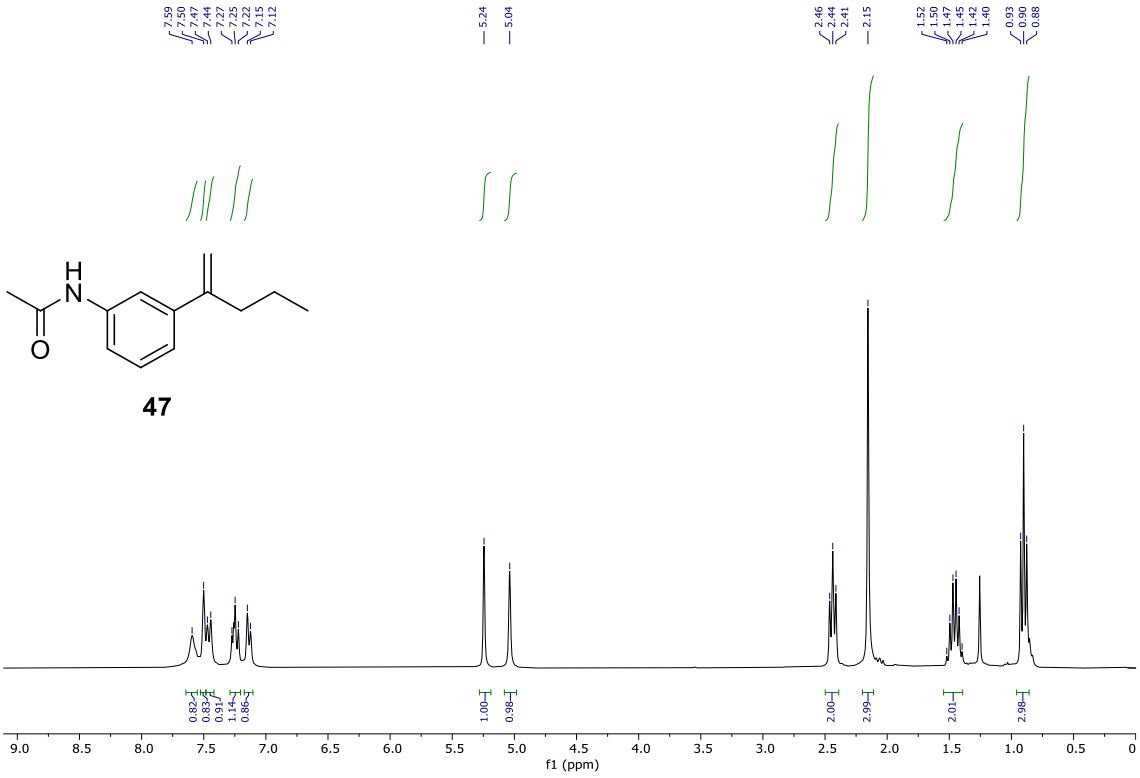

47

13C NMR (CDCl3, 126 MHz)

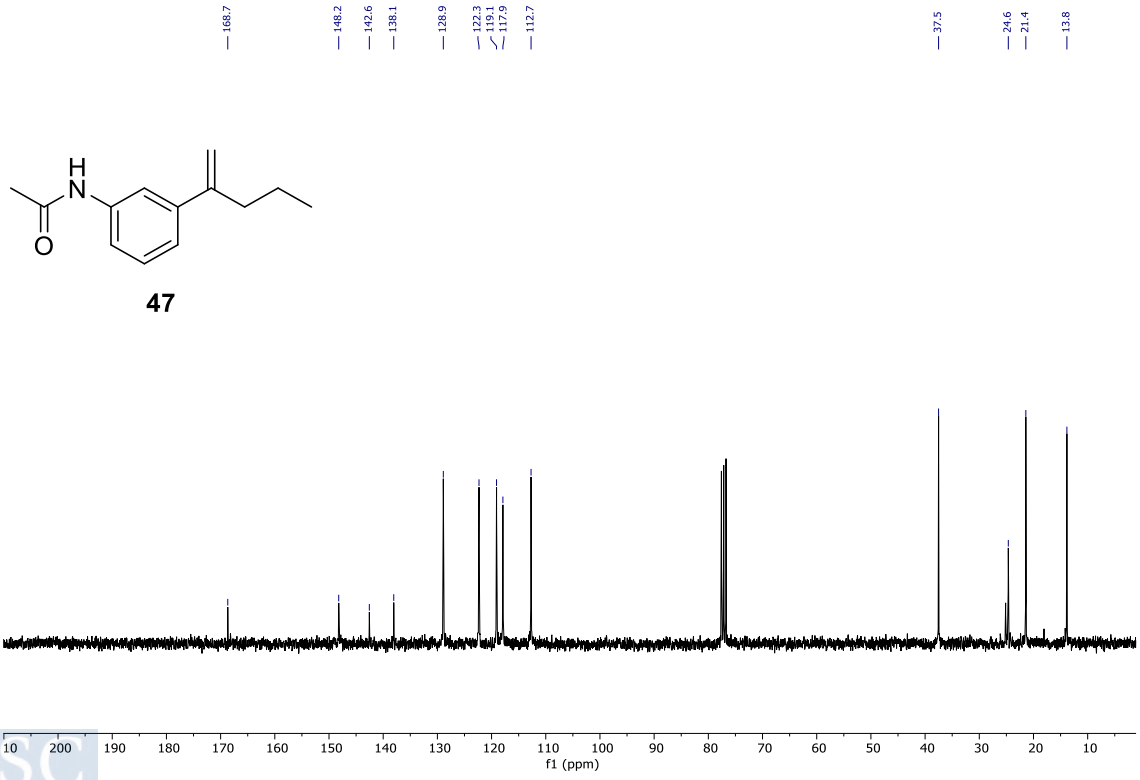

47

1H NMR (CDCl3, 300 MHz)

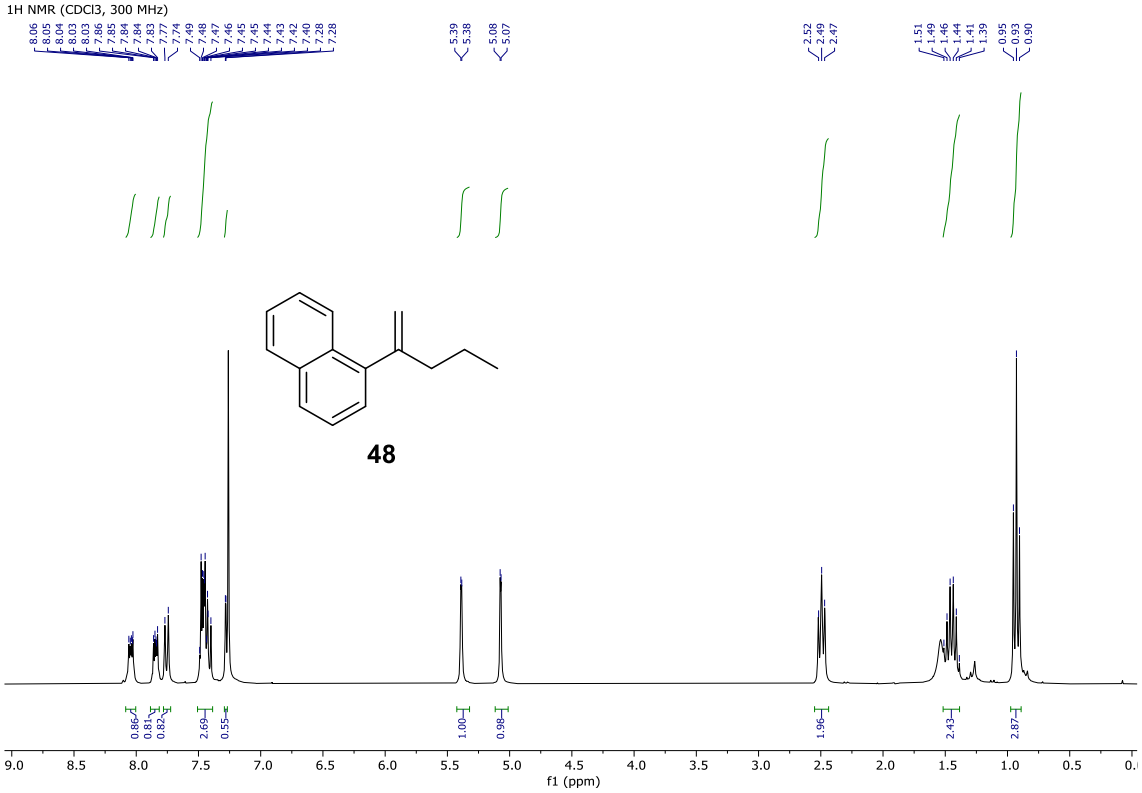

48

13C NMR (CDCl3, 125 MHz)

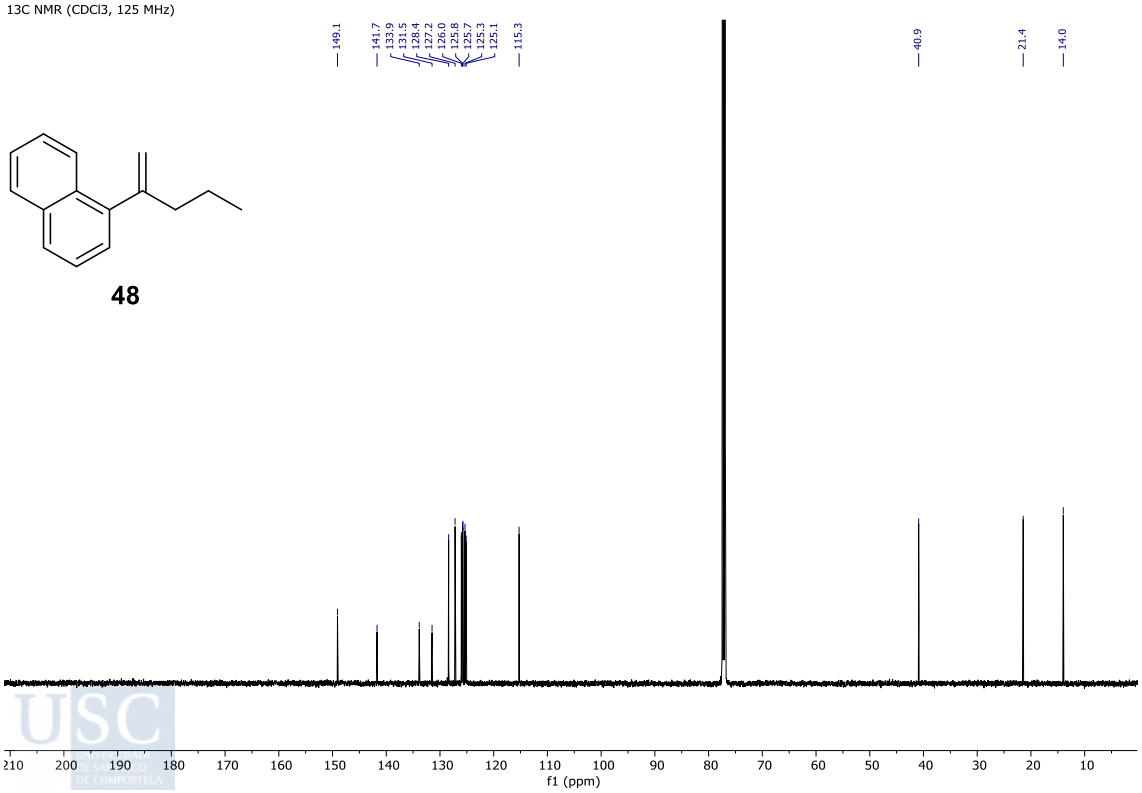

48

1H-NMR (CDCl3, 300 MHz)

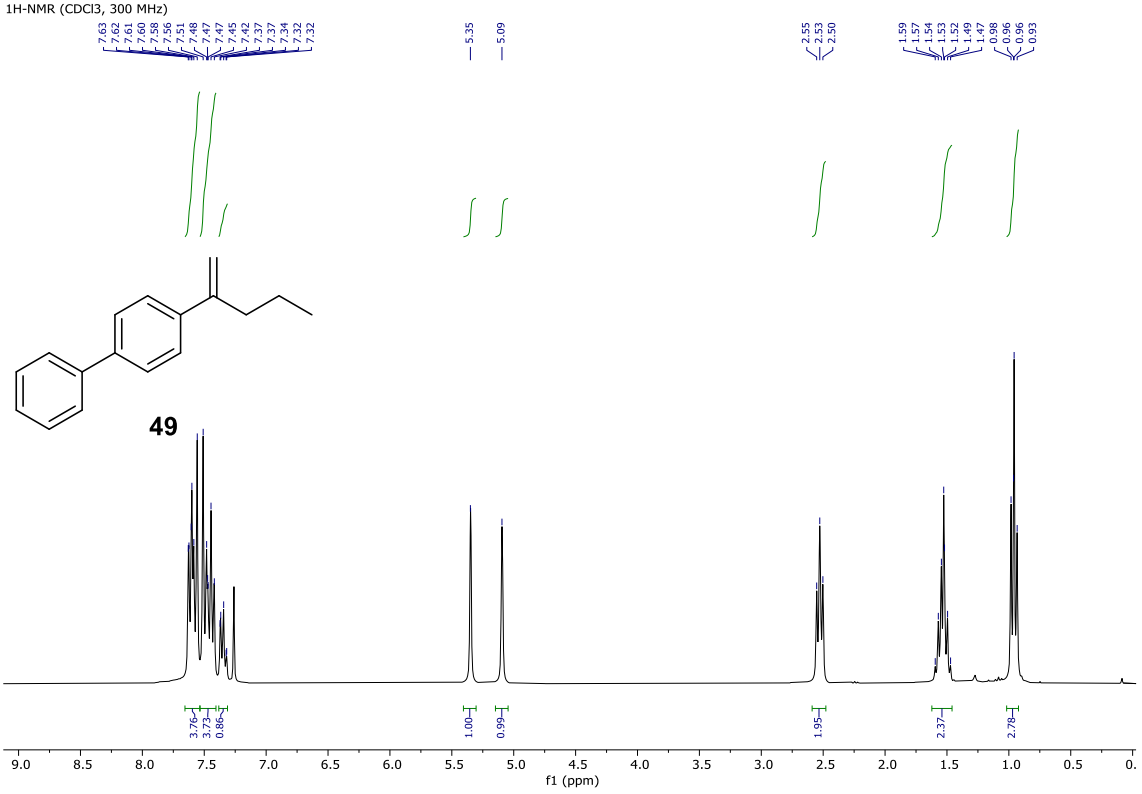

13C NMR (CDCl3, 75 MHz)

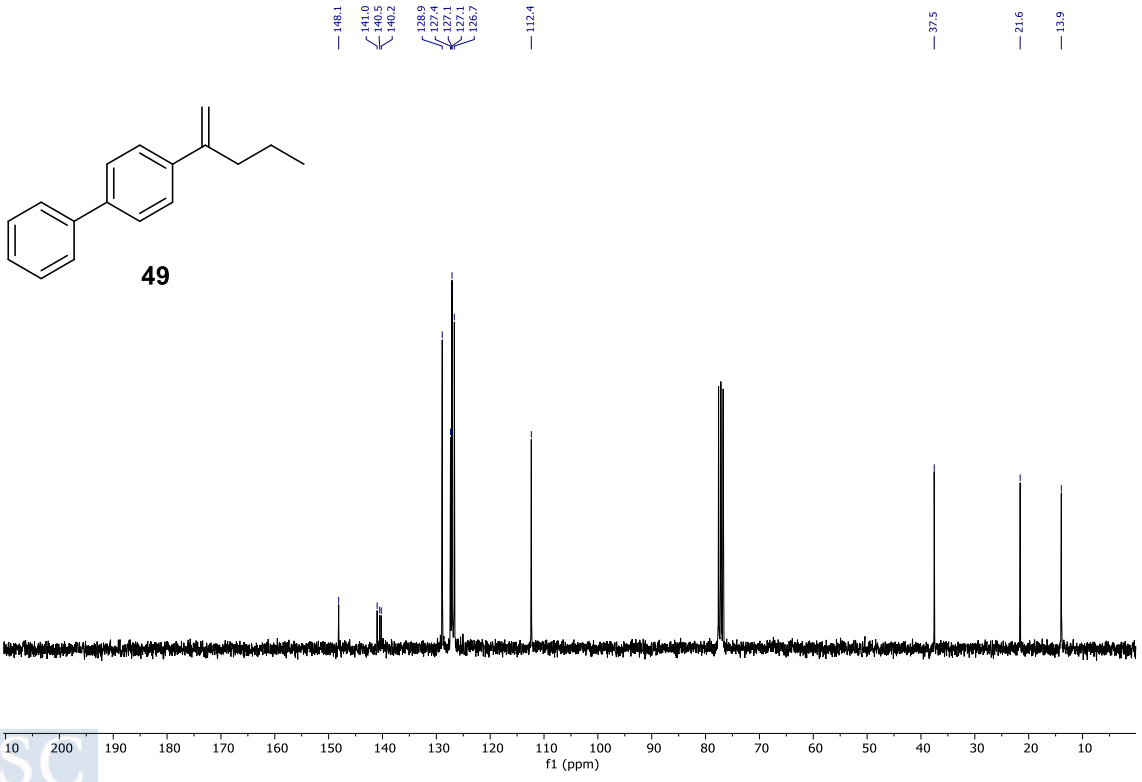

1H NMR (CDCl3, 300 MHz)

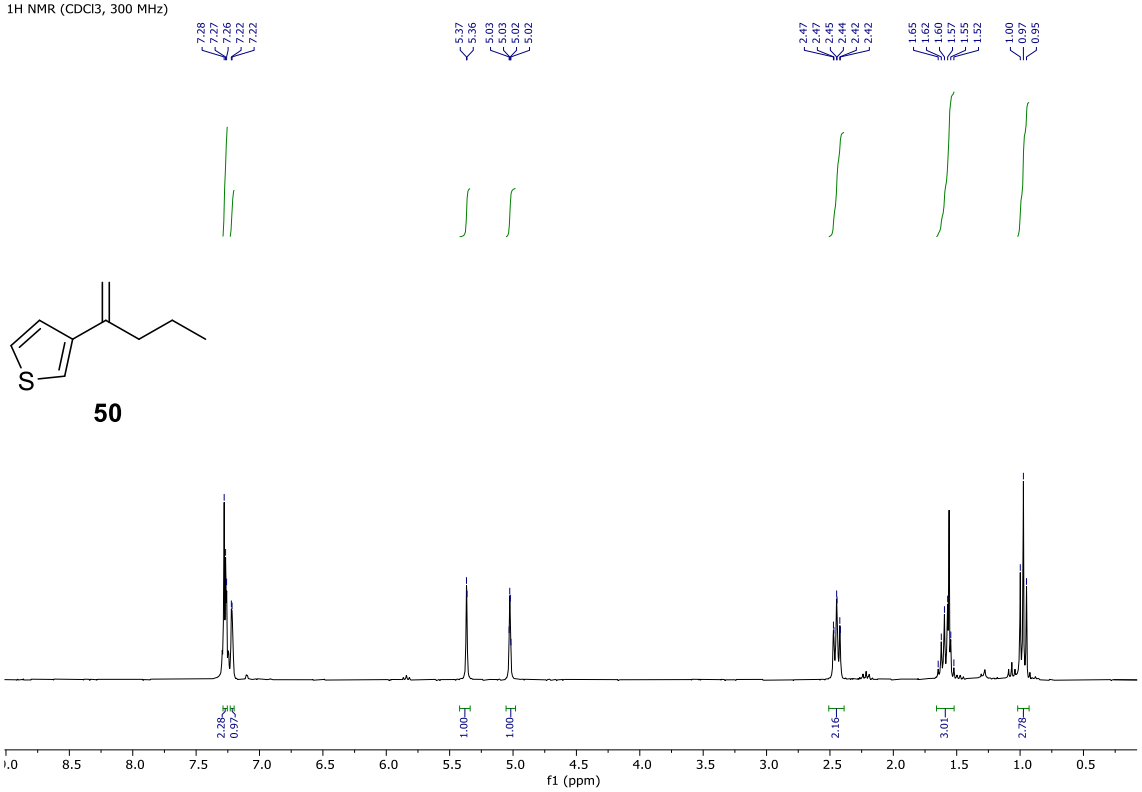

50

13C NMR (CDCl3, 126 MHz)

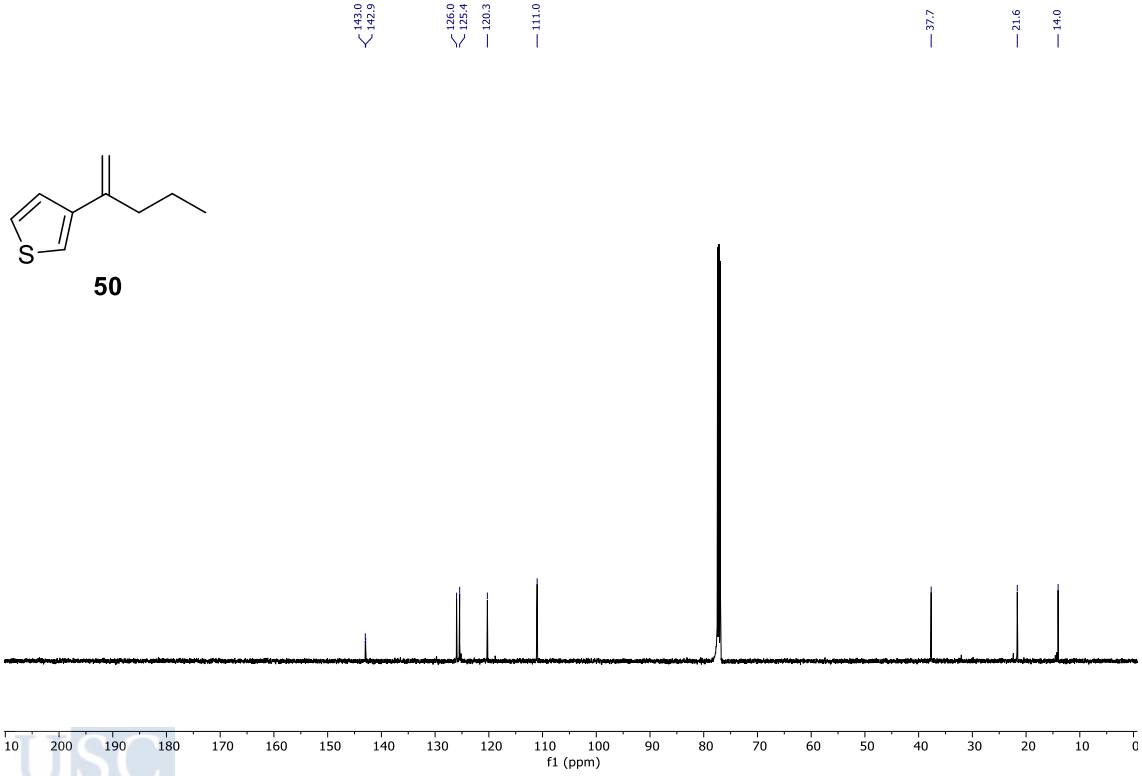

50

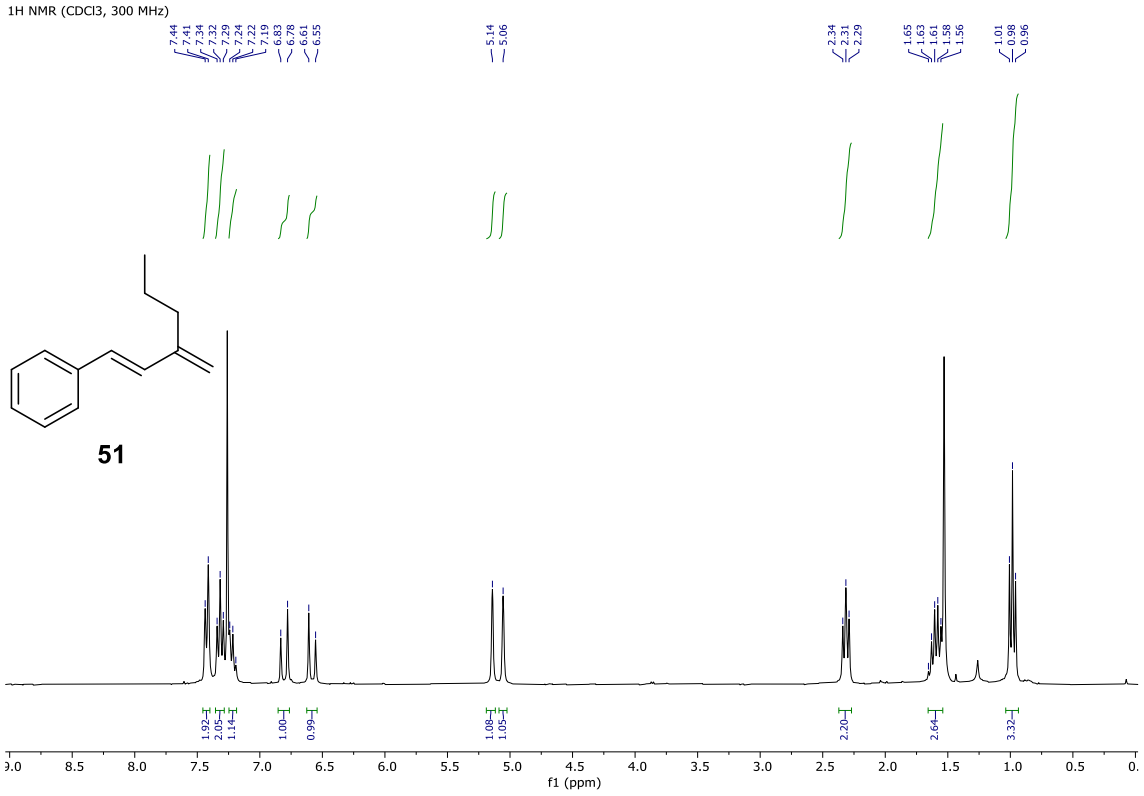

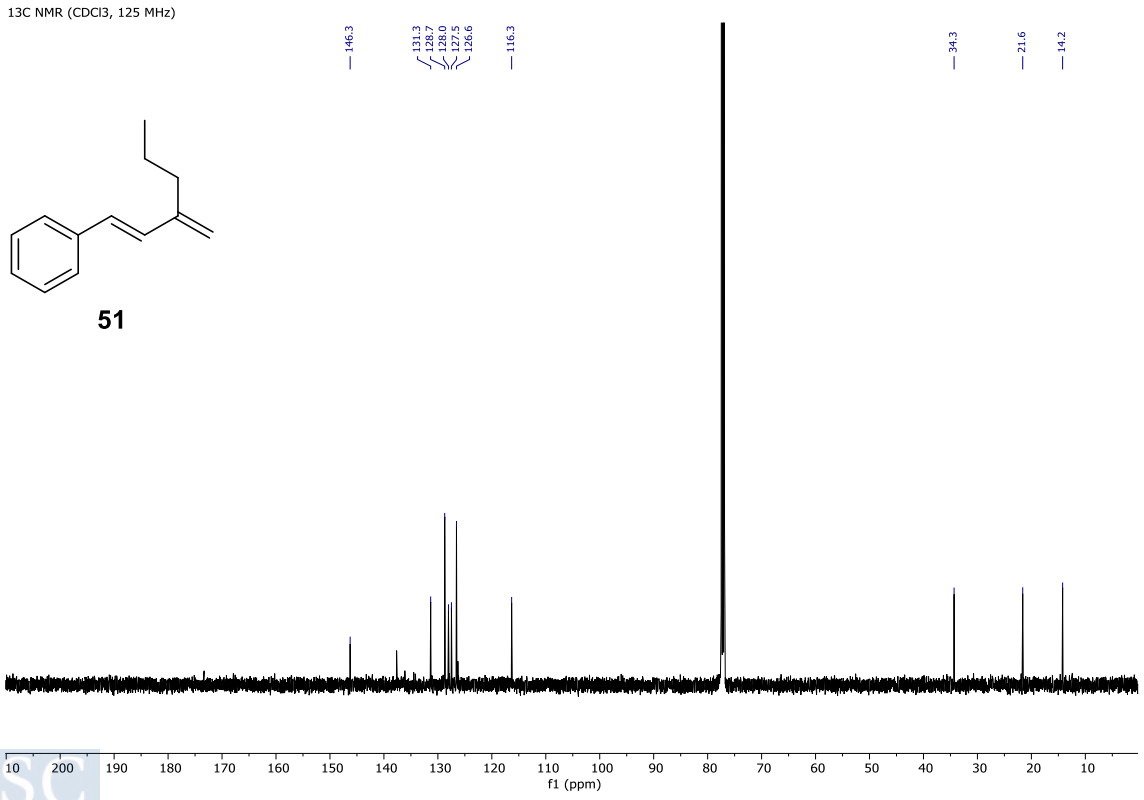

1H NMR (CDCl3, 500 MHz)

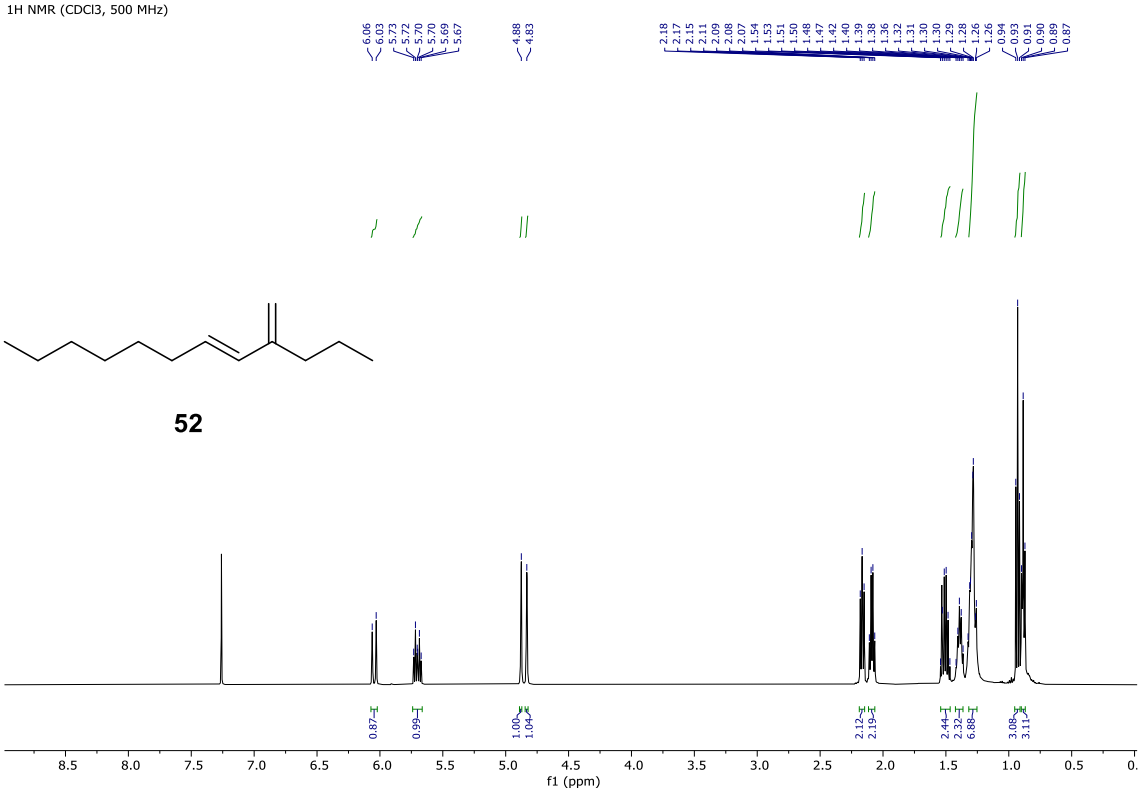

52

13C NMR (CDCl3, 125 MHz)

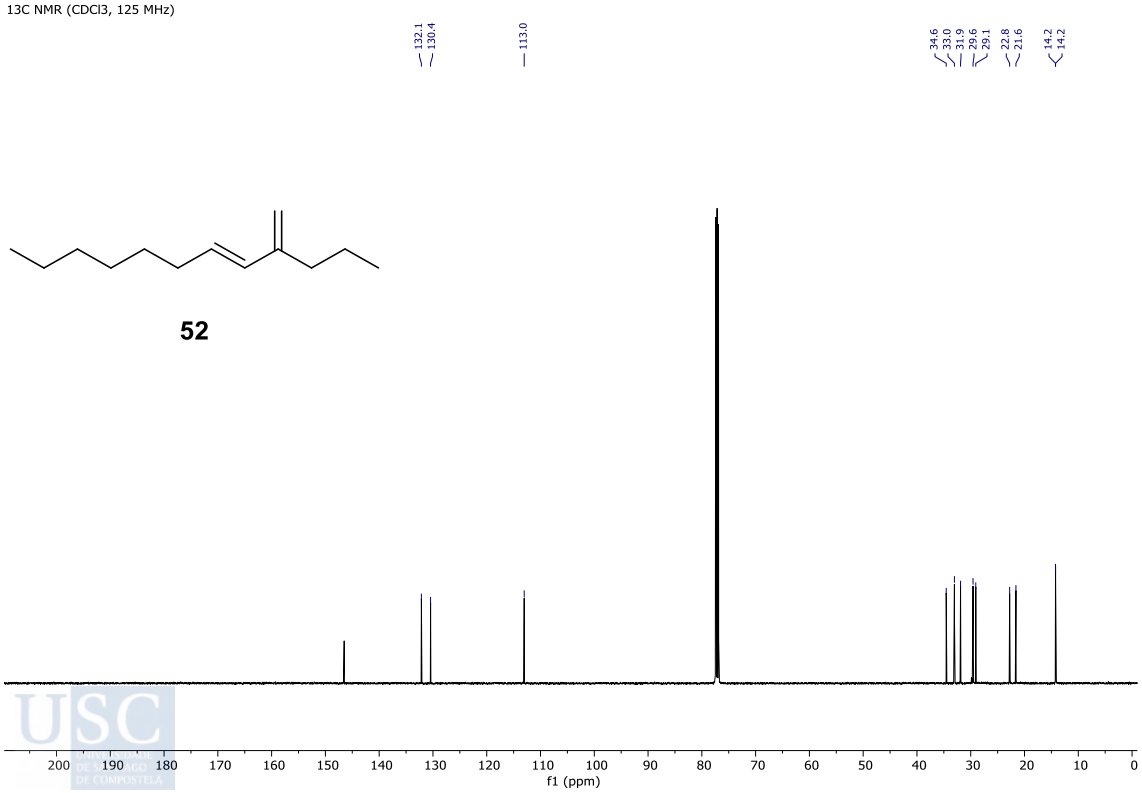

52

1H NMR (CDCl3, 300 MHz)

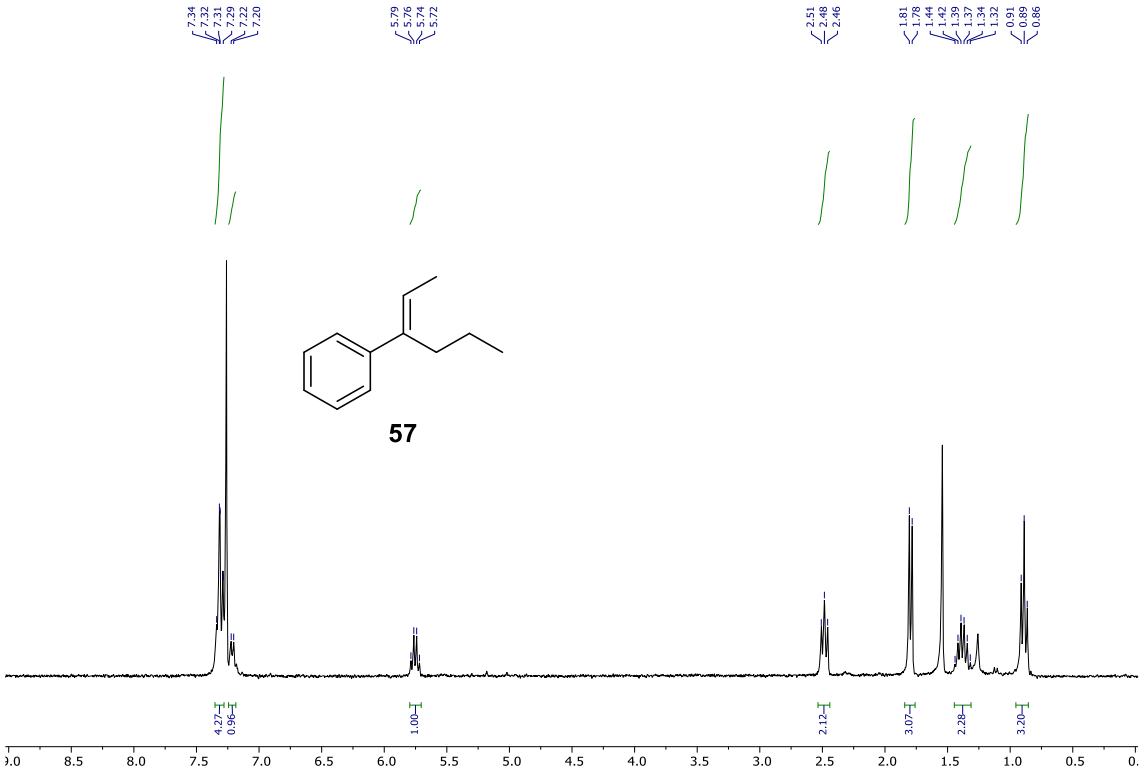

1D NOE NMR (CDCl3, 500 MHz)

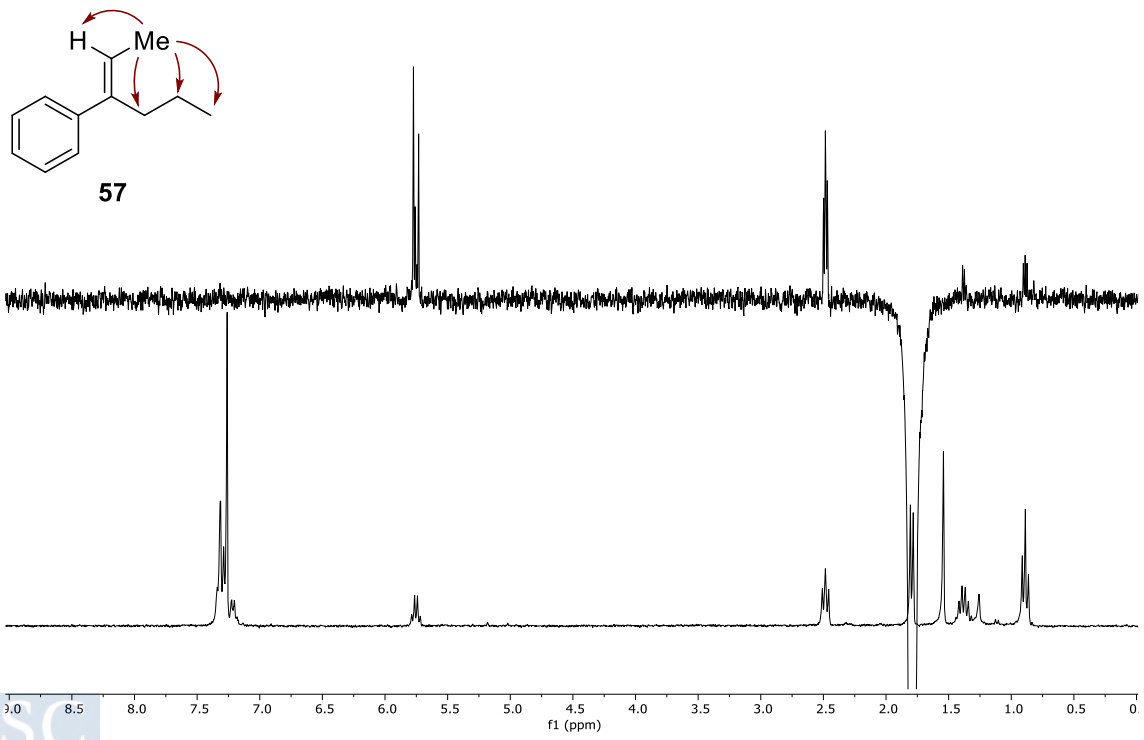

13C NMR (CDCl3, 125 MHz)

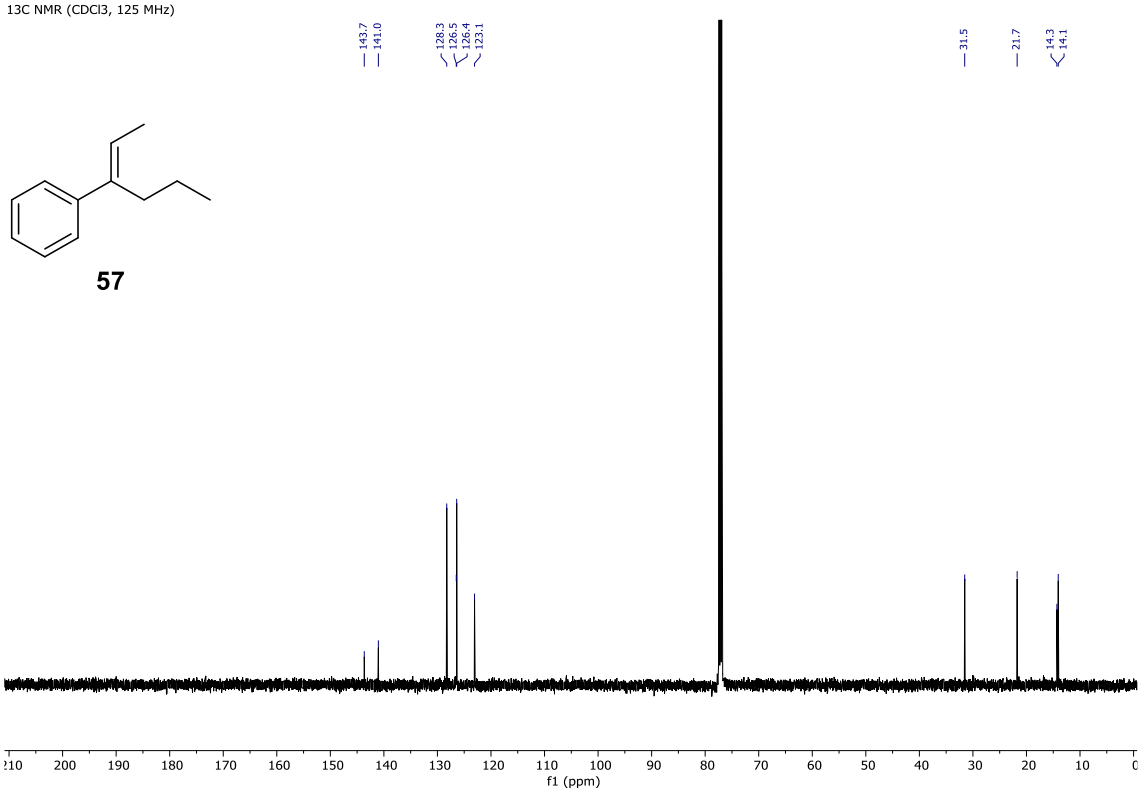

57

1H NMR (CDCl3, 300 MHz)

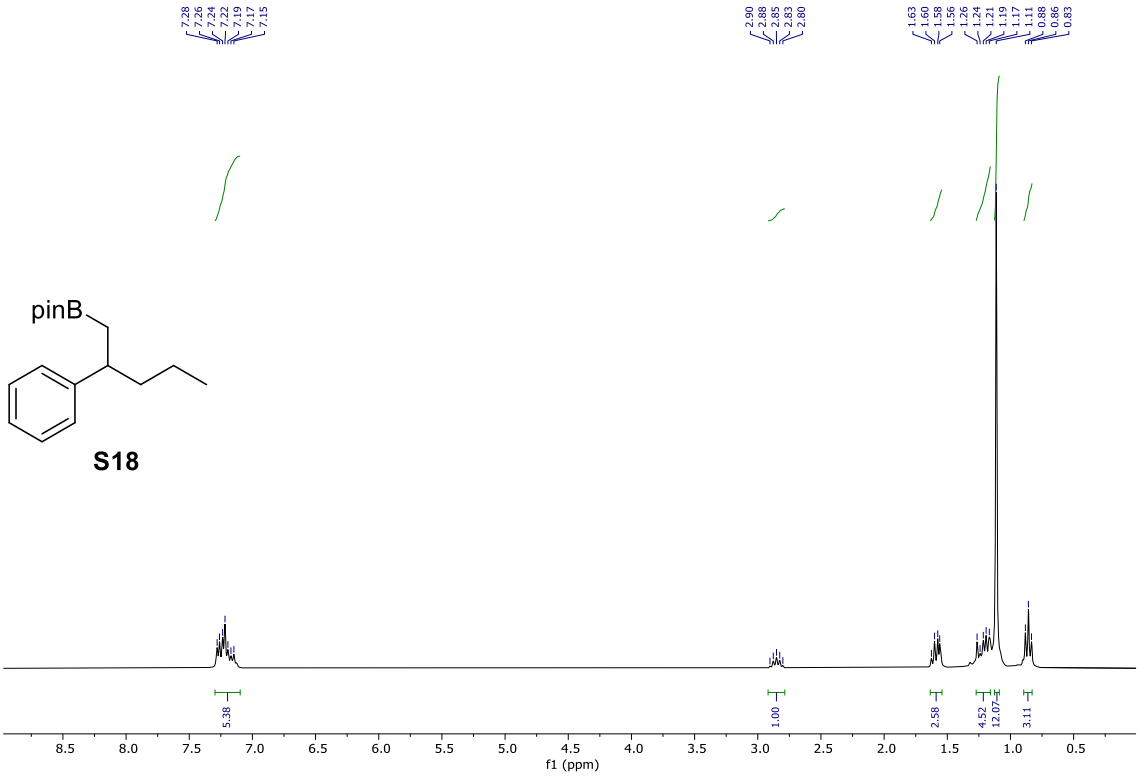

13C NMR (CDCl3, 75 MHz)

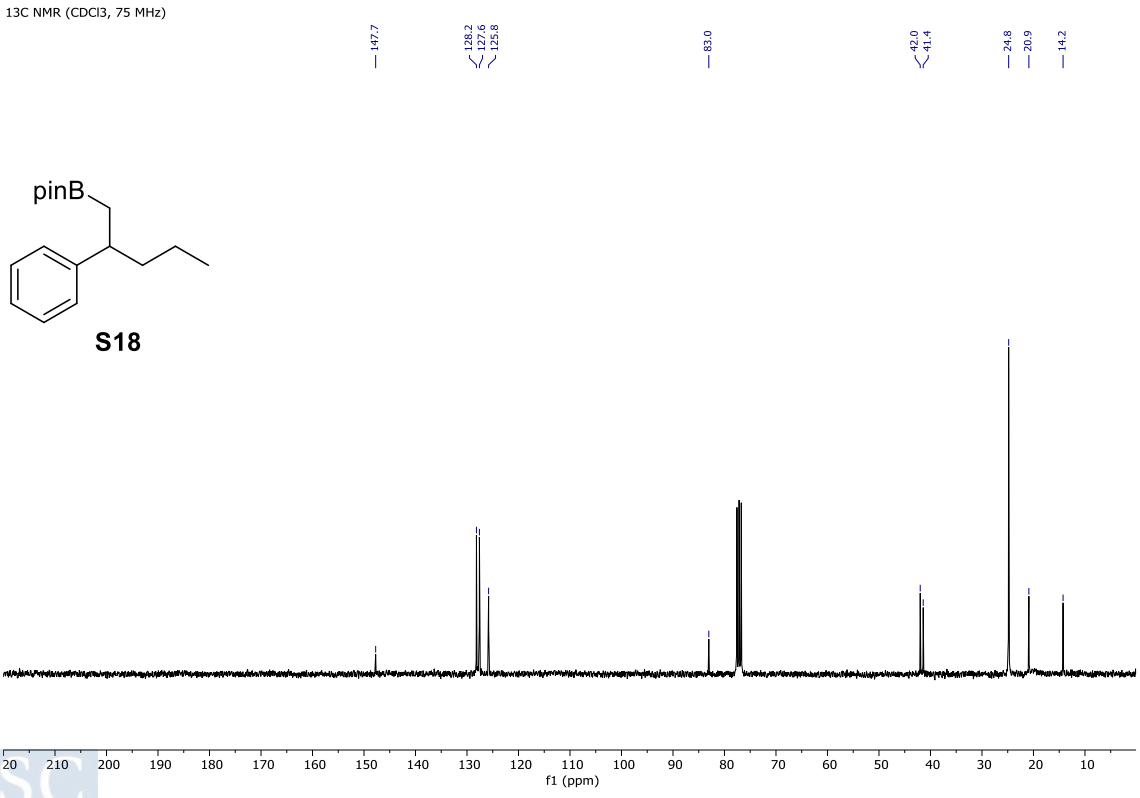

11B NMR (CDCl3, 160 MHz)

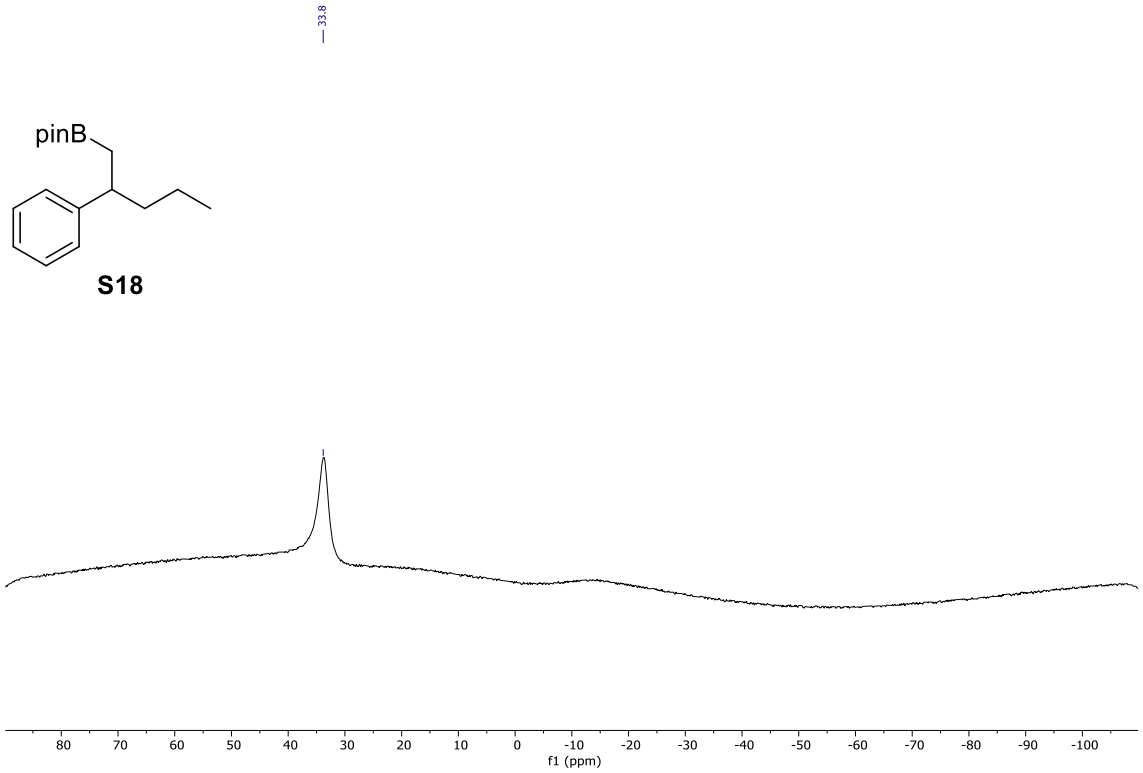

S18

1H NMR (CDCl3, 300 MHz)

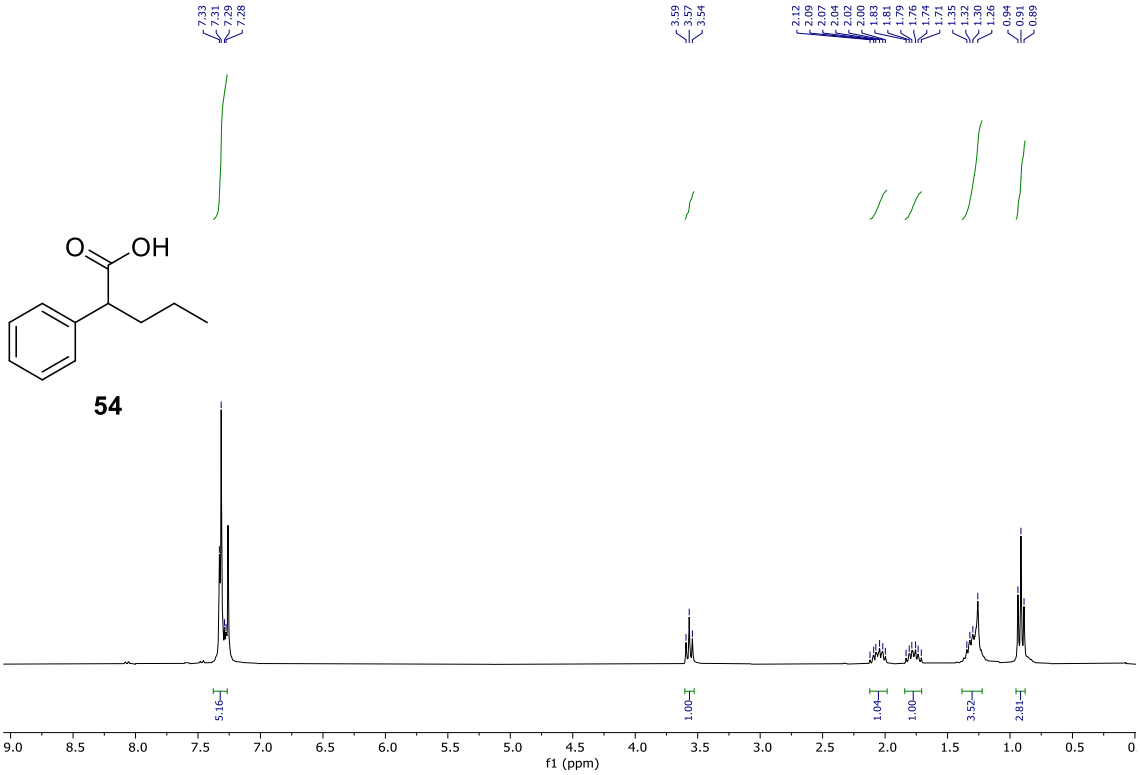

54

13C NMR (CDCl3, 126 MHz)

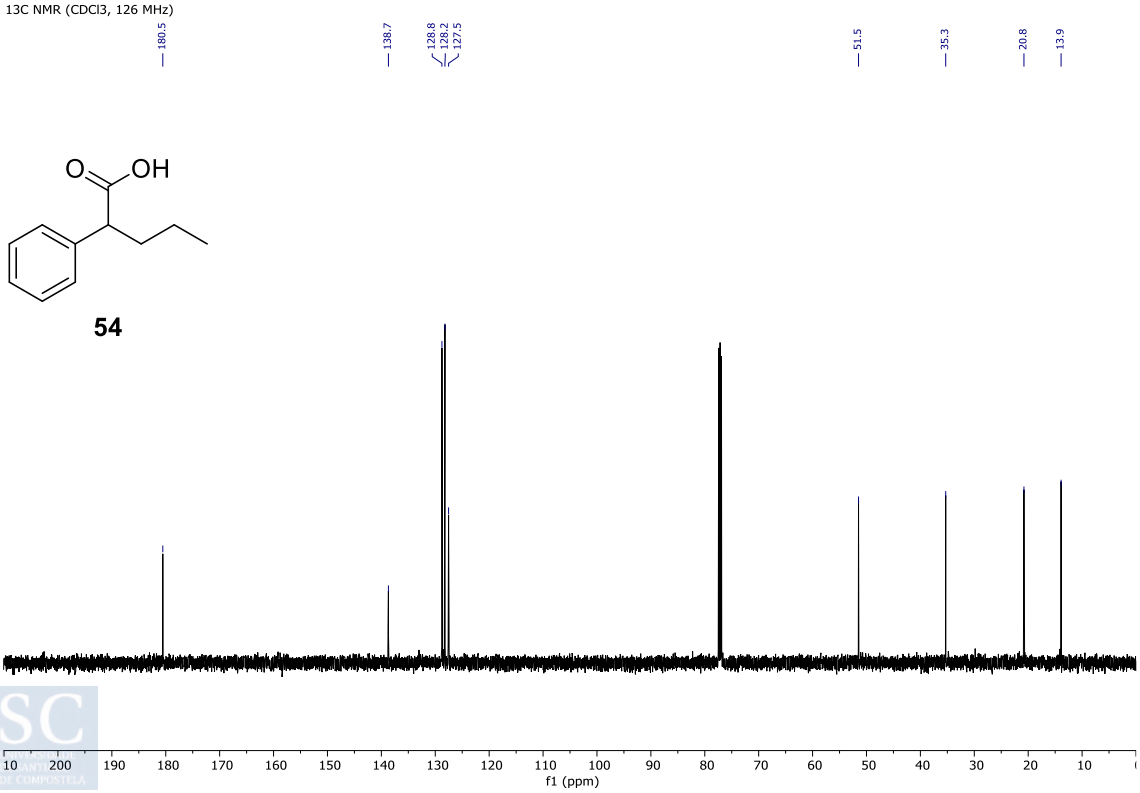

54

5.4.6 Mechanistic Studied for $FeCl_3$ Photorredox HAT Catalyzed Direct Csp^3-Csp^3 Allylation of Ethane

5.4.6.1 Evaluation of reaction mechanism nature

5.4.6.1.1 Radical trapping with TEMPO

Catalytic reaction was performed according to general procedure I in the presence of TEMPO (3 equiv) (Scheme 5.4.1). The expected product was not obtained. Conversely, the TEMPO-Et adduct was identified by GCMS, confirming the radical nature of the transformation.

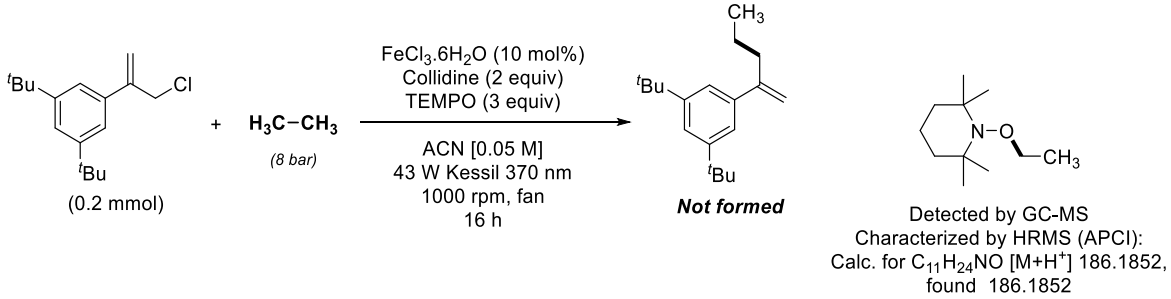

Scheme 5.4.1. Radical trapping reaction with TEMPO for ethane allylation.

5.4.6.1.2 Deuterium scrambling experiments

37-d*2* was prepared according to literature procedure.[244] Catalytic reaction was carried out following corresponding general procedure I (Scheme 5.4.2). The resulting deuterated product was characterized by **HRMS (APCI)** Calc. for $C_{11}H_{13}D_2$ [M+H$^+$] 149.1294, found 149.1300.

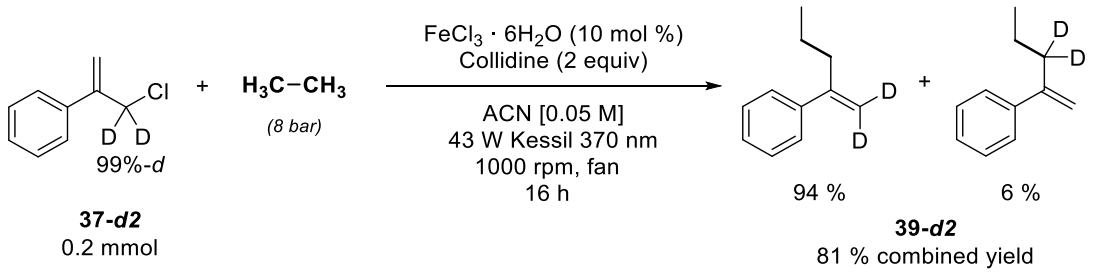

Scheme 5.4.2. Deuterium scrambling experiments for ethane allylation.

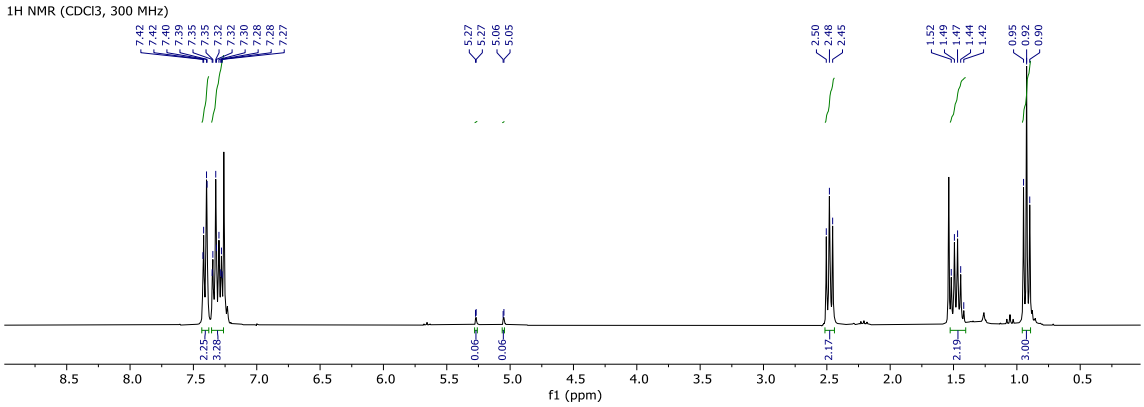

5.4.6.2 Quantum Yields determination of the catalytic reactions under 370 nm irradiation

5.4.6.2.1 Determination of the Photon Flux of the 370 nm Kessil PRL160

The photon flux of a PRL160 370 nm Kessil lamp was determined by standard ferrioxalate actinometry,[253] following described procedures.[215]

In an amber flask, a 0.15 M ferrioxalate solution (Solution A) was prepared by dissolving potassium ferrioxalate hydrate (737 mg, 1.50 mmol) in $H_2SO_{4\,(aq)}$ (0.05 M, 10 mL). In a separate amber vial, a second solution (Solution B) was prepared by dissolving 1,10-Phenanthroline monohydrate (25 mg, 0.13 mmol) and NaOAc (5.63 g, 68.63 mmol) in $H_2SO_{4\,(aq)}$ (0.05 M, 10 mL) in an amber vial.

To determine the photon flux of the lamp, 4 mL of the ferrioxalate solution (Solution A) was placed in a sealed tube, equipped with a stir bar, and irradiated for 60 seconds at 370 nm, using same setup than described in General Procedure D. After irradiation, 1 mL of this irradiated solution, 1 mL of Solution B and 4 mL of water were added to a 10 mL amber vial, equipped with a stir bar. The resulting mixture (Solution C) was stirred for 1 h under dark to allow the ferrous ions to completely coordinate to the phenanthroline.

In parallel, 1 mL of Solution A (without undergoing irradiation), 1 mL of Solution B and 4 mL of water were added to a 10 mL amber vial, equipped with a stir bar. The mixture (Solution D) was stirred for 1 h under dark to allow the ferrous ions to completely coordinate to the phenanthroline.

The absorbance of both solutions C and D was measured at 510 nm. Conversion of ferrous ions was calculated to be 7.06×10^{-6} mol using eq 10. In eq 10, V is the total volume of solution D or C, ΔA is the difference in absorbance at 510 nm between Solution C and Solution D (irradiated – non-irradiated), l is the path length of the cuvette, and ε is the molar absorptivity at 510 (11,100 L mol^{-1} cm^{-1}). The photon flux under measured conditions was calculated according to eq 11, where φ is the quantum yield for the ferrioxalate actinometry (for 365 nm: φ = 1.27),[254] t is the irradiation time (60 s) and f (f = 1 -10^{-Abs} ; where Abs is the measured absorbance of Solution D at 370 nm). The photon flux was calculated to be 8.48×10^{-8} einstein s^{-1}.

$$mol\ Fe^{2+} = \frac{V \times \Delta A}{l \times \varepsilon} = \frac{0.006\ L \times 4 \times 2.989}{1 \times 11100\ mol^{-1}\ L^{-1}} = 6.46 \times 10^{-6}\ mol \qquad (eq\ 10)$$

$$Photon\ flux = \frac{mol\ Fe^{2+}}{\varphi \times t \times f} = \frac{6.46\times10^{-6}\ mol}{1.27 \times 60\ s \times 1} = 8.48 \times 10^{-8}\ einstein\ s^{-1} \qquad (eq\ 11)$$

5.4.6.2.2 Determination of the reaction quantum yield for the photocatalytic propane allylation

Reaction was prepared as described in General Procedure D and was irradiated for 1.5 h at 370 nm. After irradiation, the reaction was quenched with water (10 mL) and extracted with pentante (3 x 10 mL). Combined organic layers were dried over $MgSO_4$, filtered, and solvent was removed under reduced pressure. The yield of the reaction was determined by ^{1}H-NMR analysis of the reaction crude using trimethyl benzene-1,3,5-tricarboxylate as internal standard.

Quantum yield of the allylation of **37** with propane was determined using eq 12. The yield of the product was calculated to be 6% (1.2×10^{-5} mol). Absorption of the reaction mixture was observed to be >3 u.a. at 370 nm. Therefore, the reaction quantum yield was calculated to be 2.6%, confirming a closed photoredox catalytic cycle with a reaction quantum yield of <1.

$$\varphi = \frac{mol\ product}{\text{photon flux} \times t \times f} = \frac{1.2\times10^{-5}\ mol}{8.48\times10^{-8} \times 5400\ s \times 1} = 0.026 \qquad (eq\ 12)$$

5.4.6.3 Time resolved reaction of Cyclohexane C-H chlorination monitored by GC-MS

In order to determine the effect of collidine regarding C-H chlorination, stoichiometric reactions with and without collidine were carried out. Reactions were run using $FeCl_3 \cdot 6H_2O$ (0.1 mmol) and CyH (0.15 mmol) in 2 mL of MeCN. When collidine was used, 20 eq were added to mimic reaction ratios. Given that C-H chlorination reaction requires two $FeCl_3$ molecules per alkane (HAT and chlorination steps), the maximum amount of formed CyCl would be 0.05 mmol (0.025 M in reaction media). For each reaction, an aliquot of 60 µL was taken and diluted until reaching a final volume of 1.25 mL of CH_2Cl_2. Therefore, the maximum amount of CyCl per aliquot would be 1.5 µmmol. Accordingly, the calibration curve was built as follows:

Stock solution was prepared following the described procedure: a vial equipped with a magnetic stir bar was charged with 1 mL of MeCN. Then, 8.9 µL of CyCl (0.075 mmol) was added and mixture was stirred. Samples for calibration curve (Figure 5.7.1) were prepared taking the indicated volume in Table 5.4.1, diluting in CH_2Cl_2 until reaching a final volume of 1.25 mL.

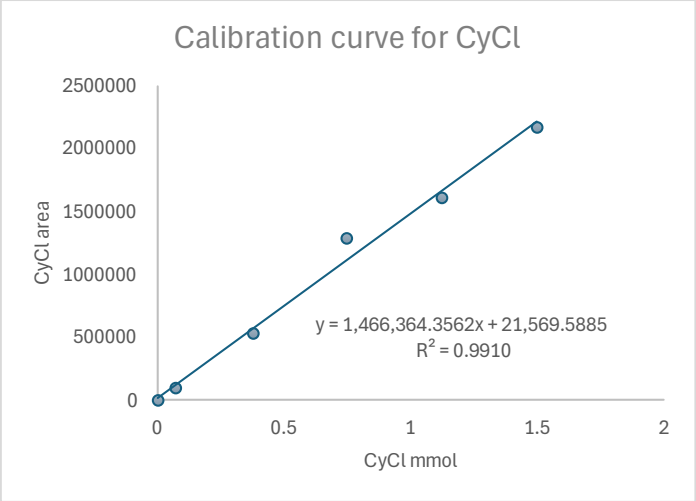

Figure 5.4.1. Calibration plot for CyCl quantification in GCMS.

Table 5.4.1. Calibration data for CyCl quantification in GCMS.

Entry	µL Stock	µmol CyCl	area CyCl
1	0	0	0
2	1	0.075	105348
3	5	0.375	537286
4	10	0.750	1291263
5	15	1.126	1623060
6	20	1.501	2184457

Once the calibration curve was built, stoichiometric reaction was evaluated. Obtained data is summarized in Figure 5.4.2 and Table 5.4.2. It can be clearly observed that collidine has a critical role in slowing down the diect C-H chlorination process.

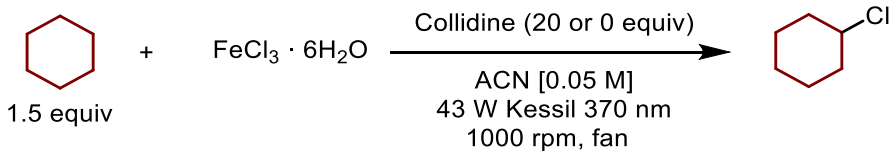

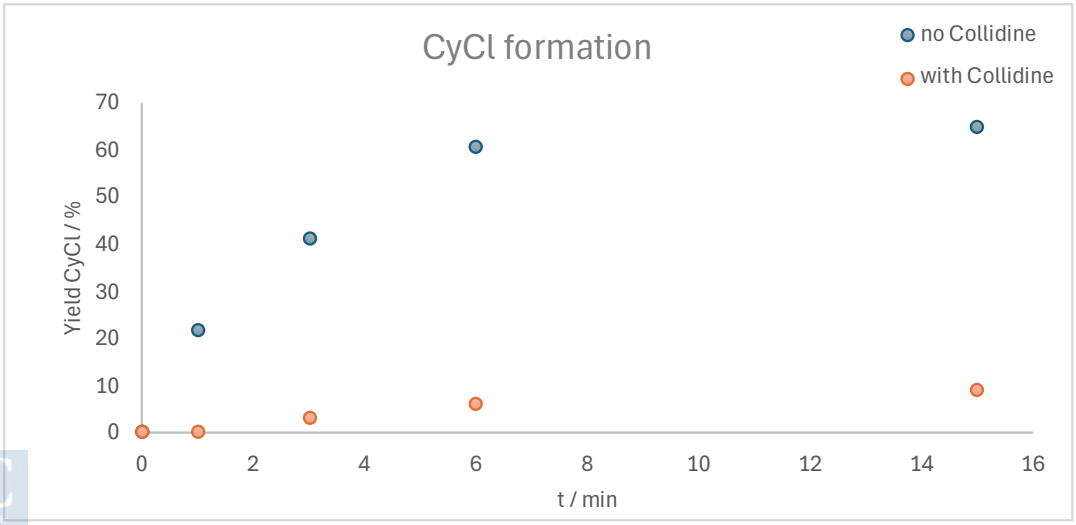

Figure 5.4.2. Formation of CyCl in stoichiometric C-H chlorination reaction, quantified by GCMS.

Table 5.4.2. Formation of CyCl in stoichiometric C-H chlorination reaction, quantified by GCMS

	No collidine			with Collidine		
t / min	area CyCl	µmol CyCl	Yield	area CyCl	µmol CyCl	Yield
0	0	0	0	0	0	0
1	493107	0.32156906	21	0	0	0
3	922092	0.61411913	41	83314	0.04210714	3
6	1358100	0.9114586	60	144045	0.08352318	6
15	1446427	0.97169397	65	214585	0.13162855	9

5.4.6.3.1 Formation of CyCl under catalytic conditions with and without collidine

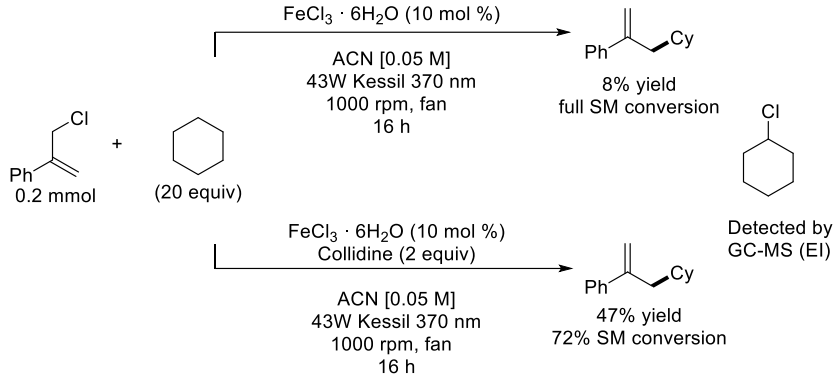

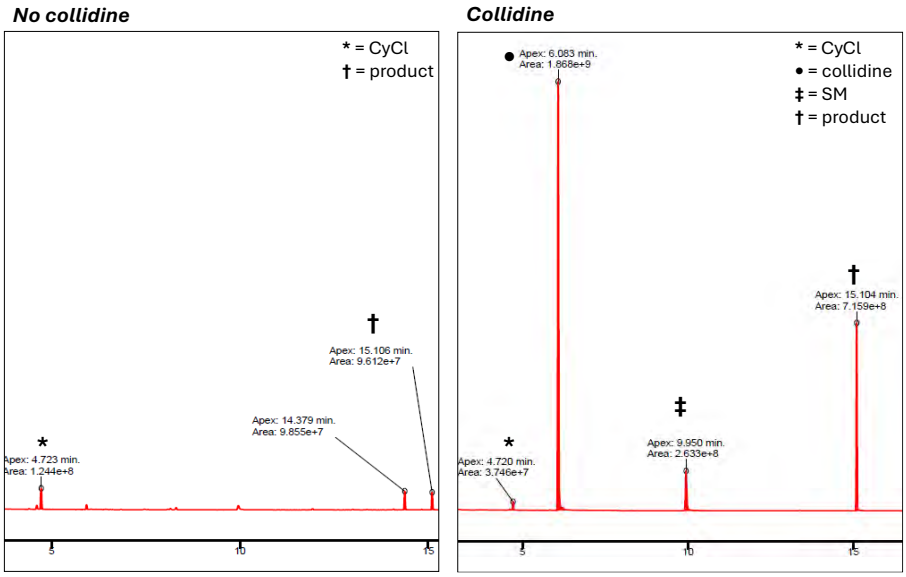

Figure 5.4.3. GC chromatogram a) without collidine and b) with collidine for reaction using CyH as alkane.

Table 5.4.3. Ratio of áreas between CyCl and Product from GCMS

	No collidine (Area)	Collidine (Area)
CyCl	1.244×10^8	3.746×10^7
Prodcut	9.612×10^7	7.159×10^8
Ratio (CyCl/Product)	56:44	7:93

5.4.6.4 Spectroscopic experiments

5.4.6.4.1 Lambert-Beer Law plots

Stock solution was prepared following the described procedure: a round-bottom flask equipped with a magnetic stir bar was charged with 33.4 mg of $FeCl_3 \cdot 6H_2O$ and closed with a septum. In a Schlenk line, the flask was purged of air and charged with Argon (3 cycles). Then, the solid was dissolved in 25 mL of MeCN. The resulting mixture was stirred for 15 minutes. Samples at different known concentrations were measured and obtained data is summarized in Figure 5.4.4 and Table 5.4.4.

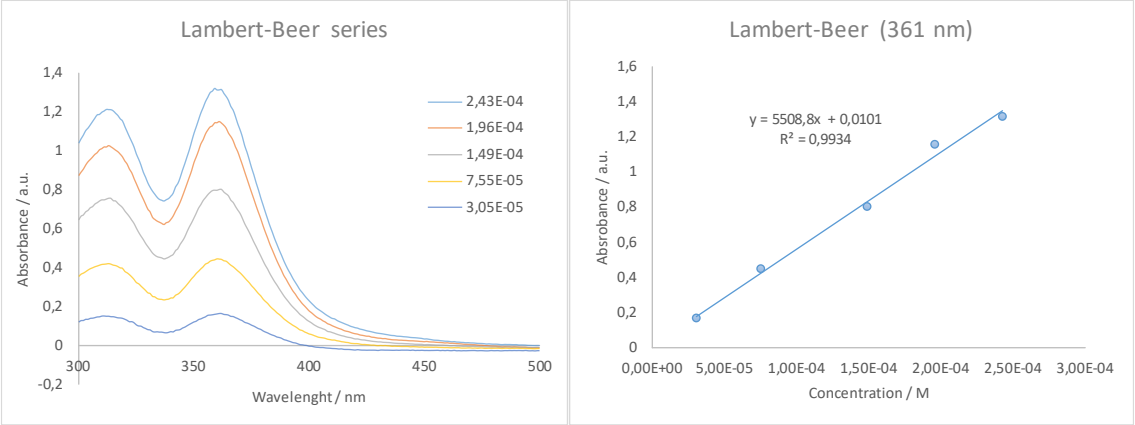

Figure 5.4.4. Lamber-Beer absorption series for $FeCl_3 \cdot 6H_2O$ in MeCN.

Table 5.4.4. Lambert-Beer law data for $FeCl_3 \cdot 6H_2O$ in MeCN.

M	Absorbance (357 nm) / a.u.	Lambert-Beer equation
2,43E-04	1,31404	
1,96E-04	1,15205	
1,49E-04	0,801098	y = 5508,8x - 0,0101
7,55E-05	0,442153	R^2 = 0.9934
3,05E-05	0,164559	

Stock solution was prepared following the described procedure: a round-bottom flask equipped with a magnetic stir bar was charged with 67.3 mg of $FeCl_3 \cdot 6H_2O$ and closed with a septum. In a Schlenk line, the flask was purged of air and charged with Argon (3 cycles). Then, the solid was dissolved in 50 mL of MeCN and 0.70 mL of distilled collidine was added. The resulting mixture was stirred for 15 minutes. Samples at different known concentrations were measured and obtained data is summarized in Figure 5.4.5 and Table 5.4.5.

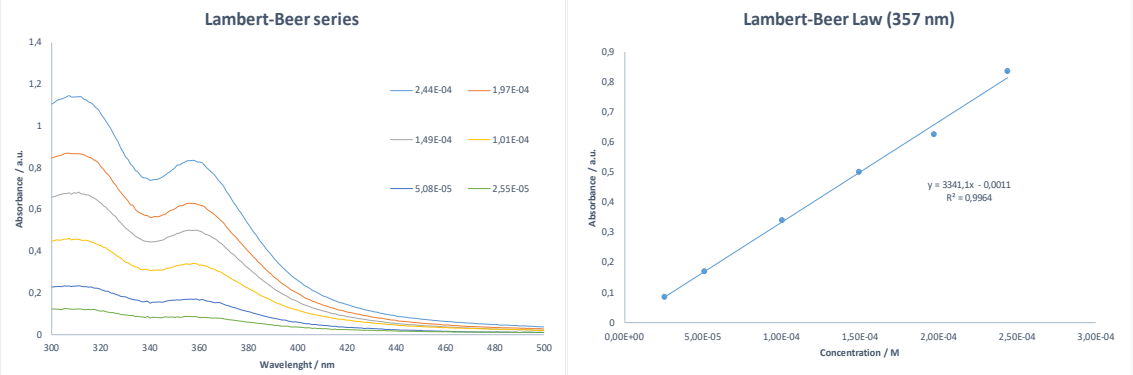

Figure 5.4.5 Lamber-Beer absorption series for $FeCl_3 \cdot 6H_2O$ in MeCN with 2,4,6-collidine as ligand.

Table 5.4.5. Lambert-Beer law data series for $FeCl_3 \cdot 6H_2O$ in MeCN with 2,4,6-collidine as ligand.

M	Absorbance (357 nm) / a.u.	Lambert-Beer equation
2,44E-04	0,835077	
1,97E-04	0,626147	
1,49E-04	0,499935	y = 3341,1x - 0,0011
1,01E-04	0,339647	R^2 = 0.9964
5,08E-05	0,1701	
2,55E-05	0,0851341	

For the sake of comparison, absorption spectra of both solutions at the same concentration were taken and plotted together in Figure 5.4.6. It can be clearly observed that formed complex with collidine displays lower absorptivity in the LMCT region band for Fe.

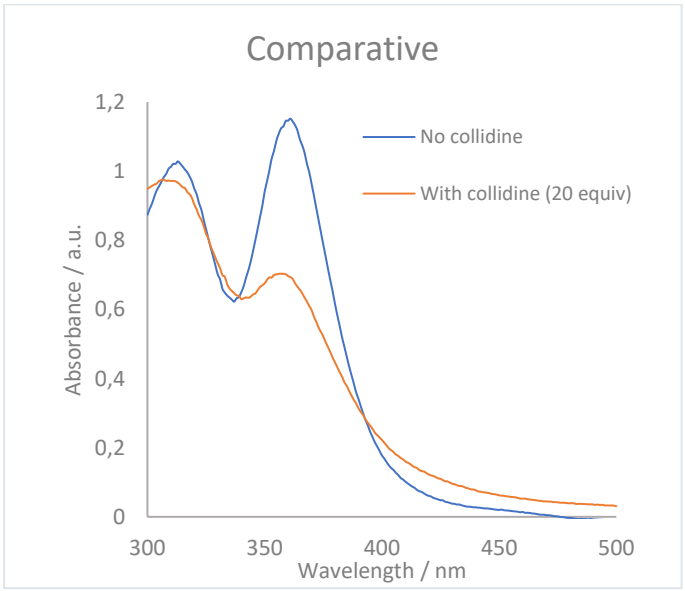

Figure 5.4.6. Comparative absorption spectra for $FeCl_3 \cdot 6H_2O$ and $FeCl_3 \cdot 6H_2O$/Collidine complex at the same concentration ($2{,}10 \times 10^{-04}$ M).

5.4.6.4.2 Kinetic measurements

In a 10 mL vial equipped with magnetic stir bar and filled with Argon, 4 mL of stock solution was added. Reactions were irradiated with 370 nm 43 W light while stirring. Absorbance spectra were acquired at the indicated time by taking an aliquot of 40 mL, which was dissolved in 970 mL of dry MeCN. Each time, one of the reactions was selected and measured and then cast aside.

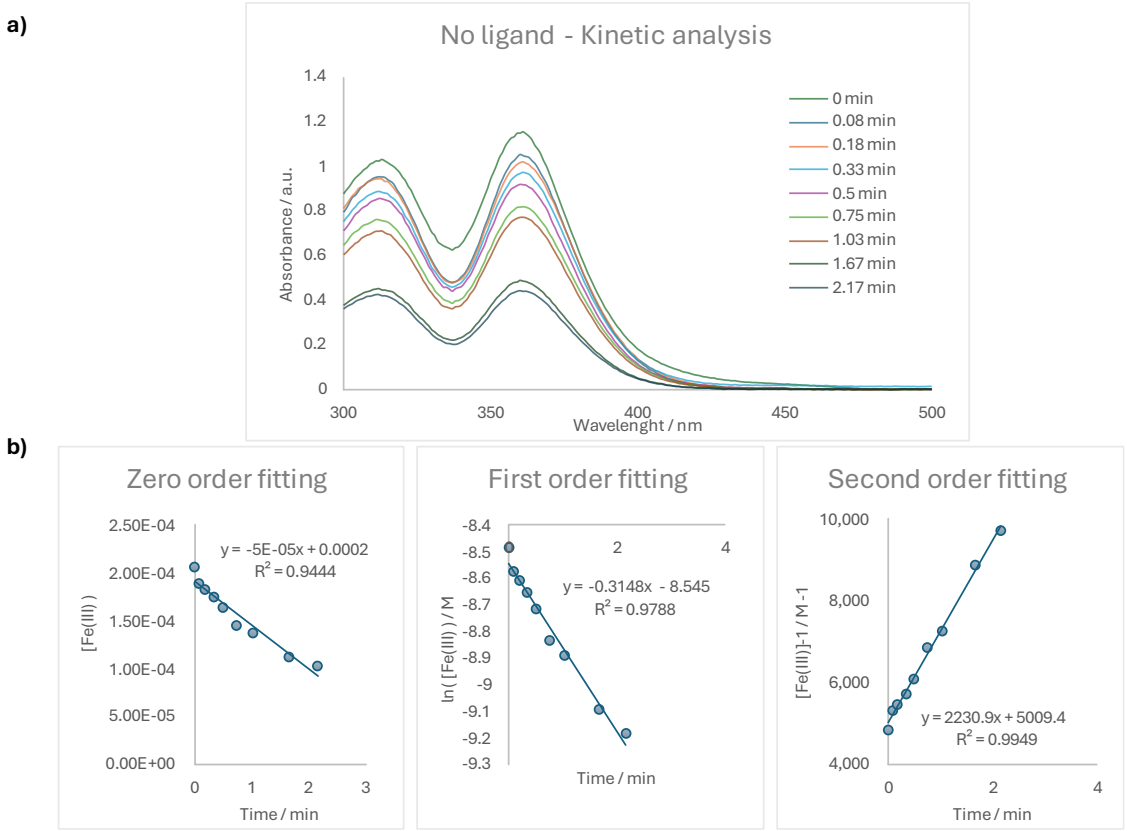

Figure 5.4.7. a) Time-resolved absorption spectra of FeCl$_3$ 6H$_2$O in MeCN. b) Straight-line plots to determine rate constant.

Table 5.4.6. Kinetic data for FeCl$_3$·6H$_2$O absorbance decaying in MeCN.

			Zero order	***First order***	***Second order***
Time / s	**Time / min**	**Abs (361 nm)**	**[Fe(III)] / M**	**Ln([Fe(III)])**	**1 / [Fe(III)]**
0	0.00	1,15205	2,07E-04	-8,48136477	4,82E+03
5	0.08	1,0509	1,89E-04	-8,57411244	5,29E+03
11	0.18	1,01902	1,83E-04	-8,60522164	5,46E+03
20	0.33	0,972942	1,75E-04	-8,65196804	5,72E+03
30	0.50	0,914966	1,64E-04	-8,71407051	6,09E+03
45	0.75	0,815461	1,46E-04	-8,83056675	6,84E+03
62	1.03	0,768647	1,38E-04	-8,89045261	7,26E+03
100	1.67	0,6311461	1,13E-04	-9,09045206	8,87E+03
130	2.17	0,57744275	1,03E-04	-9,18089375	9,71E+03
		R^2	0.9444	0.9788	0.9949

Second order in [Fe(III)]; rate = k[Fe(III)]^2; k = 2.2 × 10^3 M^{-1}·min^{-1}

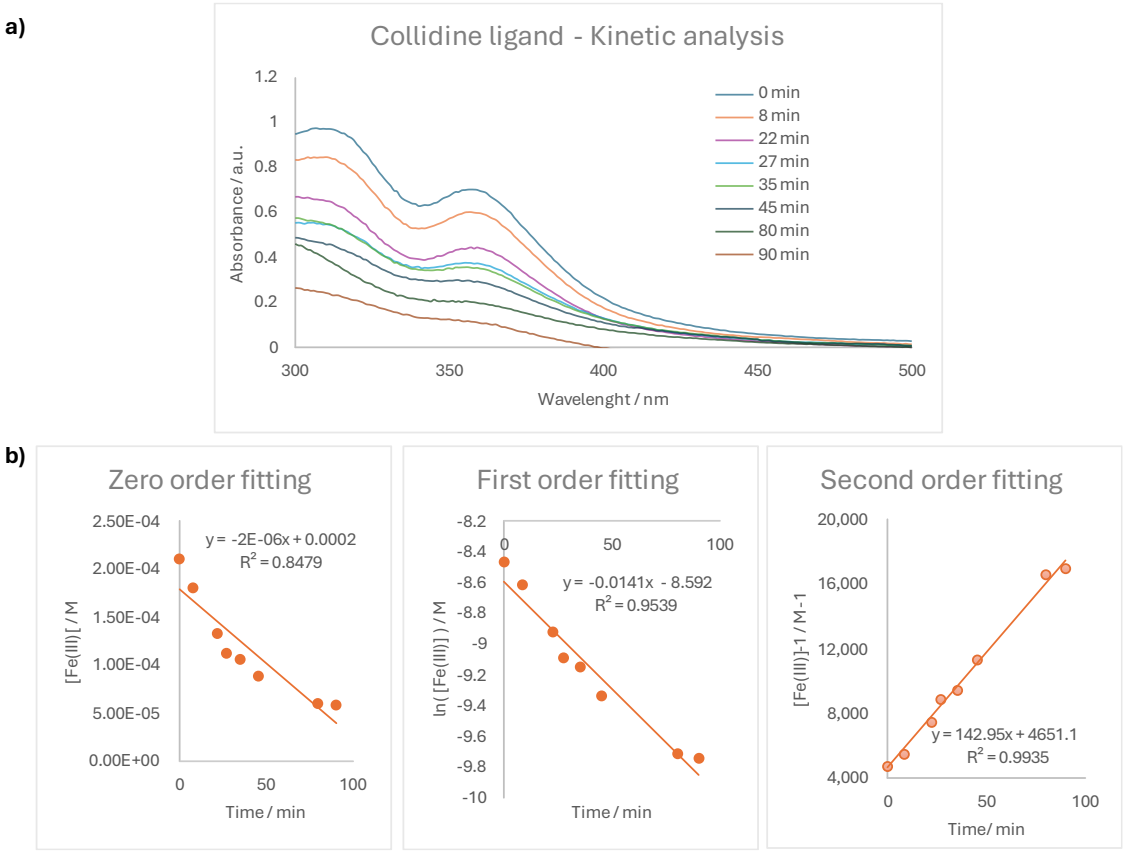

Figure 5.4.8. a) Time-resolved absorption spectra of $FeCl_3 \cdot 6H_2O$ in MeCN with 2,4,6-collidine as ligand. b) Straight-line plots to determine rate constant.

Table 5.4.7. Kinetic data for $FeCl_3 \cdot 6H_2O$ absorbance decaying in MeCN with 2,4,6-collidine as ligand.

		Zero order	***First order***	***Second order***
Time / min	**Abs (357 nm)**	**[Fe(III)] / M**	**Ln([Fe(III)])**	**1 / [Fe(III)]**
0	0,703546	2,10E-04	-8,46724212	4756,3798
8	0,604009	1,80E-04	-8,62004438	5541,6323
22	0,445411	1,33E-04	-8,92528588	7519,7328
27	0,37698	1,13E-04	-9,09254071	8888,7411
35	0,354275	1,06E-04	-9,15484697	9460,1826
45	0,295654	8,82E-05	-9,3363483	11342,9117
80	0,202232	6,02E-05	-9,71784924	16611,4790
90	0,197951	5,89E-05	-9,73936355	16972,7357
	R²	0.8479	0.9539	0.9935

Second order in [Fe(III)]; rate = k[Fe(III)]^2; k = 1.4 × 10^2 M^{-1}·min^{-1}

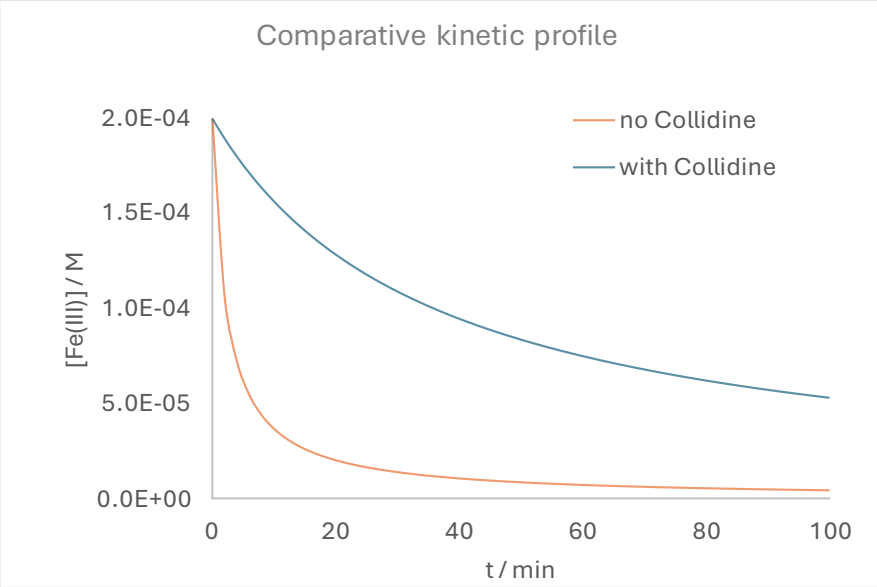

Figure 5.4.9. Kinetic profiles comparison for absorbance decaying under light irradiation (43W Kessil 370 nm) of $FeCl_3 \cdot 6H_2O$ in MeCN (orange) without and (blue) with 2,4,6-collidine as ligand.

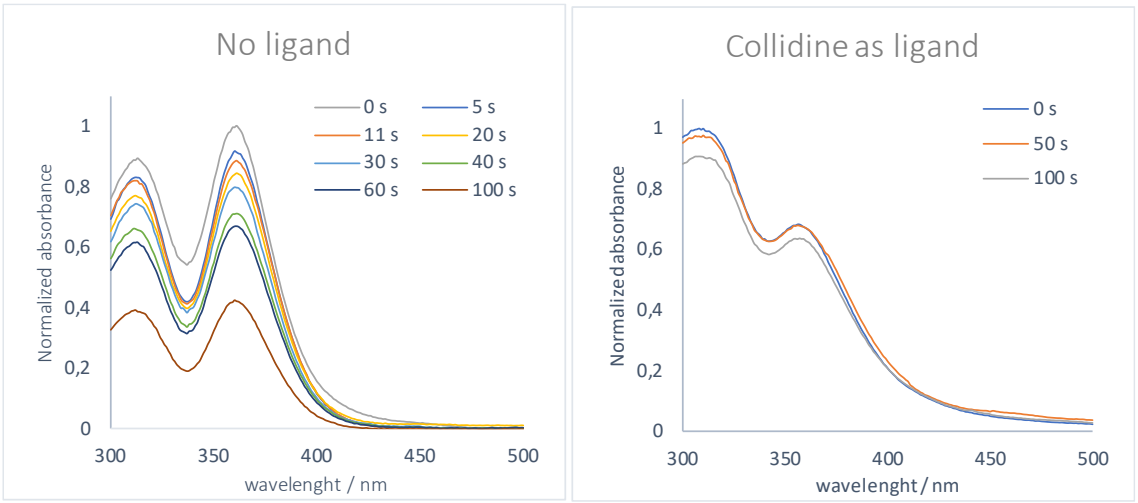

Figure 5.4.10. Comparison of absorbance decaying under light irradiation (43W Kessil 370 nm) of $FeCl_3 \cdot 6H_2O$ in MeCN (left) without and (right) with 2,4,6-collidine as ligand during the first 100 s.

5.4.6.4.3 EPR measurements

X-band EPR spectra of the $FeCl_3$ and $FeCl_3$/collidine were acquired in MeCN solution at room temperature 300 K using a quartz sample tube. Samples were charged in a capillary tube under inhert atmosphere and sealed to keep the argon atmosphere. EPR spectra was acquired after (blue) and before (orange) irradiation of both samples for 3 min, under .370 nm 43 W Kessil LED lamp irradiation.

- *$FeCl_3$ sample*: 2.7 mg of $FeCl_3 \cdot 6H_2O$, 0.5 mL of MeCN
- *$FeCl_3$/collidine sample*: 2.7 mg of $FeCl_3$, 30 µL of collidine, 0.5 mL of MeCN

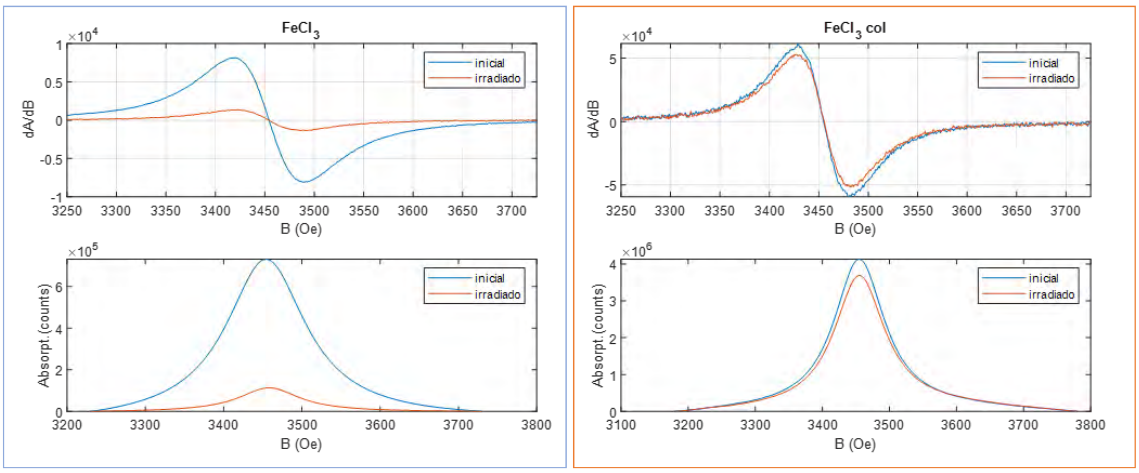

Figure 5.4.11. X-band EPR spectra for $FeCl_3$ (at room temperature) in a) absence of collidine and b) in presence of collidine. Samples were measured before and after irradiation. Upper spectra show the measurement and bottom shows the integral.

BIBLIOGRAPHY

1. Anastas, P. T.; Warner, J. C., *Green Chemistry: Theory and Practice*. Oxford University Press: 2000.
2. Anastas, P.; Eghbali, N., Green Chemistry: Principles and Practice. *Chem. Soc. Rev.* **2010,** *39* (1), 301-312.
3. Centi, G.; Perathoner, S., Catalysis and sustainable (green) chemistry. *Catal. Today* **2003,** *77* (4), 287-297.
4. Peng, Q.; Paton, R. S., Catalytic Control in Cyclizations: From Computational Mechanistic Understanding to Selectivity Prediction. *Acc. Chem. Res.* **2016,** *49* (5), 1042-1051.
5. Sterling, A. J.; Zavitsanou, S.; Ford, J.; Duarte, F., Selectivity in organocatalysis—From qualitative to quantitative predictive models. *WIREs Comput Mol Sci.* **2021,** *11* (5), e1518.
6. Blackmond, D. G., Kinetic Profiling of Catalytic Organic Reactions as a Mechanistic Tool. *J. Am. Chem. Soc.* **2015,** *137* (34), 10852-10866.
7. Methods of Investigation. In *Homogeneous Catalysis*, 2014; pp 67-94.
8. Funes-Ardoiz, I.; Schoenebeck, F., Established and Emerging Computational Tools to Study Homogeneous Catalysis—From Quantum Mechanics to Machine Learning. *Chem* **2020,** *6* (8), 1904-1913.
9. Bandar, J. S.; Ascic, E.; Buchwald, S. L., Enantioselective CuH-Catalyzed Reductive Coupling of Aryl Alkenes and Activated Carboxylic Acids. *J. Am. Chem. Soc.* **2016,** *138* (18), 5821-5824.
10. Gui, Y.-Y.; Hu, N.; Chen, X.-W.; Liao, L. L.; Ju, T.; Ye, J.-H.; Zhang, Z.; Li, J.; Yu, D.-G., Highly Regio- and Enantioselective Copper-Catalyzed Reductive Hydroxymethylation of Styrenes and 1,3-Dienes with CO2. *J. Am. Chem. Soc.* **2017,** *139* (47), 17011-17014.
11. Brechmann, L. T.; Kaewmee, B.; Teichert, J. F., H2-Mediated Copper-Catalyzed C–C Coupling Reactions: Selective Formation of Skipped Dienes. *ACS Catal.* **2023,** *13* (19), 12634-12642.
12. Hazra, C. K.; Fopp, C.; Oestreich, M., Copper(I)-Catalyzed Regioselective Addition of Nucleophilic Silicon Across Terminal and Internal Carbon–Carbon Triple Bonds. *Chem. Asian J.* **2014,** *9* (10), 3005-3010.
13. Tani, Y.; Fujihara, T.; Terao, J.; Tsuji, Y., Copper-Catalyzed Regiodivergent Silacarboxylation of Allenes with Carbon Dioxide and a Silylborane. *J. Am. Chem. Soc.* **2014,** *136* (51), 17706-17709.
14. O'Connor, T. J.; Mai, B. K.; Nafie, J.; Liu, P.; Toste, F. D., Generation of Axially Chiral Fluoroallenes through a Copper-Catalyzed Enantioselective β-Fluoride Elimination. *J. Am. Chem. Soc.* **2021,** *143* (34), 13759-13768.
15. Semba, K.; Shinomiya, M.; Fujihara, T.; Terao, J.; Tsuji, Y., Highly Selective Copper-Catalyzed Hydroboration of Allenes and 1,3-Dienes. *Chem. Eur. J.* **2013,** *19* (22), 7125-7132.
16. Jang, H.; Zhugralin, A. R.; Lee, Y.; Hoveyda, A. H., Highly Selective Methods for Synthesis of Internal (α-) Vinylboronates through Efficient NHC–Cu-Catalyzed Hydroboration of Terminal Alkynes. Utility in Chemical Synthesis and Mechanistic Basis for Selectivity. *J. Am. Chem. Soc.* **2011,** *133* (20), 7859-7871.
17. Laitar, D. S.; Tsui, E. Y.; Sadighi, J. P., Copper(I) β-Boroalkyls from Alkene Insertion: Isolation and Rearrangement. *Organometallics* **2006,** *25* (10), 2405-2408.
18. Chaves-Pouso, A.; Rivera-Chao, E.; Fañanás-Mastral, M., Catalytic Alkyne Allylboration: A Quest for Selectivity. *ACS Catal.* **2023,** *13* (19), 12656-12664.
19. Whyte, A.; Torelli, A.; Mirabi, B.; Zhang, A.; Lautens, M., Copper-Catalyzed Borylative Difunctionalization of π-Systems. *ACS Catal.* **2020,** *10* (19), 11578-11622.

20. Alfaro, R.; Parra, A.; Alemán, J.; García Ruano, J. L.; Tortosa, M., Copper(I)-Catalyzed Formal Carboboration of Alkynes: Synthesis of Tri- and Tetrasubstituted Vinylboronates. *J. Am. Chem. Soc.* **2012,** *134* (37), 15165-15168.
21. Yoshida, H.; Kageyuki, I.; Takaki, K., Copper-Catalyzed Three-Component Carboboration of Alkynes and Alkenes. *Org. Lett.* **2013,** *15* (4), 952-955.
22. Semba, K.; Bessho, N.; Fujihara, T.; Terao, J.; Tsuji, Y., Copper-Catalyzed Borylative Allyl–Allyl Coupling Reaction. *Angew. Chem. Int. Ed.* **2014,** *53* (34), 9007-9011.
23. Meng, F.; McGrath, K. P.; Hoveyda, A. H., Multifunctional organoboron compounds for scalable natural product synthesis. *Nature* **2014,** *513* (7518), 367-374.
24. Takahashi, K.; Ishiyama, T.; Miyaura, N., A borylcopper species generated from bis(pinacolato)diboron and its additions to α,β-unsaturated carbonyl compounds and terminal alkynes. *J. Organomet. Chem.* **2001,** *625* (1), 47-53.
25. Zhang, Q.; Li, M.; Liu, J.-Q.; Yu, H.-Z., Mechanistic insights into the ligand-controlled regioselectivity in Cu-catalyzed terminal alkynes alkylboration. *J. Organomet. Chem.* **2018,** *871*, 48-55.
26. Moure, A. L.; Mauleón, P.; Gómez Arrayás, R.; Carretero, J. C., Formal Regiocontrolled Hydroboration of Unbiased Internal Alkynes via Borylation/Allylic Alkylation of Terminal Alkynes. *Org. Lett.* **2013,** *15* (8), 2054-2057.
27. Gao, Y.; Yazdani, S.; Kendrick IV, A.; Junor, G. P.; Kang, T.; Grotjahn, D. B.; Bertrand, G.; Jazzar, R.; Engle, K. M., Cyclic (Alkyl)(amino)carbene Ligands Enable Cu-Catalyzed Markovnikov Protoboration and Protosilylation of Terminal Alkynes: A Versatile Portal to Functionalized Alkenes**. *Angew. Chem. Int. Ed.* **2021,** *60* (36), 19871-19878.
28. Gao, Y.; Kim, N.; Mendoza, S. D.; Yazdani, S.; Faria Vieira, A.; Liu, M.; Kendrick, A. I. V.; Grotjahn, D. B.; Bertrand, G.; Jazzar, R.; Engle, K. M., (CAAC)Copper Catalysis Enables Regioselective Three-Component Carboboration of Terminal Alkynes. *ACS Catal.* **2022,** *12* (12), 7243-7247.
29. Yoshida, H.; Takemoto, Y.; Takaki, K., A masked diboron in Cu-catalysed borylation reaction: highly regioselective formal hydroboration of alkynes for synthesis of branched alkenylborons. *Chem. Commun.* **2014,** *50* (61), 8299-8302.
30. Su, W.; Gong, T.-J.; Zhang, Q.; Zhang, Q.; Xiao, B.; Fu, Y., Ligand-Controlled Regiodivergent Copper-Catalyzed Alkylboration of Unactivated Terminal Alkynes. *ACS Catal.* **2016,** *6* (10), 6417-6421.
31. Yuan, W.; Ma, S., Ligand Controlled Highly Selective Copper-Catalyzed Borylcuprations of Allenes with Bis(pinacolato)diboron. *Adv. Synth. Catal.* **2012,** *354* (10), 1867-1872.
32. Hong, S.; Zhang, X., DFT Studies on Ligand Controlled Highly Selective Copper-Catalyzed Borylations of Allenes. *Asian J. Org. Chem.* **2023,** *12* (5), e202200689.
33. Meng, F.; Jung, B.; Haeffner, F.; Hoveyda, A. H., NHC–Cu-Catalyzed Protoboration of Monosubstituted Allenes. Ligand-Controlled Site Selectivity, Application to Synthesis and Mechanism. *Org. Lett.* **2013,** *15* (6), 1414-1417.
34. Li, J.; Song, X.; Wu, F.; You, H.; Chen, F.-E., Copper-Catalyzed Asymmetric Allylic Alkylation of Racemic Cyclic Allyl Bromides with Organolithium Compounds. *Eur. J. Org. Chem.* **2022,** *2022* (34), e202200860.
35. Xiong, W.; Xu, G.; Yu, X.; Tang, W., P-Chiral Monophosphorus Ligands for Asymmetric Copper-Catalyzed Allylic Alkylation. *Organometallics* **2019,** *38* (20), 4003-4013.
36. Huang, Y.; Fañanás-Mastral, M.; Minnaard, A. J.; Feringa, B. L., A novel catalytic asymmetric route towards skipped dienes with a methyl-substituted central stereogenic carbon. *Chem. Commun.* **2013,** *49* (32), 3309-3311.

37. Manna, M. S.; Yoo, S. Y.; Sharique, M.; Choi, H.; Pudasaini, B.; Baik, M.-H.; Tambar, U. K., Copper-Catalyzed Regiodivergent Internal Allylic Alkylations. *Angew. Chem. Int. Ed.* **2023,** *62* (35), e202304848.
38. Arai, M.; Nakamura, E.; Lipshutz, B. H., Copper-catalyzed reactions of organotitanium reagents. Highly S_N2'-and anti-selective and diastereo-and chemoselective alkylation of allylic chlorides and phosphates. *J. Org. Chem.* **1991,** *56* (19), 5489-5491.
39. Bertozzi, F.; Crotti, P.; Macchia, F.; Pineschi, M.; Feringa, B. L., Highly Enantioselective Regiodivergent and Catalytic Parallel Kinetic Resolution. *Angew. Chem. Int. Ed.* **2001,** *40* (5), 930-932.
40. Piarulli, U.; Daubos, P.; Claverie, C.; Monti, C.; Gennari, C., Copper-Catalysed, Enantioselective Desymmetrisation of meso Cyclic Allylic Bis(diethyl phosphates) with Organozinc Reagents. *Eur. J. Org. Chem.* **2005,** *2005* (5), 895-906.
41. Lee, Y.; Li, B.; Hoveyda, A. H., Stereogenic-at-Metal Zn- and Al-Based N-Heterocyclic Carbene (NHC) Complexes as Bifunctional Catalysts in Cu-Free Enantioselective Allylic Alkylations. *J. Am. Chem. Soc.* **2009,** *131* (32), 11625-11633.
42. Yoshikai, N.; Nakamura, E., Mechanisms of Nucleophilic Organocopper(I) Reactions. *Chem. Rev.* **2012,** *112* (4), 2339-2372.
43. Hornillos, V.; Gualtierotti, J.-B.; Feringa, B. L., Asymmetric Allylic Substitutions Using Organometallic Reagents. In *Progress in Enantioselective Cu(I)-catalyzed Formation of Stereogenic Centers*, Harutyunyan, S. R., Ed. Springer International Publishing: Cham, 2016; pp 1-39.
44. Langlois, J.-B.; Alexakis, A., Copper-catalyzed Enantioselective Allylic Substitution. In *Transition Metal Catalyzed Enantioselective Allylic Substitution in Organic Synthesis*, Kazmaier, U., Ed. Springer Berlin Heidelberg: Berlin, Heidelberg, 2012; pp 235-268.
45. Goering, H. L.; Kantner, S. S., Alkylation of allylic derivatives. Regio- and stereochemistry of alkylation of allylic alcohols by the Murahashi method. *J. Org. Chem.* **1981,** *46* (10), 2144-2148.
46. Yamanaka, M.; Kato, S.; Nakamura, E., Mechanism and Regioselectivity of Reductive Elimination of π-Allylcopper (III) Intermediates. *J. Am. Chem. Soc.* **2004,** *126* (20), 6287-6293.
47. Nakamura, E.; Sekiya, K.; Arai, M.; Aoki, S., Virtually complete diastereofacial selectivity in the SN2' allylation of organocopper reagents. *J. Am. Chem. Soc.* **1989,** *111* (8), 3091-3093.
48. Yamamoto, Y.; Yamamoto, S.; Yatagai, H.; Maruyama, K., Lewis acid mediated reactions of organocopper reagents. A remarkably enhanced regioselective. gamma.-attack of allylic halides and direct alkylation of allylic alcohols via RCu. cntdot. BF3 system. *J. Am. Chem. Soc.* **1980,** *102* (7), 2318-2325.
49. Corey, E. J.; Boaz, N. W., d-orbital stereoelectronic control of the stereochemistry of SN2′ displacements by organocuprate reagents. *Tetrahedron Lett.* **1984,** *25* (29), 3063-3066.
50. Nakamura, E.; Mori, S., Wherefore Art Thou Copper? Structures and Reaction Mechanisms of Organocuprate Clusters in Organic Chemistry. *Angew. Chem. Int. Ed.* **2000,** *39* (21), 3750-3771.
51. Pérez, M.; Fañanás-Mastral, M.; Hornillos, V.; Rudolph, A.; Bos, P. H.; Harutyunyan, S. R.; Feringa, B. L., Asymmetric Allylic Alkylation of Acyclic Allylic Ethers with Organolithium Reagents. *Chem. Eur. J.* **2012,** *18* (38), 11880-11883.
52. Palais, L.; Bournaud, C.; Micouin, L.; Alexakis, A., Copper-Catalysed Ring Opening of Polycyclic meso-Hydrazines with Trialkylaluminium Reagents and SimplePhos Ligands. *Chem. Eur. J.* **2010,** *16* (8), 2567-2573.

53. Yoshikai, N.; Miura, K.; Nakamura, E., Enantioselective Copper-Catalyzed Allylic Substitution Reaction with Aminohydroxyphosphine Ligand. *Adv. Synth. Catal.* **2009,** *351* (7-8), 1014-1018.
54. Yoshikai, N.; Zhang, S.-L.; Nakamura, E., Origin of the Regio- and Stereoselectivity of Allylic Substitution of Organocopper Reagents. *J. Am. Chem. Soc.* **2008,** *130* (39), 12862-12863.
55. Rivera-Chao, E.; Mitxelena, M.; Varela, J. A.; Fañanás-Mastral, M., Copper-Catalyzed Enantioselective Allylboration of Alkynes: Synthesis of Highly Versatile Multifunctional Building Blocks. *Angew. Chem. Int. Ed.* **2019,** *58* (50), 18230-18234.
56. Rivera-Chao, E.; Fañanás-Mastral, M., Synthesis of Stereodefined Borylated Dendralenes through Copper-Catalyzed Allylboration of Alkynes. *Angew. Chem. Int. Ed.* **2018,** *57* (31), 9945-9949.
57. Shi, Y.; Jung, B.; Torker, S.; Hoveyda, A. H., N-Heterocyclic Carbene–Copper-Catalyzed Group-, Site-, and Enantioselective Allylic Substitution with a Readily Accessible Propargyl(pinacolato)boron Reagent: Utility in Stereoselective Synthesis and Mechanistic Attributes. *J. Am. Chem. Soc.* **2015,** *137* (28), 8948-8964.
58. Lee, J.; Torker, S.; Hoveyda, A. H., Versatile Homoallylic Boronates by Chemo-, SN2′-, Diastereo- and Enantioselective Catalytic Sequence of Cu−H Addition to Vinyl-B(pin)/Allylic Substitution. *Angew. Chem. Int. Ed.* **2017,** *56* (3), 821-826.
59. Hoveyda, A. H.; Zhou, Y.; Shi, Y.; Brown, M. K.; Wu, H.; Torker, S., Sulfonate N-Heterocyclic Carbene–Copper Complexes: Uniquely Effective Catalysts for Enantioselective Synthesis of C−C, C−B, C−H, and C−Si Bonds. *Angew. Chem. Int. Ed.* **2020,** *59* (48), 21304-21359.
60. Vázquez-Galiñanes, N.; Sciortino, G.; Piñeiro-Suárez, M.; Tóth, B. L.; Maseras, F.; Fañanás-Mastral, M., Switching Selectivity in Borylative Allyl–Allyl Cross-Coupling through Synergistic Catalysis. *J. Am. Chem. Soc.* **2024**.
61. Plattner, D. A.; Li, Y.; Houk, K. N., Modern Computational and Theoretical Aspects of Acetylene Chemistry. In *Modern Acetylene Chemistry*, 1995; pp 1-32.
62. Palke, W. E., Double bonds are bent equivalent hybrid (banana) bonds. *J. Am. Chem. Soc.* **1986,** *108* (21), 6543-6544.
63. Trotuş, I.-T.; Zimmermann, T.; Schüth, F., Catalytic Reactions of Acetylene: A Feedstock for the Chemical Industry Revisited. *Chem. Rev.* **2014,** *114* (3), 1761-1782.
64. Zhang, S.; Li, J.; Li, G.; Nie, Y.; Qiang, L.; Bai, B.; Ma, X., Life cycle assessment of acetylene production from calcium carbide and methane in China. *Journal of Cleaner Production* **2021,** *322*, 129055.
65. Pässler, P.; Hefner, W.; Buckl, K.; Meinass, H.; Meiswinkel, A.; Wernicke, H.-J.; Ebersberg, G.; Müller, R.; Bässler, J.; Behringer, H.; Mayer, D., Acetylene. In *Ullmann's Encyclopedia of Industrial Chemistry*, Wiley: Weinheim, 2011; Vol. 1, pp 278-326.
66. Schobert, H., Production of Acetylene and Acetylene-based Chemicals from Coal. *Chem. Rev.* **2014,** *114* (3), 1743-1760.
67. H. A. Wittcoff, B. G. R., J. S. Plotkin, Chemicals from methane. In *Industrial Organic Chemicals*, Wiley: New Jersey, 2012; Vol. 3, pp 417-423.
68. Voronin, V. V.; Ledovskaya, M. S.; Bogachenkov, A. S.; Rodygin, K. S.; Ananikov, V. P., Acetylene in Organic Synthesis: Recent Progress and New Uses. *Molecules* **2018,** *23* (10), 2442.
69. Xue, F.; Deng, H.; Xue, C.; Mohamed, D. K. B.; Tang, K. Y.; Wu, J., Reaction discovery using acetylene gas as the chemical feedstock accelerated by the "stop-flow" micro-tubing reactor system. *Chem. Sci.* **2017,** *8* (5), 3623-3627.

70. Sonogashira, K.; Tohda, Y.; Hagihara, N., A convenient synthesis of acetylenes: catalytic substitutions of acetylenic hydrogen with bromoalkenes, iodoarenes and bromopyridines. *Tetrahedron Lett.* **1975,** *16* (50), 4467-4470.
71. Fu, R.; Li, Z., Direct synthesis of symmetric diarylethynes from calcium carbide and arylboronic acids/esters. *Eur. J. Org. Chem.* **2017,** *2017* (45), 6648-6651.
72. Cao, C.; Shi, Y.; Odom, A. L., Intermolecular Alkyne Hydroaminations Involving 1,1-Disubstituted Hydrazines. *Org. Lett.* **2002,** *4* (17), 2853-2856.
73. Hou, J.; Yuan, M.-L.; Xie, J.-H.; Zhou, Q.-L., Nickel-catalyzed hydrocarboxylation of alkynes with formic acid. *Green Chemistry* **2016,** *18* (10), 2981-2984.
74. Díaz Velázquez, H.; Ruiz García, Y.; Vandichel, M.; Madder, A.; Verpoort, F., Water-soluble NHC-Cu catalysts: applications in click chemistry, bioconjugation and mechanistic analysis. *Org. Biomol. Chem.* **2014,** *12* (46), 9350-9356.
75. Hu, H.; Ohno, A.; Sato, T.; Mase, T.; Uozumi, Y.; Yamada, Y. M. A., Self-Assembled Polymeric Pyridine Copper Catalysts for Huisgen Cycloaddition with Alkynes and Acetylene Gas: Application in Synthesis of Tazobactam. *Org. Process Res. Dev.* **2019,** *23* (4), 493-498.
76. Huang, F.; Zhang, Y.; Yao, Y.; Yang, W.; Tao, Y., Synthesis of (4E,6Z,10Z)-hexadeca-4,6,10-trien-1-ol and (4E,6E,10Z)-hexadeca-4,6,10-trien-1-ol, the pheromone components of cocoa pod borer moth Conopomorpha cramerella. *RSC Adv.* **2017,** *7* (57), 35575-35580.
77. Lü, S.; Wang, Z.; Zhu, S., Thiol-Yne click chemistry of acetylene-enabled macrocyclization. *Nat. Commun.* **2022,** *13* (1), 5001.
78. Yang, B.; Lu, S.; Wang, Y.; Zhu, S., Diverse synthesis of C2-linked functionalized molecules via molecular glue strategy with acetylene. *Nat. Commun.* **2022,** *13* (1), 1858.
79. Lü, S.; Wang, Z.; Gao, X.; Chen, K.; Zhu, S., 1,2-Difunctionalization of Acetylene Enabled by Light. *Angew. Chem. Int. Ed.* **2023,** *62* (16), e202300268.
80. Lin, Z.; Liu, B.; Wang, Y.; Li, S.; Zhu, S., Synthesis of vinyl-substituted alcohols using acetylene as a C2 building block. *Chem. Sci.* **2023,** *14* (7), 1912-1918.
81. Liu, B.; Lin, Z.; Wang, Y.; Cheng, T.; Cao, T.; Zhu, S., Trimerization of Acetylene and Alkene: Rapid Access to Polyenes. *CCS Chemistry* **2023,** *5* (5), 1077-1085.
82. Liu, B.; Lin, Z.; Cheng, T.; Cao, T.; Zhu, S., Synthesis of *E*-Dienyl Esters Using Acetylene as C2 Synthon. *Org. Lett.* **2023,** *25* (19), 3573-3577.
83. Cheng, T.; Liu, B.; Wu, R.; Zhu, S., Cu-catalyzed carboboration of acetylene with Michael acceptors. *Chem. Sci.* **2022,** *13* (25), 7604-7609.
84. Scharnagel, D.; Escofet, I.; Armengol-Relats, H.; de Orbe, M. E.; Korber, J. N.; Echavarren, A. M., Acetylene as a Dicarbene Equivalent for Gold(I) Catalysis: Total Synthesis of Waitziacuminone in One Step. *Angew. Chem. Int. Ed.* **2020,** *59* (12), 4888-4891.
85. Hammarback, L. A.; Medina-Gil, T.; Sadurní, A.; Echavarren, A. M., Three-Component Gold(I)-Catalyzed Alkoxyvinylation. *Org. Lett.* **2024,** *26* (30), 6375-6379.
86. Kong, J. R.; Krische, M. J., Catalytic Carbonyl Z-Dienylation via Multicomponent Reductive Coupling of Acetylene to Aldehydes and α-Ketoesters Mediated by Hydrogen: Carbonyl Insertion into Cationic Rhodacyclopentadienes. *J. Am. Chem. Soc.* **2006,** *128* (50), 16040-16041.
87. Skucas, E.; Kong, J. R.; Krische, M. J., Enantioselective Reductive Coupling of Acetylene to N-Arylsulfonyl Imines via Rhodium Catalyzed C−C Bond-Forming Hydrogenation: (*Z*)-Dienyl Allylic Amines. *J. Am. Chem. Soc.* **2007,** *129* (23), 7242-7243.
88. Del Valle, D. J.; Krische, M. J., Total Synthesis of (+)-Trienomycins A and F via C–C Bond-Forming Hydrogenation and Transfer Hydrogenation. *J. Am. Chem. Soc.* **2013,** *135* (30), 10986-10989.

89. Medina-Gil, T.; Sadurní, A.; Hammarback, L. A.; Echavarren, A. M., Gold(I)-Catalyzed Intermolecular Aryloxyvinylation with Acetylene Gas. *ACS Catal.* **2023,** *13* (16), 10751-10755.
90. Schmidt, R.; Griesbaum, K.; Behr, A.; Biedenkapp, D.; Voges, H.-W.; Garbe, D.; Paetz, C.; Collin, G.; Mayer, D.; Höke, H., Hydrocarbons. In *Ullmann's Encyclopedia of Industrial Chemistry*, pp 1-74.
91. Hagen, A.; Roessner, F., Ethane to Aromatic Hydrocarbons: Past, Present, Future. *Catalysis Reviews* **2000,** *42* (4), 403-437.
92. Kang, H.-s.; Lee, D. h.; Kim, K.-t.; Jo, S.; Pyun, S.; Song, Y.-h.; Yu, S., Methane to acetylene conversion by employing cost-effective low-temperature arc. *Fuel Process. Technol.* **2016,** *148*, 209-216.
93. Speight, J. G., Chapter 2 - Sources of hydrocarbons. In *Handbook of Industrial Hydrocarbon Processes (Second Edition)*, Speight, J. G., Ed. Gulf Professional Publishing: Boston, 2020; pp 45-93.
94. Speight, J. G., Chapter 4 - Hydrocarbons from natural gas and natural gas hydrates. In *Handbook of Industrial Hydrocarbon Processes (Second Edition)*, Speight, J. G., Ed. Gulf Professional Publishing: Boston, 2020; pp 143-192.
95. Faraday, M., VI. Experimental researches in electricity.-Seventh Series. *Philosophical Transactions of the Royal Society of London* **1834,** (124), 77-122.
96. Kolbe, H.; Frankland, E., VIII. On the products of the action of potassium on cyanide of ethyl. *Q. J. Chem. Soc.* **1849,** *1* (1), 60-74.
97. Frankland, E., XXVII.—On the isolation of the organic radicals. *Q. J. Chem. Soc.* **1850,** *2* (3), 263-296.
98. Schorlemmer, C., Ueber die Identität des Aethylwasserstoffs und des Methyls. *Justus Liebigs Ann. Chem.* **1864,** *132* (2), 234-238.
99. Zimmermann, H.; Walzl, R., Ethylene. In *Ullmann's Encyclopedia of Industrial Chemistry*.
100. Najari, S.; Saeidi, S.; Concepcion, P.; Dionysiou, D. D.; Bhargava, S. K.; Lee, A. F.; Wilson, K., Oxidative dehydrogenation of ethane: catalytic and mechanistic aspects and future trends. *Chem. Soc. Rev.* **2021,** *50* (7), 4564-4605.
101. Markofsky, S. B., Nitro Compounds, Aliphatic. In *Ullmann's Encyclopedia of Industrial Chemistry*.
102. Olah, G. A., Electrophilic methane conversion. *Acc. Chem. Res.* **1987,** *20* (11), 422-428.
103. Shilov, A. E.; Shul'pin, G. B., Activation of C−H Bonds by Metal Complexes. *Chem. Rev.* **1997,** *97* (8), 2879-2932.
104. Crabtree, R. H., The organometallic chemistry of alkanes. *Chem. Rev.* **1985,** *85* (4), 245-269.
105. Caballero, A.; Despagnet-Ayoub, E.; Mar Díaz-Requejo, M.; Díaz-Rodríguez, A.; González-Núñez, M. E.; Mello, R.; Muñoz, B. K.; Ojo, W.-S.; Asensio, G.; Etienne, M.; Pérez, P. J., Silver-Catalyzed C-C Bond Formation Between Methane and Ethyl Diazoacetate in Supercritical CO_2. *Science* **2011,** *332* (6031), 835-838.
106. Liskey, C. W.; Hartwig, J. F., Iridium-Catalyzed Borylation of Secondary C–H Bonds in Cyclic Ethers. *J. Am. Chem. Soc.* **2012,** *134* (30), 12422-12425.
107. Chen, H.; Schlecht, S.; Semple, T. C.; Hartwig, J. F., Thermal, Catalytic, Regiospecific Functionalization of Alkanes. *Science* **2000,** *287* (5460), 1995-1997.
108. Chen, H.; Hartwig, J. F., Catalytic, Regiospecific End-Functionalization of Alkanes: Rhenium-Catalyzed Borylation under Photochemical Conditions. *Angew. Chem. Int. Ed.* **1999,** *38* (22), 3391-3393.

109. Cook, A. K.; Schimler, S. D.; Matzger, A. J.; Sanford, M. S., Catalyst-controlled selectivity in the C–H borylation of methane and ethane. *Science* **2016,** *351* (6280), 1421-1424.
110. Smith, K. T.; Berritt, S.; González-Moreiras, M.; Ahn, S.; Smith, M. R.; Baik, M.-H.; Mindiola, D. J., Catalytic borylation of methane. *Science* **2016,** *351* (6280), 1424-1427.
111. Hartwig, J. F.; Cook, K. S.; Hapke, M.; Incarvito, C. D.; Fan, Y.; Webster, C. E.; Hall, M. B., Rhodium Boryl Complexes in the Catalytic, Terminal Functionalization of Alkanes. *J. Am. Chem. Soc.* **2005,** *127* (8), 2538-2552.
112. Lee, J.; Jin, S.; Kim, D.; Hong, S. H.; Chang, S., Cobalt-Catalyzed Intermolecular C–H Amidation of Unactivated Alkanes. *J. Am. Chem. Soc.* **2021,** *143* (13), 5191-5200.
113. Fuentes, M. Á.; Gava, R.; Saper, N. I.; Romero, E. A.; Caballero, A.; Hartwig, J. F.; Pérez, P. J., Copper-Catalyzed Dehydrogenative Amidation of Light Alkanes. *Angew. Chem. Int. Ed.* **2021,** *60* (34), 18467-18471.
114. Michos, D.; Sassano, C. A.; Krajnik, P.; Crabtree, R. H., Amination of Methane and Ethane by Mercury Photosensitization in the Presence of Ammonia. *Angewandte Chemie International Edition in English* **1993,** *32* (10), 1491-1492.
115. Velasco-Rubio, Á.; Martínez-Balart, P.; Álvarez-Constantino, A. M.; Fañanás-Mastral, M., C–C bond formation via photocatalytic direct functionalization of simple alkanes. *Chem. Commun.* **2023,** *59* (62), 9424-9444.
116. Pulcinella, A.; Mazzarella, D.; Noël, T., Homogeneous catalytic C(sp3)–H functionalization of gaseous alkanes. *Chem. Commun.* **2021,** *57* (78), 9956-9967.
117. Bonciolini, S.; Noël, T.; Capaldo, L., Synthetic Applications of Photocatalyzed Halogen-Radical Mediated Hydrogen Atom Transfer for C−H Bond Functionalization. *Eur. J. Org. Chem.* **2022,** *2022* (34), e202200417.
118. Capaldo, L.; Ravelli, D., Hydrogen Atom Transfer (HAT): A Versatile Strategy for Substrate Activation in Photocatalyzed Organic Synthesis. *Eur. J. Org. Chem.* **2017,** *2017* (15), 2056-2071.
119. Duncan, D. C.; Netzel, T. L.; Hill, C. L., Early-Time Dynamics and Reactivity of Polyoxometalate Excited States. Identification of a Short-Lived LMCT Excited State and a Reactive Long-Lived Charge-Transfer Intermediate following Picosecond Flash Excitation of $[W_{10}O_{32}]^{4-}$ in Acetonitrile. *Inorg. Chem.* **1995,** *34* (18), 4640-4646.
120. Tanielian, C., Decatungstate photocatalysis. *Coord. Chem. Rev.* **1998,** *178-180*, 1165-1181.
121. Tzirakis, M. D.; Lykakis, I. N.; Orfanopoulos, M., Decatungstate as an efficient photocatalyst in organic chemistry. *Chem. Soc. Rev.* **2009,** *38* (9), 2609-2621.
122. Perez-Prieto, J.; Galian, R. E.; Miranda, M. A., Diaryl Ketones as Photoactivators. *Mini-Rev. Org. Chem.* **2006,** *3* (2), 117-135.
123. Dormán, G.; Nakamura, H.; Pulsipher, A.; Prestwich, G. D., The Life of Pi Star: Exploring the Exciting and Forbidden Worlds of the Benzophenone Photophore. *Chem. Rev.* **2016,** *116* (24), 15284-15398.
124. Mateos, J.; Cuadros, S.; Vega-Peñaloza, A.; Dell'Amico, L., Unlocking the Synthetic Potential of Light-Excited Aryl Ketones: Applications in Direct Photochemistry and Photoredox Catalysis. *Synlett* **2021,** *33* (02), 116-128.
125. Prier, C. K.; Rankic, D. A.; MacMillan, D. W. C., Visible Light Photoredox Catalysis with Transition Metal Complexes: Applications in Organic Synthesis. *Chem. Rev.* **2013,** *113* (7), 5322-5363.
126. Meger, F. S.; Murphy, J. A., Recent Advances in C–H Functionalisation through Indirect Hydrogen Atom Transfer. *Molecules* **2023,** *28* (16), 6127.

127. Chiba, S.; Chen, H., sp3 C–H oxidation by remote H-radical shift with oxygen- and nitrogen-radicals: a recent update. *Org. Biomol. Chem.* **2014,** *12* (24), 4051-4060.
128. Salamone, M.; Bietti, M., Tuning Reactivity and Selectivity in Hydrogen Atom Transfer from Aliphatic C–H Bonds to Alkoxyl Radicals: Role of Structural and Medium Effects. *Acc. Chem. Res.* **2015,** *48* (11), 2895-2903.
129. Sadeghi, M., C(sp3)−H Functionalization Using Chlorine Radicals. *Adv. Synth. Catal.* **2024,** *366* (13), 2898-2918.
130. Laudadio, G.; Deng, Y.; van der Wal, K.; Ravelli, D.; Nuño, M.; Fagnoni, M.; Guthrie, D.; Sun, Y.; Noël, T., C(sp^3)-H functionalizations of light hydrocarbons using decatungstate photocatalysis in flow. *Science* **2020,** *369* (6499), 92-96.
131. Li, J.; Lopez, S. A., Computational Chemistry for Photochemical Reactions. In *Comprehensive Computational Chemistry (First Edition)*, Yáñez, M.; Boyd, R. J., Eds. Elsevier: Oxford, 2024; pp 658-698.
132. Nair, A. M.; Martínez-Balart, P.; Barbeira-Arán, S.; Fañanás-Mastral, M., Cross-Coupling of Gaseous Alkanes with (Hetero)Aryl Bromides via Dual Nickel/Photoredox Catalysis. *Angew. Chem. Int. Ed. n/a* (n/a), e202416957.
133. Pulcinella, A.; Chandra Tiwari, P.; Luridiana, A.; Yamazaki, K.; Mazzarella, D.; Sadhoe, A. K.; Alfano, A. I.; Tiekink, E. H.; Hamlin, T. A.; Noël, T., C1-4 Alkylation of Aryl Bromides with Light Alkanes enabled by Metallaphotocatalysis in Flow. *Angew. Chem. Int. Ed. n/a* (n/a), e202413846.
134. Hu, A.; Guo, J.-J.; Pan, H.; Zuo, Z., Selective functionalization of methane, ethane, and higher alkanes by cerium photocatalysis. *Science* **2018,** *361* (6403), 668-672.
135. An, Q.; Xing, Y.-Y.; Pu, R.; Jia, M.; Chen, Y.; Hu, A.; Zhang, S.-Q.; Yu, N.; Du, J.; Zhang, Y.; Chen, J.; Liu, W.; Hong, X.; Zuo, Z., Identification of Alkoxy Radicals as Hydrogen Atom Transfer Agents in Ce-Catalyzed C–H Functionalization. *J. Am. Chem. Soc.* **2023,** *145* (1), 359-376.
136. Yang, Q.; Wang, Y.-H.; Qiao, Y.; Gau, M.; Carroll, P. J.; Walsh, P. J.; Schelter, E. J., Photocatalytic C–H activation and the subtle role of chlorine radical complexation in reactivity. *Science* **2021,** *372* (6544), 847-852.
137. Deng, H.-P.; Zhou, Q.; Wu, J., Microtubing-Reactor-Assisted Aliphatic C−H Functionalization with HCl as a Hydrogen-Atom-Transfer Catalyst Precursor in Conjunction with an Organic Photoredox Catalyst. *Angew. Chem. Int. Ed.* **2018,** *57* (39), 12661-12665.
138. Li, D.-S.; Liu, T.; Hong, Y.; Cao, C.-L.; Wu, J.; Deng, H.-P., Stop-Flow Microtubing Reactor-Assisted Visible Light-Induced Hydrogen-Evolution Cross Coupling of Heteroarenes with C(sp3)–H Bonds. *ACS Catal.* **2022,** *12* (8), 4473-4480.
139. Jin, Y.; Zhang, Q.; Wang, L.; Wang, X.; Meng, C.; Duan, C., Convenient C(sp3)–H bond functionalisation of light alkanes and other compounds by iron photocatalysis. *Green Chemistry* **2021,** *23* (18), 6984-6989.
140. Zhang, Q.; Liu, S.; Lei, J.; Zhang, Y.; Meng, C.; Duan, C.; Jin, Y., Iron-Catalyzed Photoredox Functionalization of Methane and Heavier Gaseous Alkanes: Scope, Kinetics, and Computational Studies. *Org. Lett.* **2022,** *24* (10), 1901-1906.
141. Jin, Y.; Wang, L.; Zhang, Q.; Zhang, Y.; Liao, Q.; Duan, C., Photo-induced direct alkynylation of methane and other light alkanes by iron catalysis. *Green Chemistry* **2021,** *23* (23), 9406-9411.
142. Panetti, G. B.; Yang, Q.; Gau, M. R.; Carroll, P. J.; Walsh, P. J.; Schelter, E. J., Discovery and mechanistic investigation of photoinduced sp^3 C-H activation of hydrocarbons by the simple anion hexachlorotitanate. *Chem Catal.* **2022,** *2* (4), 853-866.

143. Dai, Z.-Y.; Zhang, S.-Q.; Hong, X.; Wang, P.-S.; Gong, L.-Z., A practical $FeCl_3$/HCl photocatalyst for versatile aliphatic C–H functionalization. *Chem Catal.* **2022,** *2* (5), 1211-1222.
144. Martínez-Balart, P.; Velasco-Rubio, Á.; Barbeira-Arán, S.; Jiménez-Cristóbal, H.; Fañanás-Mastral, M., Chemodivergent alkylation of trifluoromethyl alkenes via photocatalytic coupling with alkanes. *Green Chemistry* **2024**.
145. Fañanás-Mastral, M.; Feringa, B. L., Copper-Catalyzed Regio- and Enantioselective Synthesis of Chiral Enol Acetates and β-Substituted Aldehydes. *J. Am. Chem. Soc.* **2010,** *132* (38), 13152-13153.
146. Langlois, J.-B.; Alexakis, A., Identification of a Valuable Kinetic Process in Copper-Catalyzed Asymmetric Allylic Alkylation. *Angew. Chem. Int. Ed.* **2011,** *50* (8), 1877-1881.
147. Giannerini, M.; Fañanás-Mastral, M.; Feringa, B. L., *Z*-Selective Copper-Catalyzed Asymmetric Allylic Alkylation with Grignard Reagents. *J. Am. Chem. Soc.* **2012,** *134* (9), 4108-4111.
148. Frisch, M. J.; Trucks, G. W.; Schlegel, H. B.; Scuseria, G. E.; Robb, M. A.; Cheeseman, J. R.; Scalmani, G.; Barone, V.; Petersson, G. A.; Nakatsuji, H.; Li, X.; Caricato, M.; Marenich, A. V.; Bloino, J.; Janesko, B. G.; Gomperts, R.; Mennucci, B.; Hratchian, H. P.; Ortiz, J. V.; Izmaylov, A. F.; Sonnenberg, J. L.; Williams; Ding, F.; Lipparini, F.; Egidi, F.; Goings, J.; Peng, B.; Petrone, A.; Henderson, T.; Ranasinghe, D.; Zakrzewski, V. G.; Gao, J.; Rega, N.; Zheng, G.; Liang, W.; Hada, M.; Ehara, M.; Toyota, K.; Fukuda, R.; Hasegawa, J.; Ishida, M.; Nakajima, T.; Honda, Y.; Kitao, O.; Nakai, H.; Vreven, T.; Throssell, K.; Montgomery Jr., J. A.; Peralta, J. E.; Ogliaro, F.; Bearpark, M. J.; Heyd, J. J.; Brothers, E. N.; Kudin, K. N.; Staroverov, V. N.; Keith, T. A.; Kobayashi, R.; Normand, J.; Raghavachari, K.; Rendell, A. P.; Burant, J. C.; Iyengar, S. S.; Tomasi, J.; Cossi, M.; Millam, J. M.; Klene, M.; Adamo, C.; Cammi, R.; Ochterski, J. W.; Martin, R. L.; Morokuma, K.; Farkas, O.; Foresman, J. B.; Fox, D. J. *Gaussian 16 Rev. C.01*, Wallingford, CT, 2016.
149. Chai, J.-D.; Head-Gordon, M., Long-range corrected hybrid density functionals with damped atom–atom dispersion corrections. *Phys. Chem. Chem. Phys.* **2008,** *10* (44), 6615-6620.
150. Ditchfield, R.; Hehre, W. J.; Pople, J. A., Self-Consistent Molecular-Orbital Methods. IX. An Extended Gaussian-Type Basis for Molecular-Orbital Studies of Organic Molecules. *J. Chem. Phys.* **1971,** *54* (2), 724-728.
151. Hehre, W. J.; Ditchfield, R.; Pople, J. A., Self—Consistent Molecular Orbital Methods. XII. Further Extensions of Gaussian—Type Basis Sets for Use in Molecular Orbital Studies of Organic Molecules. *J. Chem. Phys.* **1972,** *56* (5), 2257-2261.
152. Hariharan, P. C.; Pople, J. A., The influence of polarization functions on molecular orbital hydrogenation energies. *Theor. Chim. Acta* **1973,** *28* (3), 213-222.
153. Dill, J. D.; Pople, J. A., Self-consistent molecular orbital methods. XV. Extended Gaussian-type basis sets for lithium, beryllium, and boron. *J. Chem. Phys.* **1975,** *62* (7), 2921-2923.
154. Francl, M. M.; Pietro, W. J.; Hehre, W. J.; Binkley, J. S.; Gordon, M. S.; DeFrees, D. J.; Pople, J. A., Self-consistent molecular orbital methods. XXIII. A polarization-type basis set for second-row elements. *J. Chem. Phys.* **1982,** *77* (7), 3654-3665.
155. Gordon, M. S.; Binkley, J. S.; Pople, J. A.; Pietro, W. J.; Hehre, W. J., Self-consistent molecular-orbital methods. 22. Small split-valence basis sets for second-row elements. *J. Am. Chem. Soc.* **1982,** *104* (10), 2797-2803.
156. Rassolov, V. A.; Pople, J. A.; Ratner, M. A.; Windus, T. L., 6-31G* basis set for atoms K through Zn. *J. Chem. Phys.* **1998,** *109* (4), 1223-1229.

157. Rassolov, V. A.; Ratner, M. A.; Pople, J. A.; Redfern, P. C.; Curtiss, L. A., 6-31G* basis set for third-row atoms. *J. Comput. Chem.* **2001,** *22* (9), 976-984.
158. Marenich, A. V.; Cramer, C. J.; Truhlar, D. G., Universal Solvation Model Based on Solute Electron Density and on a Continuum Model of the Solvent Defined by the Bulk Dielectric Constant and Atomic Surface Tensions. *J. Phys. Chem. B* **2009,** *113* (18), 6378-6396.
159. Weigend, F.; Ahlrichs, R., Balanced basis sets of split valence, triple zeta valence and quadruple zeta valence quality for H to Rn: Design and assessment of accuracy. *Phys. Chem. Chem. Phys.* **2005,** *7* (18), 3297-3305.
160. Rappoport, D.; Furche, F., Property-optimized Gaussian basis sets for molecular response calculations. *J. Chem. Phys.* **2010,** *133* (13).
161. Morokuma, K., Molecular Orbital Studies of Hydrogen Bonds. III. C=O···H–O Hydrogen Bond in $H_2CO\cdots H_2O$ and $H_2CO\cdots 2H_2O$. *J. Chem. Phys.* **1971,** *55* (3), 1236-1244.
162. Bickelhaupt, F. M., Understanding reactivity with Kohn–Sham molecular orbital theory: E2–S_N2 mechanistic spectrum and other concepts. *J. Comput. Chem.* **1999,** *20* (1), 114-128.
163. Ess, D. H.; Houk, K. N., Distortion/Interaction Energy Control of 1,3-Dipolar Cycloaddition Reactivity. *J. Am. Chem. Soc.* **2007,** *129* (35), 10646-10647.
164. Bickelhaupt, F. M.; Houk, K. N., Analyzing Reaction Rates with the Distortion/Interaction-Activation Strain Model. *Angew. Chem. Int. Ed.* **2017,** *56* (34), 10070-10086.
165. Lu, T.; Chen, F., Multiwfn: A multifunctional wavefunction analyzer. *J. Comput. Chem.* **2012,** *33* (5), 580-592.
166. Humphrey, W.; Dalke, A.; Schulten, K., VMD: Visual molecular dynamics. *J. Mol. Graph.* **1996,** *14* (1), 33-38.
167. Johnson, E. R.; Keinan, S.; Mori-Sánchez, P.; Contreras-García, J.; Cohen, A. J.; Yang, W., Revealing Noncovalent Interactions. *J. Am. Chem. Soc.* **2010,** *132* (18), 6498-6506.
168. Boto, R. A.; Contreras-García, J.; Tierny, J.; Piquemal, J.-P., Interpretation of the reduced density gradient. *Mol. Phys.* **2016,** *114* (7-8), 1406-1414.
169. Price, A. J. A.; Otero-de-la-Roza, A.; Johnson, E. R., XDM-corrected hybrid DFT with numerical atomic orbitals predicts molecular crystal lattice energies with unprecedented accuracy. *Chem. Sci.* **2023,** *14* (5), 1252-1262.
170. Andrae, D.; Häußermann, U.; Dolg, M.; Stoll, H.; Preuß, H., Energy-adjustedab initio pseudopotentials for the second and third row transition elements. *Theor. Chim. Acta* **1990,** *77* (2), 123-141.
171. Ehlers, A. W.; Böhme, M.; Dapprich, S.; Gobbi, A.; Höllwarth, A.; Jonas, V.; Köhler, K. F.; Stegmann, R.; Veldkamp, A.; Frenking, G., A set of f-polarization functions for pseudo-potential basis sets of the transition metals Sc-Cu, Y-Ag and La-Au. *Chem. Phys. Lett.* **1993,** *208* (1), 111-114.
172. Petruncio, G.; Shellnutt, Z.; Elahi-Mohassel, S.; Alishetty, S.; Paige, M., Skipped dienes in natural product synthesis. *Nat. Prod. Rep.* **2021,** *38* (12), 2187-2213.
173. Sato, T.; Suto, T.; Nagashima, Y.; Mukai, S.; Chida, N., Total Synthesis of Skipped Diene Natural Products. *Asian J. Org. Chem.* **2021,** *10* (10), 2486-2502.
174. Gerth, K.; Washausen, P.; Höfle, G.; Irschik, H.; Reichenbach, H., The Jerangolids: A Family of New Antifungal Compounds from Sorangium cellulosum (Myxobacteria). Production, Physico-chemical and Biological Properties of Jerangolid A. *J. Antibiot.* **1996,** *49* (1), 71-75.
175. Macklin, T. K.; Micalizio, G. C., Convergent and stereospecific synthesis of complex skipped polyenes and polyunsaturated fatty acids. *Nat. Chem.* **2010,** *2* (8), 638-643.

176. Hamilton, J. Y.; Sarlah, D.; Carreira, E. M., Iridium-Catalyzed Enantioselective Allylic Vinylation. *J. Am. Chem. Soc.* **2013,** *135* (3), 994-997.
177. Gao, F.; Carr, J. L.; Hoveyda, A. H., A Broadly Applicable NHC–Cu-Catalyzed Approach for Efficient, Site-, and Enantioselective Coupling of Readily Accessible (Pinacolato)alkenylboron Compounds to Allylic Phosphates and Applications to Natural Product Synthesis. *J. Am. Chem. Soc.* **2014,** *136* (5), 2149-2161.
178. Wang, Z.-X.; Gao, P.-C.; Lin, E.-Z.; Li, B.-J., Stereodefined Skipped Dienes through Iridium-Catalyzed Formal Addition of Tertiary Allylic C−H Bonds to Alkynes. *Angew. Chem. Int. Ed.* **2022,** *61* (26), e202200075.
179. Chaves-Pouso, A.; Álvarez-Constantino, A. M.; Fañanás-Mastral, M., Enantio- and Diastereoselective Copper-Catalyzed Allylboration of Alkynes with Allylic gem-Dichlorides. *Angew. Chem. Int. Ed.* **2022,** *61* (23), e202117696.
180. Sun, Y.; Zhou, Y.; Shi, Y.; Del Pozo, J.; Torker, S.; Hoveyda, A. H., Copper–Hydride-Catalyzed Enantioselective Processes with Allenyl Boronates. Mechanistic Nuances, Scope, and Utility in Target-Oriented Synthesis. *J. Am. Chem. Soc.* **2019,** *141* (30), 12087-12099.
181. Zhou, Y.; Shi, Y.; Torker, S.; Hoveyda, A. H., S_N2''-Selective and Enantioselective Substitution with Unsaturated Organoboron Compounds and Catalyzed by a Sulfonate-Containing NHC-Cu Complex. *J. Am. Chem. Soc.* **2018,** *140* (48), 16842-16854.
182. Akiyama, K.; Gao, F.; Hoveyda, A. H., Stereoisomerically Pure Trisubstituted Vinylaluminum Reagents and their Utility in Copper-Catalyzed Enantioselective Synthesis of 1, 4-Dienes Containing Z or E Alkenes. *Angew. Chem. Int. Ed.* **2010,** *49* (2), 419-423.
183. Piñeiro-Suárez, M.; Álvarez-Constantino, A. M.; Fañanás-Mastral, M., Copper-Catalyzed Enantioselective Borylative Allyl–Allyl Coupling of Allenes and Allylic gem-Dichlorides. *ACS Catal.* **2023,** *13* (8), 5578-5583.
184. Pape, F.; Teichert, J. F., Dealing at Arm's Length: Catalysis with N-Heterocyclic Carbene Ligands Bearing Anionic Tethers. *Eur. J. Org. Chem.* **2017,** *2017* (29), 4206-4229.
185. Widianto, A. Y.; Aubin, J.; Xuereb, C.; Poux, M., Gas-liquid-liquid reactions: Contacting mechanisms and effective process technologies. *Catal. Today* **2020,** *346*, 46-57.
186. Krautwald, S.; Sarlah, D.; Schafroth, M. A.; Carreira, E. M., Enantio- and Diastereodivergent Dual Catalysis: α-Allylation of Branched Aldehydes. *Science* **2013,** *340* (6136), 1065-1068.
187. Krautwald, S.; Carreira, E. M., Stereodivergence in Asymmetric Catalysis. *J. Am. Chem. Soc.* **2017,** *139* (16), 5627-5639.
188. Kassem, S.; Lee, A. T. L.; Leigh, D. A.; Marcos, V.; Palmer, L. I.; Pisano, S., Stereodivergent synthesis with a programmable molecular machine. *Nature* **2017,** *549* (7672), 374-378.
189. Huo, X.; Zhang, J.; Fu, J.; He, R.; Zhang, W., Ir/Cu Dual Catalysis: Enantio- and Diastereodivergent Access to α,α-Disubstituted α-Amino Acids Bearing Vicinal Stereocenters. *J. Am. Chem. Soc.* **2018,** *140* (6), 2080-2084.
190. Carreras, J.; Caballero, A.; Pérez, P. J., Alkenyl Boronates: Synthesis and Applications. *Chem. Asian J.* **2019,** *14* (3), 329-343.
191. Johansson Seechurn, C. C. C.; Kitching, M. O.; Colacot, T. J.; Snieckus, V., Palladium-Catalyzed Cross-Coupling: A Historical Contextual Perspective to the 2010 Nobel Prize. *Angew. Chem. Int. Ed.* **2012,** *51* (21), 5062-5085.
192. Armstrong, R. J.; Aggarwal, V. K., 50 Years of Zweifel Olefination: A Transition-Metal-Free Coupling. *Synthesis* **2017,** *49* (15), 3323-3336.
193. Tsui, W.-Y.; Brown, G. D., (+)-Nyasol from Asparagus cochinchinensis. *Phytochem.* **1996,** *43* (6), 1413-1415.

194. Hirose, Y.; Oishi, N.; Nagaki, H.; Nakatsuka, T., The structure of hinokiresinol. *Tetrahedron Lett.* **1965,** *6* (41), 3665-3668.
195. McNally, M.; Capon, R. J., Phorbasin B and C: novel diterpenes from a southern Australian marine sponge, Phorbas species. *J. Nat. Prod.* **2001,** *64* (5), 645-647.
196. Zhang, H.; Capon, R. J., Phorbasins D− F: Diterpenyl-taurines from a Southern Australian Marine Sponge, Phorbas sp. *Org. Lett.* **2008,** *10* (10), 1959-1962.
197. Macklin, T. K.; Micalizio, G. C., Total synthesis and structure elucidation of (+)-phorbasin C. *J. Am. Chem. Soc.* **2009,** *131* (4), 1392-1393.
198. Zhang, H.; Major, J. M.; Lewis, R. J.; Capon, R. J., Phorbasins G–K: new cytotoxic diterpenes from a southern Australian marine sponge, Phorbas sp. *Org. Biomol. Chem.* **2008,** *6* (20), 3811-3815.
199. Makida, Y.; Takayama, Y.; Ohmiya, H.; Sawamura, M., Copper-Catalyzed γ-Selective and Stereospecific Direct Allylic Alkylation of Terminal Alkynes: Synthesis of Skipped Enynes. *Angew. Chem. Int. Ed.* **2013,** *52* (20), 5350-5354.
200. Näf, F.; Decorzant, R.; Giersch, W.; Ohloff, G., A stereocontrolled access to (±)-,(−)-, and (+)-patchouli alcohol. *Helv. Chim. Acta* **1981,** *64* (5), 1387-1397.
201. Ireland, R. E.; Anderson, R. C.; Badoud, R.; Fitzsimmons, B. J.; McGarvey, G. J.; Thaisrivongs, S.; Wilcox, C. S., The total synthesis of ionophore antibiotics. A convergent synthesis of lasalocid A (X537A). *J. Am. Chem. Soc.* **1983,** *105* (7), 1988-2006.
202. Oppolzer, W.; Jacobsen, E. J., Enantioselective syntheses of (+)-α-skytanthine, (+)-δ-skytanthine and (+)-iridomyrmecin by an intramolecular magnesium-ene reaction. *Tetrahedron Lett.* **1986,** *27* (10), 1141-1144.
203. Gadwood, R. C.; Lett, R. M.; Wissinger, J. E., Total synthesis of (±)-poitediol and (±)-dactylol. *J. Am. Chem. Soc.* **1986,** *108* (20), 6343-6350.
204. Lacharity, J. J.; Fournier, J.; Lu, P.; Mailyan, A. K.; Herrmann, A. T.; Zakarian, A., Total synthesis of unsymmetrically oxidized nuphar thioalkaloids via copper-catalyzed thiolane assembly. *J. Am. Chem. Soc.* **2017,** *139* (38), 13272-13275.
205. Tang, F.; Lan, P.; Bolte, B.; Banwell, M. G.; Ward, J. S.; Willis, A. C., Total synthesis of (+)-viridianol, a marine-derived sesquiterpene embodying the decahydrocyclobuta [d] indene framework. *J. Org. Chem.* **2018,** *83* (22), 14049-14056.
206. Clive, D. L. J.; Murthy, K. S. K.; Wee, A. G. H.; Prasad, J. S.; Da Silva, G. V. J.; Majewski, M.; Anderson, P. C.; Evans, C. F.; Haugen, R. D., Total synthesis of both (+)-compactin and (+)-mevinolin. A general strategy based on the use of a special titanium reagent for dicarbonyl coupling. *J. Am. Chem. Soc.* **1990,** *112* (8), 3018-3028.
207. Zhang, Z.; Xie, H.; Li, H.; Gao, L.; Song, Z., Total Synthesis of (−)-Exiguolide. *Org. Lett.* **2015,** *17* (19), 4706-4709.
208. Makida, Y.; Ohmiya, H.; Sawamura, M., Regio- and Stereocontrolled Introduction of Secondary Alkyl Groups to Electron-Deficient Arenes through Copper-Catalyzed Allylic Alkylation. *Angew. Chem. Int. Ed.* **2012,** *51* (17), 4122-4127.
209. Kamijo, S.; Kamijo, K.; Maruoka, K.; Murafuji, T., Aryl Ketone Catalyzed Radical Allylation of C(sp3)–H Bonds under Photoirradiation. *Org. Lett.* **2016,** *18* (24), 6516-6519.
210. Jin, Y.; Ng, E. W. H.; Fan, T.; Hirao, H.; Gong, L.-Z., Photochemical Allylation of Alkanes Enabled by Nickel Catalysis. *ACS Catal.* **2022,** *12* (16), 10039-10046.
211. Martínez-Balart, P.; Tóth, B. L.; Velasco-Rubio, Á.; Fañanás-Mastral, M., Direct C–H Allylation of Unactivated Alkanes by Cooperative W/Cu Photocatalysis. *Org. Lett.* **2022,** *24* (37), 6874-6879.
212. Meggers, E.; Ye, C.-X.; Shen, X.; Zhou, B. Method for preparing alpha-amino acids. 2023.

213. Long, Y.; Tu, Z.; Hu, W. Preparation of imidazo[1,5-a]quinazoline-5(4H)-one derivatives as BET protein inhibitors. 2020.
214. Seidel, H. M.; Roush, W. R.; Venkatraman, S. Compounds and compositions for treating conditions associated with STING activity such as cancer using STING inhibitors. 2020.
215. Cismesia, M. A.; Yoon, T. P., Characterizing chain processes in visible light photoredox catalysis. *Chem. Sci.* **2015,** *6* (10), 5426-5434.
216. Reiß, B.; Hu, Q.; Riedle, E.; Wagenknecht, H.-A., The Dependence of Chemical Quantum Yields of Visible Light Photoredox Catalysis on the Irradiation Power. *ChemPhotoChem* **2021,** *5* (11), 1009-1019.
217. Liu, W.; Wu, Q.; Wang, M.; Huang, Y.; Hu, P., Iron-Catalyzed C–C Single-Bond Cleavage of Alcohols. *Org. Lett.* **2021,** *23* (21), 8413-8418.
218. Canle L., M.; Maskill, H.; Santaballa, J. A., Experimental Methods for Investigating Kinetics. In *The Investigation of Organic Reactions and Their Mechanisms*, 2006; pp 46-78.
219. Rodríguez, F.; Moreno, M., $FeCl_3$ solutions in isopropanol-water. *Transition Met. Chem.* **1985,** *10* (3), 108-112.
220. Wyrzykowski, D.; Kruszyński, R.; Kłak, J.; Mroziński, J.; Warnke, Z., Synthesis and magnetic characteristics of new tetrachloroferrates(III) with 2-methylpyridinium, 3-methylpyridinium and 4-methylpyridinium cations: X-ray crystal structure of 4-methylpyridinium tetrachloroferrate(III). *Inorg. Chim. Acta* **2007,** *360* (10), 3354-3360.
221. Jeffrey, G. A., *An introduction to hydrogen bonding*. Oxford University Press: New York, 1997.
222. Drew, M. G. B.; McKee, V.; Nelson, S. M., Crystal and molecular structure and some properties of pyridinium μ-oxo-bis[trichioroferrate(III)]–pyridine. *J. Chem. Soc., Dalton Trans.* **1978,** (1), 80-84.
223. Gao, Y.; Guery, J.; Jacoboni, C., $FeCl_3$ behavior in acetonitrile: structures of $[FeCl_2(CH_3CN)_4][FeCl_4]$ and $[AlCl(CH_3CN)_5][FeCl_4]$ 2 CH_3CN. *Acta Crystallogr. Sect. C: Cryst. Struct. Commun.* **1993,** *49* (1), 147-151.
224. Sessler, J. L.; Sibert, J. W.; Lynch, V., Bulky substituent effects on the iron(III) complexation of 1,4,7-triazacyclononane. *Inorg. Chim. Acta* **1994,** *216* (1), 89-95.
225. Cervone, E.; Diomedi Camassei, F., Cyclic chlorination reactions induced by visible light with chlorocopper(II) complexes as mediators. *J. Photochem.* **1981,** *15* (3), 203-212.
226. Breslow, R.; Brandl, M.; Hunger, J.; Adams, A. D., Selective steroid chlorinations directed by attached pyridine ester templates. *J. Am. Chem. Soc.* **1987,** *109* (12), 3799-3801.
227. Breslow, R.; Brandl, M.; Hunger, J.; Turro, N.; Cassidy, K.; Krogh-Jespersen, K.; Westbrook, J. D., Pyridine complexes of chlorine atoms. *J. Am. Chem. Soc.* **1987,** *109* (23), 7204-7206.
228. Abu-Raqabah, A.; Symons, M. C. R., The pyridine-chlorine atom 3-electron-bond intermediate. *J. Am. Chem. Soc.* **1990,** *112* (23), 8614-8615.
229. Legault, C. Y. *CYLview, 1.0b*, Université de Sherbrooke: 2009.
230. Murahashi, S.; Taniguchi, Y.; Imada, Y.; Tanigawa, Y., Palladium (0)-catalyzed azidation of allyl esters. Selective synthesis of allyl azides, primary allylamines, and related compounds. *J. Org. Chem.* **1989,** *54* (14), 3292-3303.
231. Jung, B.; Hoveyda, A. H., Site-and enantioselective formation of allene-bearing tertiary or quaternary carbon stereogenic centers through NHC–Cu-catalyzed allylic substitution. *J. Am. Chem. Soc.* **2012,** *134* (3), 1490-1493.

232. Brown, M. K.; May, T. L.; Baxter, C. A.; Hoveyda, A. H., All-carbon quaternary stereogenic centers by enantioselective Cu-catalyzed conjugate additions promoted by a chiral N-heterocyclic carbene. *Angew. Chem.* **2007,** *119* (7), 1115-1118.
233. Sánchez-Sordo, I.; Chaves-Pouso, A.; Mateos-Gil, J.; Rivera-Chao, E.; Fañanás-Mastral, M., Desymmetrization of meso-dibromocycloalkenes by copper-catalyzed asymmetric borylative coupling with alkynes. *Chem Catal.* **2023,** *3* (9), 100730.
234. Corberán, R.; Mszar, N. W.; Hoveyda, A. H., NHC-Cu-Catalyzed Enantioselective Hydroboration of Acyclic and Exocyclic 1, 1-Disubstituted Aryl Alkenes. *Angew. Chem. Int. Ed.* **2011,** *50* (31), 7079-7082.
235. Ko, C.; Feltenberger, J. B.; Ghosh, S. K.; Hsung, R. P., Gassman's intramolecular [2+ 2] cationic cycloaddition. Formal total syntheses of raikovenal and epi-raikovenal. *Org. Lett.* **2008,** *10* (10), 1971-1974.
236. Mousseau, J. J.; Bull, J. A.; Ladd, C. L.; Fortier, A.; Sustac Roman, D.; Charette, A. B., Synthesis of 2-and 2, 3-substituted pyrazolo [1, 5-a] pyridines: scope and mechanistic considerations of a domino direct alkynylation and cyclization of N-iminopyridinium ylides using alkenyl bromides, alkenyl iodides, and alkynes. *J. Org. Chem.* **2011,** *76* (20), 8243-8261.
237. Oketch-Rabah, H.; Dossaji, S.; Christensen, S. B.; Frydenvang, K.; Lemmich, E.; Cornett, C.; Olsen, C. E.; Chen, M.; Kharazmi, A.; Theander, T., Antiprotozoal compounds from Asparagus africanus. *J. Nat. Prod.* **1997,** *60* (10), 1017-1022.
238. Lorion, M. M.; Koch, V.; Nieger, M.; Chen, H. Y.; Lei, A.; Bräse, S.; Cossy, J., Cobalt-Catalyzed α-Arylation of Substituted α-Bromo α-Fluoro β-Lactams with Diaryl Zinc Reagents: Generalization to Functionalized Bromo Derivatives. *Chem. Eur. J.* **2020,** *26* (58), 13163-13169.
239. Bui, P. P.; Oyama, S. T.; Takagaki, A.; Carrow, B. P.; Nozaki, K., Reactions of 2-methyltetrahydropyran on silica-supported nickel phosphide in comparison with 2-methyltetrahydrofuran. *ACS Catal.* **2016,** *6* (7), 4549-4558.
240. Ushimaru, R.; Ding, Y.; Mori, T.; Miyamoto, K.; Uchiyama, M.; Abe, I., Structural and Mechanistic Insights into the C–C Bond-Forming Rearrangement Reaction Catalyzed by Heterodimeric Hinokiresinol Synthase. *J. Am. Chem. Soc.* **2023,** *145* (40), 21966-21973.
241. Lassen, P. R.; Skytte, D. M.; Hemmingsen, L.; Nielsen, S. F.; Freedman, T. B.; Nafie, L. A.; Christensen, S. B., Structure and Absolute Configuration of Nyasol and Hinokiresinol via Synthesis and Vibrational Circular Dichroism Spectroscopy. *J. Nat. Prod.* **2005,** *68* (11), 1603-1609.
242. Negishi, E.; Swanson, D. R.; Rousset, C. J., Clean and convenient procedure for converting primary alkyl iodides and. alpha.,. omega.-diiodoalkanes into the corresponding alkyllithium derivatives by treatment with tert-butyllithium. *J. Org. Chem.* **1990,** *55* (19), 5406-5409.
243. Upadhyaya, K.; Crich, D., Synthesis of 10-Aza-9-oxakalkitoxin by N–O Bond Formation. *Org. Lett.* **2022,** *24* (9), 1833-1836.
244. Xu, B.; Tambar, U. K., Remote Allylation of Unactivated C(sp3)–H Bonds Triggered by Photogenerated Amidyl Radicals. *ACS Catal.* **2019,** *9* (5), 4627-4631.
245. Hosokawa, A.; Yoshida, K. Process for preparation of 2-phenyl-1-propene derivatives by substitution. 1997.
246. Eckenhoff, W. T.; Biernesser, A. B.; Pintauer, T., Structural characterization and investigation of iron(III) complexes with nitrogen and phosphorus based ligands in atom transfer radical addition (ATRA). *Inorg. Chim. Acta* **2012,** *382*, 84-95.

247. Liao, S.; Porta, A.; Cheng, X.; Ma, X.; Zanoni, G.; Zhang, L., Bifunctional Ligand Enables Efficient Gold-Catalyzed Hydroalkenylation of Propargylic Alcohol. *Angew. Chem. Int. Ed.* **2018,** *57* (27), 8250-8254.
248. Brooks, W. L. A.; Deng, C. C.; Sumerlin, B. S., Structure–Reactivity Relationships in Boronic Acid–Diol Complexation. *ACS Omega* **2018,** *3* (12), 17863-17870.
249. Huleatt, P. B.; Khoo, M. L.; Chua, Y. Y.; Tan, T. W.; Liew, R. S.; Balogh, B.; Deme, R.; Gölöncsér, F.; Magyar, K.; Sheela, D. P.; Ho, H. K.; Sperlágh, B.; Mátyus, P.; Chai, C. L. L., Novel Arylalkenylpropargylamines as Neuroprotective, Potent, and Selective Monoamine Oxidase B Inhibitors for the Treatment of Parkinson's Disease. *J. Med. Chem.* **2015,** *58* (3), 1400-1419.
250. Zhu, B.; Shen, T.; Huang, X.; Zhu, Y.; Song, S.; Jiao, N., Selective Aerobic Oxygenation of Tertiary Allylic Alcohols with Molecular Oxygen. *Angew. Chem. Int. Ed.* **2019,** *58* (32), 11028-11032.
251. Wang, Z.-C.; Wang, M.; Gao, J.; Shi, S.-L.; Xu, Y., n BuLi-promoted anti-Markovnikov selective hydroboration of unactivated alkenes and internal alkynes. *Org. Chem. Front.* **2019,** *6* (16), 2949-2953.
252. Hunsen, M., Carboxylic Acids from Primary Alcohols and Aldehydes by a Pyridinium Chlorochromate Catalyzed Oxidation. *Synthesis* **2005,** *2005* (15), 2487-2490.
253. Kuhn, H. J.; Braslavsky, S. E.; Schmidt, R., Chemical actinometry (IUPAC Technical Report). *Pure Appl. Chem.* **2004,** *76* (12), 2105-2146.
254. Demas, J. N.; Bowman, W. D.; Zalewski, E. F.; Velapoldi, R. A., Determination of the quantum yield of the ferrioxalate actinometer with electrically calibrated radiometers. *J. Phys. Chem.* **1981,** *85* (19), 2766-2771.

APPENDIX A – RIGHTS AND PERMISSIONS

APPENDIX A.I: LIST OF PUBLICATIONS AND CONTRIBUTION STATEMENT

Data compiled from Web of Science (Clarivate Analytics) on November 18th, 2024.

1. Chaves-Pouso, A.; Álvarez-Constantino, A. M.; Fañanás-Mastral., M., Enantio- and Diastereoselective Copper-Catalyzed Allylboration of Alkynes with Allylic *gem*-Dichlorides. *Angew. Chem. Int. Ed.* **2022**, *61*, e202117696. (DOI: 10.1002/anie.202117696)

   Impact factor (2022): 16.6

   Journal Ranking (2022): Chemistry, multidisciplinary, Q1 13/178

   Contribution statement: I carried out all computational studies, including DFT calculations for energy profile building, distortion-interaction analysis and non-covalent interaction analysis, processed obtained data, data treatment and drafted the results. Andrea Chaves-Pouso carried out the overall experimental work. All authors contributed with critical feedback and helped to shape the final version of the manuscript.

2. Piñeiro-Suárez, M.; Álvarez-Constantino, A. M.; Fañanás-Mastral, M., Copper-Catalyzed Enantioselective Borylative Allyl–Allyl Coupling of Allenes and Allylic *gem*-Dichlorides. *ACS Catal.* **2023**, *13*, 5578-5583. (DOI: 10.1021/acscatal.3c00536)

   Impact factor (2023): 11.7

   Journal Ranking (2023): Chemistry, physical, Q1 21/178

   Contribution statement: I carried out all computational studies, including DFT calculations for energy profile building, distortion-interaction analysis and non-covalent interaction analysis, processed obtained data, data treatment and drafted the results. Martín Piñeiro-Suárez carried out the overall experimental work. All authors contributed with critical feedback and helped to shape the final version of the manuscript.

3. Álvarez-Constantino, A. M.; Chaves-Pouso, A.; Fañanás-Mastral, M, Enantioselective Allylboration of Acetylene: A Versatile Tool for the Stereodivergent Synthesis of Natural Products. *Angew. Chem. Int. Ed.* **2024**, *63*, e202407813. (DOI: 10.1002/anie.202407813)

   Impact factor (2023): 16.1

   Journal Ranking (2023): Chemistry, multidisciplinary, Q1 14/231

   Contribution statement: I worked as a lead author, in partnership with Andrea Chaves-Pouso (ACP). I contributed with the overall reaction optimization, scope and computational studies (including DFT calculations for energy profile building and non-covalent interaction analysis, processing and treating obtained). Synthesis of chiral ligands, starting materials, natural products and stereodivergent reactions were performed in collaboration with ACP. Writing and editing of the article was performed with the assistance of Prof. Martín Fañanás-Mastral. All authors

contributed with critical feedback and helped to shape the final version of the manuscript.

APPENDIX A.II: PERMISSIONS TO REPRODUCE PAPERS

Permission associated with section 3.1.1:

Chaves-Pouso, A.; Álvarez-Constantino, A. M.; Fañanás-Mastral., M., Enantio- and Diastereoselective Copper-Catalyzed Allylboration of Alkynes with Allylic *gem*-Dichlorides. *Angew. Chem. Int. Ed.* **2022**, *61*, e202117696. (DOI: 10.1002/anie.202117696)

JOHN WILEY AND SONS LICENSE TERMS AND CONDITIONS

Nov 18, 2024

This Agreement between Andrés Manuel Álvarez Constantino ("You") and John Wiley and Sons ("John Wiley and Sons") consists of your license details and the terms and conditions provided by John Wiley and Sons and Copyright Clearance Center.

License Number	5911820216702
License date	Nov 18, 2024
Licensed Content Publisher	John Wiley and Sons
Licensed Content Publication	Angewandte Chemie International Edition
Licensed Content Title	Enantio- and Diastereoselective Copper-Catalyzed Allylboration of Alkynes with Allylic gem-Dichlorides
Licensed Content Author	Martín Fañanás-Mastral, Andrés M. Álvarez-Constantino, Andrea Chaves-Pouso
Licensed Content Date	Mar 21, 2022
Licensed Content Volume	61
Licensed Content Issue	23
Licensed Content Pages	7
Type of Use	Dissertation/Thesis
Requestor type	Author of this Wiley article
Format	Print and electronic
Portion	Text extract
Number of Pages	2
Will you be translating?	No
Title of new work	Catalytic methodologies for the valorization of C2 hydrocarbons and mechanistic studies
Institution name	Universidade de Santiago de Compostela
Expected presentation date	Feb 2025
Portions	Last paragraph page 4 and page 5
The Requesting Person / Organization to Appear on the License	Andrés Manuel Álvarez Constantino
Requestor Location	Mr. Andrés Manuel Álvarez Constantino Rua Jenaro de la Fuente, s/n, CiQUS Santiago De Compostela, Galicia / A Coruña 15705 Spain
Publisher Tax ID	EU826007151
Total	**0.00 EUR**
Terms and Conditions	

JOHN WILEY AND SONS LICENSE TERMS AND CONDITIONS

Nov 18, 2024

This Agreement between Andrés Manuel Álvarez Constantino ("You") and John Wiley and Sons ("John Wiley and Sons") consists of your license details and the terms and conditions provided by John Wiley and Sons and Copyright Clearance Center.

License Number	5911820409596
License date	Nov 18, 2024
Licensed Content Publisher	John Wiley and Sons
Licensed Content Publication	Angewandte Chemie International Edition
Licensed Content Title	Enantio- and Diastereoselective Copper-Catalyzed Allylboration of Alkynes with Allylic gem-Dichlorides
Licensed Content Author	Martín Fañanás-Mastral, Andrés M. Álvarez-Constantino, Andrea Chaves-Pouso
Licensed Content Date	Mar 21, 2022
Licensed Content Volume	61
Licensed Content Issue	23
Licensed Content Pages	7
Type of Use	Dissertation/Thesis
Requestor type	Author of this Wiley article
Format	Print and electronic
Portion	Figure/table
Number of figures/tables	2
Will you be translating?	No
Title of new work	Catalytic methodologies for the valorization of C2 hydrocarbons and mechanistic studies
Institution name	Universidade de Santiago de Compostela
Expected presentation date	Feb 2025
Portions	Figure 1, Figure 2
The Requesting Person / Organization to Appear on the License	Andrés Manuel Álvarez Constantino
Requestor Location	Mr. Andrés Manuel Álvarez Constantino Rua Jenaro de la Fuente, s/n, CiQUS Santiago De Compostela, Galicia / A Coruña 15705 Spain
Publisher Tax ID	EU826007151
Total	**0.00 EUR**
Terms and Conditions	

Permission associated with section 3.1.2:

Piñeiro-Suárez, M.; Álvarez-Constantino, A. M.; Fañanás-Mastral, M., Copper-Catalyzed Enantioselective Borylative Allyl–Allyl Coupling of Allenes and Allylic *gem*-Dichlorides. *ACS Catal.* **2023**, *13*, 5578-5583. (DOI: 10.1021/acscatal.3c00536)

Permission associated with section 3.2:

Álvarez-Constantino, A. M.; Chaves-Pouso, A.; Fañanás-Mastral, M, Enantioselective Allylboration of Acetylene: A Versatile Tool for the Stereodivergent Synthesis of Natural Products. *Angew. Chem. Int. Ed.* **2024**, *63*, e202407813. (DOI: 10.1002/anie.202407813)

JOHN WILEY AND SONS LICENSE TERMS AND CONDITIONS

Nov 18, 2024

This Agreement between Andrés Manuel Álvarez Constantino ("You") and John Wiley and Sons ("John Wiley and Sons") consists of your license details and the terms and conditions provided by John Wiley and Sons and Copyright Clearance Center.

License Number	5911821177235
License date	Nov 18, 2024
Licensed Content Publisher	John Wiley and Sons
Licensed Content Publication	Angewandte Chemie International Edition
Licensed Content Title	Enantioselective Allylboration of Acetylene: A Versatile Tool for the Stereodivergent Synthesis of Natural Products
Licensed Content Author	Martín Fañanás-Mastral, Andrea Chaves-Pouso, Andrés M. Álvarez-Constantino
Licensed Content Date	Jul 24, 2024
Licensed Content Volume	63
Licensed Content Issue	34
Licensed Content Pages	9
Type of Use	Dissertation/Thesis
Requestor type	Author of this Wiley article
Format	Print and electronic
Portion	Full article
Will you be translating?	No
Title of new work	Catalytic methodologies for the valorization of C2 hydrocarbons and mechanistic studies
Institution name	Universidade de Santiago de Compostela
Expected presentation date	Feb 2025
The Requesting Person / Organization to Appear on the License	Andrés Manuel Álvarez Constantino
Requestor Location	Mr. Andrés Manuel Álvarez Constantino Rua Jenaro de la Fuente, s/n, CiQUS Santiago De Compostela, Galicia / A Coruña 15705 Spain
Publisher Tax ID	EU826007151
Total	**0.00 EUR**
Terms and Conditions	

APPENDIX A.III: PERMISSIONS TO PUBLISH IMAGES, TABLE AND FIGURES

Permission associated to Figure 1.1.9:

Hong, S.; Zhang, X., DFT Studies on Ligand Controlled Highly Selective Copper-Catalyzed Borylations of Allenes. *Asian J. Org. Chem.* **2023,** *12* (5), e202200689.

JOHN WILEY AND SONS LICENSE TERMS AND CONDITIONS

Nov 17, 2024

This Agreement between Andrés Manuel Álvarez Constantino ("You") and John Wiley and Sons ("John Wiley and Sons") consists of your license details and the terms and conditions provided by John Wiley and Sons and Copyright Clearance Center.

License Number	5910841084242
License date	Nov 16, 2024
Licensed Content Publisher	John Wiley and Sons
Licensed Content Publication	Asian Journal of Organic Chemistry
Licensed Content Title	DFT Studies on Ligand Controlled Highly Selective Copper-Catalyzed Borylations of Allenes
Licensed Content Author	Xue Zhang, Shichao Hong
Licensed Content Date	Mar 15, 2023
Licensed Content Volume	12
Licensed Content Issue	5
Licensed Content Pages	5
Type of Use	Dissertation/Thesis
Requestor type	University/Academic
Format	Print and electronic
Portion	Figure/table
Number of figures/tables	2
Will you be translating?	No
Title of new work	Catalytic methodologies for the valorization of C2 hydrocarbons and mechanistic studies
Institution name	Universidade de Santiago de Compostela
Expected presentation date	Feb 2025
Portions	Figure 2b, Figure 6b
The Requesting Person / Organization to Appear on the License	Andrés Manuel Álvarez Constantino
Requestor Location	Mr. Andrés Manuel Álvarez Constantino Rua Jenaro de la Fuente, s/n, CiQUS Santiago De Compostela, Galicia / A Coruña 15705 Spain
Publisher Tax ID	EU826007151
Total	**0.00 EUR**
Terms and Conditions	

Permission associated to Figure 1.1.16c:

Manna, M. S.; Yoo, S. Y.; Sharique, M.; Choi, H.; Pudasaini, B.; Baik, M.-H.; Tambar, U. K., Copper-Catalyzed Regiodivergent Internal Allylic Alkylations. *Angew. Chem. Int. Ed.* **2023,** *62* (35), e202304848.

JOHN WILEY AND SONS LICENSE TERMS AND CONDITIONS

Nov 18, 2024

This Agreement between Andrés Manuel Álvarez Constantino ("You") and John Wiley and Sons ("John Wiley and Sons") consists of your license details and the terms and conditions provided by John Wiley and Sons and Copyright Clearance Center.

License Number	5911831196666
License date	Nov 18, 2024
Licensed Content Publisher	John Wiley and Sons
Licensed Content Publication	Angewandte Chemie International Edition
Licensed Content Title	Copper-Catalyzed Regiodivergent Internal Allylic Alkylations
Licensed Content Author	Seok Yeol Yoo, Mohammed Sharique, Hyoju Choi, et al
Licensed Content Date	Jul 17, 2023
Licensed Content Volume	62
Licensed Content Issue	35
Licensed Content Pages	9
Type of Use	Dissertation/Thesis
Requestor type	University/Academic
Format	Print and electronic
Portion	Figure/table
Number of figures/tables	1
Will you be translating?	No
Title of new work	Catalytic methodologies for the valorization of C2 hydrocarbons and mechanistic studies
Institution name	Universidade de Santiago de Compostela
Expected presentation date	Feb 2025
Portions	Figure 4
The Requesting Person / Organization to Appear on the License	Andrés Manuel Álvarez Constantino
Requestor Location	Mr. Andrés Manuel Álvarez Constantino Rua Jenaro de la Fuente, s/n, CiQUS Santiago De Compostela, Galicia / A Coruña 15705 Spain
Publisher Tax ID	EU826007151
Total	**0.00 EUR**
Terms and Conditions	

Permission associated to Figure 1.1.16c:

Vázquez-Galiñanes, N.; Sciortino, G.; Piñeiro-Suárez, M.; Tóth, B. L.; Maseras, F.; Fañanás-Mastral, M., Switching Selectivity in Borylative Allyl–Allyl Cross-Coupling through Synergistic Catalysis. *J. Am. Chem. Soc.* **2024**.

Permission associated to Figure 1.3.13c:

Dai, Z.-Y.; Zhang, S.-Q.; Hong, X.; Wang, P.-S.; Gong, L.-Z., A practical $FeCl_3$/HCl photocatalyst for versatile aliphatic C–H functionalization. *Chem Catal.* **2022,** *2* (5), 1211-1222.

ELSEVIER LICENSE TERMS AND CONDITIONS

Nov 17, 2024

This Agreement between Andrés Manuel Álvarez Constantino ("You") and Elsevier ("Elsevier") consists of your license details and the terms and conditions provided by Elsevier and Copyright Clearance Center.

License Number	5910750041588
License date	Nov 16, 2024
Licensed Content Publisher	Elsevier
Licensed Content Publication	Chem Catalysis
Licensed Content Title	A practical FeCl3/HCl photocatalyst for versatile aliphatic C–H functionalization
Licensed Content Author	Zhen-Yao Dai,Shuo-Qing Zhang,Xin Hong,Pu-Sheng Wang,Liu-Zhu Gong
Licensed Content Date	May 19, 2022
Licensed Content Volume	2
Licensed Content Issue	5
Licensed Content Pages	12
Start Page	1211
End Page	1222
Type of Use	reuse in a thesis/dissertation
Portion	figures/tables/illustrations
Number of figures/tables/illustrations	1
Format	both print and electronic
Are you the author of this Elsevier article?	No
Will you be translating?	No
Title of new work	Catalytic methodologies for the valorization of C2 hydrocarbons and mechanistic studies
Institution name	Universidade de Santiago de Compostela
Expected presentation date	Feb 2025
Portions	Figure 6B
The Requesting Person / Organization to Appear on the License	Andrés Manuel Álvarez Constantino
Requestor Location	Mr. Andrés Manuel Álvarez Constantino Rua Jenaro de la Fuente, s/n, CiQUS Santiago De Compostela, Galicia / A Coruña 15705 Spain
Publisher Tax ID	GB 494 6272 12
Total	**0.00 EUR**
Terms and Conditions	

APPENDIX B – OPTIMIZED GEOMETRIES OF DFT CALCULATIONS

APPENDIX B.I: STRUCTURES RELATED TO SECTION 3.1.1

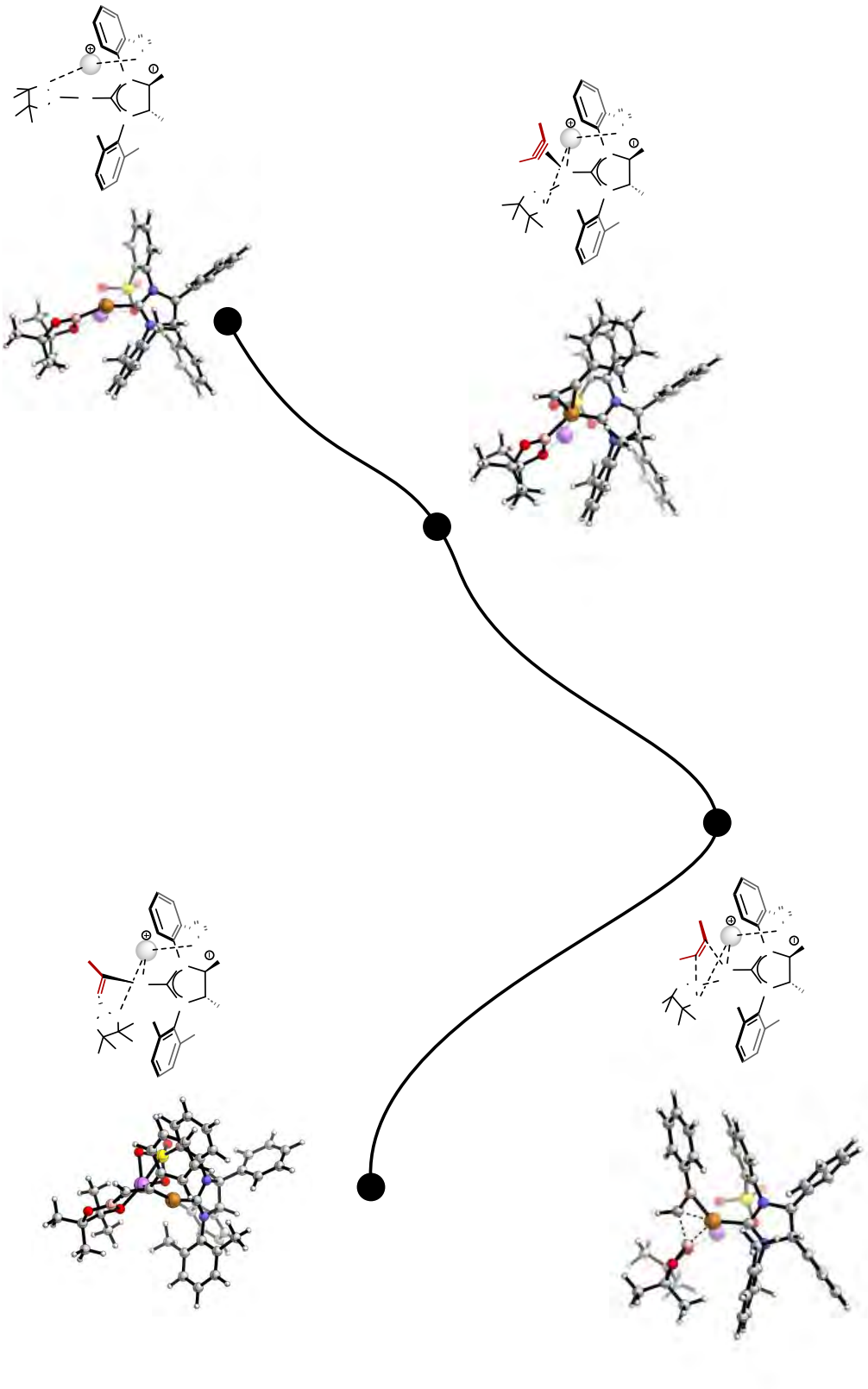

Figure B.I.1. Computed structures related to the alkyne coordination and insertion with Li as metal cation.

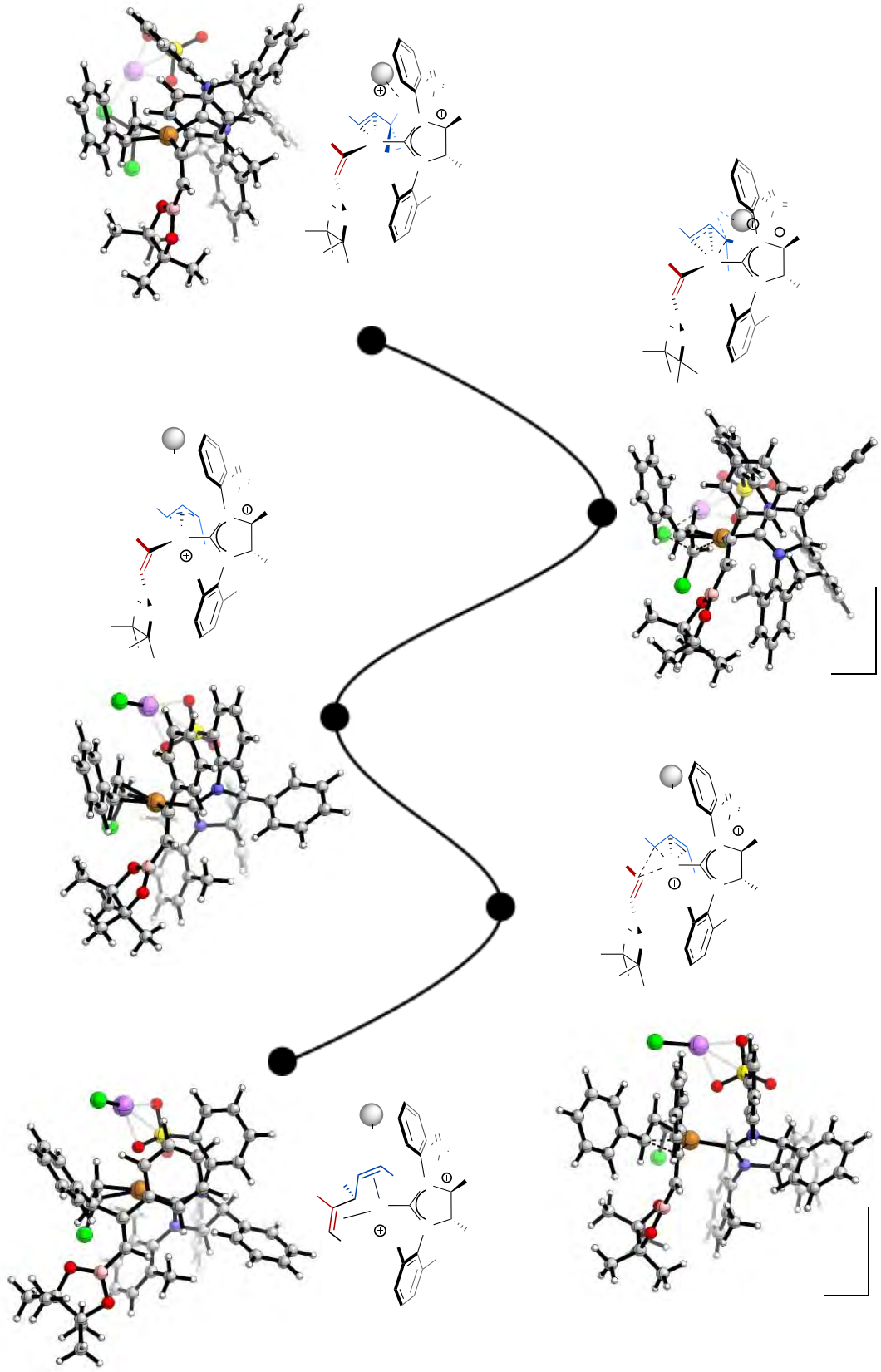

Figure B.I.2. Computed structures related to the oxidative addition and reductive elimination steps associated with the formation of **(*R*)-3-*E*,*Z*** (black pathway of Figure 3.1.2) with Li as metal cation.

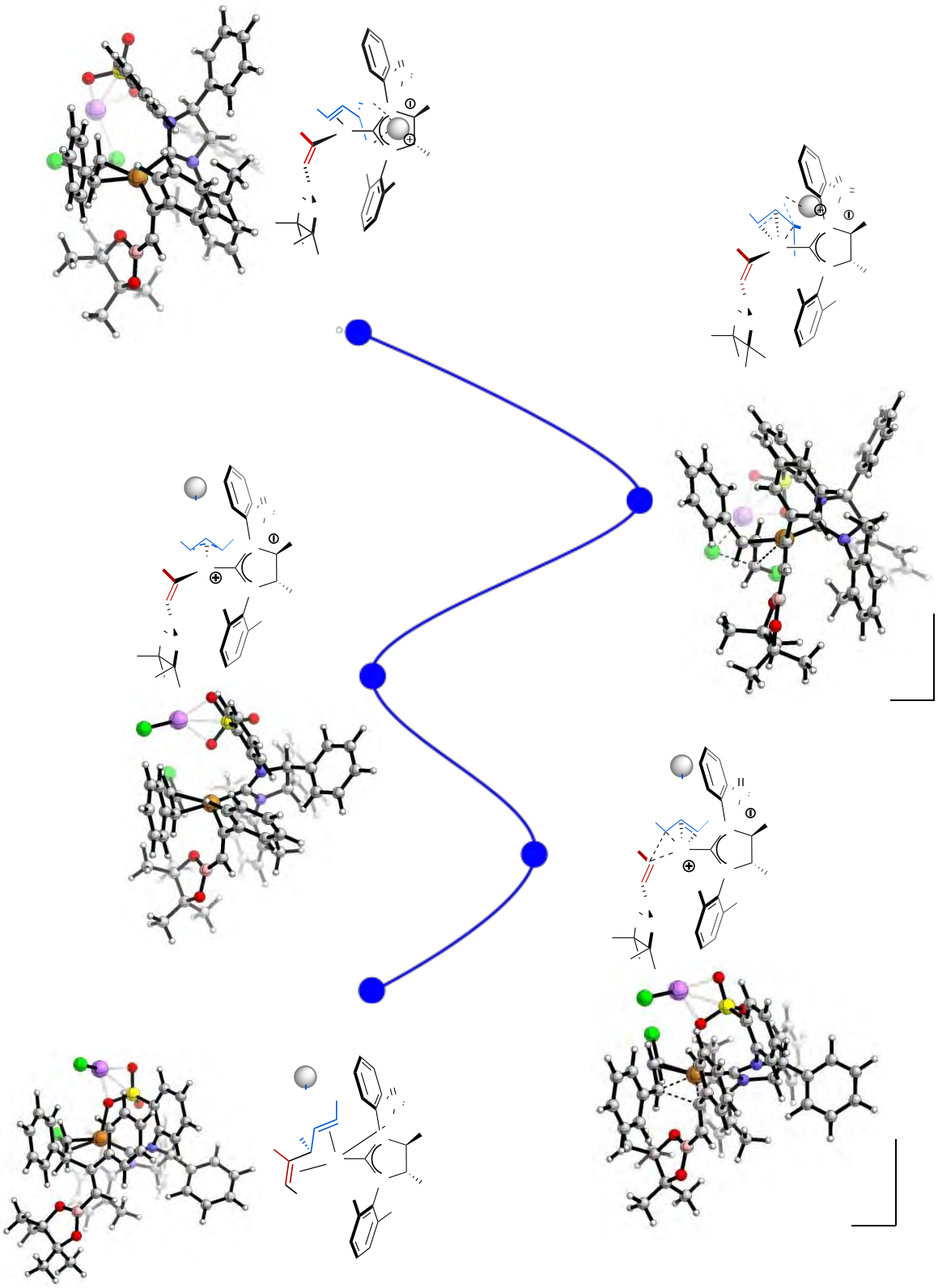

Figure B.I.3. Computed structures related to the oxidative addition and reductive elimination steps associated with the formation of ***(R)*-3-*E*,*E*** (blue pathway of Figure 3.1.2) with Li as metal cation.

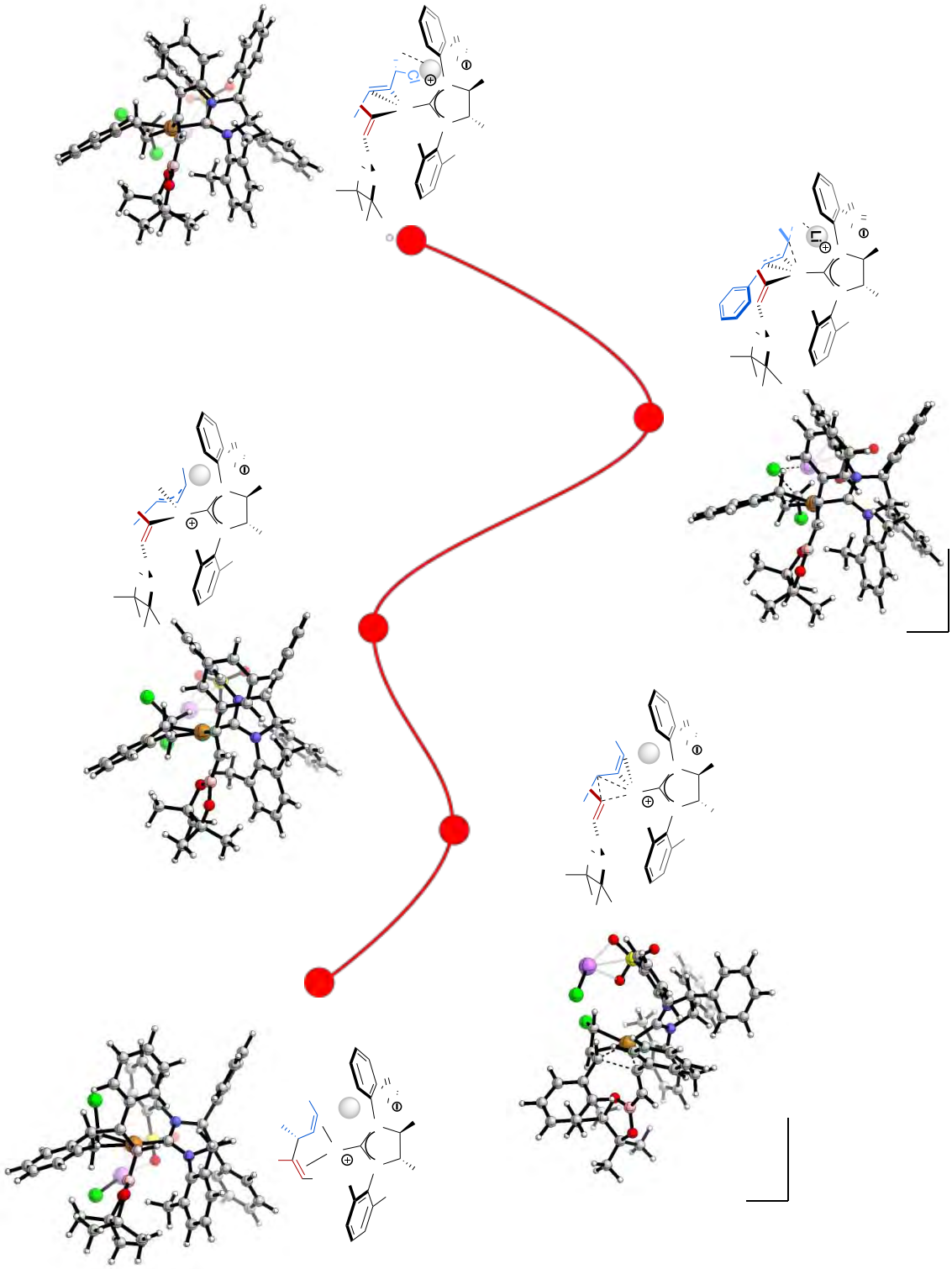

Figure B.I.4. Computed structures related to the oxidative addition and reductive elimination steps associated with the formation of **(*S*)-3-*E*,*Z*** (red pathway of Figure 3.1.2) with Li as metal cation.

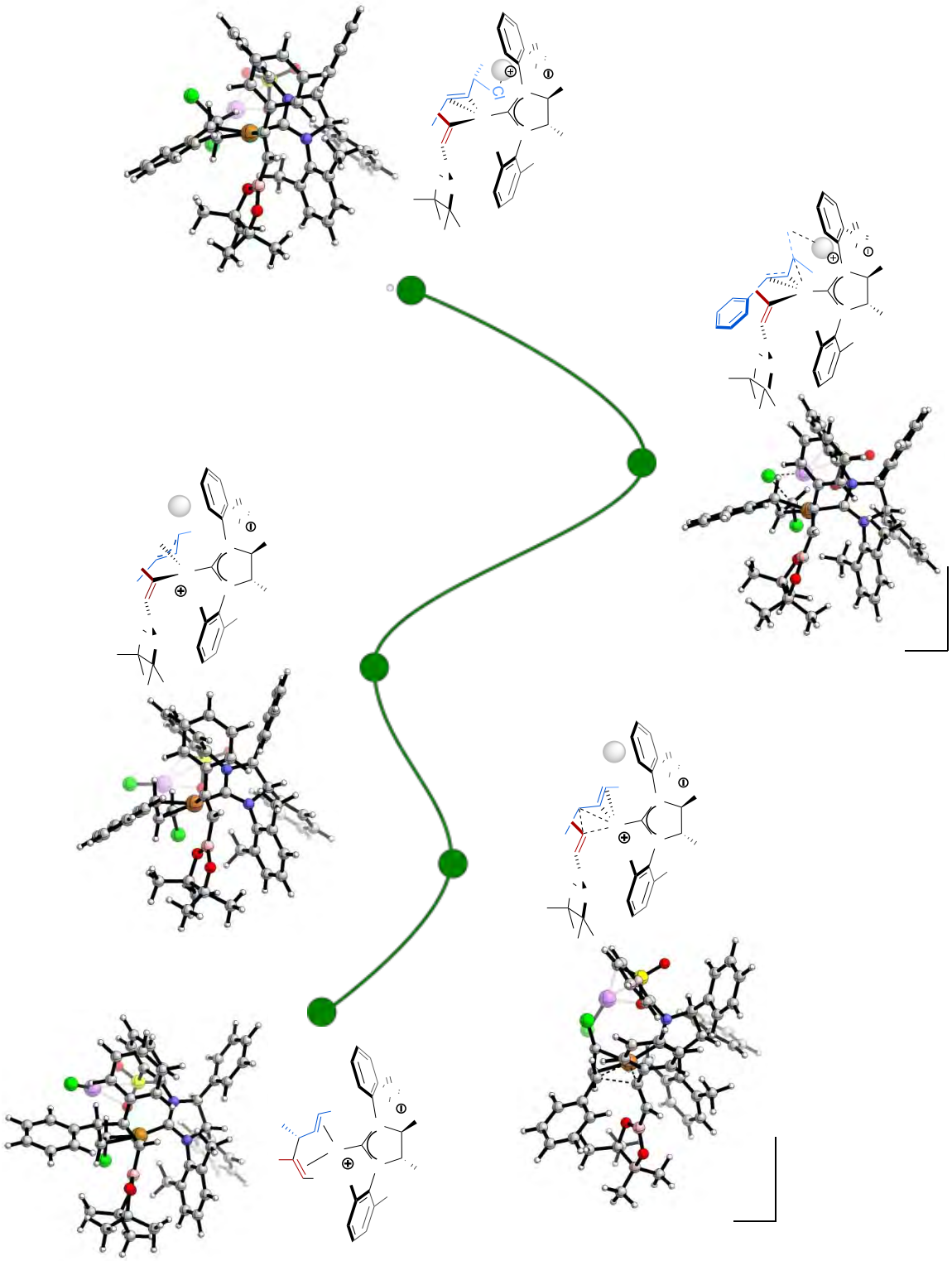

Figure B.I.5. Computed structures related to the oxidative addition and reductive elimination steps associated with the formation of ***(S)*-3-*E*,*E*** (green pathway of Figure 3.1.2) with Li as metal cation.

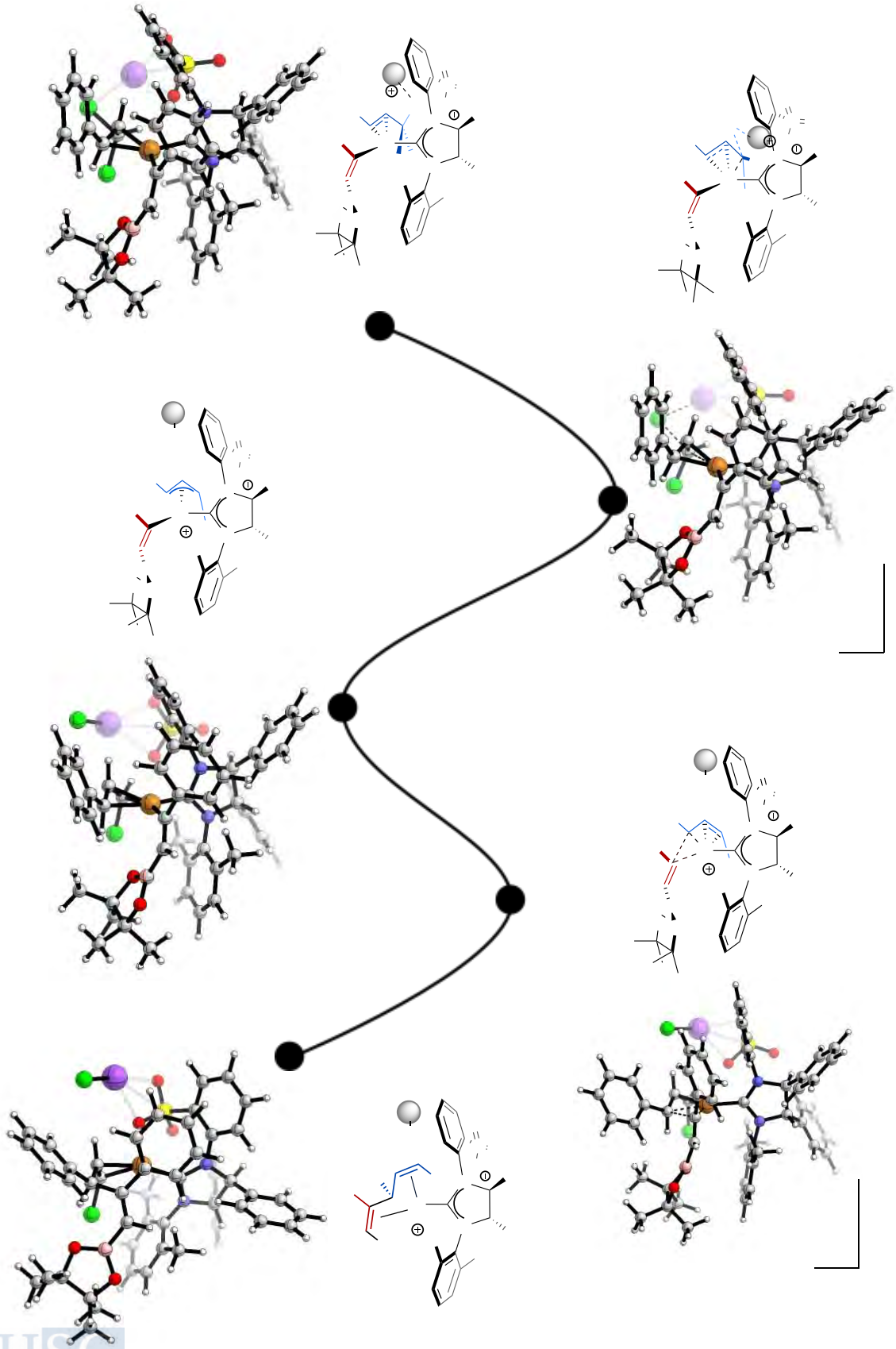

Figure B.I.6. Computed structures related to the oxidative addition and reductive elimination steps associated with the formation of ***(R)*-3-*E*,*Z*** (black pathway of Figure 3.1.4) with Na as metal cation.

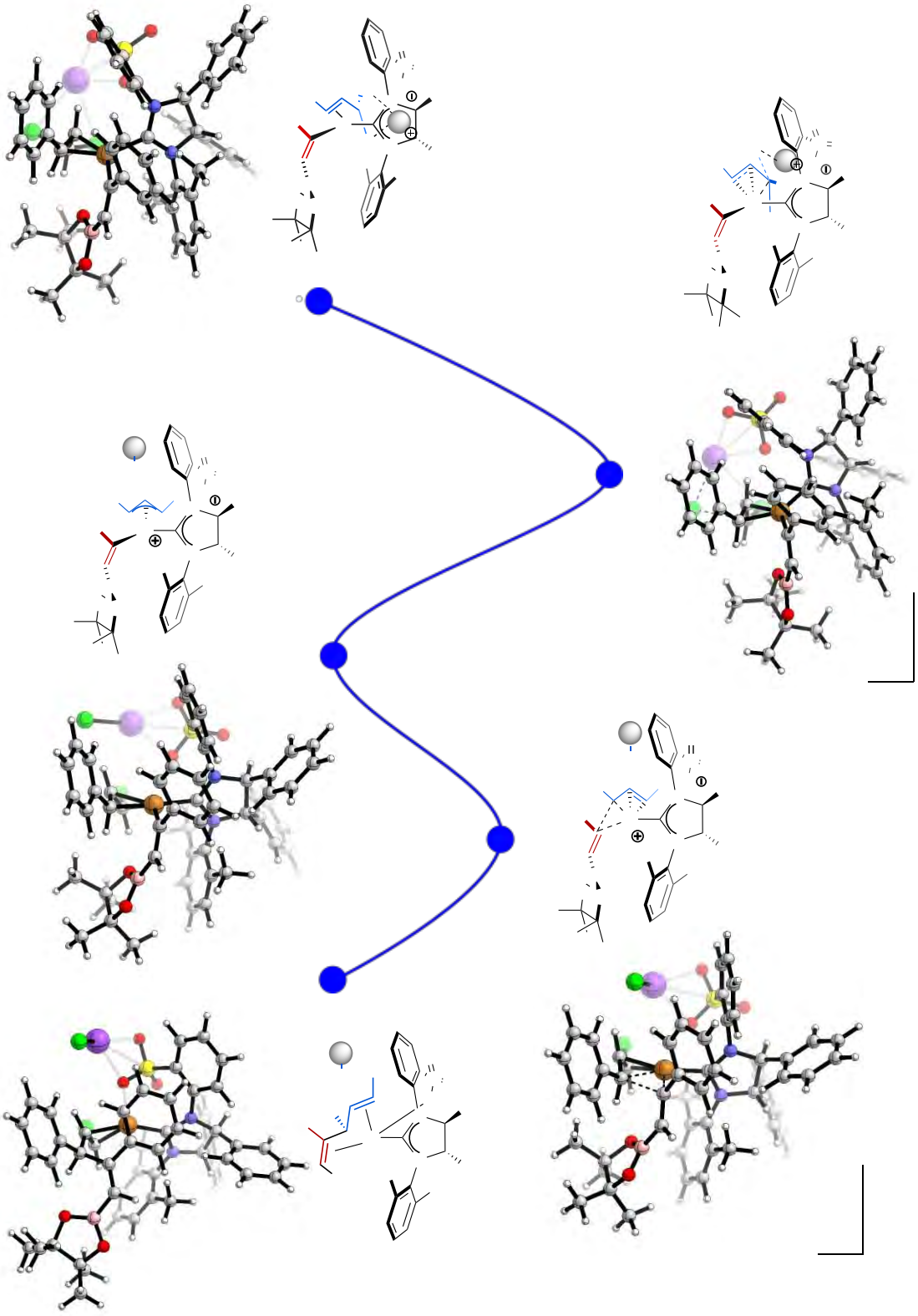

Figure B.I.7. Computed structures related to the oxidative addition and reductive elimination steps associated with the formation of ***(R)*-3-*E*,*E*** (blue pathway of Figure 3.1.4) with Na as metal cation.

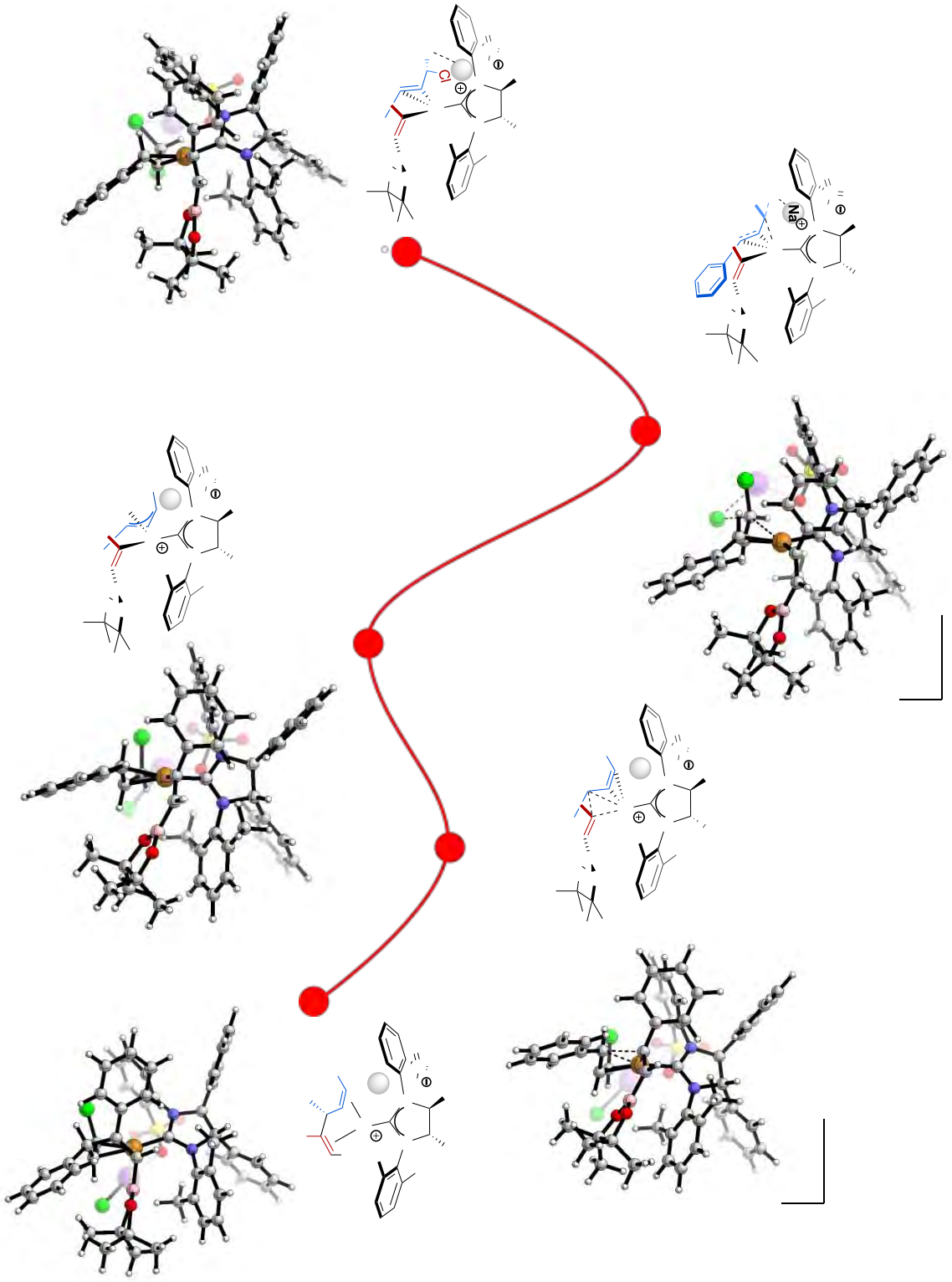

Figure B.I.8. Computed structures related to the oxidative addition and reductive elimination steps associated with the formation of **(*S*)-3-*E*,*Z*** (red pathway of Figure 3.1.4) with Na as metal cation.

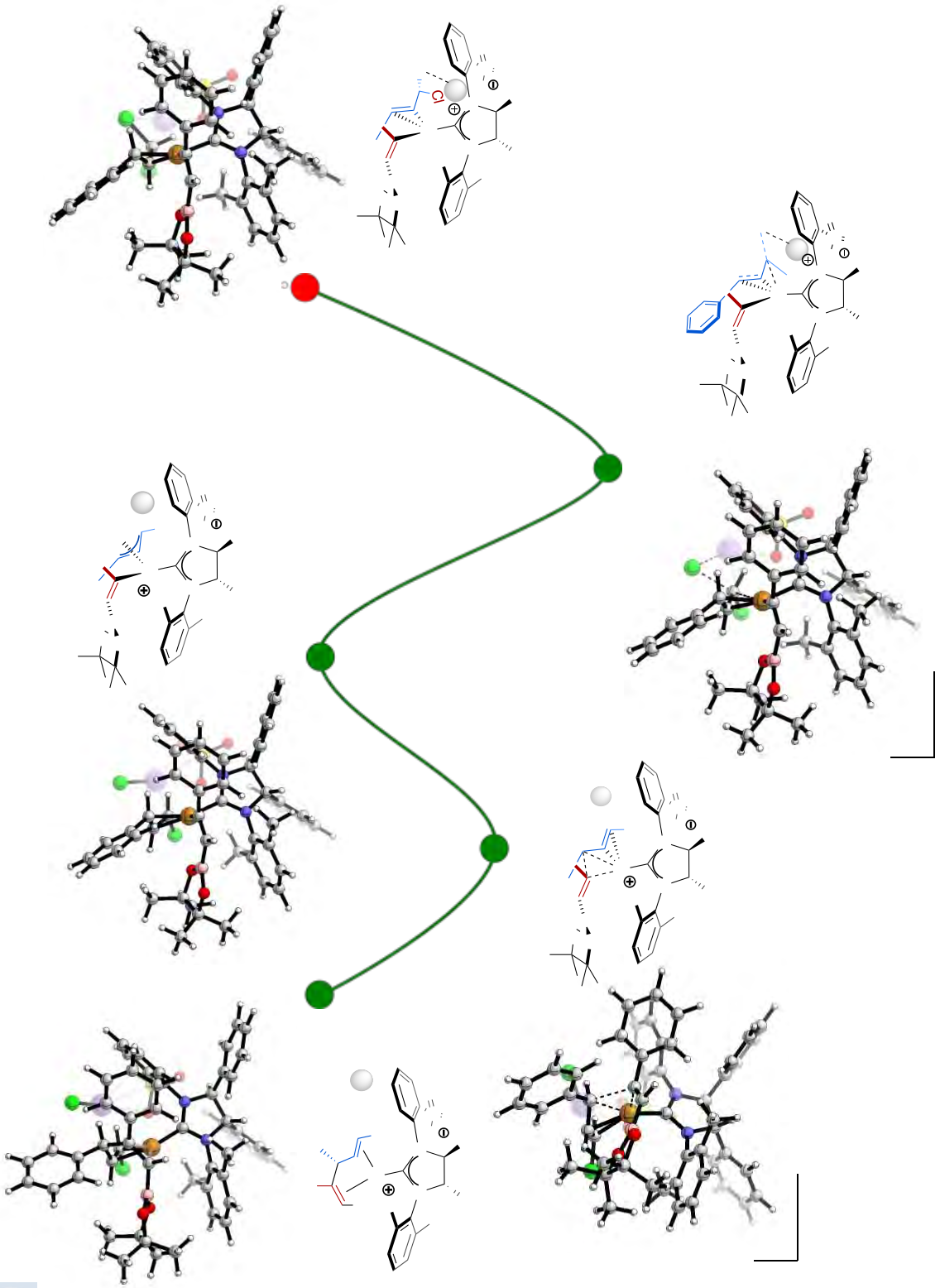

Figure B.I.9. Computed structures related to the oxidative addition and reductive elimination steps associated with the formation of **(*S*)-3-*E*,*E*** (green pathway of Figure 3.1.4) with Na as metal cation.

APPENDIX B.II: STRUCTURES RELATED TO SECTION 3.1.2

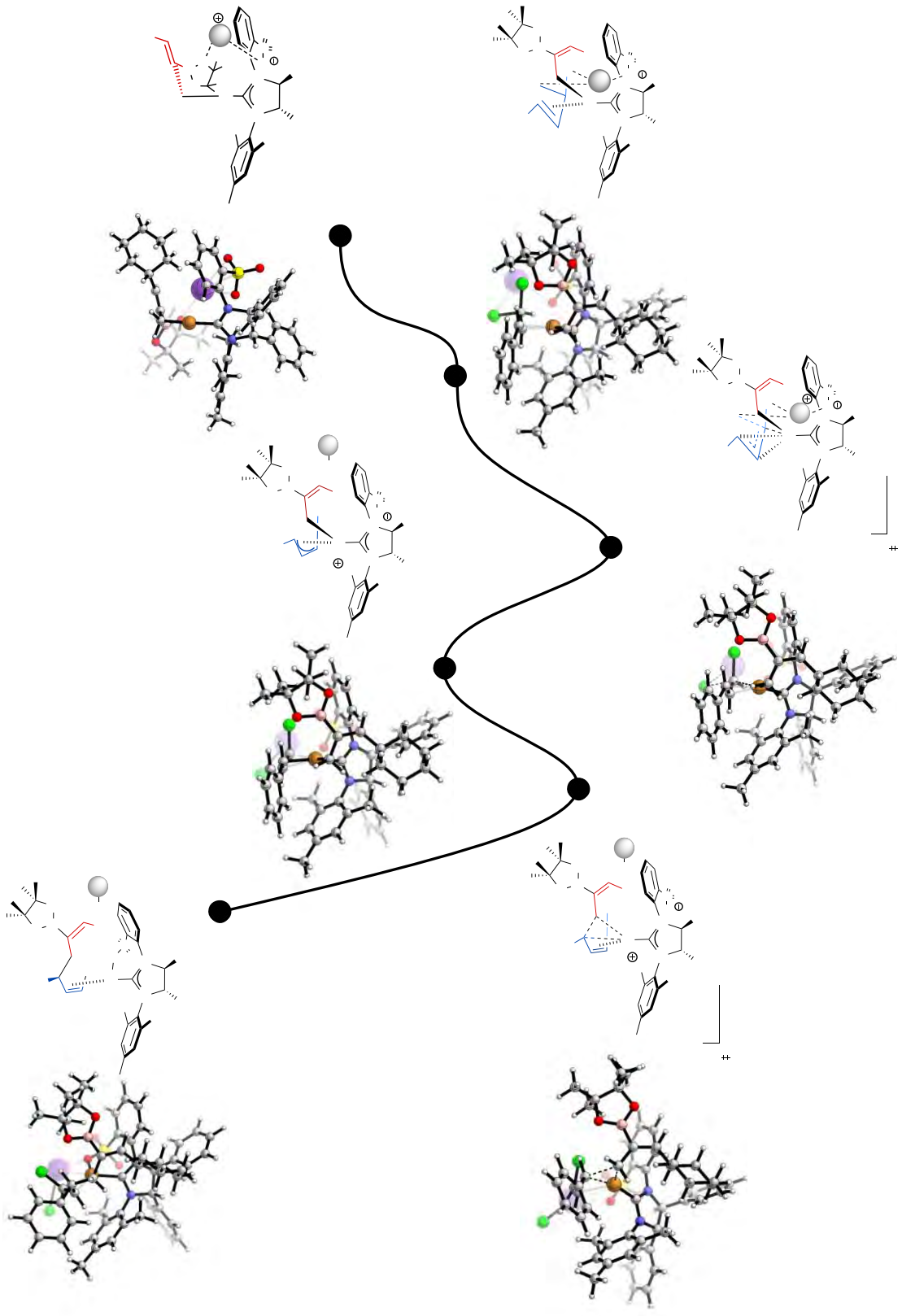

Figure B.II.1. Computed structures related to the oxidative addition and reductive elimination steps associated with the formation of ***(S)*-5-*Z*,*Z*** from **VIIa** with K as metal cation (black pathway of Figure 3.1.10).

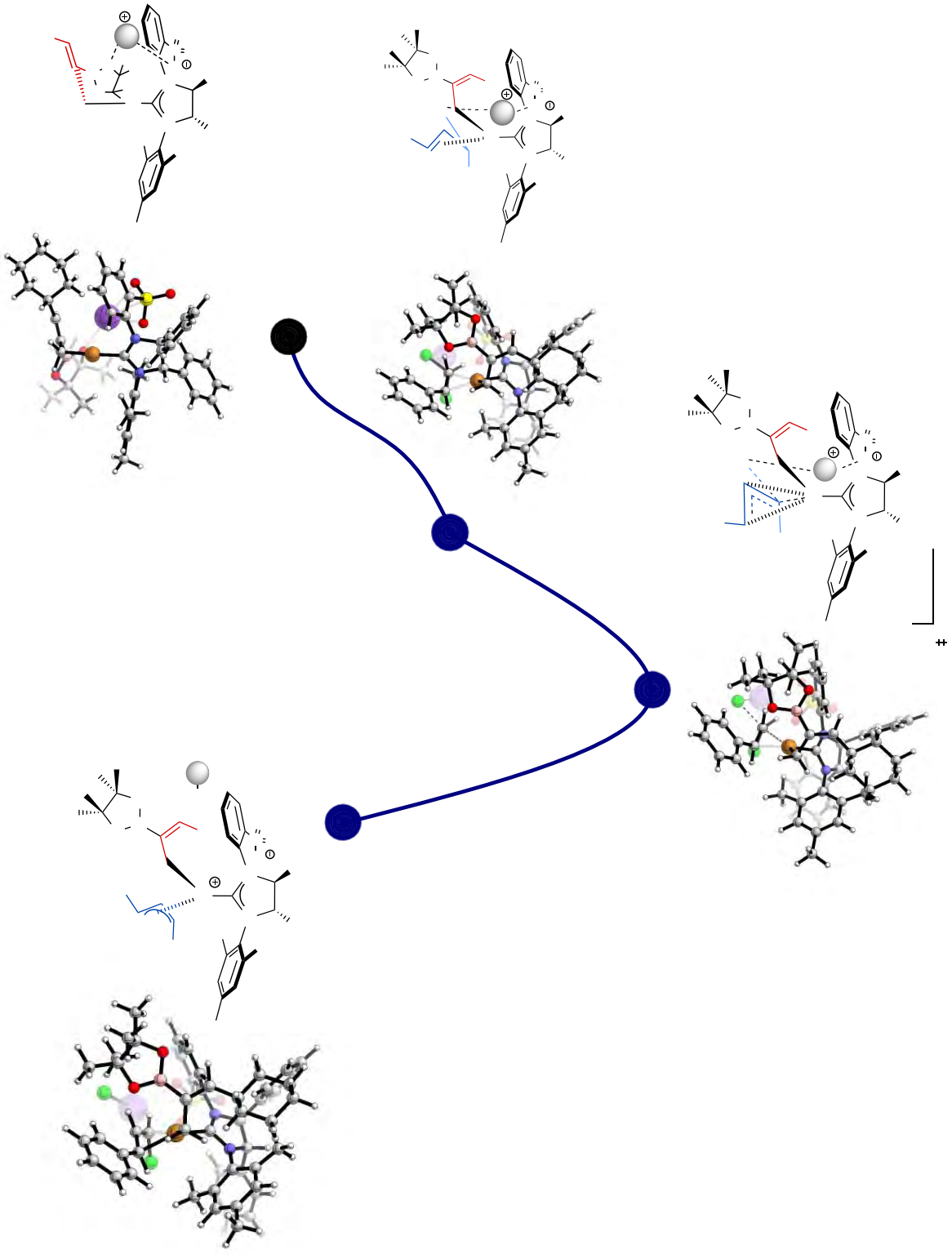

Figure B.II.2. Computed structures related to the oxidative addition step associated with the formation of **(*R*)-5-*Z*,*Z*** from **VIIa** with K as metal cation (blue pathway of Figure 3.1.10).

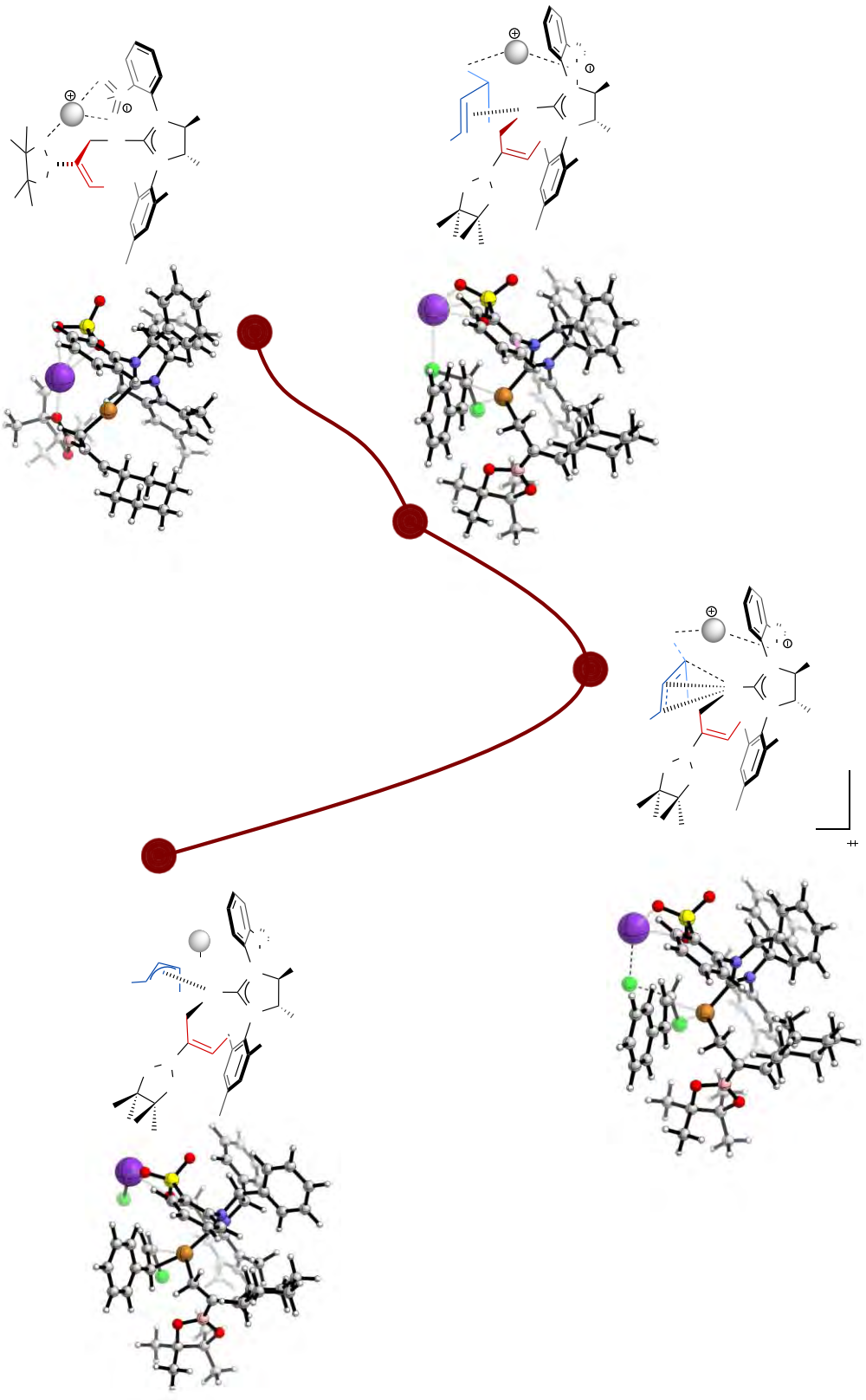

Figure B.II.3. Computed structures related to the oxidative addition step associated with the formation of ***(R)*-5-*Z*,*Z*** from **VIIb** with K as metal cation (dark red pathway of Figure 3.1.10).

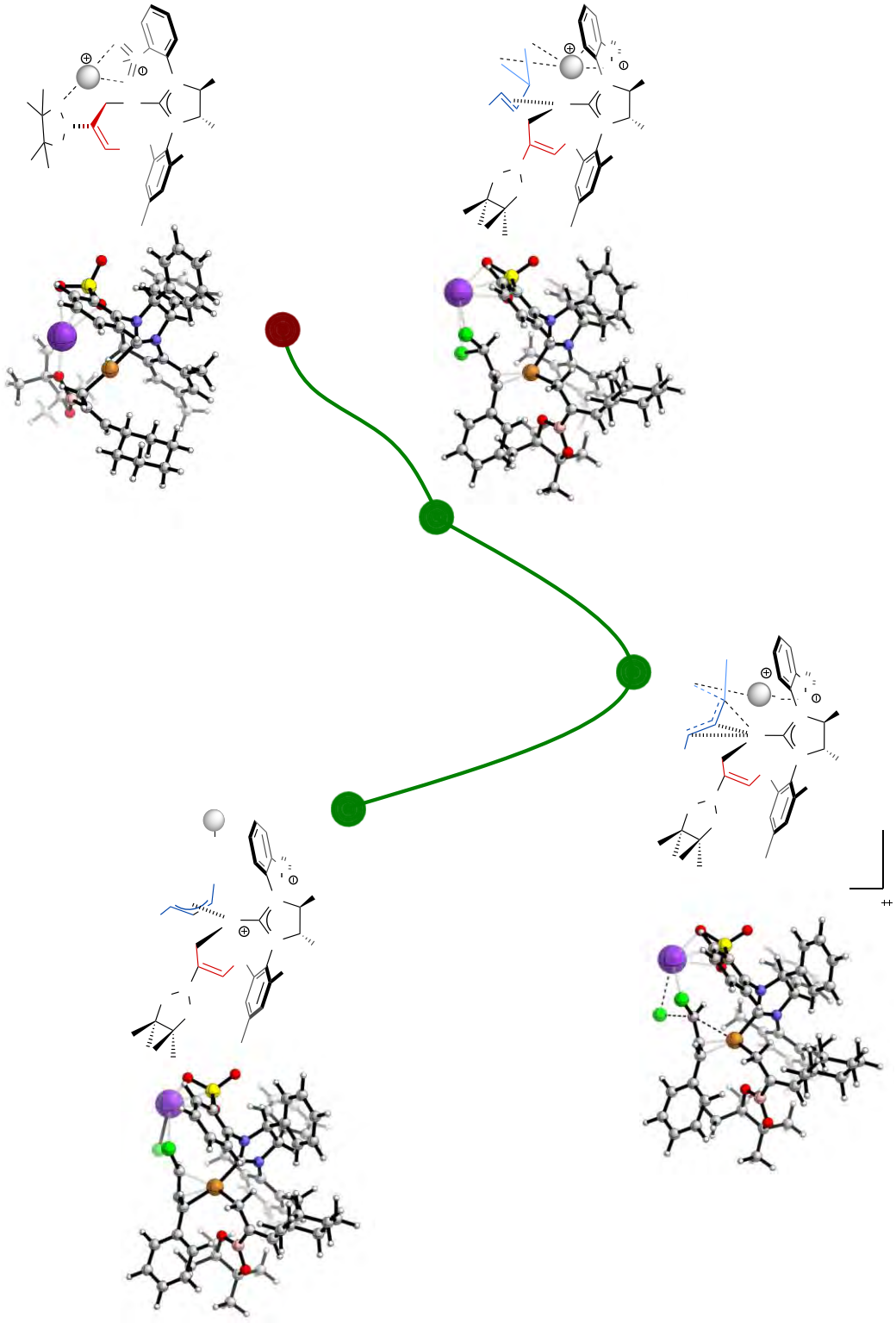

Figure B.II.4. Computed structures related to the oxidative addition step associated with the formation of **(*S*)-5-*Z*,*Z*** from **VIIb** with K as metal cation (green pathway of Figure 3.1.10).

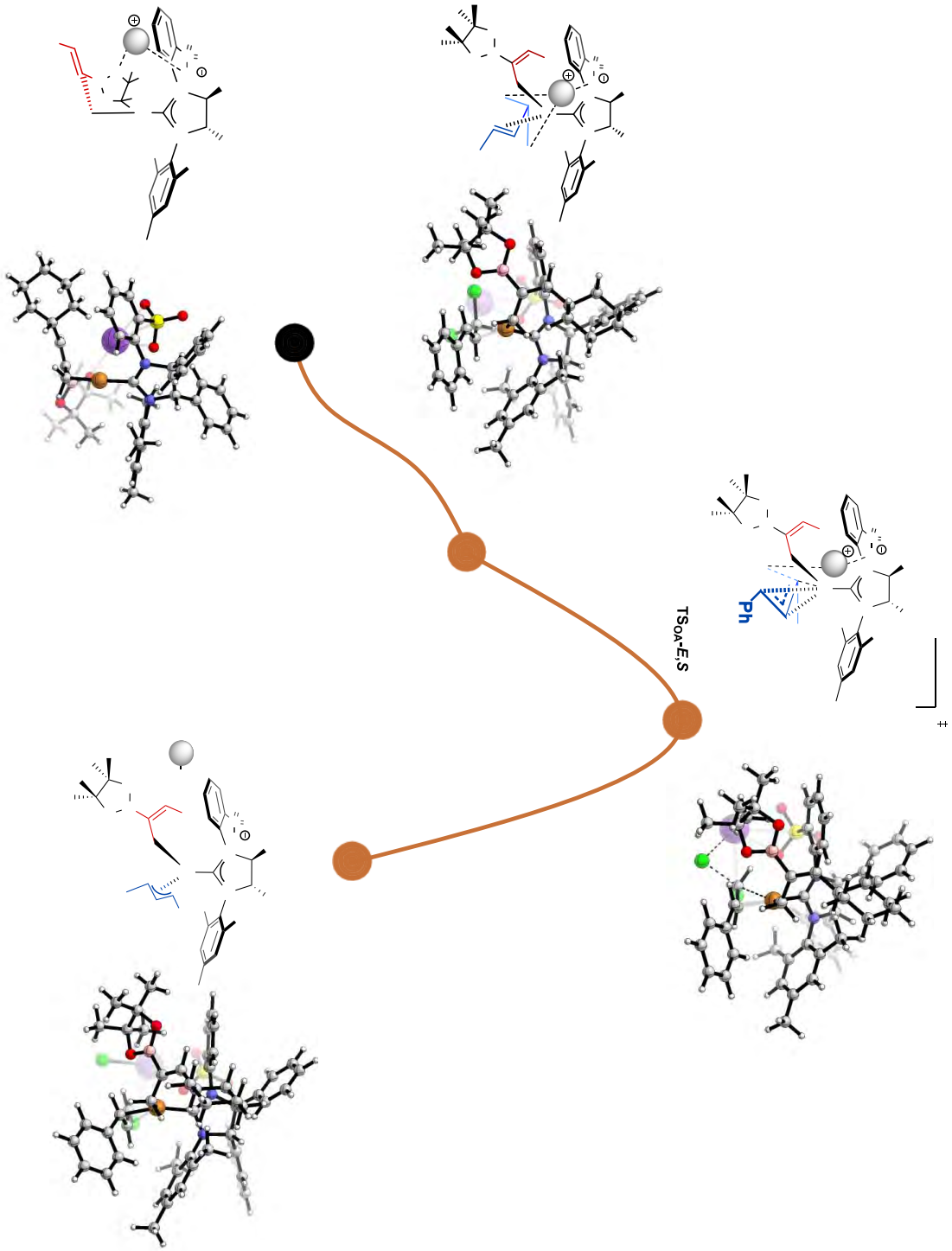

Figure B.II.5. Computed structures related to the oxidative addition step associated with the formation of ***(R)*-5-*Z*,*E*** from **VIIa** with K as metal cation (orange pathway of Figure 3.1.12).

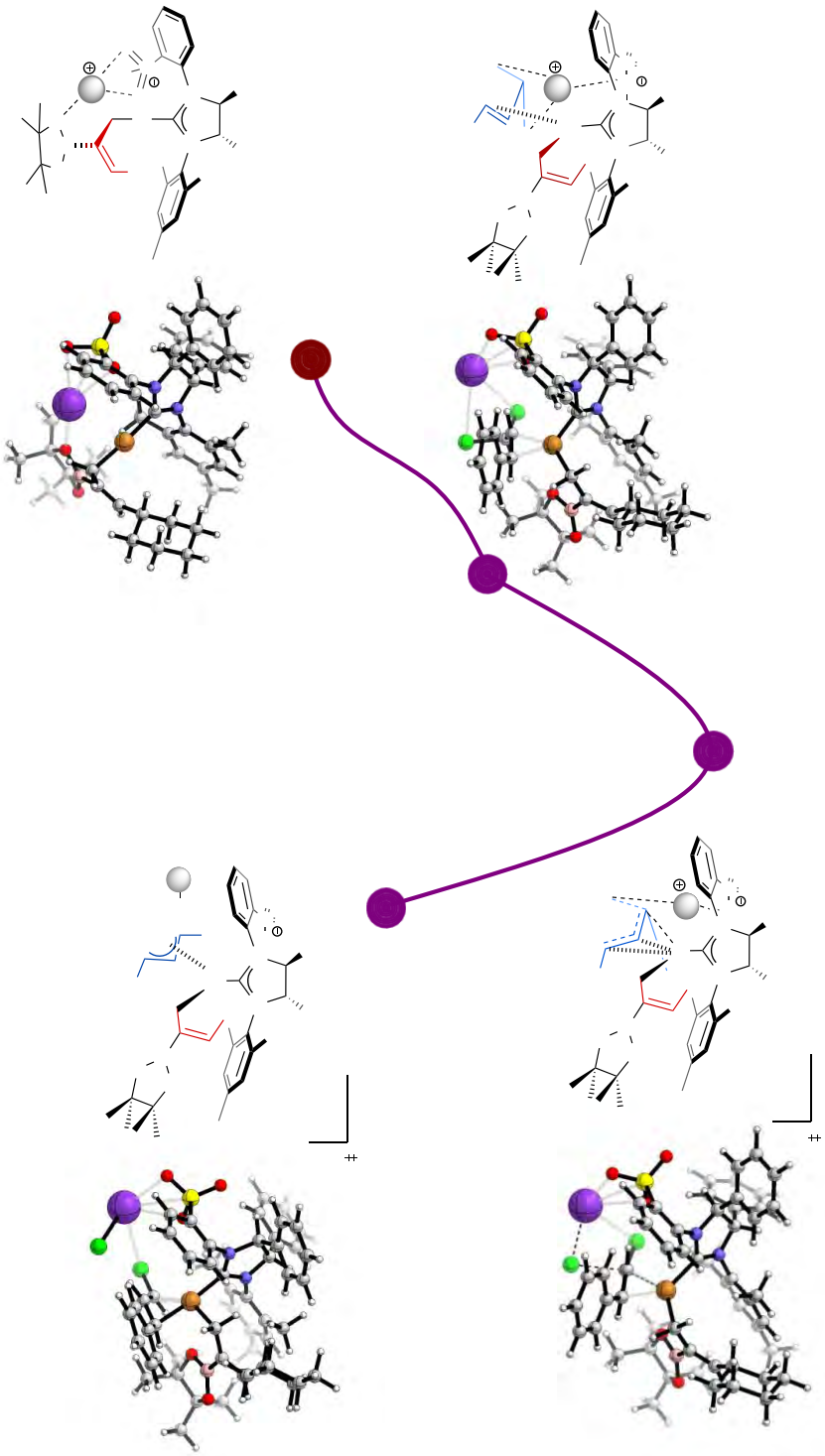

Figure B.II.6. Computed structures related to the oxidative addition step associated with the formation of **(*R*)-5-*Z*,*E*** from **VIIb** with K as metal cation (purple pathway of Figure 3.1.12).

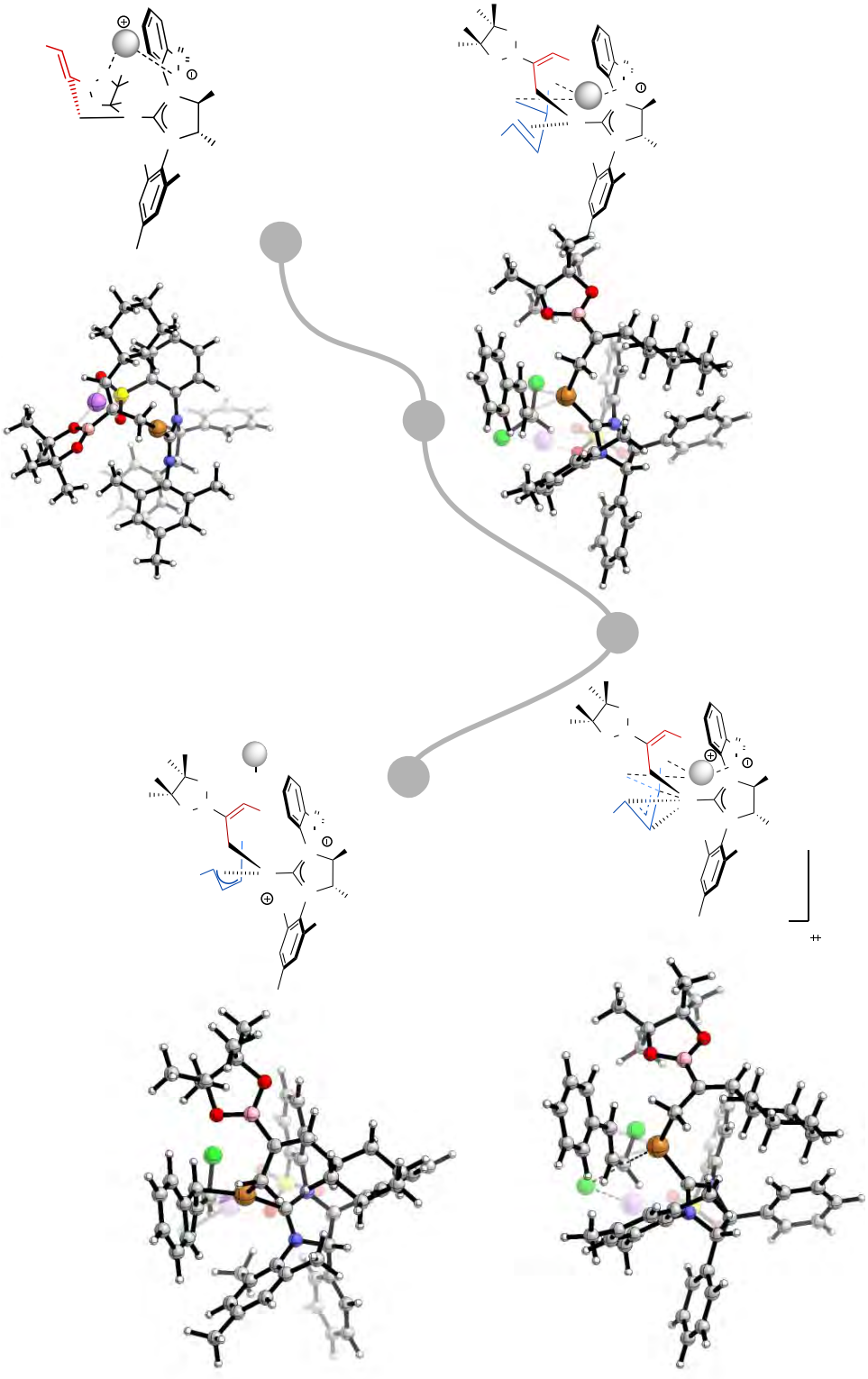

Figure B.II.7. Computed structures related to the oxidative addition step associated with the formation of ***(S)*-5-*Z*,*Z*** from **VIIa-Li** with Li as metal cation (grey pathway of Figure 3.1.14).

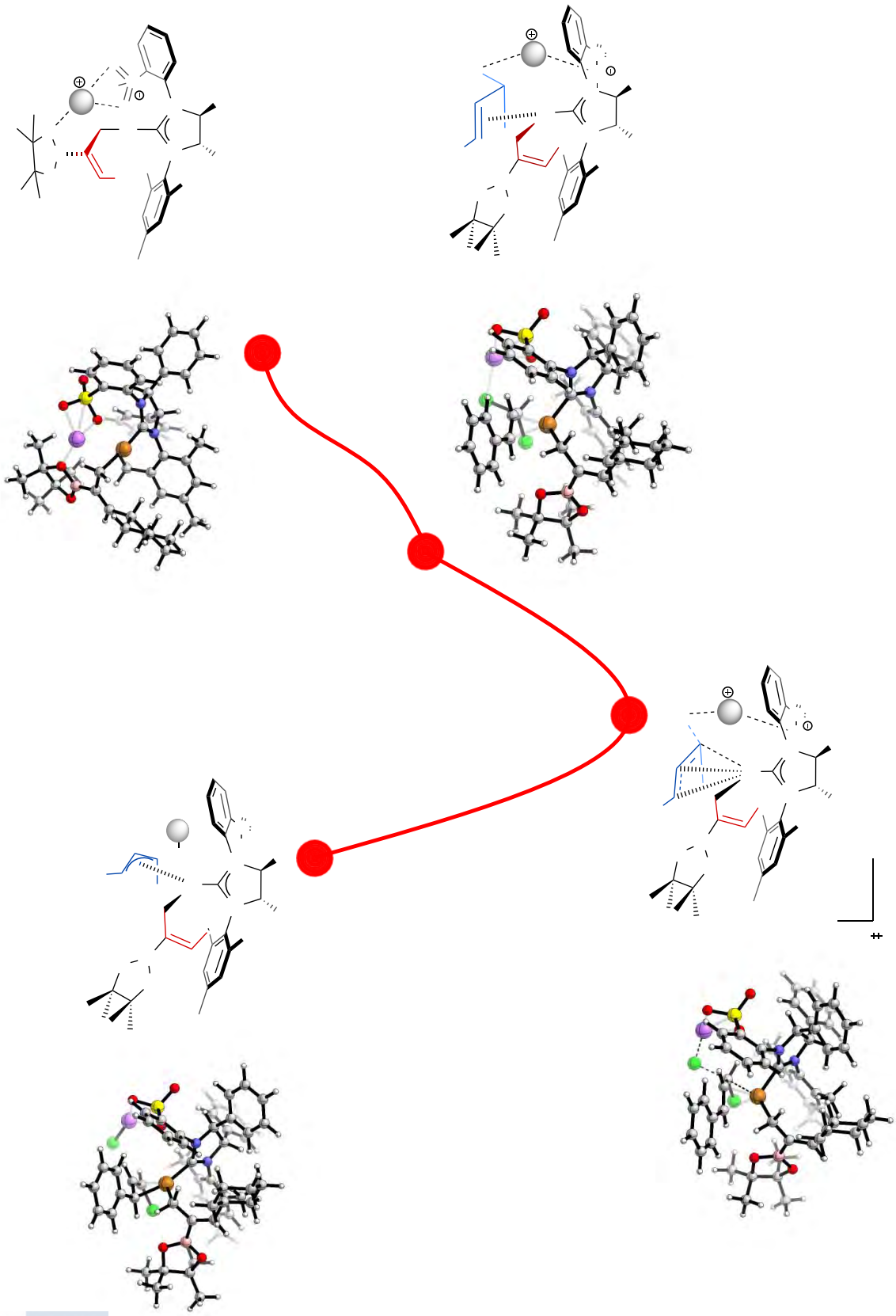

Figure B.II.8. Computed structures related to the oxidative addition step associated with the formation of **(*R*)-5-*Z*,*Z*** from **VIIb-Li** with Li as metal cation (red pathway of Figure 3.1.14).

APPENDIX B.III: STRUCTURES RELATED TO SECTION 3.2

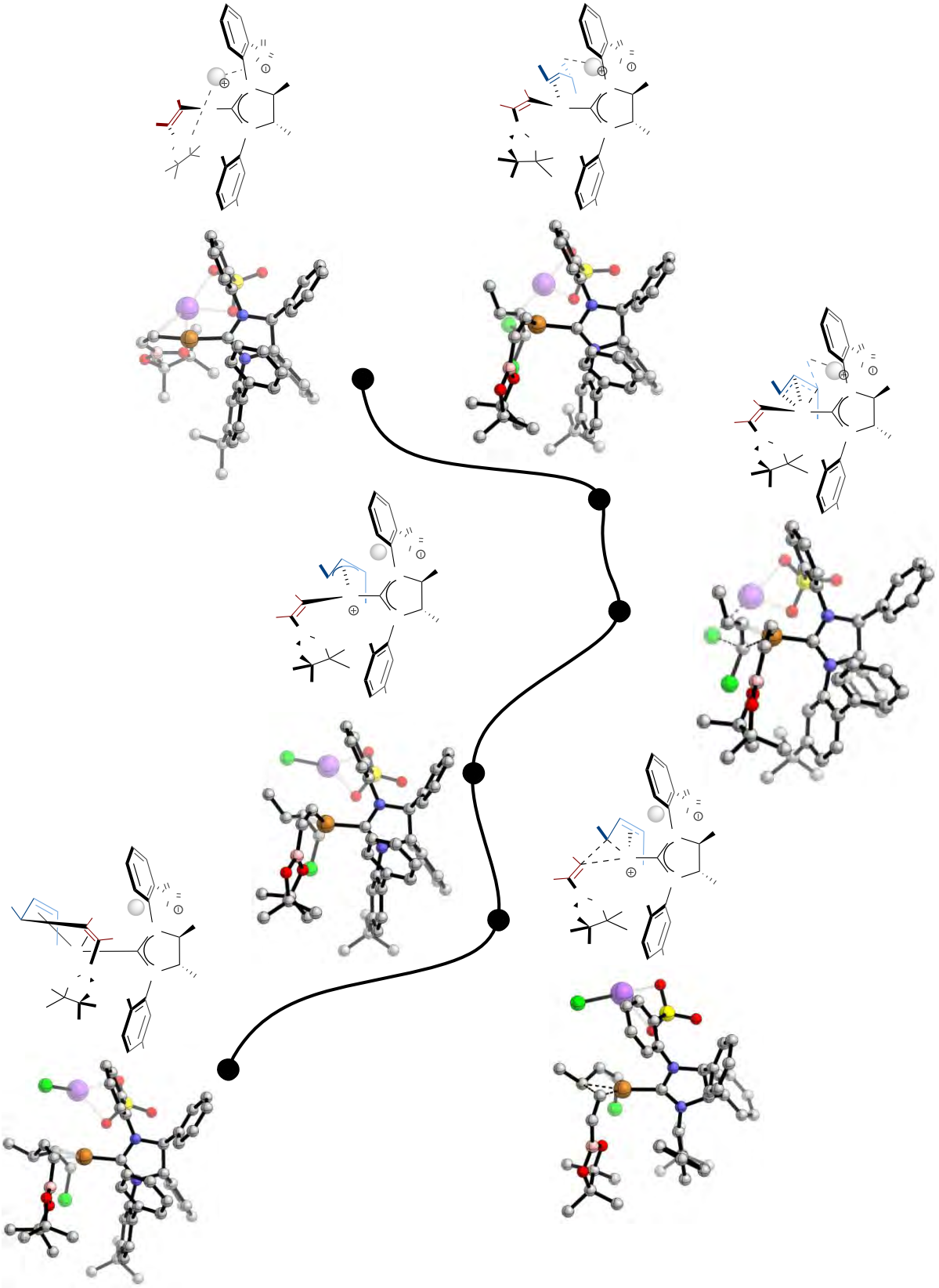

Figure B.III.1. Computed structures related to the oxidative addition and reductive elimination steps associated with the formation of ***(R)*-12-*Z*,*Z*** from **XI** (black pathway of Figure 3.2.2).

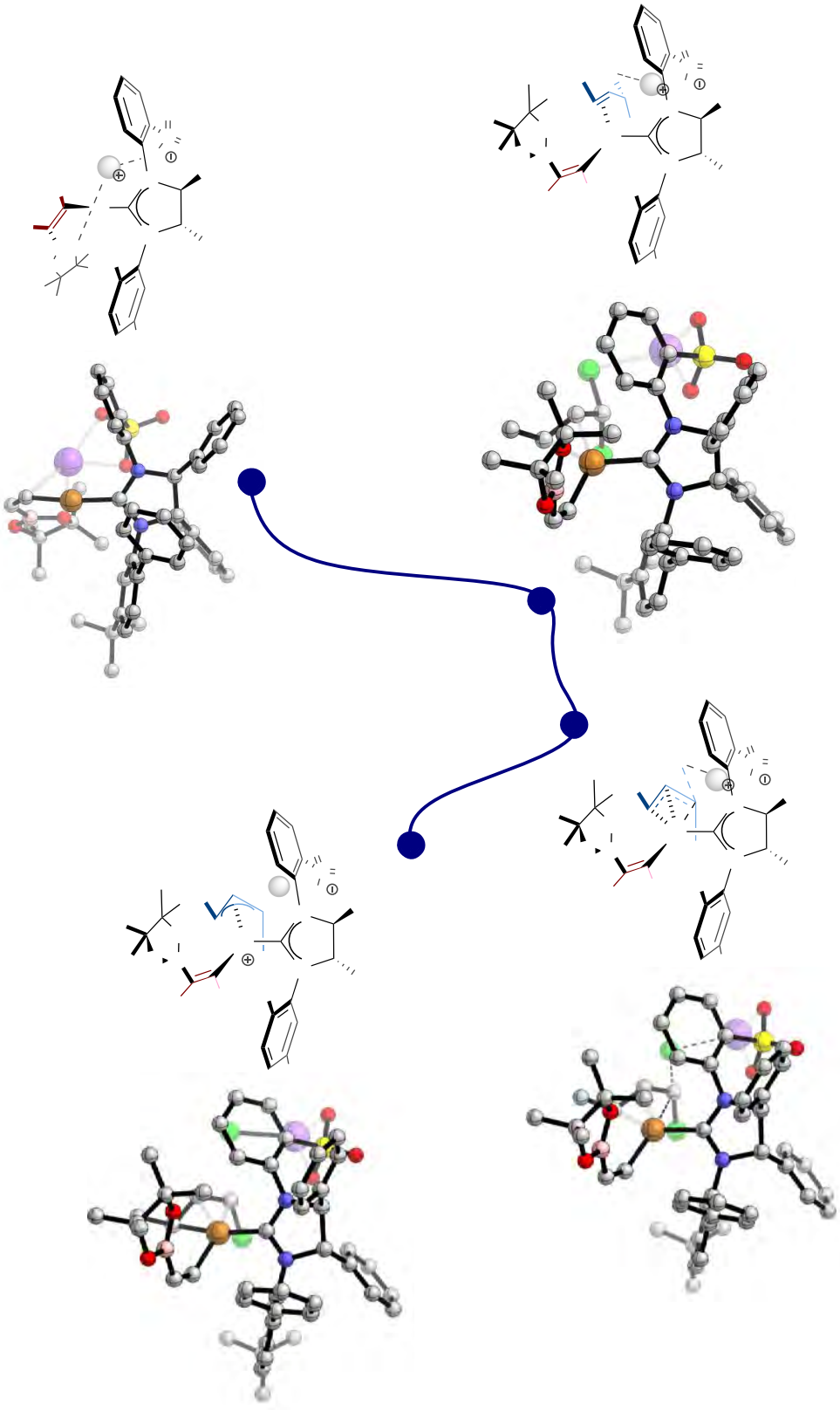

Figure B.III.2. Computed structures related to the oxidative addition step associated with the formation of **(*R*)-12-*Z*,*Z*** from **XI** (blue pathway of Figure 3.2.2).

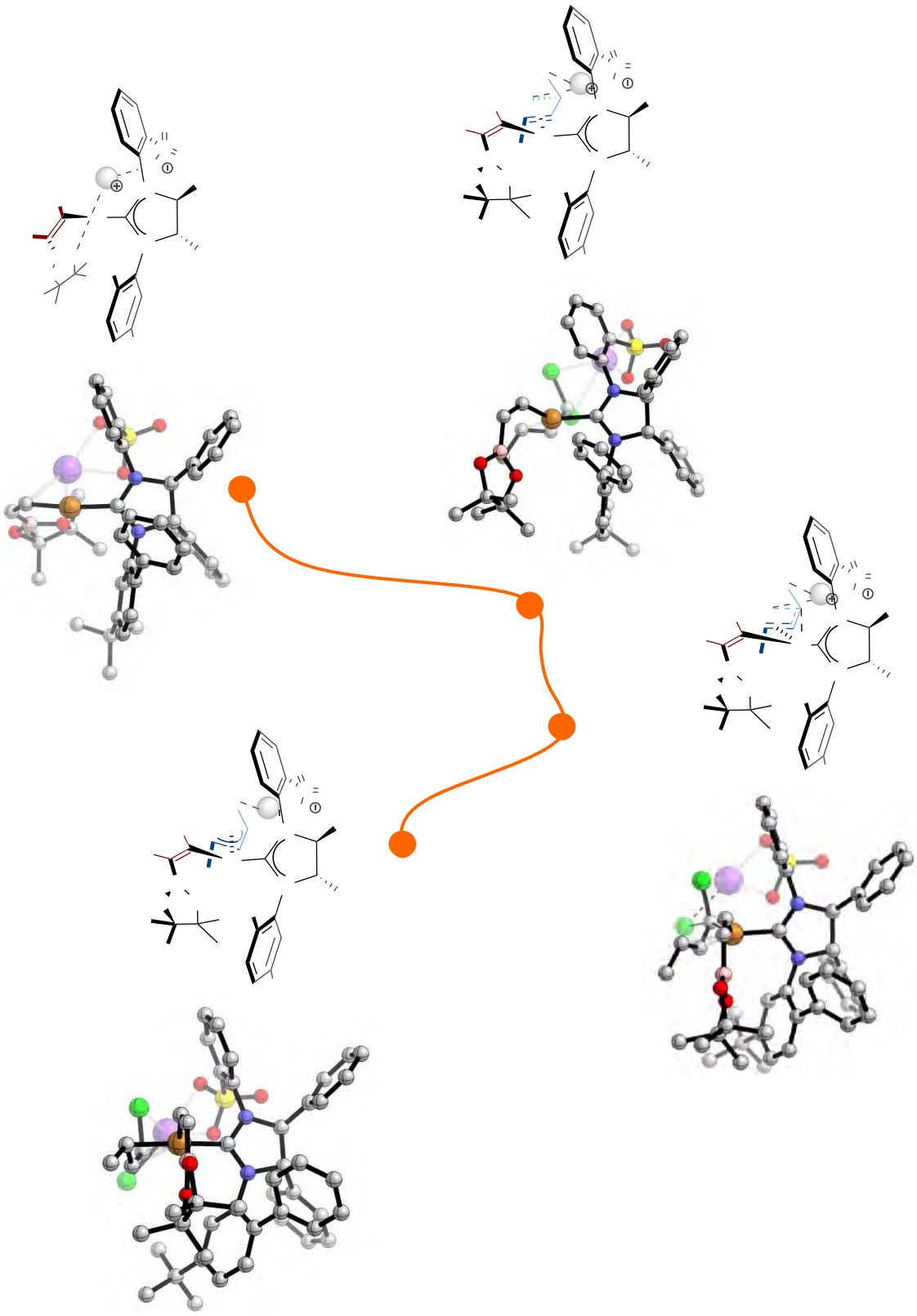

Figure B.III.3. Computed structures related to the oxidative addition step associated with the formation of **(*S*)-12-*Z*,*Z*** from **XI** (orange pathway of Figure 3.2.2).

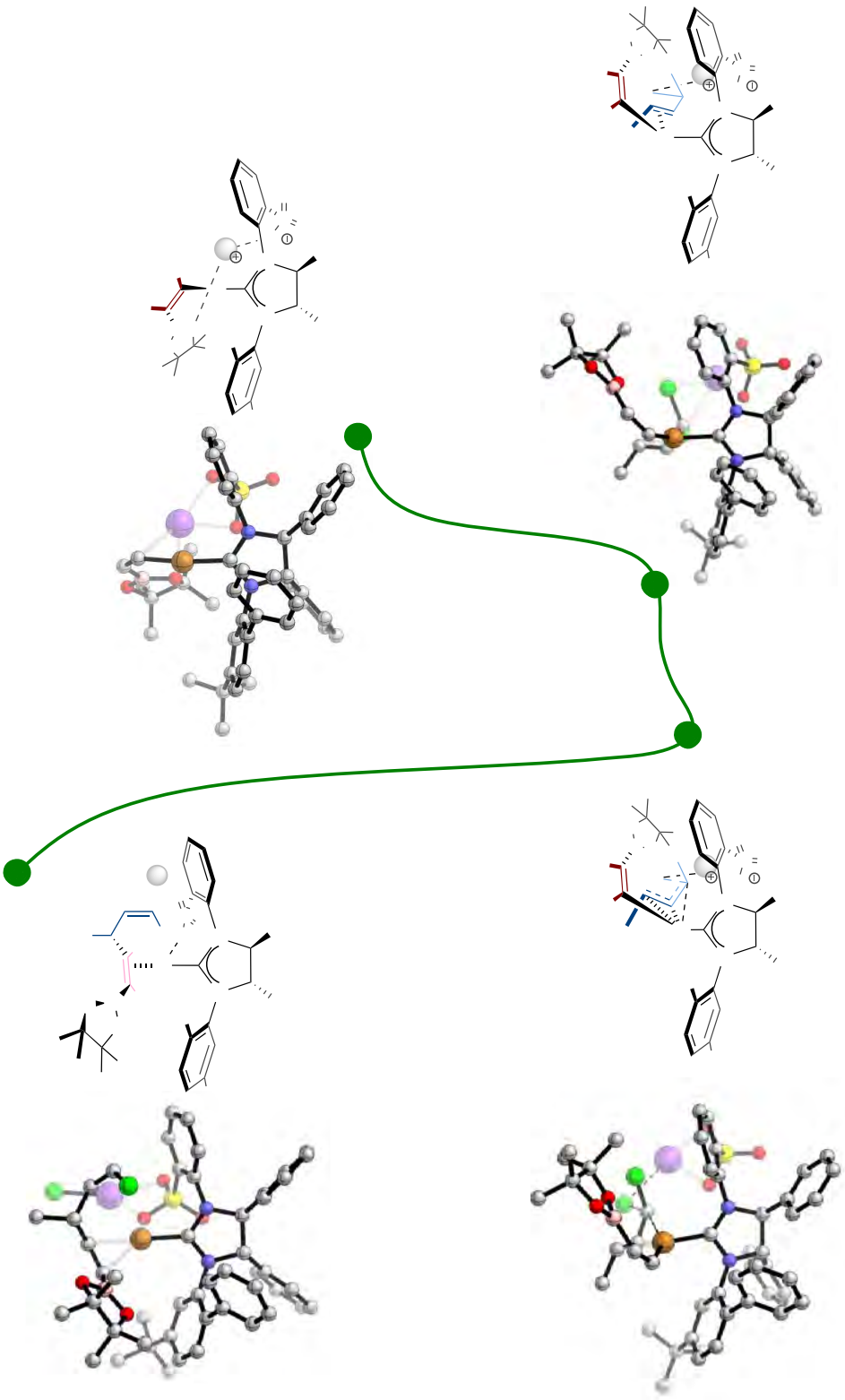

Figure B.III.4. Computed structures related to the oxidative addition step associated with the formation of **(*S*)-12-*Z*,*Z*** from **XI** (green pathway of Figure 3.2.2).

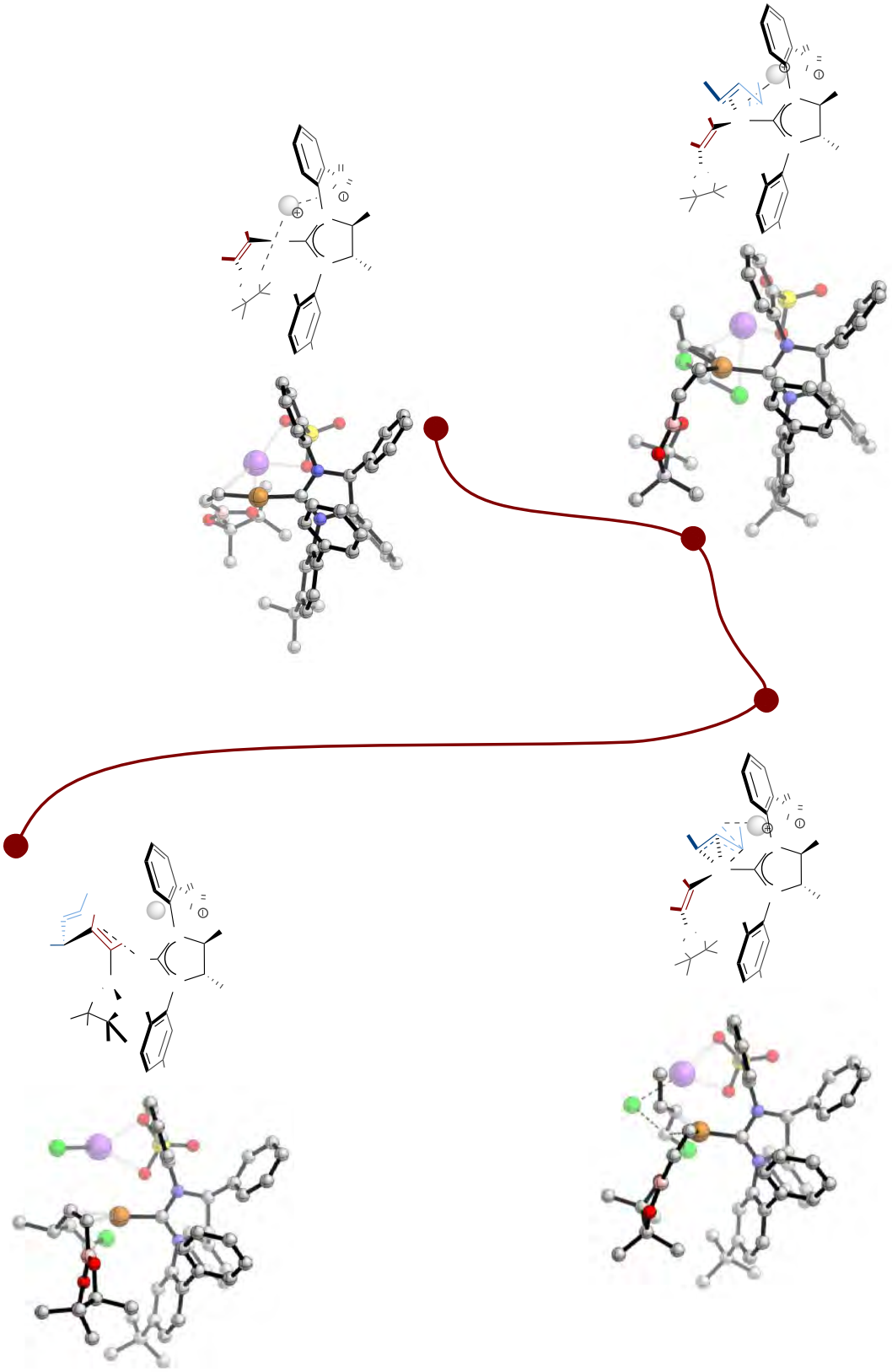

Figure B.III.5. Computed structures related to the oxidative addition step associated with the formation of **(*R*)-12-*E*,*Z*** from **XI** (dark red pathway of Figure 3.2.3).

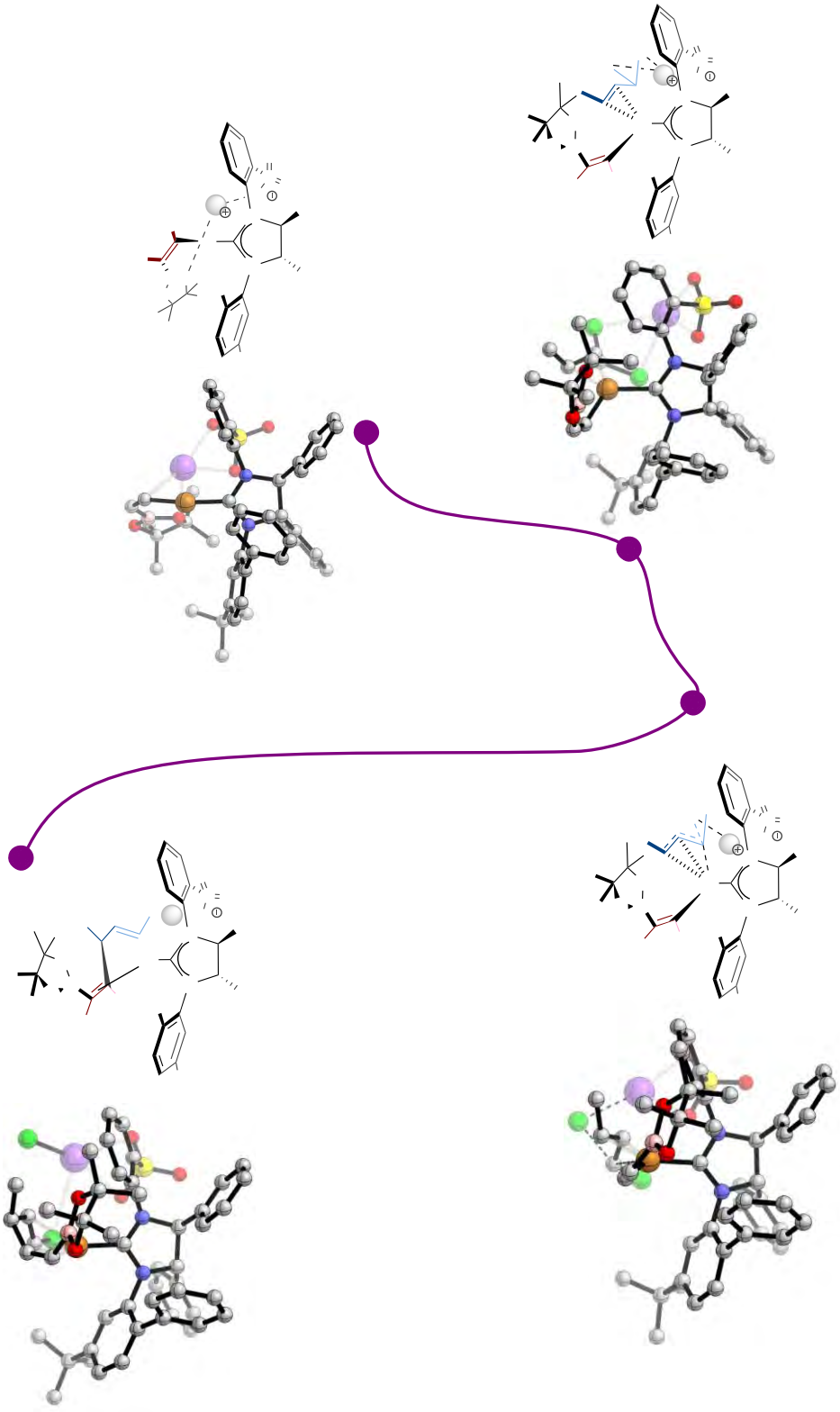

Figure B.III.6. Computed structures related to the oxidative addition step associated with the formation of **(*S*)-12-*E*,*Z*** from **XI** (dark red pathway of Figure 3.2.3).

APPENDIX C – NON-COVALENT INTERACTION PLOTS

APPENDIX C.I: NON-COVALENT INTERACTION PLOTS FOR SECTION 3.1.1

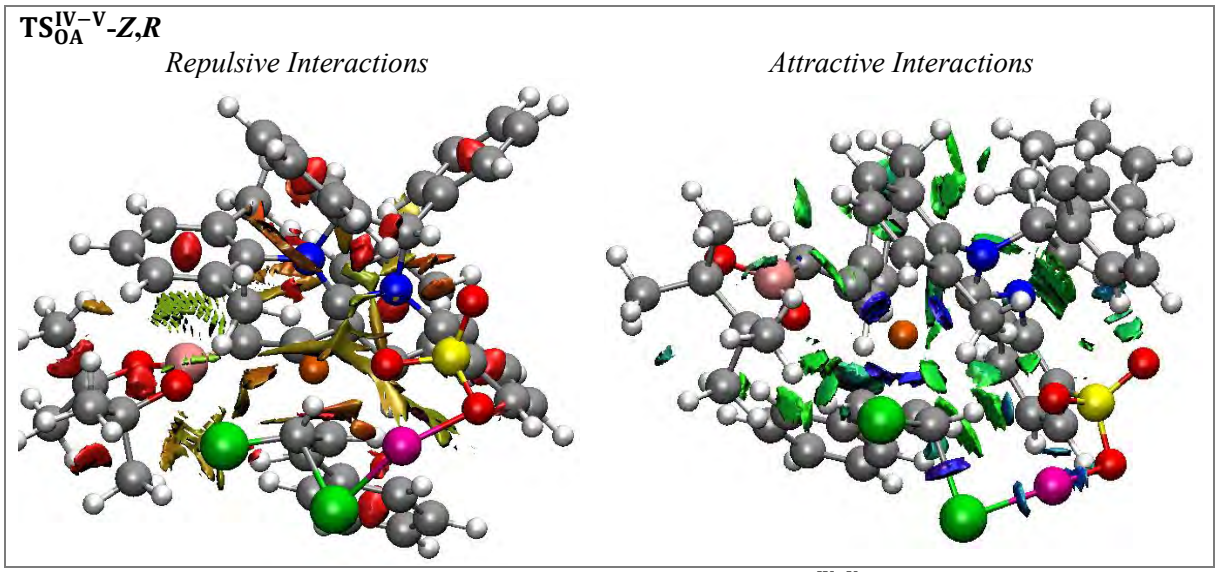

Figure C.I.1. NCI plots showing repulsive and attractive interactions for TS_{OA}^{IV-V}-*Z*,*R*

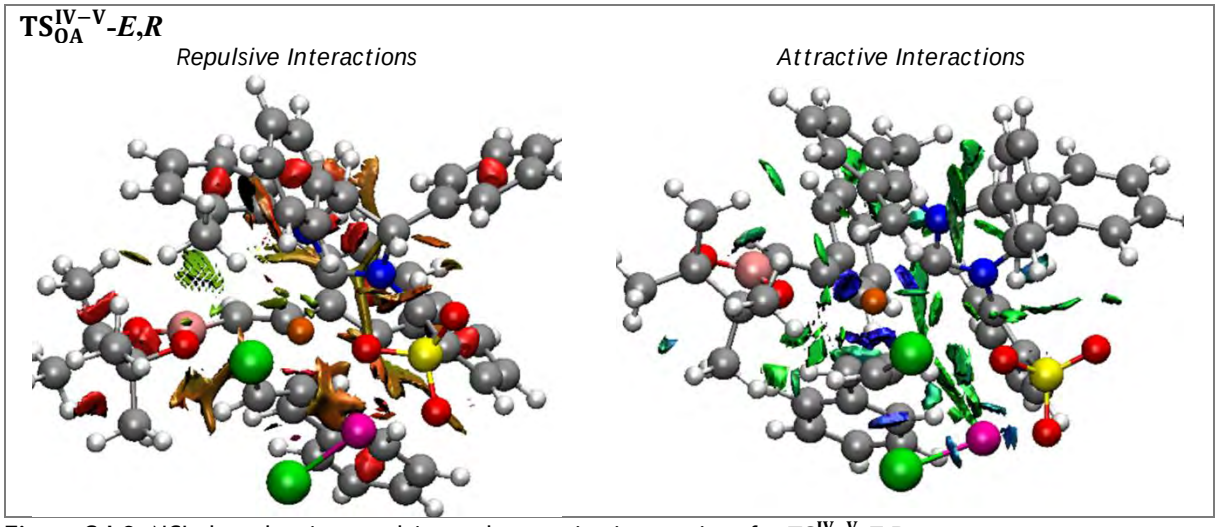

Figure C.I.2. NCI plots showing repulsive and attractive interactions for TS_{OA}^{IV-V}-*E*,*R*

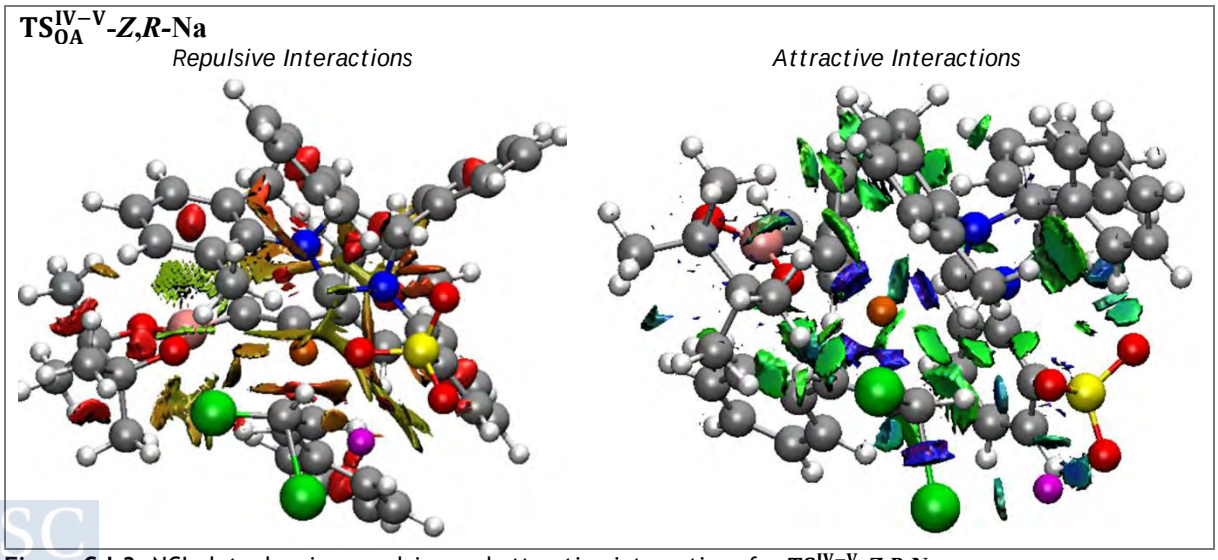

Figure C.I.3. NCI plots showing repulsive and attractive interactions for TS_{OA}^{IV-V}-*Z*,*R*-Na

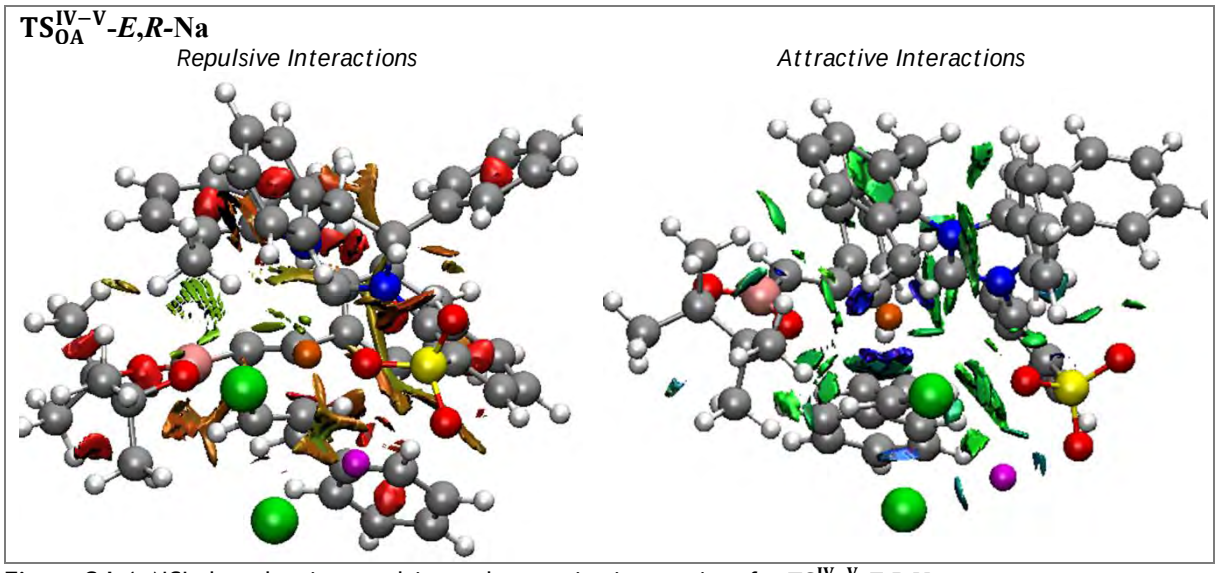

Figure C.I.4. NCI plots showing repulsive and attractive interactions for TS_{OA}^{IV-V}-*E*,*R*-Na

APPENDIX C.II: NON-COVALENT INTERACTION PLOTS FOR SECTION 3.1.2

$TS_{OA}^{VIII-IX}$-*Z*,*S*	$TS_{OA}^{VIII-IX}$-*Z*,*R*
Attractive Interactions	*Attractive Interactions*
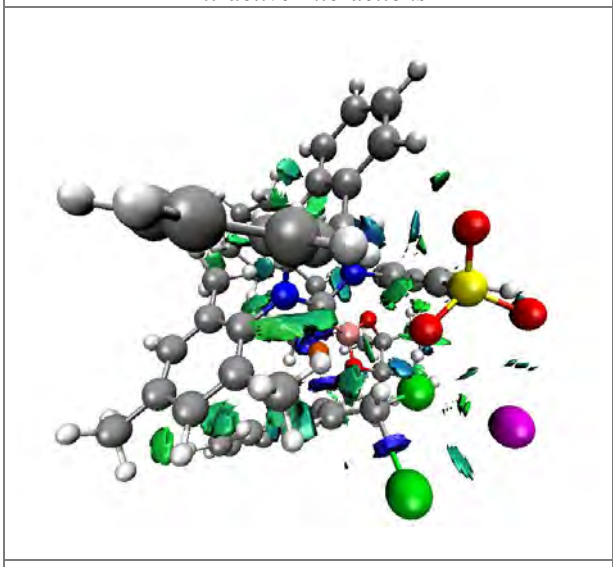	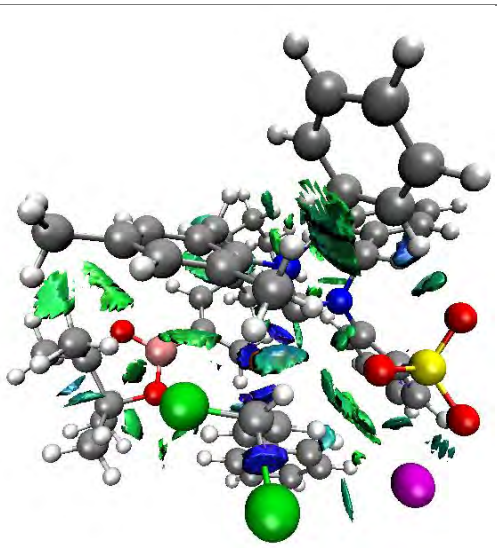
Repulsive Interactions	*Repulsive Interactions*
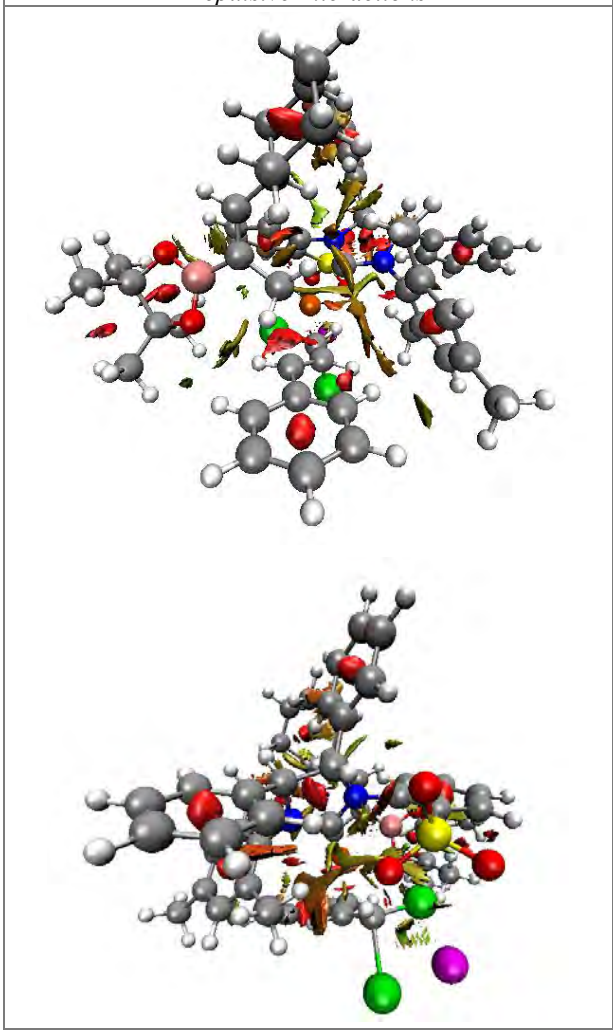	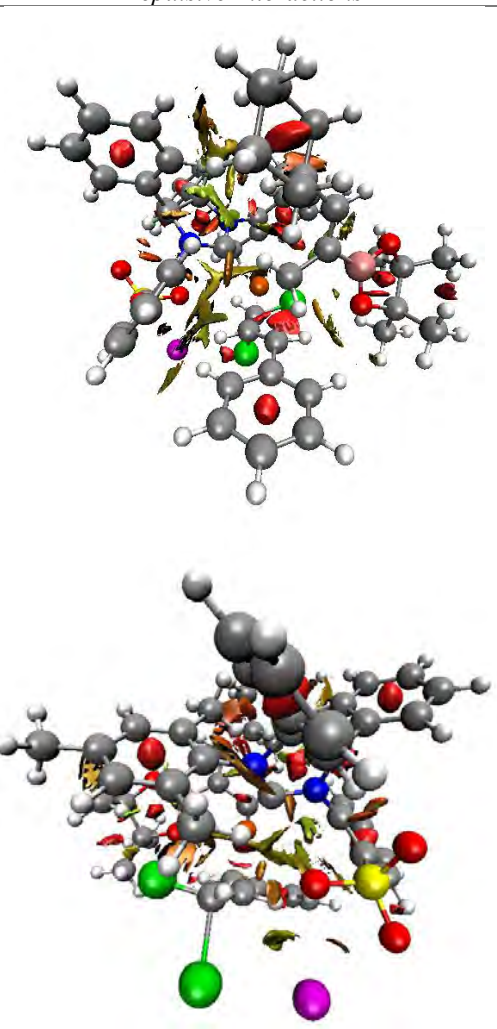

Figure C.II.1. NCI plots comparing attractive and repulsive interactions of $TS_{OA}^{VIII-IX}$-*Z*,*S* and $TS_{OA}^{VIII-IX}$-*Z*,*R*

$TS_{OA}^{XII-XIII}$-*Z*,*S*-Li	$TS_{OA}^{XII-XIII}$-*Z*,*R*-Li
Attractive Interactions	*Attractive Interactions*
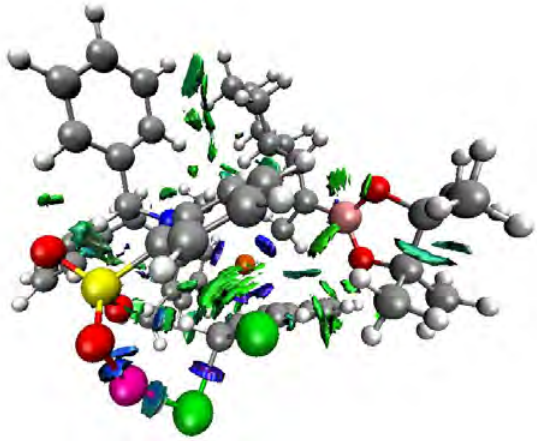	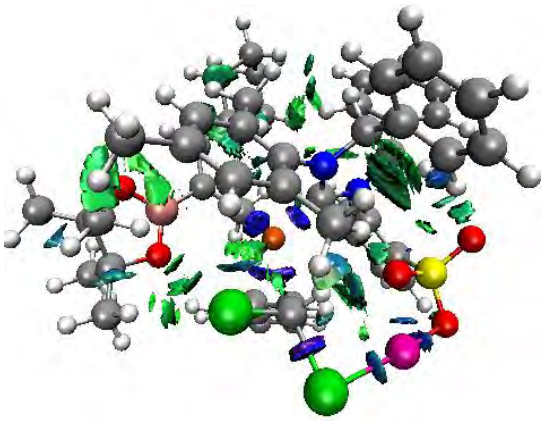
Repulsive Interactions	*Repulsive Interactions*
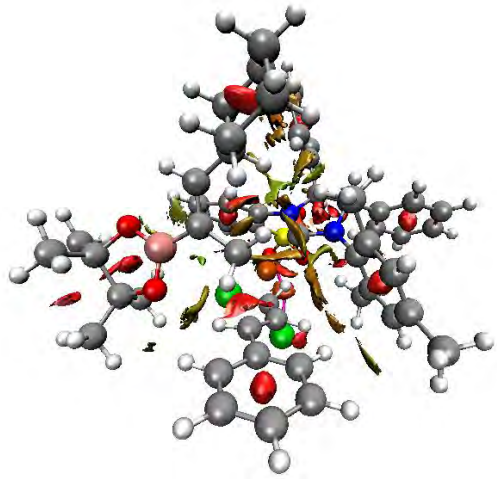 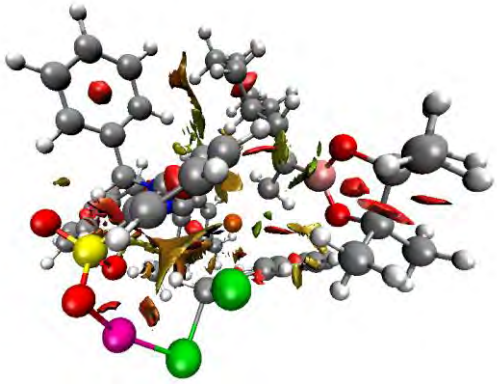	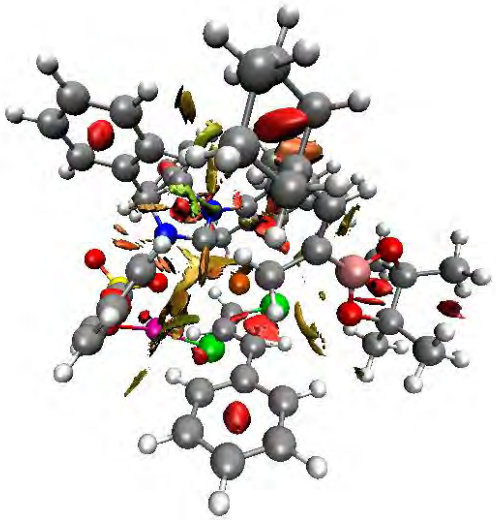 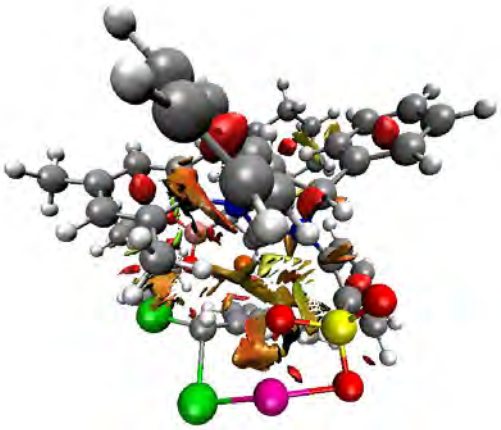

Figure C.II.2. NCI plots comparing attractive and repulsive interactions of $TS_{OA}^{XII-XIII}$-*Z*,*S*-Li and $TS_{OA}^{XII-XIII}$-*Z*,*R*-Li

$TS_{OA}^{XII-XIII}$-*Z*,*S*	$TS_{OA}^{XII-XIII}$-*Z*,*S*-Li
Attractive Interactions	*Attractive Interactions*
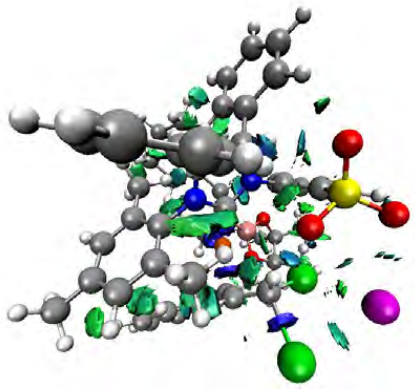	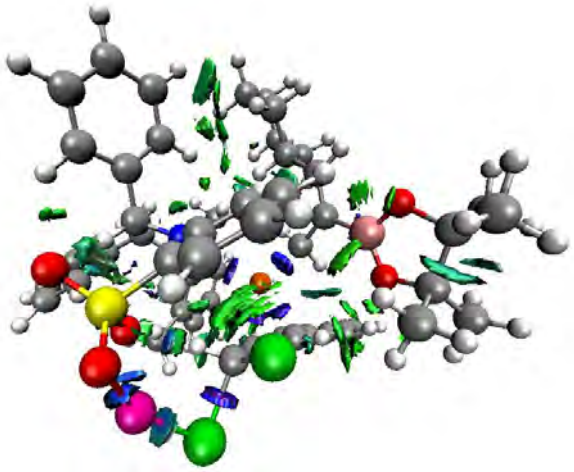
Repulsive Interactions	*Repulsive Interactions*
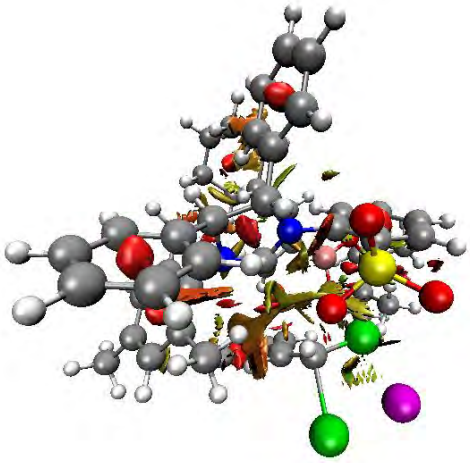	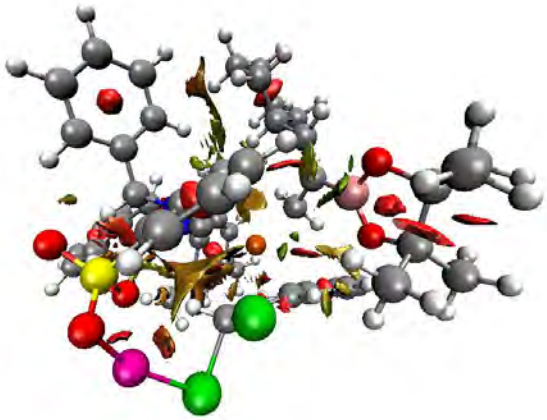

Figure C.II.3. NCI plots comparing attractive and repulsive interactions of $TS_{OA}^{XII-XIII}$-*Z*,*S* and $TS_{OA}^{XII-XIII}$-*Z*,*S*-Li

$TS_{OA}^{XII-XIII}$-*Z*,*S*	$TS_{OA}^{XII-XIII}$-*E*,*S*-Li
Attractive Interactions	*Attractive Interactions*
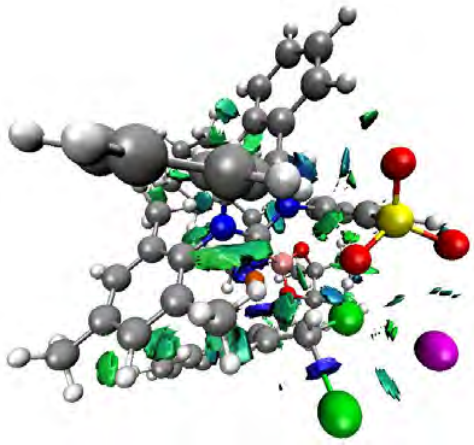	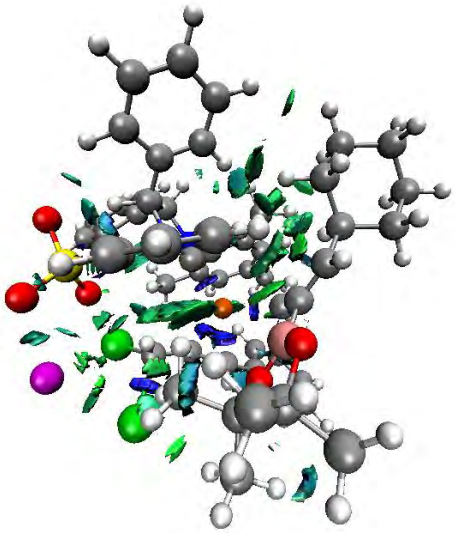
Repulsive Interactions	*Repulsive Interactions*
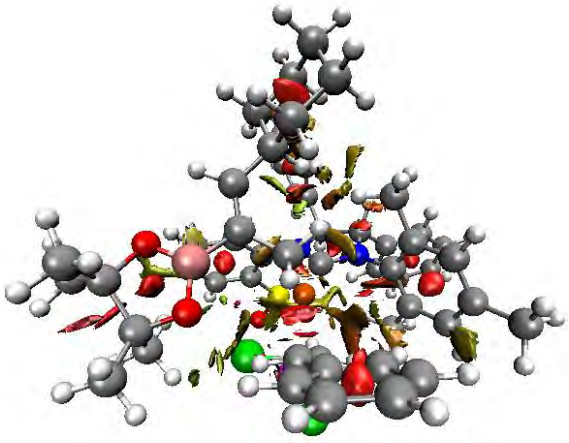	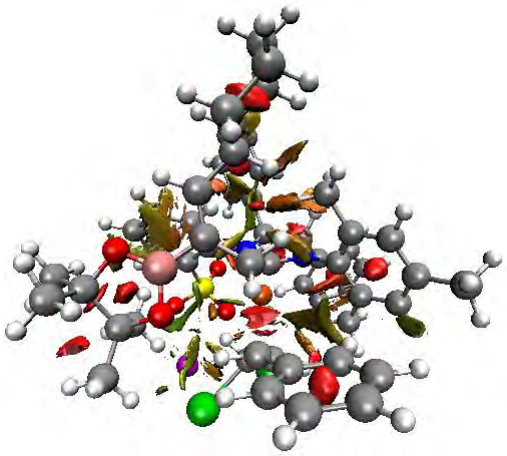

Figure C.II.4. NCI plots comparing attractive and repulsive interactions of $TS_{OA}^{XII-XIII}$-*Z*,*S* and $TS_{OA}^{XII-XIII}$-*E*,*S*-Li

APPENDIX C.III: NON-COVALENT INTERACTION PLOTS FOR SECTION 3.2

$TS_{OA}^{XII-XIII}$-*Z*,*R*	$TS_{OA}^{XII-XIII}$-*Z*,*S*
Attractive Interactions	*Attractive Interactions*
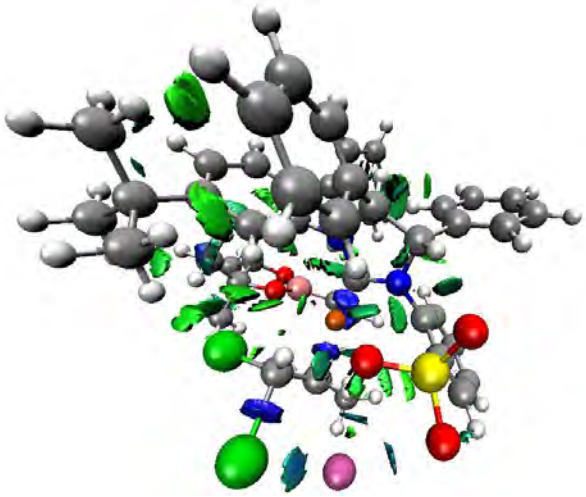	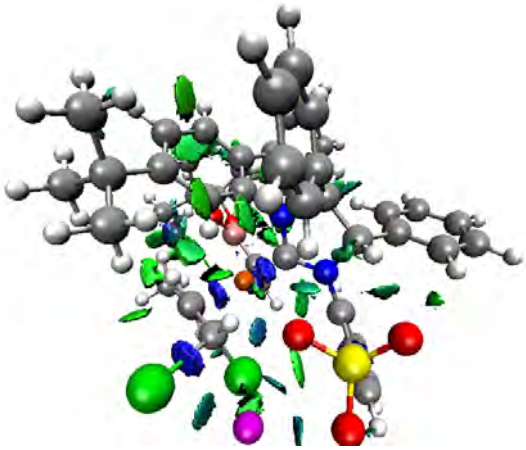
Repulsive Interactions	*Repulsive Interactions*
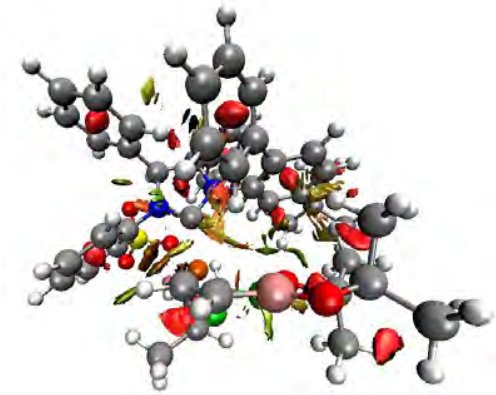	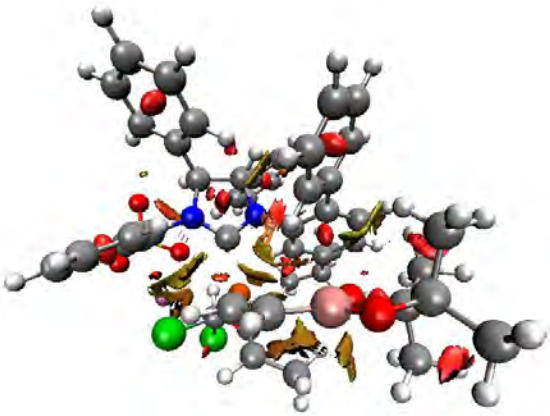
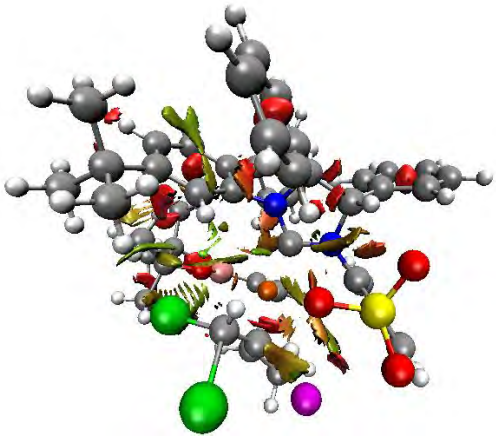	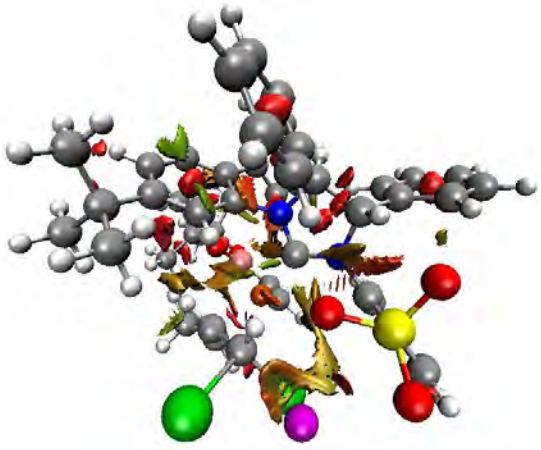

Figure C.III.1. NCI plots comparing attractive and repulsive interactions of $TS_{OA}^{XII-XIII}$-*Z*,*R* and $TS_{OA}^{XII-XIII}$-*Z*,*S*

$TS_{OA}^{XII-XIII}$-*Z*,*R*	$TS_{OA}^{XII-XIII}$-*E*,*R*
Attractive Interactions	*Attractive Interactions*
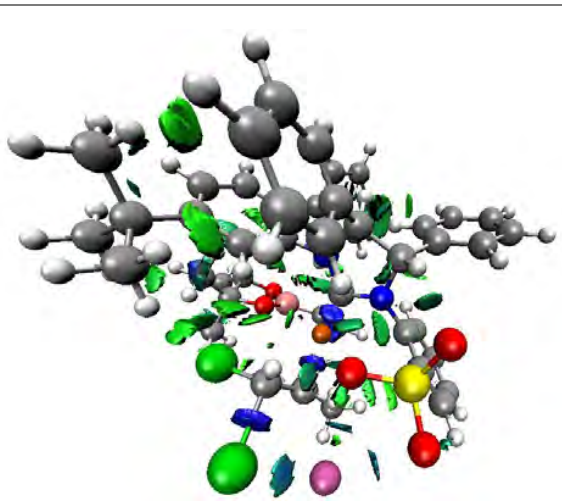	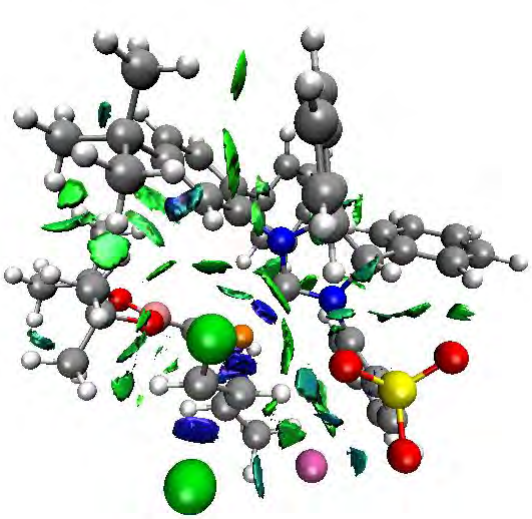
Repulsive Interactions	*Repulsive Interactions*
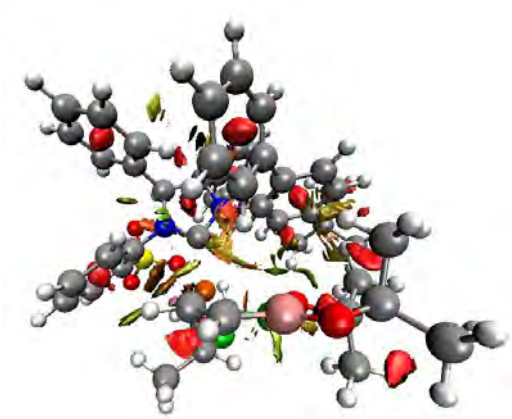	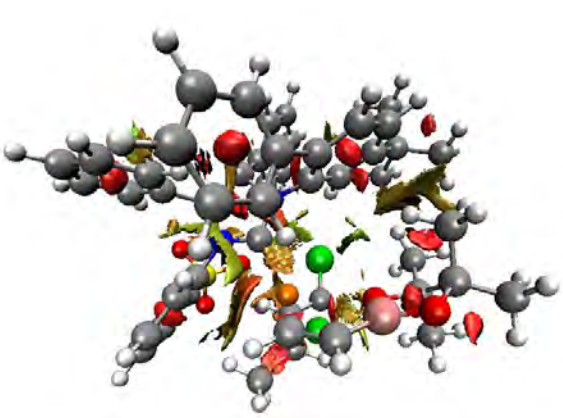
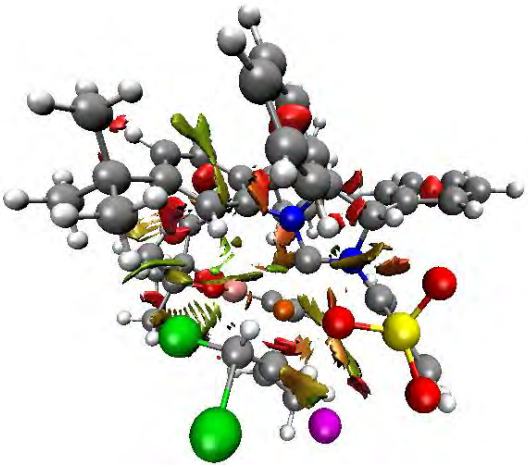	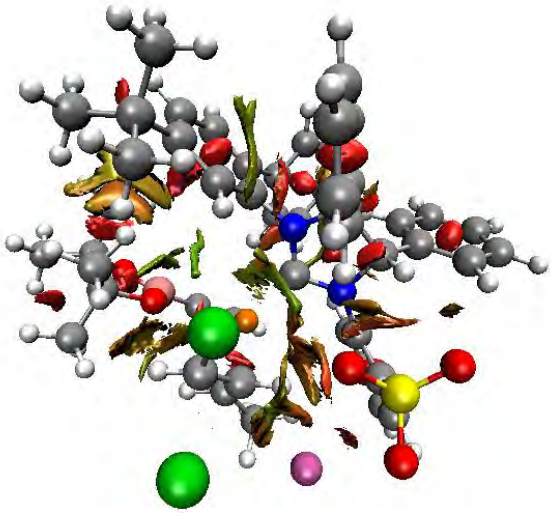

Figure C.III.2. NCI plots comparing attractive and repulsive interactions of $TS_{OA}^{XII-XIII}$-*Z*,*R* and $TS_{OA}^{XII-XIII}$-*E*,*R*

This thesis dissertation presents a compilation of the principal results obtained in the investigation of the design, development and mechanistic analysis of Cu and Fe-catalyzed allylation reactions. The Cu-catalyzed transformations have been focused on multicomponent allylboration reactions, involving a boron source, an unsaturated compound (alkynes, allenes and acetylene) and allylic substrates (allylic *gem*- dichlorides and phosphates). Regarding the Fe-catalyzed transformations, these involved the use of ethane and allylic chlorides. All the developed methodologies were applied in the synthesis of target natural products and versatile intermediates. Moreover, a series of DFT calculations and experimental mechanistic studies have been performed in order to gain insights into the factor controlling the reactions.